

Physicochemical Characterization of Chelation and Transport of Iron by Low Molecular
Weight Chelators

by
James M. Harrington

Department of Chemistry
Duke University

Date: _____

Approved:

Alvin L. Crumbliss, Supervisor

Richard A. Palmer

Michael C. Fitzgerald

Katherine J. Franz

David Needham

Dissertation submitted in partial fulfillment of
the requirements for the degree of Doctor
of Philosophy in the Department of
Chemistry in the Graduate School
of Duke University

2010

ABSTRACT

Physicochemical Characterization of Chelation and Transport of Iron by Low Molecular
Weight Chelators

by
James M. Harrington

Department of Chemistry
Duke University

Date: _____

Approved:

Alvin L. Crumbliss, Supervisor

Richard A. Palmer

Michael C. Fitzgerald

Katherine J. Franz

David Needham

An abstract of a dissertation submitted in partial
fulfillment of the requirements for the degree
of Doctor of Philosophy in the Department of
Chemistry in the Graduate School
of Duke University

2010

Copyrighted by
James Michael Harrington
2010

Abstract

The research presented here aims to expand our understanding of the structural factors that contribute to selectivity for iron and to iron complex stability in siderophores, as well as iron transport processes in siderophore systems. This work also investigates the factors that contribute to therapeutic applications of chelating agents, both for chelation therapy and for antimicrobial agents.

The thermodynamics of iron(III) binding of a number of molecules, both natural and synthetic, are determined using pH-dependent spectrophotometric titrations and potentiometric titrations. Three of the synthetic siderophore analogs studied here are a tris-hydroxypyridinone ($N^3(\text{etLH})_3$, $\log \beta_{110} = 27.34$ and $\text{pFe} = 23.49$) and two bis-hydroxypyridinone ligands ($N^2(\text{prLH})_2$, $\log \beta_{230} = 27.34$ and $\text{pFe} = 22.07$; $N^2(\text{etLH})_2$, $\log \beta_{230} = 21.08$). A determination of the solution thermodynamics of the iron(III) complex of a water-soluble analog of Brasilibactin A, a membrane-bound mycobactin-type bacterial siderophore is also presented and related to the role of mycobactins in iron uptake of mycobacteria. The analog Bbtan forms a stable complex with iron ($\log \beta_{110} = 26.96$, $\text{pFe} = 22.73$) and exhibits a relatively positive redox potential for the iron-Bbtan complex ($E_{1/2} = -300$ mV vs NHE). The thermodynamics of chelation of iron(III) by a synthetic Trojan Horse antimicrobial agent featuring a 3-hydroxy-4-pyridinone moiety, L^{PF} were also determined. The binding by L^{PF} occurs exclusively through the 3-hydroxy-4-pyridinone donor group and allows the formation of a 3:1 $L^{\text{PF}}:\text{Fe}^{3+}$ complex with $\log \beta_{130} = 31.91$. In these studies, the thermodynamic stability constants of the iron-chelator complexes are

determined through a series of spectrophotometric and potentiometric titrations. Also, the redox chemistry of the iron-chelator complexes is investigated using cyclic voltammetry. The structural features that contribute to complex stability in a series of tripodal tris-hydroxamate siderophores using computational techniques is presented, and it is shown that the position of the arm of an exocyclic siderophore system can contribute to differences in complex stability, as can the orientation of the donor group.

Kinetic studies of the iron(III) exchange reactions of the polydentate chelators desferrioxamine B, $N^3(\text{etLH})_3$, and $N^2(\text{prLH})_2$ are presented. The study of the kinetics of some reactions of iron complexes featuring hydroxypyridinone donor-group chelators is performed by spectrophotometric kinetics experiments. The mechanism of exchange between desferrioxamine B and an iron(III)-trishydroxypyridinone complex is determined through spectrophotometric monitoring of the reaction. The mechanism for this reaction is found to occur by a parallel pathway mechanism, where one pathway involves initial formation of a host-guest supramolecular assembly, followed by ternary complex formation and exchange of iron to ferrioxamine B (second order rate constant $k_{5\text{app}} = 1.7 \times 10^{-1} \text{ M}^{-1}\text{s}^{-1}$), and the other pathway involves direct reaction of the iron- $N^3(\text{etLH})_3$ with desferrioxamine B, likely through a ternary complex intermediate ($k_7 = 2.1 \times 10^{-2} \text{ M}^{-1}\text{s}^{-1}$). Also, a determination of the mechanism of proton-driven complex dissociation of a bishydroxypyridinone siderophore mimic is shown. The first step involves proton-driven dissociation of the Fe_2L_3 complex by a parallel pathway mechanism, where one pathway is proton-dependent ($k_{39} = 570 \text{ M}^{-1}\text{s}^{-1}$) and the other

pathway is proton-independent ($k_{38} = 4.8 \text{ s}^{-1}$). The second step of the reaction involves the proton-independent dissociation of the $\text{Fe}\{\text{N}^2(\text{prL})_2\}$ complex to form the monoprotonated $\text{Fe}\{\text{N}^2(\text{etL})(\text{etLH})\}$ complex ($k_{40} = 1.0 \times 10^{-2} \text{ s}^{-1}$). The ability of a bidentate hydroxypyridinone chelator to catalyze the exchange of iron(III) from desferrioxamine B to EDTA is explored and the mechanism is determined. It is shown that the mechanism of catalysis likely occurs through the formation of an inner sphere ternary complex between ferrioxamine B and the bidentate chelator.

Finally, an investigation into the efficacy of chelation therapy treatments to protect from metal toxicity using the nematode *C. elegans* as a model organism is presented. It is shown that a high degree of metal formation is necessary, but not sufficient, to predict efficiency of chelator as having a protective effect from metal toxicity. EDTA is shown to be an effective chelating agent due to its ability to protect consistently from all four metals tested. The model developed therein can also be used as a model for soil remediation of toxic metals using chelating agents.

Contents

Abstract.....	iv
List of Tables.....	xv
List of Schemes.....	xvii
List of Figures.....	xix
List of Abbreviations.....	xxxiv
Acknowledgements.....	xxxvi
1. Introduction.....	1
1.1. Iron bioavailability.....	2
1.2. Iron geochemistry.....	3
1.3. Siderophore features and architecture.....	4
1.3.1. Common siderophore architectures.....	5
1.3.2. Common siderophore binding moieties.....	17
1.4. Siderophore complex thermodynamics.....	21
1.4.1. Alternative expressions of thermodynamic stability.....	25
1.5. Iron redox chemistry.....	27
1.6. Mechanisms of iron release from siderophore complexes.....	41
1.6.1. The Reductive Hypothesis: A molecular switch.....	41
1.7. Iron in human health.....	42
1.7.1. Iron chelation therapy.....	43
1.8. Statement of problem and research objectives.....	46
2. Iron sequestration equilibria for some new tetradentate and hexadentate 3-hydroxy-2-	

pyridinone donor group siderophore mimics.....	49
2.1. Introduction.....	49
2.2. Statement of chapter objectives.....	52
2.3. Experimental.....	54
2.3.1. Materials.....	54
2.3.2. Potentiometric measurements.....	55
2.3.3. Spectrophotometric titrations.....	56
2.3.4. EDTA competition titrations.....	57
2.3.5. ESI-MS measurements of bishydroxypyridinone complexes...65	
2.3.6. Iron-trishydroxypyridinone complex redox chemistry.....	65
2.4. Results and discussion.....	66
2.4.1. HOPO ligand protonation constants.....	66
2.4.2. Fe(III)-HOPO complex stability and protonation constants: General Observations.....	70
2.4.3. Fe(III)-HOPO complex stability and protonation constants: Bishydroxypyridinone complexes $N^2(\text{prLH})_2$ and $N^2(\text{etLH})_2$	72
2.4.4. Fe(III)-HOPO complex stability and protonation constants: Trishydroxypyridinone ligand $N^3(\text{etLH})_3$	81
2.4.5. Iron-trishydroxypyridinone complex redox chemistry.....	85
2.4.6. Comparison of bis- and tris-HOPO ligands.....	88
2.5. Conclusions.....	92

3.Characterization of the mechanism of exchange of iron(III) bound by hydroxypyridinone siderophore mimics.....	93
3.1. Introduction.....	93
3.2. Statement of chapter objectives.....	95
3.3. Experimental.....	96
3.3.1. Materials.....	96
3.3.2. Exchange of iron(III) between desferrioxamine B and $N^3(\text{etLH})_3$	97
3.3.3. ESI-MS of the interactions between desferrioxamine B and $N^3(\text{etLH})_3$	98
3.3.4. Proton-driven dissociation of the iron(III)- $N^2(\text{prLH})_2$ complex	99
3.4. Results and discussion.....	101
3.4.1. Desferrioxamine B- $N^3(\text{etLH})_3$ iron(III) exchange reaction.....	101
3.4.2. Proton-driven dissociation of the Fe- $N^2(\text{prLH})_2$ complex.....	124
3.4.3. Overall mechanism of proton-driven dissociation of the Fe- $N^2(\text{prLH})_2$ Complex.....	138
3.5. Conclusions.....	138
4.Catalysis of iron(III) exchange between hexadentate chelators by a bidentate Hydroxypyridinone.....	141
4.1. Introduction.....	141
4.2. Statement of chapter objectives.....	143

4.3. Experimental.....	143
4.3.1. Materials.....	143
4.3.2. Iron(III) exchange from desferrioxamine B to EDTA in the presence of DMHP.....	145
4.3.3. Iron(III) exchange from ferrioxamine B to DMHP.....	146
4.3.4. Iron(III) exchange from DMHP to EDTA.....	147
4.4. Results.....	147
4.4.1. Iron(III) exchange from ferrioxamine B to EDTA: General observations.....	147
4.4.2. Kinetics of iron(III) exchange from ferrioxamine B to EDTA in the absence of DMHP (Eq. 1).....	149
4.4.3. Kinetics of iron(III) exchange from ferrioxamine B to EDTA in the presence of DMHP (Eq. 2).....	153
4.4.4. Kinetics of iron(III) exchange from ferrioxamine B to DMHP (Eq. 4.3).....	160
4.4.5. Kinetics of iron(III) exchange from DMHP to EDTA (Eq. 4.4)...	165
4.4.6. Summary of kinetics results.....	189
4.5. Discussion.....	193
4.5.1. Kinetics and mechanism of the iron(III) exchange reaction from ferrioxamine B to EDTA in the presence of DMHP.....	193
4.5.2. Reaction of ferrioxamine B with DMHP.....	197
4.5.3. Reaction of Fe(DMHP) ₃ with EDTA.....	203

4.6. Conclusions.....	209
5.Characterization of iron(III) sequestration by an analog of the cytotoxic siderophore Brasilibactin A.....	210
5.1. Introduction.....	210
5.2. Statement of chapter objectives.....	214
5.3. Experimental.....	214
5.3.1. Materials.....	214
5.3.2. Protonation constant determination.....	215
5.3.3. Protonation stability assay.....	217
5.3.4. Iron(III) complex thermodynamic characterization.....	217
5.3.5. Electrochemistry of Bbtan.....	220
5.3.6. Potentiometric titration of Zn(II) and Ni(II).....	220
5.4. Results.....	221
5.4.1. Determination of protonation constants.....	221
5.4.2. Structural and thermodynamic characterization of the iron(III)- Bbtan complex.....	227
5.4.3. Fe-Bbtan complex redox chemistry.....	230
5.4.4. Ni(II) and Zn system titrations.....	234
5.5. Discussion.....	234
5.5.1. Equilibrium constant determination strategies.....	234
5.5.2. Protonation constants.....	237
5.5.3. Thermodynamic characterization of the iron-Bbtan system....	240

5.5.4. Complex redox chemistry.....	247
5.5.5. Implications for iron uptake in mycobacteria.....	247
5.6. Conclusions.....	254
6.Characterization of the iron binding ability of the Trojan Horse antimicrobial agent, PF-02538084.....	255
6.1. Introduction.....	255
6.2. Statement of chapter objectives.....	259
6.3. Experimental.....	259
6.3.1. Materials.....	259
6.3.2. Protonation constant determination.....	260
6.3.3. Solution equilibria.....	261
6.3.4. Electrochemical studies of the Fe-L ^{PF} system.....	263
6.4. Results and discussion.....	264
6.4.1. Ligand protonation constants.....	264
6.4.2. Iron complex equilibria: Complex structure.....	268
6.4.3. Iron complex equilibria: Determination of stepwise formation constants.....	279
6.4.4. Electrochemical characterization.....	285
6.5. Conclusions.....	290
7.Computational comparison of strain energies in synthetic saccharide-backbone siderophore mimics.....	292
7.1. Introduction.....	292

7.2. Statement of chapter objectives.....	295
7.3. Experimental.....	296
7.4. Results.....	299
7.5. Discussion.....	303
7.5.1. Ligand design related to complex strain.....	305
7.5.2. Ligand design related to complex stereochemistry.....	307
7.5.3. Complex protonation scheme.....	308
7.6. Conclusions.....	310
8. Heavy metal toxicity and the protective effects of chelating agents on <i>Caenorhabditis elegans</i> growth.....	313
8.1. Introduction.....	313
8.2. Statement of chapter objectives.....	317
8.3. Experimental.....	318
8.3.1. Nematode culture.....	318
8.3.2. Materials.....	318
8.3.3. Growth assay.....	319
8.4. Results.....	322
8.4.1. Chelator and metal toxicity assays.....	322
8.4.2. Metal chelation protection assays.....	323
8.5. Discussion.....	327
8.5.1. Chelator and metal toxicity assays.....	328
8.5.2. Metal chelation protection assays.....	330

8.5.3. Alternative applications.....	340
8.6. Conclusions.....	340
Appendix A. Calculation of pFe values.....	342
Appendix B. Synthesis of 3-hydroxy-2-pyridinone siderophore mimics.....	354
Appendix C. Synthesis of an analog of the cytotoxic siderophore Brasilibactin A...	359
Appendix D. Synthesis and purity analysis of 2-(((1E)-1-(2-amino-1,3-thiazol-4-yl)-2- (((3S)-1-((4-methyl-3-(5-hydroxy-4-oxo-1,4-dihydropyridin-2-yl)-5-oxo-4,5-dihydro-1H- 1,2,4-triazol-1-yl)sulfonyl)carbamoyl)-2-oxoazetidin-3-yl]amino)-2- oxoethylidene]amino)oxy)-2-methylpropanoic acid (PF-02538084).....	364
Appendix E. Statistical analysis and speciation diagrams for the metal-ligand systems of toxicity studies with <i>C. elegans</i>	371
References.....	388
Biography of the Author.....	399

List of Tables

Table 2.1. Complete proton dissociation equilibria for HOPO ligands and their iron(III) complexes.....	58
Table 2.2. Wavelengths of maximum absorbance for Fe-HOPO complexes in aqueous solution. The wavelengths recorded for the complexes studied here correspond well to those of a similar iron-tris-HOPO complex, supporting the identity of the complexes. Approximate molar absorptivity values (in $\text{dm}^3 \text{mol}^{-1} \text{cm}^{-1}$) from an average of four measurements are shown below the wavelength in parentheses.....	72
Table 2.3. Calculated pFe values for a number of siderophores.....	90
Table 4.1. Rate constants observed in the reactions studied for the Fe-HDFB-DMHP-EDTA systems. Conditions: $T = 25 \text{ }^\circ\text{C}$, $\mu = 0.10 \text{ M (NaClO}_4\text{)}$, $\text{pH} = 4.35$	159
Table 4.2. Relative second order rate constants for the catalyzed iron(III) exchange reactions, $k_{\text{obs, cat}}/k_{\text{obs}}$ with 4 bidentate ligands, acetohydroxamic acid, N-methylacetohydroxamic acid, benzylhydroxamic acid, and 1,2-dimethyl-3-hydroxy-4-pyridinone.....	209
Table 5.1. Measured equilibrium constants for the Fe(III)-Bbtan system. All constants were measured at $T = 25 \text{ }^\circ\text{C}$ and $\mu = 0.10 \text{ M (NaClO}_4\text{)}$. Water molecules omitted for clarity.....	219
Table 5.2. Calculated $\log \beta_{110}$, pFe values, and redox potentials for a series of natural siderophores.....	245
Table 6.1. Equilibrium constants determined for the proton-dependent and proton-independent reactions of L^{PF} with Fe(III). Numbers shown in parentheses are the standard deviation of the value as determined from the program, HYPERQUAD. All experiments were performed at $T = 25 \text{ }^\circ\text{C}$ and $\mu = 0.10 \text{ M (NaClO}_4\text{)}$	266
Table 6.2. Observed wavelengths of maximum absorbance for the iron(III)- L^{PF} complex system and molar absorptivities of the complexes, calculated by the program HYPERQUAD. Literature values for the FeL through FeL ₃ complexes of the iron(III)-DMHP system are shown for comparison. L represents the respective hydroxypyridinone-donor chelators, L^{PF} or DMHP.....	273
Table 7.1. Strain energy calculations for iron(III) complexes of desferrioxamine B, desferrioxamine D, desferrioxamine E, $\text{H}_3\text{L}_\text{N}^{236}$, $\text{H}_3\text{L}_\text{R}^{234}$, $\text{H}_3\text{L}_\text{R}^{236}$, and $\text{H}_3\text{L}_\text{N}^{234}$	297

Table 7.2. Average Fe-O-C bond angles of hydroxamate iron(III) complex crystal structures in the Cambridge Data Base.	300
Table 7.3. Fe-O-C bond angles for calculated structures of iron-tris-hydroxamate complexes.....	301
Table 7.4. Strain energies of complexation for <i>fac</i> and <i>mer</i> isomers of normal and retro hydroxamate saccharide models for ferrichrome.....	301
Table 7.5. Calculated complexation strain energies for FeL _N ²³⁶ and FeL _R ²³⁴ after removal of a single hydroxamate moiety and pendant arm.....	302
Table 8.1. Results of metal-chelator protection assays. Concentrations of metal are listed at the top of the column, while concentrations of each chelator used is listed in each box. Symbols: 0 – no protection, + - slight protection, ++ - full protection, -- - death of all specimens.....	324
Table 8.2. Statistical analysis of the results of metal-chelator protection assays. Concentrations of all chemicals are the same as in Table 8.1.....	325
Table 8.3. pM value of the chelators studied here for the metals used in this study.	331

List of Schemes

Scheme 3.1. Proposed mechanism of exchange from $N^3(\text{etLH})_3$ to desferrioxamine B under the steady-state assumption. Pathway 1 of the reaction proceeds through initial rapid formation of a host-guest supramolecular assembly (k_8 representing the forward reaction and k_{-8} representing the reverse reaction), followed by the formation of an inner-sphere ternary complex between $\text{Fe}\{N^3(\text{etL})_3\}$ and a hydroxamate donor group of desferrioxamine B (represented by the rate constant k_9). The ternary complex formation facilitates complete exchange of iron to ferrioxamine B. Pathway 2 involves direct exchange of iron(III) from $N^3(\text{etLH})_3$ to desferrioxamine B with the second order rate constant $k_7 = 2.12 \times 10^{-3} \text{ M}^{-1} \text{ s}^{-1}$111

Scheme 3.2. Reaction scheme corresponding to the pre-equilibrium interpretation of Reaction 1, shown in Mechanism 2. Initial reaction involves the equilibrium formation of a host-guest complex ($K_{\text{H-G}}$), followed by formation of the inner-sphere ternary complex (k_{19}). This reaction leads to rapid exchange of iron(III) from the ternary complex to ferrioxamine B. Pathway 2 of the reaction involves direct exchange of iron(III) from $N^3(\text{etLH})_3$ to desferrioxamine B with the second order rate constant $k_3 = 2.12 \times 10^{-3} \text{ M}^{-1} \text{ s}^{-1}$115

Scheme 3.3. Reaction scheme corresponding to Mechanism 3, where iron(III) exchange occurs through two sequential reversible steps. The first reversible step represents formation of the host-guest supramolecular assembly, while the second step involves formation of the ternary inner sphere complex. The final step, involving complete exchange of iron from the ternary complex to desferrioxamine B is more rapid than the ternary complex formation.....121

Scheme 3.4. Proposed sequential reaction mechanism for the acid-driven dissociation of the $\text{Fe}_2\{\text{HN}^2(\text{prL})_2\}_3$ complex. Initial dissociation of one lobe takes place in a proton-independent manner, followed by protonation of the FeLLH complex to produce the FeL complex.....132

Scheme 3.5. Proposed parallel reaction mechanism for the acid-driven dissociation of the $\text{Fe}_2\{\text{HN}^2(\text{prL})_2\}_3$ complex. Initial dissociation of one lobe can proceed with or without protonation of the hydroxypyridinone donor group. The remaining FeLLH complex may then dissociate with or without protonation of the formerly bridging hydroxypyridinone ligand.....133

Scheme 3.6. Reaction mechanism of the proton-driven dissociation of the $\text{Fe}_2\{\text{HN}^2(\text{prL})_2\}_3$ complex. Initial dissociation from trishydroxypyridinone complex takes place through a parallel pathway mechanism with $k_{38} = 4.8 \text{ s}^{-1}$ and $k_{39} = 570 \text{ M}^{-1} \text{ s}^{-1}$. This is followed by protonation of the bishydroxypyridinone FeL complex to form the monohydroxypyridinone FeLH complex with $k_{40} = 1.0 \times 10^{-2} \text{ s}^{-1}$. Complete dissociation of the monohydroxypyridinone complex was not observed.....139

Scheme 4.1. The proposed parallel path mechanism of the iron(III) exchange reaction between desferrioxamine B and EDTA in the presence of DMHP (Eq. 2). Pathway 1 represents the catalyzed exchange mechanism, in which DMHP takes part to form a reactive ternary complex, and Pathway 2 represents the direct exchange reaction between DFB and EDTA.....	195
Scheme 4.2. The proposed mechanism of iron(III) exchange from desferrioxamine B to DMHP (reaction 3). The first step is rate determining and involves the formation of a ternary inner-sphere complex between ferrioxamine B and one mole of DMHP...	199
Scheme 4.3. Proposed mechanism of the iron(III) exchange reaction from DMHP to EDTA (Reaction 4) involving initial dissociation of one mole of DMHP, followed by reaction of EDTA with the bis-DMHP complex.....	206
Scheme 5.1. Proposed reaction scheme for hydrolysis of Bbtan in basic solution (top and right), reaction with Fe_{aq}^{3+} (left) and dissociation of the Fe-Bbtan complex in basic solution (bottom).....	216
Scheme 5.2. Flow chart demonstrating the strategy for characterizing the equilibria of the Fe(III)-Bbtan system.....	239
Scheme 7.1. Counter-clockwise from bottom-left to top-left illustrates the step-wise chelation of Fe^{3+} by $H_3L_N^{236}$ showing equilibrium constants (pK_n) for each step and position of coordinated arms. Clockwise from top-left illustrates proton-driven dissociation of pendant arms starting with the 2-arm.....	311
Scheme 7.2. Counter-clockwise from bottom-left to top-left illustrates the step-wise chelation of Fe^{3+} by $H_3L_R^{234}$ showing equilibrium constants (pK_n) for each step and position of coordinated arms. Clockwise from top-left illustrates proton-driven dissociation of pendant arms starting with the 4-arm.....	312

List of Figures

- Figure 1.1. General scheme of common architectures exhibited in natural hexadentate siderophores, linear, exocyclic, and endocyclic. D represents a generic bidentate donor unit.....5
- Figure 1.2. Chemical structure of select natural siderophores featuring the linear architecture.....7
- Figure 1.3. Chemical structure of select natural siderophores featuring the endocyclic architecture, neurosporin and desferrioxamine E.....8
- Figure 1.4. Chemical structure of select natural siderophores featuring the exocyclic architecture, enterobactin and ferrichrome.....8
- Figure 1.5. General scheme of architectures exhibited in natural tetradentate siderophores, linear, exocyclic, and endocyclic. D represents a bidentate donor moiety, usually a hydroxamic acid or a catechol group.....10
- Figure 1.6. Chemical structures of some natural tetradentate siderophores, mugineic acid, alcaligin, bisucaberin, and rhodotorulic acid.....11
- Figure 1.7. General structure of protonated iron(III)-hexadentate siderophore complex, the MLH complex.....12
- Figure 1.8. Protonation reaction of the catecholamide donor group, resulting in salicylate-mode coordination of iron(III).....13
- Figure 1.9. Chemical structure of the monohydroxamate, biscatecholate siderophore mimic L-01. Its iron(III) complex has been shown to exhibit a salicylate shift at both catecholamide donor groups upon lowering the solution pH.....13
- Figure 1.10. All possible solution structures of iron(III)-tetradentate siderophore complexes. The actual structure of the complex will vary based on the structure of the chelator, solution pH, and the L:M ratio in solution.....15
- Figure 1.11. Structure of common binding groups in natural siderophores, including the (a) catechol, (b) hydroxamic acid, (c) α -hydroxycarboxylic acid, (d) amine, (e) carboxylic acid, and (f) hydroxypyridinone donor groups. Also shown is the mode of iron binding at physiological pH.....18
- Figure 1.12. Scheme representing the Z-E conversion observed in hydroxamic acid donor group siderophores involving rotation around the CN-bond.....20

Figure 1.13. Chemical structures of the marine siderophores incorporating the α -hydroxycarboxylic acid donor group, aquachelin and marinobactin.....20

Figure 1.14. Plot of pFe as a function of pH for four natural siderophores. Conditions: $[\text{Fe}]_{\text{tot}} = 1 \mu\text{M}$, $[\text{Sid}]_{\text{tot}} = 10 \mu\text{M}$, $\mu = 0.10 \text{ M}$, $T = 25 \text{ }^\circ\text{C}$. Legend: diamonds – enterobactin, triangles – desferrioxamine B, squares – aerobactin, circles – rhodotorulic acid....28

Figure 1.15. Range of observable redox potentials for the Fe(III)/Fe(II) redox couple of a number of iron complexes. The redox potential of the complex varies depending on the identity of the chelator bound to iron.....29

Figure 1.16. Plot of reduction potentials ($E_{1/2}$) as a function of pFe^{3+} values for a series of hexadentate, tetradentate and bidentate hydroxamic acid siderophore and siderophore mimic complexes with iron. Legend: 1 – ferrioxamine E; 2 – ferrioxamine B; 3 – $\text{H}_3\text{LR}^{234}$; 4 – $\text{H}_3\text{LN}^{236}$; 5 – coprogen; 6 – ferricrocin; 7 – ferrichrome; 8 – alcaligin; 9 – rhodotorulic acid; 10 – NMAHA; 11 – AHA; 12 – Ly-AHA.....32

Figure 1.17. Plot of reduction potentials ($E_{1/2}$) as a function of pFe^{3+} values for hexadentate siderophore and siderophore mimic complexes with iron. Solid line represents a linear least squares fit to the data with slope = 0.0615 V. Legend: 1 – enterobactin; 2 – 3,4-LI(TAMmeg); 3 – TREN CAM; 4 – 5-LIO(TAMmeg)₂TAM; 5 – exochelin MN; 6 – 3,4-LI(Me-3,2-HOPO)(TAMmeg)₂; 7 – pyoverdine; 8 – azotobactin; 9 – ferrioxamine E; 10 – $\text{H}_3\text{LR}^{234}$; 11 – ferrioxamine B; 12 – $\text{H}_3\text{LN}^{236}$; 13 – ferricrocin; 14 – HOPObactin; 15 – 3,4-LI(Me-3,2-HOPO)₂(TAMmeg); 16 – coprogen; 17 – TR322-Me-3,2-HOPO; 18 – TREN-Me-3,2-HOPO; 19 – ferrichrome; 20 – exochelin MS; 21 – 3,4-LI(Me-3,2-HOPO); 22 – TR332-Me-3,2-HOPO; 23 – aerobactin; 24 – TRPN-Me-3,2-HOPO; 25 – rhizoferrin. $E_{1/2}$ values and pFe values taken from Ref.(1).....33

Figure 1.18. Redox potentials ($E_{1/2}$) of Fe^{3+} siderophore and siderophore mimic complexes as a function of pH. Lines represents a fit of Eq. (31) to the data, which are taken from Refs. (70-73). Adapted from Ref. (9).....35

Figure 1.19. Tetradentate natural siderophore, pyochelin (A) and the ternary complex formed with ferric iron, pyochelin, and cepabactin (B).....38

Figure 1.20. Current small molecule chelation therapy agents for iron overload, deferasirox (trade name Exjade) and 1,2-dimethyl-3-hydroxy-4-pyridinone (trade name Defेरiprone).....44

Figure 2.1. The electronic structures of the hydroxypyridinone donor group and of the catechol donor group are the same, resulting in similar thermodynamics of complex formation between the two donor groups.....51

Figure 2.2. Structures of the synthetic exocyclic 3-hydroxy-2-pyridinone donor group siderophores studied here. Two exocyclic bishydroxypyridinone siderophores based

around a [6]ane-N₂ central ring system, N²(etLH)₂ and N²(prLH)₂, and an exocyclic trishydroxypyridinone siderophore based around a [9]ane-N₃ central ring system, N³(etLH)₃. Determined protonation constants are indicated on the structures of the molecules.....53

Figure 2.3. Spectrophotometric measurements of the competition reactions between the Fe-HOPO complexes and EDTA. (A) Fe₂(HN²(prLH)₂)₃ competition reaction with EDTA, [Fe³⁺] = 2.5 × 10⁻⁴ M, [N²(prLH)₂] = 3.8 × 10⁻⁴ M, pH = 7.1, μ = 0.10 (NaCl), [EDTA] = 0 – 2.5 × 10⁻³ M; (B) Fe(HN³(etLH)₃) competition reaction with EDTA, [Fe³⁺] = [N³(etLH)₃] = 4.0 × 10⁻⁴ M, pH = 6.5, μ = 0.10 (NaCl), [EDTA] = 0 – 1.0 × 10⁻² M; (C) Fe(EDTA) competition reaction with N²(etLH)₂, [Fe³⁺] = 1.0 × 10⁻⁴ M, [EDTA] = 1.0 × 10⁻⁴ M, pH = 2.3, μ = 0.10 (NaCl), [N²(etLH)₂] = 0 – 1.0 × 10⁻³ M. In each case, an arrow indicates the direction in which the spectrum changes as competing ligand is added.....62

Figure 2.4. Potentiometric titration of two hydroxypyridinone-Fe³⁺ systems. (A) Fe-N²(prLH)₂ system. [Fe³⁺] = 4.0 × 10⁻⁴ M, [N²(prLH)₂] = 6.0 × 10⁻⁴ M, μ = 0.10 (NaCl). The triangles represent the ligand only titration ([N²(prLH)₂] = 6.7 × 10⁻⁴), while the diamonds represent the Fe-N²(prLH)₂ complex titration. (B) Fe-N³(etLH)₃ system. [Fe³⁺] = 3.98 × 10⁻⁴ M, [N³(etLH)₃] = 3.99 M, μ = 0.10 (NaCl). The squares represent the ligand only titration, while the diamonds represent the potentiometric titration performed in the presence of 1 equivalent of metal.....67

Figure 2.5. Spectrophotometric titration of the synthetic exocyclic hydroxypyridinone siderophores with 0.010 M NaOH. (A) N²(prLH)₂ over the pH range of 3.25 to 10.90. [N²(prLH)₂] = 1.0 × 10⁻⁵ M, μ = 0.10, T = 25 °C. (B) N³(etLH)₃ over the pH range of 2.6 to 11.8. [N²(prLH)₂] = 2.92 × 10⁻⁵ M, μ = 0.10, T = 25 °C. (C) N²(etLH)₂ over the pH range of 2.76 to 10.71. [N²(etLH)₂] = 5.0 × 10⁻⁵ M, μ = 0.10, T = 25 °C. Arrows indicate the direction the spectrum changes upon addition of base.....68

Figure 2.6. Spectrophotometric titrations of the Fe-N²(prLH)₂ system. (A) Spectra measured during the low-pH spectrophotometric titration of the Fe-N²(prLH)₂ system over the pH range of 2.14 to ~0.2. [Fe³⁺] = 3.3 × 10⁻⁴ M, [N²(prLH)₂] = 5.0 × 10⁻⁴ M, T = 25 °C, μ = 0.10 (NaCl). (B) pH 3.5 to 7.5. [Fe³⁺] = 2.0 × 10⁻⁴ M, [N²(prLH)₂] = 3.0 × 10⁻⁴ M, μ = 0.10 (NaCl), T = 25 °C. Arrow indicates the direction of spectral change upon addition of acid.....74

Figure 2.7. Species distribution diagram for the completely characterized systems of N²(prLH)₂ and N³(etLH)₃ in aqueous solution, showing percent total Fe³⁺ vs pH of solution. Values were calculated from determined stability constants of complexes and hydrolysis constants for Fe³⁺. T = 25 °C, μ = 0.10. (A) Fe-N²(prLH)₂ system, with [Fe³⁺]_{total} = 2.00 × 10⁻⁴ M, and [N²(prLH)₂]_{total} = 3.00 × 10⁻⁴ M. a = free Fe³⁺, b = Fe(HN²(prL)₂)(H₂O)₂²⁺ complex, c = Fe₂(HN²(prL)₂)₃³⁺ complex, d = Fe(OH)₄⁻, e = Fe(HN²(prLH)(prL))₃³⁺ and f = Fe(OH)₂⁺. (B) Fe-N³(etLH)₃ system, [Fe³⁺] = 1.00 × 10⁻⁴ M, [N³(etLH)₃] = 1.00 × 10⁻⁴ M. a =

free Fe^{3+} , b = $\text{Fe}(\text{HN}^3(\text{etL})_2(\text{etLH}))^{2+}$, c = $\text{Fe}(\text{HN}^3(\text{etL})_3)^+$, d = $\text{Fe}(\text{N}^3(\text{etL})_3)$, e = $\text{Fe}(\text{OH})_4^-$, f = $\text{Fe}(\text{OH})_2^{2+}$, and G = $\text{Fe}(\text{OH})_2^+$76

Figure 2.8. Spectra measured during the low-pH spectrophotometric titration of the $\text{Fe}(\text{N}^2(\text{etLH})_2)$ system. The absorbance decreases due in part to dilution and in part due to the change in spectral intensity upon conversion to the bicoordinate complex. $[\text{Fe}^{3+}] = 3.5 \times 10^{-4} \text{ M}$, $[\text{N}^2(\text{etLH})_2] = 3.5 \times 10^{-4} \text{ M}$, $T = 25 \text{ }^\circ\text{C}$, $\mu = 0.10$ (NaCl). Arrow indicates the arrow in which the spectrum is moving upon addition of base.....77

Figure 2.9. ESI-Mass spectra measured for the bishydroxypyridinone complex solutions. Solutions were prepared in the range indicative of formation of the 1:1 complex, pH 2.5. $T = 125 \text{ }^\circ\text{C}$, nebulizer pressure = 15 psi, dry gas flow rate = 7 L/min. (A) Mass spectrum of the $\text{Fe}-\text{N}^2(\text{etLH})_2$ system. $[\text{Fe}^{3+}] = 3.2 \times 10^{-4} \text{ M}$ and $[\text{N}^2(\text{etLH})_2] = 4.8 \times 10^{-4} \text{ M}$. (B) Mass spectrum of the $\text{Fe}-\text{N}^2(\text{prLH})_2$ system. $[\text{Fe}^{3+}] = 4.2 \times 10^{-4} \text{ M}$ and $[\text{N}^2(\text{prLH})_2] = 6.3 \times 10^{-4} \text{ M}$79

Figure 2.10. Proposed solution structure of the $\text{Fe}-\text{N}^2(\text{etLH})_2$ complex at pH 2.5 based on ESI-MS spectra.....80

Figure 2.11. Low pH spectrophotometric titration of the iron(III)- $\text{N}^3(\text{etLH})_3$ system over the pH range of 2.5 to ~0.2. Conditions: $[\text{Fe}^{3+}] = [\text{N}^3(\text{etLH})_3] = 3.6 \times 10^{-4} \text{ M}$, $T = 25 \text{ }^\circ\text{C}$, $\mu = 0.10$ (NaCl). Arrow indicates the direction of spectral change with decreasing pH. Spectral absorbance adjusted for dilution.....82

Figure 2.12. Spectrophotometric titration of the $\text{Fe}-\text{N}^3(\text{etLH})_3$ system, $[\text{Fe}^{3+}] = [\text{N}^3(\text{etLH})_3] = 4.4 \times 10^{-4} \text{ M}$, $T = 25 \text{ }^\circ\text{C}$, $\mu = 0.10$ (NaCl). Arrows indicate the direction of spectral change as the titration proceeded. (A) Titration over the pH range of 2.9 – 8.0. (B) Titration over the pH range 8.0 to 10.44.....84

Figure 2.13. Representative cyclic voltammograms of the iron- $\text{N}^3(\text{etLH})_3$ system. (A) Cyclic voltammogram measured at pH 2.0. (B) Cyclic voltammogram measured at pH 7.58. Conditions: $[\text{Fe}^{3+}] = [\text{N}^3(\text{etLH})_3] = 1.5 \text{ mM}$, $T = 25 \text{ }^\circ\text{C}$, $\mu = 0.10$ (NaCl), working electrode: HDME, reference electrode: Ag/AgCl (3.5 M NaCl), auxiliary electrode: Pt wire, scan rate = 50 mV/s.....86

Figure 2.14. Cyclic voltammogram measured for the iron- $\text{N}^3(\text{etLH})_3$ system at increased scan rate to show increased reversibility. Conditions: $[\text{Fe}^{3+}] = [\text{N}^3(\text{etLH})_3] = 1.5 \text{ mM}$, $T = 25 \text{ }^\circ\text{C}$, $\mu = 0.10$ (NaCl), working electrode: HDME, reference electrode: Ag/AgCl (3.5 M NaCl), auxiliary electrode: Pt wire, scan rate = 100 mV/s.....87

Figure 3.1. Chemical structures of the siderophore and siderophore mimics studied here. $\text{N}^3(\text{etLH})_3$ and desferrioxamine B were used in an iron(III) exchange reaction to determine the mechanism of exchange between the hexadentate ligands, while $\text{N}^2(\text{prLH})_2$ was used to investigate the mechanism of complex dissociation at low pH values.95

Figure 3.2. Spectra measured during the iron(III) exchange reaction between $N^3(\text{etLH})_3$ and desferrioxamine B (Eq. 1) over the course of 500 minutes. Conditions: $[\text{Fe}^{3+}] = [\text{N}^3(\text{etLH})_3] = 2.9 \times 10^{-4} \text{ M}$, $[\text{DFB}] = 10 \text{ mM}$, $T = 25 \text{ }^\circ\text{C}$, $\text{pH} = 7.19$ (0.20 M HEPES buffer), $\mu = 0.10 \text{ M}$ (NaClO_4). The arrow represents the direction of the spectral shift over time during the reaction.....102

Figure 3.3. Absorbance measured at 505 nm during the iron(III) exchange reaction between $N^3(\text{etLH})_3$ and desferrioxamine B (Eq. 1). The line represents the best fit line using a double exponential decay model (Eq. 2) where $k_{2\text{obs}} = 2.3 \times 10^{-3} \text{ s}^{-1}$ and $k_{3\text{obs}} = 1.63 \times 10^{-4} \text{ s}^{-1}$. Conditions: $[\text{Fe}^{3+}] = [\text{N}^3(\text{etLH})_3] = 2.9 \times 10^{-4} \text{ M}$, $[\text{DFB}] = 5 \text{ mM}$, $T = 25 \text{ }^\circ\text{C}$, $\text{pH} = 7.19$ (0.20 M HEPES buffer), $\mu = 0.10 \text{ M}$ (NaClO_4).....103

Figure 3.4. Plot of the pseudo-first order rate constants, k_{obs} as a function of DFB concentration. (A) Plot of $k_{2\text{obs}}$ as a function of $[\text{Desferrioxamine B}]$ yielding $k_{5\text{app}} = 1.7 \times 10^{-1} \text{ M}^{-1} \text{ s}^{-1}$ and $k_{6\text{app}} = 1.4 \times 10^{-3} \text{ s}^{-1}$; (B) Plot of $k_{3\text{obs}}$ as a function of $[\text{Desferrioxamine B}]$ yielding $k_7 = 2.12 \times 10^{-2} \text{ M}^{-1} \text{ s}^{-1}$. Conditions: $[\text{Fe}^{3+}] = [\text{N}^3(\text{etLH})_3] = 2.9 \times 10^{-4} \text{ M}$, $T = 25 \text{ }^\circ\text{C}$, $\text{pH} = 7.19$ (0.20 M HEPES buffer), $\mu = 0.10 \text{ M}$ (NaClO_4). Error bars represent the standard deviation of the observed rate constant at that concentration determined at 4 distinct wavelengths.....104

Figure 3.5. Electrospray mass spectrum of the desferrioxamine B- $N^3(\text{etLH})_3$ system. Conditions: 50:1 molar ratio of desferrioxamine B: $N^3(\text{etLH})_3$, in aqueous solution with no background electrolyte, $T = 125 \text{ }^\circ\text{C}$, nebulizer pressure = 15 psi, dry gas flow rate = 7 L/min.....106

Figure 3.6. Proposed structure of the host-guest supramolecular assembly between desferrioxamine B and $N^3(\text{etLH})_3$, of which the molecular weight is 1102.3 Da. The ESI-mass spectrometry peak observed at 1121.5 m/z units has been assigned to a water adduct of this complex.....107

Figure 3.7. Structures of the tripodal hexadentate iron chelators, O-TRENSEX and TRENCAMS.....109

Figure 3.8. Plots of (A) $k_{2\text{obs}} + k_{3\text{obs}}$ as a function of desferrioxamine B concentration and (B) $k_{2\text{obs}}k_{3\text{obs}}$ as a function of desferrioxamine B concentration. Kinetic parameters were obtained from the exchange of iron(III) from $N^3(\text{etLH})_3$ to desferrioxamine B. Conditions: $[\text{Fe}^{3+}] = [\text{N}^3(\text{etLH})_3] = 2.9 \times 10^{-4} \text{ M}$, $T = 25 \text{ }^\circ\text{C}$, $\text{pH} = 7.19$ (0.20 M HEPES buffer), $\mu = 0.10 \text{ M}$ (NaClO_4). Error bars represent the propagated standard deviation of the observed rate constants at that concentration determined at 4 distinct wavelengths.123

Figure 3.9. Schematic representation of the structures of singly-bridged and triply-bridged Fe_2L_3 complexes.....126

Figure 3.10. Spectra measured during the acid-driven dissociation of the $\text{Fe}_2\{\text{N}^2(\text{prL})_2\}_3$ complex. (A) Initial spectral change corresponding to dissociation of the hexacoordinate complex to the tetracoordinate complex after rapidly decreasing the solution pH from 6.0 to approximately 2.3. Conditions: $[\text{Fe}^{3+}] = 2.1 \times 10^{-4} \text{ M}$, $[\text{N}^2(\text{prLH})_2] = 3.2 \times 10^{-4} \text{ M}$, $[\text{H}^+] = 5.0 \text{ mM}$, $\mu = 0.10$ (NaNO_3), $T = 25 \text{ }^\circ\text{C}$; (B) Second spectral shift observed at higher acid concentrations by rapidly jumping the pH from approximately 6.0 to approximately 1.3. Conditions: $[\text{Fe}^{3+}] = 2.1 \times 10^{-4} \text{ M}$, $[\text{N}^2(\text{prLH})_2] = 3.2 \times 10^{-4} \text{ M}$, $[\text{H}^+] = 50.0 \text{ mM}$, $\mu = 0.10$ (NaNO_3), $T = 25 \text{ }^\circ\text{C}$127

Figure 3.11. Plot of absorbance at 503 nm as a function of time during the initial spectral shift of the acid-driven dissociation of $\text{Fe}_2\{\text{N}^2(\text{prL})_2\}_3$ (Eq. 35) over 1 second. The line represents the best fit plot to the data using a double exponential decay model (Eq. 2) with $k_{2\text{obs}} = 4.39 \text{ s}^{-1}$ and $k_{3\text{obs}} = 49.5 \text{ s}^{-1}$. Conditions: $[\text{Fe}^{3+}] = 2.1 \times 10^{-4} \text{ M}$, $[\text{N}^2(\text{prLH})_2] = 3.2 \times 10^{-4} \text{ M}$, $[\text{H}^+] = 50.0 \text{ mM}$, $\mu = 0.10$ (NaNO_3), $T = 25 \text{ }^\circ\text{C}$129

Figure 3.12. Plot of the observed pseudo-first order rate constant as a function of acid concentration for both pseudo-first order rate constants, $k_{2\text{obs}}$ and $k_{3\text{obs}}$. These plots yield a first order rate constant, $k_{38} = 4.8 \text{ s}^{-1}$ and a second order rate constant, $k_{39} = 570 \text{ M}^{-1} \text{ s}^{-1}$. Conditions: $[\text{Fe}^{3+}] = 2.1 \times 10^{-4} \text{ M}$, $[\text{N}^2(\text{prLH})_2] = 3.2 \times 10^{-4} \text{ M}$, $\mu = 0.10$ (NaNO_3), $T = 25 \text{ }^\circ\text{C}$.

.....130

Figure 3.13. Plot of absorbance at 503 nm as a function of time during the second spectral shift of the acid-driven dissociation of $\text{Fe}_2\{\text{N}^2(\text{prL})_2\}_3$ (shown in Fig. 007B) from 20-300 seconds. The line shown in the figure represents the best fit plot of the data to a single exponential decay model (Eq. 4) yielding a pseudo-first order first order rate constant of $k_{\text{obs}} = 8.9 \times 10^{-3} \text{ s}^{-1}$. Conditions: $[\text{Fe}^{3+}] = 2.1 \times 10^{-4} \text{ M}$, $[\text{N}^2(\text{prLH})_2] = 3.2 \times 10^{-4} \text{ M}$, $[\text{H}^+] = 50.0 \text{ mM}$, $\mu = 0.10$ (NaNO_3), $T = 25 \text{ }^\circ\text{C}$136

Figure 3.14. Plot of the observed pseudo-first order rate constant as a function of acid concentration for the pseudo-first order rate constant, k_{obs} of reaction 40. The observed rate constant is not dependent on proton concentration. Conditions: $[\text{Fe}^{3+}] = 2.1 \times 10^{-4} \text{ M}$, $[\text{N}^2(\text{prLH})_2] = 3.2 \times 10^{-4} \text{ M}$, $\mu = 0.10$ (NaNO_3), $T = 25 \text{ }^\circ\text{C}$137

Figure 4.1. Structures of the iron(III) chelators discussed in this study, the ferrioxamine B complex, EDTA, DMHP, and three monohydroxamic acids previously studied and shown to accelerate the exchange of iron(III) from desferrioxamine B to EDTA.....144

Figure 4.2. Spectra measured during the exchange reaction between ferrioxamine B and EDTA in the absence of DMHP (Eq. 1) measured over 250 minutes. Arrow shows the direction of spectral change with time over 250 minutes. Conditions: $[\text{Fe}^{3+}] = [\text{DFB}] = 0.4 \text{ mM}$, $[\text{EDTA}] = 10 \text{ mM}$, $\mu = 0.10 \text{ M}$ (NaClO_4), $\text{pH} = 4.35$ (100 mM NaOAc buffer), $T = 25 \text{ }^\circ\text{C}$149

Figure 4.3. Plot of absorbance at 430 nm as a function of time for the reaction of ferrioxamine B with EDTA in the absence of DMHP (Eq. 1). The points represent experimental data, while the line represents the single order exponential decay fit of the data (Eq. 5). Conditions: $[\text{Fe}^{3+}] = [\text{DFB}] = 0.4 \text{ mM}$, $[\text{EDTA}] = 10 \text{ mM}$, $[\text{DMHP}] = 1.5 \text{ mM}$, $\mu = 0.10 \text{ M}$ (NaClO_4), $\text{pH} = 4.35$ (50 mM NaOAc buffer), $T = 25 \text{ }^\circ\text{C}$150

Figure 4.4. Plot of pseudo-first order rate constant, k_{obs} as a function of $[\text{EDTA}]$ for reaction 2 at five DMHP concentrations. All reactions were performed at $[\text{Fe}^{3+}] = [\text{DFB}] = 0.4 \text{ mM}$, $[\text{EDTA}] = 5\text{-}15 \text{ mM}$, $\mu = 0.10 \text{ M}$ (NaClO_4), $\text{pH} = 4.35$ (100 mM NaOAc buffer), and $T = 25 \text{ }^\circ\text{C}$. Legend: Diamonds - $[\text{DMHP}] = 0 \text{ mM}$, squares - $[\text{DMHP}] = 0.25 \text{ mM}$, X - $[\text{DMHP}] = 1.0 \text{ mM}$, dashes - $[\text{DMHP}] = 2.5 \text{ mM}$, triangles - $[\text{DMHP}] = 5.0 \text{ mM}$. The equations show the linear best fit plots of k_{obs} as a function of $[\text{DMHP}]$ for the adjacent lines. The error bars on data points represent the standard deviation of the average observed rate constant measured at 4 discrete wavelengths in a single experiment. If an error bar is not visible, it is smaller than the data point.....152

Figure 4.5. Spectra measured during the iron(III) exchange reaction between ferrioxamine B and EDTA in the presence of DMHP (Eq. 2). Arrows show the direction of spectral change with time over 900 secs. Conditions: $[\text{Fe}^{3+}] = [\text{H}_4\text{DFB}^+] = 0.4 \text{ mM}$, $[\text{EDTA}] = 10 \text{ mM}$, $[\text{DMHP}] = 1.5 \text{ mM}$, $\mu = 0.10 \text{ M}$ (NaClO_4), $\text{pH} = 4.35$ (50 mM NaOAc buffer), $T = 25 \text{ }^\circ\text{C}$154

Figure 4.6. Plot of absorbance at 430 nm as a function of time for the reaction of ferrioxamine B with EDTA in the presence of DMHP (Eq. 2). The points represent experimental data, while the line represents the single order exponential decay fit of the data (Eq. 5) Conditions: $[\text{Fe}^{3+}] = [\text{DFB}] = 0.4 \text{ mM}$, $[\text{EDTA}] = 10 \text{ mM}$, $[\text{DMHP}] = 1.5 \text{ mM}$, $\mu = 0.10 \text{ M}$ (NaClO_4), $\text{pH} = 4.35$ (100 mM NaOAc buffer), $T = 25 \text{ }^\circ\text{C}$155

Figure 4.7. Plot of pseudo-first order rate constant, k_{obs} , as a function of $[\text{DMHP}]$ concentration for reaction 2 at five EDTA concentrations. All reactions were performed at $[\text{Fe}^{3+}] = [\text{DFB}] = 0.4 \text{ mM}$, $[\text{DMHP}] = 0\text{-}5 \text{ mM}$, $\mu = 0.10 \text{ M}$ (NaClO_4), $\text{pH} = 4.35$ (50 mM NaOAc buffer), and $T = 25 \text{ }^\circ\text{C}$. Legend: Triangles - $[\text{EDTA}] = 5.0 \text{ mM}$, X - $[\text{EDTA}] = 8 \text{ mM}$, diamonds - $[\text{EDTA}] = 10 \text{ mM}$, circles - $[\text{EDTA}] = 12 \text{ mM}$, squares - $[\text{EDTA}] = 15 \text{ mM}$. The equations to the right show the linear best fit lines of k_{obs} as a function of $[\text{DMHP}]$ in ascending order of EDTA concentration. The error bars represent the standard deviation of the average observed rate constant measured at 4 discrete wavelengths in a single experiment. If an error bar is not visible, it is smaller than the data point...156

Figure 4.8. Spectra measured during the iron(III) exchange reaction from desferrioxamine B to DMHP (Reaction 3) over the course of 20 minutes. Arrow shows direction of spectral change with time. Conditions: $[\text{Fe}^{3+}] = [\text{HDFB}] = 0.20 \text{ mM}$, $[\text{DMHP}] = 7 \text{ mM}$, $\mu = 0.10 \text{ M}$ (NaClO_4), $\text{pH} = 4.35$ (50 mM NaOAc buffer), $T = 25 \text{ }^\circ\text{C}$161

Figure 4.9. Plot of absorbance at 455 nm as a function of time for the iron(III) exchange reaction between ferrioxamine B and DMHP (Eq. 3). The line represents the single exponential decay fit to the data (Eq. 5). Conditions: $[\text{Fe}^{3+}] = [\text{HDFB}] = 0.20 \text{ mM}$, $[\text{DMHP}] = 7 \text{ mM}$, $\mu = 0.10 \text{ M}$ (NaClO_4), $\text{pH} = 4.35$ (50 mM NaOAc buffer), $T = 25 \text{ }^\circ\text{C}$162

Figure 4.10. Plot of observed pseudo-first order rate constant of the iron(III) exchange reaction between ferrioxamine B and DMHP (Eq. 3) as a function of DMHP concentration. The lower line (diamonds) represents rate constants for reaction 3 extrapolated from the intercepts of the plots in Fig. 005, while the upper line (squares) represents the values obtained experimentally. Error bars for the diamonds represent the standard deviation of the y-intercepts of the plots in Fig. 4.4. Error bars for the squares represent the standard deviation of the average observed rate constant measured at 4 discrete wavelengths in a single experiment. If error bars are not visible, they are smaller than the data points.....163

Figure 4.11. Plot of observed pseudo-first order rate constant of the iron(III) exchange reaction between ferrioxamine B and DMHP (Eq. 3) as a function of DMHP concentration at five solution pH values. The legend to the right displays the symbols for each pH value. Error bars represent the standard deviation of the average observed rate constant measured at 4 discrete wavelengths in a single experiment. If error bars are not visible, they are smaller than the data points.....166

Figure 4.12. Plot of second order rate constants for the iron(III) exchange reaction between desferrioxamine B and DMHP as a function of pH. At lower pH values, the reaction proceeds much more rapidly.....167

Figure 4.13. Spectra measured during the iron(III) exchange reaction of the $\text{Fe}(\text{DMHP})_3$ complex with EDTA (Eq. 4). Arrow shows the direction of spectral change with time over 120 secs. Conditions: $[\text{Fe}^{3+}] = 0.20 \text{ mM}$, $[\text{DMHP}] = 2.0 \text{ mM}$, $[\text{EDTA}] = 5.0 \text{ mM}$, $\mu = 0.10 \text{ M}$ (NaClO_4), $\text{pH} = 4.35$ (50 mM NaOAc buffer), $T = 25 \text{ }^\circ\text{C}$168

Figure 4.14. Plot of absorbance at 450 nm as a function of time for the iron exchange reaction between $\text{Fe}(\text{DMHP})_3$ and EDTA (Eq. 4). The line represents the single exponential decay fit to the data (Eq. 5). Conditions: $[\text{Fe}^{3+}]_{\text{tot}} = 2.0 \times 10^{-4} \text{ M}$, $[\text{DMHP}] = 5.0 \text{ mM}$, $[\text{EDTA}] = 6.0 \text{ mM}$, $25.0 \text{ }^\circ\text{C}$, $\text{pH} = 4.35$, $\mu = 0.10 \text{ M}$ (NaClO_4).....169

Figure 4.15. Plot of observed pseudo-first order rate constant for the iron(III) exchange reaction between DMHP and EDTA (Eq. 4) as a function of EDTA concentration at two DMHP concentrations. The upper plot (diamonds) represents the reaction performed at 2 mM DMHP, while the lower plot (squares) represents the reaction performed at 5 mM DMHP. Conditions: $[\text{Fe}^{3+}] = 0.20 \text{ mM}$, $\mu = 0.10 \text{ M}$ (NaClO_4), $\text{pH} = 4.35$ (50 mM NaOAc buffer), and $T = 25 \text{ }^\circ\text{C}$. Error bars on the plot at 5 mM DMHP represent the standard deviation of the average observed rate constant measured at 4 discrete wavelengths in a single experiment. Error bars on the plot at 2 mM DMHP represent the standard

deviation of the average observed rate constant measured at two discrete wavelengths, 2 replicates performed at each wavelength (4 total replicates). If error bars are not visible (as in the squares), they are smaller than the data points.....170

Figure 4.16. Plot of observed pseudo-first order rate constant for the iron(III) exchange reaction between DMHP and EDTA (Eq. 4) as a function of DMHP concentration. The line represents the best fit line to the data (excluding the data point at 1 mM DMHP) using the model shown in Eq. 30, where a is an adjustable parameter found to be 3.01×10^{-4} . Error bars represent the standard deviation of the average observed rate constant measured at 4 discrete wavelengths in a single experiment. For the error bar at 2 mM DMHP, see Fig. 4.15. Conditions: $[\text{Fe}^{3+}]_{\text{tot}} = 2.0 \times 10^{-4} \text{ M}$, $[\text{EDTA}] = 6.0 \text{ mM}$, $25.0 \text{ }^\circ\text{C}$, $\text{pH} = 4.35$, $\mu = 0.10 \text{ M (NaClO}_4\text{)}$172

Figure 4.17. Plot of observed pseudo-first order rate constant, k_{obs} , for the iron(III) exchange reaction between DMHP and EDTA (reaction 4) as a function of DMHP concentration. The line represents the best fit line to the data (excluding the data point at 1 mM DMHP) using the model shown in Eq. 38, where a is an adjustable parameter found to be 4.66×10^{-8} . Error bars represent the standard deviation of the average observed rate constant measured at 4 discrete wavelengths in a single experiment. For the error bar at 2 mM DMHP, see Fig. 4.15. Conditions: $[\text{Fe}^{3+}]_{\text{tot}} = 2.0 \times 10^{-4} \text{ M}$, $[\text{EDTA}] = 6.0 \text{ mM}$, $25.0 \text{ }^\circ\text{C}$, $\text{pH} = 4.35$, $\mu = 0.10 \text{ M (NaClO}_4\text{)}$178

Figure 4.18. Plot of observed pseudo-first order rate constant, k_{obs} , for the iron(III) exchange reaction between DMHP and EDTA (reaction 4) as a function of DMHP concentration. The line represents the best fit line to the data (excluding the data point at 1 mM DMHP) using the model shown in Eq. 40, where a and b are adjustable parameters found to be $a = 2.84 \times 10^{-4}$ and $b = 7.72 \times 10^{-3}$. Error bars represent the standard deviation of the average observed rate constant measured at 4 discrete wavelengths in a single experiment. For the error bar at 2 mM DMHP, see Fig. 4.15. Conditions: $[\text{Fe}^{3+}]_{\text{tot}} = 2.0 \times 10^{-4} \text{ M}$, $[\text{EDTA}] = 6.0 \text{ mM}$, $25.0 \text{ }^\circ\text{C}$, $\text{pH} = 4.35$, $\mu = 0.10 \text{ M (NaClO}_4\text{)}$181

Figure 4.19. Plot of observed pseudo-first order rate constant, k_{obs} , for the iron(III) exchange reaction between DMHP and EDTA (reaction 4) as a function of DMHP concentration. The line represents the best fit line to the data (excluding the data point at 1 mM DMHP) using the model shown in Eq. 42, where a and b are adjustable parameters found to be $a = 7.24 \times 10^{-8}$ and $b = 3.44 \times 10^{-4}$. Error bars represent the standard deviation of the average observed rate constant measured at 4 discrete wavelengths in a single experiment. For the error bar at 2 mM DMHP, see Fig. 009. Conditions: $[\text{Fe}^{3+}]_{\text{tot}} = 2.0 \times 10^{-4} \text{ M}$, $[\text{EDTA}] = 6.0 \text{ mM}$, $25.0 \text{ }^\circ\text{C}$, $\text{pH} = 4.35$, $\mu = 0.10 \text{ M (NaClO}_4\text{)}$183

Figure 4.20. Plot of observed pseudo-first order rate constant, k_{obs} , for the iron(III) exchange reaction between DMHP and EDTA (reaction 4) as a function of DMHP

concentration. The line represents the best fit line to the data (excluding the data point at 1 mM DMHP) using the model shown in Eq. 44, where a and b are adjustable parameters found to be $a = 3.65 \times 10^{-7}$ and $b = 0.0368$. Error bars represent the standard deviation of the average observed rate constant measured at 4 discrete wavelengths in a single experiment. For the error bar at 2 mM DMHP, see Fig. 4.15. Conditions: $[\text{Fe}^{3+}]_{\text{tot}} = 2.0 \times 10^{-4} \text{ M}$, $[\text{EDTA}] = 6.0 \text{ mM}$, $25.0 \text{ }^\circ\text{C}$, $\text{pH} = 4.35$, $\mu = 0.10 \text{ M (NaClO}_4\text{)}$185

Figure 4.21. Plot of observed pseudo-first order rate constant, k_{obs} , for the iron(III) exchange reaction between DMHP and EDTA (reaction 4) as a function of DMHP concentration. The line represents the best fit line to the data (excluding the data point at 1 mM DMHP) using the model shown in Eq. 46, where a , b , and c are adjustable parameters found to be $a = 2.55 \times 10^{-8}$, $b = 3.02 \times 10^{-4}$, and $c = 6.01 \times 10^{-3}$. Error bars represent the standard deviation of the average observed rate constant measured at 4 discrete wavelengths in a single experiment. For the error bar at 2 mM DMHP, see Fig. 009. Conditions: $[\text{Fe}^{3+}]_{\text{tot}} = 2.0 \times 10^{-4} \text{ M}$, $[\text{EDTA}] = 6.0 \text{ mM}$, $25.0 \text{ }^\circ\text{C}$, $\text{pH} = 4.35$, $\mu = 0.10 \text{ M (NaClO}_4\text{)}$188

Figure 4.22. Speciation plot of the iron(III)-DFB-DMHP-EDTA system over a range of pH values. Conditions: $[\text{Fe}]_{\text{tot}} = 0.40 \text{ mM}$, $[\text{HDFB}]_{\text{tot}} = 0.40 \text{ mM}$, $[\text{DMHP}]_{\text{tot}} = 5 \text{ mM}$, $[\text{EDTA}]_{\text{tot}} = 10 \text{ mM}$, $T = 25 \text{ }^\circ\text{C}$, $\mu = 0.10$202

Figure 4.23. Speciation diagram for the Fe-DMHP system with varying DMHP concentration. Conditions: $[\text{Fe}^{3+}]_{\text{tot}} = 0.20 \text{ mM}$, $\text{pH} = 4.35$, $T = 25 \text{ }^\circ\text{C}$, $\mu = 0.10 \text{ M}$, and $[\text{DMHP}] = 0 - 10 \text{ mM}$204

Figure 5.1. Structure of the siderophore, brasilibactin A and its synthetic analog, Bbtan. Both siderophore and analog contain two hydroxamate and a phenol-oxazole donor group. Ionizable protons are shown here in bold with their determined protonation constants for Bbtan. Also shown are mycobactin S and the related extracellular siderophores, carboxymycobactin and Exochelin MN.....211

Figure 5.2. Spectrophotometric titration of the synthetic analog of Brasilibactin A, Bbtan, over the pH range of 2.24 to 10.2. Conditions: $[\text{Bbtan}] = 1.4 \times 10^{-4} \text{ M}$, $\mu = 0.10 \text{ (NaClO}_4\text{)}$, $T = 25 \text{ }^\circ\text{C}$222

Figure 5.3. UV-Visible spectra obtained from spectrophotometric titration of Bbtan showing the lack of reversibility of the titration. Conditions: $[\text{Bbtan}] = 1.4 \times 10^{-4} \text{ M}$, $\mu = 0.10 \text{ (NaClO}_4\text{)}$, $T = 25 \text{ }^\circ\text{C}$222

Figure 5.4. pH-dependent NMR titration of the Brasilibactin A analog, Bbtan demonstrating hydrolysis of the molecule at high pH environments. Conditions: $[\text{Bbtan}] = 1.4 \times 10^{-4} \text{ M}$, $\mu = 0.10 \text{ (NaClO}_4\text{)}$, $T = 25 \text{ }^\circ\text{C}$, D_2O solvent. Experiment performed and NMR spectra collected by Heekwang Park of the Hong laboratory.....223

Figure 5.5. Potentiometric titration of Fragment 3-4 of Bbtan. [Frag34] = 5.8×10^{-4} M, T = 25 °C, and $\mu = 0.10$ (NaClO ₄).....	225
Figure 5.6. Spectrophotometric titration of Fragment 1-2 over the pH range of 2.7 to 11.0. [Frag12] = 1.7×10^{-4} M, T = 25 °C, and $\mu = 0.10$ (NaClO ₄). Arrows indicate the direction of spectral change with increasing pH.....	226
Figure 5.7. Spectrophotometric titration of the Fe(III)-Bbtan system at a 1:1 M:L molar ratio. [Bbtan] = 2.4×10^{-4} M, [Fe ³⁺] = 2.3×10^{-4} M, T = 25 °C, and $\mu = 0.10$ (NaClO ₄). Arrows indicate the direction of spectral change with increasing pH above pH 8.1.	228
Figure 5.8. Spectrophotometric titration of the Fe(III)-Bbtan system at a 1:1 molar ratio. [Bbtan] = [Fe ³⁺] = 2.1×10^{-4} M, T = 25 °C, and $\mu = 0.10$ (NaClO ₄). Arrows indicate the direction of spectral change with decreasing pH.....	229
Figure 5.9. Competition titration reaction between the Fe(III)-Bbtan complex and EDTA. [Fe ³⁺] = 2.5×10^{-4} M, [Bbtan] = 2.6×10^{-4} M, T = 25 °C, $\mu = 0.10$ (NaClO ₄), and pH = 7.03 (50 mM HEPES buffer). Spectra measured at 0 equivalents of EDTA, 2 equivalents of EDTA, and 25 equivalents of EDTA are marked for clarity.....	230
Figure 5.10. Cyclic voltammogram measured for the Fe(III)-Bbtan complex at pH 7.20. [Fe ³⁺] = [Bbtan] = 4.2×10^{-4} M, T = 25 °C, $\mu = 0.10$ M (NaClO ₄). Potential is shown on the plot against NHE. Working electrode: HDME, auxiliary electrode: Pt wire, reference electrode: Ag/AgCl, 3.5 M KCl, scan rate = 50 mV/sec.....	231
Figure 5.11. Cyclic voltammogram measured for the Fe(III)-Bbtan complex at pH 7.32. [Fe ³⁺] = [Bbtan] = 4.8×10^{-4} M, T = 25 °C, $\mu = 0.10$ M (NaClO ₄). Potential is shown on the plot against NHE. Working electrode: HDME, auxiliary electrode: Pt wire, reference electrode: Ag/AgCl, 3.5 M KCl, scan rate = 200 mV/sec.....	232
Figure 5.12. Cyclic voltammogram measured for the Fe(III)-Bbtan complex at pH 7.27. [Fe ³⁺] = 4.2×10^{-4} M, [Bbtan] = 6.3×10^{-4} M, T = 25 °C, $\mu = 0.10$ M (NaClO ₄). Potential is shown on the plot against NHE. Working electrode: HDME, auxiliary electrode: Pt wire, reference electrode: Ag/AgCl, 3.5 M KCl, scan rate = 50 mV/sec.....	232
Figure 5.13. Cyclic voltammogram measured for Bbtan in the absence of iron(III) at pH 7.24. [Bbtan] = 4.2×10^{-4} M, T = 25 °C, $\mu = 0.10$ M (NaClO ₄). Potential is shown on the plot against NHE. Working electrode: HDME, auxiliary electrode: Pt wire, reference electrode: Ag/AgCl, 3.5 M KCl, scan rate = 50 mV/sec.....	233
Figure 5.14. Cyclic voltammogram measured for Bbtan Fragment 1-2 in the absence of iron(III) at pH 9.40. [Bbtan] = 2.6×10^{-4} M, T = 25 °C, $\mu = 0.10$ M (NaClO ₄). Potential is	

shown on the plot against NHE. Working electrode: HDME, auxiliary electrode: Pt wire, reference electrode: Ag/AgCl, 3.5 M KCl, scan rate = 50 mV/sec.....235

Figure 5.15. Potentiometric titration of the Zn-Bbtan system (a) without metal present and (b and c) with 1:1 equivalent concentration of metal ion present. Titrations (b) and (c) are two replicate titrations of the same system. Conditions: without metal – [Bbtan] = 6.1×10^{-4} M, $T = 25$ °C and $\mu = 0.10$ M (NaClO₄); with metal - [Zn²⁺] = [Bbtan] = 1.4×10^{-4} M, $T = 25$ °C and $\mu = 0.10$ M (NaClO₄).....235

Figure 5.16. Potentiometric titrations of the Bbtan system in the presence of one equivalent Ni²⁺ or Zn²⁺. Concentrations of Bbtan all approximately 1.5×10^{-4} M, molar ratio of metal:ligand is 1:1 in all experiments. Numbers of nickel or zinc titrations represent the number of replicate titrations performed of that system. Conditions: Ni²⁺ titrations – [Ni²⁺] = [Bbtan] = 1.5×10^{-4} M, $T = 25$ °C and $\mu = 0.10$ M (NaClO₄); Zinc titrations - [Zn²⁺] = [Bbtan] = 1.4×10^{-4} M, $T = 25$ °C and $\mu = 0.10$ M (NaClO₄).....236

Figure 5.17. Proposed solution structure of the iron-Bbtan complex.....241

Figure 5.18. Plot of pFe as a function of pH for 3 siderophores. Legend: solid line – Bbtan, dashed line – Exochelin MS, dashed and dotted line – Exochelin MN. Conditions: [Fe³⁺] = 1 μM, [L] = 10 μM, $T = 25$ °C, $\mu = 0.10$ M (NaClO₄).....246

Figure 5.19. Schematic representation of iron acquisition and transport in mycobacteria. Diagram illustrates the effect of high inner cell membrane surface concentration on mycobactin (Mbt) extracting Fe³⁺ from the extracellular Fe-exochelin complex, followed by FMR reduction of Fe-Mbt and passage of Fe²⁺ through the membrane into the cell.

.....252

Figure 6.1. Chemical structures of the β-lactam moiety utilized in antimicrobial agents, such as the commercially-available Aztreonam and penicillin G.....256

Figure 6.2. Representative structures of β-lactam based Trojan horse antibiotics, Pirazmonam and PF-02538084 (L^{PF}). The ionizable groups of L^{PF} are highlighted in larger text. Also shown are the analogous hydroxypyridinone iron chelators, 1,2-dimethyl-3-hydroxy-4-pyridinone, DMHP, and 3-hydroxy-4-pyridinone, 3,4-HOPO.....257

Figure 6.3. UV-Visible spectra obtained from the competition experiment between the Fe(HL^{PF})₃³⁻ complex and EDTA. The concentration ratio of EDTA to iron(III) ranges from 0 equivalents EDTA to 10 equivalents EDTA. Experiment was performed in 0.25 M MES buffer at pH 6.03, $T = 25$ °C and $\mu = 0.10$ M (NaClO₄).....262

Figure 6.4. Spectra of three separate equilibria observed in the spectrophotometric titration of L^{PF}. [L^{PF}]_{tot} = 30 μM, $\mu = 0.10$ M (NaClO₄), $T = 25$ °C. (A) pH 2.1 to 5.6, (B) pH 6.9 to 9.2, (C) above pH 10.....265

Figure 6.5. Potentiometric titration of L^{PF} , showing the plot of pH versus mol OH/mol ligand. Conditions: $[L^{PF}]_{tot} = 1.0 \text{ mM}$, $\mu = 0.10 \text{ M}$ (NaClO_4), $T = 25 \text{ }^\circ\text{C}$268

Figure 6.6. Speciation diagram for (A) the free ligand L^{PF} , (B) the Fe(III)- L^{PF} system and (C) the Fe(III)-DMHP system, calculated using the determined and literature equilibrium constants. Graph shows relative amount of total iron in different forms over a range of pH values. In graph (A), $[\text{Fe}^{3+}]_{tot} = 0 \text{ M}$, $[L^{PF}]_{tot} = 10^{-5} \text{ M}$, $T = 25 \text{ }^\circ\text{C}$ and $\mu = 0.10$ (NaClO_4). In graphs (B) and (C), $[\text{Fe}^{3+}]_{tot} = 10^{-6} \text{ M}$, $[L]_{tot} = 10^{-5} \text{ M}$, $T = 25 \text{ }^\circ\text{C}$ and $\mu = 0.10$ (NaClO_4). Key: (A) I = H_4L^{PF+} , II = H_3L^{PF} , III = H_2L^{PF-} , IV = HL^{PF2-} , and V = L^{PF3-} . (B) I = $\text{Fe}(\text{HL}^{PF})(\text{H}_2\text{O})_4^+$, II = $\text{Fe}(\text{HL}^{PF})_2(\text{H}_2\text{O})_2^+$, III = $\text{Fe}(\text{HL}^{PF})_3^{3-}$, VI = $\text{Fe}(\text{HL}^{PF})_2(L^{PF})_4^+$, and V = $\text{Fe}(\text{HL}^{PF})(L^{PF})_2^{5-}$. VI-VIII represent hydrolyzed forms of free metal ion, $\text{Fe}(\text{OH})_2^+$, $\text{Fe}(\text{OH})_2^+$, and $\text{Fe}(\text{OH})_4^+$, respectively. (C) I = $\text{Fe}(\text{DMHP})(\text{H}_2\text{O})_4^{2+}$, II = $\text{Fe}(\text{DMHP})_2(\text{H}_2\text{O})_2^+$, III = $\text{Fe}(\text{DMHP})_3$, and IV = $\text{Fe}(\text{OH})_4^+$. In both (B) and (C), Fe represents free aqueous iron(III).....269

Figure 6.7. Spectrophotometric titration of the Fe(III)- L^{PF} system over a range of L^{PF} :Fe ratios from 3:2 to 4:1. Absorbances are corrected for dilution. Conditions: $[\text{Fe}^{3+}]_{tot} = 3.0 \times 10^{-4} \text{ M}$, $\text{pH} = 7.01$ (0.25 M MES buffer), $\mu = 0.10 \text{ M}$ (NaClO_4), $T = 25 \text{ }^\circ\text{C}$. Arrow indicates the change in spectral intensity as the L^{PF} :Fe ratio increased. Solutions were stored out of the light until measurement to prevent complex degradation.....271

Figure 6.8. Diamonds/left y-axis represents a plot of absorbance at 449 nm for a series of spectra measured over a range of ratios of ligand to metal for the Fe- L^{PF} system. The line/right y-axis represents a theoretical fit of percent iron bound in the $\text{Fe}(\text{HL}^{PF})_3^{3-}$ complex as a function of moles ligand:moles Fe(III). The theoretical fit was calculated from the speciation simulation of the Fe- L^{PF} system using the determined complex formation constants and the protonation constant of the hydroxypyridinone donor group as described in the text. Spectra were measured in a 0.10 M NaClO_4 solution buffered at pH 7.01 with 0.25 M MES, $T = 25 \text{ }^\circ\text{C}$. Solutions were stored out of the light until measurement to prevent complex degradation.....272

Figure 6.9. Spectrophotometric titration of the 5:1 L^{PF} :Fe system as a function of pH from pH 2.3 to 10.6. (A) Spectra measured over the pH range of 2.3 to 5.5. (B) Spectra measured over the pH range of 6.1 to 7.9. (C) Spectra measured over the pH range of 8.2 to 10.6. Conditions: $[\text{Fe}^{3+}]_{tot} = 1.05 \times 10^{-4} \text{ M}$, $[L^{PF}]_{tot} = 5.26 \times 10^{-4} \text{ M}$, $T = 25 \text{ }^\circ\text{C}$, $\mu = 0.10$ (NaClO_4). Arrows indicate the direction of spectral shifts with changes in pH.....274

Figure 6.10. Spectrophotometric titration of the 5:1 L^{PF} :Fe system as a function of pH over the pH range of 11.8 to ~2.0. (A) Spectra measured over the pH range of 11.8 to 8.1. (B) Spectra measured over the pH range of 8.1 to 6.1. (C) Spectra measured over the pH range of 6.1 to ~2.0. Conditions: $[\text{Fe}^{3+}]_{tot} = 2.9 \times 10^{-4} \text{ M}$, $[L^{PF}]_{tot} = 1.5 \times 10^{-3}$, $\mu = 0.10 \text{ M}$ (NaClO_4), $T = 25 \text{ }^\circ\text{C}$. Arrows indicate the direction of spectral shifts with decreasing pH.

.....275

Figure 6.11. Spectrophotometric titration of the 5:1 L^{PF}:Fe system as a function of pH from pH 6.3 to ~0.4. (A) Spectra measured over the pH range of 6 to 2.7. (B) Spectra measured over the pH range of 2.7 to ~0.4. Conditions: [Fe³⁺]_{tot} = 1.19 × 10⁻⁴ M, [L^{PF}]_{tot} = 6.7 × 10⁻⁴ M, T = 25 °C, μ = 0.10 (NaClO₄). Arrows indicate the direction of spectral shifts with decreasing pH.....276

Figure 6.12. Proposed structure of the 3:1 L^{PF}:Fe complex at physiological pH, Fe(HL^{PF})₃³⁻.....278

Figure 6.13. Plot of pFe values over a range of pH values for the Fe(III)-L^{PF} system (solid line), the Fe(III)-3,4-HOPO system (dotted line) and the Fe(III)-DMHP system (dashed line). For both graphs, [Fe³⁺]_{tot} = 10⁻⁶ M, [L]_{tot} = 10⁻⁵ M, and all constants used in the analysis were measured at 25 °C and μ = 0.10 (NaClO₄).....283

Figure 6.14. Cyclic voltammetric titration of a 1:5 M:L molar ratio solution of the Fe(III)-L^{PF} system. Representative voltammograms are shown for the three pH ranges observed during the titration. (A) – pH 1.4, E_{red1} = -70 mV vs NHE, E_{red2} = -500 mV vs NHE, (B) – pH 3.8, E_{red1} = -84 mV vs NHE, E_{red2} = -506 mV vs NHE, (C) – pH 7.4, E_{red1} = -30 mV vs NHE, E_{red2} = -385 mV vs NHE. Conditions: [Fe³⁺]_{tot} = 1 mM, [L^{PF}]_{tot} = 5 mM, T = 25 °C, μ = 0.20 (NaClO₄), reference electrode: Ag/AgCl, 3.5 M KCl, auxiliary electrode: Platinum wire, working electrode: hanging drop mercury electrode, scan rate: 20 mV/sec...286

Figure 6.15. Cyclic voltammogram of a 2.5 × 10⁻³ M solution of L^{PF} in the absence of Fe(III) in 0.50 M KCl/0.50 M MOPS at pH 7.2. T = 25 °C, reference electrode: Ag/AgCl, 3.5 M KCl, auxiliary electrode: Platinum wire, working electrode: hanging drop Hg electrode, scan rate: 20 mV/sec.....288

Figure 6.16. Cyclic voltammogram of a 5:1 L:M solution of Fe(III) and DMHP in 0.10 M NaNO₃/0.20 M MOPS at pH 7.2. [Fe³⁺]_{tot} = 1.5 × 10⁻³ M, [DMHP]_{tot} = 7.6 × 10⁻³ M, T = 25 °C, reference electrode: Ag/AgCl, 3.5 M KCl, auxiliary electrode: Platinum wire, working electrode: hanging drop mercury electrode, scan rate: 20 mV/sec.....289

Figure 7.1. Chemical structures of the exocyclic siderophore mimics studied here by computational simulations.....294

Figure 7.2. Chemical structures of three ferrioxamines, B, D, and E. The strain energy of complex formation of these ligands was calculated to verify the method for use on the tris-hydroxamate siderophore mimics.....298

Figure 7.3. General structures of the mer- and fac- isomers of a series of tris-hydroxamic acid synthetic chelators.....301

Figure 8.1. Chemical structures of the chelating agents studied here for toxicity and protective effects from metals.....315

Figure 8.2. Histogram correlating pM value of chelator with cadmium to calculated P-value of treatment of *C. elegans* with metal and chelator. pM values taken from Table 8.3. and P-values taken from Table 8.2.....333

Figure 8.3. Histogram correlating pM value of chelator with copper to calculated P-value of treatment of *C. elegans* with metal and chelator. pM values taken from Table 8.3. and P-values taken from Table 8.2.....334

Figure 8.4. Histogram correlating pM value of chelator with nickel to calculated P-value of treatment of *C. elegans* with metal and chelator. pM values taken from Table 8.3. and P-values taken from Table 8.2.....335

Figure 8.5. Histogram correlating pM value of chelator with zinc to calculated P-value of treatment of *C. elegans* with metal and chelator. pM values taken from Table 8.3. and P-values taken from Table 8.2.....336

List of Abbreviations

AHA	aceto-hydroxamic acid
β	proton-independent complex stability constant
Bbtan	synthetic analog of Brasilibactin A
CaEDTA	calcium disodium ethylenediamine tetracetic acid
DMHP	1,2-dimethyl-3-hydroxy-4-pyridinone, Deferiprone
$E_{1/2}$	complex half wave redox potential
EC_{50}	concentration of toxicant that reduces growth by 50%
EDTA	ethylenediamine tetracetic acid
ESI-MS	electrospray ionization mass spectroscopy
EXT	extinction, optical density
Fe(II)	iron in the 2+ oxidation state
Fe(III)	iron in the 3+ oxidation state
FMR	ferric mycobactin reductase
HDAC	histone deacetylase
HDFB	desferrioxamine B
HEPES	N-2-hydroxyethylpiperazine-N'-2-ethanesulphonic acid
HOPO	hydroxypyridinone
i_a	anodic peak current
i_c	cathodic peak current
KHP	potassium hydrogen phthalate
K	conditional equilibrium constant
k_{obs}	observed pseudo-first order rate constant
λ_{max}	wavelength of maximum absorbance
L^{234}	exocyclic configuration with arms at the 2, 3, and 4 carbon
L^{236}	exocyclic configuration with arms at the 2, 3, and 6 carbon
L_N	normal hydroxamate configuration
L^{PF}	PF-02538084

L _R	retrohydroxamate configuration
Mbt	mycobactin
MES	2-[N-morpholino]ethane sulphonic acid
NADH	β-nicotinamine adenine dinucleotide (reduced form)
NaOAc	Sodium acetate
NHE	normal hydrogen electrode
NMAHA	N-methylacetohydroxamic acid
NTBI	non-transferrin bound iron
TOF	time of flight, length

Acknowledgements

I owe a great debt of gratitude to so many people who have been there for me as I've been through my studies. I never would have guessed a number of years ago that this would be where I would end up, and getting here has been due to so many people. I would like to thank Dr. Crumbliss for being such an excellent mentor. You have given everything that you could give and have been so supportive through times of great productivity and great futility. Your guidance will not be soon forgotten as it's meant so much to me.

I also thank my parents for supporting me and being caring and understanding. Being so close to you has been exactly what I've needed just when I've needed it. I've done everything that I could to make myself into someone of whom you could be proud, even though I know that you would be proud of me no matter what.

I've been through a lot these years, and I've gone through so much of it with the people living in the desks beside me. The Crumbliss lab, Claire, Esther, Jared, Kassy, and Katherine, listened with open ears to big ideas and crummy jokes, and knowing that they understood what was going on has meant so much to me.

I would not have been able to get to this place if I hadn't been set on the path in the right way at the start. I have to thank my undergraduate advisors, Drs. Robert Hancock and S. Bart Jones. They gave me a thirst for knowledge, a passion for chemistry, and a helping hand as a confused undergrad.

Finally, I want to thank Carol Ann, my dearest. I've needed you more than anything else, and I've been so much better off having you by my side.

1. Introduction

Aspects of this chapter were taken from Crumbliss and Harrington, 2009.(1)

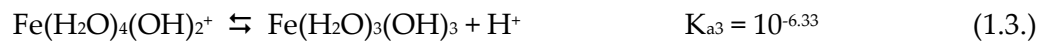
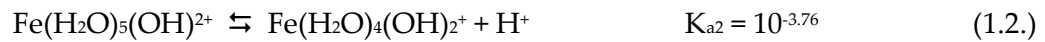
Organisms have evolved in the presence of a variety of metals, to make use of them in normal processes that maintain life. Metals are used for a variety of purposes, ranging from catalysis of biomolecular synthesis reactions to transport and storage of small molecules through the biological system. However, there are some chemical limitations that must be overcome in order for the organisms to obtain these essential metals from the environment. The problems facing organisms concerned with the use of metals are two-fold, availability and uptake.

Metal ions in solution will withdraw electron density from coordinated inner-sphere solvent molecules, increasing the likelihood that a proton will dissociate from protic solvent molecules that are so bound. This effectively causes the metal ion in a protic solvent, e.g. water, to act as an acid, and in aqueous solution will result in the formation of hydroxide and oxide complexes through loss of protons from the coordinated solvent molecules. Many of these hydroxide and oxide salts have extremely low solubility, resulting in precipitation of the metal from solution. Also, many of the metals that are present in nature are bound in large part in the matrix of a variety of minerals, making them unavailable for direct use. The second problem facing organisms with the use of metals is uptake. It is necessary for the organisms to develop

systems for selective uptake of the metals in a time- and site-specific manner. The selectively permeable membranes of cells generally prevent the uptake of many ions through simple diffusion. This has necessitated the evolution of protein or small molecule-based uptake systems directed towards selectively obtaining essential metals from the environment.

1.1 Iron bioavailability

Iron is one of the most abundant elements on the planet Earth, comprising 31.3% of the Earth's total mass.(2) It can exist in natural systems in a variety of oxidation states, most frequently 2+ and 3+. In the 3+ oxidation state, aqueous iron acts as a weak acid with pK_a's of 2.56, 3.76, and 6.33 (Eqs. 1.1.-1.3.).(3)



The metal ion will readily deprotonate and form monomeric (hydr)oxides and polymeric species and precipitate out of solution at most environmental conditions, resulting in extremely low concentrations of aqueous iron(III) on the order of 10⁻¹⁸ M. The 2+ oxidation state of the metal ion has a higher solubility than iron(III) due to lower charge density and consequently much less acidic coordinated water ligands, but it is

much less stable than the 3+ oxidation state and is oxidized upon exposure to oxygen. In the environment, iron(III) is found in the matrix of minerals such as goethite and hematite in the form of insoluble (hydr)oxides which are inaccessible to the organism.(4, 5) This makes it necessary for organisms to produce an uptake system that can solubilize the metal and compete with hydrolysis. The uptake system is often seen in the form of small organic molecules that bind to the iron with high stability thus stripping its hydrated shell and increasing its solubility.

While there are a variety of small molecules that can bind to iron with high stability, such as citrate, many organisms make use of a special class of small molecules, called siderophores to bind iron. Siderophores (from the Greek term for “iron carrying”) are molecules on the order of 1 kD that bind to iron with high stability and high specificity, preventing hydrolysis of the metal ion and providing surface features for site-specific recognition at the cell that aid in uptake of the iron-siderophore complex. These molecules are released in iron-stress conditions to aid in the uptake of the metal ion for use by the organism. A recent comprehensive review of the chemistry and reactivity of siderophores has been published.(1)

1.2 Iron geochemistry

As mentioned previously, iron in the environment is present in the form of insoluble oxide and hydroxide salts in the matrix of minerals such as goethite and

hematite. Since iron is not bioavailable in these forms, the cell requires a mechanism of making the iron bioavailable (soluble) before it can be taken up into the cell. This can be achieved primarily by two methods, excretion of ferric reductases or by chelation of the iron by the siderophore.(6) Reductases serve to convert the iron(III) to iron(II), increasing both the solubility of the iron and the kinetics of exchange in the inner coordination sphere, resulting in dissolution of the iron. Once free, the metal can then react with molecular oxygen in the aerobic system to oxidize the iron to the 3+ oxidation state. It has also been suggested that some siderophores can react with iron(II) to re-oxidize it to iron(III), providing an alternative route to re-oxidation.(7, 8) In the case of the siderophore desferrioxamine B, it has been proposed that the siderophore will bind iron(II) and then react through an inner-sphere electron transfer reaction to produce iron(III) and a DFB-monoamide reduction product. Iron that is located at the surface of the mineral may be partially hydrated, providing sites for exchange of water with donor groups from a siderophore. Once this partial chelation occurs, the kinetics of inner coordination sphere exchange increases, leading to solubilization of the iron into the environment.(5, 9, 10)

1.3 Siderophore features and architecture

Siderophores are found in a variety of systems, produced by a wide range of organisms, plant, fungal, and bacterial, but there are some unifying design concepts and architectural features that can be observed between different siderophores. Most

siderophores feature common bidentate binding groups, resulting in most siderophores featuring bidentate, tetradentate, or hexadentate binding modes.

1.3.1 Common Siderophore Architectures

In the hexadentate siderophores, the overall architecture of the siderophore can be classified into a few common categories. The most common architectures observed in natural hexadentate siderophores are linear, endocyclic, and exocyclic (Fig. 1.1.).

Siderophores exhibiting the linear architecture feature an acyclic backbone with the

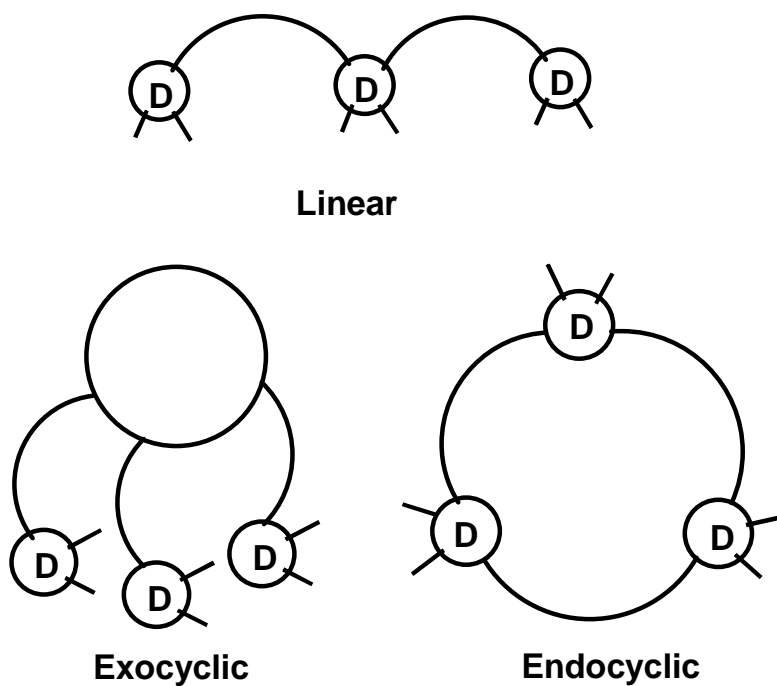


Figure 1.1. General scheme of common architectures exhibited in natural hexadentate siderophores, linear, exocyclic, and endocyclic. D represents a generic bidentate donor unit.

binding sites of the chelator contained either in the backbone of the siderophore or on arms attached to the backbone. Examples of this architecture type include most of the desferrioxamines, exochelins MN and MS, and aerobactin (Fig. 1.2.). An example of a linear siderophore featuring binding sites attached to the backbone through linkers is basidiochrome, Fig. 1.2. The endocyclic architecture features a macrocyclic backbone which incorporates the binding sites of the siderophore. This architecture type has been observed in a number of siderophores, such as the fungal tris-hydroxamate siderophores desferrioxamine E and neurosporin (Fig. 1.3.). Endocyclic architecture provides a great deal of preorganization, which can result in highly stable complexes with iron. The preorganization observed in endocyclic siderophores promotes higher complex stability with hydroxamate donor groups than with analogous linear forms.^(11, 12) However, there have been no naturally observed examples of endocyclic catecholate siderophores. It is likely that the preorganization inherent to endocyclic architecture would place too high of a steric strain on the rigid conjugated ring system of the catechol donor group. Exocyclic siderophores feature a macrocyclic backbone and binding sites attached to the macrocycle by spacers, as observed in ferrichrome and enterobactin (Fig. 1.4.). While some siderophores are difficult to classify under this system, such as the cell-wall bound mycobactin family of siderophores, the majority of hexadentate siderophores fall under one of those three general architectures.

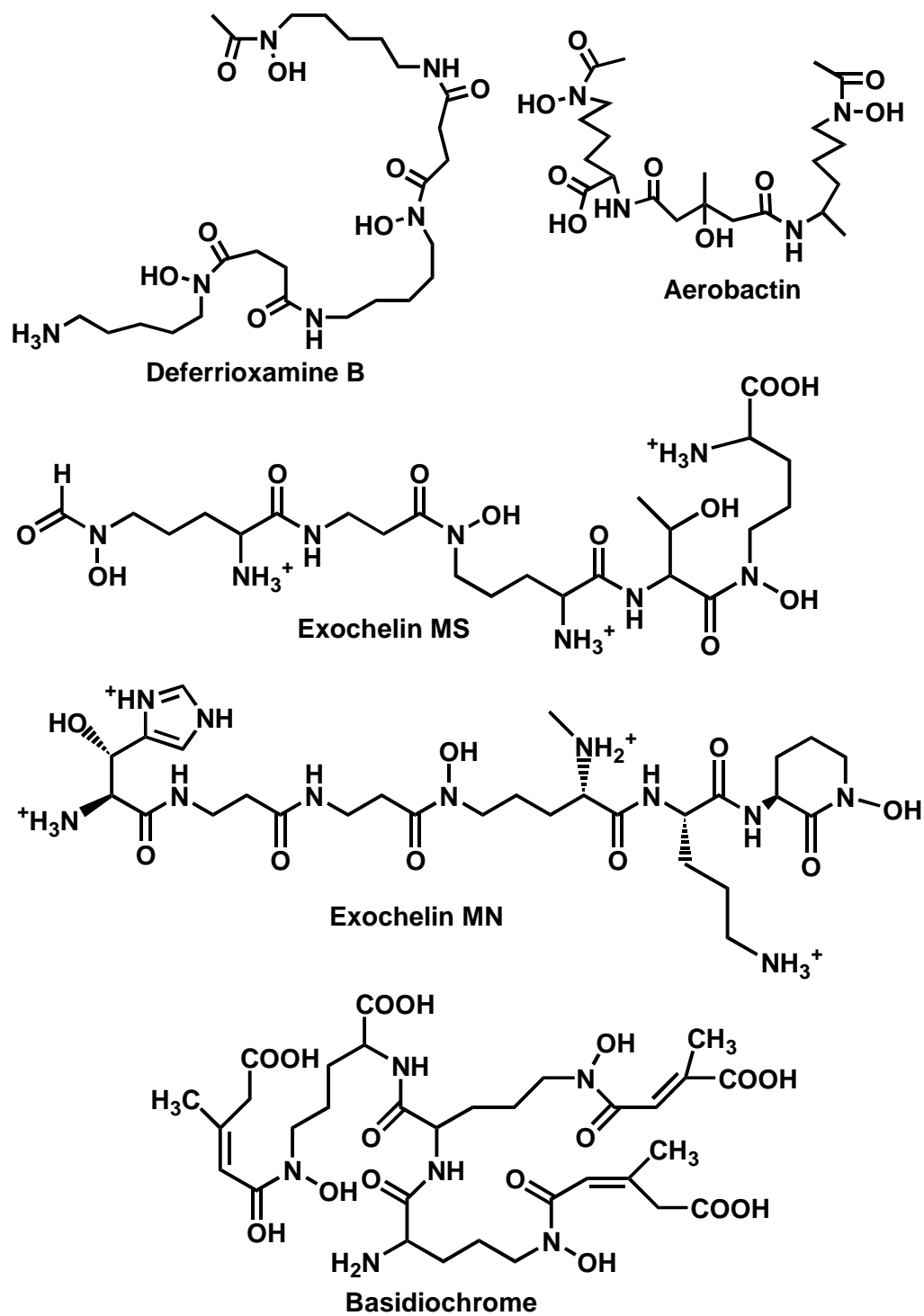


Figure 1.2. Chemical structure of select natural siderophores featuring the linear architecture.

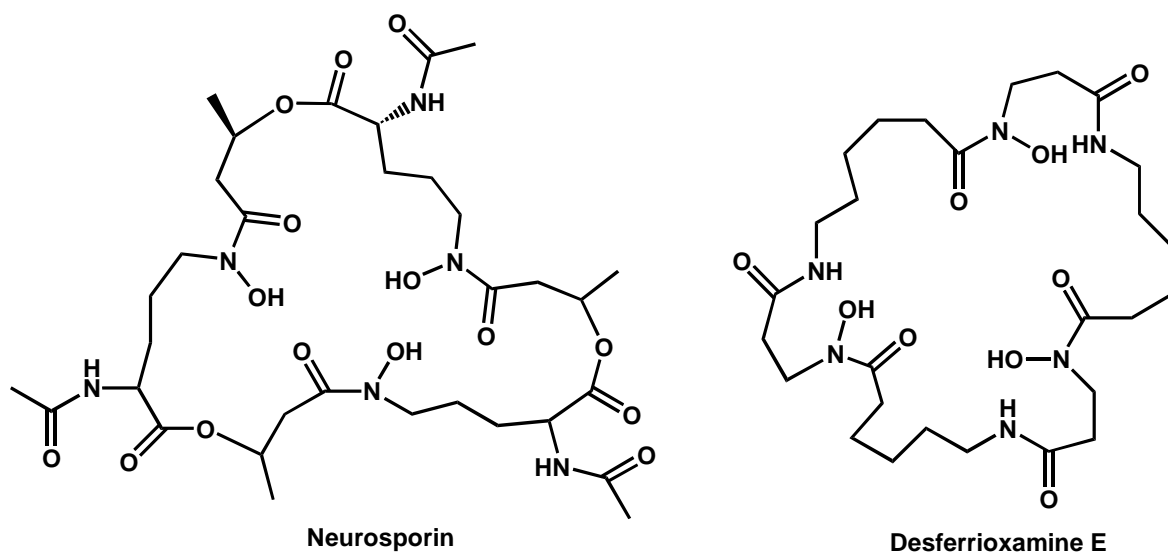


Figure 1.3. Chemical structure of select natural siderophores featuring the endocyclic architecture, neurosporin and desferrioxamine

E.

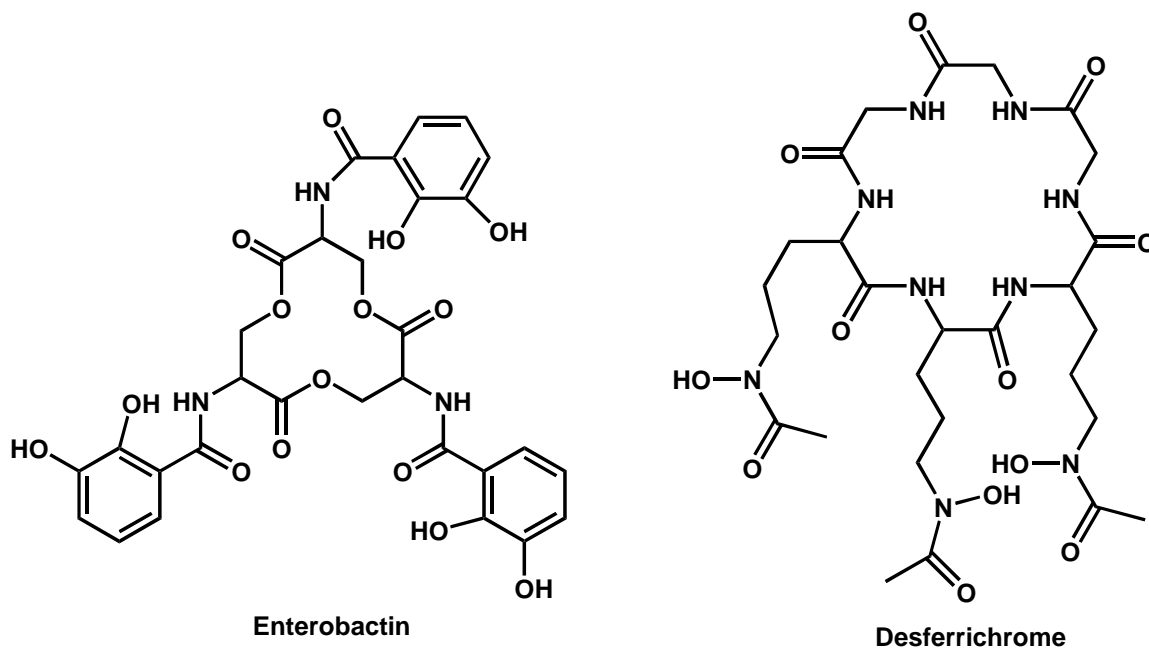
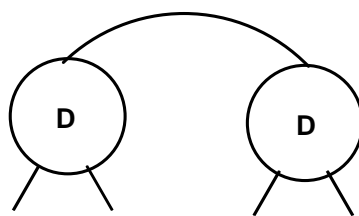


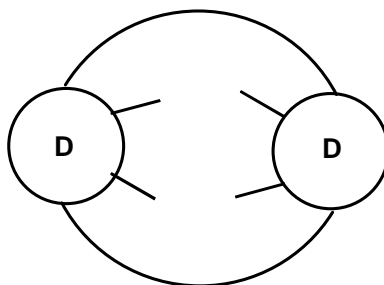
Figure 1.4. Chemical structure of select natural siderophores featuring the exocyclic architecture, enterobactin and ferrichrome.

Tetradentate siderophores can feature similar architectures as hexadentate siderophores, as linear, endocyclic, and exocyclic architectures are also observed (Fig. 1.5.). One example of a linear tetradentate siderophore is mugineic acid, a siderophore featuring an α -hydroxycarboxylic acid donor group and two carboxylate donor groups (Fig. 1.6.). Some endocyclic tetradentate siderophores are the bishydroxamate siderophores alcaligin and bisucaberin (Fig. 1.6.). Rhodotorulic acid can be viewed as an example of an exocyclic tetradentate siderophore (Fig. 1.6.), as the two hydroxamate donor groups extend at the end of arms from a central 6-membered ring.

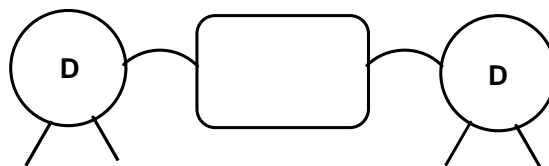
The architecture of the siderophore will contribute to the structure of the iron complex. Hexadentate siderophores will most often form 1:1 L:M complexes with iron, although it may be possible to observe polymeric species. In the case where the donor group is acidic, the coordination state of the complex will vary depending on the solution pH. At lower pH values, the concentration of protons in solution will be high enough that the protonation of the donor group will effectively compete with chelation of iron by the donor group. This will result in the formation of an MLH complex, where one donor group is protonated and the others remain chelated to the metal (Fig. 1.7.). Further decrease in the solution pH can cause a second donor group to become protonated, followed by complete dissociation of the iron-siderophore complex.



Linear

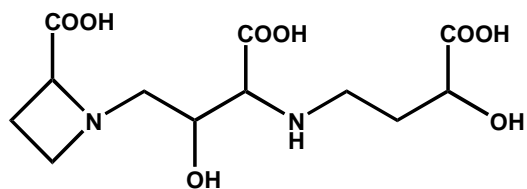


Endocyclic

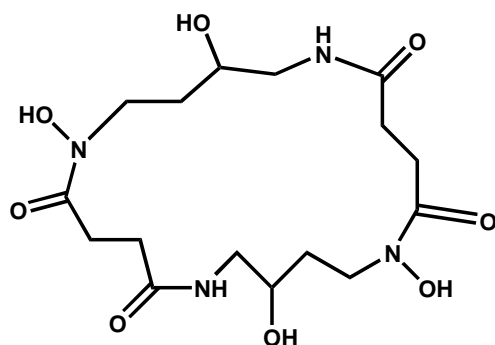


Exocyclic

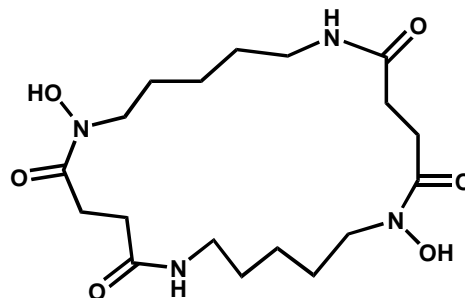
Figure 1.5. General scheme of architectures exhibited in natural tetradentate siderophores, linear, exocyclic, and endocyclic. D represents a bidentate donor moiety, usually a hydroxamic acid or a catechol group.



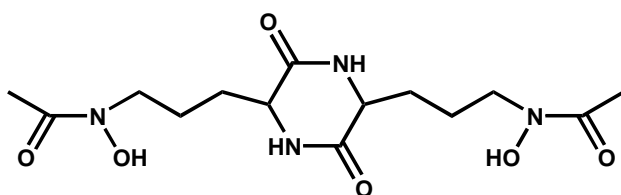
Mugineic acid



Alcaligin



Bisucaberin



Rhodotorulic acid

Figure 1.6. Chemical structures of some natural tetradentate siderophores, mugineic acid, alcaligin, bisucaberin, and rhodotorulic acid.

In the case of the catecholamide siderophores, protonation may not necessarily result in dissociation of a binding group. In many catecholate siderophores, the donor group is connected to the backbone through an amide chain spacer. Upon protonation of a catecholate donor group, the distal oxygen is preferentially protonated, resulting in

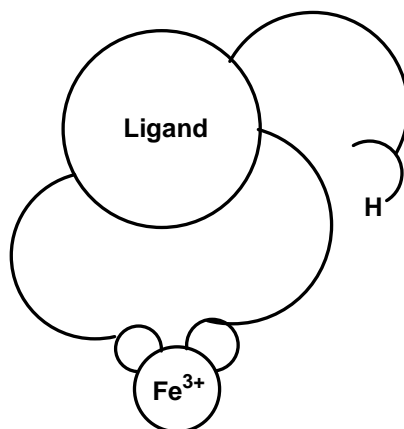


Figure 1.7. General structure of protonated iron(III)-hexadentate siderophore complex, the MLH complex.

a shift of the binding mode of the donor group from catecholate binding to salicylate binding (Fig. 1.8).(13) This shift in binding mode has been observed in the natural exocyclic siderophore enterobactin, as well as the siderophore L-01, shown in Fig. 1.9.(14) It has been proposed that this feature of catecholamide siderophores is advantageous, as the intercellular environment may be at a lower pH level than in the cellular surroundings. Upon protonation of the donor group, the binding site shifts, as evidenced by the spectral shift of the complex solution. While the shift of donor group allows the iron to remain in solution and complexed, the stability of binding of iron(III) is significantly decreased compared to the tris-catecholate binding mode. It has also been observed that the redox potential of iron-catecholamide complexes will shift depending on the solution pH, as the less stable chelation by the salicylate mode of

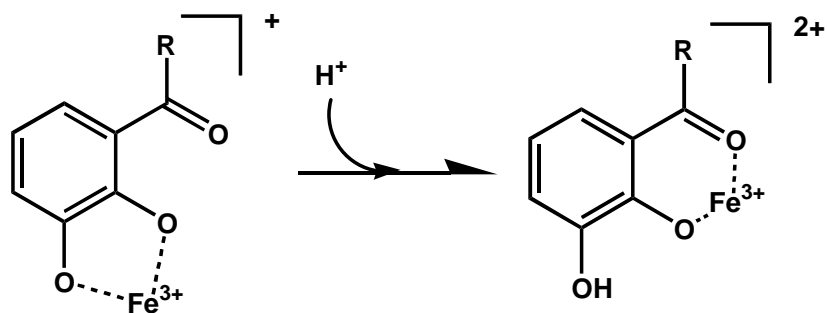


Figure 1.8. Protonation reaction of the catecholamide donor group, resulting in salicylate-mode coordination of iron(III).

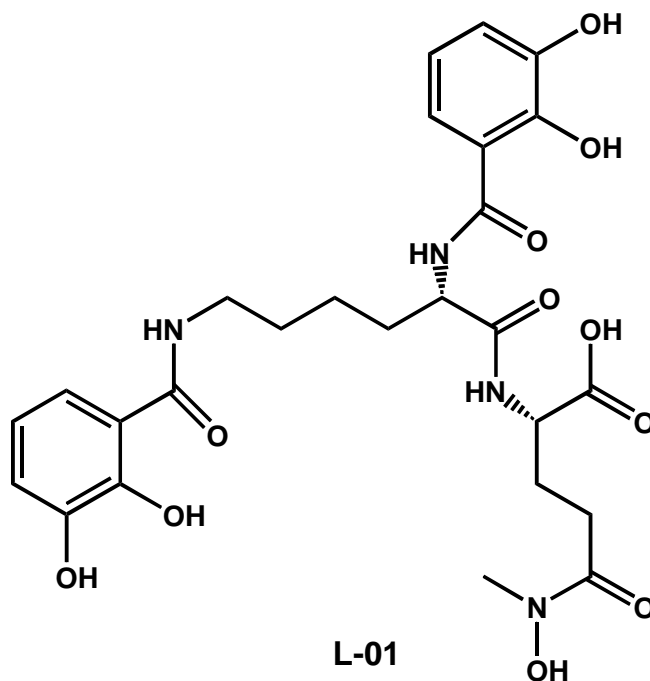


Figure 1.9. Chemical structure of the monohydroxamate, biscatecholate siderophore mimic L-01. Its iron(III) complex has been shown to exhibit a salicylate shift at both catecholamide donor groups upon lowering the solution pH.

binding results in a shift in complex redox potential (iron-siderophore redox chemistry will be discussed in more detail in Sec. 1.5.).⁽¹³⁾ When iron is bound by the catechol donor group, there are two hard, negatively charged oxygen donor atoms arranged in a five-member ring system, which is ideal for chelating iron(III). The shift to salicylate binding mode results in binding to iron through one charged oxygen donor and an uncharged ketone oxygen donor with the donor group arranged in a six-membered ring.

In the case of tetradentate siderophores, there are a number of stoichiometries and geometries that the complex can form over a range of pH values depending on the molar ratio of ligand concentration to metal concentration. At higher pH values, tetradentate siderophores can bind to iron(III) in a 2:3 Fe:L stoichiometry to fulfill the optimal hexacoordinate geometry. This complex can take two forms depending on the architecture of the siderophore; singly-bridged or triply-bridged (Fig. 1.10.). In linear tetradentate siderophores and siderophore mimics, the length of the spacer chain between the donor groups is one determining factor between formation of a singly- or triply-bridged complex. A study of synthetic models for rhodotorulic acid found that a six-carbon chain length between the hydroxamate donor groups was a crossover point from triply-bridged to singly-bridged complex formation.⁽¹⁵⁾ Chain lengths greater than 6 carbons resulted in triply-bridged complexes, while chain lengths shorter than 6 carbons resulted in singly-bridged complexes. This difference in binding mode preference is mainly due to entropic effects. In the case of rhodotorulic acid, it has been

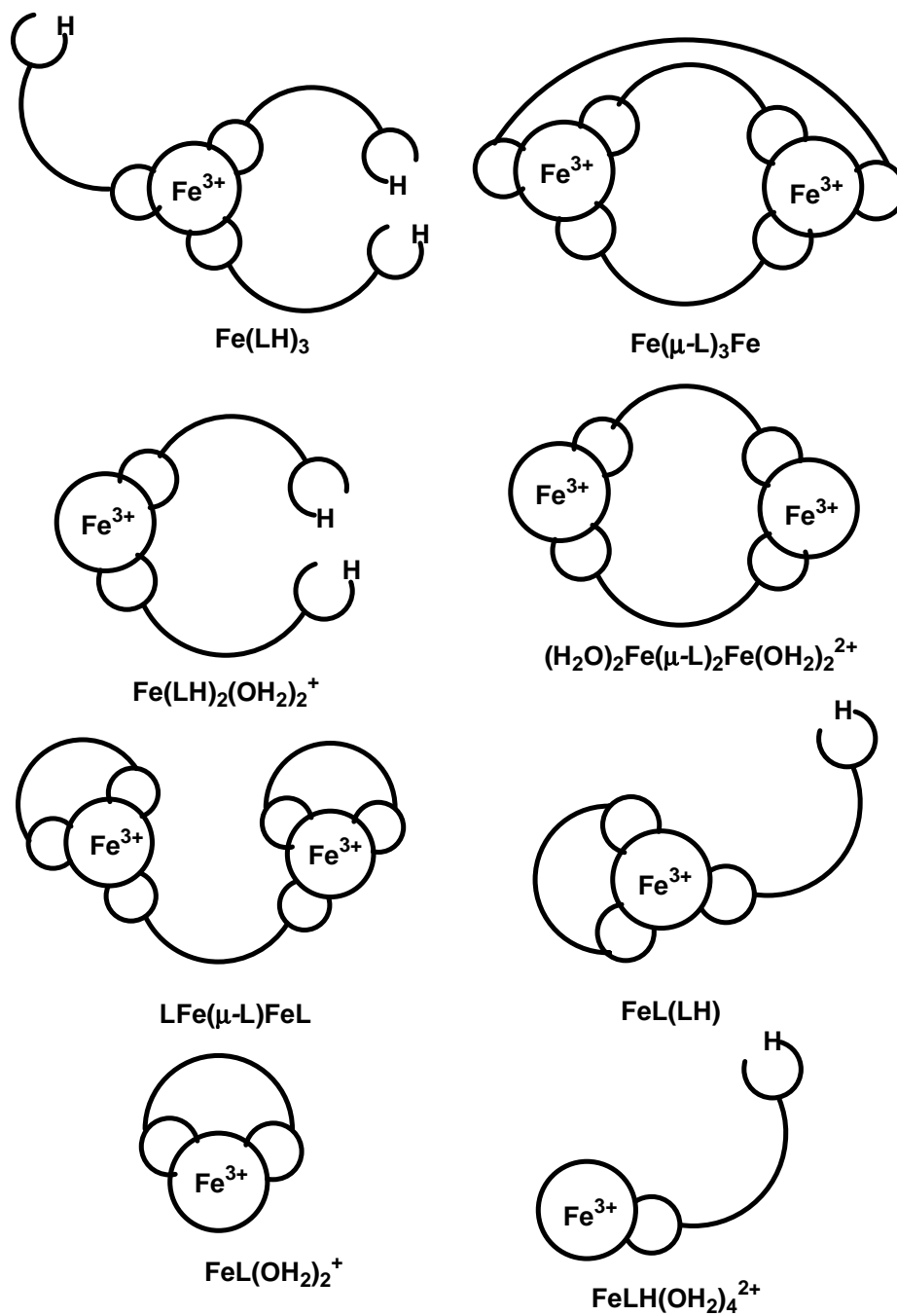


Figure 1.10. All possible solution structures of iron(III)-tetradentate siderophore complexes. The actual structure of the complex will vary based on the structure of the chelator, solution pH, and the L:M ratio in solution.

proposed to form a triply-bridged complex with iron(III) in solution based on crystallographic and mass spectrometric evidence.(16) Alcaligin, however, would exhibit a high amount of steric interaction in the triply-bridged form and as such it has been observed to form singly-bridged complexes with iron(III).(11, 17) The structure of the complex can also vary depending on the molar ratio of iron(III) to ligand in solution and the solution pH. As the Fe:L ratio decreases, there is a likelihood of complexes such as the $\text{Fe}(\text{LH})_3$ complex forming, and as the pH decreases or the Fe:L ratio increases, the FeL or FeLH complex will form (Fig. 1.10.).

Higher denticity chelating agents can also feature an increase in complex stability when compared to chelators of lower denticity with homologous donor groups, a phenomenon known as the chelate effect. This can be observed by comparing the stability constants of systems such as mono-hydroxamate molecules (such as acetohydroxamic acid) with those of bis- and tris-hydroxamate siderophore systems (such as ferrichrome or rhodotorulic acid). The chelate effect is not always observed in siderophores, however, depending on the architecture of the molecule.(16, 18-20) In cases such as desferrioxamine B, the chelate effect is not observed, likely because the spacer chain connecting hydroxamate donor groups is too long to effect the binding of the iron center by adjacent hydroxamate donor groups.(20) The chelate effect is also often not observed in exocyclic hydroxypyridinone synthetic siderophores, as the architecture of the molecules are not optimal for binding by the donor group.(19, 21)

1.3.2 Common Siderophore Binding Moieties

While siderophores can bind iron through different binding modes, there are some common donor moieties that are observed throughout nature (Fig. 1.11.). Iron(III) has a high charge-to-radius ratio and low polarizability, and is classified as a hard Lewis acid on the Pearson Hard-Soft Acid-Base scale.(22) Thus, it will bind most stably with hard donor atoms, such as charged oxygen. Due to the size of the metal ion, it also binds preferentially to five-membered chelate rings, which feature ideal bite angles for binding to larger metal ions.(23) Despite the overwhelming presence of five-membered chelate rings in natural siderophores, there are some siderophores that feature six-membered chelate rings, such as the mycobactin family, which features a six-membered chelate ring and two five-membered chelate rings.(24)

Most common siderophore binding groups feature oxygen donor groups or uncharged N-donors. The catechol donor group is a common donor group in natural siderophores, which has high affinity for binding iron(III) due to the two charged O-donors and the delocalization of electron density through the central conjugated ring system. One model for this type of donor group that is not commonly observed in nature is the hydroxypyridinone donor group, which exhibits high affinity for binding iron(III) due to a similar electronic structure to the catechol donor group (as will be discussed in Ch. 2), but binds more effectively than the catechol donor group due to its

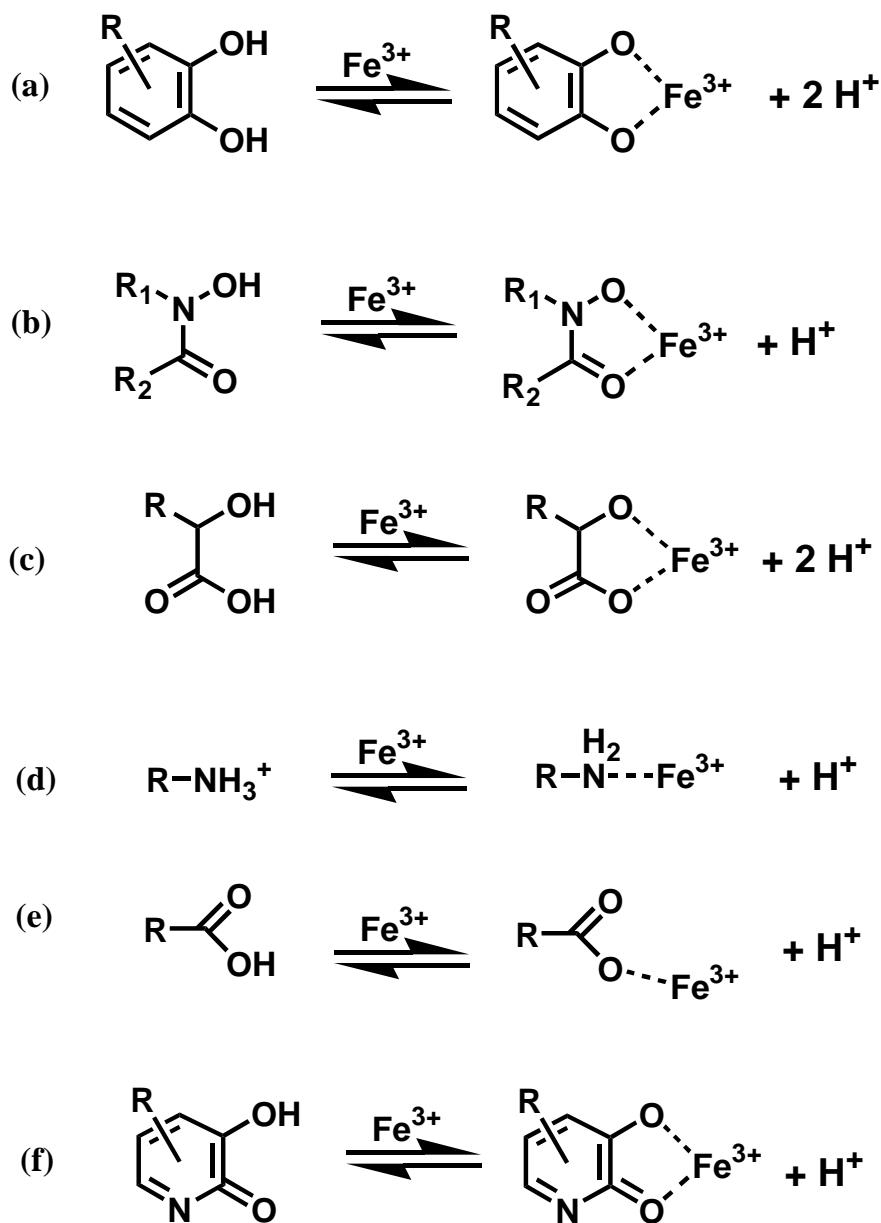


Figure 1.11. Structure of common binding groups in natural siderophores, including the (a) catechol, (b) hydroxamic acid, (c) α -hydroxycarboxylic acid, (d) amine, (e) carboxylic acid, and (f) hydroxypyridinone donor groups. Also shown is the mode of iron binding at physiological pH.

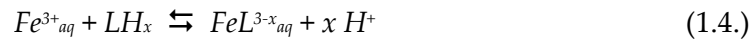
single acidic proton.(25) Another common donor group, which is featured in many fungal and bacterial siderophores is the hydroxamic acid donor group.(26) This group features a charged oxygen donor and a ketone oxygen donor for binding to the iron center. The C-N bond features partial double bond characteristics, which allows some rotation around the bond from the Z to E-configuration (Fig. 1.12.). This can make Z-to-E conversion an important step in influencing the rate of complex formation.(27, 28)

Another common donor group is the α -hydroxycarboxylic acid donor group. This donor group has been observed in many aquatic siderophores, such as aquachelin, marinobactin, and aerobactin (Fig. 1.13. and Fig. 1.2.). It has been found that many siderophores featuring this donor group are photoreactive, resulting in reduction of bound iron by the siderophore through electron transfer from the donor group to iron.(29-31) This has been hypothesized to be an advantageous characteristic for algae that live in the photic zone of the ocean, which allows for removal of iron from the extremely stable siderophore complex. Other common donor groups are the amine donor group and the carboxylic acid donor group. The order of iron(III) affinity for these common donor groups generally has been found to be catechol > hydroxamic acid > α -hydroxycarboxylic acid > single-atom donor groups.

1.4 Siderophore complex thermodynamics

As mentioned previously, many siderophore binding sites for iron(III) are acidic and therefore in aqueous solution there is a competition between H^+ and Fe^{3+} binding.

Consequently, the equilibrium expression for the formation of the iron-siderophore complex must take into account the proton dependence of the reaction (Eqs. 1.4.-1.5.).



$$K = \frac{[FeL^{3-x}][H^+]^x}{[Fe^{3+}][LH_x]} \quad (1.5.)$$

This means that the sequestration equilibrium reaction will be pH-dependent. The constant K is known as the “conditional” equilibrium constant. However, for stability comparisons between complexes of the same denticity (or number of donor atoms), it may be more convenient to compare the equilibrium constant for the proton independent reaction between iron and siderophore (Eqs. 1.6.-1.7.). This can also be useful in a theoretical sense, as it allows comparison of complex stability where siderophores have different protonation constants. However, this approach does not account for environmental or *in vivo* competition between H^+ and Fe^{3+} for binding.



$$\beta_{110} = \frac{[FeL^{3-x}]}{[Fe^{3+}][L^{x-}]} \quad (1.7.)$$

In Eq. 1.7., β_{110} corresponds to the overall stability constant of the complex, following the β_{MLH} notation. β_{MLH} is the symbol reserved for an overall stability constant, and the subscripts denote the metal (M), ligand (L), and proton (H) stoichiometry of the equilibrium expression for the complex. So, the overall stability constant expression for an $Fe_2L_3^{x-}$ complex formed from the reaction stoichiometry $2 Fe^{3+}$ and $3 L^{n-}$ would be referred to as β_{230} . In many cases, a hexadentate siderophore (L) complex can be protonated at low pH, resulting in a tetracoordinate $FeLH$ complex with a single binding group protonated, as shown in Eq. 1.8. and Fig. 1.7. (coordinated water molecules not shown for clarity).



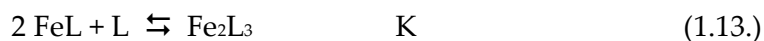
$$K = \frac{[FeLH^+]}{[FeL][H^+]} \quad (1.9.)$$

However, Eqs. 1.8. and 1.9. can be combined with the proton independent overall stability constant of the FeL complex to give an overall stability constant for the $FeLH$ complex, β_{111} .



$$\beta_{111} = \frac{[FeLH^{4-x}]}{[Fe^{3+}][L^{x-}][H^+]} \quad (1.11.)$$

Complexes formed by tetradentate siderophores have somewhat different equilibria from their hexadentate analogs, which involve stepwise complex formation. Initial chelation will occur with a tetracoordinate FeL complex forming. A subsequent equilibrium then occurs, where the FeL complexes will react in a 2:1 stoichiometry with free ligands in solution to form a single Fe₂L₃ complex (coordinated water and charges not shown for clarity).



In some cases where the siderophore architecture permits, the tetradentate siderophore will form a dimeric Fe₂L₂ complex with iron instead of the monomeric FeL form. These dimeric complexes are not discernable from their monomer counterparts by their UV-Visible spectra, although mass spectrometric methods can distinguish between the two forms as will be discussed in Ch. 2.(15)

An examination of equilibrium expressions for different siderophore denticities will illustrate nature's preference towards hexadentate siderophores. There is a concentration effect when comparing lower denticity siderophores to their higher

denticity analogs. pH-independent equilibrium expressions for generic bidentate and hexadentate siderophores are shown below, where Hx represents a hexadentate siderophore and Bd a bidentate siderophore (charges are omitted for clarity).

$$\beta_{110} = \frac{[FeHx]}{[Fe][Hx]} \quad (1.15.)$$

$$\beta_{130} = \frac{[Fe(Bd)_3]}{[Fe][Bd]^3} \quad (1.16.)$$

Rearranging these expressions to a form that displays the ratio of complexed to unbound iron gives the following equations.

$$\beta_{110}[Hx] = \frac{[FeHx]}{[Fe]} \quad (1.17.)$$

$$\beta_{130}[Bd]^3 = \frac{[Fe(Bd)_3]}{[Fe]} \quad (1.18.)$$

The stability constant equation for the bidentate complex features ligand concentration raised to the third power (Eq. 1.18.), while the hexadentate complex stability constant expression only features the ligand concentration raised to the first power (Eq. 1.17.). Consequently, assuming equivalent values for β_{110} and β_{130} , there is a much larger concentration of free bidentate siderophore required to obtain the same degree of iron

binding (e.g. 50% of total iron present where $[\text{Fe}]_{\text{bound}} = [\text{Fe}]_{\text{free}}$) than in the case of a hexadentate siderophore. Therefore, it is generally more efficient for organisms to exert the extra metabolic effort to produce hexadentate siderophores rather than their lower denticity analogs.

1.4.1 Alternative expressions of Thermodynamic stability

Stability comparisons between siderophore complexes with different binding stoichiometries are complicated by the fact that the units for the concentration equilibrium constants are different. Also, since the Fe^{3+} binding moieties have different pK_a values, competition for binding with H^+ differs, which will not be reflected in the pH independent β_{MLH} values. Therefore, it is important to have a scale for iron-siderophore complex stability that is independent of metal/ligand stoichiometry and that accounts for H^+ competition. Raymond, et al, developed the pFe scale to compare stability for a variety of complexes with different denticities and ligand pK_a values in a meaningful way at physiological conditions.(32) The pFe value is the negative logarithm of the free aqueous iron(III) concentration at arbitrary fixed $[\text{Fe}^{3+}]$, [ligand], and $[\text{H}^+]$ concentrations (Eq. 1.19.). The concentrations for pFe calculations normally found in the literature are $[\text{Fe}^{3+}]_{\text{tot}} = 1 \mu\text{M}$, $[\text{L}]_{\text{tot}} = 10 \mu\text{M}$, and $\text{pH} = 7.4$. The

$$\text{pFe} = -\log[\text{Fe}^{3+}_{\text{aq}}] \quad (1.19.)$$

calculation of pFe values takes into account the protonation constants of the siderophore and the equilibrium constants of all forms of the iron-siderophore complexes. It is important to note that these values are not a complete measure of the soluble iron concentration, as pFe values only take into account the non-hydrolyzed metal ion. As the pH increases, the proportion of non-chelated iron present in the non-hydrolyzed form will decrease as the relative complex stability decreases and bis-hydroxy- and tetrahydroxy- species will increase. At physiological pH, this difference will be significant, with the bis-hydroxy- species present at a concentration generally a few orders of magnitude higher than the fully aquated metal ion. The relative amount of iron that is hydrolyzed can be accounted for by determination of a value known as the Ringbom coefficient. The Ringbom coefficient, α , is determined from the mass balance equation as shown below for the metal Ringbom coefficient.

$$M_{tot} = [M] + [M(OH)] + [M(OH)_2] + \dots \quad (1.20.)$$

$$M_{tot} = [M] + \frac{K_{a1}[M]}{[H^+]} + \frac{\beta_{a2}[M]}{[H^+]^2} + \dots \quad (1.21.)$$

$$M_{tot} = [M] \left(1 + \frac{K_{a1}}{[H^+]} + \frac{\beta_{a2}}{[H^+]^2} + \dots \right) \quad (1.22.)$$

$$\alpha_M = 1 + \frac{K_{a1}}{[H^+]} + \frac{\beta_{a2}}{[H^+]^2} + \dots \quad (1.23.)$$

It is also important to state the conditions at which the pFe is determined, as the value will change with the conditions.(33) Figure 1.14. shows an example of how the pFe value can vary over a range of pH values. This variation is due to the inclusion of the ligand Ringbom coefficient in the determination of pFe values.

$$L_{tot} = [L] + [LH] + [LH_2] + \dots \quad (1.24.)$$

$$L_{tot} = [L] + K_{a1}[L][H^+] + \beta_{a2}[L][H^+]^2 + \dots \quad (1.25.)$$

$$L_{tot} = [L](1 + K_{a1}[H^+] + \beta_{a2}[H^+]^2 + \dots) \quad (1.26.)$$

$$\alpha_L = 1 + K_{a1}[H^+] + \beta_{a2}[H^+]^2 + \dots \quad (1.27.)$$

This variation in complex stability with change in pH is particularly important in the context of biological systems, as it can potentially play a role in the iron uptake mechanism of some organisms. In some cases, the iron-siderophore complex is taken up into compartments where the pH is lower than the surrounding environment of the organism. This change in pH can lead to lower relative stability of the iron-siderophore complex compared to other competing ligands, and can potentially facilitate the exchange of iron from one siderophore to another.

1.5 Iron redox chemistry

As mentioned earlier, iron has access to a number of oxidation states, ranging from 0 to IV+. The two most often observed oxidation states in iron biochemistry are the

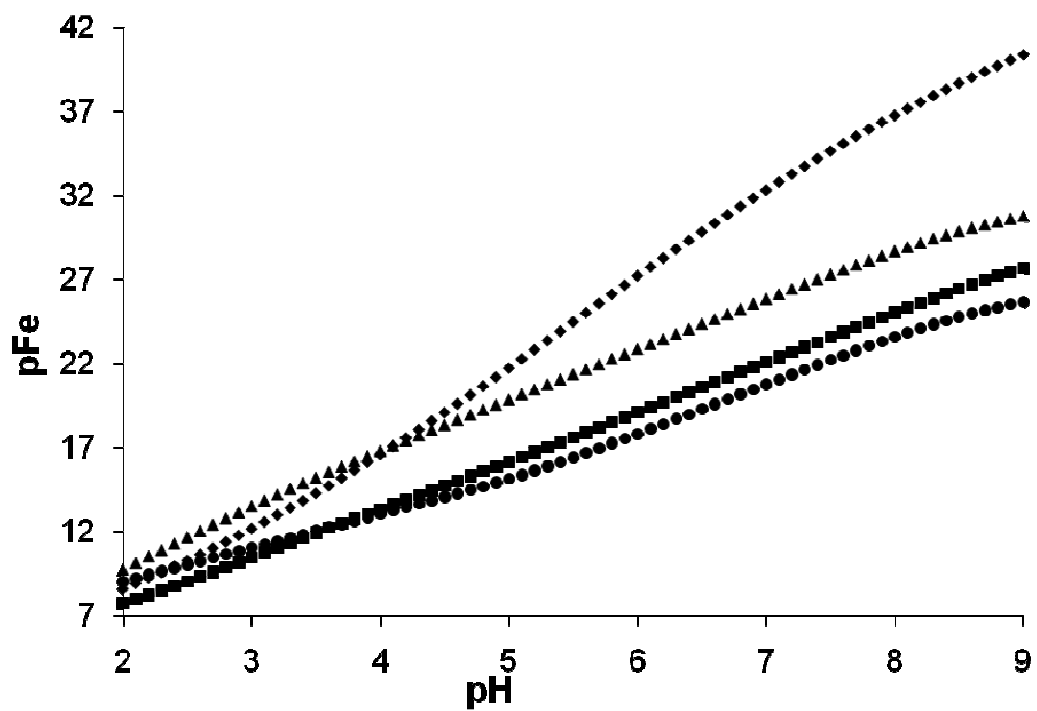


Figure 1.14. Plot of pFe as a function of pH for four natural siderophores. Conditions: $[\text{Fe}]_{\text{tot}} = 1 \mu\text{M}$, $[\text{Sid}]_{\text{tot}} = 10 \mu\text{M}$, $\mu = 0.10 \text{ M}$, $T = 25 \text{ }^\circ\text{C}$. Legend: diamonds – enterobactin, triangles – desferrioxamine B, squares – aerobactin, circles – rhodotorulic acid.

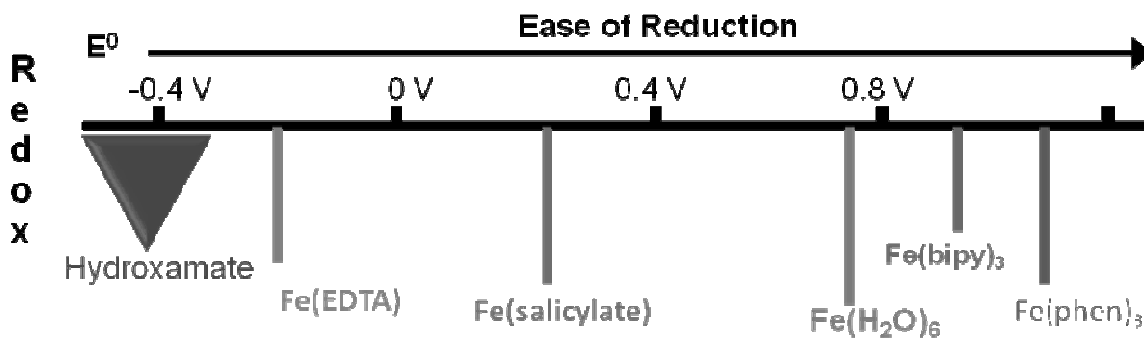


Figure 1.15. Partial range of observable redox potentials for the Fe(III)/Fe(II) redox couple of a number of iron complexes. The redox potential of the complex varies depending on the identity of the chelator bound to iron.

3+ and 2+ oxidation states. The redox potential of the $\text{Fe}^{3+}/\text{Fe}^{2+}$ couple can also vary depending on the identity of the primary coordination sphere, providing a range of observable redox potentials from -800 mV to +1000 mV against NHE (Fig. 1.15.). The exact redox potential for the $\text{Fe}^{3+}/\text{Fe}^{2+}$ couple depends on the hardness or softness of the donor atoms in the primary coordination sphere of the iron. As mentioned previously, iron(III) is considered a hard acid on the Pearson HSAB scale, resulting in more stable complex formation with hard donor atoms, such as charged oxygen atoms and carbonyl oxygens.(22) Meanwhile, iron(II) has a much lower charge-to-radius ratio, classifying it as a moderate acid. This means that it binds more stably to softer donor atoms, such as nitrogen, than does iron(III). The stability of the complex formed between iron(III) or iron(II) and the donor atoms of the ligands will have a large influence on the redox

potential of the complex. The redox chemistry of iron as it relates to the siderophores has been recently reviewed.(34)

Assuming ideal behavior and applying the Nernst equation, the relationship between β^{III} and β^{II} , the stability constants of the iron(III) and iron(II) complexes, respectively, is as follows, where E^0_{complex} represents the iron-siderophore complex redox potential and E_{aq} is the redox potential of the aquo-complex couple, $\text{Fe}(\text{H}_2\text{O})_6^{3+}/\text{Fe}(\text{H}_2\text{O})_6^{2+}$.

$$E^0_{\text{complex}} - E_{\text{aq}} = -59.16 \log(\beta^{\text{III}} / \beta^{\text{II}}) \quad (1.28.)$$

Eq. 1.28. also illustrates that the more negative the formal redox potential, the greater the differences in siderophore affinity for iron(III) versus iron(II).

When iron is bound by soft donor atoms, the 2+ oxidation state will be stabilized, resulting in easier reduction of the iron and more positive redox potentials. The opposite is true for complexes incorporating charged oxygen donors, which stabilizes the 3+ oxidation state, making it more difficult to oxidize the iron resulting in more negative complex redox potentials.(34) The most negative iron-siderophore complex redox potentials are observed for the catecholate siderophores, such as enterobactin and bacilibactin, where the hard oxygen donor atoms and the delocalized electron density of

the catechol donor groups stabilize the ferric state. Meanwhile the least negative redox potentials are observed in α -hydroxycarboxylate siderophores, such as rhizoferrin. $E_{1/2}$ values for mixed siderophore systems and hydroxamate-donor group siderophores are in the intermediate range.

Another factor that will affect the complex redox potential is the architecture of the siderophore. A plot of ferri-siderophore redox potentials as a function of pFe for a series of hydroxamate complexes of differing denticity (shown in Fig. 1.16.) exhibits a trend. The trend demonstrates that hydroxamate siderophores of higher denticity will form complexes with more negative $E_{1/2}$ values than analogous siderophores of lower denticity.

A similar plot of $E_{1/2}$ vs pFe is shown in Fig. 1.17., which is limited to hexadentate siderophores, but includes a wide variety of donor groups. Although there is significant scatter, a linear trend is evident with higher iron affinity siderophores exhibiting more negative $E_{1/2}$ values. Using the Nernst equation and the standard redox potential for the Fe^{3+}/Fe^{2+} couple, it can be shown that a linear relationship is possible between

$$E_{1/2} = E^0 - \frac{59.16}{n} \log \frac{[Fe^{2+}]}{[Fe^{3+}]} \quad (1.29.)$$

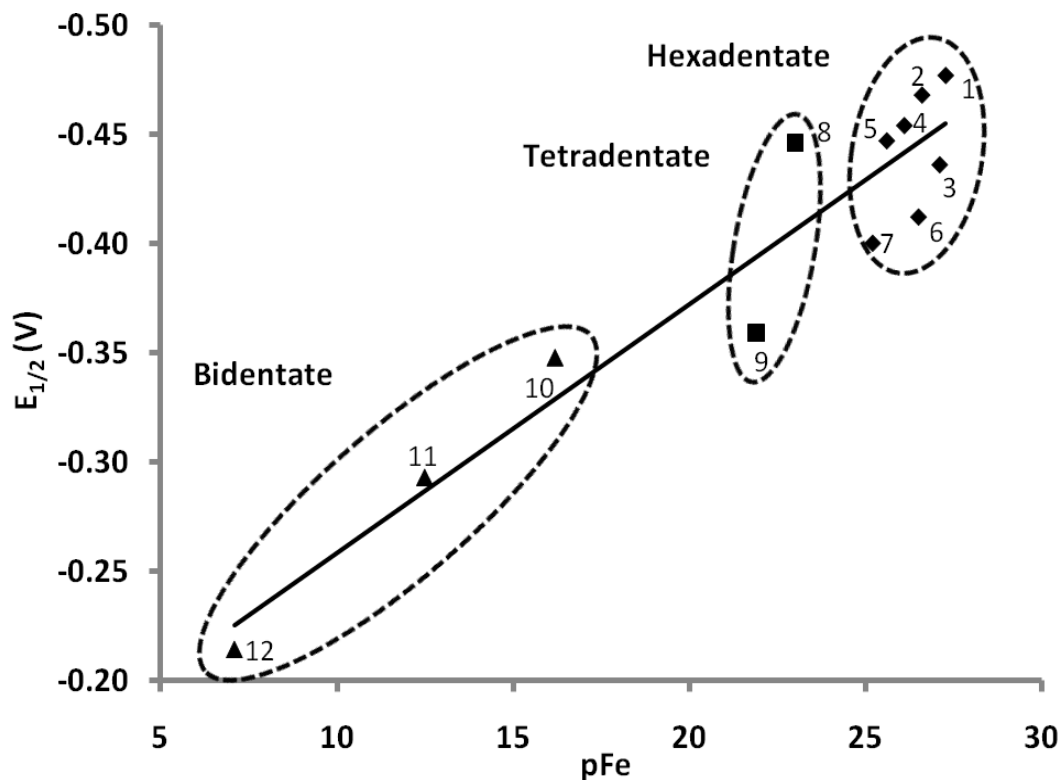


Figure 1.16. Plot of reduction potentials ($E_{1/2}$) as a function of pFe^{3+} values for a series of hexadentate, tetradentate and bidentate hydroxamic acid siderophore and siderophore mimic complexes with iron. Data taken from Ref. (1). Legend: 1 – ferrioxamine E; 2 – ferrioxamine B; 3 – H_3LR^{234} ; 4 – H_3LN^{236} ; 5 – coprogen; 6 – ferricrocin; 7 – ferrichrome; 8 – alcaligin; 9 – rhodotorulic acid; 10 – NMAHA; 11 – AHA; 12 – Ly-AHA.

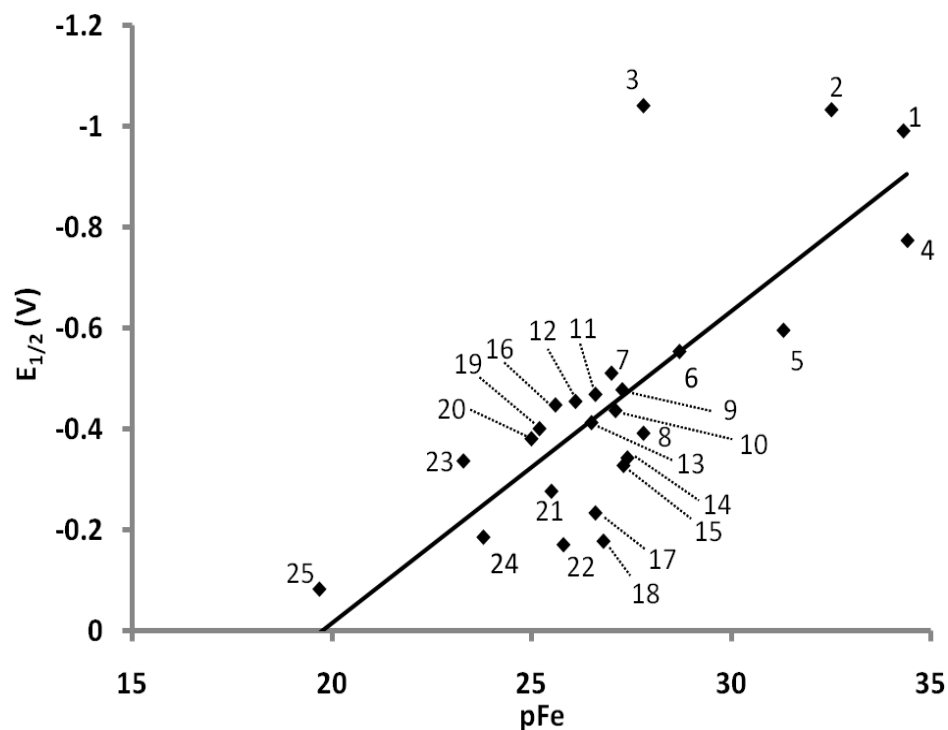


Figure 1.17. Plot of reduction potentials ($E_{1/2}$) as a function of pFe^{3+} values for hexadentate siderophore and siderophore mimic complexes with iron. Solid line represents a linear least squares fit to the data with slope = 0.0615 V. Legend: 1 – enterobactin; 2 – 3,4-LI(TAMmeg); 3 – TREN CAM; 4 – 5-LIO(TAMmeg)₂TAM; 5 – exochelin MN; 6 - 3,4-LI(Me-3,2-HOPO)(TAMmeg)₂; 7 – pyoverdine; 8 – azotobactin; 9 – ferrioxamine E; 10 – H₃L_R²³⁴; 11 – ferrioxamine B; 12 – H₃L_N²³⁶; 13 – ferricrocin; 14 – HOPObactin; 15 - 3,4-LI(Me-3,2-HOPO)₂(TAMmeg); 16 – coprogen; 17 – TR322-Me-3,2-HOPO; 18 – TREN-Me-3,2-HOPO; 19 – ferrichrome; 20 – exochelin MS; 21 – 3,4-LI(Me-3,2-HOPO); 22 – TR332-Me-3,2-HOPO; 23 – aerobactin; 24 – TRPN-Me-3,2-HOPO; 25 – rhizoferrin. $E_{1/2}$ values and pFe values taken from Ref. (1).

the $p\text{Fe}^{3+}$ value and the solution reduction potential if $p\text{Fe}^{2+}$ is a constant for all of the complexes considered.

$$-E_{1/2} = -(0.77) - c p\text{Fe}^{2+} + c p\text{Fe}^{3+} \quad (1.30.)$$

This ideal plot should have a slope of $c = 59$ mV/log unit and a y-intercept related to the standard reduction potential of the $\text{Fe}_{(\text{aq})}^{3+}/\text{Fe}_{(\text{aq})}^{2+}$ couple and the $p\text{Fe}^{2+}$ for the complexes. Linear regression of the plot in Fig. 1.17. shows a line fit to the points with a slope of approximately 60 mV/log unit, equivalent to that expected for the ideal plot. This implies limited variation of the $p\text{Fe}^{2+}$ values from 7.4 for the siderophores included in the plot. Of interest is the fact that the hexadentate catechol siderophore complexes exhibit more negative $E_{1/2}$ values than predicted from Eq. 1.30., while hydroxypyridinone-donor group siderophores exhibit less negative complex $E_{1/2}$ values than predicted.

The redox potential and reversibility of the reduction of many iron-siderophore complexes will also vary with pH. This variation is due to a number of factors, including the speciation of the Fe(III)-siderophore and Fe(II)-siderophore complex in solution over the pH range studied.(9, 35) Reduction of Fe^{3+} results in diminished competition with protons for binding to ionizable donor groups. Figure 1.18. shows the variation of the redox potential of a series of hydroxamate siderophore complexes with

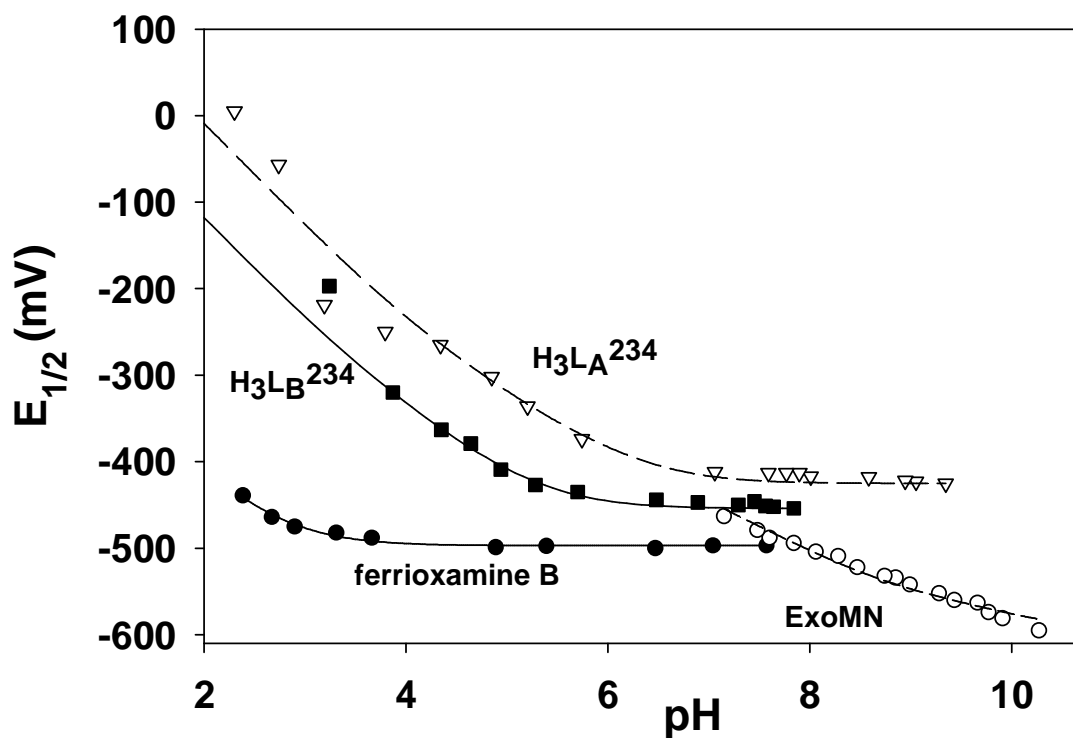


Figure 1.18. Redox potentials ($E_{1/2}$) of Fe^{3+} siderophore and siderophore mimic complexes as a function of pH. Lines represent a fit of Eq. (31) to the data, which are taken from Refs (36-39). Adapted from Ref (9).

pH. At higher pH values, the redox potential of the complex plateaus as the protonation states of the complexes do not change above this pH. This variation of $E_{1/2}$ with pH may be advantageous, as at physiological conditions the redox potential of many complexes are out of the range of biological reducing agents.(9, 35) Therefore, lower pH regions may contribute to the increased ability of an organism to obtain iron through a reductive mechanism. This is most notably observed in hydroxamate siderophores, such as alcaligin, desferrioxamine B, and rhodotorulic acid, as well as other donor group systems.(12, 40-42) The variation of $E_{1/2}$ with pH can be derived from the protonation constant expressions of the oxidized and reduced forms of the complexes and the Nernst equation:

$$E_{\text{rxn}} = E_{\text{complex}} + 59.16 \log(1 + K_{a1^{\text{III}}}[\text{H}^+] + \beta_{a2^{\text{III}}}[\text{H}^+]^2 + \dots) - 59.16 \log(1 + K_{a1^{\text{II}}}[\text{H}^+] + \dots) \quad (1.31.)$$

Using linear regression, it is possible to estimate the protonation constants of the Fe(II)-siderophore complexes where the redox potentials have been measured over a range of pH values.(43) This also explains the variation in reversibility of reduction as the pH changes, as the stability of the ferro-siderophore complex is much lower than the ferric complex, and the increased lability of ligand exchange and increased binding site competition from H^+ may result in dissociation of the complex before the iron center can be reoxidized in a cyclic voltammetry experiment.

Another factor that can possibly affect the redox potential in biological systems is the presence of secondary chelating agents that can participate in coupled equilibria.(35) When other chelators are present, coupled equilibria involving iron-siderophore redox and a secondary ligand will cause the siderophore complex effective redox potential to shift. The decrease in stability of the iron-siderophore complex upon reduction results in a more facile release of the iron. Upon release, the iron(II) is available for complexation by the secondary ligand, which results in a corresponding shift in the redox equilibrium towards production of iron(II). In cases where iron(II) is stabilized by the secondary chelators, there is a shift in the effective redox potential to more positive values, as shown in Eqs. 1.32.-1.35.



$$E_{rxn} = E_{1/2}^{Fe(III)sid} + \frac{0.0592}{n} \log \left(1 + \frac{K^{Fe(II)L} [L]}{K^{Fe(II)sid} [sid]} \right) \quad (1.35.)$$

In Eq. 1.35., $K^{Fe(II)L}$ is the stability constant for iron(II) complexation by the competing ligand, $K^{Fe(II)sid}$ is the stability constant for the complex formed between

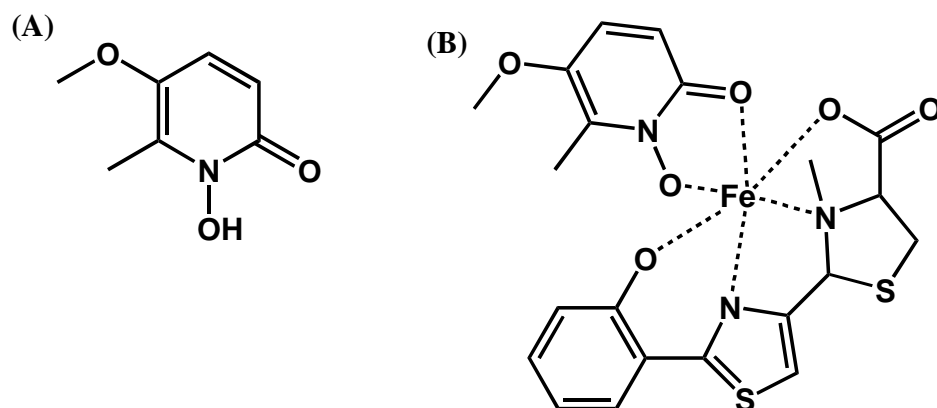


Figure 1.19. Tetradentate natural siderophore, pyochelin (A) and the ternary complex formed with ferric iron, pyochelin, and cepabactin (B).

iron(II) and the siderophore, n is the number of electrons transferred, E_{rxn} is the observed redox potential for the iron(III)-siderophore system coupled with iron(II) chelation, and $E_{1/2}^{\text{Fe(III)sid}}$ is the redox potential of the iron(III)-siderophore complex.

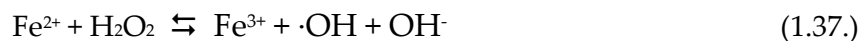
Ternary complex formation in ferrioxamine B has been shown to facilitate the reduction and release of iron in some biological model systems. The formation of a ternary complex with iron(II) chelators can shift the redox potential of iron(III) into a range accessible by biological chelators, such as NADH, glutathione, and ascorbate.^(44, 45) Evidence for the biological relevance of a hypothetical ternary complex route leading to reduction and release of siderophore bound iron comes from the siderophore pyochelin, where the tetradentate siderophore forms a complex with iron, leaving two available coordination sites. The monohydroxypyridinone siderophore, cepabactin, can

bind to the remaining two coordination sites and form a ternary complex (in Fig. 1.19).(46) Ternary complex formation may also be important in the recognition of the iron(III)-pyochelin complex by the pyochelin receptor protein, FptA.(47)

Such ternary complex formation can be facilitated by the environment surrounding the siderophore. Ferrioxamine B ternary complex formation was shown to be stabilized in the presence of SDS micelles, suggesting the possible involvement of low pH regions and cell-receptor surfaces in the formation and transport of ternary complexes in biological systems.(48) Low pH regions facilitate the dissociation of a donor group from the iron(III) center of the complex, which allows the ternary complex to be formed. These results can be viewed as a mimic of low-pH compartments inside the cell that can potentially store iron-siderophore complexes upon uptake, leading to release of the metal.

Another possible route for reduction of the iron center is photoreduction. This has been studied in a variety of marine siderophore systems, such as aquachelin, marinobactin, and aerobactin, where it was demonstrated that photolytic reduction was due to a ligand-to-metal charge transfer band of the Fe(III)-siderophore complex, eventually resulting in reduction of iron(III) and cleavage of the siderophore.(29-31) This suggests a possible role for iron reduction in iron release from marine siderophore systems.

While the variety of oxidation states and variability of reduction potentials allows for great versatility in the roles that iron can play, particularly in electron transfer capacities, it also can result in problems for organisms. The reduction potential of the aqueous $\text{Fe}^{3+}/\text{Fe}^{2+}$ redox pair is +0.770 V. If there is unbound iron present in biological systems, it can react with superoxide to produce iron(II) and oxygen. The iron(II) can then react via the Fenton reaction with hydrogen peroxide to produce hydroxyl radical.(49)



These reactions represent a catalytic cycle with harmful hydroxyl radicals as a product known as the Haber-Weiss cycle. The hydroxyl radical products and other reactive oxygen species (ROS) can lead to lipid peroxidation and oxidative damage that can over time result in cell death. Siderophores serve a second function by binding to iron and decreasing its redox potential due to the influence of the hard donor atoms stabilizing the 3+ oxidation state, effectively controlling its redox behavior and preventing participation in the Haber-Weiss cycle.

1.6 Mechanisms of iron release from siderophore complexes

One aspect of microbial iron metabolism that remains unclear in many cases is the mechanism for iron release from tight sequestration once the siderophore complex arrives at its destination; the cell surface or cell interior. Three broad hypotheses may be envisioned to describe the mechanism of iron release to the cell: i) simple release of iron driven by binding site protonation and/or conformational change; ii) siderophore ligand cleavage or hydrolysis leaving a binding site with lower iron affinity, leading to subsequent iron release; or iii) reduction of Fe^{3+} to Fe^{2+} , followed by dissociation of the siderophore.(9, 18, 50) The second mechanism has been observed in the case of enterobactin, where an enterobactin-specific esterase cleaves the backbone.(51) This results in a tris-bidentate ligand complex, which has a lower affinity for iron than the hexadentate analog, resulting in facile release of the iron. However, it has been proposed that the first and third mechanisms are more efficient, due to the metabolic cost of producing new siderophores after hydrolysis.(9, 35, 52)

1.6.1 The Reductive Hypothesis: A molecular “switch”

Reduction of the bound iron to the 2+ state results in a lower charge-to-radius ratio, making the metal center a borderline soft acid. This results in lower affinity of the metal ion for the hard donor atoms contained in most siderophores.(53) Reduction also will increase the lability of the iron as high-spin Fe^{2+} undergoes ligand exchange more

rapidly than high-spin Fe^{3+} .(54, 55) The efficacy of the reductive iron release hypothesis depends heavily on the redox potential, $E_{1/2}$, of the ferri-siderophore complex at cellular conditions.

Reduction of the iron center may be described as a molecular “switch” to indicate its possible role in the mechanism of iron release from the siderophore complex.

Reduction from Fe(III) to Fe(II) results in lower siderophore selectivity, as evidenced by a decrease in the overall complex stability with iron(III) compared to iron(II), as well as an increase in H^+ competition for the binding group resulting in iron dissociation.

Reduction also acts as a kinetic “switch,” as the rate of ligand exchange at the iron center increases greatly upon reduction.(54) All of these factors lead to much easier release of the iron from the siderophore binding site, making the process of reduction of the metal center a molecular “switch.” Although many ferri-siderophores have very negative reduction potentials, these thermodynamic potentials may be shifted to higher values through change in dielectric constant of the medium such as experienced in a receptor interior, a drop in pH, ternary complex formation, coupled reactions that trap reduced iron, and photolysis, all of which were discussed in Section 1.5.

1.7 Iron in human health

The use of iron chelators with high stability and specificity can be linked to the study of iron-siderophore chemistry, as an understanding of the structural and

architectural features microbes use to obtain iron from their environment can be used to design synthetic siderophore-like molecules for chelating iron in biological and engineered systems. Design of molecules with high binding affinity for iron and high bioavailability, and that are not biologically active in the case of iron overload therapeutic agents (or are biologically active in the case of antimicrobial siderophore mimics) requires an intimate knowledge of the binding and iron uptake mechanisms of a variety of biological systems.

1.7.1 Iron chelation therapy

Genetic disorders resulting in the mutation of hemoglobin, such as β -thalassemia and sickle cell, can result in anemia, for which a treatment is frequent blood transfusions. An indirect result of these blood transfusions is a high concentration of non-transferrin bound iron (NTBI) in the body, which over time can accumulate in organs, such as the liver.(56, 57) Accumulation of NTBI will cause oxidative damage to the organs and, after an average of 20 years, results in death of the patient.(58) Treatment with small molecule chelating agents can aid the body in removal of this excess iron.(59, 60) An understanding of iron – siderophore and siderophore mimic interactions has been a guiding principle in the development of chelators for the treatment of iron overload.

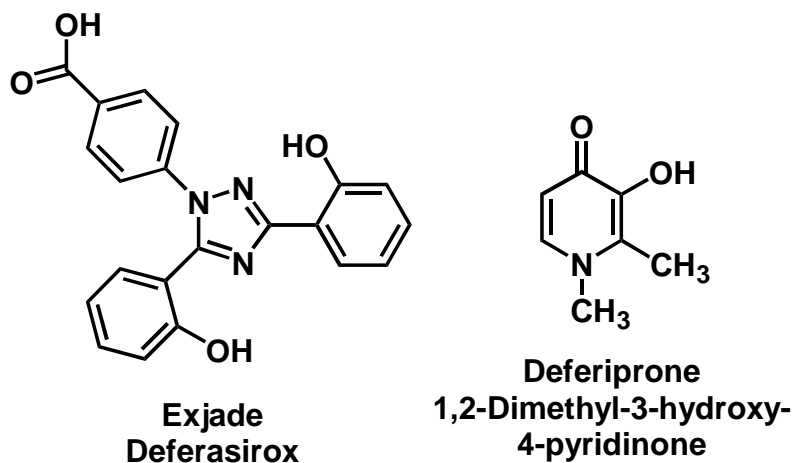


Figure 1.20. Current small molecule chelation therapy agents for iron overload, deferasirox (trade name Exjade) and 1,2-dimethyl-3-hydroxy-4-pyridinone (trade name Deferiprone).

Current chelation therapy treatments for iron overload that have been approved for clinical use by the US FDA are Desferal™, or desferrioxamine B mesylate salt (Fig. 1.1.), and Exjade™, or deferasirox (Fig. 1.20.).(61, 62) A third treatment that has been approved for use in Europe is Deferiprone™, or 1,2-dimethyl-3-hydroxy-4-pyridinone (Fig. 1.20.).(63) However, there are problems associated with all three of these treatments. Desferrioxamine B, a tri-hydroxamate siderophore, has low bioavailability and short serum half life and must be administered through frequent subcutaneous transfusions.(64) Treatments are long, painful, and expensive, resulting in low user compliance rates. While Exjade has a higher bioavailability than desferrioxamine B and can be administered orally, its structure features a variety of binding groups, which are not specific for binding iron. This can potentially lead to binding of other metal ions that

may result in undesirable side effects.(65) Deferiprone is a bidentate hydroxypyridinone molecule, which has high and specific affinity for iron and is administered orally. However, concerns have been raised regarding its toxicity and possible links between its use and diseases such as hepatic fibrosis, casting doubts on its efficacy.(66, 67) Future development of chelators for use as therapeutic agents in the treatment of iron overload diseases will likely rely on our understanding of iron-siderophore chemistry and biology.

Another potential use of iron chelators in biological systems is as antimicrobial agents. Siderophores and siderophore-like molecules can act as antimicrobial agents by multiple routes. The ability of bacteria to uptake iron has been linked to the virulence of some species of bacteria. If a chelating agent can compete effectively with bacterial siderophores for iron and not be taken up by the bacterial cell receptors, the bacterium will be deprived of essential iron, resulting in death.(68, 69) Another route of depriving the bacterium of iron is to use a siderophore mimic that will bind to the siderophore uptake protein, but not be taken up itself, preventing the bacterial siderophores from being transported across the cell membrane.(68, 70) A third route of antimicrobial activity of a siderophore is the attachment of an antimicrobial molecule to a siderophore binding moiety, which will bind iron and then be taken up by the bacterium, bypassing the defense mechanisms of the bacterium. Once inside the cell, the molecule will release

iron and undergo a reaction to activate its antimicrobial activity, killing the cell. This is known as the “Trojan Horse” approach.(68, 71)

As research continues into the field of siderophore production and iron uptake, the knowledge gained will be invaluable to the development of medical treatments for bacterial infection, iron overload, iron deficiency, and cancer (e.g. desferrioxamine B is currently used as an anticancer agent, as well as a chelation therapy agent).(60, 72, 73)

An understanding of the chelator structural factors that result in selectivity for iron, as well as the formation of more stable iron complexes, while still making use of bioavailable chelating agents, may allow treatments to become less expensive, less painful, and more convenient, which may enhance compliance. An understanding of the uptake systems used in bacterial and fungal organisms can be applied to the development of therapeutic agents as the uptake mechanism in bacteria is related to the virulence of the organism.

1.8 Statement of problem and Research Objectives

The goal of the research presented here is to expand our understanding of the structural factors that contribute to selectivity for iron and to iron complex stability in siderophores. Also, the process of iron transport in siderophore systems is investigated using model chelators. A secondary objective is to investigate the factors that contribute

to the development of successful therapeutic applications of chelating agents, both for chelation therapy and for antimicrobial agents. A study is presented to determine the thermodynamics of binding of a number of chelators, both natural and synthetic, to iron(III) using pH-dependent spectrophotometric titrations and potentiometric titrations. Chapter 2 presents a study of the thermodynamics of chelation of iron(III) by a tris-hydroxypyridinone and two bis-hydroxypyridinone synthetic siderophore mimics. Chapter 5 presents a determination of the solution thermodynamics of the iron(III) complex of Brasilibactin A, a membrane-bound mycobactin-type bacterial siderophore. Chapter 6 presents the thermodynamics of chelation of iron(III) by a synthetic Trojan Horse antimicrobial agent featuring a 3-hydroxy-4-pyridinone moiety. In these studies, the thermodynamic stability constants of the iron-chelator complexes are determined through a series of spectrophotometric and potentiometric titrations. Also, the redox chemistry of the iron-chelator complexes is investigated using cyclic voltammetry.

Chapter 7 investigates the structural features that contribute to complex stability in a series of tripodal tris-hydroxamate siderophores using computational techniques. It is shown that the position of the arm of an exocyclic siderophore system can contribute to differences in complex stability, as can the orientation of the donor group.

Chapter 3 presents a study of the kinetics of some reactions of iron complexes featuring hydroxypyridinone donor-group chelators. A determination of the

mechanism of proton-driven complex dissociation of a bishydroxypyridinone siderophore mimic is shown. Also, the mechanism of exchange between desferrioxamine B and an iron(III)-trishydroxypyridinone complex is determined through spectrophotometric monitoring of the reaction. Finally, Chapter 4 investigates the ability of a bidentate hydroxypyridinone chelator to catalyze the exchange of iron(III) from desferrioxamine B to EDTA. The catalysis of the iron(III) exchange reaction by 1,2-dimethyl-3-hydroxy-4-pyridinone is demonstrated through spectrophotometric monitoring of the reaction in the absence and presence of the catalyst. It was shown that the mechanism involves the formation of a ternary complex to facilitate exchange of iron from one chelator to another. This can be viewed as a model for iron exchange in biological systems where two highly stable chelators are involved in the iron uptake process.

Chapter 8 presents an investigation into the efficacy of chelation therapy treatments to protect from metal toxicity using the nematode *C. elegans* as a model organism. The model developed therein can also be used as a model for soil remediation of toxic metals using chelating agents.

2. Iron Sequestration Equilibria for Some New Tetradentate and Hexadentate 3-Hydroxy-2-pyridinone Donor Group Siderophore Mimics

2.1. Introduction

Aspects of this chapter were taken from Harrington, et al. (2010).(74)

As mentioned previously, the hydroxypyridinone (HOPO) donor group is rarely observed in nature, with only one observed instance in nature, cepabactin (see Section 1.5.). Preliminary studies on the use of HOPO siderophores as a treatment for iron overload disease have shown promising results with regard to iron binding ability and lack of bioavailability of the iron(III) complexes in mammalian systems.(75, 76) The development of chelation therapy agents requires that the unbound molecule has good bioavailability to allow ease of uptake, but that the metal-chelator complex that is formed has low bioavailability, to aid in removal of the metal from the system. The low bioavailability and high stability of previously observed Fe(III)-HOPO complexes suggests that the development of synthetic siderophores with hydroxypyridinone donors may be a viable route for the development of new treatments for iron overload disease. Additionally, hydroxypyridinone chelators form stable complexes with other metal ions, leading to their proposed use in other medical applications, such as novel

anti-bacterial agents, cancer prevention and treatment and chelating agents for plutonium(IV).(77, 78) Hydroxypyridinone complexes of radioactive isotopes of Ga(III) and In(III) have been proposed as useful in radiochemical imaging, and their complexes of Gd(III) have shown potential as magnetic resonance imaging agents.(79-85)

The Gopalan Lab of New Mexico State University has developed a synthetic method for a new class of hydroxypyridinone chelators that makes use of an intermediate iminium salt to attach a 3-hydroxy-2-pyridinone (3,2-HOPO) donor group to a wide variety of nucleophilic moieties (see Appendix B).(86) This allows the synthesis of a range of 3,2-HOPO-donor group chelators without the need of forming an amide bond. Current synthetic methods produce HOPO-substituted molecules featuring amide bonds at the connection points, which can be susceptible to hydrolysis or other undesirable reactions and decreases aqueous solubility of the molecules.(87) Additionally, as was discussed in Chapter 1, the presence of an amide bond may contribute to a salicylate shift in binding mode upon varying the pH. Such limitations would not be observed in the absence of the amide donor oxygen. The members of the hydroxypyridinone class of siderophore mimics to be studied here are based around a macrocyclic polyamine to allow comparison to some other exocyclic hydroxypyridinone chelators that have been investigated, TRENHOPO and HOPObactin.(88)

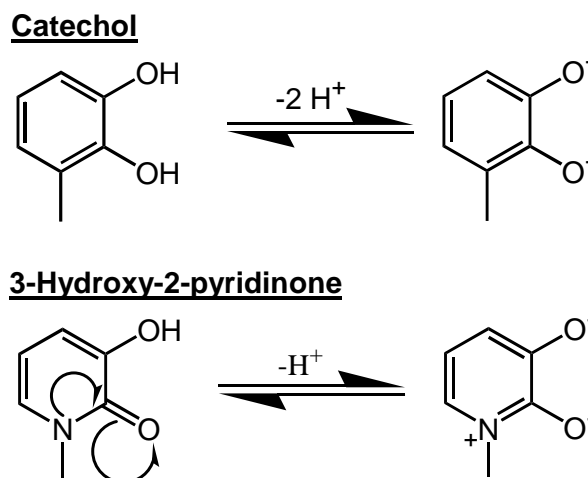


Figure 2.1. The electronic structures of the hydroxypyridinone donor group and of the catechol donor group are the same, resulting in similar thermodynamics of complex formation between the two donor groups.

Hydroxypyridinone donor groups are similar to catechol donor groups in stability due to the similar electronic configurations of the two moieties (Fig. 2.1.). However, the different number of ionizable protons of the donor moieties (one for hydroxypyridinone donors and two for catechol donors) results in more effective chelation by HOPO donor groups than catechol donor groups, as reflected in the pFe values for catechol (15.1) and 3,2-HOPO (16.26). (89-91) The charge difference in the donor moieties of catechol and hydroxypyridinone also affect the equilibrium constants for complexation. This is demonstrated by comparing the stepwise formation constants for the iron-catechol complex with those of the 3,2-HOPO complex.(90, 91) The K_1 for $\text{FeL}(\text{OH}_2)_4^{n+}$ formation is larger for $L = \text{catechol}$ than for 3,2-HOPO, at least partially due

to the greater electrostatic force of attraction between the +3 iron and the catechol dianion.

However, the higher negative charge for catechol also has a destabilizing effect due to charge repulsion in the polydentate complexes. Normally, the stepwise equilibrium constants decrease in the order $K_1 > K_2 > K_3$ for statistical reasons. However, the observed decrease is greater than expected on statistical grounds and the sequence decreases faster for catechol ($K_1 = 20.4$, $K_2 = 15.5$, $\Delta_{1-2} = 4.9$, $K_3 = 9.4$, $\Delta_{2-3} = 6.1$) than for 3,2-HOPO ($K_1 = 11.48$, $K_2 = 9.77$, $\Delta_{1-2} = 1.71$, $K_3 = 8.01$, $\Delta_{2-3} = 1.76$), due to increased charge repulsion.(91, 92)

2.2. Statement of chapter objectives

The purpose of this study is to determine the thermodynamics of aqueous iron(III) coordination of three members of a new class of bis- and trishydroxypyridinone exocyclic synthetic siderophore mimics built on an N_2 and N_3 aza-macrocyclic platform (Fig. 2.2.). The protonation equilibria of these three siderophores were elucidated through potentiometric and spectrophotometric titrations, and the stability of their complexes with Fe(III) were determined through spectrophotometric titration and competition reactions with EDTA. A thorough investigation of the aqueous solution

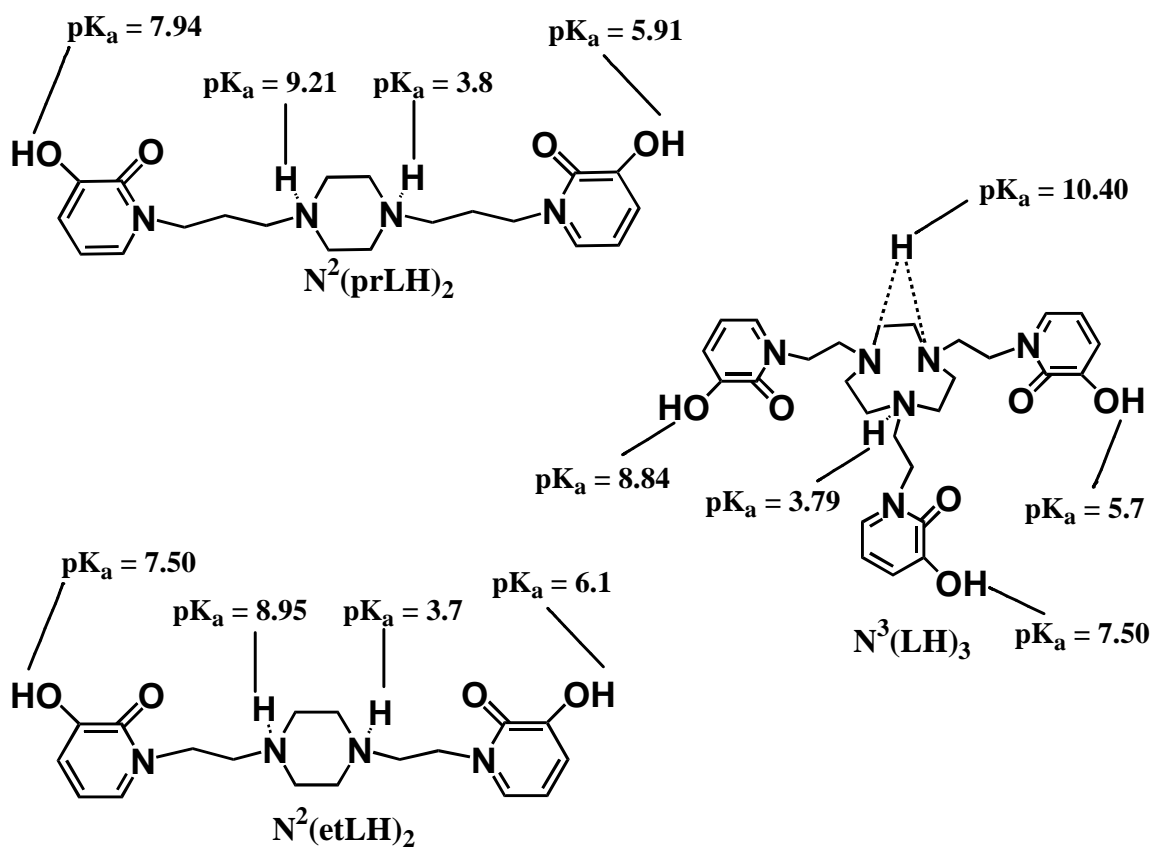


Figure 2.2. Structures of the synthetic exocyclic 3-hydroxy-2-pyridinone donor group siderophores studied here. Two exocyclic bishydroxypyridinone siderophores based around a [6]ane- N_2 central ring system, $N^2(\text{etLH})_2$ and $N^2(\text{prLH})_2$, and an exocyclic trishydroxypyridinone siderophore based around a [9]ane- N_3 central ring system, $N^3(\text{etLH})_3$. Determined protonation constants are indicated on the structures of the molecules.

equilibria for these complexes can give insight into the future development of synthetic molecules as candidates for the development of chelation therapy treatments.

2.3. Experimental

2.3.1. Materials

All solutions were prepared in deionized water. Solid NaCl (>99%, Fischer Chemicals) and solid NaClO₄ (99.99%, Sigma-Aldrich) was used to prepare the background electrolyte solution. Standardized 1 N NaOH solution (Fischer Chemicals), was used to prepare a 0.10 M solution. The base solution was standardized against KHP (Aldrich, 99.95%) to the phenolphthalein endpoint. Concentrated HCl (Malinckrodt AR, 37%) was used to prepare a 0.10 M solution, which was standardized against a standard NaOH solution to the phenolphthalein endpoint. Solid anhydrous FeCl₃ was obtained from Sigma and used to prepare 0.10 M stock solution that was standardized titrimetrically by reduction with SnCl₂, followed by titration with K₂Cr₂O₇.⁽⁹³⁾ Competition reactions were performed with a stock solution prepared with solid EDTA (Acros Organics, 99+%). Solid samples of N²(etLH)₂ • 2 HBr, and N²(prLH)₂ • 2 HBr were prepared by a previously determined synthesis (see Appendix B) and were used as received to prepare solutions of the ligands.⁽⁹⁴⁾ pK_a titrations of each of the HOPO siderophores alone were performed in NaClO₄ background electrolyte, while titrations

in the presence of iron(III) were performed in NaCl background electrolyte due to low solubility in perchlorate above pH 4.

The background electrolyte used for titrations involving the hydroxypyridinone siderophore-Fe³⁺ complexes was NaCl, due to solubility issues of the complexes in perchlorate at higher pH (above pH 4). Perchlorate is a relatively large singly charged anion, which can promote precipitation of the large iron-hydroxypyridinone complexes being studied here. The electrolyte used for the titrations of the siderophores alone for determination of the ligand pK_a's was NaClO₄, as the solubility issues did not arise for the ligand alone.

2.3.2. Potentiometric Measurements

Ligand pK_a's were determined by potentiometric and spectrophotometric titrations. All pH measurements were made with an Orion 230 A+ pH/ion meter equipped with an Orion Ross pH electrode filled with 3 M NaCl solution. The electrode was calibrated by titration of standardized 0.10 M HCl with standardized 0.10 M NaOH, as in the "classical method," and calibration data were analyzed using the computer program, GLEE. (95, 96) Ligand solutions were prepared at 10⁻⁵ M in acid and titrated with 0.010 M NaOH. Potentiometric data were analyzed with the program, EXCEL.(97)

2.3.3. Spectrophotometric Titrations

UV-visible spectra were recorded with the Cary-50 spectrophotometer equipped with an external dip probe (Hellma, USA). For spectrophotometric titrations of the siderophores alone, solutions of 1.0×10^{-5} M siderophore were prepared in 0.10 M NaClO_4 solutions. These solutions were titrated with standardized 0.010 M $\text{NaOH}/0.090$ M NaClO_4 solutions. The pH was measured after each addition, and the UV-Visible spectrum was measured in the wavelength region of 200-400 nm. Spectrophotometric data were analyzed by the program, SPECFIT to determine the protonation constants of the ligands.(98)

For the Fe(III)-tris-hydroxypyridinone complex titrations, stock solutions were prepared at Fe(III):siderophore concentration ratios of 1:1 at $[\text{Fe}^{3+}] = [\text{N}^3(\text{etLH})_3] = 3.08 \times 10^{-4}$ M. For Fe(III)-bis-hydroxypyridinone complex titrations, stock solutions were prepared at a 2:3 molar ratio (for the $\text{N}^2(\text{etLH})_2$ system $[\text{Fe}^{3+}] = 2.70 \times 10^{-4}$ M and $[\text{N}^2(\text{etLH})_2] = 4.06 \times 10^{-4}$ M, and for the $\text{N}^2(\text{prLH})_2$ system $[\text{Fe}^{3+}] = 1.99 \times 10^{-4}$ M, $[\text{N}^2(\text{prLH})_2] = 2.98 \times 10^{-4}$ M). For all the Fe(III)-siderophore mimic complex titrations, 0.10 M NaCl was used as a background electrolyte. The presence of chloride was taken into account in the determination of the stability constants by including the stability constants of the mono-, di-, and trichloro-iron(III) complexes in the determinations of the stability constants for the hydroxypyridinone complexes.

Two pH-dependent titrations (acid and base) were performed for each Fe(III)-siderophore system. In the base titration, 0.10 M NaOH was used to titrate the Fe(III)-siderophore complex from pH 2.9 to pH 10.4. UV-vis spectra from the titration were analyzed with the programs SPECFIT and HYPERQUAD to determine the protonation constants of the complexes.(98, 99) All determined complex stability constants are shown in Table 2.1.

An acid titration, using 1.0 M HCl was conducted for each Fe(III) siderophore system from pH 3 to approximately pH 0.3. For these titrations, the program EXCEL was used to analyze the spectral shifts, due to difficulty of solving for some concentrations in both SPECFIT and HYPERQUAD.(97) Electrode calibration in high-acid conditions was performed assuming Nernstian behavior with a junction potential using the program VLpH.(100)

2.3.4. EDTA Competition Titrations

UV-visible spectra were recorded using a Varian Cary 100 UV-visible spectrophotometer measuring from 350 nm – 750 nm. For the $\text{Fe}_2(\text{N}^2(\text{prL})_2)_3$ system, stock solutions of the Fe(III)-siderophore complex were prepared in a background electrolyte of 0.10 M NaCl and separated into 2.0 mL aliquots at $[\text{Fe}^{3+}] = 2.47 \times 10^{-4}$ M and $[\text{N}^2(\text{prLH})_2] = 3.70 \times 10^{-3}$ M, and a range of concentrations of

Table 2.1. Complete proton dissociation equilibria for HOPO ligands and their iron(III) complexes.

Equilibrium ^a	K or β	$\log(K \text{ or } \beta)^b$	Eq.
<u>N²(etLH)₂</u>			
H ₂ N ² (etLH) ₂ ²⁺ ⇌ HN ² (etLH) ₂ ⁺ + H ⁺	K _{a1}	-3.7±0.1 ^c	2.1-1
HN ² (etLH) ₂ ⁺ ⇌ HN ² (etL)(etLH) + H ⁺	K _{a2}	-6.1±0.1 ^c	2.1-2
HN ² (etL)(etLH) ⇌ HN ² (etL) ₂ ⁻ + H ⁺	K _{a3}	-7.50±0.08 ^c	2.1-3
HN ² (etL) ₂ ⁻ ⇌ N ² (etL) ₂ ²⁻ + H ⁺	K _{a4}	-8.95±0.02 ^c	2.1-4
2 Fe(H ₂ O) ₆ ³⁺ + 3 HN ² (etLH) ₂ ⁺ ⇌ Fe ₂ (HN ² (etL) ₂) ₃ ³⁺ + 6 H ⁺ + 12 H ₂ O	K ₂₃₀	d	2.1-5
2 Fe(H ₂ O) ₆ ³⁺ + 3 N ² (etL) ₂ ²⁻ ⇌ Fe ₂ (N ² (etL) ₂) ₃ + 6 H ₂ O	β ₂₃₀	d	2.1-6
2 Fe(HN ² (etL) ₂)(H ₂ O) ₂ ²⁺ + HN ² (etLH) ₂ ⁺ ⇌ Fe ₂ (HN ² (etL) ₂) ₃ ³⁺ + 2 H ⁺ + 4 H ₂ O	K ₂	d	2.1-7
Fe(H ₂ O) ₆ ³⁺ + N ² (etL) ₂ ²⁻ ⇌ Fe(N ² (etL) ₂)(H ₂ O) ₂ ⁺ + 4 H ₂ O	β ₁₁₀	21.08±0.01 ^e	2.1-8
Fe(H ₂ O) ₆ ³⁺ + HN ² (etLH) ₂ ⁺ ⇌ Fe(HN ² (etL) ₂)(H ₂ O) ₂ ²⁺ + 2 H ⁺ + 4 H ₂ O	K ₁₁₀	7.5 ^f	2.1-9
Fe(HN ² (etL)(etLH))(H ₂ O) ₄ ³⁺ ⇌ Fe(HN ² (etL) ₂)(H ₂ O) ₂ ²⁺ + H ⁺ + 2 H ₂ O	K _{aFe}	-0.96±0.09 ^c	2.1-10
Fe(H ₂ O) ₆ ³⁺ + N ² (etL) ₂ ²⁻ + H ⁺ ⇌ Fe(N ² (etL)(etLH))(H ₂ O) ₄ ²⁺ + 2 H ₂ O	β ₁₁₁	22.1±0.1 ^f	2.1-11
Fe(H ₂ O) ₆ ³⁺ + HN ² (etLH) ₂ ⁺ ⇌ Fe(HN ² (etL)(etLH))(H ₂ O) ₄ ³⁺ + H ⁺ + 2 H ₂ O	K	8.5 ^f	2.1-12
Fe(H ₂ O) ₆ ³⁺ + N ² (etL)(etLH) ⁻ ⇌ Fe(N ² (etL)(etLH))(H ₂ O) ₄ ²⁺ + 2 H ₂ O	β	14.6 ^f	2.1-13
<u>N²(prLH)₂</u>			
H ₂ N ² (prLH) ₂ ²⁺ ⇌ HN ² (prLH) ₂ ⁺ + H ⁺	K _{a1}	-3.8±0.1 ^c	2.1-14
HN ² (prLH) ₂ ⁺ ⇌ HN ² (prL)(prLH) + H ⁺	K _{a2}	-5.91±0.09 ^c	2.1-15
HN ² (prL)(prLH) ⇌ HN ² (prL) ₂ ⁻ + H ⁺	K _{a3}	-7.94±0.05 ^c	2.1-16
HN ² (prL) ₂ ⁻ ⇌ N ² (prL) ₂ ²⁻ + H ⁺	K _{a4}	-9.21±0.02 ^c	2.1-17
2 Fe(H ₂ O) ₆ ³⁺ + 3 HN ² (prLH) ₂ ⁺ ⇌ Fe ₂ (HN ² (prL) ₂) ₃ ³⁺ + 6 H ⁺ + 12 H ₂ O	K ₂₃₀	18.91 ^f	2.1-18
2 Fe(H ₂ O) ₆ ³⁺ + 3 N ² (prL) ₂ ²⁻ ⇌ Fe ₂ (N ² (prL) ₂) ₃ + 12 H ₂ O	β ₂₃₀	60.46±0.02 ^e	2.1-19

$2 \text{Fe}(\text{HN}^2(\text{prL})_2)(\text{H}_2\text{O})_2^{2+} + \text{HN}^2(\text{prLH})_2^+ \rightleftharpoons \text{Fe}_2(\text{HN}^2(\text{prL})_2)_3^{3+} + 2 \text{H}^+ + 4 \text{H}_2\text{O}$	K_2	5.71 ^f	2.1-20
$\text{Fe}(\text{H}_2\text{O})_6^{3+} + \text{HN}^2(\text{prLH})_2^+ \rightleftharpoons \text{Fe}(\text{HN}^2(\text{prL})_2)(\text{H}_2\text{O})_2^{2+} + 2 \text{H}^+ + 4 \text{H}_2\text{O}$	K_{110}	6.60 ^f	2.1-21
$\text{Fe}(\text{H}_2\text{O})_6^{3+} + \text{N}^2(\text{prL})_2^{2-} \rightleftharpoons \text{Fe}(\text{N}^2(\text{prL})_2)(\text{H}_2\text{O})_2^{2+} + 4 \text{H}_2\text{O}$	β_{110}	20.45±0.04 ^g	2.1-22
$\text{Fe}(\text{HN}^2(\text{prL})(\text{prLH}))(\text{H}_2\text{O})_4^{3+} \rightleftharpoons \text{Fe}(\text{HN}^2(\text{prL})_2)(\text{H}_2\text{O})_2^{2+} + \text{H}^+ + 2 \text{H}_2\text{O}$	K_{aFe}	-1.1±0.1 ^c	2.1-23
$\text{Fe}(\text{H}_2\text{O})_6^{3+} + \text{N}^2(\text{prL})_2^{2-} + \text{H}^+ \rightleftharpoons \text{Fe}(\text{N}^2(\text{prL})(\text{prLH}))(\text{H}_2\text{O})_4^{2+} + 2 \text{H}_2\text{O}$	β_{111}	21.5±0.1 ^f	2.1-24
$\text{Fe}(\text{H}_2\text{O})_6^{3+} + \text{HN}^2(\text{prLH})_2^+ \rightleftharpoons \text{Fe}(\text{HN}^2(\text{prL})(\text{prLH}))(\text{H}_2\text{O})_4^{3+} + \text{H}^+ + 2 \text{H}_2\text{O}$	K	7.65 ^f	2.1-25
$\text{Fe}(\text{H}_2\text{O})_6^{3+} + \text{N}^2(\text{prL})(\text{prLH})^- \rightleftharpoons \text{Fe}(\text{N}^2(\text{prL})(\text{prLH}))(\text{H}_2\text{O})_4^{2+} + 2 \text{H}_2\text{O}$	β	13.56 ^f	2.1-26

N³(etLH)₃

$\text{H}_2\text{N}^3(\text{etLH})_3^{2+} \rightleftharpoons \text{HN}^3(\text{etLH})_3^+ + \text{H}^+$	K_{a1}	-3.79±0.07 ^c	2.1-27
$\text{HN}^3(\text{etLH})_3^+ \rightleftharpoons \text{HN}^3(\text{etL})(\text{etLH})_2 + \text{H}^+$	K_{a2}	-5.7±0.1 ^c	2.1-28
$\text{HN}^3(\text{etL})(\text{etLH})_2 \rightleftharpoons \text{HN}^3(\text{etL})_2(\text{etLH})^- + \text{H}^+$	K_{a3}	-7.50±0.02 ^c	2.1-29
$\text{HN}^3(\text{etL})_2(\text{etLH})^- \rightleftharpoons \text{HN}^3(\text{etL})_3^{2-} + \text{H}^+$	K_{a4}	-8.84±0.03 ^c	2.1-30
$\text{HN}^3(\text{etL})_3^{2-} \rightleftharpoons \text{N}^3(\text{etL})_3^{3-} + \text{H}^+$	K_{a5}	-10.40±0.04 ^c	2.1-31

59 $\text{Fe}(\text{H}_2\text{O})_6^{3+} + \text{N}^3(\text{etL})_3^{3-} \rightleftharpoons \text{Fe}(\text{N}^3(\text{etL})_3)\text{H}_{11}^- + \text{H}^+ + 6 \text{H}_2\text{O}$	β_{11-1}	17.66±0.09 ^f	2.1-32
$\text{Fe}(\text{HN}^3(\text{etL})_3)^+ \rightleftharpoons \text{Fe}(\text{N}^3(\text{etL})_3) + \text{H}^+$	K_{aFe2}	-9.68±0.08 ^c	2.1-33
$\text{Fe}(\text{H}_2\text{O})_6^{3+} + \text{N}^3(\text{etL})_3^{3-} \rightleftharpoons \text{Fe}(\text{N}^3(\text{etL})_3) + 6 \text{H}_2\text{O}$	β_{110}	27.34±0.04 ^e	2.1-34
$\text{Fe}(\text{H}_2\text{O})_6^{3+} + \text{HN}^3(\text{etLH})_3^+ \rightleftharpoons \text{Fe}(\text{HN}^3(\text{etL})_3)^+ + 3 \text{H}^+ + 6 \text{H}_2\text{O}$	K_1	5.3 ^g	2.1-35
$\text{Fe}(\text{H}_2\text{O})_6^{3+} + \text{N}^3(\text{etL})_3^{3-} + \text{H}^+ \rightleftharpoons \text{Fe}(\text{N}^3(\text{etL})_2(\text{etLH}))(\text{H}_2\text{O})_2^+ + 4 \text{H}_2\text{O}$	β_{111}	30.44±0.08 ^g	2.1-36
$\text{Fe}(\text{HN}^3(\text{etL})_2(\text{etLH}))(\text{H}_2\text{O})_2^{2+} \rightleftharpoons \text{Fe}(\text{HN}^3(\text{etL})_3)^+ + \text{H}^+ + 2 \text{H}_2\text{O}$	K_{aFe1}	-3.10±0.07 ^f	2.1-37
$\text{Fe}(\text{H}_2\text{O})_6^{3+} + \text{N}^3(\text{etL})_2(\text{etLH})^{2-} \rightleftharpoons \text{Fe}(\text{N}^3(\text{etL})_2(\text{etLH}))(\text{H}_2\text{O})_2^+ + 4 \text{H}_2\text{O}$	β_{tet}	21.58 ^f	2.1-38
$\text{Fe}(\text{H}_2\text{O})_6^{3+} + \text{HN}^3(\text{etLH})_3^+ \rightleftharpoons \text{Fe}(\text{HN}^3(\text{etL})_2(\text{etLH}))(\text{H}_2\text{O})_2^{2+} + 2 \text{H}^+ + 4 \text{H}_2\text{O}$	K_{111}	8.4 ^f	2.1-39
$\text{Fe}(\text{H}_2\text{O})_6^{3+} + \text{HN}^3(\text{etLH})_3^+ \rightleftharpoons \text{Fe}(\text{HN}^3(\text{etL})(\text{etLH})_2)(\text{H}_2\text{O})_4^{3+} + \text{H}^+ + 2 \text{H}_2\text{O}$	K_{112}	^h	2.1-40
$\text{Fe}(\text{H}_2\text{O})_6^{3+} + \text{N}^3(\text{etL})(\text{etLH})_2^- \rightleftharpoons \text{Fe}(\text{N}^3(\text{etL})(\text{etLH})_2)(\text{H}_2\text{O})_4^{2+} + 2 \text{H}_2\text{O}$	β_{bis}	^h	2.1-41

^a Equilibria are shown as proton dissociation reactions except in log β_{111} reactions. Conditional equilibrium constants are given the symbol K and written to show the protonation state of the ligand in solution, including the protonation of the central ring system.

The protonation state of the central ring is unimportant to the equilibrium constants determined, as protons will only be released from the HOPO binding moieties of the molecule upon chelation. The overall stability constants, $\log \beta$, are shown as reactions involving completely deprotonated ligands, regardless of the protonation state of the central ring system, to simplify the representation and calculation of the stability constants.

^b All values were determined at $\mu = 0.10 \text{ M}$, $T = 25 \text{ }^\circ\text{C}$.

^c Direct determination by spectrophotometric titration

^d Not determined due to solubility problems, see text

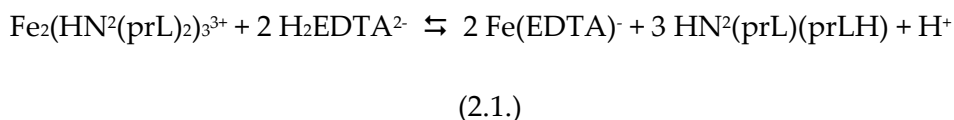
^e Indirect determination by competition reaction

^f Indirect determination by linear combination of experimental results

^g Indirect determination by spectrophotometric titration

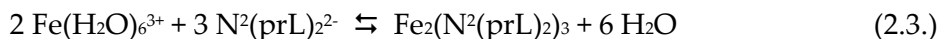
^h Not determined due to lack of protonation constant; see text

EDTA, from 0 to 25 equivalents of EDTA relative to Fe(III), were added while monitoring the pH (between 6 and 7). The competition reaction performed for the $N^2(prLH)_2$ system is shown in Eqs. 2.1.-2.2.



$$K_{obs} = \frac{[Fe(EDTA)^-]^2 [HN^2(prL)(prLH)^{2-}]^3 [H^+]}{[Fe_2(HN^2(prL)_2)_3][H_2EDTA^{4-}]^2} \quad (2.2.)$$

Solutions of the complexes were allowed to react for 24 hr at 25 °C, until the spectra of the solutions were constant, and the pH and UV-Vis spectra were measured. The spectrum of the solution containing the highest EDTA concentration corresponds to the solution spectrum of the $Fe(EDTA)^-$ complex, which has no absorbance in the visible region.⁽¹⁰¹⁾ Data from the competition titration (Fig. 2.3.A.) were used in conjunction with the published stability constant of the $Fe(EDTA)^-$ complex taken from the Critical Stability Constant database ($\log \beta_{EDTA} = 25.16$) to determine the stability constant of the Fe_2L_3 complex using Eqs. 2.3.-2.5.⁽¹⁰²⁾



$$\beta_{230} = \frac{[Fe_2(N^2(prL)_2)_3]}{[Fe(H_2O)_6^{3+}]^2 [N^2(prL)_2^{2-}]^3} \quad (2.4.)$$

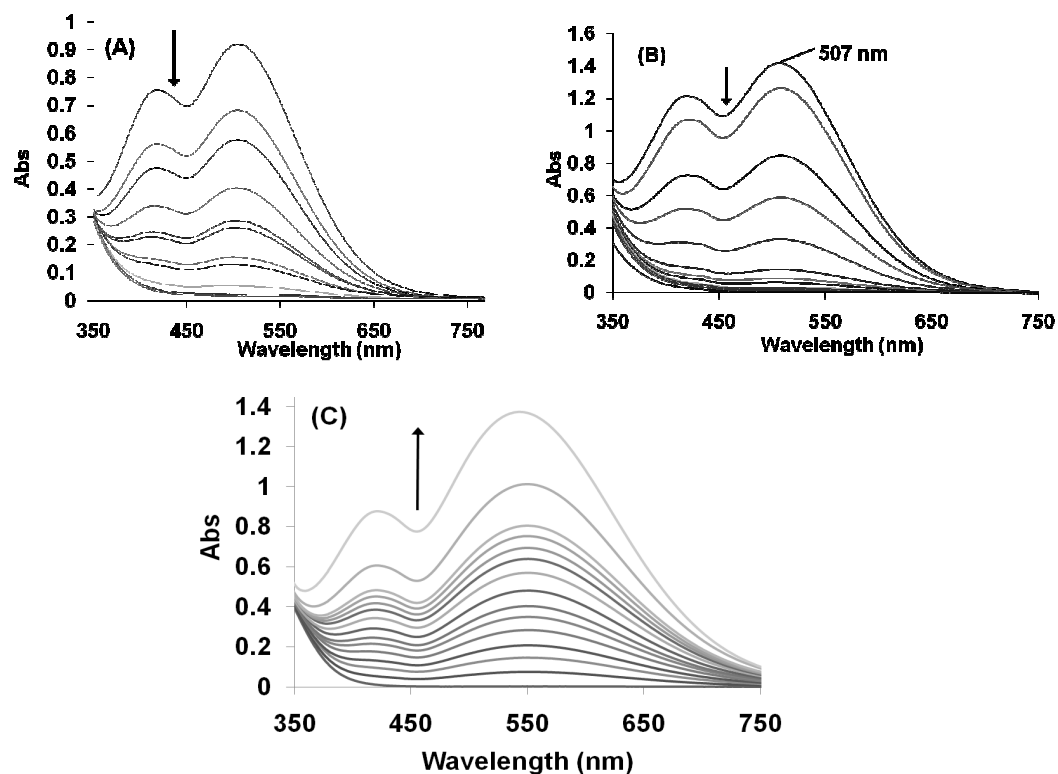


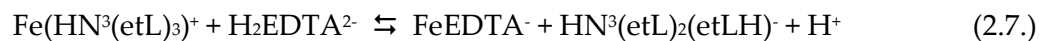
Figure 2.3. Spectrophotometric measurements of the competition reactions between the Fe-HOPO complexes and EDTA. (A) $\text{Fe}_2(\text{HN}^2(\text{prL})_2)_3$ competition reaction with EDTA, $[\text{Fe}^{3+}] = 2.5 \times 10^{-4} \text{ M}$, $[\text{N}^2(\text{prLH})_2] = 3.8 \times 10^{-4} \text{ M}$, $\text{pH} = 7.1$, $\mu = 0.10$ (NaCl), $[\text{EDTA}] = 0 - 2.5 \times 10^{-3} \text{ M}$; (B) $\text{Fe}(\text{HN}^3(\text{etL})_3)$ competition reaction with EDTA, $[\text{Fe}^{3+}] = [\text{N}^3(\text{etLH})_3] = 4.0 \times 10^{-4} \text{ M}$, $\text{pH} = 6.5$, $\mu = 0.10$ (NaCl), $[\text{EDTA}] = 0 - 1.0 \times 10^{-2} \text{ M}$; (C) $\text{Fe}(\text{EDTA})$ competition reaction with $\text{N}^2(\text{etLH})_2$, $[\text{Fe}^{3+}] = 1.0 \times 10^{-4} \text{ M}$, $[\text{EDTA}] = 1.0 \times 10^{-4} \text{ M}$, $\text{pH} = 2.3$, $\mu = 0.10$ (NaCl), $[\text{N}^2(\text{etLH})_2] = 0 - 1.0 \times 10^{-3} \text{ M}$. In each case, an arrow indicates the direction in which the spectrum changes as competing ligand is added.

$$\beta_{230} = \left(\frac{K_{obs}}{(\beta_{110,EDTA})^2} \right)^{-1} \quad (2.5.)$$

$$\beta_{110,EDTA} = \left(\frac{[Fe(EDTA)^-]}{[Fe^{3+}][EDTA^{4-}]} \right) \quad (2.6.)$$

The computer program, HYPERQUAD was used to analyze the spectral shifts in the titration of the Fe(III)-N²(prLH)₂ system. The stability constants of the Fe(EDTA)⁻ complex and the protonation constants of EDTA were taken from the Critical Stability Constant Database and held constant in the analysis, as were the siderophore protonation constants.(90)

A similar experiment was performed for the N³(etLH)₃ system with the concentrations [Fe³⁺] = [N³(etLH)₃] = 4.0 x 10⁻⁴ M and the EDTA concentration ranging from 0 to 0.010 M, following Eqs. 2.7.-2.9. The spectra measured during this experiment are shown in Fig. 2.3.B.

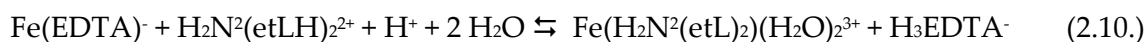


$$K_{obs} = \frac{[FeEDTA^-][HN^3(etL)_2(etLH)^{2-}]}{[Fe(HN^3(etL)_3)^+][H_2EDTA^{2-}]} \quad (2.8.)$$

$$\beta_{110} = \left(\frac{K_{obs}}{\beta_{110,EDTA}} \right)^{-1} \quad (2.9.)$$

The stability constant, $\log \beta_{110}$ was determined from the measured spectra using the program, SPECFIT. In some cases, such as the competition experiment shown above, HYPERQUAD experienced difficulties calculating free proton concentrations, resulting in the need to use SPECFIT to determine the stability constant value. However, it was determined that the programs evaluated comparable equilibrium constants for the same equilibria where both were able to calculate the constants.

For the Fe/(N²(etLH)₂) system, a stock solution of Fe(EDTA)⁻ was prepared at [Fe³⁺] = [EDTA] = 1.04 × 10⁻⁴ M and separated into 2.0 mL aliquots. The competition study was conducted by treating the stock aliquots of Fe(EDTA)⁻ complex with concentrations of N²(etLH)₂ ranging from 0 molar equivalents to 10 molar equivalents N²(etLH)₂:Fe, as described by Eqs. 2.10. and 2.11., and the solutions were



$$K_{obs} = \frac{[\text{Fe}(\text{H}_2\text{N}^2(\text{etL})_2)(\text{H}_2\text{O})_2^{3+}][\text{H}_3\text{EDTA}^-]}{[\text{Fe}(\text{EDTA})^-][\text{H}_2\text{N}^2(\text{etLH})_2^{2+}][\text{H}^+]} \quad (2.11.)$$

allowed to equilibrate for 24 hr before measuring the UV-visible spectra (Fig. 2.3.C) and the final pH. Using the condition-dependent equilibrium constant (Eq. 2.11.) and the stability constant of the Fe(EDTA)⁻ complex, it was possible to determine the $\log \beta_{110}$ (Eq. 2.12.) using the program Hyperquad.(99)

$$\beta_{110} = (K_{obs})(\beta_{110,EDTA}) \quad (2.12.)$$

2.3.5. ESI-MS measurements of bishydroxypyridinone complexes

All mass spectra were measured using an Agilent 1100 SL LC/MSD-Trap instrument. In all experiments, the LC functionality of the instrument was bypassed to obtain ESI mass spectra of the complexes in positive ion mode at a temperature of 125 °C, a nebulizer pressure of 15 psi, and a dry gas flow rate of 7 L/min. For N²(etLH)₂, a solution of [Fe³⁺]_{total} = 3.2 × 10⁻⁴ M and [N²(etLH)₂]_{total} = 4.5 × 10⁻⁴ M at pH ~ 2.5 and μ = 0.10 (NaCl) was prepared. For N²(prLH)₂, a solution of [Fe³⁺] = 4.2 × 10⁻⁴ M and [N²(prLH)₂] = 6.3 × 10⁻⁴ M was prepared at pH ~ 2.5 and μ = 0.10 (NaCl).

2.3.6. Iron-trishydroxypyridinone complex redox chemistry

The redox properties of the iron-N³(etLH)₃ complex were measured by cyclic voltammetry. A solution of iron(III)-N³(etLH)₃ was prepared at a 1:1 molar ratio by a similar procedure to that used for the spectrophotometric titrations. Cyclic voltammograms were measured from pH 2 to pH 9 by adjusting solution pH with small measured volumes of 0.10 M NaOH. Voltammograms were measured using a Cypress potentiostat with a Controlled Growth Mercury Electrode by BASi set to the static mercury drop mode as the working electrode, a Ag/AgCl (3.5 M NaCl) reference

electrode, and a platinum wire auxiliary electrode. Values of redox potentials reported here were adjusted 205 mV to report potentials against NHE.(103)

2.4. Results and Discussion

2.4.1. HOPO Ligand protonation constants

Protonation constants for $N^2(\text{etLH})_2$, $N^2(\text{prLH})_2$ and $N^3(\text{etLH})_3$ (Fig. 2.2.) in aqueous solution were determined by potentiometric and spectrophotometric titration. Potentiometric titration data for the latter two are shown in Figure 2.4. Representative spectrophotometric titration data for all three systems are shown in Figure 2.5. The spectral shifts observed in the spectrophotometric titrations correspond to the deprotonation reactions of the hydroxypyridinone moieties of the molecules. As the hydroxypyridinone groups are separate but undergoing identical deprotonation reactions, the spectral shift appeared as a single large shift corresponding to all hydroxypyridinone protonation constants instead of three spectral shifts with separate isobestic points. In the $N^2(\text{prLH})_2$ titration, isobestic points were observed at 273 and 298 nm, indicating a transition between two light absorbing species in all recorded spectra (Fig. 2.5.A.). A similar spectral shift was observed in the $N^3(\text{etLH})_3$ titration, with isobestic points observed at 276 and 300 nm (Fig. 2.5.B.). In contrast, the $N^2(\text{etLH})_2$ titration showed similar spectral shifts as in the other two experiments, but only a single isobestic point was observed at 277 nm (Fig. 2.5.C.).

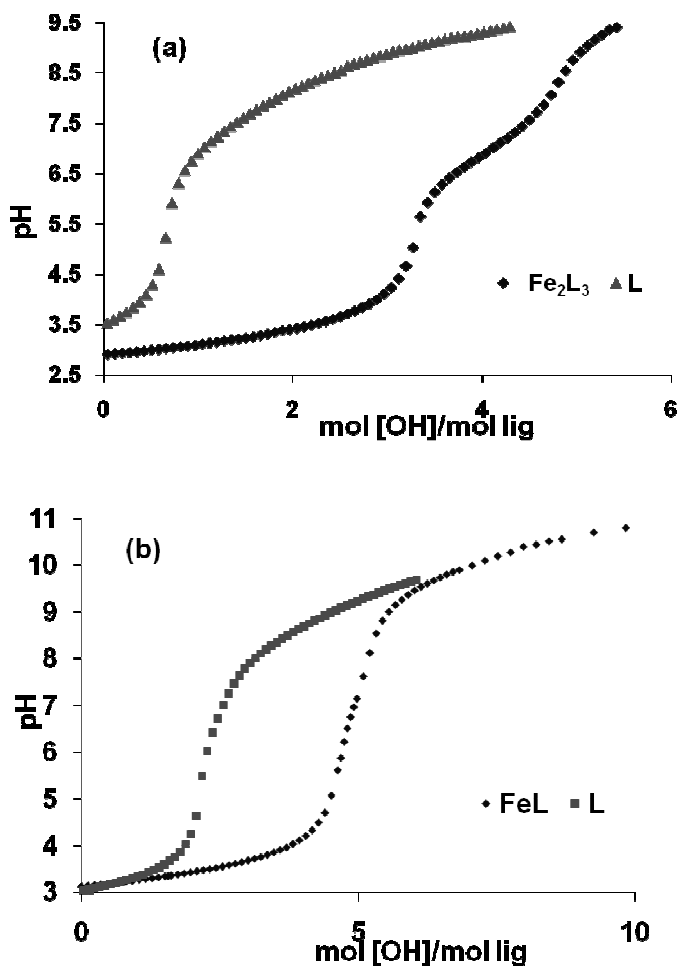


Figure 2.4. Potentiometric titration of two hydroxypyridinone-Fe³⁺ systems. (A) Fe-N²(prLH)₂ system. [Fe³⁺] = 4.0 × 10⁻⁴ M, [N²(prLH)₂] = 6.0 × 10⁻⁴ M, μ = 0.10 (NaCl). The triangles represent the ligand only titration ([N²(prLH)₂] = 6.7 × 10⁻⁴), while the diamonds represent the Fe-N²(prLH)₂ complex titration. (B) Fe-N³(etLH)₃ system. [Fe³⁺] = 3.98 × 10⁻⁴ M, [N³(etLH)₃] = 3.99 M, μ = 0.10 (NaCl). The squares represent the ligand only titration, while the diamonds represent the potentiometric titration performed in the presence of 1 equivalent of metal.

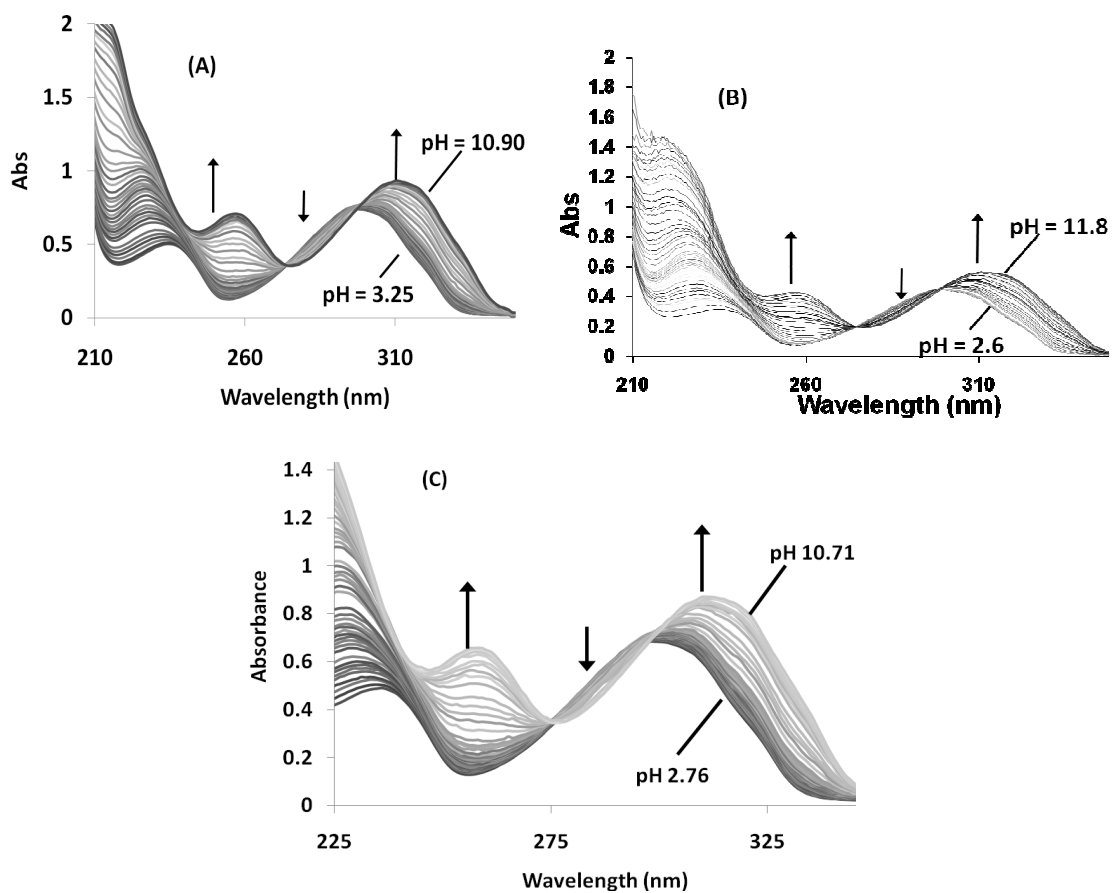


Figure 2.5. Spectrophotometric titration of the synthetic exocyclic hydroxypyridinone siderophores with 0.010 M NaOH. (A) $N^2(\text{prLH})_2$ over the pH range of 3.25 to 10.90. $[N^2(\text{prLH})_2] = 1.0 \times 10^{-5} \text{ M}$, $\mu = 0.10$, $T = 25 \text{ }^\circ\text{C}$. (B) $N^3(\text{etLH})_3$ over the pH range of 2.6 to 11.8. $[N^2(\text{prLH})_2] = 2.92 \times 10^{-5} \text{ M}$, $\mu = 0.10$, $T = 25 \text{ }^\circ\text{C}$. (C) $N^2(\text{etLH})_2$ over the pH range of 2.76 to 10.71. $[N^2(\text{etLH})_2] = 5.0 \times 10^{-5} \text{ M}$, $\mu = 0.10$, $T = 25 \text{ }^\circ\text{C}$. Arrows indicate the direction the spectrum changes upon addition of base.

The proton dissociation equilibria are described by Eqs. 2.13. and 2.14. below.

The measured deprotonation constants for all three HOPO ligands are shown in Table 2.1. and Figure 2.2.



$$K_{an} = \frac{[LH_{n-1}^{n-4}][H^+]}{[LH_n^{n-3}]} \quad (2.14.)$$

For the bishydroxypyridinones, N²(etLH)₂ and N²(prLH)₂, four separate deprotonation constants were observed (shown in Figure 2.2. and Table 2.1.), where pK_{a1} and pK_{a4} correspond to the deprotonation of the ring N atoms and pK_{a2} and pK_{a3} correspond to the hydroxypyridinone donor groups. The deprotonation constants of the ring N atoms are consistent with the observed literature values of [6]ane-N₂ ring systems.⁽¹⁰⁴⁾ The lower pK_a (≈3.7) corresponds to loss of a proton from the doubly protonated ring. This pK_a is greatly depressed due to electrostatic repulsion and steric hindrance.⁽¹⁰⁵⁾ The higher pK_a (9-10) is typical for the deprotonation of the singly protonated [6]ane-N₂ ring. The pK_a values that have been assigned to the hydroxypyridinone donor groups are lower than that observed for the 3-hydroxy-2- pyridinone donor group alone, 8.99.⁽¹⁰⁶⁾ This may be due to steric or electrostatic considerations. However, the values observed for the hydroxypyridinone donor groups of N²(etLH)₂ and N²(prLH)₂ are similar in

value to those observed in a previous study of a bishydroxypyridinone synthetic siderophore-mimic, where the pK_a 's of 8.40 and 6.87 were attributed to the HOPO donor groups.⁽¹⁰⁷⁾ The average pK_a separation for two identical acidic moieties is 0.60 in the absence of any intramolecular interactions, less than the separation observed here (1.4 for $N^2(\text{etLH})_2$ and 2.0 for $N^2(\text{prLH})_2$). This suggests the influence of intramolecular interactions on the pK_a s of the bishydroxypyridinone molecules.⁽¹⁰⁸⁾

The pK_a values observed for $N^3(\text{etLH})_3$ follow a similar pattern as that observed for the bishydroxypyridinone siderophores (Figure 2.2. and Table 2.1.). pK_{a1} and pK_{a5} correspond to the central ring system and are greatly separated due to electrostatic repulsion.⁽¹⁰⁹⁾ The third proton on the central ring has a pK_a too low to be observed, also due to steric interactions and electrostatic repulsion from the 2+ doubly protonated ring system. The hydroxypyridinone pK_{a2-4} are 5.7, 7.5, and 8.84. Two are quite low compared to a bidentate 3-hydroxy-2-pyridinone. The observed pK_a 's are separated by more than the predicted separation for three identical acidic moieties, 0.48 log units, implying a contribution from intramolecular interactions.⁽¹⁰⁸⁾

2.4.2. Fe(III)-HOPO Complex Stability and Protonation Constants: General observations

Iron may be bound by the bidentate HOPO moieties in three modalities as mono, bis and tris (bidentate, tetradentate and hexadentate) Fe(III)- HOPO complexes. These

complexes exist in solution as a dynamic equilibrium system where mono, bis, and tris complexes interconvert with changing pH due to competition between H⁺ and Fe³⁺ for the HOPO oxygen sites (as shown in Eq. 2.15.-2.17., where HOPO⁻ represents a generic anionic hydroxypyridinone donor moiety).



Changes in the Fe(III) inner coordination sphere produce observable changes in the UV-visible spectrum of the solution with pH. The spectral changes observed in this study are in agreement with those previously reported for Fe(III)-3,2-HOPO systems (Table 2.2.).(106)

The determined equilibrium constants for all possible complexation and deprotonation reactions for all three hydroxypyridinone siderophore mimics are shown in Table 2.1. The values presented were obtained from a combination of direct determination, and indirect determination from competition experiments. The equilibria determined through direct and indirect methods are related through linear combinations of constants determined by other methods and can be used as an internal check for consistency.

Table 2.2. Wavelengths of maximum absorbance for Fe-HOPO complexes in aqueous solution. The wavelengths recorded for the complexes studied here correspond well to those of a similar iron-tris-HOPO complex, supporting the identity of the complexes. Approximate molar absorptivity values (in $\text{dm}^3 \text{mol}^{-1} \text{cm}^{-1}$) from an average of four measurements are shown below the wavelength in parentheses.

Complex	$\text{N}^3(\text{etLH})_3$	$\text{N}^2(\text{etLH})_2$	$\text{N}^2(\text{prLH})_2$	3,2-HOPO*
Bis-coordinated	N/A	~600**	~600**	600
tetracoordinated	546 (2650±20)	547 (3580±20)	545 (3650±50)	548 (3690)
	413 (1760±40)	419 (2400±100)	417 (2300±200)	415 (1880)
hexacoordinated	507 (3820±10)	***	503 (4910±20)	502 (5160)
	417 (3320±10)	***	418 (4000±20)	417 (4080)

* Reference (106).

** Values were measured at high dilution and may be inaccurate.

*** Values were not determined due to low solubility of complex at higher pH.

2.4.3. Fe(III)-HOPO Complex Stability and Protonation Constants: Bishydroxypyridinone ligands $\text{N}^2(\text{prLH})_2$ and $\text{N}^2(\text{etLH})_2$

Initial complex formation occurs via deprotonation of one hydroxypyridinone donor moiety, which then coordinates to the metal center via displacement of two water ligands, as shown in Eqs. 2.1-12. and 2.1-25. in Table 2.1. (all Eq. 1-X designations refer to equilibria listed in Table 2.1.). A gradual increase in pH leads to deprotonation of the

second hydroxypyridinone donor group, followed by formation of the tetracoordinate $\text{FeL}(\text{H}_2\text{O})_2^+$ complex ($\text{L} = \text{N}^2(\text{prLH})_2$ or $\text{N}^2(\text{etLH})_2$), shown in Eqs. 2.1-10. and 2.1-23.

The potentiometric titration of the $\text{Fe}(\text{III})\text{-N}^2(\text{prLH})_2$ system (Fig. 2.4.A) showed an initial three-proton buffer region, one proton corresponding to the removal of a single proton from the central ring system and the other two corresponding to the deprotonation of the two HOPO donor groups upon chelation. Figure 2.6.A shows the low pH spectrophotometric titration of the $\text{Fe}(\text{III})\text{-N}^2(\text{prLH})_2$ system. Similar potentiometric and spectrophotometric data were obtained for the $\text{Fe}(\text{III})\text{-N}^2(\text{etLH})_2$ system (data not shown). The observed changes over the pH range of ~ 0.2 to 2.5 correspond to conversion of the complex from the biscoordinate to tetracoordinate complex, Eqs. 2.1-10. and 2.1-23. Using the spectra measured at low pH, the stability constant of the $\text{FeLH}(\text{H}_2\text{O})_4^{2+}$ complex (Eq. 2.1-11. and Eq. 2.1-24.) was calculated. The value obtained indirectly for the pH independent stability constant of the bishydroxypyridinone complexes, $\log \beta_{110}$, was 20.45 for $\text{Fe}(\text{HN}^2(\text{prL})_2)(\text{H}_2\text{O})_2^+$ (Eq. 2.1-22.) and $\log \beta_{110} = 21.08$ for $\text{Fe}(\text{HN}^2(\text{etL})_2)(\text{H}_2\text{O})_2^+$ (Eq. 1-8).

At low pH, $\text{N}^2(\text{prLH})_2$ and $\text{N}^2(\text{etLH})_2$ exhibit similar iron(III) complexation equilibria to form $\text{Fe}(\text{HN}^2(\text{prL})_2)(\text{H}_2\text{O})_2^+$ and $\text{Fe}(\text{HN}^2(\text{etL})_2)(\text{H}_2\text{O})_2^+$. However, at pH values above 3, their aqueous solution behavior diverges, as discussed below. In the $\text{Fe}(\text{III})\text{-N}^2(\text{prLH})_2$ system, as the pH increased above where the tetradentate species

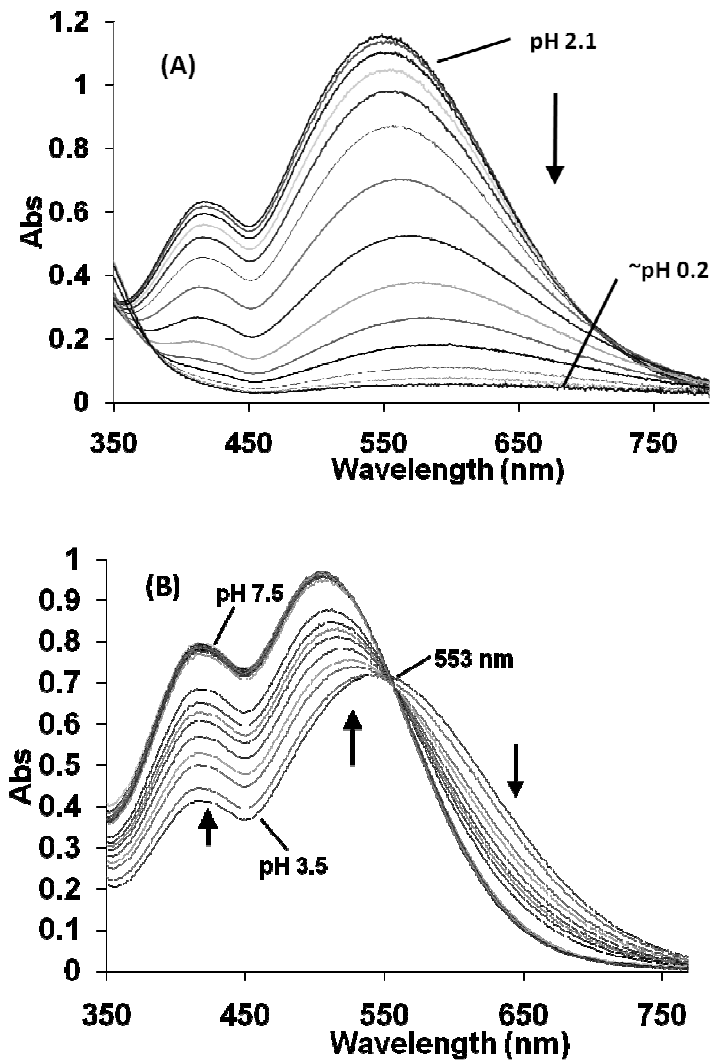


Figure 2.6. Spectrophotometric titrations of the Fe-N²(prLH)₂ system. (A) Spectra measured during the low-pH spectrophotometric titration of the Fe-N²(prLH)₂ system over the pH range of 2.14 to ~0.2. [Fe³⁺] = 3.3 × 10⁻⁴ M, [N²(prLH)₂] = 5.0 × 10⁻⁴ M, T = 25 °C, μ = 0.10 (NaCl). (B) pH 3.5 to 7.5. [Fe³⁺] = 2.0 × 10⁻⁴ M, [N²(prLH)₂] = 3.0 × 10⁻⁴ M, μ = 0.10 (NaCl), T = 25 °C. Arrow indicates the direction of spectral change upon addition of acid.

predominates, a further deprotonation of the free ligand in solution occurred as evidenced by a second buffer region observed in the potentiometric titration (Fig. 2.4.A). This second buffer region, from 3 to 5 equivalents of base added, corresponds to the formation of the hexacoordinate complex $\text{Fe}_2(\text{HN}^2(\text{prL})_2)^{3+}$, as shown in Eq. 2.1-20. Spectrophotometric titration of the Fe(III)- $\text{N}^2(\text{prLH})_2$ system over the pH range of 3.5 to 7.5 exhibits a spectral change with an isosbestic point at 557 nm (Figure 2.6.B), indicating a single protonation equilibrium. The observed shift in λ_{max} is consistent with conversion of the tetracoordinate $\text{Fe}(\text{HN}^2(\text{prL})_2)(\text{H}_2\text{O})_2^+$ complex to the hexacoordinate $\text{Fe}_2(\text{HN}^2(\text{prL})_2)^{3+}$ complex (Table 2.2. and Eq 2.1-20.).⁽¹⁰⁶⁾ The equilibrium constant for Eq. 2.1-18. is sufficiently high that direct characterization is not possible. Consequently, an indirect stability constant determination by competition with EDTA (see Experimental section) yielded a $\log \beta_{230}$ value of 60.46 for $\text{N}^2(\text{prLH})_2$ (Eq. 2.1-19.). The species distribution diagram for the Fe(III)- $\text{N}^2(\text{prLH})_2$ system (Figure 2.7.A) shows that at the chosen concentrations the Fe(III) is present as a hexacoordinate $\text{Fe}_2(\text{HN}^2(\text{prL})_2)^{3+}$ complex over the pH range of approximately 5 to 10.

Similar behavior is observed in the Fe(III)- $\text{N}^2(\text{etLH})_2$ system shown in Eqs 2.1-5 through 2.1-7, however the $\text{Fe}_2(\text{HN}^2(\text{etL})_2)^{3+}$ complex precipitates above pH 3, making it difficult to accurately determine $\log \beta_{230}$. The complex λ_{max} can be estimated from the remaining absorbance, as shown in Table 2.2. Comparison to the determined λ_{max} values of the Fe(III)- $\text{N}^2(\text{prLH})_2$ complex shows that the Fe(III)- $\text{N}^2(\text{etLH})_2$ complex exhibits a

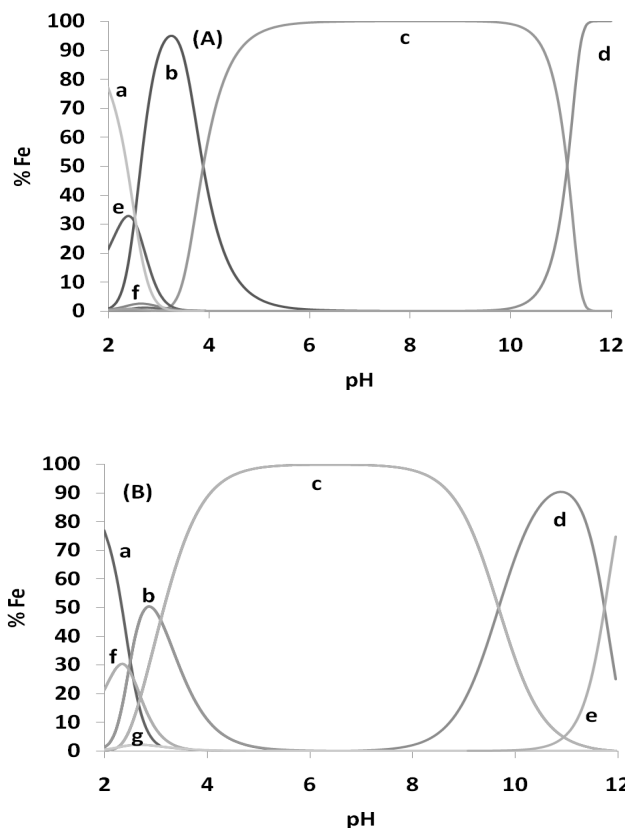


Figure 2.7. Species distribution diagram for the completely characterized systems of N²(prLH)₂ and N³(etLH)₃ in aqueous solution, showing percent total Fe³⁺ vs pH of solution. Values were calculated from determined stability constants of complexes and hydrolysis constants for Fe³⁺. T = 25 °C, μ = 0.10. (A) Fe-N²(prLH)₂ system, with [Fe³⁺]_{total} = 2.00 × 10⁻⁴ M, and [N²(prLH)₂]_{total} = 3.00 × 10⁻⁴ M. a = free Fe³⁺, b = Fe(HN²(prL)₂)(H₂O)₂²⁺ complex, c = Fe₂(HN²(prL)₂)₃³⁺ complex, d = Fe(OH)₄⁻, e = Fe(HN²(prLH)(prL))³⁺ and f = Fe(OH)₂⁺. (B) Fe-N³(etLH)₃ system, [Fe³⁺] = 1.00 × 10⁻⁴ M, [N³(etLH)₃] = 1.00 × 10⁻⁴ M. a = free Fe³⁺, b = Fe(HN³(etL)₂(etLH))₂²⁺, c = Fe(HN³(etL)₃)⁺, d = Fe(N³(etL)₃), e = Fe(OH)₄⁻, f = Fe(OH)₂⁺, and G = Fe(OH)₂⁺.

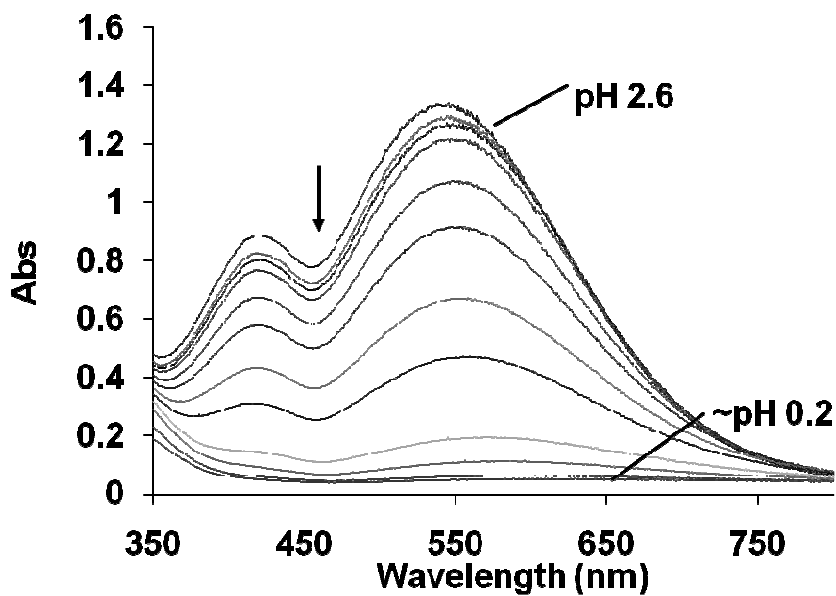


Figure 2.8. Spectra measured during the low-pH spectrophotometric titration of the $\text{Fe}(\text{N}^2(\text{etLH})_2)$ system. The absorbance decreases due in part to dilution and in part due to the change in spectral intensity upon conversion to the bicoordinate complex.

$[\text{Fe}^{3+}] = 3.5 \times 10^{-4} \text{ M}$, $[\text{N}^2(\text{etLH})_2] = 3.5 \times 10^{-4} \text{ M}$, $T = 25 \text{ }^\circ\text{C}$, $\mu = 0.10$ (NaCl). Arrow indicates the arrow in which the spectrum is moving upon addition of base.

similar inner coordination sphere as the $\text{N}^2(\text{prLH})_2$ complex at pH 7. Equilibrium constants for Eqs. 2.1-8 through 2.1-13. were calculated through EDTA competition experiments (Fig. 2.3.C) and low pH spectrophotometric titrations (Fig. 2.8.). The species distribution diagram for the $\text{Fe}(\text{III})\text{-N}^2(\text{etLH})_2$ system was not calculated due to the insolubility of the complex at $\text{pH} > 3$. The tetradentate chelators $\text{N}^2(\text{etLH})_2$ and $\text{N}^2(\text{prLH})_2$ can reasonably encapsulate a single Fe^{3+} ion or form a bridge between two Fe^{3+} ions. This impacts the possible structures for the 1:1 and 2:3 Fe:L stoichiometry

complexes described here. Specifically, the 1:1 complex can exist in monomeric form ($\text{FeL}(\text{H}_2\text{O})_2^+$) or as a doubly bridged dimer $(\text{H}_2\text{O})_2\text{Fe}(\mu\text{-L})_2\text{Fe}(\text{H}_2\text{O})_2^{2+}$ ($\text{L} = \text{N}^2(\text{etLH})_2$ or $\text{N}^2(\text{prLH})_2$). The coordinatively saturated 2:3 complex may exist as a singly $((\text{L})\text{Fe}(\mu\text{-L})\text{Fe}(\text{L}))$ or triply bridged $(\text{Fe}(\mu\text{-L})_3\text{Fe})$ species. To address this question we used ESI-MS to characterize solutions of complexes at the L:Fe and pH conditions where the only species present was FeL as indicated by the speciation plot. The isotopic ratio of ^{56}Fe (91.18% natural abundance) to ^{57}Fe (2.1% natural abundance) is a useful tool to probe the nature of the iron complexes.

There is a peak observed in the Fe(III)- $\text{N}^2(\text{etLH})_2$ ESI-MS spectrum that corresponds to the 1:1 complex without coordinated water molecules, $\text{Fe}(\text{N}^2(\text{etL})_2)^+$ ($m/z = 414.1$, Fig. 2.9.A). The isotopic peaks of the 1:1 complex signal are separated by a whole m/z unit, which implies that the 1:1 complex is present in solution as the monomeric $\text{FeL}(\text{H}_2\text{O})_2^+$ form and not as the ligand-bridged dimer form (Fig. 2.10.). A similar isotopic separation is observed in the mass spectrum of the Fe(III)- $\text{N}^2(\text{prLH})_2$ 1:1 complex system (Fig. 2.9.B., where the 442.1 m/z peak represents $\text{Fe}(\text{N}^2(\text{prL})_2)^+$ without coordinated water molecules and exhibits an isotopic peak separation of 1 m/z unit, also suggesting that the complex is present in aqueous solution as the monomeric $\text{FeL}(\text{H}_2\text{O})_2^+$ form. The isotopic splitting pattern arises due to the presence of 1% ^{13}C and 2% ^{57}Fe in the complexes formed in solution. Thus, for each carbon present in the complex, there is a 1% chance that the mass of the complex will be one greater than the mass of the base

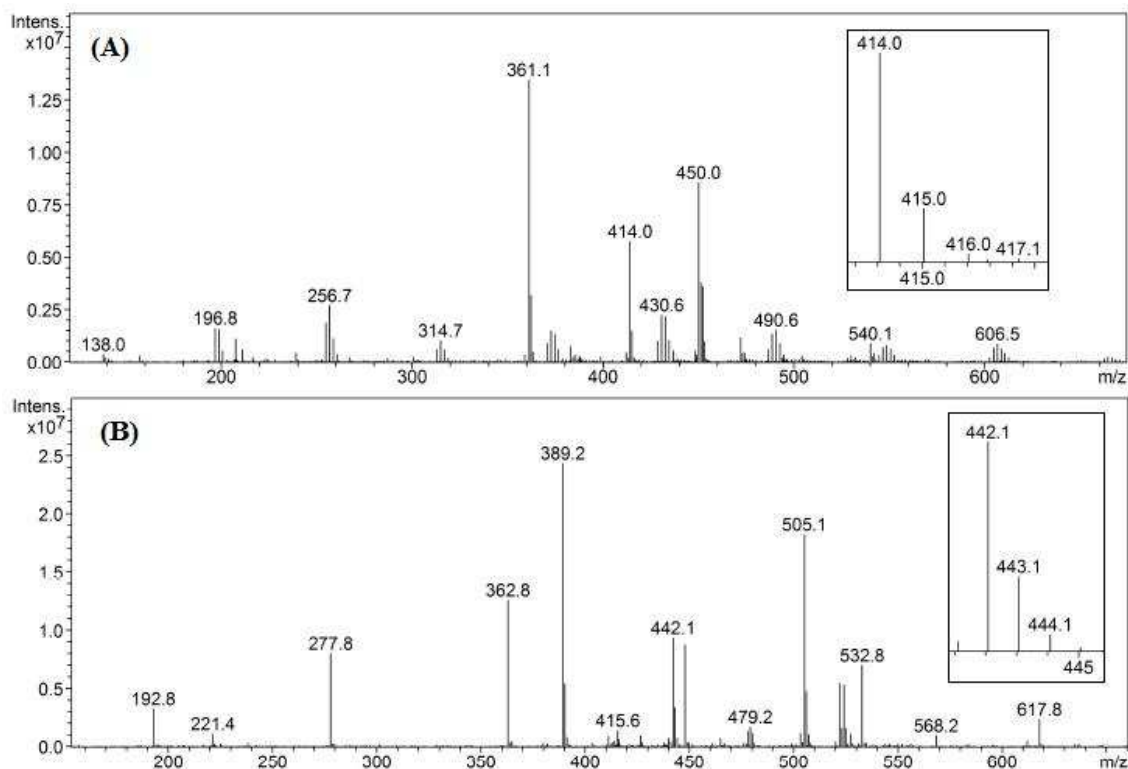


Figure 2.9. ESI-Mass spectra measured for the bis(hydroxypyridinone) complex solutions. Solutions were prepared in the range indicative of formation of the 1:1 complex, pH 2.5. T = 125 °C, nebulizer pressure = 15 psi, dry gas flow rate = 7 L/min. (A) Mass spectrum of the Fe-N²(etLH)₂ system. [Fe³⁺] = 3.2 x 10⁻⁴ M and [N²(etLH)₂] = 4.8 x 10⁻⁴ M. (B) Mass spectrum of the Fe-N²(prLH)₂ system. [Fe³⁺] = 4.2 x 10⁻⁴ M and [N²(prLH)₂] = 6.3 x 10⁻⁴ M.

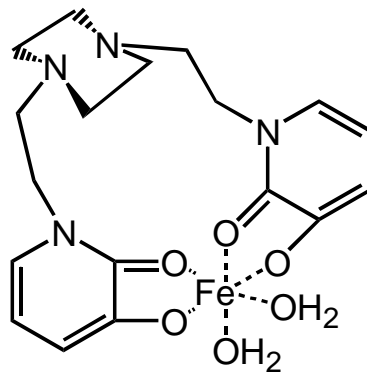
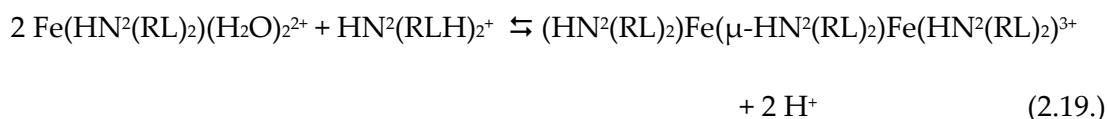
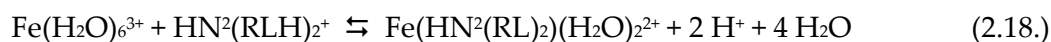


Figure 2.10. Proposed solution structure of the $\text{Fe-N}^2(\text{etLH})_2$ complex at pH 2.5 based on ESI-MS spectra.

peak and a 2% chance for each iron atom in the complex. If the complexes were found in the ligand bridged dimeric form $(\text{H}_2\text{O})_2\text{Fe}(\mu\text{-L})_2\text{Fe}(\text{H}_2\text{O})_2^{2+}$, the observed isotopic separation would be 0.5 m/z unit, as the difference in mass of the complex arising from the presence of a single ^{57}Fe metal center with the same overall charge of the complex would be 0.5 m/z unit. No peak that corresponds to a possible dimer is observed in the mass spectrum. Peak intensities provide additional evidence for the assignment of the peaks to the ML^+ complex. Theoretical calculations of the relative peak intensity of the $\text{ML}+1^+$ peak for the $\text{Fe}(\text{N}^2(\text{prL})_2)^+$ complex show that the corresponding isotopic peak should represent 23.5% of the entire peak intensity for all observed isotopes. The observed relative intensity of the $\text{ML}+1^+$ peak for the $\text{Fe}(\text{N}^2(\text{prL})_2)^+$ system was 24.6%, showing very good agreement with the predicted isotopic splitting pattern. The relative peak intensity of the $(\text{FeL} + 1)^+$ peak also provides additional evidence for the complex structure shown in Fig. 2.10. The dimer would not only exhibit 0.5 m/z peak separation

for its isotopic splitting pattern, but it would also exhibit different relative peak intensity. For the dimer Fe_2L_2 complex, the $(\text{Fe}_2\text{L}_2 + 1)^{2+}$ peak would represent 50.4% of the total peak intensity of all of the (Fe_2L_2) peaks, due to the relative abundance of each element in the complex, which is much greater than that observed in Fig. 2.9. A similar calculation for the $\text{Fe}(\text{N}^2(\text{etL})_2)^+$ system predicted 21.5% of the total peak intensity and the observed relative intensity of the $(\text{FeL} + 1)^+$ peak was 20%, also showing very good agreement with the predicted isotopic splitting pattern. Again, the dimer Fe_2L_2 complex would exhibit different relative peak intensities, where the $(\text{Fe}_2\text{L}_2 + 1)^{2+}$ peak would represent 48.2% of the total peak intensity, much greater than that observed here.

Based on these observations, we propose that the iron(III) sequestration equilibria for the teradentate HOPO ligands $\text{N}^2(\text{etLH})_2$ and $\text{N}^2(\text{prLH})_2$ proceed through the formation of the following structures (R = et or pr).



2.4.4. Fe(III)-HOPO Complex Stability and Protonation Constants: Trishydroxypyridinone ligand $\text{N}^3(\text{etLH})_3$

Initial complex formation of the trishydroxypyridinone ($\text{N}^3(\text{etLH})_3$) complex occurs in a similar manner as the bishydroxypyridinone complexes, where addition of

iron to the ligand results in displacement of two protons to form the tetracoordinate complex (Eq. 2.1-39, Table 2.1.). This complex is formed at a low pH, and the two protonation steps are not resolvable, as evidenced by the low pH spectrophotometric and potentiometric titrations. Over the pH range of ~0.2 to 2.5, the spectra that are observed correspond to the formation of the tetracoordinate complex without observing λ_{\max} values that correspond to the biscoordinate complex (Fig. 2.11). Also, the potentiometric titration (Fig. 2.4.B.) exhibits an initial 4-proton buffer region that corresponds to the removal of a proton from the central ring, followed by the removal of

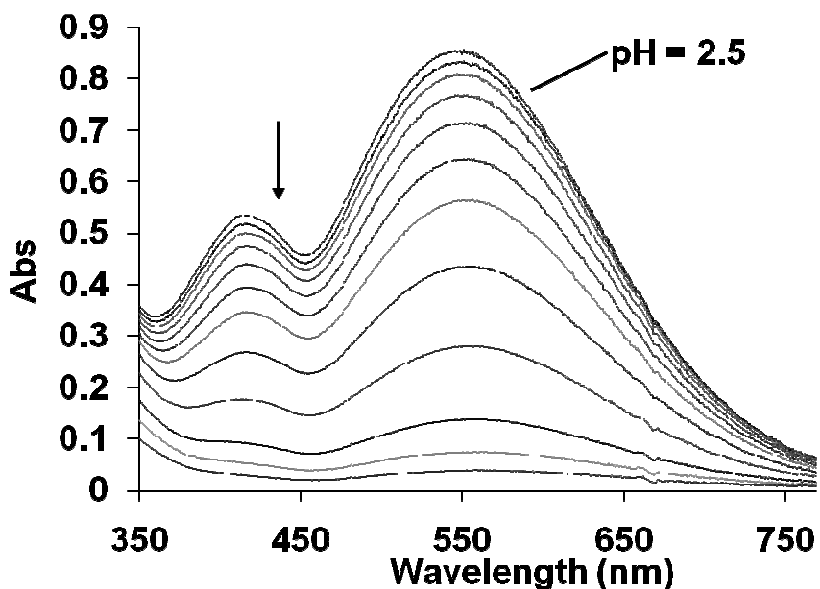


Figure 2.11. Low pH spectrophotometric titration of the iron(III)- $N^3(\text{etLH})_3$ system over the pH range of 2.5 to ~0.2. Conditions: $[\text{Fe}^{3+}] = [N^3(\text{etLH})_3] = 3.6 \times 10^{-4} \text{ M}$, $T = 25^\circ\text{C}$, $\mu = 0.10$ (NaCl). Arrow indicates the direction of spectral change with decreasing pH. Spectral absorbance adjusted for dilution.

two protons from hydroxypyridinone donor groups to form the tetracoordinate complex and subsequent removal of a third hydroxypyridinone proton to form the trishydroxypyridinone complex at higher solution pH (Eqs. 2.1-39. and 2.1-37.). Spectrophotometric titration of the complex characterized the transition from $\text{Fe}(\text{HN}^3(\text{etL})_2(\text{etLH})(\text{H}_2\text{O})_2)^{2+}$ to $\text{Fe}(\text{HN}^3(\text{etL})_3)^+$ over the pH range of ~2.5 to 8, exhibiting a spectral change consistent with the deprotonation of the third donor group to form the hexacoordinate trishydroxypyridinone complex (Fig. 2.12.A.). The isosbestic point observed is indicative of a single protonation equilibrium, suggesting deprotonation of a hydroxypyridinone donor group over that pH range (Eq. 2.1-37.). The measured stability constant for $\text{N}^3(\text{etLH})_3$ was found by indirect determination via EDTA competition to be $\log \beta_{110} = 27.34$, Eq. 2.1-34.

Between pH 8 and 10.4, a third deprotonation event, involving the dissociation of a fourth proton is observed (Fig. 2.12.B.) and exhibits an isosbestic point at 391nm. There are two possible reactions that can be attributed to this proton dissociation. It is possible that this is the removal of a proton from a water molecule coordinated to a sterically unhindered seventh coordination site on the Fe(III). This type of complex has previously been observed, such as in the seven-coordinate Fe(EDTA) complex.⁽¹¹⁰⁾ The second possibility is the deprotonation of the central polyamine ring (Eq. 2.1-33). This seems more likely, as evidenced by the small absorbance changes and λ_{max} which suggest a minimal change in the inner coordination sphere of iron. Further, this is

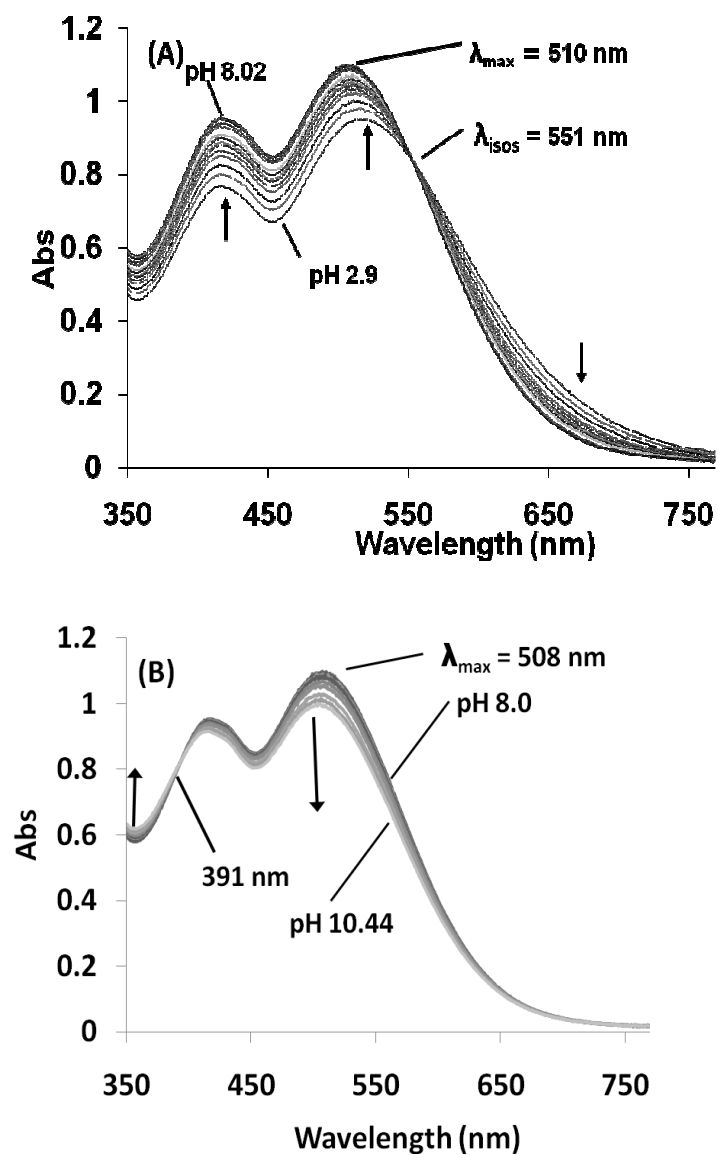


Figure 2.12. Spectrophotometric titration of the Fe-N³(etLH)₃ system, [Fe⁺³] = [N³(etLH)₃] = 4.4 × 10⁻⁴ M, T = 25 °C, μ = 0.10 (NaCl). Arrows indicate the direction of spectral change as the titration proceeded. (A) Titration over the pH range of 2.9 – 8.0. (B) Titration over the pH range 8.0 to 10.44.

consistent with the pK_a , for reaction 2.1-33., which is ~ 0.7 log units lower than the pK_a assigned to the less acidic proton dissociation ($pK_a = 10.4$) of the central ring system of $H_2N^3(etLH)_3^{2+}$. Above pH 10.4, the complex began to slowly dissociate, as evidenced by the gradual decrease of the spectral intensity to the baseline.

The species distribution diagram for the Fe(III)- $N^3(etLH)_3$ system as a function of pH is shown in Fig. 2.7.B. The distribution diagram shows that the Fe(III) is present exclusively as a hexadentate $Fe(N^3(etL)_3$ complex over the pH range of approximately 5 to 8.

2.4.5. Iron-trishydroxypyridinone redox chemistry

The cyclic voltammogram measured at pH 2.0 exhibited a single irreversible reduction at approximately 0 mV vs NHE (Fig. 2.13.A.). The potential of this peak was pH-dependent, shifting to -68 mV vs NHE at physiological pH (Fig. 2.13.B.). As the pH increased, a second quasi-reversible reduction peak appeared with a reduction peak potential of -383 mV. As the pH was increased, the peak increased in intensity and shifted to more negative potentials through physiological pH, with the lowest $E_{1/2}$ value being -389 mV vs NHE (Fig. 2.13.B.). At a scan rate of 50 mV/s, the more negative redox couple exhibited a peak current ratio $i_{pa}/i_{pc} = 0.286$, while increasing the scan rate increased the peak current ratio to 0.485 at 200 mV/s (100 mV/s shown in Fig. 2.14.). A voltammogram measured of the tris-hydroxypyridinone ligand itself at pH 7.0 exhibited

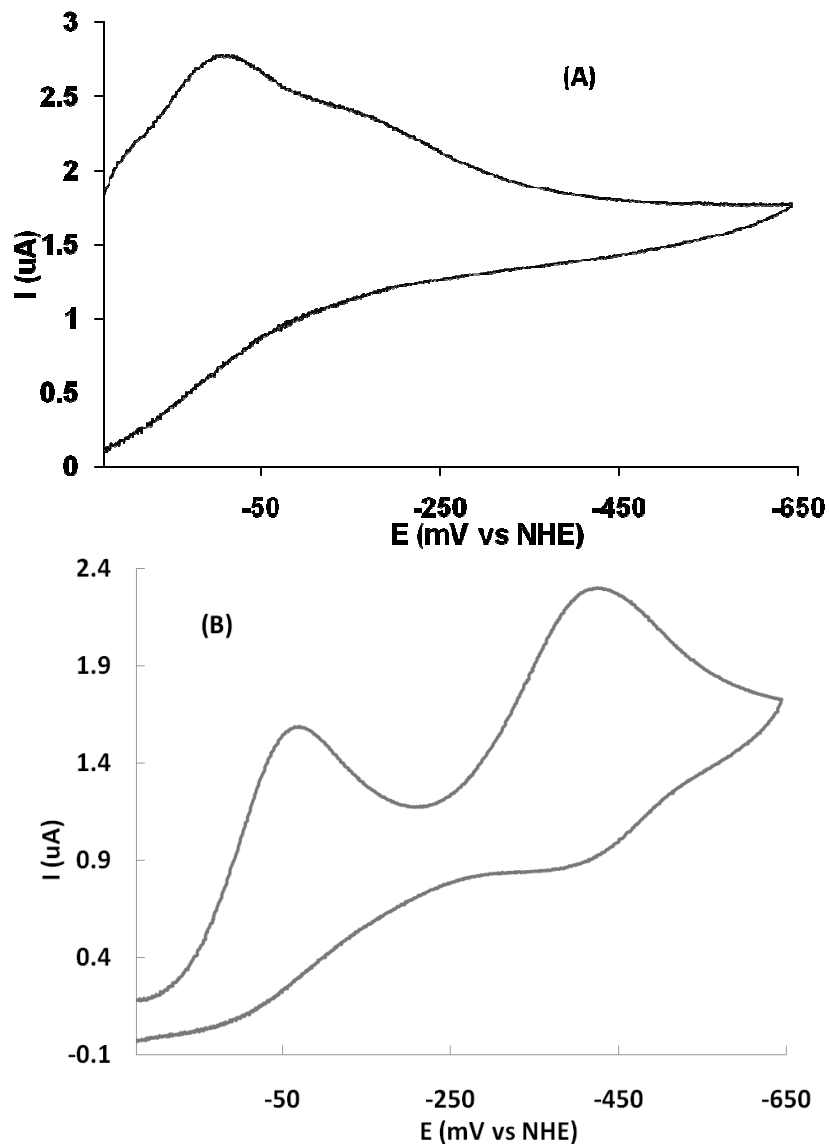


Figure 2.13. Representative cyclic voltammograms of the iron- $\text{N}^3(\text{etLH})_3$ system. (A) Cyclic voltammogram measured at pH 2.0. (B) Cyclic voltammogram measured at pH 7.58. Conditions: $[\text{Fe}^{3+}] = [\text{N}^3(\text{etLH})_3] = 1.5 \text{ mM}$, $T = 25 \text{ }^\circ\text{C}$, $\mu = 0.10$ (NaCl), working electrode: HDME, reference electrode: Ag/AgCl (3.5 M NaCl), auxiliary electrode: Pt wire, scan rate = 50 mV/s .

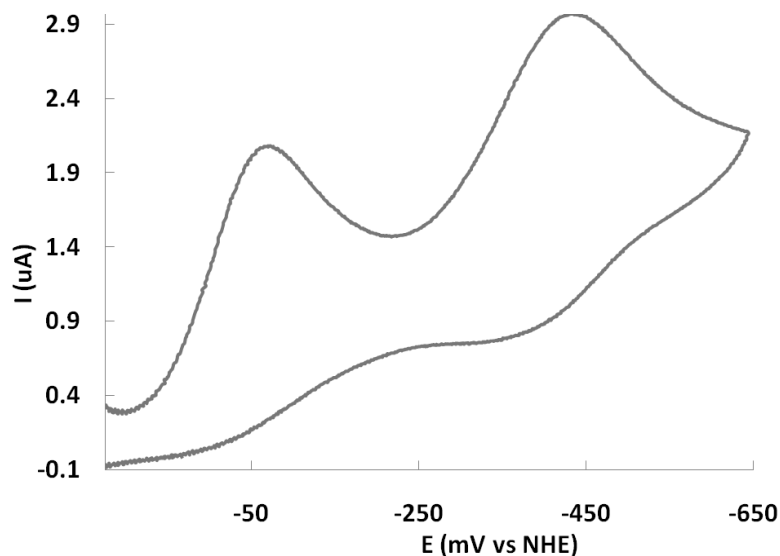


Figure 2.14. Cyclic voltammogram measured for the iron- $N^3(\text{etLH})_3$ system at increased scan rate to show increased reversibility. Conditions: $[\text{Fe}^{3+}] = [N^3(\text{etLH})_3] = 1.5 \text{ mM}$, $T = 25 \text{ }^\circ\text{C}$, $\mu = 0.10 \text{ (NaCl)}$, working electrode: HDME, reference electrode: Ag/AgCl (3.5 M NaCl), auxiliary electrode: Pt wire, scan rate = 100 mV/s.

no redox activity. These observations suggest that the more negative redox couple corresponds to the iron- $N^3(\text{etLH})_3$ complex, exhibiting a redox potential of -389 mV vs NHE. This redox potential is on the same order as that observed in some other HOPO complexes in the literature. The reported $E_{1/2}$ of HOPObactin is -342 mV vs NHE and that of TRENHOPO is -435 mV vs NHE.⁽⁸⁸⁾ Using the rearranged version of the Nernst equation (see Sec. 1.5.) and the measured complex redox potential, it is possible to calculate the stability constant of the $N^3(\text{etLH})_3$ complex for iron(II), $\log \beta^{\text{II}} = 7.75$. The

quasi-reversibility of the signal likely arises from the relatively low stability of the iron-tris-HOPO complex, in addition to the background electrolyte used in the experiment. It has been shown that chloride salts can act as a catalyst for complex dissociation reactions, which would result in a higher rate of complex dissociation upon reduction of the iron center and therefore lower reversibility than might be observed in other ligand systems. The irreversible reduction at lower potentials likely corresponds to small amount of lower order complex that is still present in solution. This is consistent with the observed potential of reduction, which is located at a less negative potential than that assigned to the hexacoordinate complex. The irreversibility of the reduction would also be consistent with the proposed complex assignment, as the tetradentate complex is more likely to dissociate upon reduction of iron(III) to iron(II), especially in the presence of chloride ion. Finally, this observation is consistent with the speciation diagram of the Fe-N³(etLH)₃ system (Fig. 2.7.B.), which shows that at pH 2.0, the bishydroxypyridinone FeLH complex is the predominant form of the complex, while the trishydroxypyridinone complex becomes the predominant complex as the pH increases through physiological pH.

2.4.6. Comparison of bis- and tris-HOPO ligands

A demonstration of the internal consistency of our model shown in Table 2.1. can be made by comparing the stability constants of complexes of similar denticity. Through linear combination of the protonation constant corresponding to the first

hydroxypyridinone moiety of $N^3(\text{etLH})_3$ (Eq. 2.1-30.) and the $\log \beta_{111}$ (Eq. 2.1-36.), one can obtain the equilibrium and stability constant shown in Eq. 2.1-38. The equilibrium constant for reaction of the doubly deprotonated trishydroxypyridinone ligand with iron(III) is $\log \beta_{\text{tet}} = 21.58$ (Eq. 2.1-38.), which is very close to the $\log \beta_{110}$ of $N^2(\text{etLH})_2$, 21.08 (Eq. 2.1-8.). The small increase in the $\log \beta_{\text{tet}}$ of $N^3(\text{etLH})_3$ compared to the $\log \beta_{110}$ of $N^2(\text{etLH})_2$ may be due to a chelate effect in $N^3(\text{etLH})_3$ or more favorable steric factors. The similarity of the two values demonstrates that the determinations are consistent between ligand systems. A similar comparison may be made for the $N^2(\text{prLH})_2$ system, where $\log \beta_{110} = 20.45$ (Eq. 2.1-22.).

pFe values are a useful criterion to compare iron chelators of different denticities and pK_as (see Sec. 1.4.1., Appendix A). Table 2.3. contains pFe values for $N^3(\text{etLH})_3$ and $N^2(\text{prLH})_2$, along with a representative group of comparable chelators listed in ascending order. The high Fe(III) affinity of $N^3(\text{etLH})_3$ and $N^2(\text{prLH})_2$ is reflected by their large pFe values, which are higher than 1- methyl-3-hydroxypyridin-2-one, consistent with their higher denticity and a modest chelate effect. The pFe value observed for $N^3(\text{etLH})_3$ is slightly less than the other tris-HOPO chelators in Table 2.3., suggesting that the triazacyclononane backbone does not confer significant additional stabilization in the arrangement of the HOPO chelating groups for iron sequestration.

Table 2.3. Calculated pFe values for a number of siderophores.

Ligand	pFe ^a
1-methyl-3-hydroxypyridin-2-one	16 ^b
Deferiprone	19.4 ^c
N ² (prLH) ₂	22.07 ^d
N ³ (etLH) ₃	23.49 ^d
Deferasirox	23.5 ^e
EDTA	24.16 ^d
3,4-LI-(Me-3,2-HOPO)	25.5 ^f
Desferrioxamine B	26.6 ^g
TRENHOPO	26.7 ^h
HOPObactin	27.4 ^h

^a pH = 7.4, [Fe³⁺] = 1.0 × 10⁻⁶ M,
[L] = 1.0 × 10⁻⁵ M.

^b Ref (111)

^c Ref (112).

^d This work

^e Ref (113)

^f Ref (114)

^g Ref (115)

^h Ref (88)

The pFe values for the chelators prepared in this study make them viable candidates for application as iron overload drugs. Their pFe values are comparable to transferrin and Deferasirox, a FDA approved drug, and superior to Deferiprone, a drug approved for use in iron overload therapy in Europe. It is useful in discussing potential iron chelation therapy agents to compare the thermodynamics of iron(III) chelation to that of transferrin, as iron overload patients are characterized by saturated serum transferrin.(116, 117) The pFe values are three log units lower than Desferal (desferrioxamine B), the other FDA approved therapeutic for this application. However, there are multiple factors involved in the effectiveness of a chelating agent in iron

chelation therapy.(118) Lower thermodynamics of iron chelation may be overcome by increasing chelator plasma concentration, and the kinetics of removal of iron from transferrin is also related to the efficiency of a molecule as an iron chelation therapy agent. Previous studies have shown that hydroxypyridinones can rapidly remove iron from transferrin, suggesting that the synthetic HOPO siderophores studied here exhibit iron binding capabilities in the range that could be of interest in the development of treatments for iron overload.(118)

Comparison of the stability of the hexacoordinate complex of $N^3(\text{etLH})_3$ with other HOPO chelators can give an indication of the structural factors that are of importance in complex formation. Interestingly, comparison of the stability constants would suggest the lack of chelate effect in these macrocyclic hydroxypyridinone siderophore mimics. The measured $\log \beta_{110}$ for $N^3(\text{etLH})_3$ (27.34) can be compared to the \log units of complex stability per iron center of the $\text{Fe}_2(\text{N}^2(\text{etL})_2)_3$ complex ($\log \beta_{230}^{1/2} = 30.23$), which would suggest higher stability in the bishydroxypyridinone complex. However, using the stability constants as the standard of comparison ignores the influence that ligand protonation constants play in aqueous solution complex formation. Therefore, in assessing the effective presence of the chelate effect, it is more appropriate to consider the ligand pFe values. Comparison of the pFe values determined for the $N^3(\text{etLH})_3$ system (23.49) to the $N^2(\text{prLH})_2$ system (22.07) seems to suggest a chelate effect in these exocyclic polyhydroxypyridinone molecules. This may have to do with

the structure of the central ring systems (cyclononane versus cyclohexane central ring system) as well as different length spacer arms ($N^3(\text{etLH})_3$ has a two carbon chain spacer and $N^2(\text{prLH})_2$ with a three carbon chain spacer), which may contribute to the difference in stability. The determined value of the $\log \beta_{110}$ of $N^3(\text{etLH})_3$ also agrees very well with a previously reported value of $\log \beta_{110} = 27.6$ for a tripodal trishydroxypyridinone siderophore mimic HOPOHL with Fe(III).⁽¹¹⁹⁾

2.5. Conclusions

The hydroxypyridinone donor group has been shown to allow the formation of siderophore mimic molecules that feature stable complexation of iron in aqueous environments. The tris-hydroxypyridinone and bis-hydroxypyridinone ligands studied here follow a similar trend, forming complexes with relatively high stability constants, $\log \beta_{110} = 27.34$ and $\text{pFe} = 23.49$ for $N^3(\text{etLH})_3$, $\log \beta_{230} = 27.34$ and $\text{pFe} = 22.07$ for $N^2(\text{prLH})_2$, and $\log \beta_{230} = 21.08$ for $N^2(\text{etLH})_2$. The stability of these complexes is in the range observed for natural and synthetic iron chelators, suggesting favorable complex stability for application of the molecules as chelation therapy agents.

3. Characterization of the mechanism of exchange of iron(III) bound by hydroxypyridinone siderophore mimics

3.1. Introduction

In nature, the uptake of iron can take place by a number of mechanisms. Some of these possible mechanisms were introduced in Chapter 1, although the reductive mechanism was the only process discussed in any depth. Another possible mechanism involves the exchange of iron from a highly stable siderophore complex to another iron chelator, which may be more or less stable than the extracellular siderophore. This has been proposed to be the case in some species of mycobacterium, where the extracellular siderophores, called exochelins, are proposed to exchange iron through some mechanism with membrane-bound siderophores, the mycobactins, which then transport the iron across the membrane through some uncharacterized mechanism (this will be discussed further in Chapter 5). While it is also possible that the metabolite salicylate molecules may also play a role in the exchange mechanism, as will discussed in Chapter 4, the exchange of iron from one hexadentate chelator to another can still serve as a useful model for this natural process.

A third possible transport mechanism involves the exposure of the iron-siderophore complex to a low pH environment, such as in an endosome. The exposure to low pH would result in the dissociation of some donor groups from the metal center and lead to the ability to exchange more easily with intracellular chelators. This mechanism has not been considered feasible due to the extremely low pH values that would be required in some cases to promote dissociation of donor groups from the iron center. However, any decrease in pH would make the contribution from this route greater than at neutral environmental conditions. The presence of secondary chelators of lower denticity could also facilitate the dissociation or exchange of iron from stable siderophore complexes, as will be addressed in Chapter 4.

The study of iron exchange reactions in such situations can lead to a greater understanding of the iron uptake mechanisms in natural systems. However, it may be difficult to obtain natural product chelator samples. It is also possible that the molecules in such a case are not yet characterized, as they may be attached to cellular membranes or have yet to be identified. Additionally, removing the actual molecules from the natural system may affect the nature of their reactions such that they take place at different rates or through different mechanisms. This is especially the case for proteins, which may require their natural environment to function normally. These systems are best analyzed using models of the types of molecules that might be involved in the exchange mechanisms taking place in the system.

3.2. Statement of chapter objectives

The purpose of this chapter is to describe the study of some iron(III) exchange reactions between polydentate ligands using model systems to provide insight into the mechanism of reactions likely found in natural cellular iron uptake processes. These studies use kinetic methods to provide insight into the mechanism of iron exchange between polydentate siderophore mimics. The model siderophore system that will be investigated is the hydroxypyridinone donor group siderophores thermodynamically characterized in Chapter 2. The exchange of iron(III) from $N^3(\text{etLH})_3$ (Fig. 3.1.) to

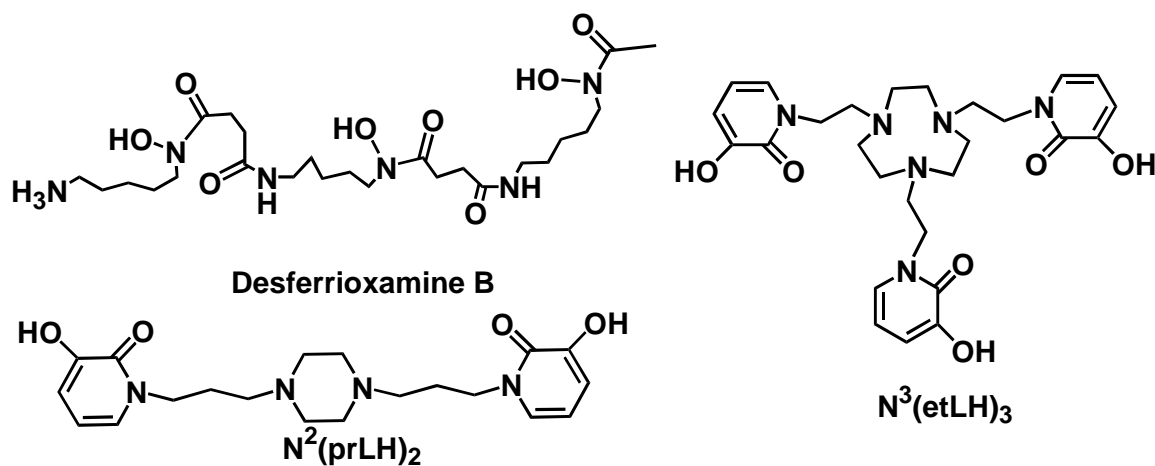


Figure 3.1. Chemical structures of the siderophore and siderophore mimics studied here. $N^3(\text{etLH})_3$ and desferrioxamine B were used in an iron(III) exchange reaction to determine the mechanism of exchange between the hexadentate ligands, while $N^2(\text{prLH})_2$ was used to investigate the mechanism of complex dissociation at low pH values.

desferrioxamine B (also Fig. 3.1.) will be investigated mechanistically, and by comparison of potential parallel or sequential reaction pathways it will be proposed that exchange occurs through a parallel pathway mechanism where one reaction pathway occurs through an intermediate outer sphere host-guest complex, followed by an inner-sphere ternary complex and the other pathway involves direct reaction of the trishydroxypyridinone complex with desferrioxamine B. In addition, the proton-driven dissociation of the $\text{Fe}_2\{\text{HN}^2(\text{prLH})_2\}_3^{3+}$ (Fig. 3.1.) complex will be characterized spectrophotometrically, and the mechanism of dissociation will be determined based on the structure of the complex. The proposed mechanism of proton-driven dissociation will proceed through a two-step mechanism, the first step involving dissociation of the trishydroxypyridinone complex to the bishydroxypyridinone complex through a parallel pathway mechanism.

3.3. Experimental

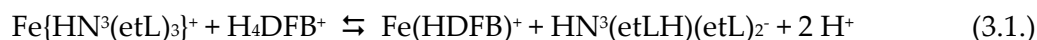
3.3.1. Materials

All solutions were prepared in deionized water. Solid NaNO_3 (>99%, Fischer Chemicals) was used to prepare background electrolyte solution. Solid anhydrous $\text{Fe}(\text{NO}_3)_3$ was obtained from Sigma and used to prepare 0.10 M stock solution in 0.10 M HNO_3 . The stock solution was standardized titrimetrically by reduction with SnCl_2 , followed by titration with $\text{K}_2\text{Cr}_2\text{O}_7$.(93) In the DFB exchange reaction, solid HEPES was used to prepare a 0.20 M HEPES in 0.10 M NaNO_3 buffered background solution. The

pH of the buffered background solution was adjusted to 7.19 using solid NaOH to minimize dilution. Solid samples of $N^3(\text{etLH})_3 \cdot 2 \text{HBr}$, and $N^2(\text{prLH})_2 \cdot 2 \text{HBr}$ were prepared by the Gopalan research group at New Mexico State University using the synthetic procedure described in Appendix A, and were used as received to prepare stock solutions of the ligands.⁽⁹⁴⁾

3.3.2. Exchange of iron(III) between desferrioxamine B and $N^3(\text{etLH})_3$

A kinetic experiment spectrophotometrically monitoring the exchange of iron(III) from $N^3(\text{etLH})_3$ to ferrioxamine B as a function of time was performed as shown in Eq. 3.1. UV-visible spectra for the ferrioxamine B exchange reactions were recorded using



a Cary-100 spectrophotometer equipped with a dual cell peltier accessory and the reaction temperature was maintained at 25 °C. A stock solution of 0.25 mM iron(III)- $N^3(\text{etLH})_3$ was prepared as described in the previous chapter by addition of all components, followed by adjustment of the solution pH using the background electrolyte buffered at pH 7.19 by 200 mM HEPES. The final concentration of the complex was verified spectrophotometrically using molar absorbance values determined in previous studies of the complex (see Chapter 2). Solutions of DFB in buffered background electrolyte (also pH 7.04) were prepared in a range of

concentrations from 20 mM to 47 mM. The solutions were mixed together in 1:1 ratios with a final pH of 7.19 and allowed to react over the course of 8 hours and the reaction was monitored spectrophotometrically over the range of 400-650 nm. The identity of the complex product was verified by comparison to the known spectral properties of Fe(HDFB)⁺.⁽²⁰⁾ The absorbance was taken at four distinct wavelengths and modeled to a double exponential decay equation (Eq. 3.2.), where A represents the absorbance at

$$A = m_1 e^{-k_{2obs}t} + m_2 e^{-k_{3obs}t} + A_{inf} \quad (3.2.)$$

time t, m₁ and m₂ represent the amplitude of the first and second components of absorbance change, respectively, k_{2obs} and k_{3obs} represent the observed rate constants of the first and second components of absorbance change, respectively, and A_{inf} represents the absorbance at infinite time.

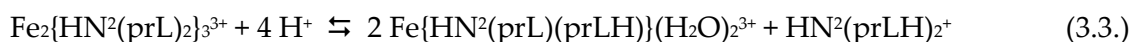
3.3.3. ESI-MS of the interactions between desferrioxamine B and N³(etLH)₃

The ESI-mass spectrum was measured of an aqueous solution containing a 30:1 excess of desferrioxamine B to N³(etLH)₃. Mass spectra were measured using an Agilent 1100 SL LC/MSD-Trap instrument in positive ion mode at a temperature of 125 °C, a nebulizer pressure of 15 psi, and a dry gas flow rate of 7 L/min. No background electrolyte was used in this experiment due to the propensity of perchlorate to form

adducts in ESI mass spectrometry experiments, which would complicate the ESI mass spectrum.

3.3.4. Proton-driven dissociation of the iron(III)-N²(prLH)₂ complex

A spectrophotometric kinetics experiment was performed to monitor the dissociation reaction of the Fe₂{HN²(prL)₂}₃ complex as a function of time at decreased pH (Eq. 3.3.). A stock solution of 0.30 mM N²(prLH)₂/0.20 mM Fe³⁺ was prepared in



unbuffered 0.10M NaNO₃ background electrolyte at approximately pH 6. A range of concentrations of HNO₃ from 0.010 M to 1.0 M were prepared from concentrated HNO₃ and then standardized against a standard 0.10 M NaOH solution or a standard 1.0 M NaOH solution to the phenolphthalein endpoint. Solutions were insulated at 25 °C until mixing to maintain reaction temperature. The final solution pH varied from 2.5 to less than 1 depending on the concentration of acid added. Spectra were measured during the reaction on an Applied Photophysics stopped-flow spectrophotometer, model SX.18MV. The detector used for full spectrum scans was a photodiode array detector, while the detector used for single wavelength scans was a photomultiplier tube. Simultaneous mixing of the solutions initiated the reaction, which was monitored at 3 different wavelengths. The absorbance was monitored over 1000 seconds and two

spectral shifts were observed. The spectrum of the final product was compared to the known spectra of lower order coordination species (see Chapter 2) to determine the identity of the final product. The change in absorbance at four distinct wavelengths was monitored and then fit to a double exponential decay model (Eq. 3.2.).

In these experiments, NaNO_3 is used as the background electrolyte. It was discussed in the previous chapter why chloride salts were used rather than perchlorate salts for the background electrolyte in thermodynamic studies. In kinetic experiments, it is undesirable to use chloride salts as the background electrolyte, as chloride has been shown to catalyze iron complex dissociation reactions through the formation of transient ternary complexes.⁽¹²⁰⁾ The anionic ternary ligand donates electron density to the iron center, accelerating release of the iron center by the chelating ligand. The same study showed that nitrate anion will accelerate complex dissociation reactions, but to a much lesser extent than chloride salts. Nitrate is generally not used in spectrophotometric experiments, as nitrate exhibits an absorbance at 297 nm with a molar absorptivity of approximately $7 \text{ M}^{-1} \text{ cm}^{-1}$ (data not shown). In these experiments, the range of wavelengths being measured is significantly remote from the wavelength of maximum absorbance of nitrate, which results in minimal interference in the absorbance spectrum by the nitrate anion. In the iron exchange reaction between $\text{N}^3(\text{etLH})_3$ and desferrioxamine B, it is assumed that catalysis by the chloride anion will play a negligible role in the rate of reaction due to the high thermodynamics of binding of the

trishydroxypyridinone ligand, as well as the possible formation of ternary complexes by a donor group of desferrioxamine B during the reaction.

3.4. Results and Discussion

3.4.1. Desferrioxamine B- $N^3(\text{etLH})_3$ iron(III) exchange reaction

The exchange of iron(III) to desferrioxamine B from the tris-hydroxypyridinone siderophore mimic, $N^3(\text{etLH})_3$ was monitored spectrophotometrically at pH 7.04 (Eq. 3.1), shown in Fig. 3.2. The initial spectrum of the reaction corresponds to that of the $\text{Fe}\{\text{HN}^3(\text{etL})_3\}$ complex, while the final spectrum of the exchange reaction corresponds to the ferrioxamine B complex. This suggests that the overall reaction proceeds corresponding to Eq. 3.1. No isosbestic point was observed during the reaction, although it is unclear if that is due to the narrow range of wavelengths being monitored. The absorbance measured at a single wavelength was plotted as a function of time, as shown in Fig. 3.3., and then fit to a double exponential decay model (Eq. 3.2). The double exponential decay model gave an acceptable theoretical fit to the experimental data with the minimum number of variables necessary (Fig. 3.3.), while a single exponential decay model (Eq. 3.4.) did not provide an acceptable fit.

$$A = me^{-kt} + A_{\text{inf}} \quad (3.4.)$$

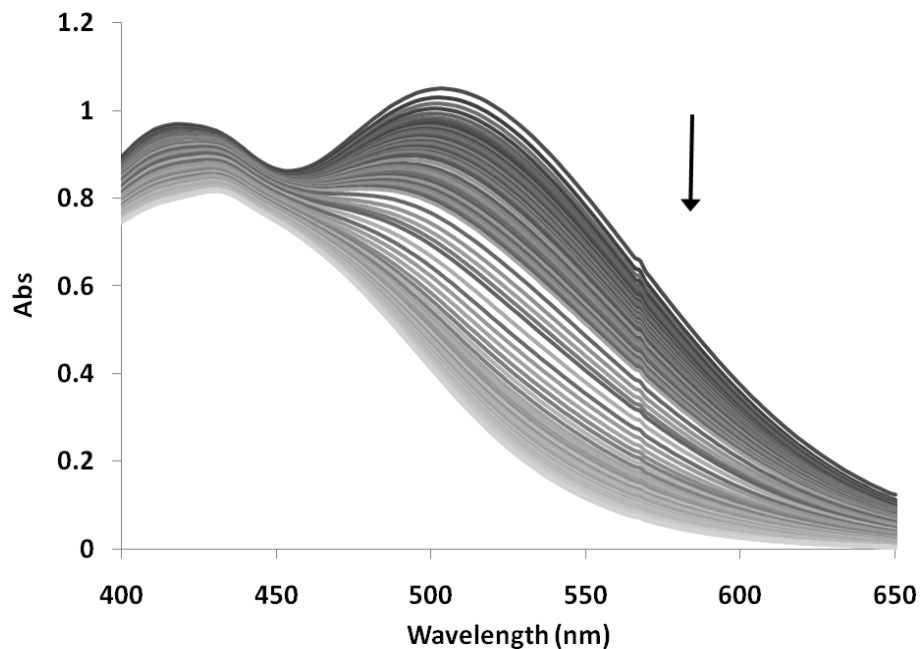


Figure 3.2. Spectra measured during the iron(III) exchange reaction between $N^3(\text{etLH})_3$ and desferrioxamine B (Eq. 1) over the course of 500 minutes. Conditions: $[\text{Fe}^{3+}] = [N^3(\text{etLH})_3] = 2.9 \times 10^{-4} \text{ M}$, $[\text{DFB}] = 10 \text{ mM}$, $T = 25 \text{ }^\circ\text{C}$, $\text{pH} = 7.19$ (0.20 M HEPES buffer), $\mu = 0.10 \text{ M}$ (NaClO_4). The arrow represents the direction of the spectral shift over time during the reaction.

In Eq. 3.4., A represents the absorbance at time t , m represents the amplitude of the absorbance change, k represents the observed rate constant, and A_{inf} represents the observed absorbance at time $= \infty$. The form of the rate law for reaction 1 is shown in Eq. 3.5.

$$\text{Rate} = (k_{2\text{obs}} + k_{3\text{obs}})[\text{Fe}\{\text{HN}^3(\text{etL})_3\}] \quad (3.5.)$$

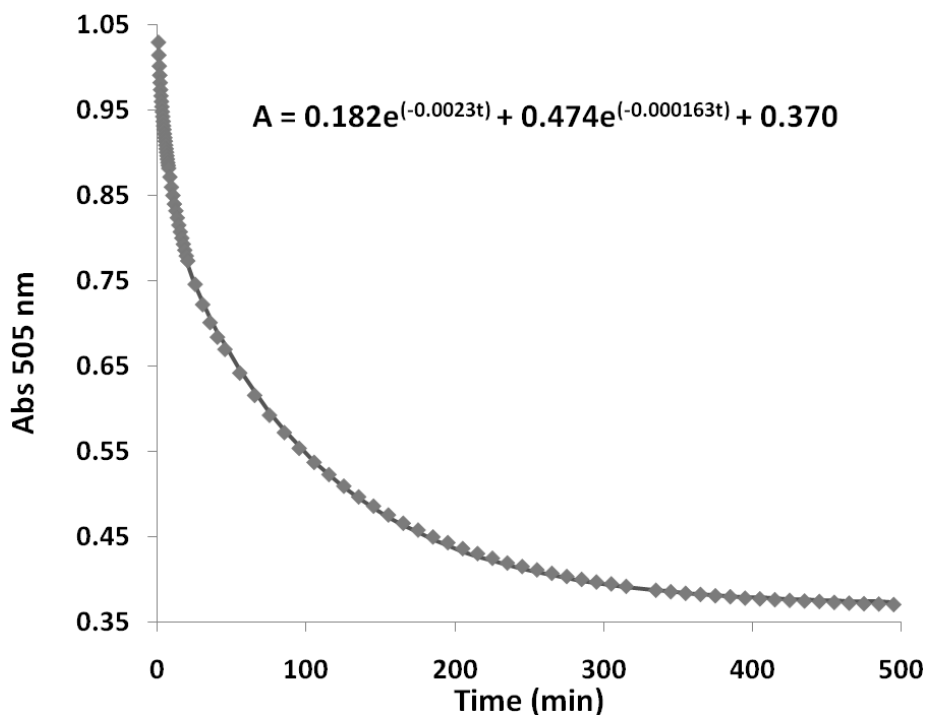


Figure 3.3. Absorbance measured at 505 nm during the iron(III) exchange reaction between $N^3(\text{etLH})_3$ and desferrioxamine B (Eq. 3.1.). The line represents the best fit line using a double exponential decay model (Eq. 3.2.) where $k_{2\text{obs}} = 2.3 \times 10^{-3} \text{ s}^{-1}$ and $k_{3\text{obs}} = 1.63 \times 10^{-4} \text{ s}^{-1}$. Conditions: $[\text{Fe}^{3+}] = [N^3(\text{etLH})_3] = 2.9 \times 10^{-4} \text{ M}$, $[\text{DFB}] = 5 \text{ mM}$, $T = 25 \text{ }^\circ\text{C}$, $\text{pH} = 7.19$ (0.20 M HEPES buffer), $\mu = 0.10 \text{ M}$ (NaClO_4).

The exponential fit of the experimental data suggests single order dependence of the rate law on $\text{Fe}\{\text{HN}^3(\text{etL})_3\}$ concentration, as shown in Eq. 3.5. A plot of $k_{2\text{obs}}$ as a function of desferrioxamine B concentration (Fig. 3.4.A.) and of $k_{3\text{obs}}$ as a function of desferrioxamine B concentration (Fig. 3.4.B.) demonstrates a linear relationship of both observed rate constants with respect to desferrioxamine B concentration, indicative of single order

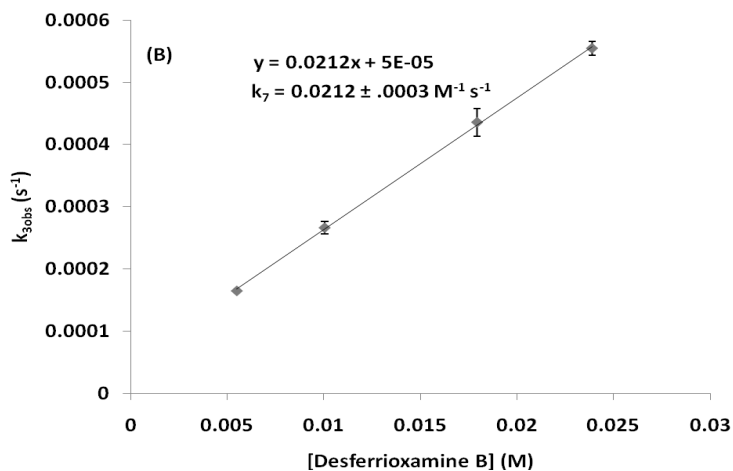
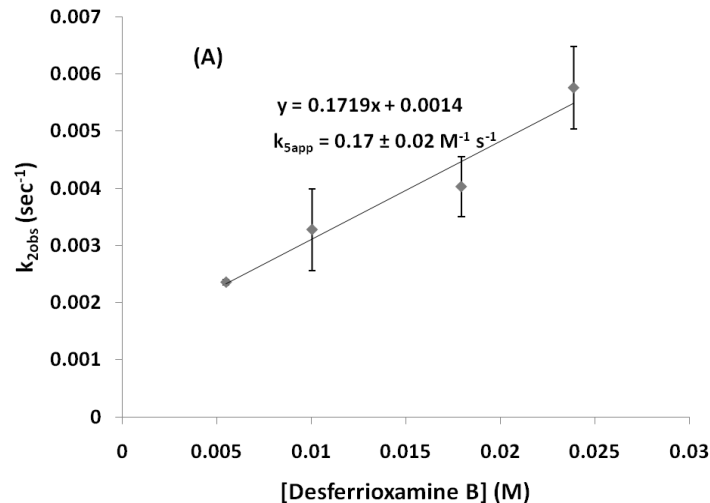


Figure 3.4. Plot of the pseudo-first order rate constants, k_{obs} as a function of DFB concentration. (A) Plot of k_{2obs} as a function of [Desferrioxamine B] yielding $k_{5app} = 1.7 \times 10^{-1} \text{ M}^{-1} \text{ s}^{-1}$ and $k_{6app} = 1.4 \times 10^{-3} \text{ s}^{-1}$; (B) Plot of k_{3obs} as a function of [Desferrioxamine B] yielding $k_7 = 2.12 \times 10^{-2} \text{ M}^{-1} \text{ s}^{-1}$. Conditions: $[\text{Fe}^{3+}] = [\text{N}^3(\text{etLH})_3] = 2.9 \times 10^{-4} \text{ M}$, $T = 25 \text{ }^\circ\text{C}$, $\text{pH} = 7.19$ (0.20 M HEPES buffer), $\mu = 0.10 \text{ M}$ (NaClO_4). Error bars represent the standard deviation of the observed rate constant at that concentration determined at 4 distinct wavelengths.

dependence of the rate law on desferrioxamine B concentration, as indicated in Eqs. 3.6.-3.7. Eqs. 3.6 and 3.7 represent the linear fits of the plots shown in Fig. 3.4.A. and 3.4.B.,

$$k_{2\text{obs}} = k_{5\text{app}}[\text{DFB}] + k_{6\text{app}} \quad (3.6.)$$

$$k_{3\text{obs}} = k_7[\text{DFB}] \quad (3.7.)$$

respectively. This suggests the involvement of a single molecule of desferrioxamine B in the rate determining step of both kinetically observable processes of reaction 3.1.

Additionally, the plot of $k_{2\text{obs}}$ as a function of desferrioxamine B concentration exhibits a non-zero y-intercept (Eq. 3.6.), suggesting the observation of a reversible reaction in the mechanism. The double exponential decay model suggests two parallel or sequential processes occurring during the exchange reaction. As one apparent rate constant is almost an order of magnitude larger than the other ($k_{5\text{app}} = 1.7 \pm 0.2 \times 10^{-1} \text{ M}^{-1} \text{ s}^{-1}$, $k_7 = 2.12 \pm 0.03 \times 10^{-2} \text{ M}^{-1} \text{ s}^{-1}$) and both observed rate constants ($k_{2\text{obs}}$ and $k_{3\text{obs}}$) are dependent on desferrioxamine B concentration, it is likely that the two processes are parallel rather than sequential.

Additional information pertinent to determining the reaction mechanism of Eq. 3.1. was obtained from an ESI-mass spectrometric investigation of a solution of 30:1 molar ratio desferrioxamine B: $\text{N}^3(\text{etLH})_3$ in aqueous solution in the absence of iron(III), shown in Fig. 3.5. The mass spectrum produced a signal at 1121.5 m/z units, and this

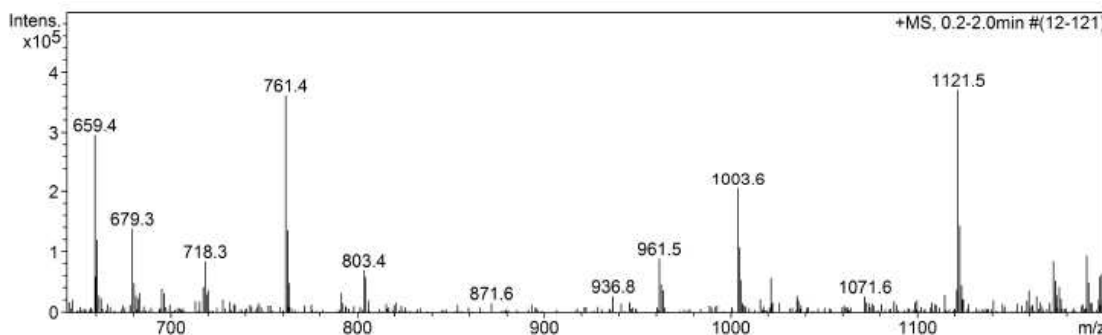


Figure 3.5. Electrospray mass spectrum of the desferrioxamine B- $N^3(\text{etLH})_3$ system.

Conditions: 50:1 molar ratio of desferrioxamine B: $N^3(\text{etLH})_3$, in aqueous solution with no background electrolyte, $T = 125\text{ }^\circ\text{C}$, nebulizer pressure = 15 psi, dry gas flow rate = 7 L/min.

mass-to-charge ratio can be assigned to the host-guest complex shown in Fig. 3.6. with the addition of a molecule of water (1121 m/z units). The structure of the trishydroxypyridinone ligand $N^3(\text{etLH})_3$ features a [9]ane N^3 central macrocycle where the secondary amine groups are positioned such that they can donate electron density to the formation of hydrogen bonds with the protonated pendant amine tail of desferrioxamine B, as shown in Fig. 3.6. While this interaction appears to be relatively weak based on the low intensity of the ESI peak, it is possible that the intermolecular interaction could provide some basis for the initial interaction of the complex and the receiving ligand in solution. These types of interactions have been studied previously in the context of host-guest complexes formed between ferrioxamine B and crown ethers, which showed that the host-guest interaction with crown ethers featured stability

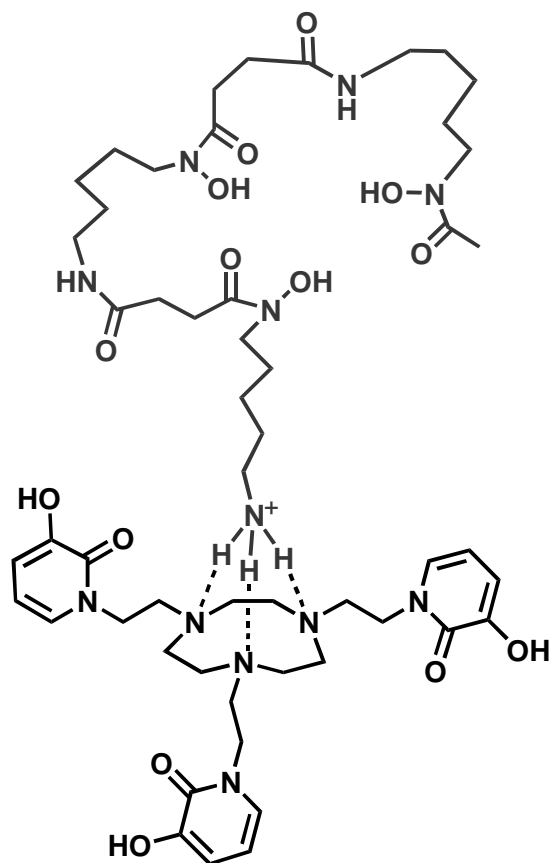
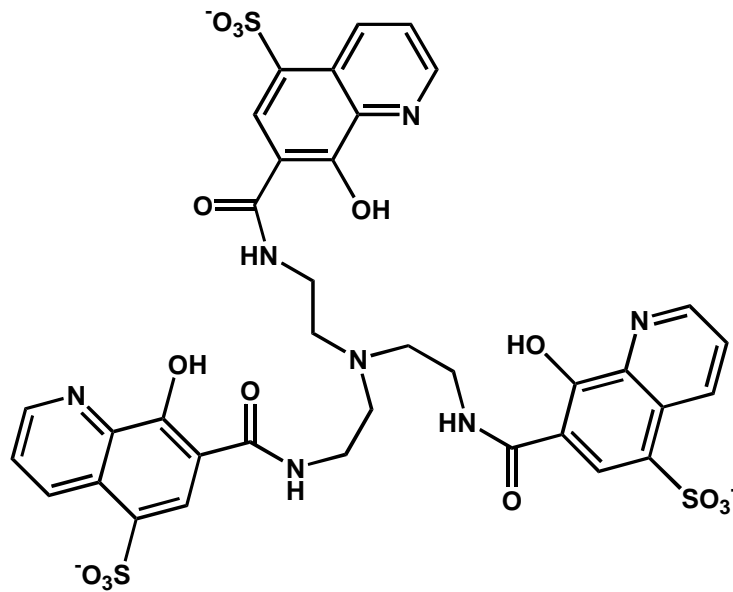


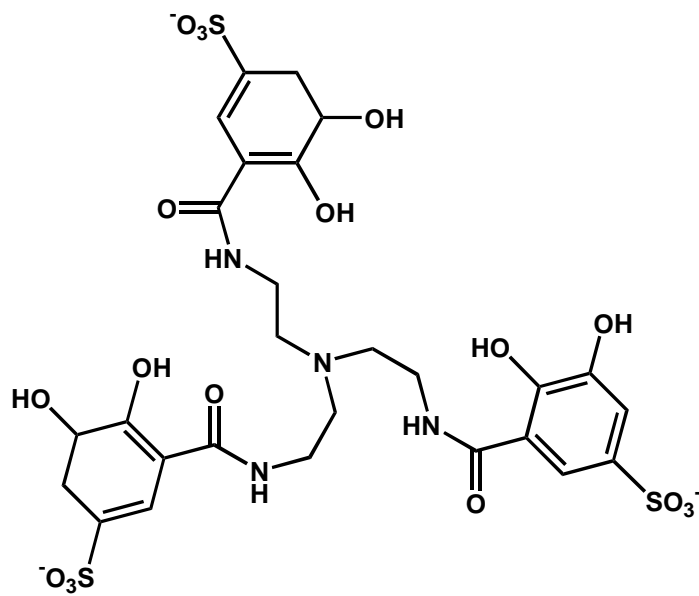
Figure 3.6. Proposed structure of the host-guest supramolecular assembly between desferrioxamine B and $N^3(\text{etLH})_3$, of which the molecular weight is 1102.3 Da. The ESI-mass spectrometry peak observed at 1121.5 m/z units has been assigned to a water adduct of this complex.

constants on the order of $\log K = 3$.⁽¹²¹⁾ However, this value for the host-guest interaction equilibrium constant was characterized in methanol, and it is likely that the hydrogen bonding interactions of the central ring in aqueous solution would hinder the formation of hydrogen bond interactions between desferrioxamine B and the central ring, leading to less stable formation of the host-guest complex in the desferrioxamine B- $N^3(\text{etLH})_3$ system. Additionally, it is possible that the smaller diameter of the triazacyclononane compared to the diameter of the crown ethers used in the previous study results in even weaker host-guest interactions. While the interaction may be weakened in the system studied here compared to the previously studied host-guest complex systems due to the factors discussed above, mass spectrometric evidence suggests that the host-guest complex is still formed in solution, and it is most likely that the complex exhibits the structure predicted in Fig. 3.6.

A previous study of the iron(III) exchange reaction between the hexadentate siderophore mimics, O-TRENTOX and TRENCAMS (Fig. 3.7.) suggested that the exchange between two hexadentate chelators proceeds by way of an inner sphere ternary complex between the complexing ligand and the receiving ligand.⁽¹²²⁾ While no readily characterized intermediate species was observed during the exchange reaction between $N^3(\text{etLH})_3$ and desferrioxamine B, it is possible that a similar mechanism is observed in this reaction.



O-TRENSEX

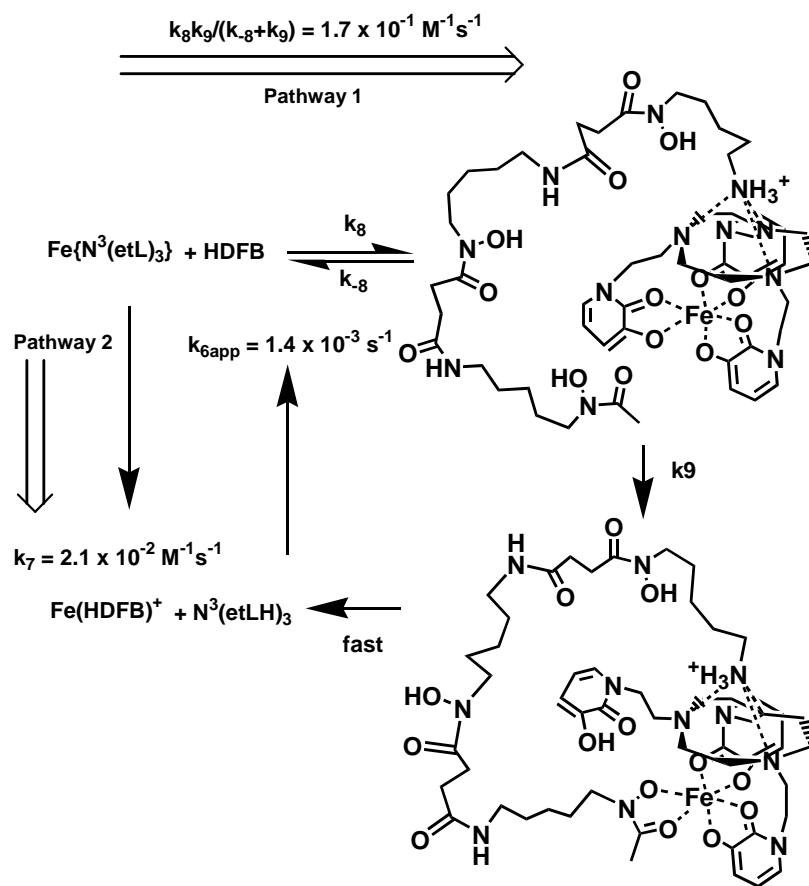


TRENAMS

Figure 3.7. Structures of the tripodal hexadentate iron chelators, O-TRENSEX and TRENAMS.

The observed host-guest supramolecular assembly between $N^3(\text{etLH})_3$ and desferrioxamine B, the observation of ternary complex intermediates in hexadentate ligand exchange reactions, and the difference between $k_{2\text{obs}}$ and $k_{3\text{obs}}$ are important characteristics of reaction 1. These three pieces of information can be used to propose three reaction mechanisms for reaction 1. These three mechanisms are described as follows. Two mechanisms involve parallel pathways, one pathway involving reaction via ternary complex formation and the other pathway involving a direct reaction pathway, where $k_{2\text{obs}}$ and $k_{3\text{obs}}$ are treated separately as representing one pathway each. The third mechanism involves a sequential pathway with two reversible steps where $k_{2\text{obs}}$ and $k_{3\text{obs}}$ are treated as representing a composite of the rate constants for the two steps.

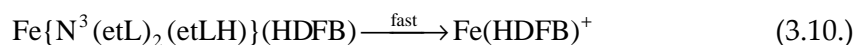
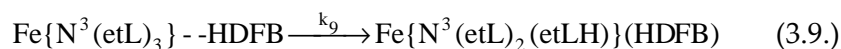
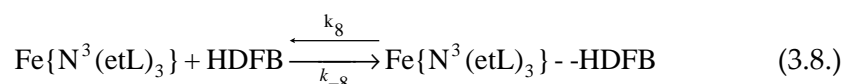
The first proposed reaction mechanism, Mechanism 1, involves two parallel pathways, designated Pathway 1 and Pathway 2 in Scheme 3.1. and applies the steady state approximation to the host-guest assembly intermediate to determine the rate law, as will be discussed below. In Mechanism 1, the mechanistic interpretation of Pathway 1 can be arrived at by analysis of $k_{2\text{obs}}$. In Pathway 1, the initial step involves formation of a host-guest supramolecular assembly, in a rapid step with forward rate constant k_s and reverse rate constant k_{-s} , and would not result in a spectral change. This host-guest supramolecular assembly would facilitate the formation of the inner-sphere ternary



Scheme 3.1. Proposed mechanism of exchange from $\text{N}^3(\text{etLH})_3$ to desferrioxamine B under the steady-state assumption. Pathway 1 of the reaction proceeds through initial rapid formation of a host-guest supramolecular assembly (k_8 representing the forward reaction and k_{-8} representing the reverse reaction), followed by the formation of an inner-sphere ternary complex between $\text{Fe}\{\text{N}^3(\text{etL})_3\}$ and a hydroxamate donor group of desferrioxamine B (represented by the rate constant k_9). The ternary complex formation facilitates complete exchange of iron to ferrioxamine B. Pathway 2 involves direct exchange of iron(III) from $\text{N}^3(\text{etLH})_3$ to desferrioxamine B with the second order rate constant $k_7 = 2.12 \times 10^{-3} \text{ M}^{-1} \text{ s}^{-1}$.

complex between desferrioxamine B and the $Fe\{N^3(etL)_3\}$ complex with the rate constant k_9 . The reactions represented by Pathway 1 of Scheme 3.1. would be as follows:

Mechanism 1



The final step of the exchange mechanism involves dissociation of the remaining hydroxypyridinone donor groups of $N^3(etLH)_3$ to be replaced by desferrioxamine B, which would be more rapid than the formation of the ternary complex. Thus, the formation of the ternary complex can be viewed as the rate limiting step of the reaction.

One method for deriving a rate law for Eqs. 3.8.-3.10. can be done by applying a steady state assumption to the concentration of the host-guest complex (Eq. 3.9.). That is, the rate of formation of the host-guest complex is equal to the rate of consumption of the host-guest complex in this reaction.

$$\frac{d[Fe(N^3(etL)_3) - HDFB]}{dt} = 0 = k_8[Fe\{N^3(etL)_3\}][HDFB] - k_{-8}[Fe\{N^3(etL)_3\} - HDFB] - k_9[Fe\{N^3(etL)_3\} - DF B] \quad (3.11.)$$

In Eq. 3.11., k_8 represents the rate constant of formation of the host-guest complex, k_{-8} represents the rate constant of dissociation of the host-guest complex, and k_9 is the rate constant of formation of the ternary inner sphere complex as shown in Eqs. 3.8. and 3.9. This assumption is reasonable, as the consumption of the complex is slow and when the formation of the host-guest complex is at a steady state, additional complex can only be produced when some is consumed.

Using the steady state assumption, it is possible to determine the concentration of the host-guest complex for relation to the rate law, shown in Eqs. 3.12.-3.15.

$$k_8[\text{Fe}\{\text{N}^3(\text{etL})_3\}\text{--}(\text{HDFB})] + k_9[\text{Fe}\{\text{N}^3(\text{etL})_3\}\text{--}(\text{HDFB})] = k_8[\text{Fe}\{\text{N}^3(\text{etL})_3\}][\text{HDFB}] \quad (3.12.)$$

$$[\text{Fe}\{\text{N}^3(\text{etL})_3\}\text{--}(\text{HDFB})] = \frac{k_8[\text{Fe}\{\text{N}^3(\text{etL})_3\}][\text{HDFB}]}{k_{-8} + k_9} \quad (3.13.)$$

$$\text{Rate} = k_9[\text{Fe}\{\text{N}^3(\text{etL})_3\}\text{--}(\text{HDFB})] \quad (3.14.)$$

$$\text{Rate} = \frac{k_8 k_9 [\text{HDFB}][\text{Fe}\{\text{N}^3(\text{etL})_3\}]}{k_{-8} + k_9} \quad (3.15.)$$

$$\text{Rate} = k_{\text{obs}}[\text{Fe}\{\text{N}^3(\text{etL})_3\}] \quad (3.16.)$$

This means that the observed rate constant of the reaction can be described with a linear relationship with respect to desferrioxamine B shown in Eq. 3.17.

$$k_{2obs} = \frac{k_8 k_9 [HDFB]}{k_{-8} + k_9} \quad (3.17.)$$

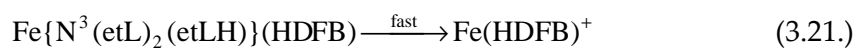
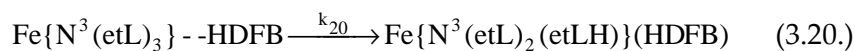
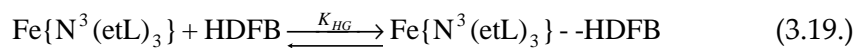
Therefore, from the plot shown in Fig. 3.4.A., we see that

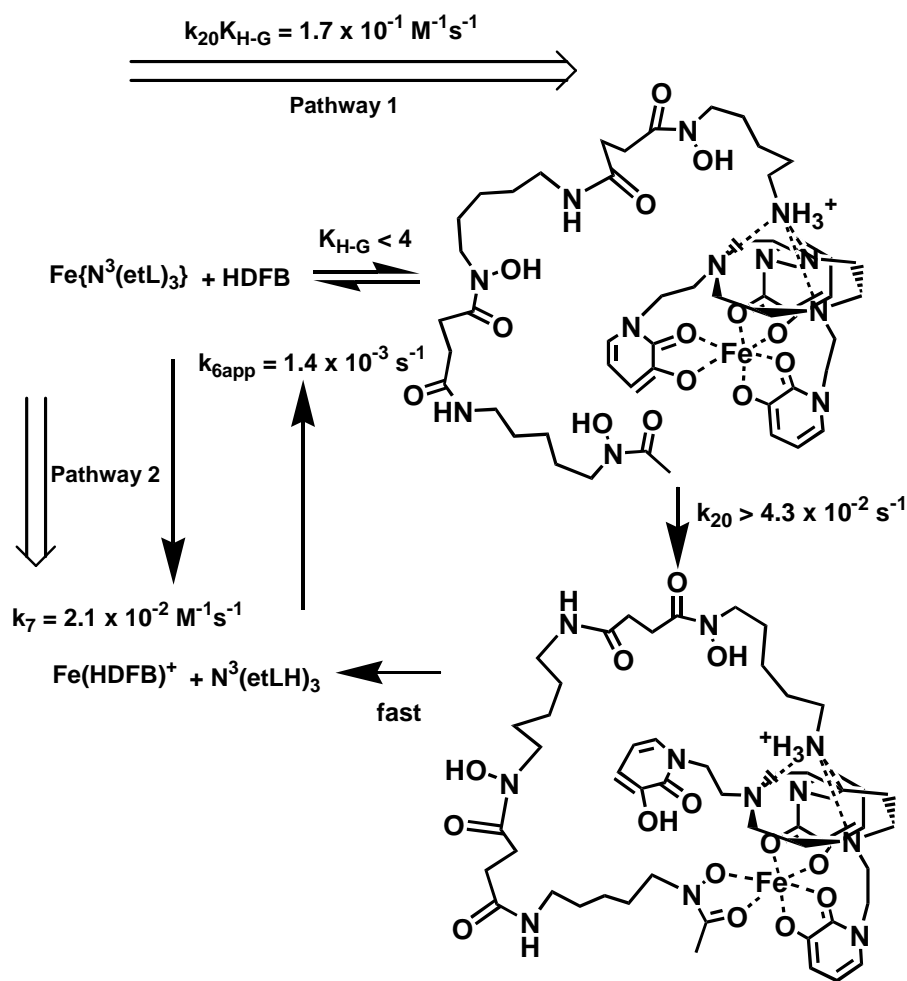
$$k_{5app} = \frac{k_8 k_9}{k_{-8} + k_9} = 1.7 \times 10^{-1} M^{-1} s^{-1} \quad (3.18.)$$

Without more information, it is not possible to determine the values of the microscopic rate constants k_8 , k_{-8} , or k_9 using this model.

Another interpretation of the reaction that can lead to the derivation of a rate law for the reaction is that the reaction occurs through a pre-equilibrium step, which will be referred to as Mechanism 2 as shown in Scheme 3.2. As with Mechanism 1, the mechanistic interpretation of Pathway 1 for Mechanism 2 can be arrived at by analysis of k_{2obs} . In this interpretation, Eqs. 3.8.-3.10. are rewritten as

Mechanism 2





Scheme 3.2. Reaction scheme corresponding to the pre-equilibrium interpretation of Reaction 1, shown in Mechanism 2. Initial reaction involves the equilibrium formation of a host-guest complex ($K_{\text{H-G}}$), followed by formation of the inner-sphere ternary complex (k_{19}). This reaction leads to rapid exchange of iron(III) from the ternary complex to ferrioxamine B. Pathway 2 of the reaction involves direct exchange of iron(III) from $N^3(\text{etLH})_3$ to desferrioxamine B with the second order rate constant $k_7 = 2.12 \times 10^{-3} \text{ M}^{-1} \text{ s}^{-1}$.

The rate of reaction can be expressed in terms of the production of the product $\text{Fe}\{\text{HDFB}\}^+$, which assuming that the initial equilibrium is a rapid equilibrium, can in turn be expressed in terms of the loss of both $\text{Fe}\{\text{N}^3(\text{etL})_3\}$ and the host-guest complex

$$d[\text{Fe}(\text{HDFB})^+]/dt = k_{\text{obs}}([\text{Fe}\{\text{N}^3(\text{etL})_3\}] + [\text{Fe}\{\text{N}^3(\text{etL})_3\} \text{--} \text{HDFB}]) \quad (3.22.)$$

Since the rate limiting step of the reaction is the reaction of the host-guest complex to form the ternary complex, the equilibrium expression of the formation of the host-guest complex must be taken into account.

$$K_{\text{H-G}} = \frac{[\text{Fe}\{\text{N}^3(\text{etL})_3\} \text{--} \text{HDFB}]}{[\text{Fe}\{\text{N}^3(\text{etL})_3\}][\text{HDFB}]} \quad (3.23.)$$

$$K_{\text{H-G}}[\text{Fe}\{\text{N}^3(\text{etL})_3\}][\text{HDFB}] = [\text{Fe}\{\text{N}^3(\text{etL})_3\} \text{--} \text{HDFB}] \quad (3.24.)$$

$$d[\text{Fe}(\text{HDFB})^+]/dt = k_{20}[\text{Fe}\{\text{N}^3(\text{etL})_3\} \text{--} \text{HDFB}] \quad (3.25.)$$

$$d[\text{Fe}(\text{HDFB})^+]/dt = k_{20}K_{\text{H-G}}[\text{HDFB}][\text{Fe}\{\text{N}^3(\text{etL})_3\}] \quad (3.26.)$$

The expression to describe the observed rate constant can be obtained by setting Eq. 3.22. equal to Eq. 3.26.

$$k_{\text{obs}}([\text{Fe}\{\text{N}^3(\text{etL})_3\}] + [\text{Fe}\{\text{N}^3(\text{etL})_3\} \text{--} \text{HDFB}]) = k_{20}K_{\text{H-G}}[\text{HDFB}][\text{Fe}\{\text{N}^3(\text{etL})_3\}] \quad (3.27.)$$

It can be shown that

$$k_{obs} = \frac{k_{20} K_{H-G} [HDFB] [Fe\{N^3(etL)_3\}]}{[Fe\{N^3(etL)_3\}] + [Fe\{N^3(etL)_3\} - HDFB]} \quad (3.28.)$$

$$k_{obs} = \frac{k_{20} K_{H-G} [HDFB]}{1 + K_{H-G} [HDFB]} \quad (3.29.)$$

The relationship shown in Eq. 3.29. suggests that at low desferrioxamine B concentrations (where $1 \gg K_{H-G}[HDFB]$), the observed rate of reaction should be linearly dependent with respect to concentration of desferrioxamine B, while at high desferrioxamine B concentration (where $1 \ll K_{H-G}[HDFB]$), the observed rate constant should be independent of desferrioxamine B concentration ($k_{5obs} \approx k_{20}$). The plot of observed rate constant k_{2obs} as a function of desferrioxamine B concentration (Fig. 3.4.A.) exhibits a straight line fit with a non-zero intercept, and the slope of the linear fit of the plot in Fig. 3.4.A. is $1.7 \pm 0.2 \times 10^{-1} \text{ M}^{-1} \text{ s}^{-1}$. In the range of desferrioxamine B concentrations studied here, there is no indication that the rate constant deviates from linearity, suggesting that if Mechanism 2 is the appropriate interpretation, the value of $K_{H-G}[HDFB]$ is still much less than 1. In order for this relationship to be true, $K_{H-G}[HDFB]$ must be less than 0.1. Using the highest concentration of desferrioxamine B used in the exchange reaction, 25 mM, the maximum value of K_{H-G} must be 4. This extremely low formation constant for the host-guest supramolecular assembly is consistent with the results of the ESI-mass spectrometry experiments described above,

which suggested very weak formation of the host-guest complex due to hydrogen bonding by the solvent and protonation of the [9]aneN³ central ring system.

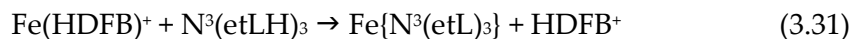
Determination of the maximum value of the host-guest supramolecular assembly formation constant also allows determination of the minimum value of the rate constant k_{20} . As discussed above, when $K_{H-G}[HDFB]$ is small, the slope of the plot shown in Fig. 3.4.A. is

$$k_{5app} = k_{20}K_{H-G} \quad (3.30.)$$

Using the value determined for the maximum value of K_{H-G} and the slope of the plot shown in Fig. 3.4.A. ($1.7 \times 10^{-1} \text{ M}^{-1}\text{s}^{-1}$), it is seen that the minimum value of k_{20} is $4.3 \times 10^{-2} \text{ s}^{-1}$. The minimum rate constant for formation of the ternary inner sphere complex (k_{20}) is a reasonable value for the formation of a ternary inner sphere complex, as the reaction involves dissociation of a single donor group from a hexadentate complex. Such a dissociation reaction is generally a very slow reaction, especially at approximately neutral pH.

Both mechanisms 1 and 2 provide rate laws that allow interpretation of the slope of the plot in Fig. 3.4.A, however neither provide rate laws that take into account the y-intercept. This observation leads to the interpretation that the y-intercept represents the

reverse reaction, direct reaction of the ferrioxamine B complex with $N^3(\text{etLH})_3$ to form the $\text{Fe}\{N^3(\text{etL})_3\}$ complex, as shown in Eq. 3.31.



The observed rate constant for this reverse reaction obtained from the y-intercept of the plot in Fig. 3.4.A. is $k_{6\text{app}} = 1.4 \times 10^{-3} \text{ s}^{-1}$. While this apparent rate constant, $k_{6\text{app}}$ is a first order observed rate constant, the mechanism of the reverse reaction in Eq. 3.31. is likely a bimolecular reaction with a second order rate constant in the rate law of the reaction. Therefore, it is not possible to comment on the validity of $k_{6\text{app}}$ as determined from Fig. 3.4.A. The value of the second order rate constant can be determined by performing the exchange reaction over a range of excess $N^3(\text{etLH})_3$ concentrations.

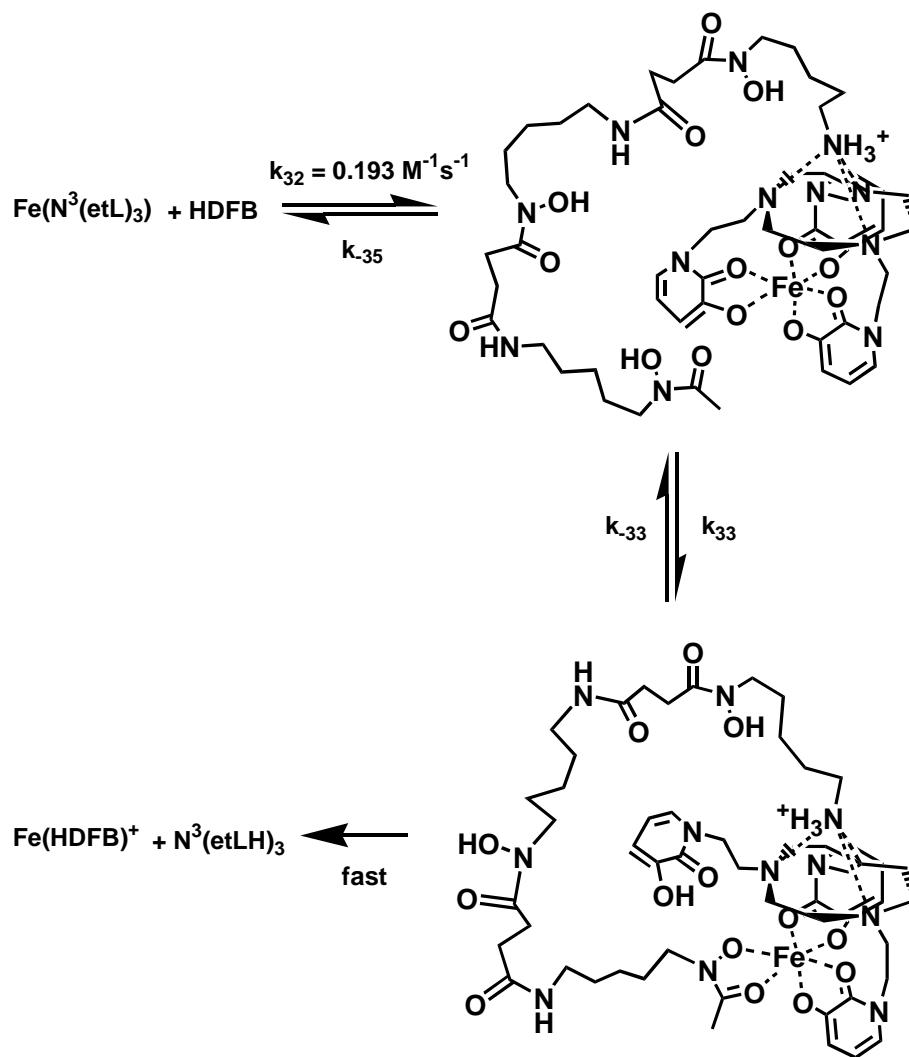
Under either of the above interpretations, the observation that the ternary complex reacts rapidly to exchange iron(III) suggests that $k_{3\text{obs}}$ does not represent a second step of the reaction, but rather a parallel reaction pathway, as shown in Eq. 3.32.



The plot of $k_{3\text{obs}}$ as a function of DFB concentration (Fig. 3.4.B.) exhibits a linear dependence with respect to desferrioxamine B concentration and an approximately zero

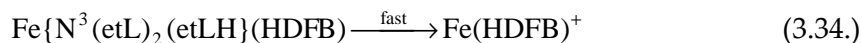
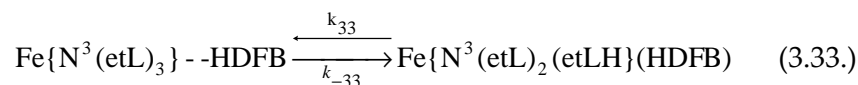
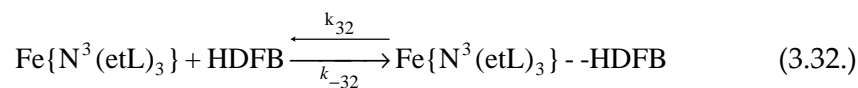
y-intercept. The second order rate constant for this pathway ($k_7 = 2.12 \pm 0.03 \times 10^{-2} \text{ M}^{-1} \text{ s}^{-1}$) is an order of magnitude lower than the second order rate constant of pathway 1, $k_{5\text{app}}$, suggesting that the second pathway of the iron(III) exchange reaction between $\text{N}^3(\text{etLH})_3$ and desferrioxamine B involves direct reaction of desferrioxamine B with the $\text{Fe}\{\text{HN}^3(\text{etL})_3\}$ complex, as shown in Pathway 2 of Scheme 3.1. and Scheme 3.2. Direct reaction via Pathway 2 likely involves the formation of a ternary inner sphere complex without the formation of the host-guest supramolecular assembly. Comparison of k_7 to k_{20} demonstrates that the value of k_7 and the minimum value of k_{20} , representing the formation of the ternary inner sphere complex are very similar to each other. This observation suggests that if Mechanism 2 of Pathway 1 is the appropriate model, then k_7 is suggestive of ternary inner sphere complex formation in Pathway 2 of Scheme 3.1. and Scheme 3.2.

A third mechanism represented by sequential pathway reaction (Scheme 3.3.) would also offer a rate law consistent with a double exponential decay by assuming reversibility of both steps, followed by rapid conversion of the intermediate ternary complex to the final product, as shown in Eqs. 3.32.-3.34., which will be referred to as Mechanism 3.



Scheme 3.3. Reaction scheme corresponding to Mechanism 3, where iron(III) exchange occurs through two sequential reversible steps. The first reversible step represents formation of the host-guest supramolecular assembly, while the second step involves formation of the ternary inner sphere complex. The final step, involving complete exchange of iron from the ternary complex to desferrioxamine B is more rapid than the ternary complex formation.

Mechanism 3



In Mechanisms 1 and 2, $k_{2\text{obs}}$ and $k_{3\text{obs}}$ are treated as representing separate parallel reaction pathways. However, under Mechanism 3, $k_{2\text{obs}}$ and $k_{3\text{obs}}$ are treated as representing a single sequential pathway. It can be shown that under this model, a biphasic absorbance change (two distinct kinetic ranges, as described by a double exponential decay model) would be observed and the reaction would exhibit the rate law

$$k_{2\text{obs}} + k_{3\text{obs}} = k_{32}[\text{HDFB}] + k_{-32} + k_{33} + k_{-33} \quad (3.35.)$$

$$k_{2\text{obs}}k_{3\text{obs}} = k_{32}(k_{33} + k_{-33})[\text{HDFB}] + k_{-32}k_{-33} \quad (3.36.)$$

with first-order dependence on desferrioxamine B concentration.⁽⁵⁵⁾ The plot of $k_{2\text{obs}} + k_{3\text{obs}}$ as a function of desferrioxamine B concentration and of $k_{2\text{obs}}k_{3\text{obs}}$ as a function of desferrioxamine B concentration are shown in Fig. 3.8.A. and B, respectively. By comparing Eq. 3.35. to Fig. 3.8.A., it is seen that the rate constant for the formation of the host-guest supramolecular assembly is $k_{32} = 1.93 \times 10^{-1} \text{ M}^{-1}\text{s}^{-1}$. This rate constant seems

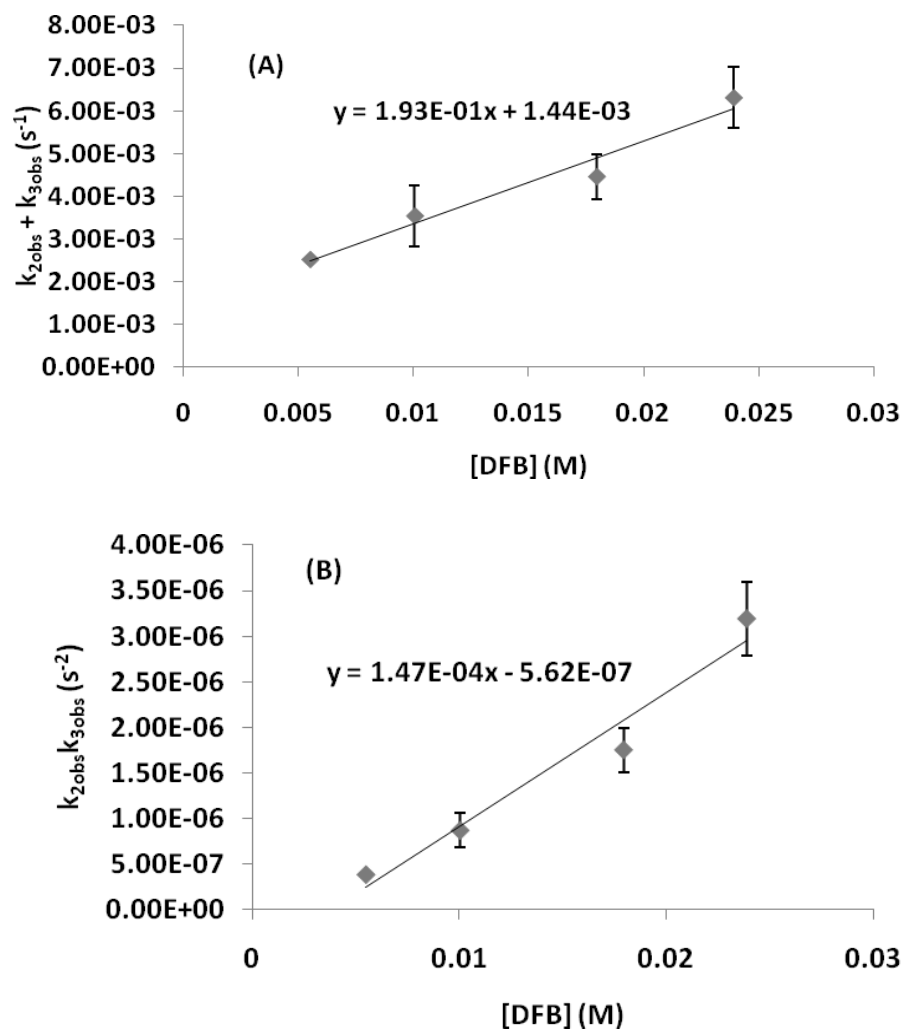


Figure 3.8. Plots of (A) $k_{2obs} + k_{3obs}$ as a function of desferrioxamine B concentration and (B) $k_{2obs}k_{3obs}$ as a function of desferrioxamine B concentration. Kinetic parameters were obtained from the exchange of iron(III) from $N^3(etLH)_3$ to desferrioxamine B. Conditions: $[Fe^{3+}] = [N^3(etLH)_3] = 2.9 \times 10^{-4}$ M, $T = 25$ °C, $pH = 7.19$ (0.20 M HEPES buffer), $\mu = 0.10$ M ($NaClO_4$). Error bars represent the propagated standard deviation of the observed rate constants at that concentration determined at 4 distinct wavelengths.

relatively slow for the formation of a host-guest supramolecular assembly, which takes place by the breaking and formation of hydrogen bonds. Additionally, it seems that this interpretation is not appropriate for the system, as the plot shown in Fig. 3.8.B.

corresponding to Eq. 3.36. exhibits a negative y-intercept which is significantly less than zero (compared to the values of $k_{2\text{obs}}k_{3\text{obs}}$). This observation is not consistent with Eq. 3.36., due to the magnitude of the negative y-intercept of the plot.

Based on these observations, it possible to say that the iron(III) exchange reaction mechanism between desferrioxamine B and $\text{N}^3(\text{etLH})_3$ is consistent with both Mechanism 1 (Scheme 3.1.) and Mechanism 2 (Scheme 3.2.). Without more information, it is not possible to determine the values of the microscopic rate constants k_s , k_{-s} , and k_9 , which prevents comparison to similar reactions. Additionally, both Mechanism 1 and Mechanism 2 are consistent with the observations provided by ESI-mass spectrometry.

3.4.2. Proton-driven dissociation of the $\text{Fe-N}^2(\text{prLH})_2$ complex

Exposure of a complex featuring ionizable donor groups to low pH environments can result in the dissociation of some donor groups from the complex due to their competitive protonation at higher proton concentrations. This reaction can be viewed as a loose model for a biological system where an iron-siderophore complex may be exposed to low pH compartments inside the cell, intended to facilitate the release of iron from siderophore complexes with high thermodynamic stability or to decrease the

complex stability to facilitate exchange between ligands. The reaction can also be viewed as a general model of dechelation reactions of polydentate chelators from the inner coordination shell of a metal ion.

A previous study of the proton-driven dissociation of some bishydroxamate complexes with iron(III) showed that the tetradentate complexes can exist in solution as both a singly-bridged Fe_2L_3 complex and as a triply-bridged Fe_2L_3 complex where all three tetradentate ligands contribute one donor group to both of the iron centers, as shown in Fig. 3.9. These two structures will provide multiple pathways for proton-driven dissociation of the complex.⁽¹²³⁻¹²⁵⁾ The structure of this complex is an important factor in proposing a mechanism for the proton-driven dissociation reaction. Thus, it is important to determine the structure of the hexacoordinate complex in solution at the beginning of the reaction. This was achieved by performing an ESI-mass spectrometry experiment on the $\text{Fe-N}^2(\text{prLH})_2$ system at low pH, where spectral evidence suggested that the complex was predominantly present in the form of the monomeric FeL complex. As discussed in Section 2.3.3, the complex structure was proposed to be the singly-bridged Fe_2L_3 form at physiological pH values (Fig. 3.9.), as this is the most likely form of the Fe_2L_3 complex upon increasing the solution pH, starting from the monomeric FeL complex.

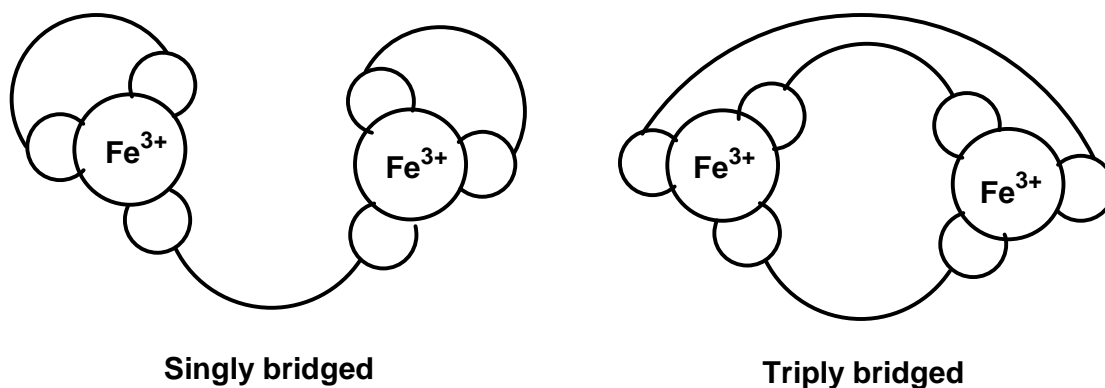


Figure 3.9. Schematic representation of the structures of singly-bridged and triply-bridged Fe_2L_3 complexes.

In the experiments performed here, the initial solution pH was approximately 6, well into the region where the Fe_2L_3 complex is the predominant species in solution (see speciation diagrams, Sec. 2.4.). Upon mixing the complex solution with a strongly acidic solution, the system pH was decreased rapidly, resulting in a shift in complex coordination number at the iron centers from hexacoordinate to tetra-coordinate. This can be established by comparing the λ_{max} values observed at the beginning of the reaction (506 nm) and at the end of the reaction (547 nm) to those observed in the thermodynamic studies of the complex described in chapter 2. In the thermodynamic study, it was shown that the λ_{max} corresponding to the hexadentate complex is 503 nm, while the λ_{max} corresponding to the tetradentate complex is 548 nm. At even lower pH values, the coordination number was decreased further to bidentate.

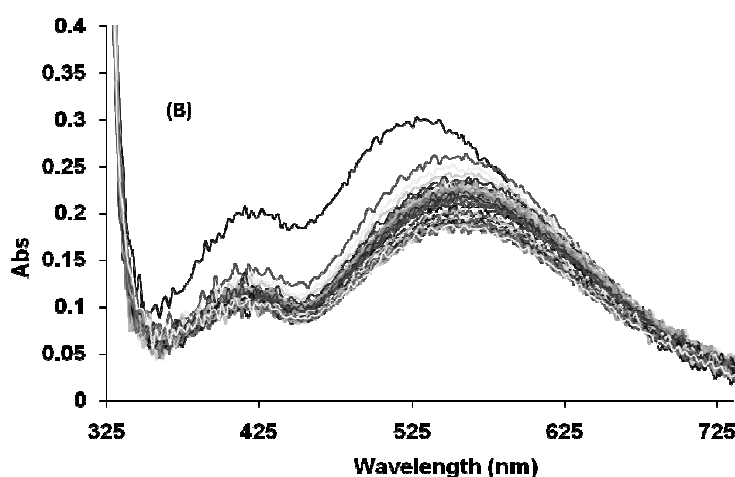
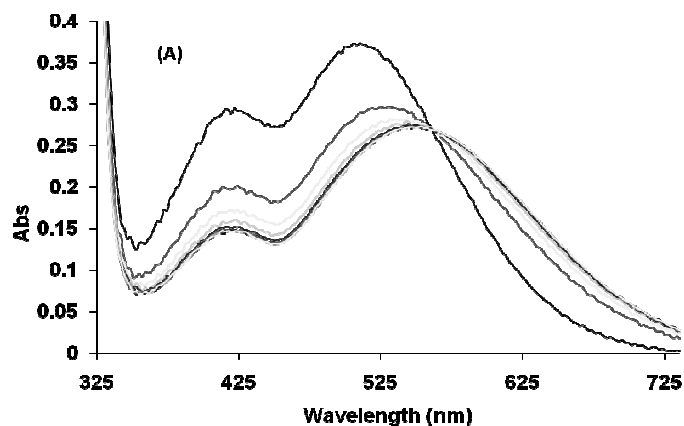
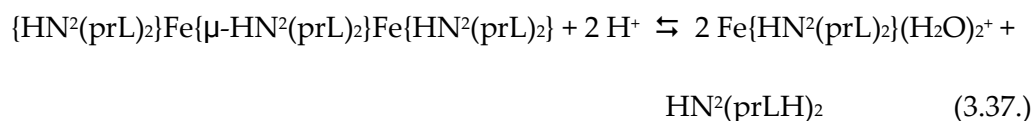


Figure 3.10. Spectra measured during the acid-driven dissociation of the $\text{Fe}_2\{\text{N}^2(\text{prL})_2\}_3$ complex (Eq. 3.35). (A) Initial spectral change corresponding to dissociation of the hexacoordinate complex to the tetracoordinate complex after rapidly decreasing the solution pH from 6.0 to approximately 2.3. Conditions: $[\text{Fe}^{3+}] = 2.1 \times 10^{-4} \text{ M}$, $[\text{N}^2(\text{prLH})_2] = 3.2 \times 10^{-4} \text{ M}$, $[\text{H}^+] = 5.0 \text{ mM}$, $\mu = 0.10$ (NaNO_3), $T = 25 \text{ }^\circ\text{C}$; (B) Second spectral shift observed at higher acid concentrations by rapidly jumping the pH from approximately 6.0 to approximately 1.3. Conditions: $[\text{Fe}^{3+}] = 2.1 \times 10^{-4} \text{ M}$, $[\text{N}^2(\text{prLH})_2] = 3.2 \times 10^{-4} \text{ M}$, $[\text{H}^+] = 50.0 \text{ mM}$, $\mu = 0.10$ (NaNO_3), $T = 25 \text{ }^\circ\text{C}$.

At all acid concentrations investigated, an initial shift in the solution spectrum was observed (Fig. 3.10.A.), representing conversion of the complex from the hexacoordinate Fe_2L_3 form to the tetradentate $\text{FeL}(\text{H}_2\text{O})_2$ form, shown in Eq. 3.37., as determined by comparison of observed λ_{max} here to thermodynamic UV-Visible



titrations (see Chapter 2). In this experiment, the initial λ_{max} was observed at approximately 510 nm, which is indicative of the tris-hydroxypyridinone complex. This is as expected, as the initial solution pH (approximately 6.0) is in the range expected from the speciation diagram of this complex for the formation of the trishydroxypyridinone complex. At low acid concentrations, the final λ_{max} was found to be approximately 545 nm, indicative of formation of the bis-hydroxypyridinone complex. This initial spectral change was rapid, taking place over the course of 2 seconds or less.

The absorbance at a single wavelength was plotted as a function of time (Fig. 3.11.) and fit to a double exponential decay model (Eq. 3.2.), suggesting two parallel or sequential kinetically observable processes in the reaction. A plot of the observed rate constants for reaction 3.35. as a function of proton concentration is shown in Fig. 3.12.

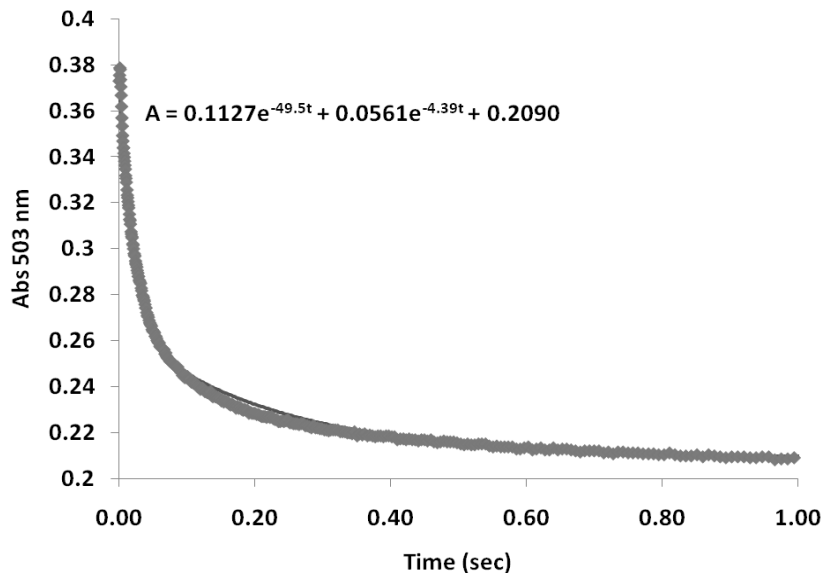


Figure 3.11. Plot of absorbance at 503 nm as a function of time during the initial spectral shift of the acid-driven dissociation of $\text{Fe}_2\{\text{N}^2(\text{prL})_2\}_3$ (Eq. 3.35.) over 1 second.

The line represents the best fit plot to the data using a double exponential decay model (Eq. 3.2.) with $k_{2\text{obs}} = 4.39 \text{ s}^{-1}$ and $k_{3\text{obs}} = 49.5 \text{ s}^{-1}$. Conditions: $[\text{Fe}^{3+}] = 2.1 \times 10^{-4} \text{ M}$, $[\text{N}^2(\text{prLH})_2] = 3.2 \times 10^{-4} \text{ M}$, $[\text{H}^+] = 50.0 \text{ mM}$, $\mu = 0.10$ (NaNO_3), $T = 25 \text{ }^\circ\text{C}$.

This plot demonstrates independence of $k_{2\text{obs}}$ on proton ion concentration, suggesting that one process occurs without a proton in the rate determining step. Additionally, the second observed rate constant, $k_{3\text{obs}}$ exhibits linear dependence on proton ion concentration, suggesting the involvement of one proton in the rate limiting step of the reaction. These observations allow us to propose a rate law for the observed reaction, shown in Eqs. 3.38.-3.39.

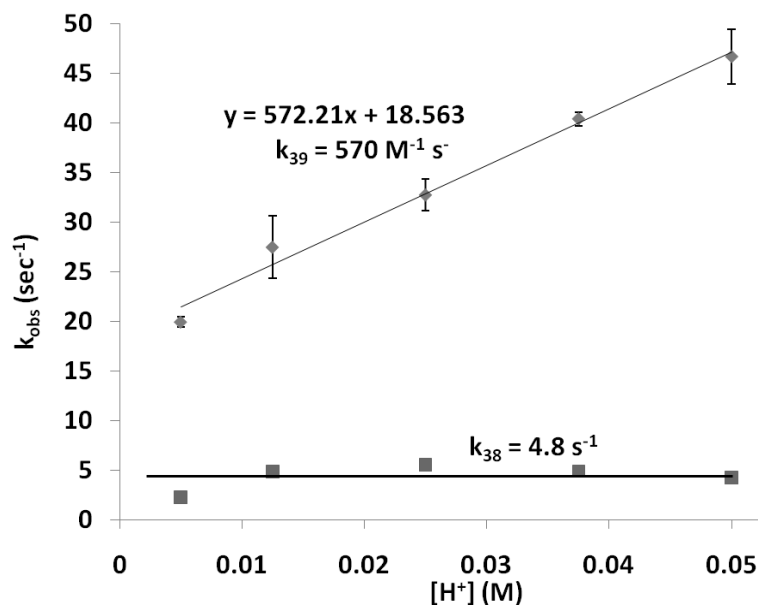


Figure 3.12. Plot of the observed pseudo-first order rate constant as a function of acid concentration for both pseudo-first order rate constants, k_{2obs} and k_{3obs} . These plots yield a first order rate constant, $k_{38} = 4.8 \text{ s}^{-1}$ and a second order rate constant, $k_{39} = 570 \text{ M}^{-1} \text{ s}^{-1}$. Conditions: $[\text{Fe}^{3+}] = 2.1 \times 10^{-4} \text{ M}$, $[\text{N}^2(\text{prLH})_2] = 3.2 \times 10^{-4} \text{ M}$, $\mu = 0.10$ (NaNO_3), $T = 25 \text{ }^\circ\text{C}$.

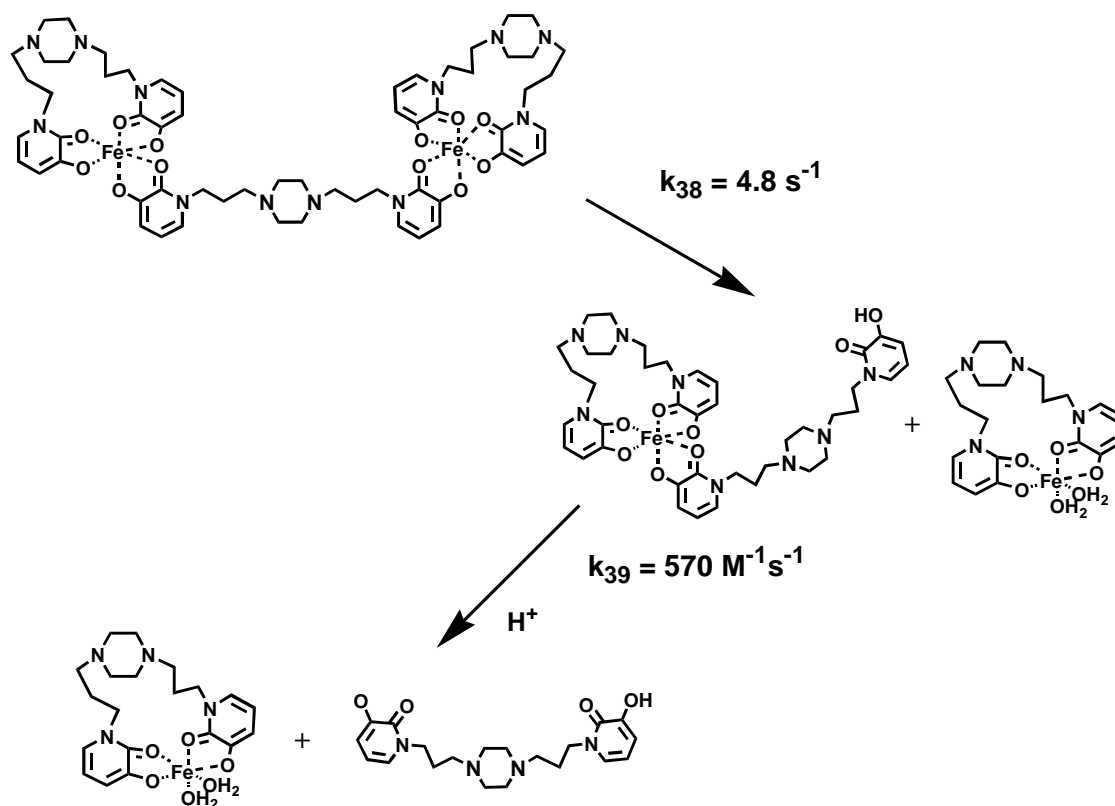
$$\text{Rate} = (k_{38} + k_{39}[\text{H}^+])[\text{Fe}_2(\text{HN}^2(\text{prL})_2)_3] \quad (3.38.)$$

$$k_{38} = 4.8 \pm 0.4 \text{ s}^{-1} \quad k_{39} = 570 \text{ M}^{-1} \text{ s}^{-1} \quad (3.39.)$$

This information, combined with the mass spectral evidence for the complex structure allows two mechanisms of proton-driven dissociation to be proposed, shown in Schemes 3.4. and 3.5. As mentioned earlier, there are two observable processes in the hexacoordinate-to- tetracoordinate conversion reaction, as evidenced by the double

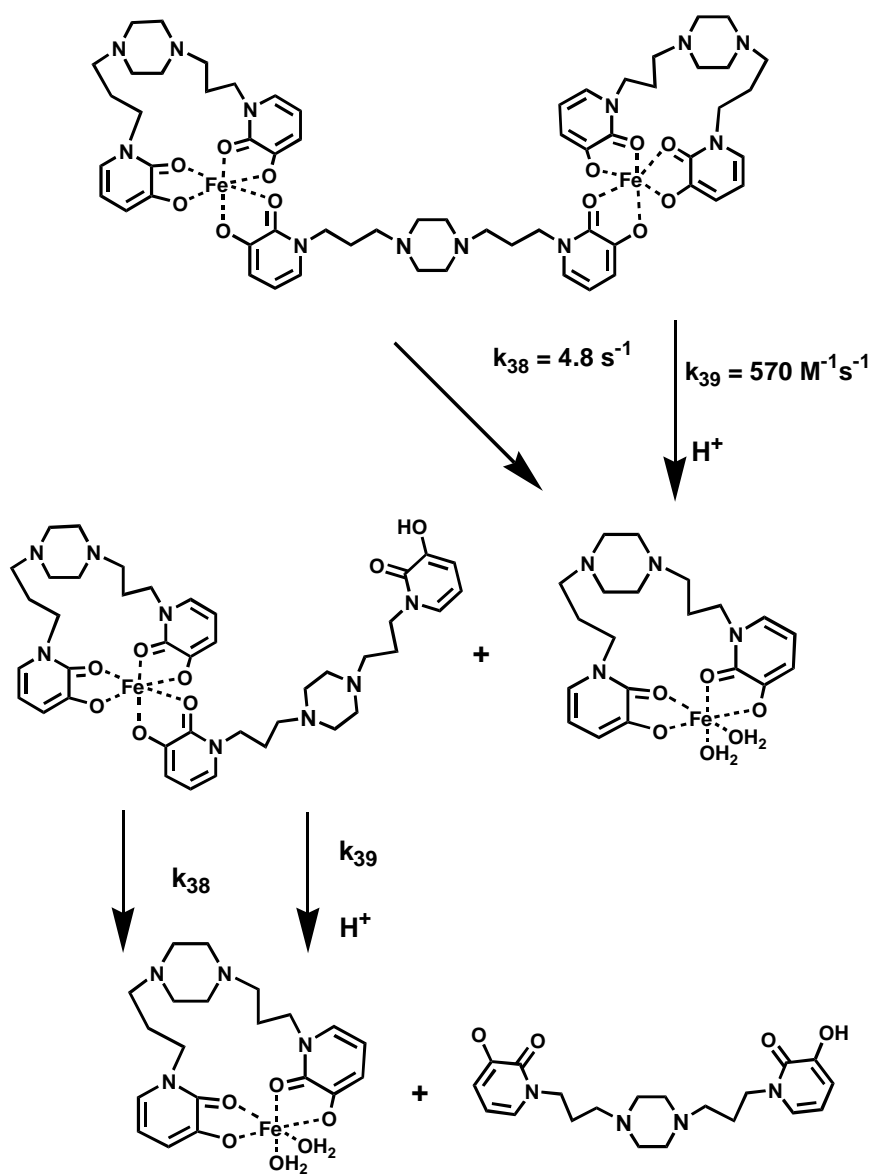
exponential decay fit for the kinetic data. The two possible mechanisms involve a parallel reaction pathway, where two reactions occur to produce the same product, or a sequential reaction pathway, where one reaction occurs to produce a meta-stable intermediate, followed by conversion of the intermediate to the final product.

The possible sequential reaction mechanism for the dissociation of the Fe_2L_3 complex is shown in Scheme 3.4., where one lobe of the $\text{Fe}_2\{\text{HN}^2(\text{prL})_2\}_3$ complex dissociates in a proton independent manner to produce the $\text{Fe}\{\text{HN}^2(\text{prL})_2\}\{\text{HN}^2(\text{prL})(\text{prLH})\}$ complex, followed by dissociation of the former bridging ligand from the $\text{Fe}\{\text{HN}^2(\text{prL})_2\}\{\text{HN}^2(\text{prL})(\text{prLH})\}$ complex in a proton-dependent manner to produce the $\text{Fe}\{\text{HN}^2(\text{prL})_2\}$ complex. Dissociation may proceed in that order, as steric interactions between the two $\text{Fe}\{\text{HN}^2(\text{prL})_2\}$ lobes would promote the dissociation of one of the two $\text{Fe}\{\text{HN}^2(\text{prL})_2\}$ units, driven by the sterics of the interaction and not requiring a proton to drive the dissociation. Dissociation of the bidentate ligand from the $\text{Fe}\{\text{HN}^2(\text{prL})_2\}\{\text{HN}^2(\text{prL})(\text{prLH})\}$ complex would then likely be proton-dependent, as the steric interaction between lobes would be removed. This also suggests why the observed pseudo-first order rate constant assigned to this reaction appears greater than the observed pseudo-first order rate constant assigned to the initial dissociation at every proton concentration studied. The dependence of the rate of reaction on the proton ion concentration drives the reaction thermodynamically.



Scheme 3.4. Proposed sequential reaction mechanism for the acid-driven dissociation of the $\text{Fe}_2\{\text{HN}^2(\text{prL})_2\}_3$ complex. Initial dissociation of one lobe takes place in a proton-independent manner, followed by protonation of the FeLLH complex to produce the FeL complex.

The proposed parallel reaction mechanism for the complex dissociation reaction is shown in Scheme 3.5., where two pathways exist for dissociation of the $\text{Fe}_2\{\text{HN}^2(\text{prL})_2\}_3$ complex to form the $\text{Fe}\{\text{HN}^2(\text{prL})_2\}\{\text{HN}^2(\text{prL})(\text{prLH})\}$ complex, one by a proton-dependent dissociation and the other by a proton-independent dissociation



Scheme 3.5. Proposed parallel reaction mechanism for the acid-driven dissociation of the $\text{Fe}_2\{\text{HN}^2(\text{pRL})_2\}_3$ complex. Initial dissociation of one lobe can proceed with or without protonation of the hydroxypyridinone donor group. The remaining FeLLH complex may then dissociate with or without protonation of the formerly bridging hydroxypyridinone ligand.

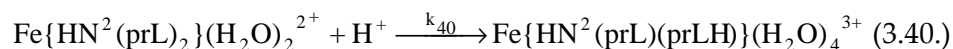
reaction. $\text{Fe}\{\text{HN}^2(\text{prL})_2\}\{\text{HN}^2(\text{prL})(\text{prLH})\}$ complex would then dissociate to form the $\text{Fe}\{\text{HN}^2(\text{prL})_2\}(\text{H}_2\text{O})_2$ complex through the same two parallel proton-dependent and -independent pathways. This mechanism requires that the two lobes of the $\text{Fe}_2\{\text{HN}^2(\text{prL})_2\}_3$ complex be equivalent in steric interactions, and that the iron center of the $\text{Fe}\{\text{HN}^2(\text{prL})_2\}\{\text{HN}^2(\text{prL})(\text{prLH})\}$ complex be roughly equivalent to those of the $\text{Fe}_2\{\text{HN}^2(\text{prL})_2\}_3$ complex. This would be facilitated by a greater distance between the two iron centers of the $\text{Fe}_2\{\text{HN}^2(\text{prL})_2\}_3$ complex, as a greater distance between the two lobes would result in a decrease in steric interactions between the two lobes.

The spectral shifts alone are not indicative of either of the two pathways. In both reaction pathways, the intermediate complex is the same $\text{Fe}\{\text{HN}^2(\text{prL})_2\}\{\text{HN}^2(\text{prL})(\text{prLH})\}$, resulting in the same UV-Visible spectrum corresponding to the trishydroxypyridinone complex. The transition observed during the reaction would be identical, as the spectral transition corresponds to the hexacoordinate-to-tetracoordinate complex transition, as seen in Eq. 3.37. Also, the spectral handles observed in the transition species ($\text{Fe}\{\text{HN}^2(\text{prL})_2\}\{\text{HN}^2(\text{prL})(\text{prLH})\}$) corresponds to the trishydroxypyridinone complex, which would be virtually the same as the absorbance spectrum of the hexacoordinate $\text{Fe}_2\{\text{HN}^2(\text{prL})_2\}_3$ complex.

We propose that the latter mechanism (the parallel mechanism shown in Scheme 3.5.) is the more likely of the two proposed mechanisms, as the two lobes of the Fe_2L_3

complex are able to separate sufficiently in solution due to the single bridging ligand, resulting in minimal steric interactions between the two lobes.

At high acid concentrations, a second spectral shift is evident, corresponding to dissociation of the tetracoordinate $\text{FeL}(\text{H}_2\text{O})_2^{2+}$ complex to the biscoordinate $\text{FeLH}(\text{H}_2\text{O})_4^{2+}$ complex (Fig. 3.10.B., Eq. 3.40.). The assignment of reactant and product



complex are based on the observed λ_{max} of the system at the beginning and the end of the slower transition. The starting complex is the tetracoordinate complex, as discussed above. Meanwhile, the shift in λ_{max} that is observed in the spectra over time towards longer wavelengths is indicative of transition to the monohydroxypyridinone complex, as observed in the low-pH thermodynamic experiment discussed in the previous chapter. Direct comparison between the two values is difficult, as the λ_{max} was observed at high dilution in the thermodynamic experiments, and with increasing proton concentration, a larger amount of the complex completely dissociates. However, the observed λ_{max} shown in the final spectrum of Fig. 3.10.B. is approximately 575 nm, approaching that estimated for the bishydroxypyridinone complex shown in Table 2 of Chapter 2. This spectral shift takes place much slower after the initial spectral shift from hexacoordinate to tetracoordinate complex. The absorbance plotted as a function of time

(Fig. 3.13.) was fit to a single exponential decay model (Eq. 3.4.), suggesting only a single kinetically observable process taking place during the course of the reaction. The observed rate constant obtained from the kinetic curve was plotted as a function of proton concentration (Fig. 3.14.) and exhibited zero order dependence on proton concentration with a rate constant of $k_{40} = 1.0 \pm 0.2 \times 10^{-2} \text{ s}^{-1}$, suggesting that no proton

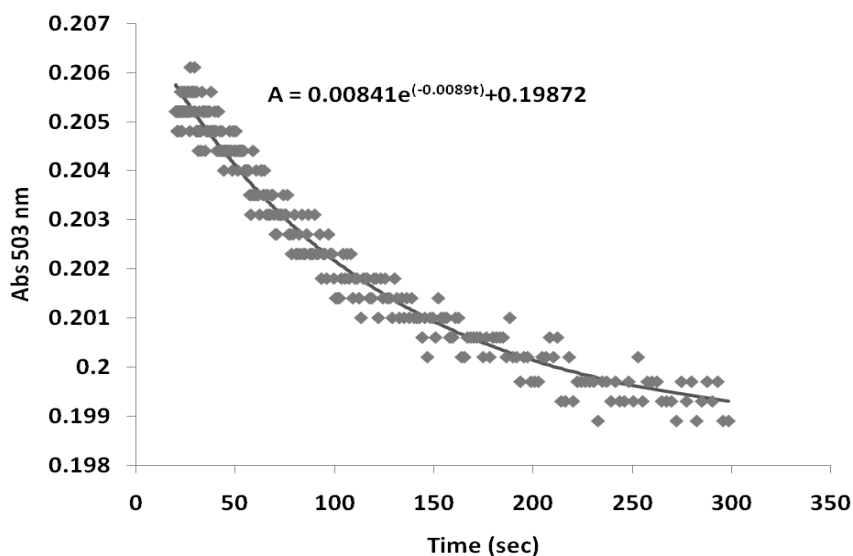


Figure 3.13. Plot of absorbance at 503 nm as a function of time during the second spectral shift of the acid-driven dissociation of $\text{Fe}_2\{\text{N}^2(\text{prL})_2\}_3$ (shown in Fig. 3.10.B) from 20-300 seconds. The line shown in the figure represents the best fit plot of the data to a single exponential decay model (Eq. 3.4.) yielding a pseudo-first order rate constant of $k_{\text{obs}} = 8.9 \times 10^{-3} \text{ s}^{-1}$. Conditions: $[\text{Fe}^{3+}] = 2.1 \times 10^{-4} \text{ M}$, $[\text{N}^2(\text{prLH})_2] = 3.2 \times 10^{-4} \text{ M}$, $[\text{H}^+] = 50.0 \text{ mM}$, $\mu = 0.10 \text{ (NaNO}_3\text{)}$, $T = 25 \text{ }^\circ\text{C}$.

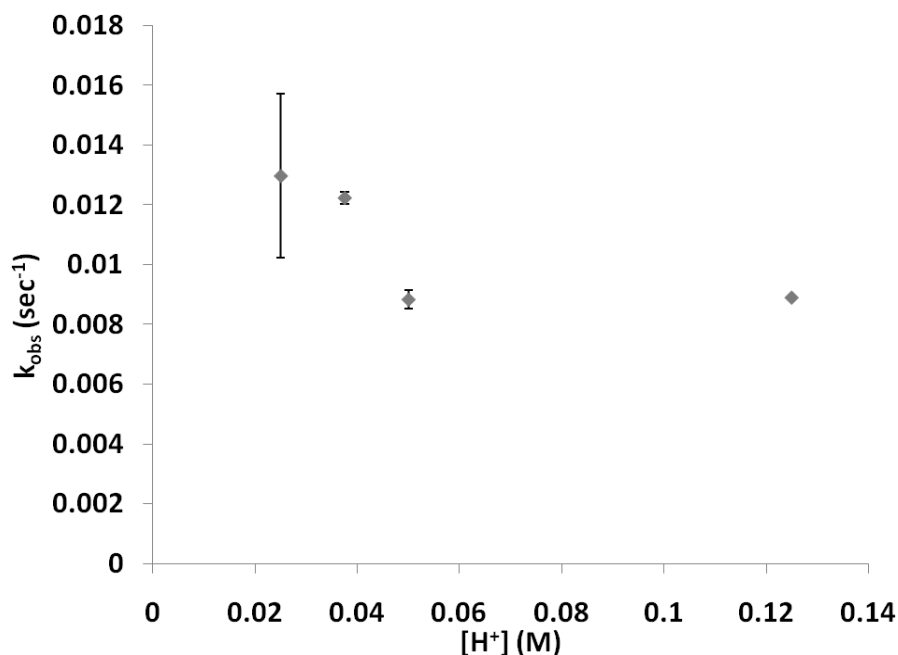


Figure 3.14. Plot of the observed pseudo-first order rate constant as a function of acid concentration for the pseudo-first order rate constant, k_{obs} of reaction 40. The observed rate constant is not dependent on proton concentration. Conditions: $[\text{Fe}^{3+}] = 2.1 \times 10^{-4} \text{ M}$, $[\text{N}^2(\text{prLH})_2] = 3.2 \times 10^{-4} \text{ M}$, $\mu = 0.10 \text{ (NaNO}_3\text{)}$, $T = 25 \text{ }^\circ\text{C}$.

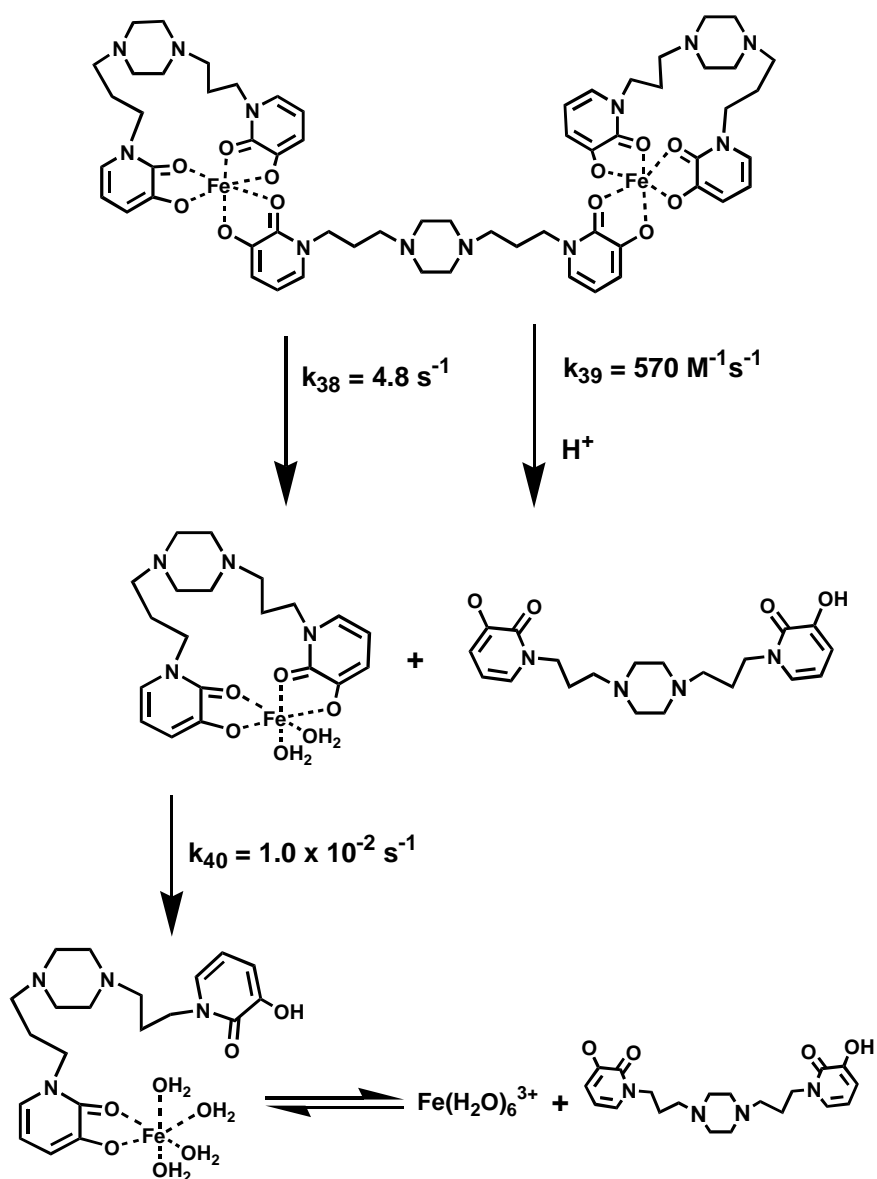
was involved in the rate-limiting step of the conversion from tetracoordinate to biscoordinate complex, Eq. 3.38. This suggests that the rate limiting step of the protonation reaction is dissociation of the hydroxypyridinone donor group, which is then protonated to prevent rechelation. At much higher acid concentrations, the complex would likely dissociate completely, but those experiments were not performed as the complex began to precipitate out of solution at high nitrate ion concentrations.

3.4.3. Overall mechanism of proton-driven dissociation of the Fe-N²(prLH)₂ complex

The complete mechanism of proton-driven dissociation of the Fe₂{HN²(prL)₂}₃ complex (Eq. 3.35) is shown in Scheme 3.6. Initial transition of the trishydroxypyridinone Fe₂L₃ complex occurs through two steps. Both steps involve parallel pathways of complex dissociation, one pathway involving simple solvation ($k_{38} = 4.8 \text{ s}^{-1}$) and proton-driven dissociation ($k_{39} = 570 \text{ M}^{-1} \text{ s}^{-1}$). The second step of the reaction involves dissociation of the bishydroxypyridinone FeL complex to form the monohydroxypyridinone FeLH complex ($k_{40} = 9.0 \times 10^{-3} \text{ s}^{-1}$) in a proton-independent reaction. The final reaction would involve complete dissociation of the FeLH complex to aquated iron, however, this reaction was not studied due to precipitation of the complex at high nitrate anion concentrations.

3.5. Conclusions

The exchange of iron between polydentate ligands is an important model for iron exchange reactions that occur in biological systems. While it is difficult to obtain samples of natural molecules in large quantities, information about the natural exchange processes can be obtained through the use of model chelators. The exchange of iron from N³(etLH)₃ to desferrioxamine B is an example of such a model reaction, where iron is exchanged between hexadentate iron chelators. The mechanism for this reaction was found to occur by a parallel pathway mechanism, where one pathway involves initial



Scheme 3.6. Reaction mechanism of the proton-driven dissociation of the $\text{Fe}_2\{\text{HN}^2(\text{prL})_2\}_3$ complex. Initial dissociation from trishydroxypyridinone complex takes place through a parallel pathway mechanism with $k_{38} = 4.8 \text{ s}^{-1}$ and $k_{39} = 570 \text{ M}^{-1} \text{ s}^{-1}$.¹ This is followed by protonation of the bishydroxypyridinone FeL complex to form the monohydroxypyridinone FeLH complex with $k_{40} = 1.0 \times 10^{-2} \text{ s}^{-1}$. Complete dissociation of the monohydroxypyridinone complex was not observed.

formation of a host-guest supramolecular assembly, followed by ternary complex formation and exchange of iron to ferrioxamine B (second order rate constant $k_{5app} = 1.7 \times 10^{-1} \text{ M}^{-1}\text{s}^{-1}$), and the other pathway involves direct reaction of the iron- $\text{N}^3(\text{etLH})_3$ with desferrioxamine B, likely through a ternary complex intermediate ($k_7 = 2,1 \times 10^{-2} \text{ M}^{-1} \text{ s}^{-1}$). Another model reaction for a possible natural iron release process is hydrolysis of iron-siderophore complexes. The iron- $\text{N}^2(\text{prLH})_2$ complex was found to dissociate at high proton concentrations by a two step mechanism. The first step involves proton-driven dissociation of the Fe_2L_3 complex by a parallel pathway mechanism, where one pathway is proton-dependent ($k_{39} = 570 \text{ M}^{-1}\text{s}^{-1}$) and the other pathway is proton-independent ($k_{38} = 4.8 \text{ s}^{-1}$). The second step of the reaction involves the proton-independent dissociation of the $\text{Fe}\{\text{N}^2(\text{prL})_2\}$ complex to form the monoprotonated $\text{Fe}\{\text{N}^2(\text{etL})(\text{etLH})\}$ complex ($k_{40} = 1.0 \times 10^{-2} \text{ s}^{-1}$).

4. Catalysis of iron(III) exchange between hexadentate chelators by a bidentate hydroxypyridinone

4.1. Introduction

In nature, iron uptake can occur through a variety of mechanisms, as discussed in Chapter 3. One important step in the uptake process may involve the exchange of iron between two chelators. This exchange process is important in systems such as the mycobactins, the membrane-bound siderophores produced by many species of mycobacteria that receive iron(III) from the extracellular siderophores, the exochelins and the carboxymycobactins (this will be discussed in further detail later in Chapter 5). Chelator exchange is also of importance in pathogenic bacteria, where the siderophores produced by the bacterium remove iron from the host iron chelators to sequester it for the bacterium.

One factor that has been proposed as having a role in some biological iron exchange mechanisms is the presence of secondary chelating agents.⁽¹⁸⁾ Secondary chelating agents have been shown to affect the iron chelation equilibria of siderophore systems in a variety of ways. A previous study has shown that secondary chelators that are specific for iron(II) can affect the redox potential of iron-siderophore complexes.⁽⁴⁴⁾ The presence of chelators that are specific for iron(II) act to shift the redox potential to more positive values, as the chelators serve as “iron(II) sinks” that shift the redox

equilibrium towards more facile production of iron(II). In the ferrioxamine B system, it was shown that the presence of bathophenanthroline disulfonate, a secondary chelator specific for iron(II), would facilitate reduction of iron(III) in the ferrioxamine B complex by ascorbate and glutathione. While the redox potential of the ferrioxamine B complex is too negative to be reduced by these biologically relevant reducing agents, the presence of the secondary chelator shifted the effective redox potential through coupled equilibria and promoted the reduction of iron(III) to iron(II), which was then trapped by the secondary chelator. It is unclear whether the shift in apparent redox potential is due to coupled equilibria, as stated above, or to the formation of a ternary complex, leading to a shift in the actual redox potential of the metal center.

Another study showed that the presence of secondary chelators results in acceleration of the exchange of iron(III) from ferrioxamine B to another hexadentate chelator, EDTA by a non-redox mechanism.⁽¹²⁶⁾ The exchange of iron(III) between hexadentate chelators is a slow process, due to relatively slow kinetics of inner coordination sphere exchange at the high spin d^5 metal center. Addition of hydroxamic acid chelators to the exchange reaction resulted in acceleration of the observed rate of reaction. This was proposed to be due to the formation of a ternary inner sphere complex between iron(III), desferrioxamine B, and the hydroxamate chelator.

4.2. Statement of chapter objectives

The purpose of this study is to characterize the kinetics and mechanism of a similar iron(III) exchange reaction using a hydroxypyridinone chelator, 1,2-dimethyl-3-hydroxy-4-pyridinone (DMHP, Fig. 4.1.), as the ternary chelator. The exchange reaction in the presence of DMHP was monitored spectrophotometrically, and the mechanism was shown to involve a ternary complex formed between ferrioxamine B and DMHP. Additionally, it was shown that DMHP is a more effective catalyst than the simple mono-hydroxamic acids previously investigated, acetohydroxamic acid, N-methylacetohydroxamic acid, and benzylhydroxamic acid (Fig. 4.1.), likely due to the relative chelating strength of the hydroxamic acids and DMHP.(126)

4.3. Experimental

4.3.1. Materials

All solutions were prepared in deionized water. A solution of 0.10 M NaClO_4 with 0.20 M sodium acetate was used as the background electrolyte with the pH adjusted to 4.35 by 1.0 M HClO_4 . The minimum volume of acid necessary to adjust the pH was used to minimize the effect on solution ionic strength which was held at 0.10 M. Solid anhydrous $\text{Fe}(\text{ClO}_4)_3$ (low chloride content, <0.005%) was obtained from Sigma and used to prepare 0.10 M stock solution in 0.10 M HClO_4 to prevent hydrolysis of the metal ion. The stock solution was standardized titrimetrically by reduction with SnCl_2 ,

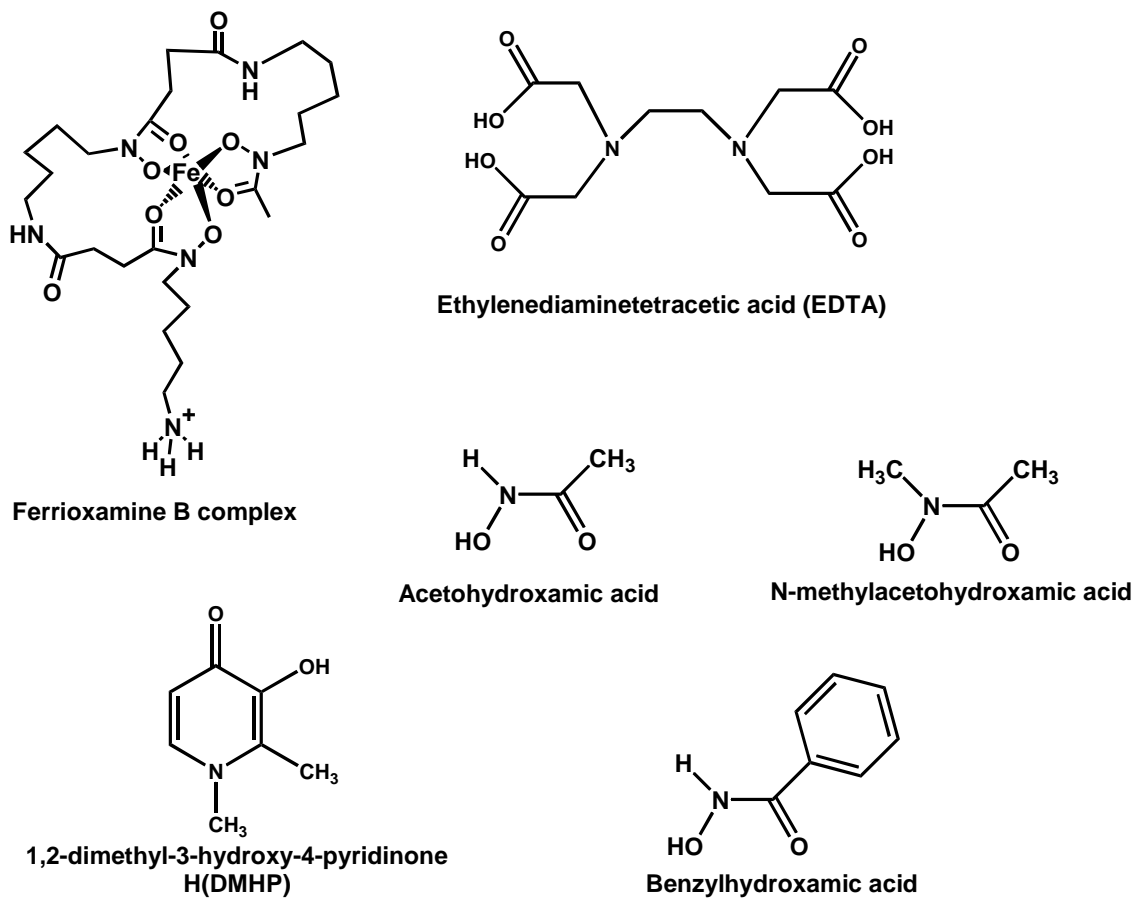


Figure 4.1. Structures of the iron(III) chelators discussed in this study, the ferrioxamine B complex, EDTA, DMHP, and three monohydroxamic acids previously studied and shown to accelerate the exchange of iron(III) from desferrioxamine B to EDTA.

followed by titration with $K_2Cr_2O_7$.⁽⁹³⁾ Stock EDTA solutions were prepared with solid EDTA (Acros Organics, 99+%) dissolved in 0.10 M $NaClO_4$ with 100 mM $NaOAc$. Desferrioxamine B mesylate (95%) and 1,2-dimethyl-3-hydroxy-4-pyridinone (98%) were obtained from Sigma-Aldrich and used as received to prepare stock solutions. Solutions of ferrioxamine B were prepared by slow addition with stirring to an unbuffered solution of desferrioxamine B mesylate in 0.10 M $NaClO_4$ with a final pH of approximately 2-3, followed by dilution to volume with the buffered electrolyte background to a final concentration of 100 mM acetate buffer and a final solution pH of 4.35. A stock solution of ferric DMHP was prepared similarly by slow addition with stirring to an unbuffered solution, followed by dilution to volume with the buffered electrolyte at a final solution pH of 4.35. All stock solutions of ligands were prepared similarly to maintain buffer concentration.

4.3.2. Iron(III) exchange from ferrioxamine B to EDTA in the presence of DMHP

Stock solutions of 3 mM ferrioxamine B, 30 mM EDTA, and 31 mM DMHP were prepared for use in the first set of experiments. UV-visible spectra for the ferrioxamine B exchange reactions were recorded with the Varian Cary-100 spectrophotometer equipped with a dual cell peltier accessory and the reaction temperature was maintained at 25 °C. The reaction was prepared by mixture of the EDTA and DMHP stock solutions, followed by rapid addition to the ferrioxamine B solution. The final

concentration of ferrioxamine B complex in all experiments was 0.4 mM at a final pH of 4.35 (100 mM NaOAc buffer), 25 °C and an ionic strength of 0.10 (NaClO₄). A set of experiments was performed under pseudo-first order reaction conditions with respect to EDTA at EDTA concentrations of 5 mM, 7 mM, 10 mM, 12 mM, and 15 mM. At each EDTA concentration, the concentration of DMHP was varied over the range of 0 to 5 mM. The reaction was monitored until the spectrum was constant.

4.3.3. Iron(III) exchange from ferrioxamine B to DMHP

Iron exchange reactions were performed between ferrioxamine B and DMHP under similar conditions as the reactions in the presence of EDTA. Spectra were measured using a Varian Cary 50 spectrophotometer equipped with a jacketed cell holder and a water bath set to 25 °C. Solutions were mixed to result in final concentrations of 0.2 mM ferrioxamine B and a range of DMHP concentrations from 4 mM to 10 mM at a pH of 4.35 (100 mM NaOAc buffer) and an ionic strength of 0.10 (NaClO₄). Reactions were monitored over the range of 325 to 650 nm until the spectrum was constant and the final spectrum was compared to expected absorbance values determined from literature reports of the molar absorptivity of the Fe(DMHP)₃ complex to verify the product.⁽¹²⁷⁾ The reactions were also repeated over a range of pH values. The solution pH was varied by changing the pH of the buffer system. The experiments

were repeated in 100 mM NaOAc/100 mM NaClO₄ buffer at pH 4.56 and in 100 mM MES/100 mM NaClO₄ buffer at pH 4.85, pH 5.50, and pH 6.00.

4.3.4. Iron(III) exchange from DMHP to EDTA

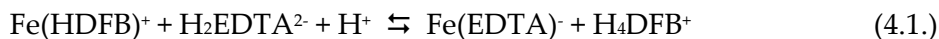
The exchange of iron(III) from DMHP to EDTA was monitored spectrophotometrically using similar equipment as the ferrioxamine B-DMHP exchange reaction. Solutions of 0.4 mM iron(III) with 4 mM DMHP and 0.4 mM iron(III) with 10 mM DMHP were prepared in 0.10 M NaClO₄ buffered at pH 4.35 with 100 mM sodium acetate and a range of EDTA concentrations from 4 to 20 mM were prepared. The solutions were mixed in a 1:1 ratio and the reaction was monitored spectrophotometrically over the range of 325 to 650 nm until the solution spectrum was constant. The identity of the final product was verified as Fe(EDTA) by comparison to the known solution spectrum from previous experiments (see Chapter 2).

4.4. Results

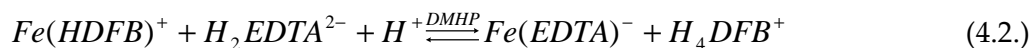
4.4.1. Iron(III) exchange from ferrioxamine B to EDTA: General observations

The iron(III) exchange reaction from ferrioxamine B to EDTA is incredibly slow, with an observed second order rate constant of 0.030 M⁻¹ s⁻¹ at pH 4.35 (see section 4.3.2.),

as the reaction involves exchange of the metal between two hexadentate chelators, shown in Eq. 4.1.



We observed however, that addition of DMHP catalyzes the iron(III) exchange reaction shown in Eq. 4.1. In order to determine the mechanism of catalysis, it was necessary to investigate the kinetics of exchange of iron(III) between ferrioxamine B and EDTA in the presence of the catalyst, Eq. 4.2. (see Sec. 4.3.3.).



Indirect information about potential intermediate species involved in the catalysis mechanism of Eq. 4.2. can be obtained by investigating the reaction mechanisms of the iron(III) exchange reaction between desferrioxamine B and DMHP, shown in Eq. 4.3. (see Sec. 4.3.4.), and the iron(III) exchange reaction between DMHP and EDTA, shown in Eq. 4.4. (see Sec. 4.3.5.).



The determined rate laws for reactions 4.3. and 4.4. will allow us to propose a mechanism of catalysis of Eq. 4.2. by DMHP.

4.4.2. Kinetics of iron(III) exchange from ferrioxamine B to EDTA in the absence of DMHP (Eq. 4.1.)

The spectra measured for reaction 4.1. at a concentration of 10 mM EDTA and Fe(HDFB)⁺ concentration of 0.40 mM are shown in Fig. 4.2., while the absorbance measured at a single wavelength over time is shown in Fig. 4.3. The reaction takes place

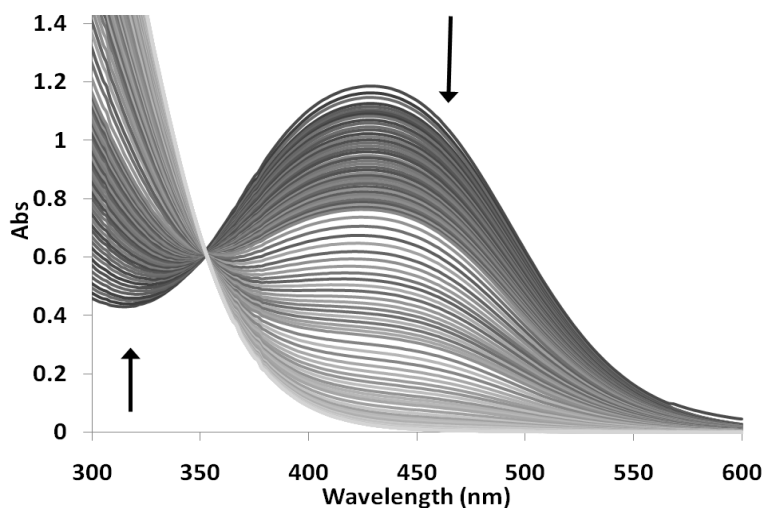


Figure 4.2. Spectra measured during the exchange reaction between ferrioxamine B and EDTA in the absence of DMHP (Eq. 4.1.) measured over 250 minutes. Arrow shows the direction of spectral change with time over 250 minutes. Conditions: [Fe³⁺] = [DFB] = 0.4 mM, [EDTA] = 10 mM, μ = 0.10 M (NaClO₄), pH = 4.35 (100 mM NaOAc buffer), T = 25 °C.

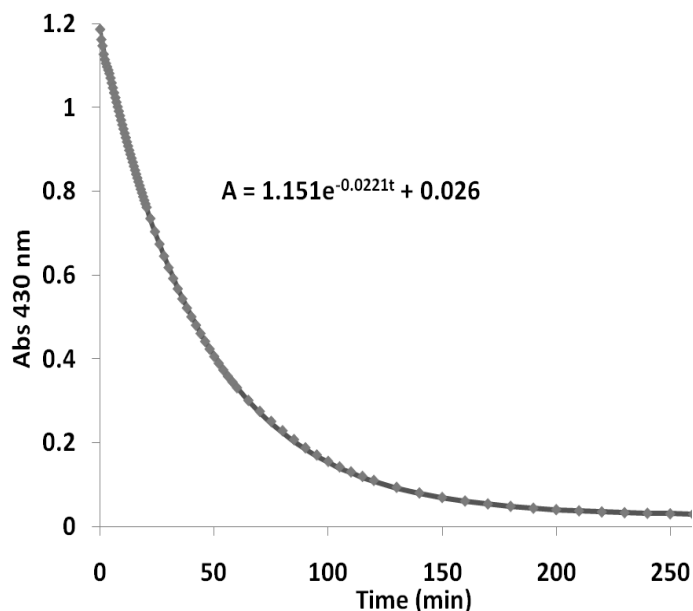


Figure 4.3. Plot of absorbance at 430 nm as a function of time for the reaction of ferrioxamine B with EDTA in the absence of DMHP (Eq. 4.1.). The points represent experimental data, while the line represents the single order exponential decay fit of the data (Eq. 4.5.). Conditions: $[\text{Fe}^{3+}] = [\text{DFB}] = 0.4 \text{ mM}$, $[\text{EDTA}] = 10 \text{ mM}$, $[\text{DMHP}] = 1.5 \text{ mM}$, $\mu = 0.10 \text{ M}$ (NaClO_4), $\text{pH} = 4.35$ (50 mM NaOAc buffer), $T = 25 \text{ }^\circ\text{C}$.

over the course of 2-5 hours at $\text{pH} = 4.35$ depending on the concentration of EDTA present. The initial spectrum is consistent with iron being bound by desferrioxamine B as the $\text{Fe}(\text{HDFB})^+$ complex ($\lambda_{\text{max}} = 430 \text{ nm}$), while the final spectrum is consistent with the $\text{Fe}(\text{EDTA})^-$ complex (see Chapter 2).^(20, 126) Additionally, an isosbestic point is observed during the reaction, suggesting that only two absorbing species are present during the iron(III) exchange reaction. The absorbance over time was fit to a single exponential decay model, shown in Eq. 4.5.

$$A = me^{-k_{\text{obs}}t} + A_{\text{inf}} \quad (4.5.)$$

In Eq. 4.5., A represents the absorbance at time t , m represents the amplitude of the absorbance change, k_{obs} represents the observed rate constant for the first-order reaction, and A_{inf} represents the final absorbance of the decay. The observed pseudo-first order rate constants, k_{obs} , obtained from this analysis were plotted as a function of EDTA concentration, yielding a linear relationship, shown in diamonds in Fig. 4.4. The single exponential decay model suggests that the rate law for the rate limiting step of the reaction is first order with respect to $\text{Fe}(\text{HDFB})^+$:

$$\text{Rate} = k_{\text{obs}}[\text{Fe}(\text{HDFB})] \quad (4.6.)$$

Also, the linear relationship between k_{obs} and EDTA suggests first order dependence on EDTA concentration.

$$k_{\text{obs}} = k_1[\text{EDTA}] \quad (4.7.)$$

From the slope of the line in Fig. 4.4. we obtain a value for $k_1 = 0.030$ (8) $\text{M}^{-1}\text{s}^{-1}$ for the uncatalyzed iron(III) exchange reaction (Eq. 4.1.) between ferrioxamine B and EDTA at pH 4.35. The mechanism of exchange will be discussed later.

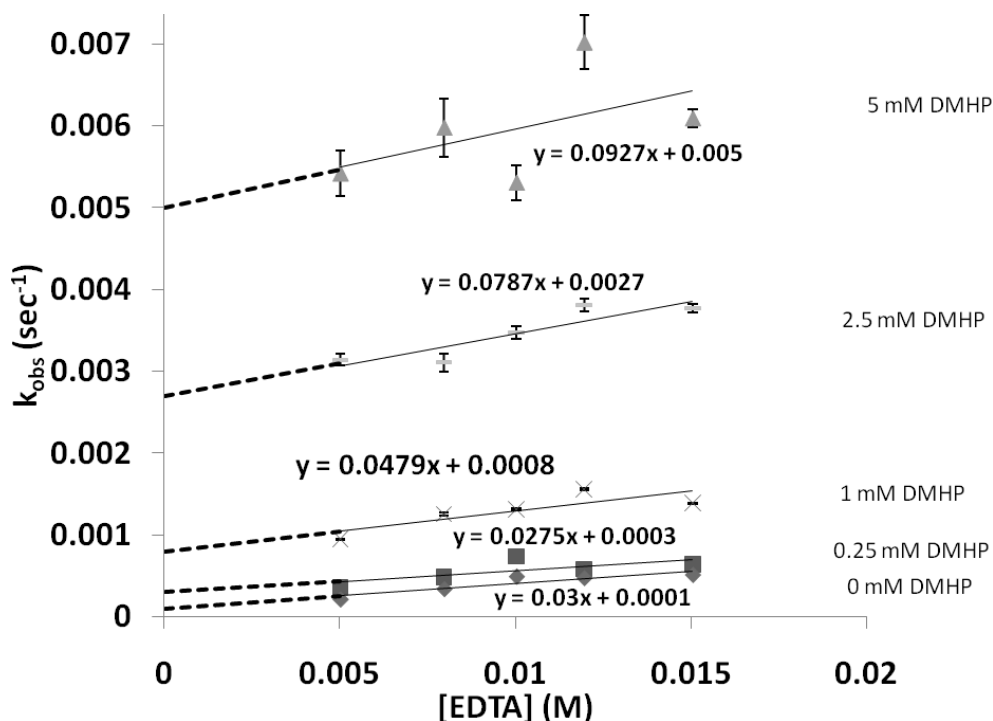


Figure 4.4. Plot of pseudo-first order rate constant, k_{obs} as a function of [EDTA] for reaction 4.2. at five DMHP concentrations. All reactions were performed at $[\text{Fe}^{3+}] = [\text{DFB}] = 0.4 \text{ mM}$, $[\text{EDTA}] = 5\text{-}15 \text{ mM}$, $\mu = 0.10 \text{ M}$ (NaClO_4), $\text{pH} = 4.35$ (100 mM NaOAc buffer), and $T = 25 \text{ }^\circ\text{C}$. Legend: Diamonds - [DMHP] = 0 mM, squares - [DMHP] = 0.25 mM, X - [DMHP] = 1.0 mM, dashes - [DMHP] = 2.5 mM, triangles - [DMHP] = 5.0 mM. The equations show the linear best fit plots of k_{obs} as a function of [DMHP] for the adjacent lines. The error bars on data points represent the standard deviation of the average observed rate constant measured at 4 discrete wavelengths in a single experiment. If an error bar is not visible, it is smaller than the data point.

4.4.3. Kinetics of iron(III) exchange from ferrioxamine B to EDTA in the presence of DMHP (Eq. 4.2.)

The spectra measured during a representative exchange reaction of iron(III) from ferrioxamine B to EDTA in the presence of DMHP (Eq. 4.2.) at pH 4.35 are shown in Fig. 4.5. The initial spectrum is consistent with that of ferrioxamine B at pH 4.35 and the final spectrum exhibits no absorbance in the visible range, consistent with production of the Fe(EDTA) complex as shown in Eq. 4.2. The absorbance at four wavelengths was plotted as a function of time, producing kinetic curves for the reaction, and the kinetic curves were fit to a single exponential decay model (Eq. 4.5.) (as shown for the single wavelength measurement of the reaction between ferrioxamine B and EDTA in the presence of DMHP, Fig. 4.6.). The observed rate constants for reaction 4.2. were plotted as a function of DMHP concentration for five different EDTA concentrations (Fig. 4.7.), and then the observed rate constants were plotted as a function of EDTA concentration at 5 different DMHP concentrations (Fig. 4.4.). The rate constants determined at all four wavelengths were the same within experimental error, consistent with the presence of an isosbestic point and suggesting that no stable intermediate is present in the reaction. The rate law of the iron(III) exchange reaction from ferrioxamine B to EDTA in the presence of DMHP based on the plot of k_{obs} against [DMHP] at a constant EDTA concentration (Fig. 4.7.) is:

$$\text{Rate} = k_{\text{obs}}[\text{Fe}(\text{HDFB})] \quad (4.8.)$$

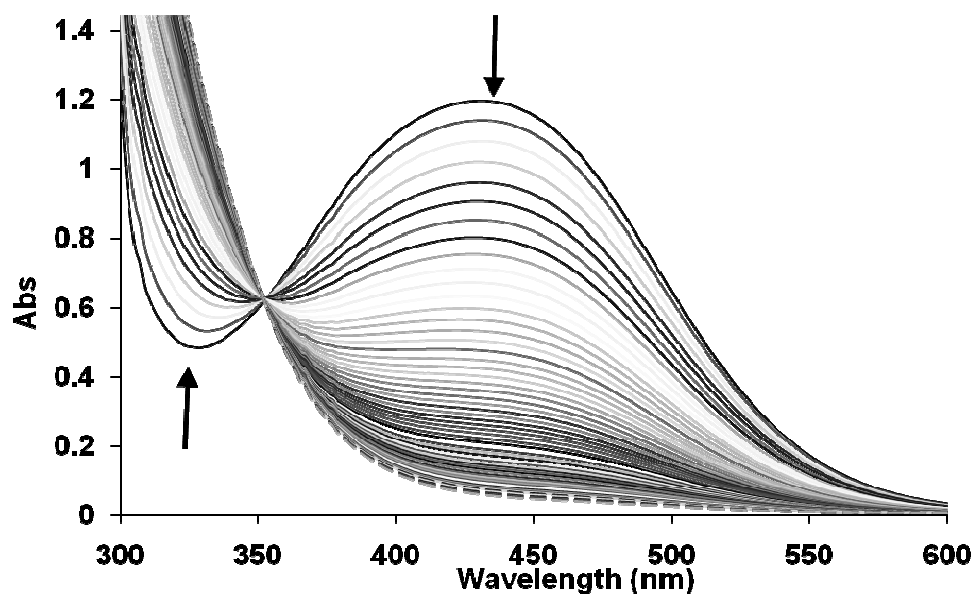


Figure 4.5. Spectra measured during the iron(III) exchange reaction between ferrioxamine B and EDTA in the presence of DMHP (Eq. 4.2.). Arrows show the direction of spectral change with time over 900 secs. Conditions: $[\text{Fe}^{3+}] = [\text{H}_4\text{DFB}^+] = 0.4$ mM, $[\text{EDTA}] = 10$ mM, $[\text{DMHP}] = 1.5$ mM, $\mu = 0.10$ M (NaClO_4), pH = 4.35 (50 mM NaOAc buffer), $T = 25$ °C.

$$k_{\text{obs}} = k_2[\text{DMHP}] + C_2 \quad (4.9.)$$

where k_{obs} represents the observed apparent first-order rate constant, k_2 represents the second-order rate constant for the reaction with DMHP at a fixed constant EDTA concentration obtained from the slope of the linear plots shown in Fig. 4.7., and C_2 represents a constant component to the observed rate constant which is dependent on

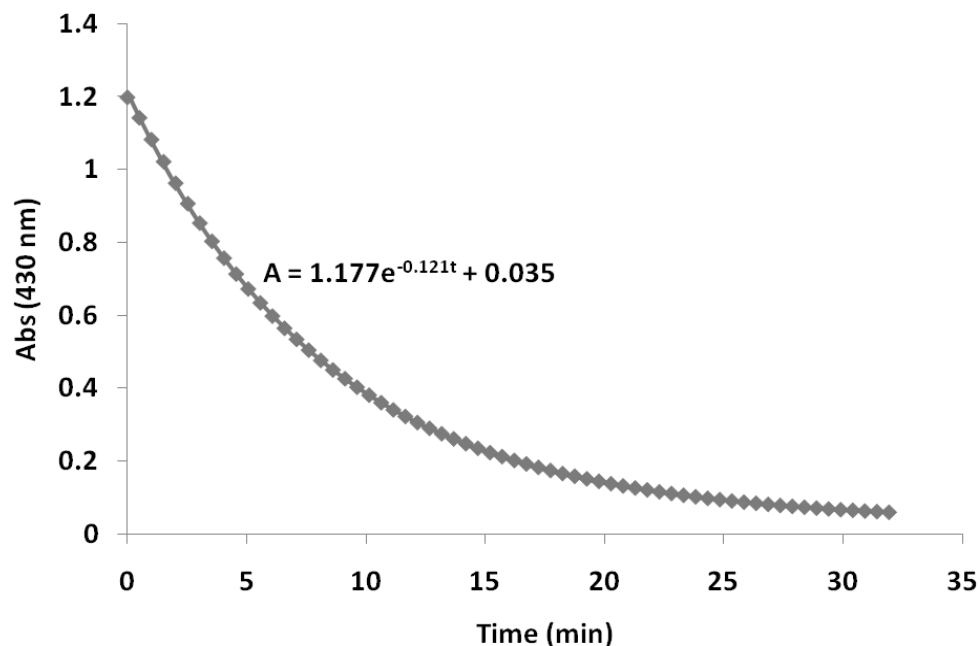


Figure 4.6. Plot of absorbance at 430 nm as a function of time for the reaction of ferrioxamine B with EDTA in the presence of DMHP (Eq. 4.2). The points represent experimental data, while the line represents the single order exponential decay fit of the data (Eq. 4.5.) Conditions: $[\text{Fe}^{3+}] = [\text{DFB}] = 0.4 \text{ mM}$, $[\text{EDTA}] = 10 \text{ mM}$, $[\text{DMHP}] = 1.5 \text{ mM}$, $\mu = 0.10 \text{ M}$ (NaClO_4), $\text{pH} = 4.35$ (100 mM NaOAc buffer), $T = 25 \text{ }^\circ\text{C}$.

the concentration of EDTA and obtained from the y-intercept of the linear plots of Eq. 4.9. shown in Fig. 4.7. The implications of this relationship will be explored in more depth later.

A series of experiments was also performed for reaction 4.2. at constant DMHP concentration over a range of EDTA concentrations. The observed rate constant for the

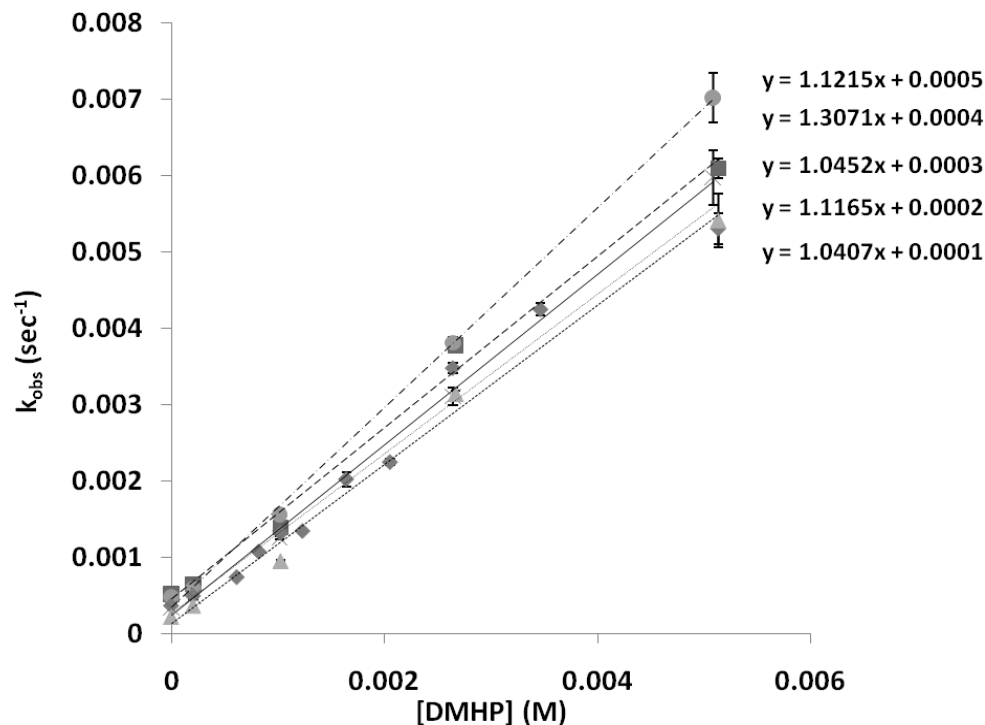


Figure 4.7. Plot of pseudo-first order rate constant, k_{obs} , as a function of $[\text{DMHP}]$ concentration for reaction 4.2. at five EDTA concentrations. All reactions were performed at $[\text{Fe}^{3+}] = [\text{DFB}] = 0.4 \text{ mM}$, $[\text{DMHP}] = 0\text{-}5 \text{ mM}$, $\mu = 0.10 \text{ M}$ (NaClO_4), $\text{pH} = 4.35$ (50 mM NaOAc buffer), and $T = 25 \text{ }^\circ\text{C}$. Legend: Triangles - $[\text{EDTA}] = 5.0 \text{ mM}$, X - $[\text{EDTA}] = 8 \text{ mM}$, diamonds - $[\text{EDTA}] = 10 \text{ mM}$, circles - $[\text{EDTA}] = 12 \text{ mM}$, squares - $[\text{EDTA}] = 15 \text{ mM}$. The equations to the right show the linear best fit lines of k_{obs} as a function of $[\text{DMHP}]$ in ascending order of EDTA concentration. The error bars represent the standard deviation of the average observed rate constant measured at 4 discrete wavelengths in a single experiment. If an error bar is not visible, it is smaller than the data point.

reaction showed a linear dependence on the concentration of EDTA (Fig. 4.4.), suggesting first-order dependence of the reaction on EDTA concentration. The linear plot of observed rate constant against EDTA concentration at a constant DMHP concentration takes the form of

$$k_{\text{obs}} = C_3 + k_3[\text{EDTA}] \quad (4.10.)$$

where k_3 represents the second order rate constant for reaction 4.2. with respect to EDTA at a constant fixed DMHP concentration obtained from the slope of the linear plots shown in Fig. 4.4. and C_3 represents a constant component that varies with DMHP concentration in the reaction obtained from the y-intercepts of the linear plots shown in Fig. 4.4.

The values calculated for k_2 and k_3 from Figs. 4.4 and 4.7. are shown in Table 4.1. The value for k_2 determined from the linear plots in Fig. 4.7. is $1.12 (9) \text{ M}^{-1} \text{ s}^{-1}$. The value for k_3 determined from the linear plots in Fig. 4.4. is $0.06 (2) \text{ M}^{-1} \text{ s}^{-1}$.

The importance of the y-intercepts of the linear plots of the iron(III) exchange reaction in Figs. 4.4. and 4.7. can be demonstrated by comparing the slopes of the plots obtained at one constant component to the y-intercept of the plots obtained at the other

constant component. As shown in Eq. 4.11.-4.12., there is a relationship between the constants, C_2 (Eq. 4.9.) and C_3 (Eq. 4.10.)

$$C_2 = k_3[\text{EDTA}] \quad (4.11.)$$

$$C_3 = k_2[\text{DMHP}] \quad (4.12.)$$

and the rate constants, k_3 and k_2 . By dividing the y-intercept of the linear plots in Figure 4.7. at varying DMHP concentration by the EDTA concentration of each line, the second order rate constant that is calculated is $0.028 (5) \text{ M}^{-1} \text{ s}^{-1}$, which is close to the second order rate constant observed in the linear plots in Fig. 4.4. corresponding to $k_3 (0.06 (2) \text{ M}^{-1} \text{ s}^{-1})$. It is important to note that the values of the rate constants k_3 that are determined both from Fig. 4.4. and Fig. 4.7. are the same as the value of the rate constant for the iron(III) exchange reaction performed without DMHP (Eq. 1) within experimental error, $0.030 (8) \text{ M}^{-1} \text{ s}^{-1}$. The same observation can be made for the y-intercepts of the plots of k_{obs} against EDTA concentration in Fig. 4.4., where the second order rate constant, k_2 calculated from the y-intercepts through division by the DMHP concentration of each line is $1.0 (1) \text{ M}^{-1} \text{ s}^{-1}$, the same value within experimental error as that observed in the plots of k_{obs} against DMHP concentration in Fig. 4.7. ($1.13 (9) \text{ M}^{-1} \text{ s}^{-1}$).

The rate laws derived from the experiments performed at constant EDTA concentration and at constant DMHP concentration feature second order rate constants

Table 4.1. Rate constants observed in the reactions studied for the Fe-HDFB-DMHP-EDTA systems. Conditions: T = 25 °C, μ = 0.10 M (NaClO₄), pH = 4.35.

Reaction	Symbol	Constant
$\text{Fe}(\text{HDFB})^+ + \text{H}_2\text{EDTA}^{2-} + \text{H}^+ \rightleftharpoons \text{Fe}(\text{EDTA})^- + \text{H}_4\text{DFB}^+$	k_1	0.030 (8) M ⁻¹ s ⁻¹
$\text{Fe}(\text{HDFB})^+ + \text{H}_2\text{EDTA}^{2-} + \text{H}^+ \xrightleftharpoons{\text{DMHP}} \text{Fe}(\text{EDTA})^- + \text{H}_4\text{DFB}^+$	k_2	1.12 (9) M ⁻¹ s ⁻¹ ^a
		1.0 (1) M ⁻¹ s ⁻¹ ^b
	k_3	0.06 (2) M ⁻¹ s ⁻¹ ^c
		0.028(5) M ⁻¹ s ⁻¹ ^d
$\text{Fe}(\text{HDFB})^+ + 3 \text{H}(\text{DMHP}) \rightleftharpoons \text{Fe}(\text{DMHP})_3 + \text{H}_4\text{DFB}^+$	k_4	1.13 (9) M ⁻¹ s ⁻¹ ^e
		0.96 (3) M ⁻¹ s ⁻¹ ^f
$\text{Fe}(\text{DMHP})_3 + \text{H}_2\text{EDTA}^{2-} + \text{H}^+ \rightleftharpoons \text{FeEDTA}^- + 3 \text{H}(\text{DMHP})$	k_5	377 (7) M ⁻¹ s ⁻¹ ^g

^a Value obtained from the slopes of the plots shown in Fig. 4.7.

^b Value obtained from the y-intercepts of the plots shown in Fig. 4.4.

^c Value obtained from the slopes of the plots shown in Fig. 4.4.

^d Value obtained from the y-intercepts of the plots shown in Fig. 4.7.

^e Value obtained from the slope of the experimental plot shown in Fig. 4.10.

^f Value obtained from the slope of the theoretical plot shown in Fig. 4.10.

^g Value obtained from the best fit line shown in Fig. 4.15. and the slopes of the plots shown in Fig. 4.16.

k_2 and k_3 that differ by over an order of magnitude. The combined rate law obtained from Eqs. 4.9. and 4.10. is shown in Eqs. 4.13. and 4.14.

$$\text{Rate} = k_{\text{obs}}[\text{FeHDFB}^+] = k_2[\text{DMHP}][\text{FeHDFB}^+] + k_3[\text{EDTA}^{4-}][\text{FeHDFB}^+] \quad (4.13.)$$

$$k_{\text{obs}} = k_2[\text{DMHP}] + k_3[\text{EDTA}] \quad (4.14.)$$

4.4.4. Kinetics of iron(III) exchange from ferrioxamine B to DMHP (Eq. 4.3.)

The iron(III) exchange reaction of $\text{Fe}(\text{HDFB})^+$ with DMHP to form $\text{Fe}(\text{DMHP})_3$ occurs relatively slowly, over the course of 10-60 minutes depending on the DMHP concentration at pH 4.35, following Eq. 4.3. The spectra measured during the course of the reaction (Fig. 4.8.) support the identity of the product as $\text{Fe}(\text{DMHP})_3$, suggesting complete conversion of the $\text{Fe}(\text{HDFB})^+$ complex to the product. The observed λ_{max} of the product was 457 nm, which is significantly different from that of $\text{Fe}(\text{HDFB})^+$, and is consistent with the value reported for the tris-DMHP-iron(III) system at pH 4.35, $\lambda_{\text{max}} \approx 460 \text{ nm}$.⁽¹²⁷⁾ No isosbestic point is observed during this reaction, due to the narrow frame of wavelengths measured during the experiment. The absorbance measured at a single wavelength (Fig. 4.9.) can be fit with a single exponential decay model (Eq. 4.5.), suggesting a single kinetically observable reaction acting as the rate-limiting step as well as confirming first order dependence of the rate-determining step on $\text{Fe}(\text{HDFB})^+$ concentration. The observed pseudo-first order rate constant was plotted as a function of DMHP concentration, yielding a straight line over the range of 4 to 10 mM DMHP (see Fig. 4.10.), which is consistent with first-order dependence of the rate law on DMHP concentration. This first-order dependence suggests the involvement of one equivalent of DMHP in the rate-determining step of the reaction. Using this information, it is possible to propose the following rate law for the rate limiting step:

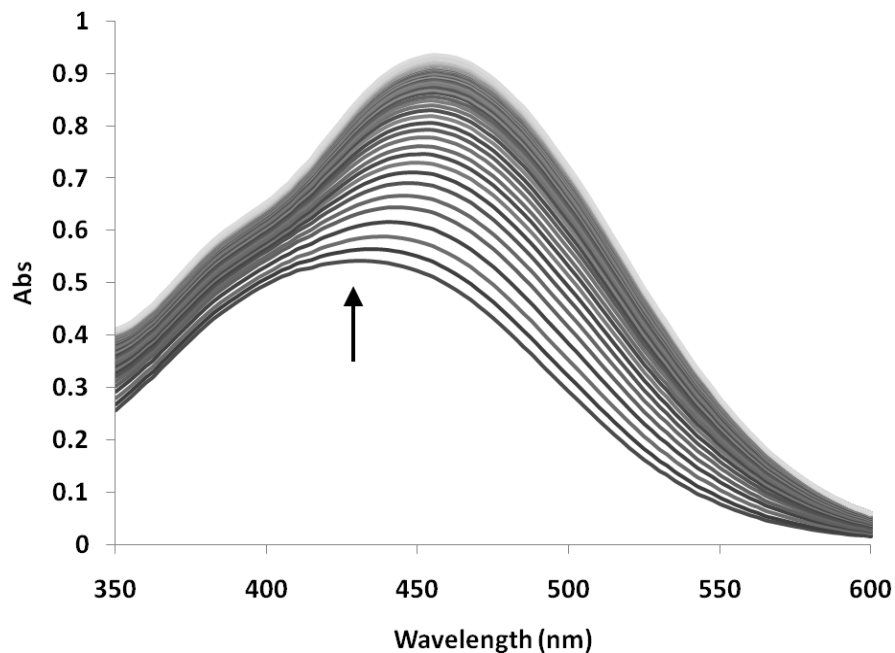


Figure 4.8. Spectra measured during the iron(III) exchange reaction from desferrioxamine B to DMHP (Reaction 4.3.) over the course of 20 minutes. Arrow shows direction of spectral change with time. Conditions: $[\text{Fe}^{3+}] = [\text{HDFB}] = 0.20 \text{ mM}$, $[\text{DMHP}] = 7 \text{ mM}$, $\mu = 0.10 \text{ M}$ (NaClO_4), $\text{pH} = 4.35$ (50 mM NaOAc buffer), $T = 25 \text{ }^\circ\text{C}$.

$$\text{Rate} = k_4[\text{DMHP}][\text{FeHDFB}^+] \quad (4.15.)$$

and where in the presence of excess DMHP,

$$k_{\text{obs}} = k_4[\text{DMHP}] \quad (4.16.)$$

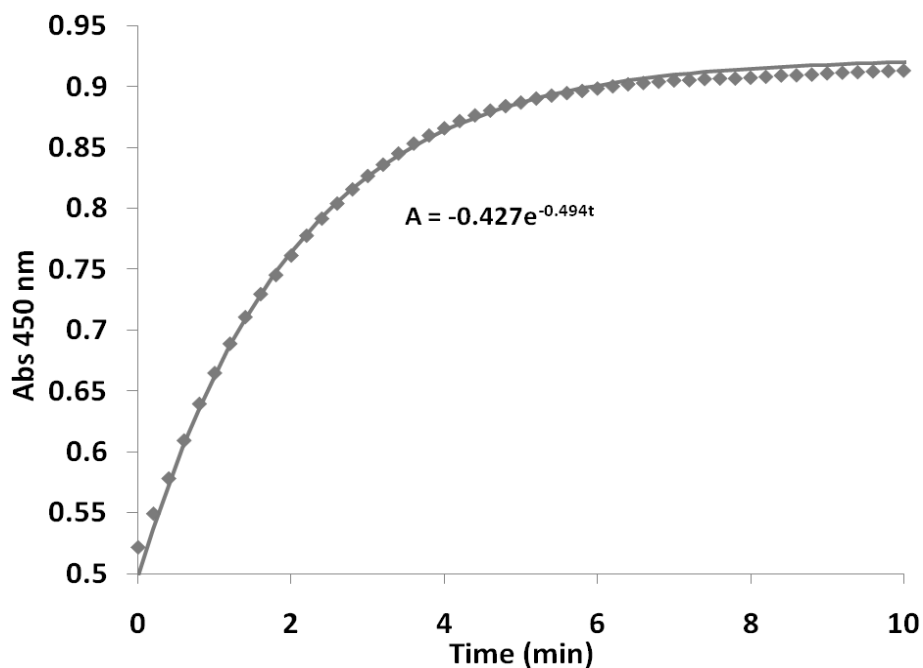


Figure 4.9. Plot of absorbance at 455 nm as a function of time for the iron(III) exchange reaction between ferrioxamine B and DMHP (Eq. 4.3.). The line represents the single exponential decay fit to the data (Eq. 4.5.). Conditions: $[\text{Fe}^{3+}] = [\text{HDFB}] = 0.20$ mM, $[\text{DMHP}] = 7$ mM, $\mu = 0.10$ M (NaClO_4), $\text{pH} = 4.35$ (50 mM NaOAc buffer), $T = 25$ °C.

The determined rate law shows high sensitivity of the reaction rate to the concentration of DMHP, $k_4 = 1.13$ (9) $\text{M}^{-1} \text{s}^{-1}$ as determined from the slope of the plot of k_{obs} as a function of $[\text{DMHP}]$, Fig. 4.10., and a first order dependence of the reaction on the concentration of DMHP, suggesting the presence of only one equivalent of DMHP involved in or before the rate-limiting step.

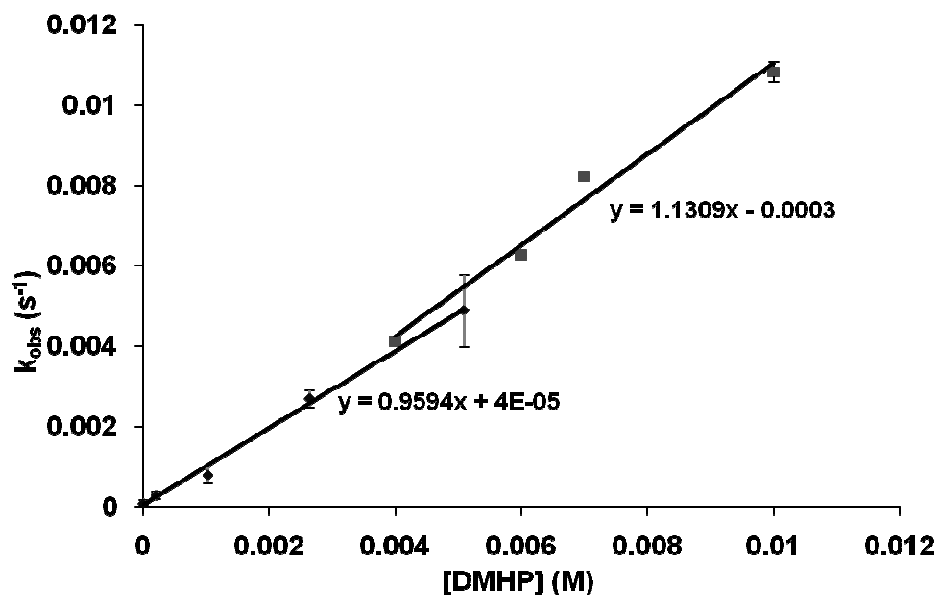


Figure 4.10. Plot of observed pseudo-first order rate constant of the iron(III) exchange reaction between ferrioxamine B and DMHP (Eq. 4.3.) as a function of DMHP concentration. The lower line (diamonds) represents rate constants for reaction 3 extrapolated from the intercepts of the plots in Fig. 4.4., while the upper line (squares) represents the values obtained experimentally. Error bars for the diamonds represent the standard deviation of the y-intercepts of the plots in Fig. 4.4. Error bars for the squares represent the standard deviation of the average observed rate constant measured at 4 discrete wavelengths in a single experiment. If error bars are not visible, they are smaller than the data points.

Linear regression of the plots in Fig. 4.4. allows us to calculate an observed rate constant for the reaction of desferrioxamine B with DMHP from the y- intercept of the plot. This determination of the second order rate constant of reaction 4.3. from extrapolation of the rate constants of reaction 4.2. to $[EDTA] = 0$ can be compared to the experimentally determined value of the second order rate constant of reaction 4.3. Fig. 4.10. shows this comparison, where the slopes of the lines, representing the second order rate constant of reaction 4.3., are similar ($0.96 (3) \text{ M}^{-1} \text{ s}^{-1}$ for the data extrapolated from reaction 4.2. and $1.13 (9) \text{ M}^{-1} \text{ s}^{-1}$ for the experimental data of reaction 4.3.), as are the y-intercepts, which are both approximately zero, suggesting no appreciable back-reaction of desferrioxamine B with the $\text{Fe}(\text{DMHP})_3$ complex. The second order rate constant for reaction 4.3., k_4 , obtained from the slope of the experimental data can be compared to the slope of the best fit line to the y-intercepts of the lines in Fig. 4.4. The values have been shown to be similar, and the rate laws obtained from those two sets of data both suggest that reaction 4.3. occurs with first order dependence on DMHP concentration. Since the rate laws of the reaction obtained from the slope of the experimental data and from the intercepts of Fig. 4.4. are the same, and they exhibit the same second order rate constant within experimental error, we can propose that reactions 4.2. and 4.3. proceed by the same rate determining step, which will be discussed later.

Additional experiments were performed over a range of pH values, from pH 4.35 to pH 6.00, and similar spectral shifts were obtained for all experiments, suggesting that

at all pH values, the reaction followed Eq. 4.3. All experiments were able to be fit to a single exponential decay model, Eq. 4.5., suggesting that the reactions proceed by the same mechanism at all pH values. The plots of k_{obs} as a function of DMHP concentration are shown in Fig. 4.11. The slopes of the lines, representing the second order rate constant of reaction 4.3., k_4 , vary with pH as shown in Fig. 4.12., demonstrating pH-dependence of the rate of the iron(III) exchange reaction.

4.4.5. Kinetics of iron(III) exchange from DMHP to EDTA (Eq. 4.4.)

Finally, experiments were performed to determine the mechanism and rate of exchange of iron(III) from DMHP to EDTA. Comparison of the rate law and mechanism of exchange from $\text{Fe}(\text{DMHP})_3$ can provide information about the role of the iron(III)-DMHP complex in the catalyzed iron(III) exchange reaction, Eq. 4.2.

Spectra for exchange reaction 4.4. are shown in Fig. 4.13. for the reaction of 0.20 mM Fe(III) and 2 mM DMHP with 5 mM EDTA at pH 4.35. The initial and final spectra are indicative of reactant and products as shown in Eq. 4.4., taking into account the protonation states of the ligands at pH 4.35. The initial λ_{max} of the system is consistent with the $\text{Fe}(\text{DMHP})_3$ complex, as discussed in section 4.3.3., and the final product is consistent with the $\text{Fe}(\text{EDTA})^-$ complex, as discussed in section 4.3.2. The time-dependent absorbance change at 4 discrete wavelengths was monitored to investigate

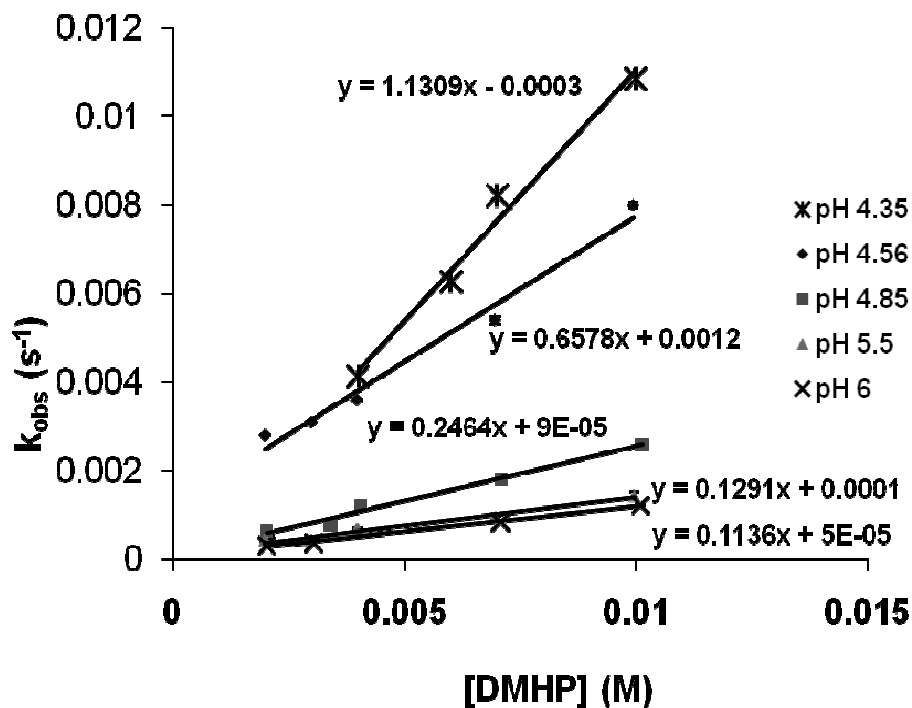


Figure 4.11. Plot of observed pseudo-first order rate constant of the iron(III) exchange reaction between ferrioxamine B and DMHP (Eq. 4.3.) as a function of DMHP concentration at five solution pH values. The legend to the right displays the symbols for each pH value. Error bars represent the standard deviation of the average observed rate constant measured at 4 discrete wavelengths in a single experiment. If error bars are not visible, they are smaller than the data points.

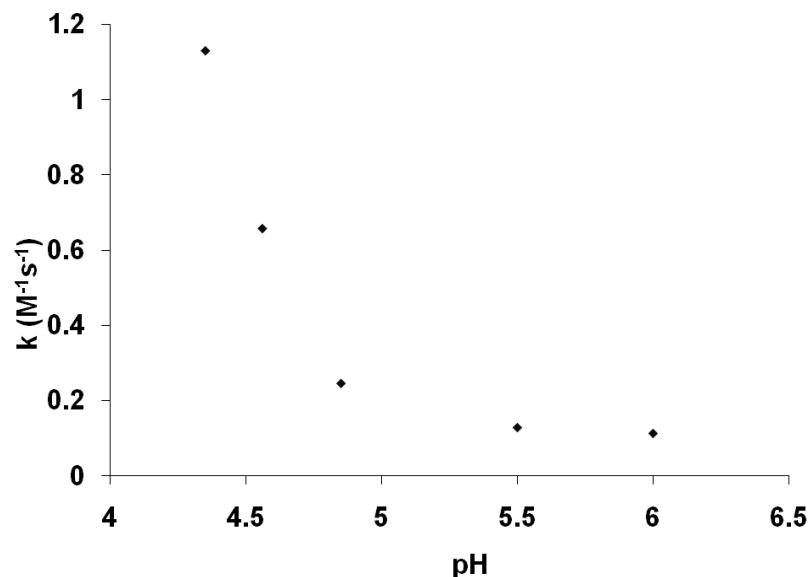


Figure 4.12. Plot of second order rate constants for the iron(III) exchange reaction between desferrioxamine B and DMHP (reaction 4.3.) as a function of pH. At lower pH values, the reaction proceeds much more rapidly.

the possible wavelength dependence of the measured rate constant (Fig. 4.14.). The observed rate constants were wavelength independent, again suggesting that no stable intermediate was present. A single exponential decay model (Eq. 4.5.) was fit to the data, suggesting that a single reaction was spectrophotometrically observable during the exchange process and that the rate law of the rate-limiting step of iron exchange is first order with respect to the iron-DMHP complex concentration. Additionally, a plot of observed pseudo-first order rate constants as a function of EDTA concentration yielded a linear relationship (Fig. 4.15.), suggesting that the reaction is first-order with respect to EDTA.

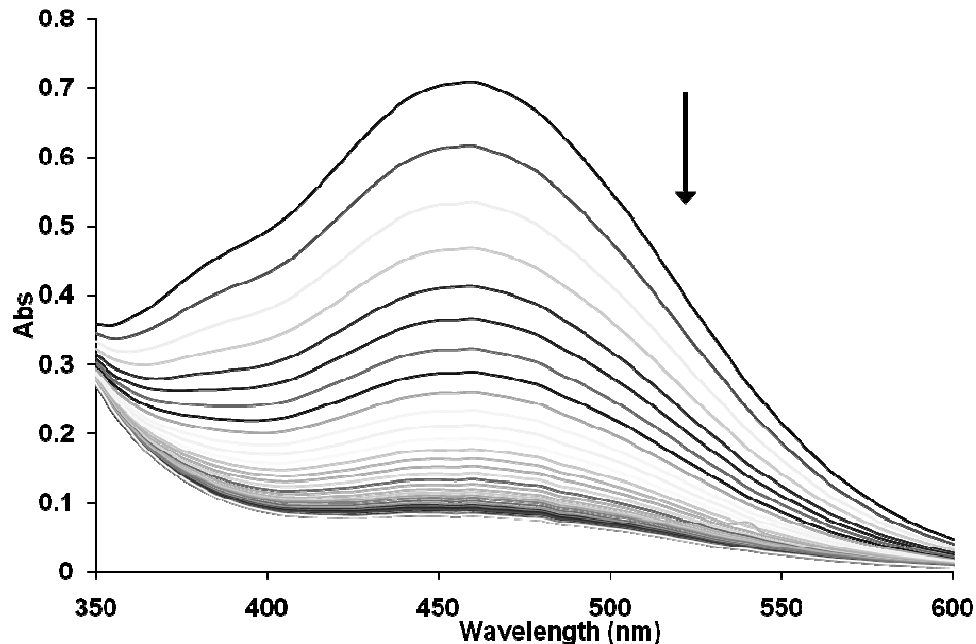


Figure 4.13. Spectra measured during the iron(III) exchange reaction of the $\text{Fe}(\text{DMHP})_3$ complex with EDTA (Eq. 4.4.). Arrow shows the direction of spectral change with time over 120 secs. Conditions: $[\text{Fe}^{3+}] = 0.20 \text{ mM}$, $[\text{DMHP}] = 2.0 \text{ mM}$, $[\text{EDTA}] = 5.0 \text{ mM}$, $\mu = 0.10 \text{ M}$ (NaClO_4), $\text{pH} = 4.35$ (50 mM NaOAc buffer), $T = 25 \text{ }^\circ\text{C}$.

No isosbestic point was obtained over the wavelength range measured in this experiment, again likely due to the narrow frame of wavelengths measured.

At both DMHP concentrations, the plots in Figure 4.15. exhibit approximately zero y-intercepts, suggesting no appreciable back reaction of the $\text{Fe}(\text{EDTA})^-$ complex with DMHP at our conditions. Another interesting facet of the linear plots is the observed second-order rate constant of the reactions, represented by the slope of the

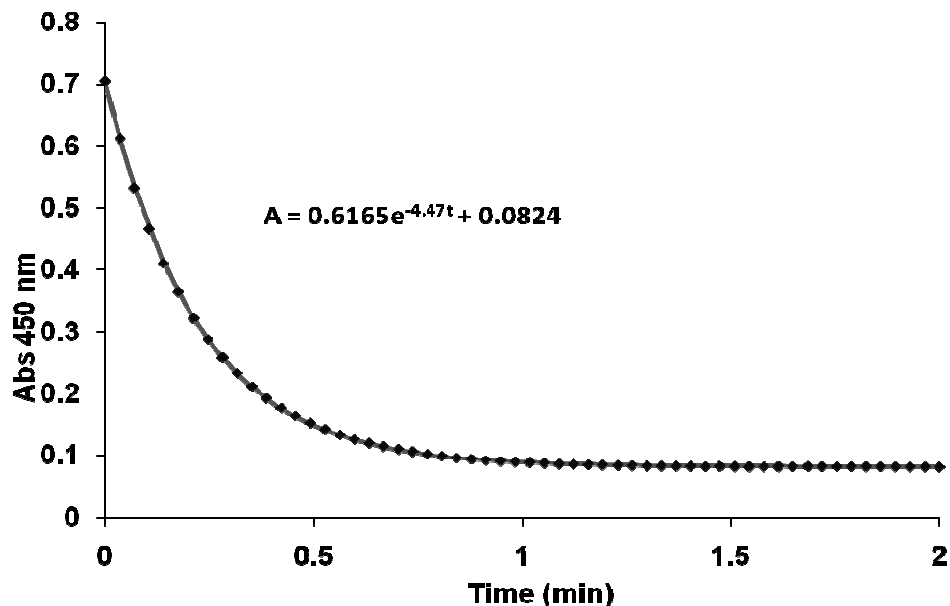


Figure 4.14. Plot of absorbance at 450 nm as a function of time for the iron exchange reaction between $\text{Fe}(\text{DMHP})_3$ and EDTA (Eq. 4.4.). The line represents the single exponential decay fit to the data (Eq. 4.5.). Conditions: $[\text{Fe}^{3+}]_{\text{tot}} = 2.0 \times 10^{-4} \text{ M}$, $[\text{DMHP}] = 5.0 \text{ mM}$, $[\text{EDTA}] = 6.0 \text{ mM}$, $25.0 \text{ }^\circ\text{C}$, $\text{pH} = 4.35$, $\mu = 0.10 \text{ M}$ (NaClO_4).

lines. For the plot at 2 mM DMHP, the apparent second-order rate constant is $36 \text{ M}^{-1} \text{ s}^{-1}$, while the apparent second order rate constant at 5 mM DMHP is $11 \text{ M}^{-1} \text{ s}^{-1}$, suggesting an inverse dependence of the reaction rate on DMHP concentration.

A third series of experiments was performed by varying the concentration of DMHP present in solution at a constant EDTA concentration. A plot of the observed pseudo first order rate constant as a function of DMHP concentration is shown in Fig. 4.16. This plot showed an inverse relationship of the observed rate constant of the

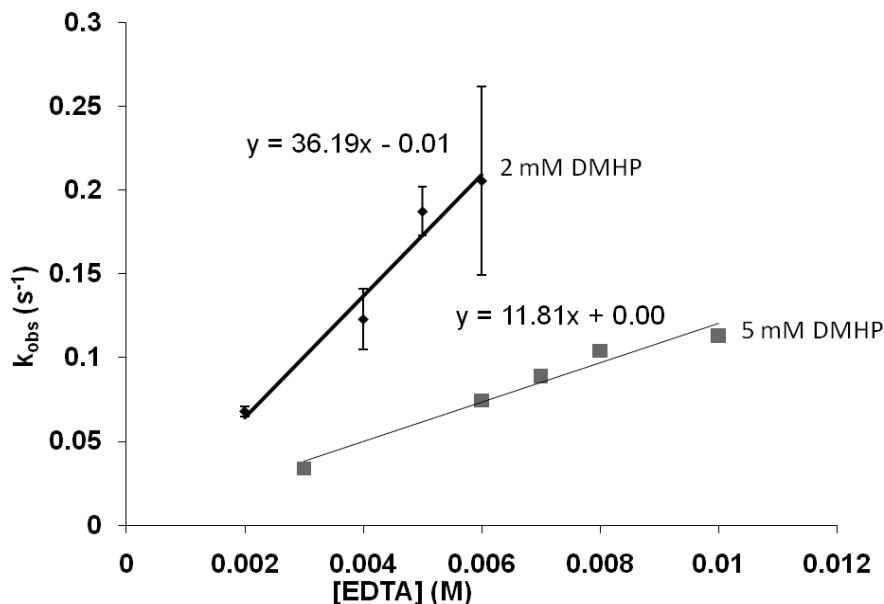


Figure 4.15. Plot of observed pseudo-first order rate constant for the iron(III) exchange reaction between DMHP and EDTA (Eq. 4.4.) as a function of EDTA concentration at two DMHP concentrations. The upper plot (diamonds) represents the reaction performed at 2 mM DMHP, while the lower plot (squares) represents the reaction performed at 5 mM DMHP. Conditions: $[Fe^{3+}] = 0.20$ mM, $\mu = 0.10$ M ($NaClO_4$), pH = 4.35 (50 mM NaOAc buffer), and $T = 25$ °C. Error bars on the plot at 5 mM DMHP represent the standard deviation of the average observed rate constant measured at 4 discrete wavelengths in a single experiment. Error bars on the plot at 2 mM DMHP represent the standard deviation of the average observed rate constant measured at two discrete wavelengths, 2 replicates performed at each wavelength (4 total replicates). If error bars are not visible (as in the squares), they are smaller than the data points.

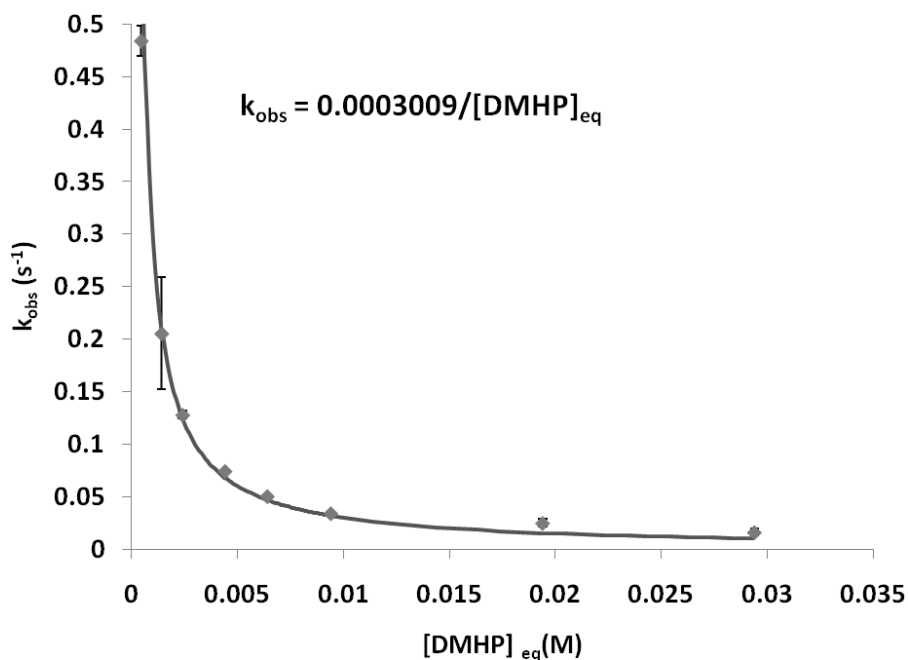


Figure 4.16. Plot of observed pseudo-first order rate constant for the iron(III) exchange reaction between DMHP and EDTA (Eq. 4.4.) as a function of DMHP concentration.

The line represents the best fit line to the data (excluding the data point at 1 mM DMHP) using the model shown in Eq. 4.30., where a is an adjustable parameter found to be 3.01×10^{-4} . Error bars represent the standard deviation of the average observed rate constant measured at 4 discrete wavelengths in a single experiment. For the error bar at 2 mM DMHP, see Fig. 4.15. Conditions: $[\text{Fe}^{3+}]_{\text{tot}} = 2.0 \times 10^{-4} \text{ M}$, $[\text{EDTA}] = 6.0 \text{ mM}$, $25.0 \text{ }^\circ\text{C}$, $\text{pH} = 4.35$, $\mu = 0.10 \text{ M (NaClO}_4\text{)}$.

iron(III) exchange reaction on the concentration of DMHP. In order to determine the exact mechanism of iron(III) exchange, it is necessary to determine the mathematical model that gives the best fit of predicted rate constant to experimentally determined rate constant. As such, we will discuss the contribution to the rate law from each possible species of the $\text{Fe}(\text{DMHP})_x$ complex ($x = 1, 2, \text{ or } 3$). The most simple complex that could participate in the exchange reaction is the tris-DMHP complex, $\text{Fe}(\text{DMHP})_3$. The rate law for $\text{Fe}(\text{DMHP})_3$ exchanging iron(III) with EDTA is:

$$\text{Rate} = k_x[\text{EDTA}][\text{Fe}(\text{DMHP})_3]_{\text{eq}} \quad (4.17.)$$

where k_x represents the rate constant for the exchange of iron(III) from $\text{Fe}(\text{DMHP})_3$ to EDTA. One important estimation that can be made for the reactions at high DMHP concentration is that essentially all iron(III) in solution is found in the tris-DMHP complex.

$$[\text{Fe}(\text{DMHP})_3]_{\text{eq}} \approx [\text{Fe}^{3+}]_{\text{tot}} \quad (4.18.)$$

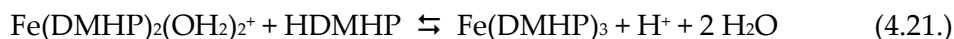
The rate law shown in Eq. 4.17. cannot be the sole contributor to the overall rate law of the reaction, however, as the equation representing the observed pseudo-first order rate constant is

$$k_{\text{obs}} = k_x[\text{EDTA}] \quad (4.19.)$$

which is constant with respect to DMHP concentration. Both Figs. 4.15. and 4.16. demonstrate the dependence of k_{obs} on DMHP concentration. The next lower order of complex that may participate in the iron(III) exchange reaction with EDTA is the bis-DMHP complex, $\text{Fe}(\text{DMHP})_2(\text{H}_2\text{O})_2^+$. The rate law corresponding to the iron(III) exchange reaction between EDTA and $\text{Fe}(\text{DMHP})_2(\text{H}_2\text{O})_2^+$ takes the form shown in Eq. 4.20.

$$\text{Rate} = k_{\text{yapp}}[\text{EDTA}][\text{Fe}(\text{DMHP})_2(\text{OH}_2)_2^+] \quad (4.20.)$$

The concentration of $\text{Fe}(\text{DMHP})_2(\text{OH}_2)_2^+$ is relatively low at the DMHP concentrations chosen for the experiment, so the complex formation equilibrium constant must be considered. Also, since the reaction is being carried out at pH 4.35, the majority of free DMHP that is present in solution will be found in the mono-protonated form, HDMHP.

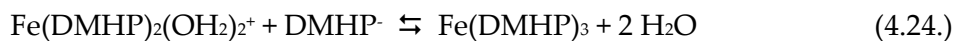


$$K_3 = \frac{[\text{Fe}(\text{DMHP})_3]_{\text{eq}}[\text{H}^+]}{[\text{Fe}(\text{DMHP})_2(\text{H}_2\text{O})_2^+]_{\text{eq}}[\text{HDMHP}]_{\text{eq}}} \quad (4.22.)$$

By rearranging the equilibrium constant expression shown in Eq. 4.22., it is possible to solve for the equilibrium concentration of $Fe(DMHP)_2(H_2O)_2^+$.

$$[Fe(DMHP)_2(H_2O)_2^+]_{eq} = \frac{[Fe(DMHP)_3][H^+]}{K_3[HDMHP]_{eq}} \quad (4.23.)$$

The numerical value of K_3 can be obtained by linear combination of the third proton-independent step-wise complex equilibrium constant, β_3 and the second protonation constant of DMHP.



$$\beta_3 = \frac{[Fe(DMHP)_3]}{[Fe(DMHP)_2(H_2O)_2^+][DMHP^-]} \quad (4.25.)$$

$$K_{a2} = \frac{[DMHP^-][H^+]}{[HDMHP]} \quad (4.26.)$$

$$K_3 = \beta_3 K_{a2} \quad (4.27.)$$

Substitution of Eq. 4.27. into Eq. 4.23., and then Eq. 4.23. into Eq. 4.20. with the assumption shown in Eq. 4.18. yields the rate law for the reaction, Eq. 4.28.

$$Rate = \frac{k_y [EDTA][H^+][Fe]_{tot}}{\beta_3 K_{a2} [HDMHP]_{eq}} \quad (4.28.)$$

$$k_{obs} = \frac{k_y [EDTA][H^+]}{\beta_3 K_{a2} [HDMHP]_{eq}} \quad (4.29.)$$

Where k_y is the second-order rate constant for the reaction of EDTA with $Fe(DMHP)_2(OH)_2$, K_{a2} represents the second deprotonation constant of DMHP (Eq. 4.26., obtained from the literature, $10^{9.72}$), β_3 represents the third proton-independent formation constant of the Fe-DMHP complex (Eq. 4.25., also obtained from the literature, $10^{9.24}$), and $[Fe]_{tot}$ represents the total iron(III) concentration in solution.(127)

A plot of the best fit line using the theoretical model determined above to the experimentally determined rate constants allows evaluation of the quality of the model. The best fit line was calculated for the plot of k_{obs} as a function of DMHP concentration using the inverse first order model:

$$y = \frac{a}{x} \quad (4.30.)$$

Where $y = k_{obs}$, $x = [HDMHP]_{eq}$, and $a = k_y [EDTA][H^+] / \beta_3 K_{a2}$ from Eq. 4.29. The fit of this model to the experimental data determined at 2 mM DMHP to 10 mM DMHP is shown in Fig. 4.16. The data point measured at 1 mM DMHP was excluded, as the high rate of reaction may have led to decreased accuracy in the determined value of the

observed rate constant. A good fit of the data to Eq. 4.30. is obtained, demonstrating the viability of this model for the exchange mechanism.

The final species that could participate in the iron(III) exchange reaction with EDTA is the mono-DMHP complex, $Fe(DMHP)(H_2O)_4^{2+}$. The rate law that corresponds to the reaction of EDTA with $Fe(DMHP)(H_2O)_4^{2+}$ is shown in Eq. 4.31.

$$\text{Rate} = k_{zapp}[\text{EDTA}][Fe(DMHP)(OH_2)_4^{2+}] \quad (4.31.)$$

Where k_{zapp} represents the apparent rate constant of the iron(III) exchange reaction between $[Fe(DMHP)(OH_2)_4^{2+}]$ and EDTA. As with $Fe(DMHP)_2(H_2O)_2^{2+}$, the equilibrium expression for the mono-DMHP complex will factor in to the rate law expression.



$$K_2 = \frac{[Fe(DMHP)_2(OH_2)_2^{2+}]_{eq} [H^+]}{[Fe(DMHP)(H_2O)_4^{2+}]_{eq} [HDMHP]_{eq}} \quad (4.33.)$$

$$K_2 = \beta_2 K_{a2} \quad (4.34.)$$

By rearranging Eq. 4.33., it is possible to solve for the concentration of $Fe(DMHP)(H_2O)_4^{2+}$.

$$[Fe(DMHP)(H_2O)_4^{2+}]_{eq} = \frac{[Fe(DMHP)_2(H_2O)_2^+]_{eq}[H^+]}{K_2[HDMHP]_{eq}} \quad (4.35.)$$

Substitution of Eq. 4.35. and Eq. 4.23. into Eq. 4.31., as well as substitution of Eq. 4.27. and Eq. 4.34. gives the rate law for iron(III) exchange from $Fe(DMHP)(H_2O)_4^{2+}$, shown in Eq. 4.36.

$$Rate = \frac{k_z[EDTA][H^+]^2[Fe]_{tot}}{\beta_3\beta_2K_{a2}^2[HDMHP]_{eq}^2} \quad (4.36.)$$

$$k_{obs} = \frac{k_z[EDTA][H^+]^2}{\beta_3\beta_2K_{a2}^2[HDMHP]_{eq}^2} \quad (4.37.)$$

A best fit line of the experimental data using the model proposed in Eq. 4.36. was calculated using the mathematical model

$$y = \frac{a}{x^2} \quad (4.38.)$$

Where $y = k_{obs}$, $x = [DMHP]$, and $a = k_z[EDTA][H^+]^2/\beta_3\beta_2K_{a2}^2$ from Eq. 4.37., as is shown in Fig. 4.17. The model in Eq. 4.38. does not provide a satisfactory fit to the

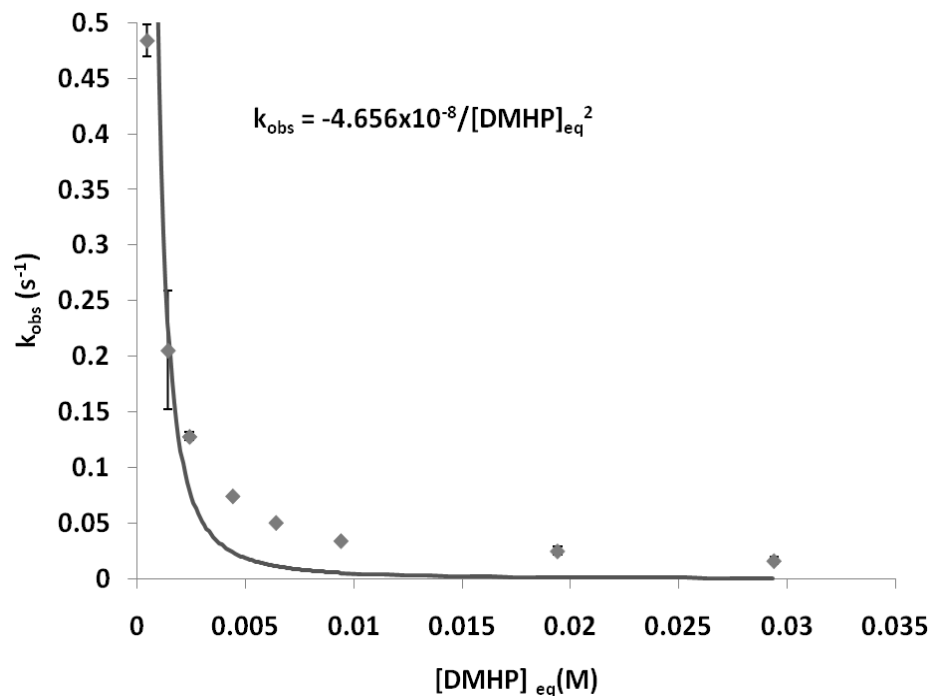


Figure 4.17. Plot of observed pseudo-first order rate constant, k_{obs} , for the iron(III) exchange reaction between DMHP and EDTA (reaction 4.4.) as a function of DMHP concentration. The line represents the best fit line to the data (excluding the data point at 1 mM DMHP) using the model shown in Eq. 4.38., where a is an adjustable parameter found to be 4.66×10^{-8} . Error bars represent the standard deviation of the average observed rate constant measured at 4 discrete wavelengths in a single experiment. For the error bar at 2 mM DMHP, see Fig. 4.15. Conditions: $[\text{Fe}^{3+}]_{\text{tot}} = 2.0 \times 10^{-4}$ M, $[\text{EDTA}] = 6.0$ mM, 25.0 °C, $\text{pH} = 4.35$, $\mu = 0.10$ M (NaClO_4).

experimental data, suggesting that the rate law of the reaction does not exclusively involve reactivity through the mono-DMHP complex.

It is also possible that the reaction mechanism involves parallel pathways, where different iron(III)-DMHP complex species contribute to the observed rate of reaction. Therefore, the rate laws of a combination of species must be derived and compared to the experimental data. The first possible combination of reactive species is the bis- and tris-DMHP complexes, shown in Eq. 4.39.-4.40. The rate law for a parallel reaction



mechanism for those two species can be obtained through linear combination of the rate laws of the individual species, or the sum of Eq. 4.17. and Eq. 4.28. to give Eq. 4.41.

$$\text{Rate} = \frac{k_y [\text{EDTA}][\text{H}^+][\text{Fe}]_{\text{tot}}}{\beta_3 K_{a2} [\text{HDMHP}]_{\text{eq}}} + k_x [\text{EDTA}][\text{Fe}]_{\text{tot}} \quad (4.41.)$$

$$\text{Rate} = k_{\text{obs}}[\text{Fe}]_{\text{tot}} \quad (4.42.)$$

$$k_{\text{obs}} = \frac{k_y [\text{EDTA}][\text{H}^+]}{\beta_3 K_{a2} [\text{HDMHP}]_{\text{eq}}} + k_x [\text{EDTA}] \quad (4.43.)$$

This suggests that the best fit line to the experimental data would take the form of

$$y = \frac{a}{x} + b \quad (4.44.)$$

Where $y = k_{obs}$, $x = [DMHP]$, $a = k_y[EDTA][H^+]/\beta_3K_{a2}$, and $b = k_x[EDTA]$ from Eq. 4.43.

The best fit line to the experimental data with this mathematical model is shown in Fig. 4.18, demonstrating a good fit of the model in Eq. 4.44. to the observed rate constants, even while including the data point measured at 1 mM DMHP. While it is difficult to distinguish between the quality of the theoretical fit to the experimental data using the model shown in Eq. 4.30. and the model shown in Eq. 4.44., it is possible that the improved fit using the model in Eq. 4.44. is solely due to the additional variable included.

The next possible combination of reactive species is the bis- and mono-DMHP complexes, shown in Eqs. 4.40. and 4.45.



The sum of Eqs. 4.28. and 4.36. provides the rate law of this proposed parallel mechanism, shown in Eq. 4.46.

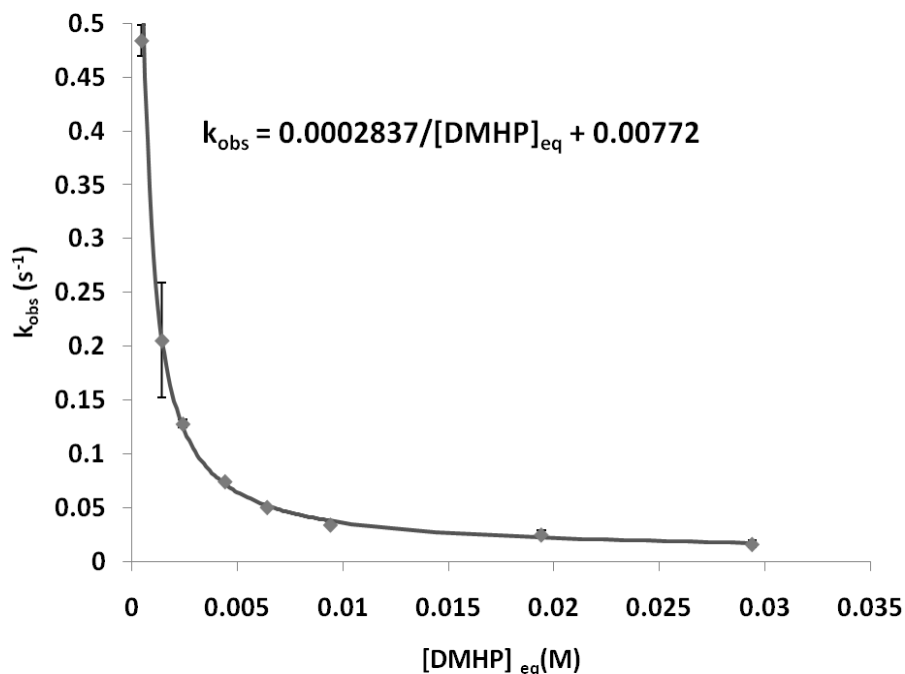


Figure 4.18. Plot of observed pseudo-first order rate constant, k_{obs} , for the iron(III) exchange reaction between DMHP and EDTA (reaction 4.4.) as a function of DMHP concentration. The line represents the best fit line to the data (excluding the data point at 1 mM DMHP) using the model shown in Eq. 4.40., where a and b are adjustable parameters found to be $a = 2.84 \times 10^{-4}$ and $b = 7.72 \times 10^{-3}$. Error bars represent the standard deviation of the average observed rate constant measured at 4 discrete wavelengths in a single experiment. For the error bar at 2 mM DMHP, see Fig. 4.15. Conditions: $[Fe^{3+}]_{tot} = 2.0 \times 10^{-4}$ M, $[EDTA] = 6.0$ mM, 25.0 °C, $pH = 4.35$, $\mu = 0.10$ M ($NaClO_4$).

$$Rate = \frac{k_z [EDTA][H^+]^2 [Fe]_{tot}}{\beta_3 \beta_2 K_{a1}^2 [HDMHP]_{eq}^2} + \frac{k_y [EDTA][H^+] [Fe]_{tot}}{\beta_3 K_{a1} [HDMHP]_{eq}} \quad (4.46.)$$

$$k_{obs} = \frac{k_z [EDTA][H^+]^2}{\beta_3 \beta_2 K_{a1}^2 [HDMHP]_{eq}^2} + \frac{k_y [EDTA][H^+]}{\beta_3 K_{a1} [HDMHP]_{eq}} \quad (4.47.)$$

The form of the theoretical fit of rate constants to experimental data will then be

$$y = \frac{a}{x^2} + \frac{b}{x} \quad (4.48.)$$

Where $y = k_{obs}$, $x = [DMHP]$, $a = k_z [EDTA][H^+]^2 / \beta_3 \beta_2 K_{a2}^2$, and $b = k_y [EDTA][H^+] / \beta_3 K_{a2}$ from Eq. 4.47. The plot of the best fit line using this model is shown in Fig. 4.19., demonstrating a very good fit of Eq. 4.48. to the experimental data. However, the fit exhibits a negative coefficient for the term corresponding to the rate constant of the mono-complex, which is not physically meaningful. This suggests that the model incorporating both mono- and bis- complexes is not the appropriate model for analysis of the mechanism.

Another possible combination of possible reactive species in iron(III) exchange reaction 4.4. is the mono- and tris-complexes, the reaction scheme of which would include reactions 4.39. and 4.45.

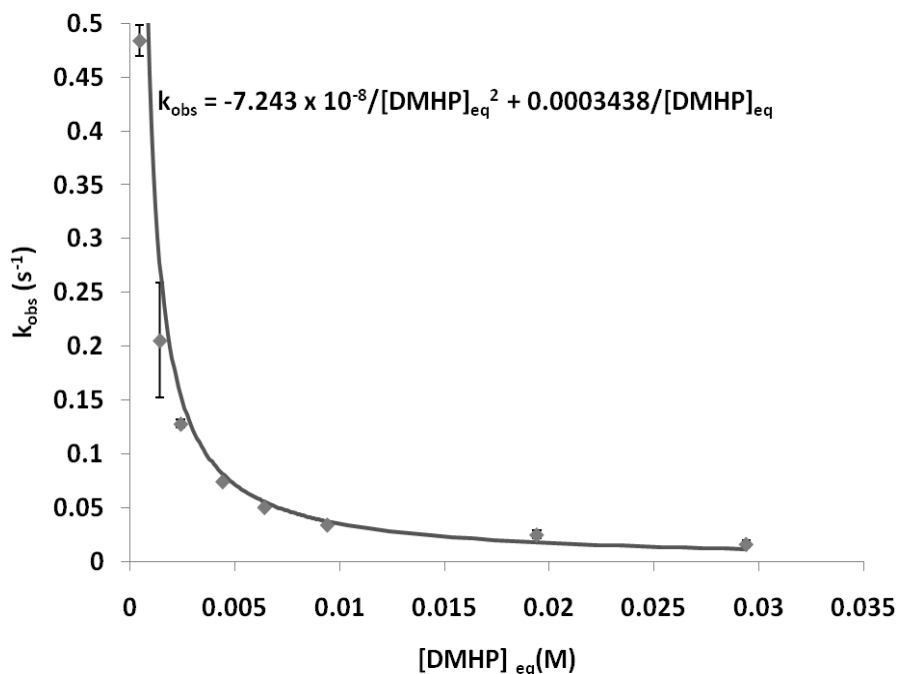


Figure 4.19. Plot of observed pseudo-first order rate constant, k_{obs} , for the iron(III) exchange reaction between DMHP and EDTA (reaction 4.4.) as a function of DMHP concentration. The line represents the best fit line to the data (excluding the data point at 1 mM DMHP) using the model shown in Eq. 4.42., where a and b are adjustable parameters found to be $a = 7.24 \times 10^{-8}$ and $b = 3.44 \times 10^{-4}$. Error bars represent the standard deviation of the average observed rate constant measured at 4 discrete wavelengths in a single experiment. For the error bar at 2 mM DMHP, see Fig. 4.15. Conditions: $[Fe^{3+}]_{tot} = 2.0 \times 10^{-4} M$, $[EDTA] = 6.0 mM$, $25.0\text{ }^{\circ}C$, $pH = 4.35$, $\mu = 0.10 M (NaClO_4)$.



The rate law for this model obtained from linear combination of Eqs. 4.17. and 4.36. is shown in Eq. 4.49.

$$\text{Rate} = \frac{k_z[\text{EDTA}][\text{H}^+]^2[\text{Fe}]_{\text{tot}}}{\beta_3\beta_2K_{a1}^2[\text{HDMHP}]_{\text{eq}}^2} + k_x[\text{EDTA}][\text{Fe}]_{\text{tot}} \quad (4.49.)$$

$$k_{\text{obs}} = \frac{k_z[\text{EDTA}][\text{H}^+]^2}{\beta_3\beta_2K_{a1}^2[\text{HDMHP}]_{\text{eq}}^2} + k_x[\text{EDTA}] \quad (4.50.)$$

However, the mathematical model for this mechanism

$$y = \frac{a}{x^2} + b \quad (4.51.)$$

where $y = k_{\text{obs}}$, $x = [\text{DMHP}]$, $a = k_z[\text{EDTA}][\text{H}^+]^2/\beta_3\beta_2K_{a1}^2$, and $b = k_x[\text{EDTA}]$ from Eq. 4.50.

does not provide a good fit of Eq. 4.51. to the experimental data (Fig. 4.20.) and

exhibits a negative coefficient a , suggesting that this is not the appropriate model for

analyzing the observed rate constants.

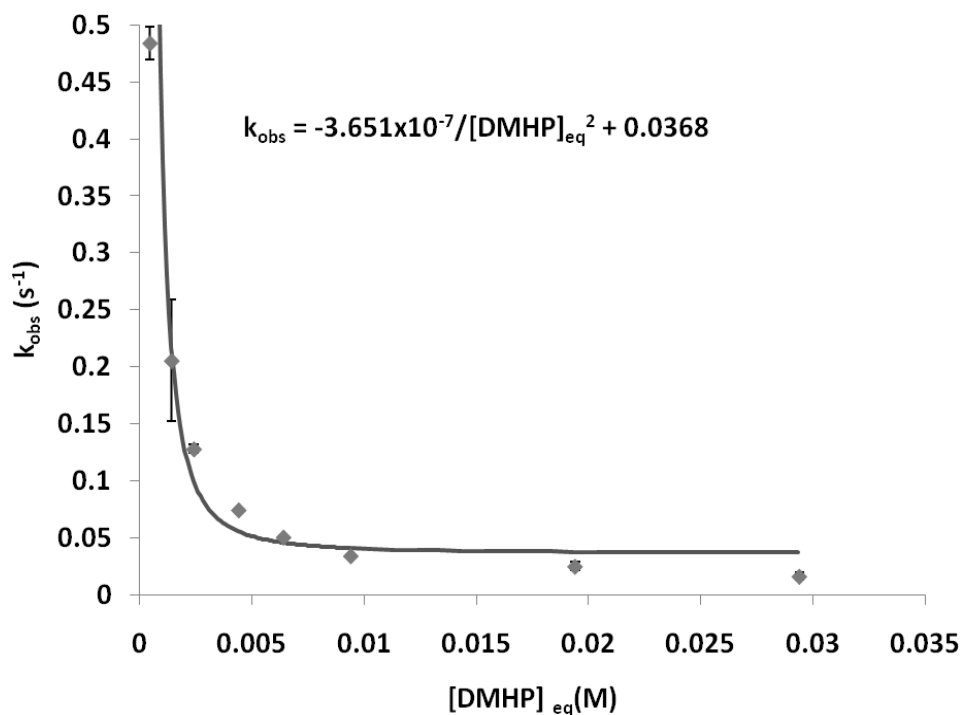


Figure 4.20. Plot of observed pseudo-first order rate constant, k_{obs} , for the iron(III) exchange reaction between DMHP and EDTA (reaction 4.4.) as a function of DMHP concentration. The line represents the best fit line to the data (excluding the data point at 1 mM DMHP) using the model shown in Eq. 4.44., where a and b are adjustable parameters found to be $a = 3.65 \times 10^{-7}$ and $b = 0.0368$. Error bars represent the standard deviation of the average observed rate constant measured at 4 discrete wavelengths in a single experiment. For the error bar at 2 mM DMHP, see Fig. 4.15.

Conditions: $[Fe^{3+}]_{tot} = 2.0 \times 10^{-4} M$, $[EDTA] = 6.0 mM$, $25.0 \text{ } ^\circ C$, $pH = 4.35$, $\mu = 0.10 M$ ($NaClO_4$).

The final possible combination of species that could contribute to the exchange mechanism of reaction 4.4. is all 3 species, the mono-, bis-, and tris-DMHP complexes, as shown in the mechanism incorporating all three reactions 4.39., 4.40., and 4.45. The rate



law that would correspond to the parallel pathway mechanism featuring all three complexes is found through linear combination of Eqs. 4.17., 4.28., and 4.36., shown in Eq. 4.52.

$$\text{Rate} = \frac{k_z[\text{EDTA}][\text{H}^+]^2[\text{Fe}]_{\text{tot}}}{\beta_3\beta_2K_{a1}^2[\text{HDMHP}]_{\text{eq}}^2} + \frac{k_y[\text{EDTA}][\text{H}^+][\text{Fe}]_{\text{tot}}}{\beta_3K_{a1}[\text{HDMHP}]_{\text{eq}}} + k_x[\text{EDTA}][\text{Fe}]_{\text{tot}} \quad (4.52.)$$

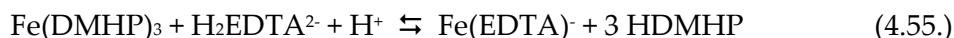
$$k_{\text{obs}} = \frac{k_z[\text{EDTA}][\text{H}^+]^2}{\beta_3\beta_2K_{a1}^2[\text{HDMHP}]_{\text{eq}}^2} + \frac{k_y[\text{EDTA}][\text{H}^+]}{\beta_3K_{a1}[\text{HDMHP}]_{\text{eq}}} + k_x[\text{EDTA}] \quad (4.53.)$$

The mathematical model that describes the best fit line for this proposed mechanism is

$$y = \frac{a}{x^2} + \frac{b}{x} + c \quad (4.54.)$$

where $y = k_{\text{obs}}$, $x = [\text{DMHP}]$, $a = k_z[\text{EDTA}][\text{H}^+]^2/\beta_3 \beta_2 K_{a2}^2$, $b = k_y[\text{EDTA}][\text{H}^+]/\beta_3 K_{a2}$, and $c = k_x[\text{EDTA}]$ from Eq. 4.53. The plot showing the best fit line to the data using the model in Eq. 4.54. is shown in Fig. 4.21., demonstrating a good fit of Eq. 4.54. to the experimental data. However, as with the mono- and bis-complex species model, this model exhibits a negative coefficient for the mono-DMHP complex rate constant, k_z . This suggests that the proposed parallel reaction pathway is not appropriate for analyzing the experimental data.

Using the information obtained from the preceding statistical analysis, it seems most likely that the appropriate reaction mechanism for iron(III) exchange from DMHP to EDTA occurs exclusively through the bis-DMHP complex, as shown in Eqs. 4.20.-4.29. While both the bis-DMHP complex rate law and the parallel tris-bis-DMHP complex rate law provide good fits of the mathematical model to the observed rate constants, it is most likely that any reaction involving the tris-DMHP complex will have to occur through dissociation to the bis-complex, as there would be likely too much steric interaction to allow an associative reaction between EDTA and the $\text{Fe}(\text{DMHP})_3$ complex. Therefore, the proposed rate law for the reaction of the $\text{Fe}(\text{DMHP})_3$ complex with EDTA is



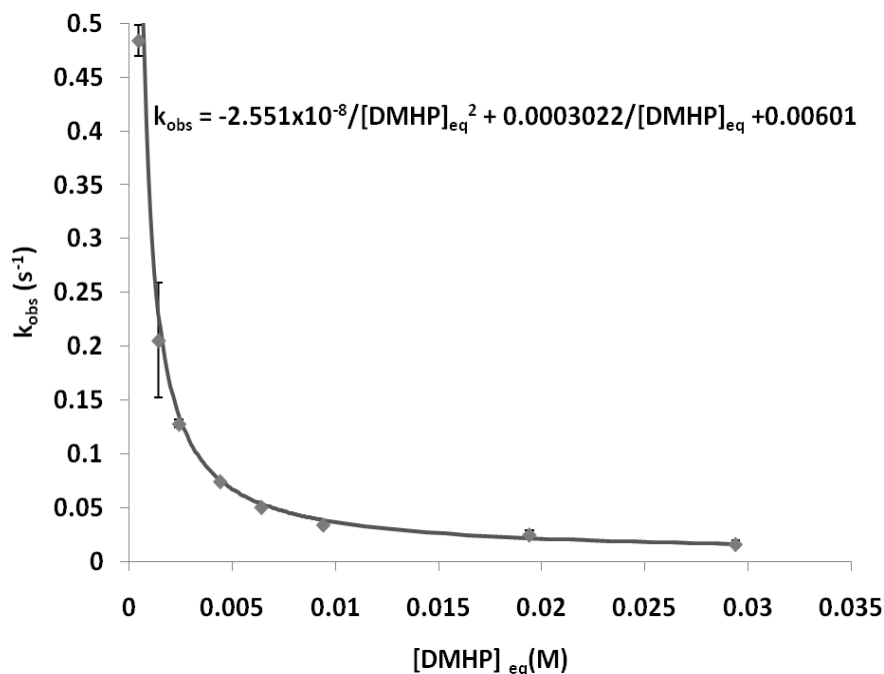


Figure 4.21. Plot of observed pseudo-first order rate constant, k_{obs} , for the iron(III) exchange reaction between DMHP and EDTA (reaction 4.4.) as a function of DMHP concentration. The line represents the best fit line to the data (excluding the data point at 1 mM DMHP) using the model shown in Eq. 4.46., where a , b , and c are adjustable parameters found to be $a = 2.55 \times 10^{-8}$, $b = 3.02 \times 10^{-4}$, and $c = 6.01 \times 10^{-3}$. Error bars represent the standard deviation of the average observed rate constant measured at 4 discrete wavelengths in a single experiment. For the error bar at 2 mM DMHP, see Fig. 4.15. Conditions: $[Fe^{3+}]_{tot} = 2.0 \times 10^{-4} M$, $[EDTA] = 6.0 mM$, $25.0 \text{ } ^\circ C$, $pH = 4.35$, $\mu = 0.10 M (NaClO_4)$.

$$Rate = \frac{k_5[EDTA][H^+][Fe]_{tot}}{\beta_3 K_{a1}[HDMHP]_{eq}} \quad (4.56.)$$

$$k_{obs} = \frac{k_5[EDTA][H^+]}{\beta_3 K_{a1}[HDMHP]_{eq}} \quad (4.57.)$$

We can make the approximation that $[HDMHP]_{eq}$ is equal to any DMHP that is not bound to iron, or

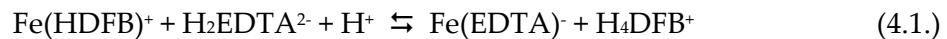
$$[HDMHP]_{eq} = [DMHP]_{tot} - 3[Fe(DMHP)_3] - 2[Fe(DMHP)_2(H_2O)_2] \quad (4.58.)$$

Analysis of the best fit plot shown in Fig. 4.16. yields a rate constant from Eq. 4.57. of $k_5 = 377 \text{ M}^{-1} \text{ s}^{-1}$.

4.4.6. Summary of Kinetics Results

The rate law analysis of the iron(III) exchange reactions involving desferrioxamine B, DMHP, and EDTA can be summarized as follows;

The rate law for the exchange of iron(III) from desferrioxamine B to EDTA in the absence of DMHP follows the chemical equation:

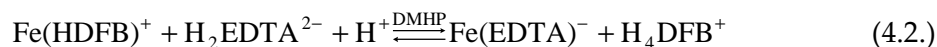


This reaction was found to be first order with respect to EDTA and ferrioxamine B, giving a rate law and second order rate constant as follows:

$$\text{Rate} = k_1[\text{EDTA}] [\text{Fe}(\text{HDFB})] \quad (4.58.)$$

$$k_1 = 0.030 \text{ (8) } \text{M}^{-1}\text{s}^{-1} \quad (4.59.)$$

The iron(III) exchange reaction performed in the presence of DMHP is accelerated, and no observable species includes DMHP, suggesting that DMHP acts as a catalyst for the reaction as shown in Eq. 4.2.



The rate law for catalyzed reaction 4.2. exhibits first order dependence on $\text{Fe}(\text{HDFB})^+$ concentration, as well as first order dependence on DMHP and EDTA concentrations.

$$\text{Rate} = k_2[\text{DMHP}^-][\text{FeHDFB}^+] + k_3[\text{EDTA}^{4-}][\text{FeHDFB}^+] \quad (4.13.)$$

$$k_2 = 1.12 \text{ (9) } \text{M}^{-1}\text{s}^{-1}; \quad k_3 = 0.06 \text{ (2) } \text{M}^{-1}\text{s}^{-1} \quad (4.60.)$$

The iron(III) exchange reaction between desferrioxamine B and DMHP (Eq. 4.3.) can provide information with regards to the identity of any intermediate species that may be present in catalyzed reaction 4.2.



The rate-limiting step of reaction 4.3. was found to be first order with respect to ferrioxamine B complex concentration and first order with respect to DMHP concentration. The rate law and second order rate constant for reaction 4.3. is shown in Eq. 4.15. and 4.53.

$$\text{Rate} = k_4[\text{DMHP}][\text{FeHDFB}] \quad (4.15.)$$

$$k_4 = 1.13 \text{ (9) } \text{M}^{-1}\text{s}^{-1}; \quad (4.61.)$$

The iron(III) exchange reaction between the iron-DMHP complex and EDTA (Eq. 4.4.) exhibits a rate law that is first order with respect to EDTA and inversely proportional to DMHP concentration, shown in Eq. 4.26., with a second order rate constant shown in Eq. 4.54.



$$Rate = \frac{k_5[EDTA][H^+][Fe]_{tot}}{\beta_3 K_{a1}[HDMHP]_{eq}} \quad (4.62.)$$

$$k_{obs} = \frac{k_5[EDTA][H^+]}{\beta_3 K_{a1}[HDMHP]_{eq}} \quad (4.63.)$$

By measuring the observed rate constant at a constant DMHP concentration, it was possible to fit the mathematical model to the data:

$$y = \frac{a}{x} \quad (4.30.)$$

where $y = k_{obs}$, $x = [HDMHP]_{eq}$, and $a = k_5[EDTA][H^+]/\beta_3 K_{a2}$. Using the value obtained from the literature for β_3 and $K_{a2}(127)$ and the experimental values of $[EDTA]$ and $[H^+]$, it was possible to solve for k_5

$$k_5 = 377 (7) \text{ M}^{-1}\text{s}^{-1}; \quad \beta_3 = 10^{9.24} \text{ M}^{-1} \quad (4.64.)$$

These kinetic parameters along with the corresponding chemical reactions are listed in Table 4.1.

4.5. Discussion

4.5.1. Kinetics and mechanism of the iron(III) exchange reaction from ferrioxamine B to EDTA in the presence of DMHP

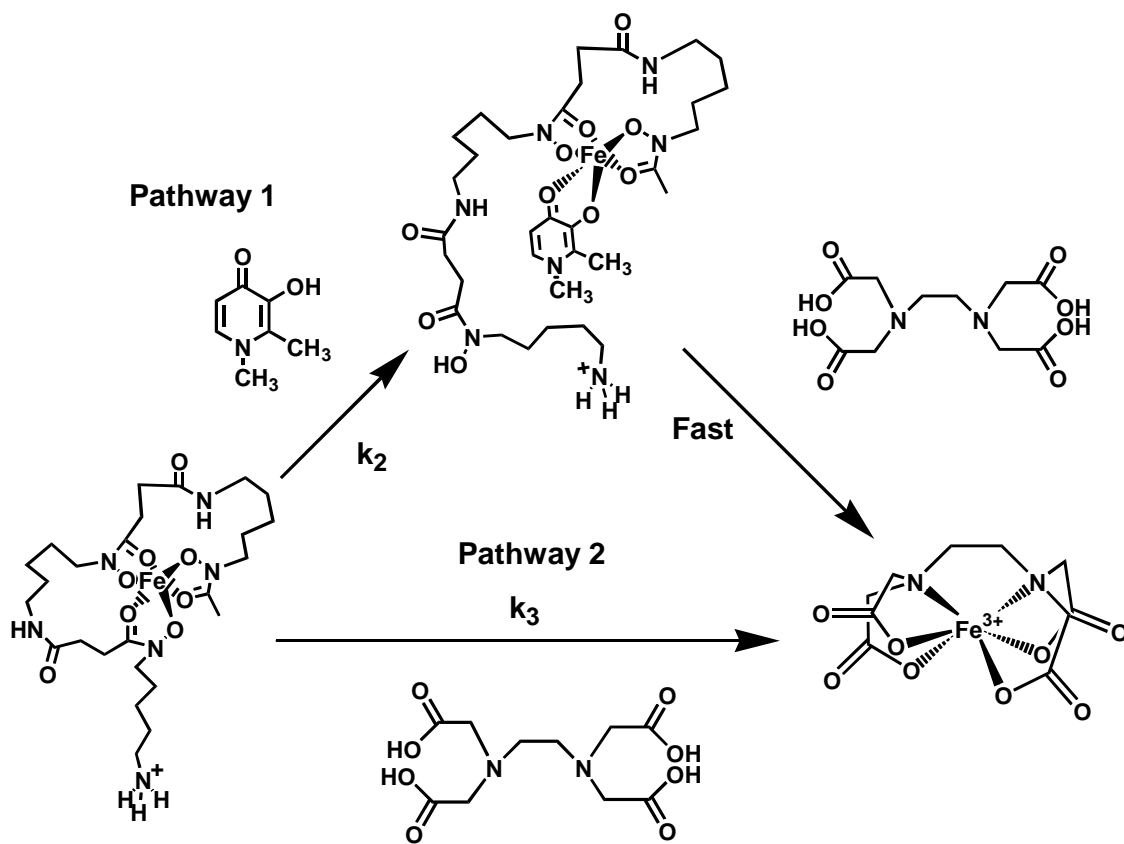
The reaction of ferrioxamine B with EDTA (Eq. 4.1.) was initially characterized previously.⁽¹²⁸⁾ It was observed that the reaction occurs fairly slowly due in part to the oxidation state of iron (iron(III) has slow inner coordination sphere ligand exchange as a high spin d^5 electronic configuration metal ion) and the architecture of the ligands (it is more difficult for hexadentate ligands to fully exchange in the first coordination sphere than for lower order chelators).⁽¹²⁹⁾ The second order rate constant for reaction 1 (k_1 from Eq. 4.58.) was found to be approximately $0.030 \text{ M}^{-1} \text{ s}^{-1}$. Another previous study found that the rate of reaction was pH-dependent, suggesting that protonation of the donor groups attached to iron(III) could play a role in the exchange reaction.⁽¹²⁸⁾ Protonation of a donor group would leave open coordination sites available on the metal for partial chelation by the receiving ligand. Protonation of the donor group would also prevent ring closure of the chelate complex, driving the complex towards dissociation. However, even over a range of pH values, the rate of this exchange reaction is relatively slow, likely too slow to play a major role in the exchange of iron in a biological context.

Addition of DMHP was found to accelerate the rate of iron(III) exchange from ferrioxamine B to EDTA (Eq. 4.2.), with a linear dependence of the observed rate constant on the DMHP concentration (as shown in Eq. 4.9.). The final product of

reaction 2 is the $\text{Fe}(\text{EDTA})^-$ complex, as evidenced by the UV-Visible spectrum of the product (see section 2.2.). Linearity of the observed rate constant with respect to $[\text{DMHP}]$ is obtained, even at less than stoichiometric concentrations, suggesting that DMHP acts as a true catalyst which is not consumed during the course of the reaction. The acceleration of the observed rate of reaction occurs from 0.25 molar equivalents of DMHP (with respect to $\text{Fe}(\text{III})$) through 12-fold excess. Determination of the rate law of the rate limiting step of the iron(III) exchange reaction can allow for the proposal of a mechanism of catalysis by DMHP.

The rate law (Eq. 4.11.) represents a reaction mechanism as shown in Scheme 4.1., where two parallel reactions are observed, one where the initial step involves the reaction of ferrioxamine B with a single molecule of DMHP, followed by a number of more rapid steps that result in the exchange of iron from ferrioxamine B to EDTA and another where ferrioxamine B reacts directly with EDTA to exchange iron. One potential mechanism of reaction between ferrioxamine B and DMHP would involve the dissociation of one ferrioxamine B hydroxamate donor, leaving two open coordination sites that could be filled through the formation of a ternary inner sphere complex with DMHP, $\text{Fe}(\text{H}_2\text{DFB})(\text{DMHP})^+$.

The proposed reaction mechanism of Pathway 1 from Scheme 4.1., involving a ternary complex intermediate is interesting, as the spectra measured during the reaction



Scheme 4.1. The proposed parallel path mechanism of the iron(III) exchange reaction between desferrioxamine B and EDTA in the presence of DMHP (Eq. 4.2.). Pathway 1 represents the catalyzed exchange mechanism, in which DMHP takes part to form a reactive ternary complex, and Pathway 2 represents the direct exchange reaction between DFB and EDTA.

exhibit an isosbestic point (Fig. 4.5.), which suggests only two light-absorbing species present in solution during the reaction. Two possible explanations of this are that the ternary complex intermediate is formed relatively slowly and reacts rapidly to form the final product, resulting in a transient intermediate species and a lack of observed spectrum, or that the intermediate ternary complex has an absorbance spectrum that is very similar to that of $\text{Fe}(\text{HDFB})^+$, resulting in little observed change in absorbance upon formation of the ternary complex. The former explanation seems much more likely, however, as the electronic structure of hydroxamate groups (as in ferrioxamine B) are very different from that of hydroxypyridinone groups, resulting in different λ_{max} values for the mono-, bis-, and tris-complexes of hydroxypyridinone and hydroxamate complexes.(18, 130)

The parallel pathway reaction mechanism illustrated in Scheme 4.1. exhibits the ability of DMHP to catalyze the exchange of iron from DFB to EDTA. The second order rate constant for the reaction pathway involving the direct reaction of ferrioxamine B with EDTA, k_3 in Pathway 2, is $0.06 \text{ M}^{-1} \text{ s}^{-1}$. Meanwhile, the second order rate constant for the reaction pathway involving the reaction of ferrioxamine B with DMHP, k_2 in Pathway 1, has a second order rate constant of $1.13 \text{ M}^{-1} \text{ s}^{-1}$. This demonstrates an acceleration of the rate of reaction 19-fold in the presence of DMHP at pH 4.35. Additional evidence for the proposed parallel pathway mechanism is the comparison of k_1 , the second-order rate constant of the iron(III) exchange reaction between HDFB and

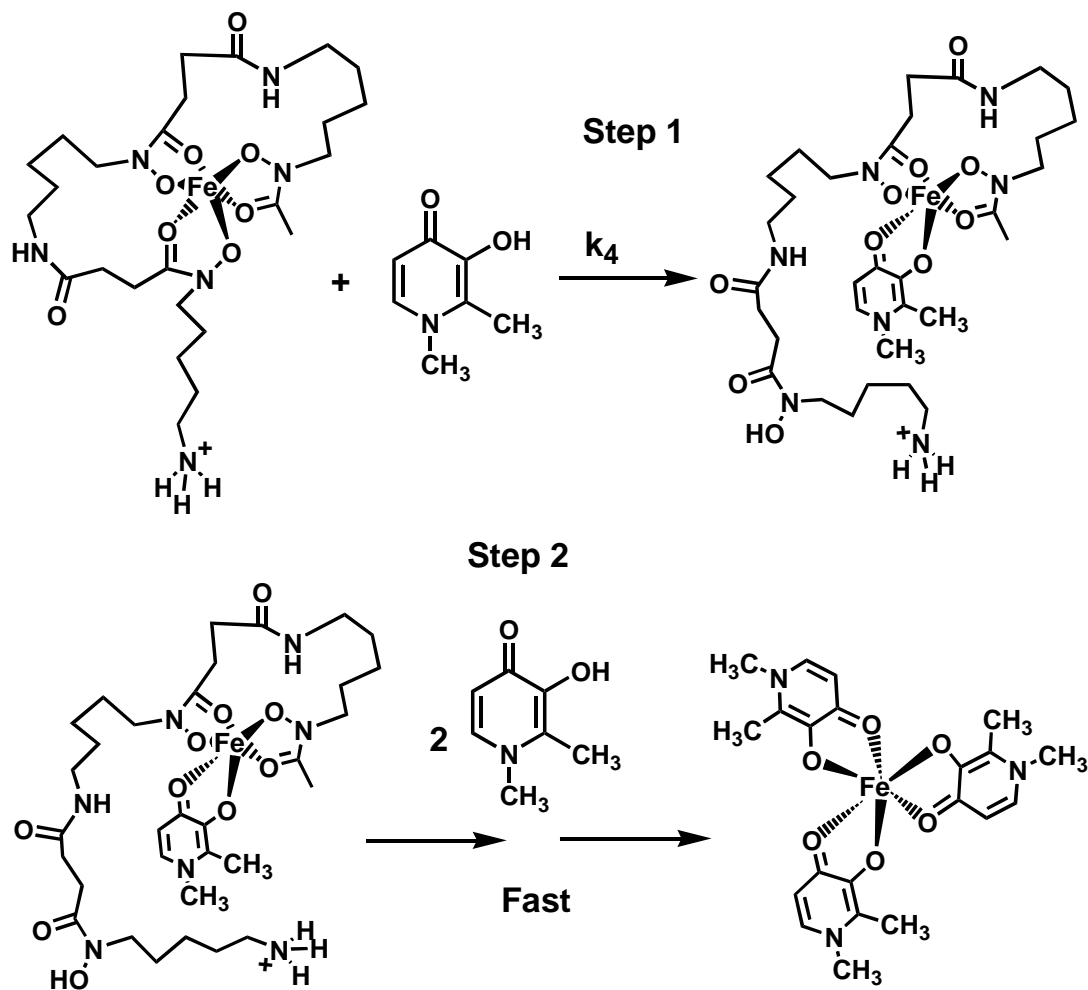
EDTA in the absence of DMHP, and k_3 , the second-order rate constant of Pathway 2 of the reaction in the presence of EDTA. Both rate laws corresponding to reaction 1 and Pathway 2 have the same dependence on EDTA concentration and have similar second order rate constants ($k_1 = 0.030$ (8) $M^{-1} s^{-1}$ and $k_3 = 0.06$ (2) $M^{-1} s^{-1}$). However, the second order rate constant k_3 was determined from two sources, the y-intercepts of the plots in Fig. 4.4. and from the slope of the plots in Fig. 4.7. Comparison of the values obtained from Fig. 4.4. gives a closer comparison ($k_3 = 0.028$ (5) $M^{-1} s^{-1}$) with higher precision than the values obtained from Fig. 4.7. The comparison of these values shows that the rate law of Pathway 2 for the catalyzed reaction, Eq. 4.2., is consistent with the rate law of the reaction in the absence of DMHP, suggesting that both reaction 1 and Pathway 2 occur through the same activated complex in the rate determining step.

4.5.2. Reaction of ferrioxamine B with DMHP

By examining the reaction of ferrioxamine B with DMHP (Eq. 4.3.), it is possible to gain information about the mechanism of the DMHP catalyzed reaction of iron exchange from ferrioxamine B with EDTA (Eq. 4.2.). The iron(III) exchange reaction between desferrioxamine B and DMHP (reaction 4.3.) may take place through a mechanism involving similar intermediate complexes or transition states as the catalyzed iron exchange reaction between ferrioxamine B and EDTA, reaction 4.2. The plot of k_{obs} as a function of DMHP concentration shows first-order dependence of the rate law on DMHP concentration, as shown in Fig. 4.10. The rate law is shown in Eq. 4.15. Based on

this observation, we propose that the rate-limiting step for reaction 4.3. involves the formation of a ternary inner-sphere complex following dissociation of a single hydroxamate donor group, shown in Scheme 4.2. and that this step is the rate-limiting step and the only observable step of the reaction, as the absorbance change can be fit by a single exponential model. Subsequent formation of the bis- and tris-DMHP complexes would likely be more rapid than the initial formation of the mono-DMHP ternary complex. Formation of the ternary complex would result in more rapid dissociation of the second hydroxamate donor group, which would be replaced by a second mole of DMHP. Finally, replacement of the third hydroxamate donor of desferrioxamine B by DMHP would be much more rapid than either of the other two exchange processes. Therefore, the only kinetically observable step in reaction 4.3. would be initial formation of the ternary complex. In addition, comparison of the values of the second order rate constants for Pathway 1 of reaction 4.2. ($k_2 = 1.12 (9) \text{ M}^{-1} \text{ s}^{-1}$) to the second order rate constant of reaction 4.3. ($k_4 = 1.13 (9) \text{ M}^{-1} \text{ s}^{-1}$) reveals that the rate limiting steps of those reactions occur with the same dependence on DMHP concentration and with the same rate constant. This comparison makes it possible to conclude that those reactions correspond to the formation of the same transition state, the ternary inner sphere complex $\text{Fe}(\text{H}_2\text{DFB})(\text{DMHP})^{2+}$.

The increasingly rapid substitution of hydroxamic acid donor groups with hydroxypyridinone donor groups is not inconsistent with the observations made in the



Scheme 4.2. The proposed mechanism of iron(III) exchange from desferrioxamine B to DMHP (reaction 4.3.). The first step is rate determining and involves the formation of a ternary inner-sphere complex between ferrioxamine B and one mole of DMHP.

rate law of the rate limiting step of reaction 4.2., and so it is necessary to determine whether the bis- or tris-DMHP iron(III) complexes ($\text{Fe}(\text{DMHP})_2(\text{H}_2\text{O})_2^+$ and $\text{Fe}(\text{DMHP})_3$) can play a role in catalyzing the iron(III) exchange reaction between ferrioxamine B and EDTA.

Linear regression of the observed rate constants with varying EDTA from the catalysis experiments (reaction 4.2.) allows prediction of the observed rate constant for the catalysis experiment at $[\text{EDTA}] = 0 \text{ M}$, or the reaction of ferrioxamine B with DMHP. Plotting the y-intercepts of those plots against their DMHP concentration produces a plot of pseudo-first order rate constants over a range of DMHP concentrations. The slope of that line represents the second order rate constant for reaction 4.3., $k_4 = 0.96 \text{ M}^{-1} \text{ s}^{-1}$ (Fig. 4.10.). As discussed above, the intercepts of the plots in Fig. 4.4. are extrapolated rate constants for the iron exchange reaction of Eq. 4.3. While the value of k_4 obtained from y-intercepts of Fig. 4.4. ($0.096 \text{ M}^{-1} \text{ s}^{-1}$) and directly from reaction 4.3. ($1.13 \text{ M}^{-1} \text{ s}^{-1}$) were obtained using separate methods, the two rate constants are the same, with the same mechanism. The similarity of the mechanism of Pathway 1 of reaction 4.2. (Scheme 4.1.) to the mechanism of reaction 4.3. (Scheme 4.2.) also suggests that the bis- and tris-DMHP complexes would not play a role in the iron exchange process of reaction 4.2., due to the increased lability of the $\text{Fe}(\text{DMHP})(\text{H}_2\text{DFB})^+$ complex.

In order to determine the source of protonation of the dissociated hydroxamate donor group in Eq. 4.2., it is necessary to investigate the rate of reaction over a range of pH values. This reveals the pH dependence of the reaction and also can provide information about the overall mechanism of iron(III) exchange reactions 4.2. and 4.3. While it would be desirable to compare the rate constants of the iron(III) exchange reaction from desferrioxamine B to EDTA in the presence of DMHP over a range of pH values, speciation diagrams of the system suggest that at high DMHP concentrations, DMHP and desferrioxamine B would be able to out-compete EDTA for chelating iron (Fig. 4.22.). The speciation diagram is calculated by the program, Hyss at a varying pH and constant concentrations of DMHP, desferrioxamine B, and EDTA, using the literature values of the stability constants of the Fe-DMHP system.(102, 131) Such a multiple equilibrium system does not proceed with the same mechanism as the reactions observed in Section 4.5.2. As reaction 4.3. proceeds with the same mechanism of the rate limiting step as Reaction 4.2, and as there is less chance for undesirable side reactions to occur in reaction 4.3, reaction 4.3. was chosen as the model reaction for reaction 4.2. for experiments carried out over a range of pH values. The second order rate constant of reaction 4.3. was observed to increase as the pH value decreased. The increase in k values with decreasing pH is shown in Fig. 4.12. It is likely that this increase in rate of reaction is due to protonation of a hydroxamate donor group in ferrioxamine B by a proton from the solvent instead of proton exchange between DMHP and the hydroxamate group. This observation suggests that as the pH decreases, a rapid

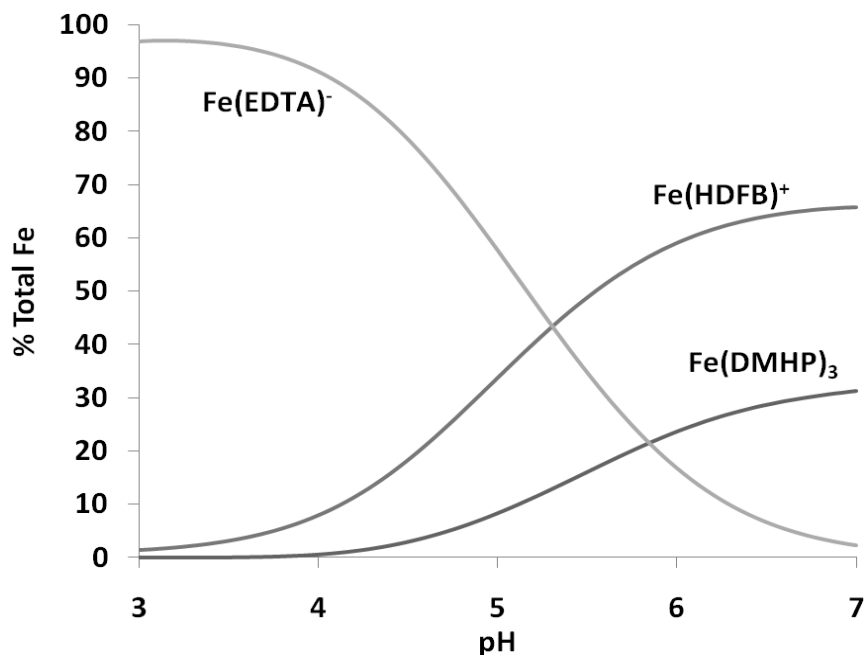


Figure 4.22. Speciation plot of the iron(III)-DFB-DMHP-EDTA system over a range of pH values. Conditions: $[\text{Fe}]_{\text{tot}} = 0.40 \text{ mM}$, $[\text{HDFB}]_{\text{tot}} = 0.40 \text{ mM}$, $[\text{DMHP}]_{\text{tot}} = 5 \text{ mM}$, $[\text{EDTA}]_{\text{tot}} = 10 \text{ mM}$, $T = 25 \text{ }^\circ\text{C}$, $\mu = 0.10$.

increase in the second order rate constant of the reaction will be observed until a very low pH value, where the maximum rate of reaction is the rate of solvent exchange at the metal center. At this low pH, the majority of ferrioxamine B will be present in solution as the protonated FeLH complex, leaving two coordination sites filled by water. In the FeLH complex, substitution of the water molecules is much more rapid than that of the hydroxamate donor group in the hexadentate $\text{Fe}(\text{HDFB})^+$ complex.

4.5.3. Reaction of Fe(DMHP)₃ with EDTA

In order to verify the role of the Fe(DMHP)(H₂DFB)²⁺ ternary complex as the intermediate species in the catalyzed iron(III) exchange reaction between ferrioxamine B and EDTA (Eq. 4.2.), it was necessary to investigate other possible participating complexes in the system. The specific complex of interest is the most prevalent DMHP complex at physiological conditions, the Fe(DMHP)₃ complex. A possible mechanistic assignment for reaction 4.2. involves the exchange of iron(III) from desferrioxamine B to DMHP to form the tris complex, Fe(DMHP)₃, followed by rapid iron(III) exchange to EDTA. To verify our mechanism of Eq. 4.2., we must demonstrate that no Fe(DMHP)_x complexes can act as an intermediate in Eq. 4.2. Determination of the rate law of Eq. 4.4. will allow us to assess the role of the Fe(DMHP)₃ complex in the mechanism of catalysis of the iron(III) exchange reaction from ferrioxamine B to EDTA, reaction 4.2. Reaction 4.4. occurs much faster than the exchange of iron(III) from desferrioxamine B (Eq. 4.1.-4.3.), as the hexacoordinate starting material is a tris-bidentate chelator complex instead of a hexadentate chelator. For these experiments, three conditions were tested. The first two series of experiments featured constant DMHP concentrations at a 10-fold excess and at a 25-fold excess with respect to iron(III) concentration and varying EDTA concentrations. A third series of experiments featured a range of DMHP concentrations at a set EDTA concentration of 6 mM. The data from the third series of experiments also incorporated data from the first two sets of data that were performed at 6 mM EDTA for consistency. The thermodynamics of complex formation requires an excess of DMHP in

solution to promote full complex formation as shown in the speciation diagram for the Fe-DMHP system in Fig. 4.23.

The speciation diagram is calculated by the program, Hyss at a varying DMHP concentration and constant pH of 4.35 using the literature values of the stability constants of the Fe-DMHP system.(102, 131) This speciation diagram shows that at a total iron(III) concentration of 2×10^{-4} M and total DMHP concentration of 2 mM, only

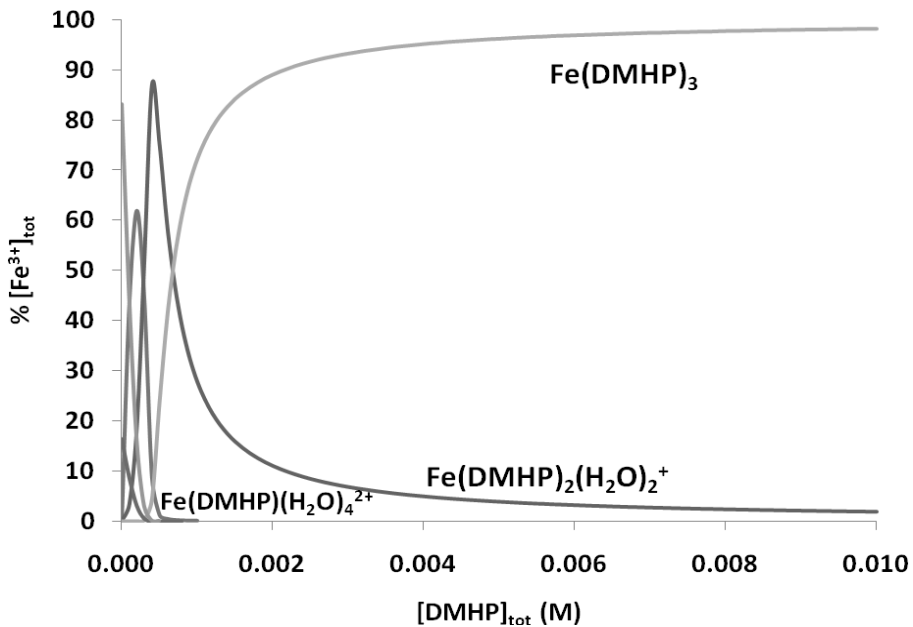
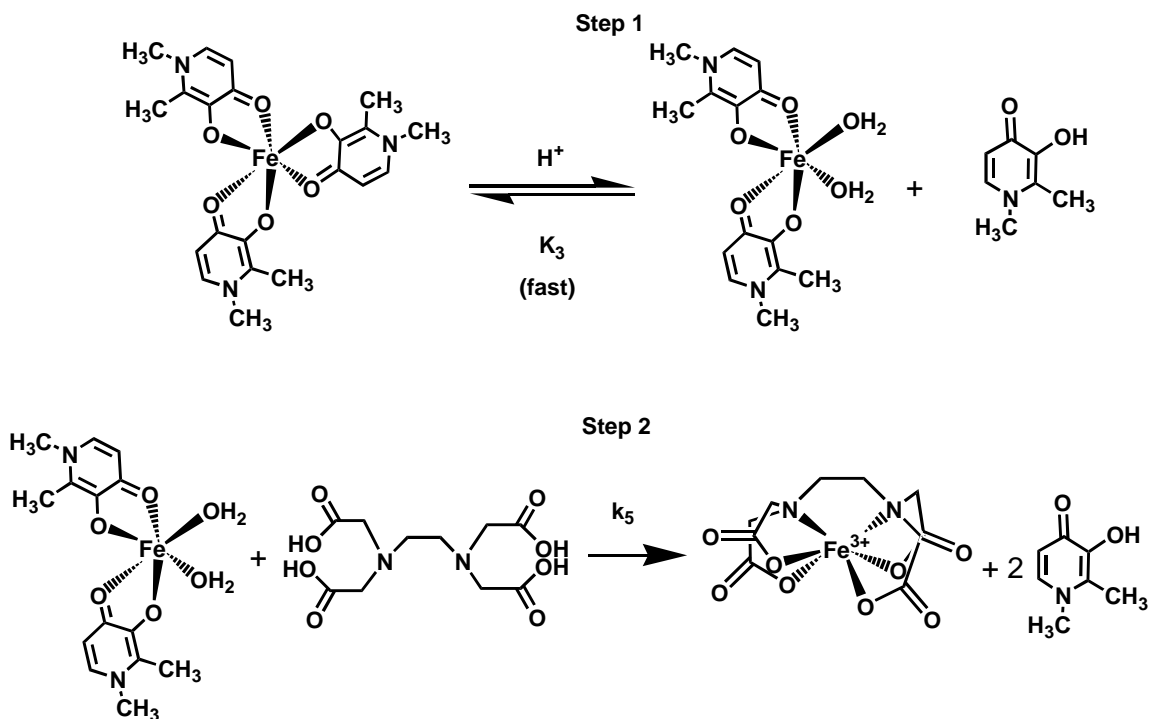


Figure 4.23. Speciation diagram for the Fe-DMHP system with varying DMHP concentration. The concentrations were calculated using the literature values of the complex formation constants obtained from reference (127). Conditions: $[\text{Fe}^{3+}]_{\text{tot}} = 0.20$ mM, pH = 4.35, T = 25 °C, $\mu = 0.10$ M, and $[\text{DMHP}] = 0 - 10$ mM.

90% of iron(III) is found in the tris-DMHP complex, with the remaining 10% found as the bis- DMHP complex. However, it is also possible that the concentration of DMHP could affect the rate of reaction due to the back-reaction of $\text{Fe}(\text{EDTA})^-$ with DMHP to produce $\text{Fe}(\text{DMHP})_x$ or other ternary complexes.

The plot of the observed rate constants against EDTA concentration for both DMHP concentrations in reaction 4.4. are shown in Fig. 4.15. A linear dependence of observed rate constant on EDTA concentration is observed at both DMHP concentrations, suggesting that the reaction is first-order with respect to EDTA. This is not surprising, as the stoichiometry of the product complex is 1:1 Fe(III):EDTA and there is no reason to propose a priori that more than one molecule of EDTA would take part in the rate-limiting step of the exchange reaction. The plot of observed rate constant as a function of DMHP concentration is shown in Fig. 4.16., exhibiting an inverse relationship of observed rate constant to DMHP concentration, as discussed in Section 4.3.4. This can be explained by examining the reactivity of the species in solution in an exchange reaction. Similar to how desferrioxamine B must partially dissociate to provide open coordination sites for the exchange reaction to proceed, the $\text{Fe}(\text{DMHP})_3$ complex must dissociate partially to allow reaction with the competing ligand. This makes the likely reactive species in solution $\text{Fe}(\text{DMHP})_2(\text{OH}_2)_2^+$. The proposed mechanism for this exchange reaction is shown in Scheme 4.3.



Scheme 4.3. Proposed mechanism of the iron(III) exchange reaction from DMHP to EDTA (Reaction 4.4.) involving initial dissociation of one mole of DMHP, followed by reaction of EDTA with the bis-DMHP complex.

The observations made in this experiment also support the proposed interpretation of the catalysis mechanism of reaction 4.3. and Pathway 1 in Scheme 4.1. The reaction of EDTA with $\text{Fe}(\text{DMHP})_x$ exhibits a much more rapid second order rate constant than that observed in the catalysis reactions ($k_2 = 1.13 \text{ M}^{-1} \text{ s}^{-1}$, $k_5 = 3.8 \times 10^2 \text{ M}^{-1} \text{ s}^{-1}$). This suggests that the reaction of a ternary complex or a complex that has a coordination number lower than 6 with EDTA will result in more rapid exchange than in reactions removing iron(III) from a hexadentate. This suggests that the reaction step involving EDTA cannot be the rate-limiting step in the catalysis reaction, as it is very fast

compared to the formation of the ternary inner sphere complex. Additionally, it supports the assertion that the intermediate species in the catalyzed pathway of iron exchange (Scheme 4.1., Pathway 1) cannot involve $\text{Fe}(\text{DMHP})_3$, as the reactive species in the exchange of iron from DMHP to EDTA is $\text{Fe}(\text{DMHP})_2(\text{H}_2\text{O})_2^+$, which is unlikely to form in the presence of the hexadentate chelator desferrioxamine B. Further, the inverse relationship of the observed second order rate constant with DMHP concentration is not observed in reaction 4.3., further supporting that $\text{Fe}(\text{DMHP})_3$ is not involved in the mechanism of catalysis of iron(III) exchange by DMHP.

A previous study showed that addition of acetohydroxamic acid, N-methylacetohydroxamic acid, and benzylhydroxamic acid (Fig. 4.1.) to reaction 4.1. would accelerate the exchange of iron from desferrioxamine B to EDTA, and that the mechanism of catalysis was through the formation of a ternary complex.⁽¹²⁶⁾ The exchange of iron(III) from desferrioxamine B occurs through a number of steps, the first of which is dissociation of a terminal donor group of the linear desferrioxamine B. In cases where the receiving ligand in an exchange reaction is a hexadentate ligand, steric interactions can occur that make chelation of the metal center more difficult. This combines with the slow inner-sphere exchange rate of high-spin d^5 iron(III) to result in a slow exchange reaction. The introduction of a smaller bidentate chelator provides a route of dechelation of the remaining binding sites, accelerating the dissociation of the

donor groups of the original chelator, in this case, desferrioxamine B. This also prevents rechelation of the iron by the dissociated donor group of desferrioxamine B.

In the previous study, it was shown that the acceleration of the exchange of iron(III) from desferrioxamine B to EDTA was dependent on the structure of the ternary chelator, such that N-methylacetohydroxamic acid was most rapid and acetohydroxamic acid was the least rapid. In all three cases, a significant acceleration of the reaction was only observed at the higher concentrations of ternary ligand, at least 0.10 M ligand and even then only increasing the rate of reaction by 30-to-70-fold. In the case of DMHP, the observed rate constant was predicted to increase by a factor of 126 at 10 mM DMHP and 3 mM EDTA (Table 4.2., values calculated using Eq. 4.14. and values for k_2 and k_3 shown in Table 4.1.), suggesting more efficient catalysis by DMHP than the hydroxamic acid chelators. This may be related to the strength of the complex formed between iron and DMHP, which is stronger than that formed with the hydroxamates. The $\log \beta_{110}$ value of DMHP is 15.1, much greater than the $\log \beta_{110}$ of AHA, 11.42.(102, 127) The greater catalytic ability of DMHP compared to the hydroxamic acids may also be related to the characteristics of the ternary chelator. DMHP features a conjugated ring system as part of the donor group, which would result in delocalization of electron density and increased complex stability. This can be demonstrated by comparing the equilibria of AHA to that of 1-hydroxy-2-pyridinone, which behaves as a cyclic hydroxamate ($\log \beta_{110}$ of 1,2-HOPO is similar at 10.3, but it is much more acidic with a $pK_a = 5.78$). (130)

Table 4.2. Relative second order rate constants for the catalyzed iron(III) exchange reactions, $k_{\text{obs, cat}}/k_{\text{obs}}$ with 4 bidentate ligands, acetohydroxamic acid, N-methylacetohydroxamic acid, benzylhydroxamic acid, and 1,2-dimethyl-3-hydroxy-4-pyridinone.^a

Concentration	AHA	NMAHA	BzHA	DMHP
0 M	1	1	1	1
0.010 M	1.4	2.7	1.8	126 ^b

^a Conditions: $[\text{FeHDFB}^+] = 1.60 \times 10^{-4} \text{ M}$, $[\text{EDTA}]_{\text{tot}} = 3.21 \times 10^{-3} \text{ M}$, $\text{pH} = 4.30$, $\mu = 2.00 \text{ M}$ for hydroxamic acid ligand studies. Values taken from Ref. (126).

^b For hydroxypyridinone study, value calculated using predicted k_{obs} at conditions: $[\text{FeHDFB}^+]_{\text{tot}} = 4.00 \times 10^{-4} \text{ M}$, $[\text{EDTA}]_{\text{tot}} = 3.21 \times 10^{-3} \text{ M}$, and $[\text{DMHP}]_{\text{tot}} = 5.00 \times 10^{-3} \text{ M}$ for calculation of $k_{\text{obs, cat}}$, $\text{pH} = 4.35$, $\mu = 0.10 \text{ M}$.

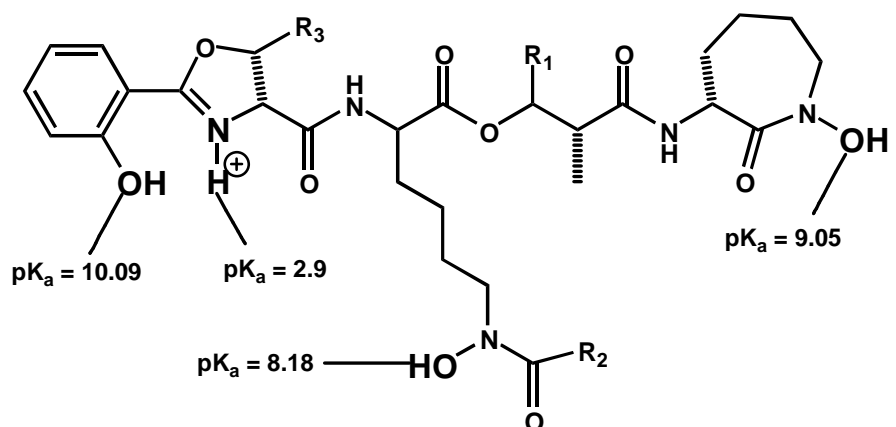
4.6. Conclusions

As discussed in previous chapters, the mechanism of exchange of iron in biological systems is of vital importance to the role of siderophores in cellular uptake processes. It has been proposed that the exchange of iron can be facilitated by the presence of small molecule chelators, which can catalyze the normally slow exchange reactions. The hydroxypyridinone molecule, DMHP, has shown the ability to catalyze the exchange of iron from ferrioxamine B to EDTA involves the formation of an inner sphere ternary complex, followed by rapid exchange of iron from ferrioxamine B to EDTA. It was also shown that iron-DMHP complexes likely are not involved in the catalysis reaction, due to the rapid exchange kinetics and favorable thermodynamics of chelation of iron by desferrioxamine B.

5. Characterization of iron(III) sequestration by an analog of the cytotoxic siderophore Brasilibactin A


5.1. Introduction

Brasilibactin A is a siderophore produced by the actinomycete *Nocardia brasiliensis*, that features a mycobactin backbone tethered to the exterior cell wall of the bacterium by a long hydrophobic carbon chain (Figure 5.1.).(132) It has been shown that brasilibactin A has an extremely strong cytotoxic effect on human epidermoid carcinoma KB cells at concentrations of 50 nM, resulting in its classification as a cytotoxic siderophore.(132) Brasilibactin A activates the protein caspase-3, a proteolytic enzyme of central importance to the apoptosis cellular pathway, which may be the cause of its high cytotoxicity.(132) Previous studies on caspase-3 have shown that the inactivation of the protein and halting of the apoptotic pathway containing caspase-3 is iron-dependent, where iron acts as a reversible inhibitor of caspase-3.(133) It has also been shown that treatment of caspase-3 with iron, followed by the siderophore desferrioxamine B, results in loss of the inhibitory effect of the iron. It has been proposed that the reactivation of the protein is due to chelation of the iron by desferrioxamine B, preventing it from interacting with the inhibitory site of caspase-3.(133) The activation of caspase-3 in cells treated with iron chelators could lead to the development of more effective treatments for cancer.



Brasilibactin A: $R_1 = C_{15}H_{31}$, $R_2 = R_3 = H$

Brasilibactin A analog, Bbtan: $R_1 = R_2 = R_3 = H$

Carboxymycobactins: $R_1 = C_2H_5$, $R_3 = CH_3$, $R_2 =$ 

Mycobactin S: $R_1 = CH_3$, $R_2 = C_{15}H_{31}$, $R_3 = H$

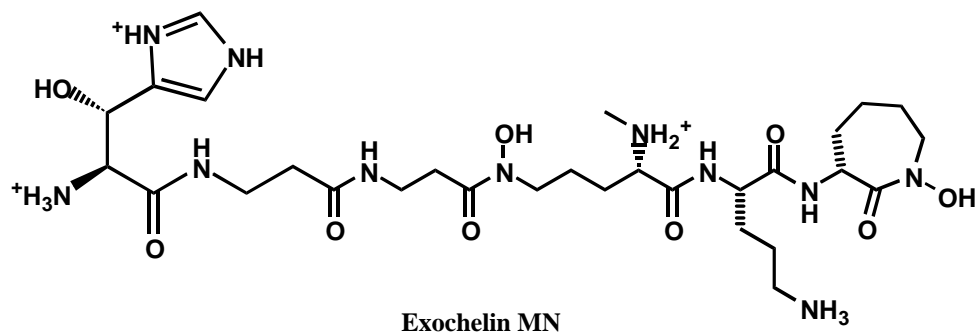


Figure 5.1. Structure of the siderophore, brasilibactin A and its synthetic analog, Bbtan. Both siderophore and analog contain two hydroxamate and a phenol-oxazole donor group. Ionizable protons are shown here in bold with their determined protonation constants for Bbtan. Also shown are mycobactin S and the related extracellular siderophores, carboxymycobactin and Exochelin MN.

Mycobactins (Fig. 5.1.) are a class of membrane-bound siderophore molecules featuring a similar four-residue backbone structure with varying lengths and positions of a long carbon chain that acts as a tether to connect the molecule to the exterior side of the cell wall of the mycobacterium or in some cases to lipid pools contained in macrophages to facilitate the removal of iron from the host.(24) A related class of chelators, the carboxymycobactins (Fig. 5.1.), differs from the mycobactins in that the ornithine residue terminates in an extended carbon chain with a carboxylate group or an ester group, which can act to increase the water solubility of the molecules. In all of these cases, the iron-binding moieties are the same, a hydroxamate-modified ornithine residue, a cyclic hydroxamic acid moiety, and a phenoloxazoline donor moiety. The mycobactin backbone structure is a commonly recurring motif observed in a number of amphiphilic siderophore classes, including the amamistatins and the nocardimicins.(134-136) In most mycobacteria, an extracellular siderophore, an exochelin or a carboxymycobactin, is produced to bind the iron and return it to the cell, where it exchanges the iron with the cell membrane-bound mycobactin.(137) In most mycobacteria, an extracellular siderophore, an exochelin or a carboxymycobactin, is produced to diffuse into the external environment to sequester iron and return it to the cell, where the siderophore may either transport the iron into the cell or exchange the iron with the cell membrane-bound mycobactin. The receiving mycobactin acts as a cellular membrane-bound "iron sink" or temporary storage until needed, and then reaction with a ferrireductase presumably occurs, followed by transport of the iron(II)

into the cell through some uncharacterized mechanism.(137, 138) These siderophores (water soluble external siderophores called exochelins for non-pathogenic and carboxymycobactins for pathogenic mycobacteria, and membrane-bound mycobactins) serve a critical role in the iron acquisition process of mycobacteria. It is also important to note that the type of mycobactin used by one species of mycobacterium can be lethal to other mycobacterium.(139) As of this writing, the only mycobactin siderophore for which its Fe(III) affinity has been characterized is mycobactin S.(140)

The water-solubility of brasilibactin A is severely limited due to the long carbon chain (R_1 in Fig. 5.1.) attached to the backbone, preventing study of the molecule itself. One way of addressing this issue is by studying a derivative of the molecule without the carbon tail, limiting the focus to the mycobactin backbone. This increases the water solubility of the molecule, presumably without affecting its iron binding properties, as the donor moieties that contribute to complex stability remain unchanged in the analog. The synthesis of the natural product Brasilibactin A has been recently reported.(141) A modification to the synthetic procedure allows study of a structural analog of the natural product Brasilibactin A that lacks the 15-carbon chain and features much higher water solubility than the natural product.

5.2. Statement of chapter objectives

The first purpose of this study is to investigate the Fe(III)-binding abilities of brasilibactin A and to determine the architectural features of importance to iron-binding in brasilibactin A for potential development of anti-cancer agents. This characterization was done using a combination of potentiometric and spectrophotometric titrations of the water-soluble brasilibactin A analog molecule (Bbtan, Fig. 5.1., R = H) lacking the long carbon chain tail, both in the presence and the absence of Fe(III). This brasilibactin A analog was kindly made available to us by the Hong research group at Duke University.⁽¹⁴²⁾ Additionally, the characteristics of the iron(III)-Bbtan complex will be related to the iron uptake mechanism in mycobacteria and related bacteria and it will be argued that the relative Fe(III) affinity and ease of Fe(III) reduction are integral parts of the mechanism. In addition to our studies with Fe(III), we have studied the binding of zinc with brasilibactin. We use potentiometric titrations of Bbtan in the presence of zinc to determine whether or not protons are being displaced by the metal. Potentiometric investigations of the binding of Ni(II) with Bbtan were also performed.

5.3. Experimental

5.3.1. Materials

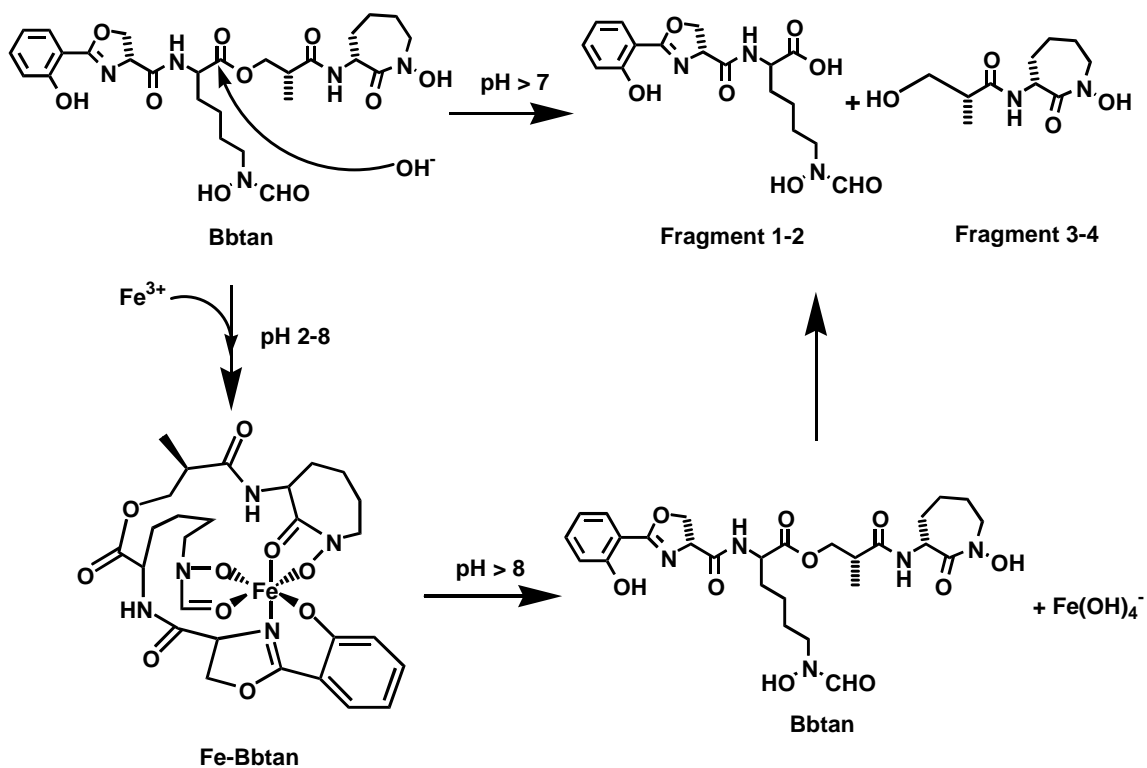
All solutions were prepared in deionized water with 0.10 M NaClO₄ as the background electrolyte for ionic strength. Ligands were synthesized and purified by the

Hong Lab at Duke University according to previously established methods (see Appendix C) and were used without further purification.⁽¹⁴¹⁾ Solid anhydrous FeCl_3 (Sigma) was used to prepare 0.10 M stock solution that was standardized titrimetrically by reduction with SnCl_2 , followed by titration with $\text{K}_2\text{Cr}_2\text{O}_7$. Solutions of $\text{Ni}(\text{ClO}_4)_2$ and $\text{Zn}(\text{ClO}_4)_2$ were prepared and standardized by titration with EDTA.⁽⁹³⁾

5.3.2. Protonation constant determination

Characterization of the Bbtan (Fig. 5.1.) protonation constants was done through a combination of spectrophotometric and potentiometric titrations. A spectrophotometric titration of Bbtan was performed, where a 1.4×10^{-4} M solution was titrated with measured volumes of standardized 0.10 M NaOH. The titration proceeded over the pH range 2.2 to 10.2. All pH measurements were made with an Orion 230 A+ pH/ion meter equipped with an Orion Ross pH electrode filled with 3 M NaCl solution. The electrode was calibrated by the “classical method,” titration of standardized 0.10 M HClO_4 with standardized 0.10 M NaOH. Calibration data were analyzed using the computer program, GLEE. ^(95, 96) UV-visible spectra were recorded with the Cary-50 spectrophotometer equipped with an external dip probe (Hellma, USA).

Additionally, a potentiometric titration of fragment 3-4 (Shown in Scheme 5.1.) was performed. A 5.8×10^{-4} M solution of fragment 3-4 was prepared and titrated with standardized 0.10 M NaOH. The data were fit to a single proton model and analyzed



Scheme 5.1. Proposed reaction scheme for hydrolysis of Bbtan in basic solution (top and right), reaction with $\text{Fe}_{\text{aq}}^{3+}$ (left) and dissociation of the Fe-Bbtan complex in basic solution (bottom).

using the computer program, HYPERQUAD.⁽¹⁴³⁾ A spectrophotometric titration was used to determine the protonation constants of fragment 1-2 (Scheme 5.1). A 1.7×10^{-4} M solution of fragment 1-2 was prepared and titrated with standardized 0.10 M NaOH, measuring the UV-Visible spectrum of the solution over the range of 250 nm – 400 nm. The pH range of the experiment was from pH 2.7-11.0. Analysis of the spectrophotometric data of the protonation of fragment 3-4 was performed again using the program, HYPERQUAD with a 4-proton model.

5.3.3. Protonation stability assay

To ensure the stability of Bbtan, a $^1\text{H-NMR}$ experiment was performed by the Hong research group to mimic the spectrophotometric titration.⁽¹⁴²⁾ The $^1\text{H-NMR}$ spectrum of Bbtan was measured at a pH of approximately 2, and the pH was raised to approximately 11 by addition of 0.1 M NaOD. The $^1\text{H-NMR}$ spectrum was then measured at 25 minutes and 11 hours after adjustment was made to the pH. For comparison, the $^1\text{H-NMR}$ spectrum of fragment 1-2 and the $^1\text{H-NMR}$ spectrum of fragment 3-4 were measured under basic conditions, approximately pH 10.

5.3.4. Iron(III) complex thermodynamic characterization

The stability of the iron-Bbtan complex was then characterized using spectrophotometric titrations. Two pH-dependent spectrophotometric titrations of the iron-Bbtan complex were performed, one going from low pH to high pH and another going from moderate pH to low pH. The low-to-high pH titration was performed by increasing the solution pH of a 1:1 Fe:Bbtan molar ratio solution through measured additions of standardized 0.1 M NaOH over the pH range of 2.1 to 11.3. The moderate-to-low pH titration was performed by titrating a 1:1 Fe:Bbtan molar ratio solution with 1.0 M HClO_4 over the pH range of 6.7 to approximately 0.5. To measure low pH values, the electrode was calibrated assuming Nernstian behavior with a junction potential. Calibration data was analyzed using the program, VLpH. ⁽¹⁰⁰⁾

Determination of the iron(III)-Bbtan complex stability constant was done through a competition reaction between Bbtan and EDTA. The experiment was performed in a pH range such that EDTA would react with the Fe-Bbtan complex in a 1:1 fashion following the equilibrium shown in Eq. 5.1., where K_{obs} represents the experimentally determined conditional equilibrium constant, $\beta_{a2,EDTA}$ represents the product of the first two protonation constants of EDTA obtained from the literature, $\beta_{a3,Bbtan}$ represents the product of the first three protonation constants of Bbtan determined above, and $\beta_{110,EDTA}$ represents the overall stability constant for the $Fe(EDTA)^-$ complex obtained from the literature.(102) In this experiment, a 1:1 solution of



$$K_{obs} = \frac{[FeEDTA^-][H_3Bbtan]}{[Fe(Bbtan)^+][H_2EDTA^{2-}][H^+]} \quad (5.2.)$$

$$\beta_{110} = \left(\frac{K_{obs} \beta_{a2,EDTA}}{\beta_{110,EDTA} \beta_{a3,Bbtan}} \right)^{-1} \quad (5.3.)$$

Fe(III)-Bbtan complex was prepared at pH 7 in HEPES buffer (to maintain a constant solution pH) with a 0.10 M $NaClO_4$ background electrolyte to maintain the solution ionic strength and separated into 2.0 mL aliquots. Varying concentrations of EDTA were added over the range of 0-25 equivalents of EDTA:Fe and the solutions were allowed to equilibrate. The reaction was found to be very slow, likely due to the kinetics

of release of iron by Bbtan, so equilibration was allowed to take place over the course of 2 months to ensure completeness. The reaction was stored in the dark at a constant temperature to ensure the stability of the complex and that no photochemistry would occur. The final product of the reaction was the Fe(EDTA)⁻ complex as determined from the UV-visible spectrum at equilibrium (see Section 2.3.4). Spectral data were analyzed using the protonation constants determined from potentiometric titration of the ligand and the data measured from the separate solutions using the program, HYPERQUAD. The value of K_{obs} was determined using the program, Excel. All determined equilibrium constants for the Fe(Bbtan) complex are shown in Table 5.1.

Table 5.1. Measured equilibrium constants for the Fe(III)-Bbtan system. All constants were measured at T = 25 °C and μ = 0.10 M (NaClO₄). Water molecules omitted for clarity.

Equilibrium	log K (β)
$\text{Bbtan}^{-3} + \text{H}^+ \rightleftharpoons \text{HBbtan}^{-2}$	10.09 ± 0.03
$\text{Bbtan}^{-2} + 2 \text{H}^+ \rightleftharpoons \text{H}_2\text{Bbtan}^{-}$	19.14 ± 0.08
$\text{Bbtan}^{-} + 3 \text{H}^+ \rightleftharpoons \text{H}_3\text{Bbtan}$	27.3 ± 0.1
$\text{Bbtan} + 4 \text{H}^+ \rightleftharpoons \text{H}_4\text{Bbtan}^+$	30.2 ± 0.2
$\text{Fe}^{3+} + \text{Bbtan}^{-3} \rightleftharpoons \text{Fe}(\text{Bbtan})$	26.96 ± 0.02
$\text{Fe}^{3+} + \text{H}_3\text{Bbtan} \rightleftharpoons \text{Fe}(\text{Bbtan}) + 3 \text{H}^+$	1.0
$\text{Fe}^{3+} + \text{H}_2\text{EDTA} \rightleftharpoons \text{Fe}(\text{EDTA}) + 2 \text{H}^+$	7.51
$\text{Fe}(\text{Bbtan}) + \text{H}_2\text{EDTA} + \text{H}^+ \rightleftharpoons \text{Fe}(\text{EDTA}) + \text{H}_3\text{Bbtan}$	6.5 ± 0.4

5.3.5. Electrochemistry of Fe-Bbtan

A solution of the Fe(Bbtan) complex was prepared at a 1:1 Fe(III):Bbtan molar ratio by dissolving the ligand in acidic electrolyte solution, followed by slow addition of the iron(III) solution with stirring. The cyclic voltammogram of the solution was measured using a Cypress potentiostat with a Controlled Growth Mercury Electrode by BASi set to static mercury drop electrode mode as the working electrode, platinum wire auxiliary electrode, and Ag/AgCl, 3.5 M KCl reference electrode. All values reported here were adjusted by 205 mV to obtain redox potentials versus NHE. Solution pH was adjusted over the range of 2.3 to 8 by measured addition of 0.10 M NaOH. Between each addition, 5 minutes was allowed for stirring, degassing and equilibration.

5.3.6. Potentiometric titration of Zn(II) and Ni(II)

Potentiometric titrations were performed on the Ni(II) and Zn(II) systems with Bbtan. In the Ni(II)-Bbtan system, a 1:1 molar ratio solution of Ni(II) and Bbtan was prepared at $[\text{Ni}^{2+}] = [\text{Bbtan}] = 1.6 \times 10^{-4} \text{ M}$ in 0.10 M NaClO₄, and the solution was titrated with standardized 0.10 M NaOH. A similar titration was performed for the Zn-Bbtan system, with $[\text{Zn}^{2+}] = [\text{Bbtan}] = 1.4 \times 10^{-4} \text{ M}$ in 0.10 M NaClO₄. Both systems were titrated in triplicate.

5.4. Results

5.4.1. Determination of protonation constants

An attempt was made to determine the protonation constants of Bbtan through direct spectrophotometric titration of the whole molecule with standardized NaOH. The spectra measured in the spectrophotometric titration of Bbtan show two separate pH ranges, one from pH 2.2 to pH 6.1 characterized by a slow shift in the λ_{\max} and a slight decrease in the intensity of the spectrum, and a second one from pH 6.1 to pH 10.2, characterized by a major shift in the λ_{\max} and in spectral intensity (Fig. 5.2.). However, it was noticed that the system exhibited a gradual shift in the solution pH to lower values when allowed 15-60 minutes equilibration time, accompanied by a corresponding shift in the spectrum. Also, upon returning the solution pH to the initial value (pH 2.3), the spectral shift was found to be irreversible (Figure 5.3.). This observation indicates the occurrence of some irreversible chemical reaction of Bbtan, possibly including hydrolysis of the molecule. $^1\text{H-NMR}$ experiments which replicated the spectrophotometric titration performed by the Hong group (Fig. 5.4.) showed that the shift of $^1\text{H-NMR}$ spectrum observed for the whole Bbtan molecule at high pH was similar to the additive product of the measured spectra of fragment 1-2 and of fragment 3-4.(142) At high pH, the spectrum of Bbtan featured a triplet at approximately 6.55 ppm and a doublet at approximately 6.67 ppm, which was not observed at low pH conditions. A similar multiplet was observed in the spectrum of fragment 1-2, which

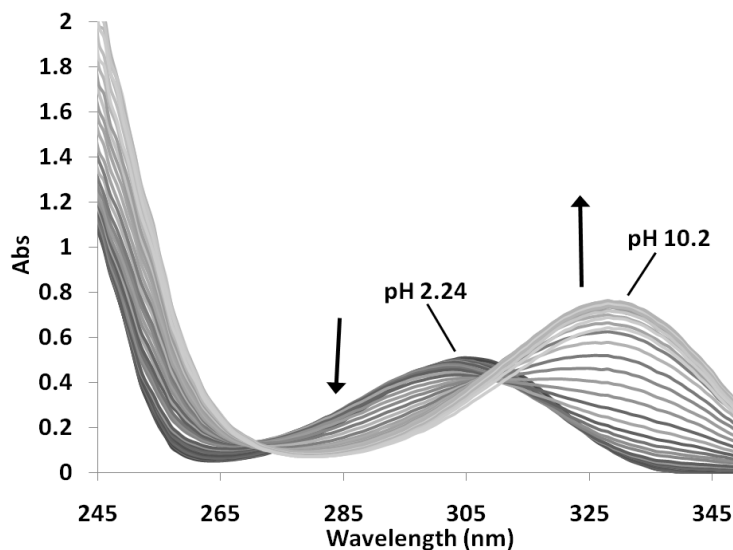


Figure 5.2. Spectrophotometric titration of the synthetic analog of Brasilibactin A, Bbtan, over the pH range of 2.24 to 10.2. Conditions: [Bbtan] = 1.4×10^{-4} M, $\mu = 0.10$ (NaClO₄), T= 25 °C.

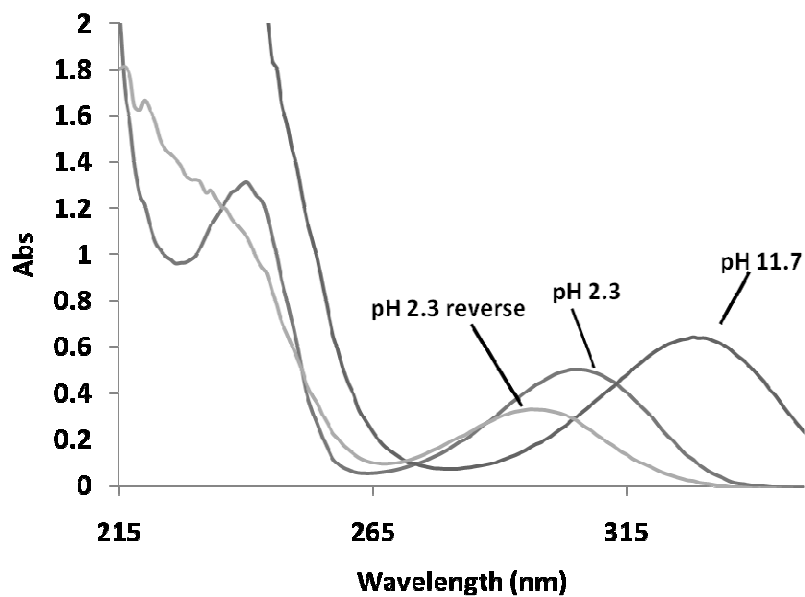


Figure 5.3. UV-Visible spectra obtained from spectrophotometric titration of Bbtan showing the lack of reversibility of the titration. Conditions: [Bbtan] = 1.4×10^{-4} M, $\mu = 0.10$ (NaClO₄), T = 25 °C.

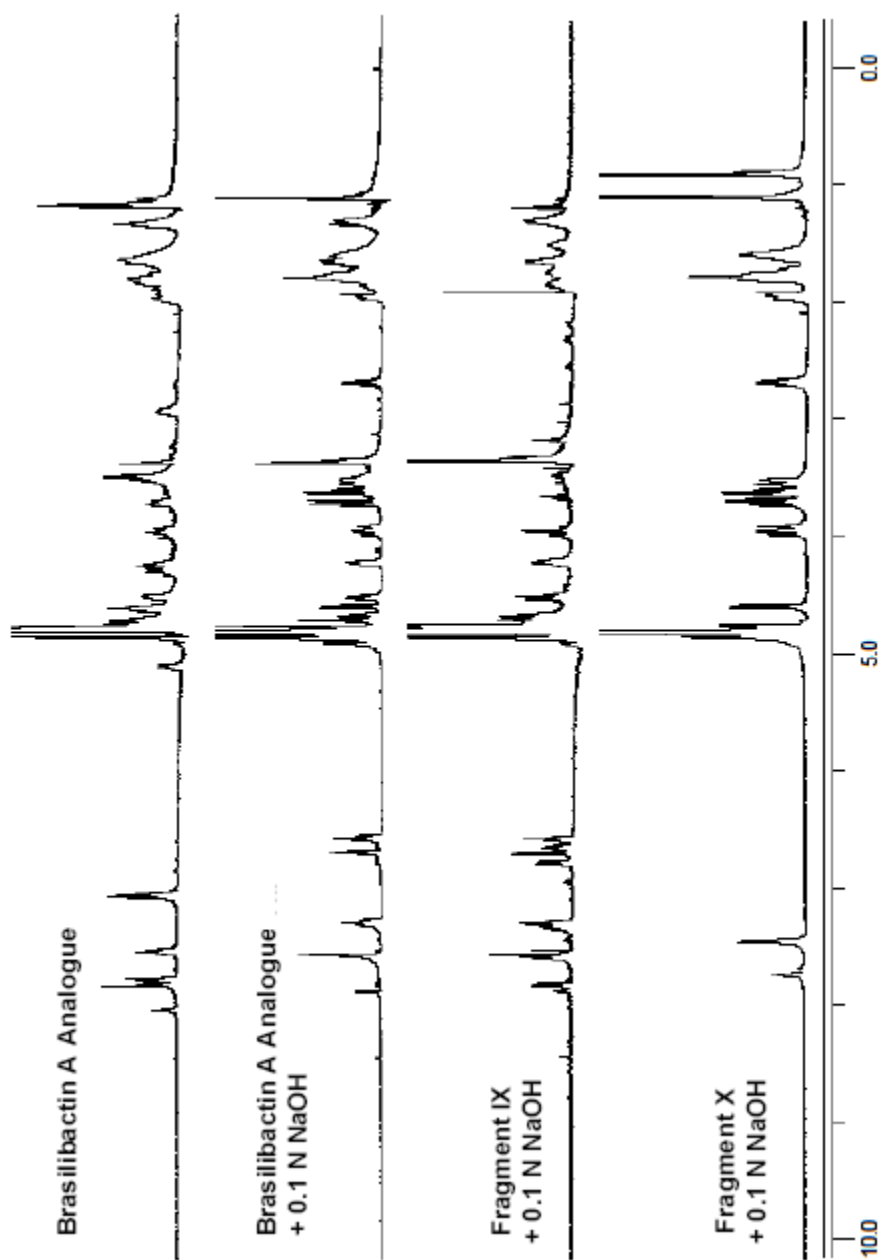


Figure 5.4. pH-dependent NMR titration of the Brasilibactin A analog, Bbtan demonstrating hydrolysis of the molecule at high pH environments. Conditions: [Bbtan] = 1.4×10^{-4} M, $\mu = 0.10$ (NaClO₄), T = 25 °C, D₂O solvent. Experiment performed and NMR spectra collected by Heekwang Park of the Hong laboratory.

was also measured at high pH conditions. Also at high pH, Bbtan featured a multiplet at approximately 3.6 ppm, which was shifted from that observed at low pH. A similar pattern of multiplet was observed in the ^1H -NMR spectrum measured at high pH of fragment 3-4. This spectral shift and the similarity of the spectra between the high pH solution of Bbtan and fragments 1-2 and 3-4 suggest hydrolysis of Bbtan at high pH. It seems likely that at high pH, the ester bond of the mycobactin backbone is cleaved through hydrolysis. This suggests that the molecule is being hydrolyzed at the ester bond moiety of the backbone in basic solution to produce fragments 1-2 and 3-4.

Direct determination of the protonation constants is not possible due to the hydrolysis of the molecules at the ester bond, as illustrated in Scheme 5.1. Comparison of the protonation constants of the two product fragments in Scheme 5.1., Fragment 1-2 and 3-4 allows estimation of the protonation constants of the intact Bbtan molecule, disregarding intramolecular interactions that could affect the thermodynamics of protonation. Fragment 3-4 has two ionizable protons, a hydroxamic acid and a hydroxyl group. The data obtained from the potentiometric titration of Fragment 3-4 exhibited a single protonation constant in the pH range measured, as can be seen in Fig. 5.5. The protonation constant was determined by fitting it to a single proton model, which yielded the protonation constant for Fragment 3-4 of 9.05 ± 0.08 . Fragment 1-2 is expected to exhibit 4 ionizable protons. As shown in Fig. 5.6, the UV-visible spectra of Fragment 1-2 measured during the spectrophotometric titration are very similar to those

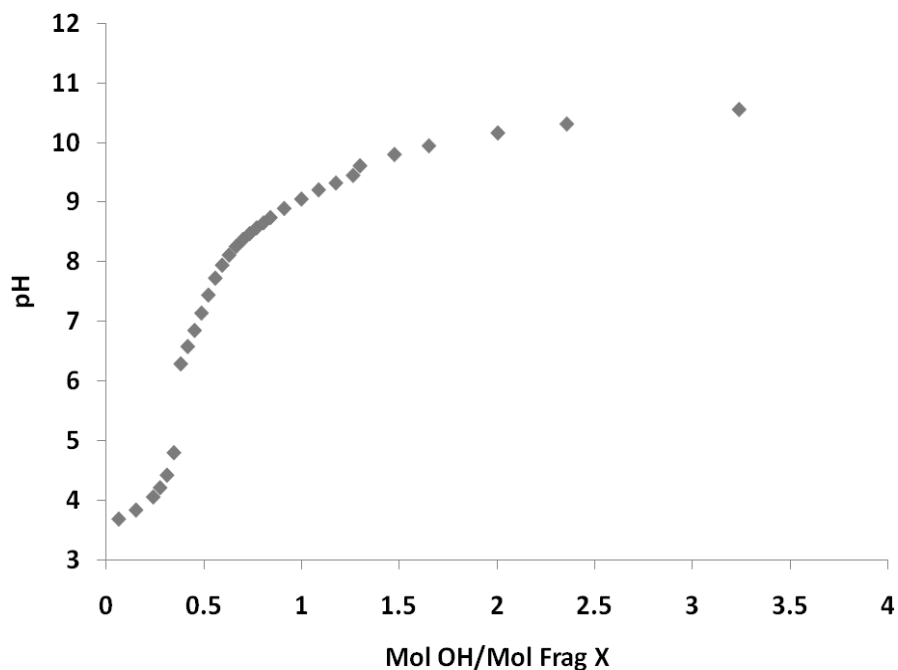


Figure 5.5. Potentiometric titration of Fragment 3-4 of Bbtan. [Frag34] = 5.8×10^{-4} M, T = 25 °C, and $\mu = 0.10$ (NaClO₄).

observed in the titration of the whole molecule, presumably because the major chromophore of Bbtan is the phenoloxazoline moiety. Data analysis of the measured spectra was performed using the program, HYPERQUAD by separating the spectral shifts into two segments, from pH 2.7 to pH 6.0 and from pH 6.0 to pH 10.6. Both segments of the spectral change were solved using a 2-proton model. The best-fit model produced four protonation constants for Fragment 1-2 of $pK_{a1} = 2.9 \pm 0.1$, $pK_{a2} = 4.8 \pm 0.2$, $pK_{a3} = 8.18 \pm 0.09$, and $pK_{a4} = 10.09 \pm 0.03$. Upon completing the titration, the reversibility was tested in a similar manner as the whole molecule, and the spectrum exhibited a similar shift as that observed in the whole Bbtan molecule, as shown in Fig. 5.3. This

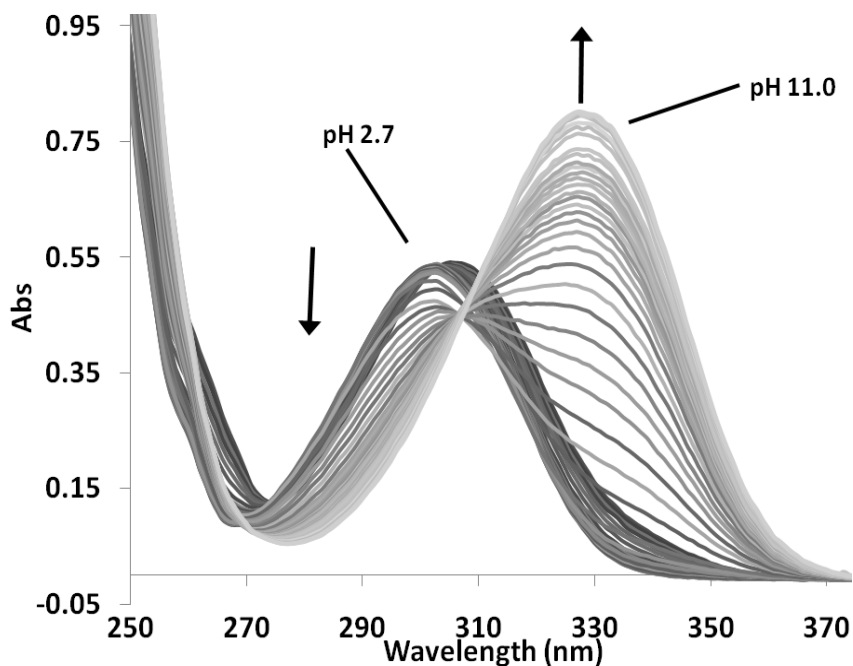


Figure 5.6. Spectrophotometric titration of Fragment 1-2 over the pH range of 2.7 to 11.0. [Frag12] = 1.7×10^{-4} M, T = 25 °C, and $\mu = 0.10$ (NaClO₄). Arrows indicate the direction of spectral change with increasing pH.

implies some degree of hydrolysis of fragment 1-2 over the course of the experiment, likely at the phenoxazoline ring.

By combining the determined protonation constants for the hydrolyzed fragments, it is possible to predict the protonation constants for the entire molecule Bbtan, ignoring the possibility of some intramolecular interactions. The assigned protonation constants for the molecule Bbtan are shown with their assigned acidic moieties in Fig. 5.1. and in Table 5.1.

5.4.2. Structural and thermodynamic characterization of the iron(III)-Bbtan complex

Addition of iron(III) to solutions of Bbtan results in complex formation, as evidenced by the spectral change of the solution. However, comparisons of the rate of Fe(III) complex formation with Bbtan to that of complex formation with a simple model monohydroxamic acid, acetoacetoacetic acid (data not shown) indicate a 3-fold slower rate of formation for Bbtan. This is possibly due to protonation of the phenoloxazoline moiety, which forms a 6-membered ring that is more stable than the 5-membered rings formed by protonation of other donor moieties.

Over the entire pH range of the spectrophotometric titration of the Fe-Bbtan complex, very little change in the solution UV-Visible spectrum is observed, indicating no change in the inner coordination sphere environment of the metal upon addition of base over the pH range of ~1 to 8.1, above which the complex begins to slowly dissociate (Fig. 5.7.). The λ_{max} of the complex spectrum is 455 nm, suggesting that more than two hydroxamate groups ($\lambda_{\text{max}} = 460$ nm) are binding the iron center.⁽¹⁴⁴⁾ The mode of binding of Bbtan (and by inference brasilibactin A) appears to occur through the two hydroxamate donor groups and the phenol-oxazoline donor group, as shown in Scheme 5.1. The spectral change at high pH was also found to be irreversible, implying some chemical reaction in the system, possibly hydrolysis of Bbtan. This result was not unexpected, as upon dissociation of the complex, the exposure of the ligand to the basic

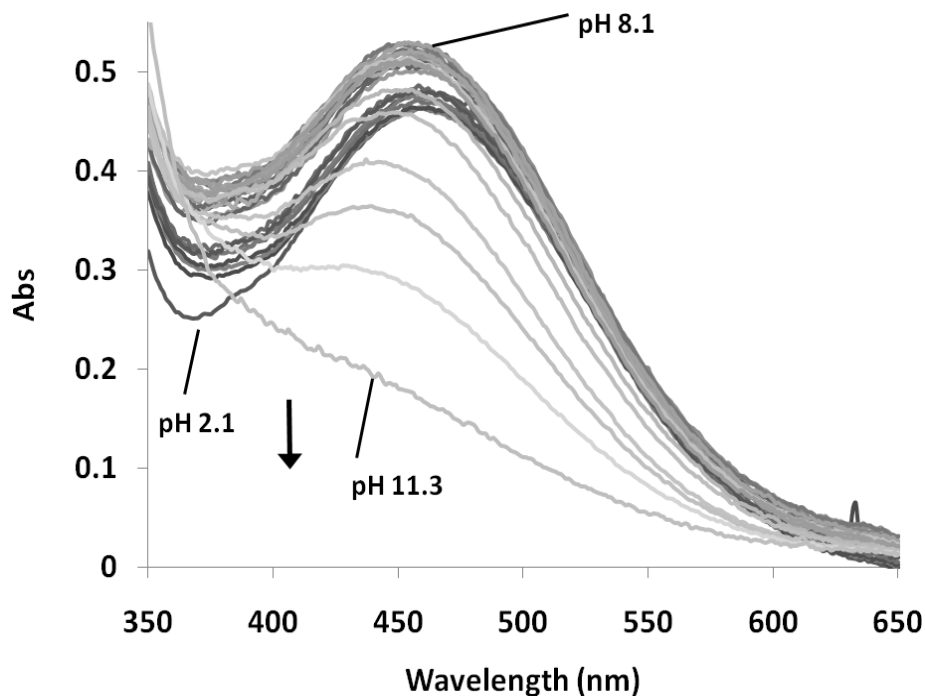


Figure 5.7. Spectrophotometric titration of the Fe(III)-Bbtan system at a 1:1 M:L molar ratio. [Bbtan] = 2.4×10^{-4} M, $[\text{Fe}^{3+}] = 2.3 \times 10^{-4}$ M, $T = 25$ °C, and $\mu = 0.10$ (NaClO₄). Arrows indicate the direction of spectral change with increasing pH above pH 8.1.

solution causes hydrolysis of the ester bond. The spectra obtained from the low pH spectrophotometric titration are shown in Fig. 5.8. During this titration, there appears to be little spectral change aside from dilution until very low pH, at which point the degree of dilution due to addition of titrant, and slow kinetics of complex dissociation made it difficult to determine the spectral characteristics of the complex. It was found, however, that the Fe(III)-Bbtan complex dissociation reaction was reversible, as addition of base to return the pH to higher values resulted in a return of the original spectrum.

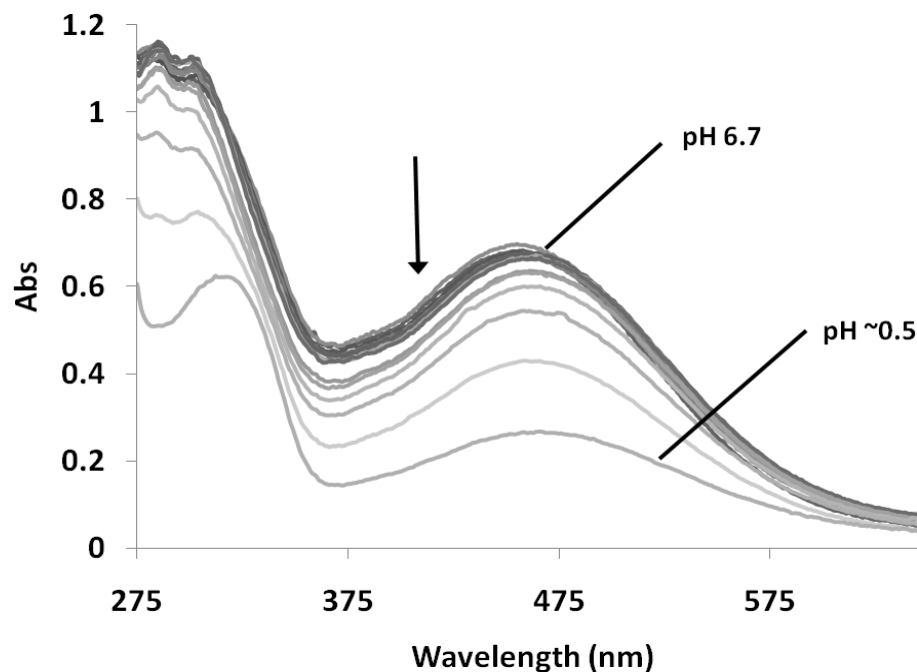


Figure 5.8. Spectrophotometric titration of the Fe(III)-Bbtan system at a 1:1 molar ratio. [Bbtan] = [Fe³⁺] = 2.1 × 10⁻⁴ M, T = 25 °C, and μ = 0.10 (NaClO₄). Arrows indicate the direction of spectral change with decreasing pH.

At circumneutral pH, the Fe³⁺-Bbtan complex is stable for extended periods of time, allowing determination of the iron(III) affinity. Due to the high value of the complex formation constant was done through competition with EDTA (See Section 5.2.4.). The spectra obtained from the EDTA competition experiment are shown in Figure 5.9. At our conditions, Bbtan is unable to effectively compete with EDTA for binding iron above 2 equivalents of EDTA present, implying relatively weak Bbtan binding compared to EDTA at these conditions. The spectra were then used with the program, HYPERQUAD to determine the stability constant of the Fe(III)-Bbtan complex, β₁₁₀ (Eq 5.4.-5.5., Table 5.1.).

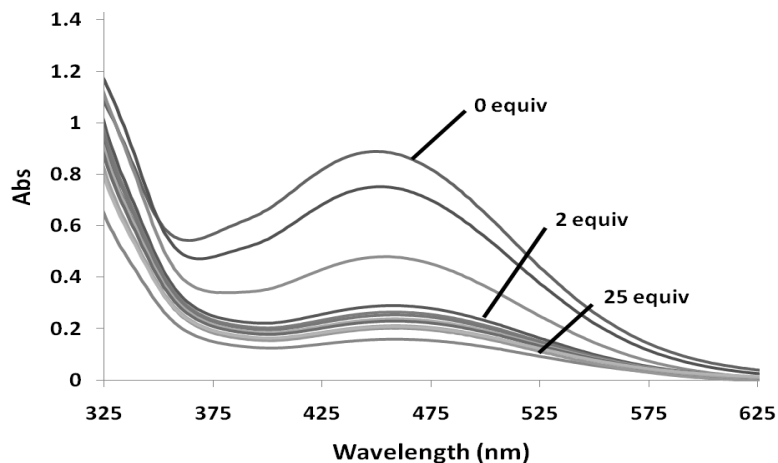


Figure 5.9. Competition titration reaction between the Fe(III)-Bbtan complex and EDTA. $[\text{Fe}^{3+}] = 2.5 \times 10^{-4} \text{ M}$, $[\text{Bbtan}] = 2.6 \times 10^{-4} \text{ M}$, $T = 25 \text{ }^\circ\text{C}$, $\mu = 0.10$ (NaClO_4), and $\text{pH} = 7.03$ (50 mM HEPES buffer). Spectra measured at 0 equivalents of EDTA, 2 equivalents of EDTA, and 25 equivalents of EDTA are marked for clarity.



$$\beta_{110} = \frac{[\text{Fe}(\text{Bbtan})]}{[\text{Fe}^{3+}][\text{Bbtan}^{3-}]} = 10^{26.96} \quad (5.5.)$$

Also included in Table 5.1. is the equilibrium constant for the EDTA competition reaction (Eq. 5.1.; Methods) and the pH dependent equilibrium constant for the Fe^{3+} sequestration by H_3Bbtan (Eq. 5.2.).

5.4.3. Fe-Bbtan complex redox chemistry

A representative cyclic voltammogram measured for the $\text{Fe}(\text{Bbtan})$ complex at $\text{pH} 7.2$ is shown in Fig. 5.10. The complex exhibits a single irreversible reduction with a

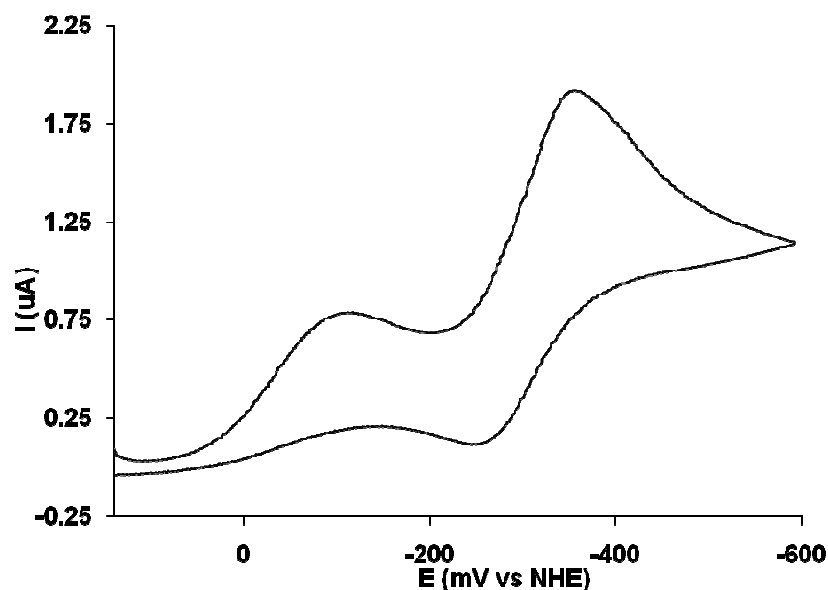


Figure 5.10. Cyclic voltammogram measured for the Fe(III)-Bbtan complex at pH 7.20. $[\text{Fe}^{3+}] = [\text{Bbtan}] = 4.2 \times 10^{-4} \text{ M}$, $T = 25 \text{ }^\circ\text{C}$, $\mu = 0.10 \text{ M}$ (NaClO_4). Potential is shown on the plot against NHE. Working electrode: HDME, auxiliary electrode: Pt wire, reference electrode: Ag/AgCl, 3.5 M KCl, scan rate = 50 mV/sec.

peak potential of -70 mV vs NHE, accompanied by a quasi-reversible redox couple with $E_{1/2} = -300 \text{ mV vs NHE}$ that is assigned to an Fe(III)/Fe(II) redox couple. Cyclic voltammograms obtained over the pH range of 3.5 to 8 were invariant, indicating no change in the inner coordination shell over a range of pH, consistent with our spectrophotometric titrations. The redox couple exhibited a peak current ratio (i_a/i_c) of 0.5, or quasi-reversible behavior (Fig. 5.10.), likely due to dissociation of the complex upon reduction to iron(II). The signal became more reversible as the scan rate was increased up to $i_a/i_c = 0.70$ at 200 mV/sec (Fig. 5.11.), as well as a peak-to-peak ratio of 0.59 at a Fe:Bbtan ratio of 1:1.5 and a scan rate of 50 mV/sec (Fig. 5.12.).

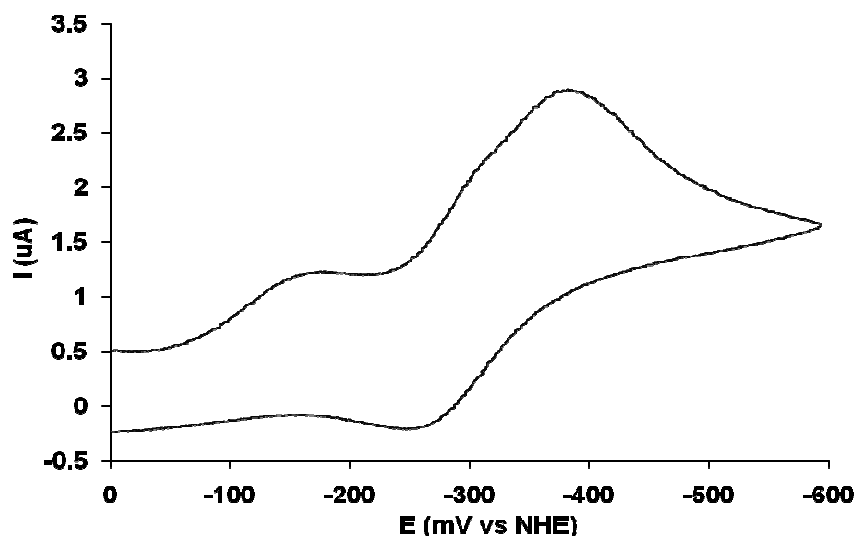


Figure 5.11. Cyclic voltammogram measured for the Fe(III)-Bbtan complex at pH 7.32. $[\text{Fe}^{3+}] = [\text{Bbtan}] = 4.8 \times 10^{-4} \text{ M}$, $T = 25 \text{ }^\circ\text{C}$, $\mu = 0.10 \text{ M}$ (NaClO_4). Potential is shown on the plot against NHE. Working electrode: HDME, auxiliary electrode: Pt wire, reference electrode: Ag/AgCl, 3.5 M KCl, scan rate = 200 mV/sec.

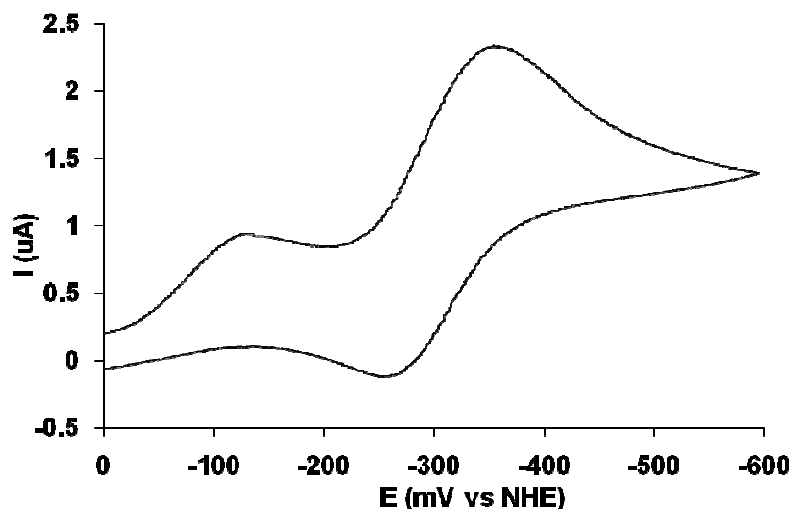


Figure 5.12. Cyclic voltammogram measured for the Fe(III)-Bbtan complex at pH 7.27. $[\text{Fe}^{3+}] = 4.2 \times 10^{-4} \text{ M}$, $[\text{Bbtan}] = 6.3 \times 10^{-4} \text{ M}$, $T = 25 \text{ }^\circ\text{C}$, $\mu = 0.10 \text{ M}$ (NaClO_4). Potential is shown on the plot against NHE. Working electrode: HDME, auxiliary electrode: Pt wire, reference electrode: Ag/AgCl, 3.5 M KCl, scan rate = 50 mV/sec.

A voltammogram of Bbtan in the absence of iron (Fig. 5.13.) exhibits a single irreversible reduction with a peak potential of -70 mV vs NHE, suggesting that the irreversible reduction wave at -70 mV vs NHE observed in the voltammogram of Fe(Bbtan) corresponds to the reduction of the ligand in solution. Additionally, a voltammogram was measured of fragment 1-2 in solution (Fig. 5.14.), which exhibited a similar behavior to Bbtan, suggesting that the reduction of the Bbtan ligand involves an irreversible reduction of the phenoloxazoline moiety.

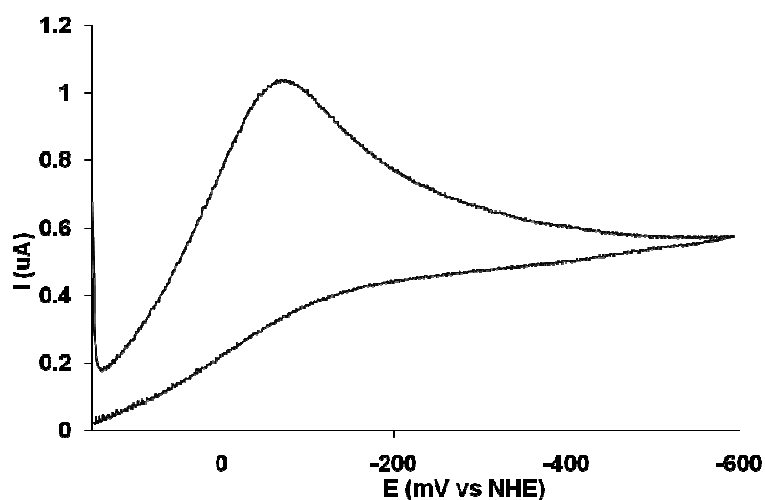


Figure 5.13. Cyclic voltammogram measured for Bbtan in the absence of iron(III) at pH 7.24. [Bbtan] = 4.2×10^{-4} M, T = 25 °C, μ = 0.10 M (NaClO₄). Potential is shown on the plot against NHE. Working electrode: HDME, auxiliary electrode: Pt wire, reference electrode: Ag/AgCl, 3.5 M KCl, scan rate = 50 mV/sec.

5.4.4. Ni(II) and Zn system titrations

The titrations of the Ni(II) and Zn(II) systems with Bbtan are shown in Figs. 5.15. and 5.16. It was found that the titrations of the Bbtan molecule in the presence of Zn and Ni(II) were non-reproducible and irreversible. Attempts were made to solve for the stability constants of the complex using HYPERQUAD, but solutions could not be obtained using the 4-protonation constant model.

5.5. Discussion

5.5.1. Equilibrium constant determination strategies

The water-solubility of brasilibactin A is severely limited due to the long carbon chain (R_1 in Fig. 001) attached to the backbone, preventing study of the molecule in aqueous solution. One way of addressing this issue is by studying an analog of the molecule without the 15-carbon tail, limiting the focus to the mycobactin backbone and iron binding moieties. This increases the water solubility, presumably without affecting the iron binding properties of the molecule as the donor moieties that contribute to iron affinity remain unchanged in the analog. The synthesis of the natural product Brasilibactin A has been recently reported.⁽¹⁴¹⁾ The synthesis of the water soluble analogue (Bbtan; Fig. 5.1) was developed by the Hong group based on the reported Brasilibactin A synthesis (see Appendix C).⁽¹⁴²⁾ Early experiments suggested significant hydrolysis of the molecule above neutral pH, which could result in incorrect

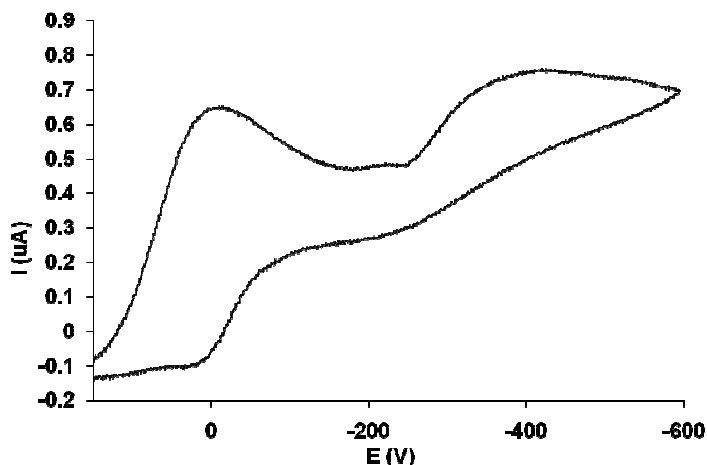


Figure 5.14. Cyclic voltammogram measured for Bbtan Fragment 1-2 in the absence of iron(III) at pH 9.40. $[Bbtan] = 2.6 \times 10^{-4} \text{ M}$, $T = 25 \text{ }^\circ\text{C}$, $\mu = 0.10 \text{ M (NaClO}_4\text{)}$. Potential is shown on the plot against NHE. Working electrode: HDME, auxiliary electrode: Pt wire, reference electrode: Ag/AgCl, 3.5 M KCl, scan rate = 50 mV/sec.

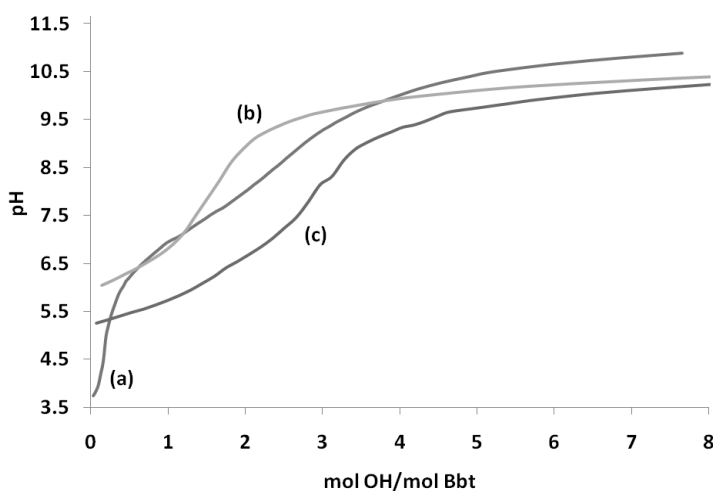


Figure 5.15. Potentiometric titration of the Zn-Bbtan system (a) without metal present and (b and c) with 1:1 equivalent concentration of metal ion present. Titrations (b) and (c) are two replicate titrations of the same system. Conditions: without metal – $[Bbtan] = 6.1 \times 10^{-4} \text{ M}$, $T = 25 \text{ }^\circ\text{C}$ and $\mu = 0.10 \text{ M (NaClO}_4\text{)}$; with metal - $[Zn^{2+}] = [Bbtan] = 1.4 \times 10^{-4} \text{ M}$, $T = 25 \text{ }^\circ\text{C}$ and $\mu = 0.10 \text{ M (NaClO}_4\text{)}$.

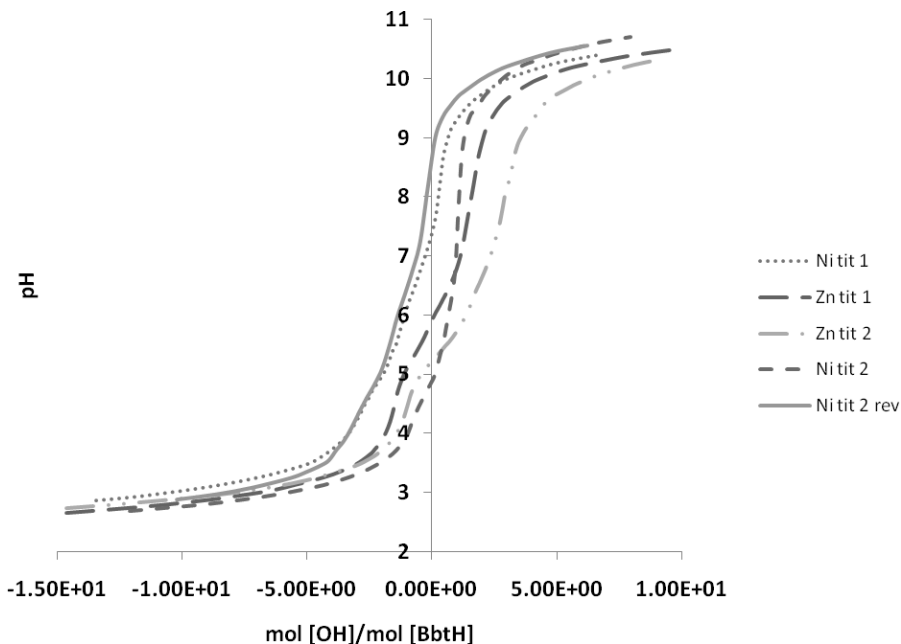


Figure 5.16. Potentiometric titrations of the Bbtan system in the presence of one equivalent Ni^{2+} or Zn^{2+} . Concentrations of Bbtan all approximately 1.5×10^{-4} M, molar ratio of metal:ligand is 1:1 in all experiments. Numbers of nickel or zinc titrations represent the number of replicate titrations performed of that system. Conditions: Ni^{2+} titrations – $[\text{Ni}^{2+}] = [\text{Bbtan}] = 1.5 \times 10^{-4}$ M, $T = 25$ °C and $\mu = 0.10$ M (NaClO_4); Zinc titrations - $[\text{Zn}^{2+}] = [\text{Bbtan}] = 1.4 \times 10^{-4}$ M, $T = 25$ °C and $\mu = 0.10$ M (NaClO_4).

protonation constant determinations. As protonation constants are required for accurate determination of iron(III) complex formation constants, we propose that high quality estimates of the protonation constants can be achieved using the hydrolyzed fragments of Bbtan, labeled 1-2 and 3-4, shown in Scheme 5.1.

After determining the protonation constants of the two fragments, Fe(III) competition experiments between the analog Bbtan and EDTA were performed, and the protonation constants determined from the hydrolysis products were used to calculate the stability constant of the Fe(Bbtan) complex. The difference between the analog Bbtan and the natural product Brasilibactin A is the carbon chain tail, which is not directly involved in the binding of iron(III). Due to this similarity, it is possible to accurately estimate the stability constant of the Brasilibactin A complex of iron(III) using the stability constant of the analog, Bbtan. A schematic representation of the subunit process used to determine the protonation constants and complex stability constant is shown in Scheme 5.2.

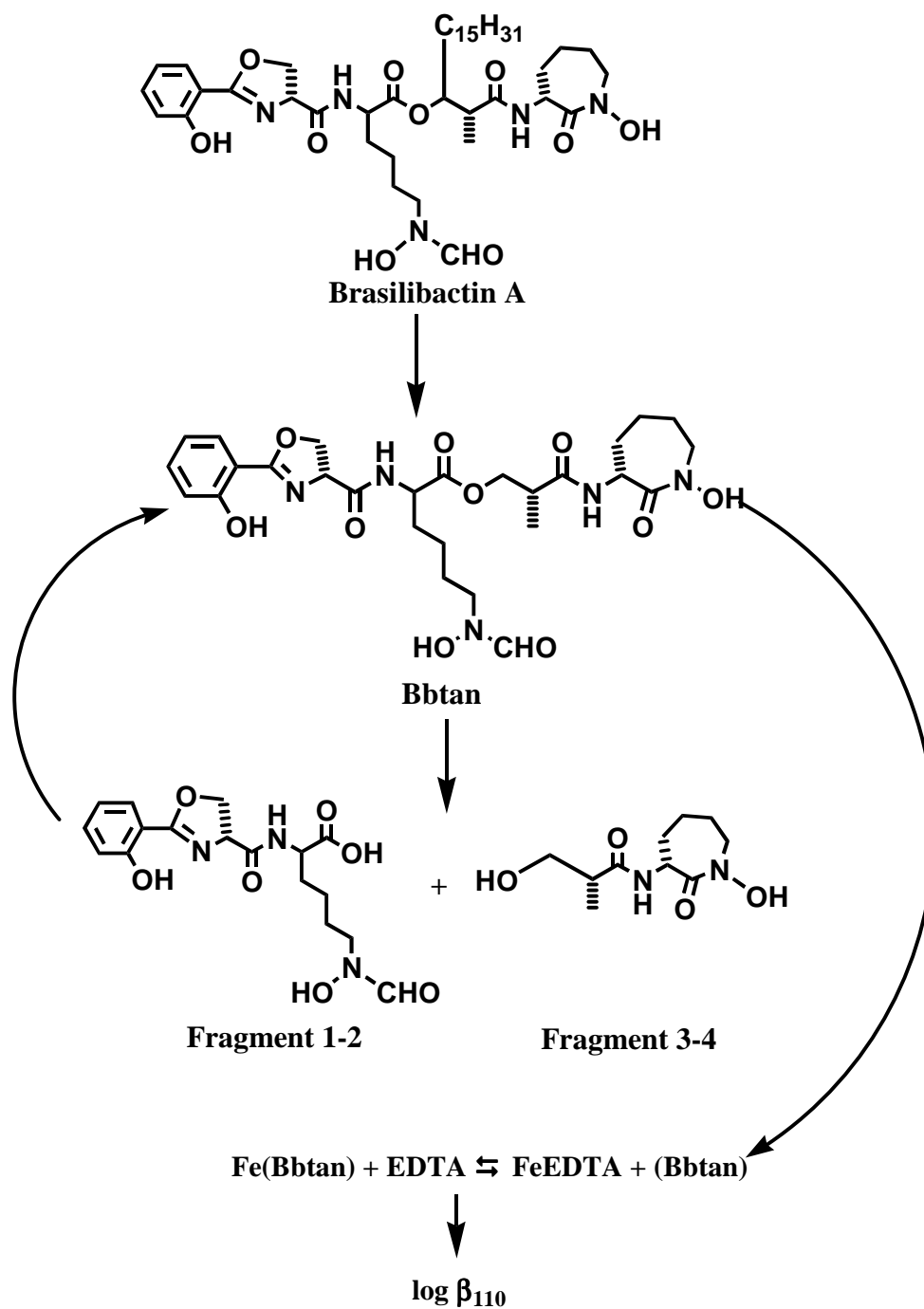
5.5.2. Protonation constants

Spectrophotometric titration of Bbtan with standardized NaOH, shown in Fig. 5.2, suggests an irreversible reaction upon increasing the solution pH. The ¹H-NMR titration performed by the Hong group (Fig. 5.4.) compared the spectrum of Bbtan to the spectra of the two halves of the molecule, fragments 1-2 and 3-4, shown in Scheme 5.1. As the only factor that is changing in solution during the titrations is the pH of the solution, it is reasonable to propose that hydrolysis occurs to the molecule at the ester moiety of the mycobactin backbone at high pH. This type of reaction may be feasible when compared to another siderophore featuring an ester backbone, vibrioferrin.⁽¹⁴⁵⁾ It was observed that the ester backbone of vibrioferrin was hydrolyzed under basic conditions, although

those experiments used much higher concentrations of NaOH, higher temperatures, and longer equilibration times than those seen here. Because of this reaction, it is difficult to accurately determine the protonation constants directly from the spectrophotometric or potentiometric titrations.

To address the issue of ligand hydrolysis, experiments were performed to determine the protonation constants of the two fragments produced by hydrolysis separately and assign the determined protonation constants to the corresponding groups of Bbtan. Fragment 3-4 has two ionizable protons, one hydroxamate proton and a hydroxyl group, although the hydroxyl group ionizes at a much higher pH than is observable using the techniques described here. The value determined from the potentiometric titration of fragment 3-4 for the hydroxamate group, 9.05 ± 0.08 is in the expected range for hydroxamic acids ($pK_a = 8-9$). However, it is higher than that observed for the cyclic hydroxamic acid of Exochelin MN (8.01) possibly due to electrostatic factors.⁽¹⁴⁶⁾

Fragment 1-2 features 4 possible protonation sites, a carboxylate, a hydroxamate, a phenol, and an oxazoline ring. The protonation constants measured for fragment 1-2 (see Sec. 5.4.1.) are also in the expected range for their assigned groups. The calculated value for pK_{a4} is slightly higher than the literature range for the protonation constant of a phenol, but pK_{a3} is consistent with literature reports of hydroxamate protons, pK_{a2} is



Scheme 5.2. Flow chart demonstrating the strategy for characterizing the equilibria of the Fe(III)-Bbtan system.

consistent with observed values of carboxylate protons, and pK_{a1} is consistent with literature reports of oxazoline ring protons.⁽¹⁴⁷⁾ By combining the protonation constants for the two fragments, the determined protonation constants for the molecule, Bbtan are shown in Fig. 5.1 and Table 5.1.

5.5.3. Thermodynamic characterization of the iron-Bbtan system

Having determined the protonation constants for the molecule, it is possible to determine the stability constant for the Fe(III)-Bbtan complex. The spectrophotometric titration of the complex showed very little change in the UV-visible spectrum of the complex over the pH range of approximately 2 to 8, suggesting no change in the inner coordination sphere of the metal until very low pH or very high pH, where ligand protonation and metal hydrolysis, respectively, begin to compete with the complexation of the iron. The proposed structure of the Fe-Bbtan complex is shown in Fig. 5.17. where iron is bound by two hydroxamate donor groups and one phenoloxazoline moiety. In the high pH titration, it was also found that the spectral shift at higher pH was irreversible, as would be expected if ligand hydrolysis was occurring upon dissociation of the brasilibactin analog at high pH. In the low pH titration, the reaction was found to be reversible, implying that the ligand remained largely intact upon dissociation at low pH.

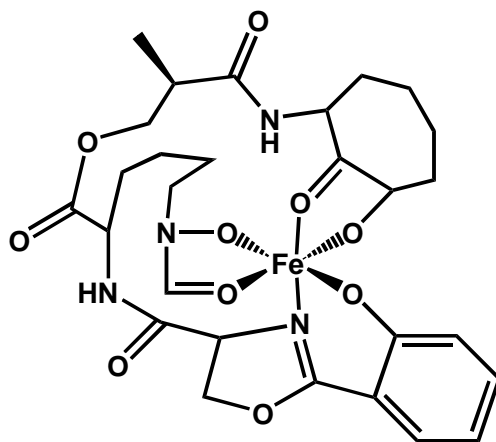


Figure 5.17. Proposed solution structure of the iron-Bbtan complex.

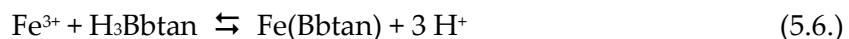
The competition titration between Bbtan and EDTA showed that Bbtan binds iron relatively weakly and is not as effective as other siderophores at competing with EDTA at the experimental conditions (Eq. 5.1., see Sec. 2.3.). The EDTA and Bbtan compete for chelation of the iron at a constant pH maintained by a buffer solution, and the spectral changes indicate the relative amount of iron(III) chelated by EDTA or by Bbtan. Through linear combination of the stability constants of EDTA and the equilibrium constant for Eq. 5.1., the stability constant for the Fe-Bbtan complex, β_{110} can be determined (Eq. 5.4.-5.5.). At 2 equivalents of EDTA added, the iron had been almost completely removed from Bbtan (Fig. 5.9.). Using the protonation constants obtained from previous experiments, the value for $\log \beta_{110} = 26.96$ (2) for reaction 5.4. The value of $\log \beta_{110}$ can also be compared to that of EDTA to give a comparison of relative stability of the complexes ignoring protonation of the ligands. This comparison ($\log \beta_{110} = 25.16$ for EDTA) shows that, as observed in the experiment, Bbtan has little advantage over EDTA for iron complex stability. Comparison of the conditional stability constants for EDTA

and Bbtan (both shown in Table 5.1.) exhibit a marked preference for formation of the Fe(EDTA)⁻ complex ($\log K_{\text{Bbtan}} = 1.0$, $\log K_{\text{EDTA}} = 7.51$), as evidenced by the results of the experiment where low concentrations of EDTA were required to remove iron from Bbtan.

The stability constant of the iron(III)-Bbtan complex ($\log \beta_{110} = 26.96$) compares favorably to the stability constant of the iron(III) complex of at least one similar molecule, $\log \beta_{110} = 25.5$ for mycobactin S, which confirms our reliable determination of the stability constant of the Fe-Bbtan complex. (140, 148) The small difference in determined stability constant may arise from the techniques used in the determination of the mycobactin S stability constant. Due to the low solubility of mycobactin S in aqueous solution, organic-aqueous extraction techniques with ⁵⁹Fe were used over a range of acid concentrations to determine the percent iron(III) uptake, which was extrapolated to determine the mycobactin-iron(III) affinity. Also, ionic strength effects may be a factor, as the acid concentrations used were as high as 5 M. (140, 149)

There are a variety of ways that the equilibria observed in the competition experiment can be expressed. One way is to directly calculate the equilibrium constant for the reaction as observed in the experiment, described by Eq. 5.1.-5.2. The equilibrium expression represents the ligands in their predominant protonation state at the experimental conditions, pH 7.03, and its equilibrium constant is a conditional equilibrium, as the expression depends on the solution pH at which the experiment is

being performed. By directly taking the spectra measured and determining the relative amount of iron present in the form of the Bbtan complex and in the form of the EDTA complex and calculating the amounts of free ligand present through mass balance equations, it is possible to calculate the conditional equilibrium constant for Eq. 5.4. Using the program, Excel, the equilibrium constant for Eq. 5.4. was found to be $\log K_{\text{obs}} = 6.5 \pm 0.4$. This indicates, as observed, that the equilibrium strongly prefers formation of the Fe(EDTA) complex at these experimental conditions. Another method of expressing the relative strength of complex formation is to calculate the proton-dependent stability constant of the ML complex, shown in Equation 5.6.



This can be obtained by linear combination of the experimental equilibrium constant for the competition reaction (Eq. 5.1.), the protonation equilibria of EDTA (Eq. 5.7.) and the stability constant of the Fe(EDTA) complex (Eq. 5.8.).



The equilibrium constant for the proton-dependent reaction of Bbtan with iron(III) (Eq. 5.6.) was found to be $\log K = 1.0$. This value also serves as an internal

calibrant for the determination of the stability constant $\log \beta_{110}$ as the difference between the cumulative protonation constant of Bbtan and the determined $\log \beta_{110}$ is approximately 1 log unit. All of the determined equilibrium constants are summarized in Table 5.1.

Another method of comparing relative stabilities of siderophores for binding iron(III) in cases where the molecules have different denticities and protonation constants is the pFe value (see Sec. 1.4.1.).⁽³²⁾ By using the $\log \beta_{110}$ determined above ($\log \beta_{110} = 26.96$) and the determined protonation constants, the pFe value for Bbtan is found to be 22.73. The determined values of the pFe^{3+} and the complex stability constant compared to some other natural siderophores are shown in Table 5.2. The determined pFe^{3+} is relatively low when compared to many other siderophores, which have pFe values in the range of 21.9 (for rhodotorulic acid) to higher than 30 for many tris-catecholate siderophores.^(1, 150) The value for Bbtan is closest to aerobactin, a photoreactive marine siderophore and rhodotorulic acid, a tetradentate siderophore. It is also interesting that the pFe and $\log \beta_{110}$ values are so much lower than that of the exochelins MN and MS, since mycobactins, which feature the same backbone structure as Bbtan are proposed to accept iron from exochelins to facilitate iron uptake. A plot of pFe over a range of pH values (Fig. 5.18.) shows that at all physiologically relevant pH values, the pFe value of Bbtan is multiple orders of magnitude lower than both Exochelin MN and exochelin MS, which suggests that a change in pH, as upon

Table 5.2. Calculated $\log \beta_{110}$, pFe values, and redox potentials for a series of natural siderophores.

Siderophore	$\log \beta_{110}$	pFe ^a	E _{1/2} ^b
Rhodotorulic Acid	62.2 ^c	21.9	-359
Mycobactin S	25.5 ^d	N/A	N/A
Bbtan	26.96 ^e	22.73	-300
Aerobactin	27.6 ^f	23.3	-336
Desferrioxamine B	30.6 ^g	26.6	-468
Exochelin MN	39.12 ^h	31.1	-595

^a Conditions: $[\text{Fe}^{3+}]_{\text{tot}} = 10^{-6} \text{ M}$, $[\text{L}] = 10^{-5} \text{ M}$, $T = 25 \text{ }^\circ\text{C}$, $\text{pH} = 7.4$.

^b Values reported as mV versus NHE, potential-limiting high-pH conditions

^c This value represents a $\log \beta_{230}$. Ref (12)

^d Ref (140, 148)

^e This work

^f Ref (151)

^g Ref (20, 32)

^h Ref (146)

endocytosis, would not affect the relative stabilities of the mycobactin and exochelin complexes, suggesting that change in pH plays a minimal role in iron(III) exchange from exochelins to mycobactins.

Upon mixing solutions of Bbtan with iron(III), the solution color was found to change very slowly, indicating slow rate of complex formation (data not shown). The amount of time required for the solution spectrum to stop changing was approximately three times as long as that observed for acetohydroxamic acid. It is possible that this

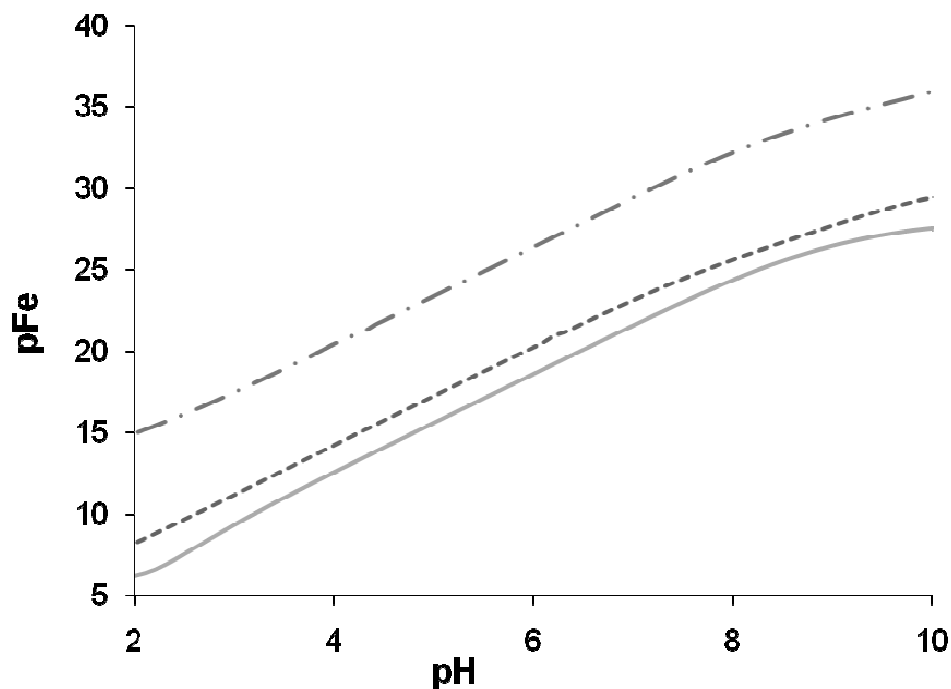


Figure 5.18. Plot of pFe as a function of pH for 3 siderophores. Ligand protonation constants and stability constants were taken from this work, (152), and (43). Legend: solid line – Bbtan, dashed line – Exochelin MS, dashed and dotted line – Exochelin MN. Conditions: $[Fe^{3+}] = 1 \mu M$, $[L] = 10 \mu M$, $T = 25 \text{ }^\circ C$, $\mu = 0.10 \text{ M (NaClO}_4\text{)}$.

decreased rate of complex formation is due to protonation of the phenoxazoline ring. Protonation of the phenol moiety allows the formation of a 6-membered ring including the oxazoline N-donor, which would deprotonate less rapidly than in other acidic moieties due to the stability of the ring, preventing chelation of iron by the phenoxazoline group.

5.5.4. Complex redox chemistry

Cyclic voltammetry of the complex exhibited two signals, one irreversible reduction assigned to the oxazoline moiety of the molecule and a reversible redox couple assigned to the iron(III) redox couple for the Fe-Bbtan complex. One literature report of the cathodic reduction of 2-substituted oxazoline groups in organic solvents showed that reduction of the molecules occurs across the C-N double bond of the oxazoline moiety.(153)

The quasi-reversible redox potential assigned to a $\text{Fe}^{3+}/\text{Fe}^{2+}$ centered redox couple, -300 mV vs NHE, is more positive than the redox potentials of a number of other natural siderophores (Table 5.2.), consistent with the relatively low pFe value of the ligand.(1) The redox potential of the Fe(Bbtan) complex is likely to be very close to that of a number of other natural mycobactin-type siderophore complexes, suggesting that the high redox potential of the complex (less negative, more easily reduced) plays a role in the ability of membrane-bound reductases to reduce iron(III) bound by mycobactins to facilitate uptake of the iron in its 2+ oxidation state.

5.5.5. Implications for iron uptake in mycobacteria

The chemical structure of Bbtan is identical in backbone and donor groups to that of brasilibactin A, which suggests that the iron chelating properties and iron(III)

complex redox chemistry will be the same for Bbtan and brasilibactin A. Thus, it is possible to use the results of the thermodynamic characterization done here to comment on the role of mycobactins in the iron uptake mechanisms of mycobacteria. Brasilibactin A exhibits a structure that is similar to many mycobactins. Thus, it is significant that a siderophore that plays a role in iron sequestration and uptake exhibits relatively low Fe(III) affinity and high redox potential. Siderophores with identical mycobactin backbones and varying pendant hydrophobic carbon chain lengths have been identified from other strains of *Nocardia* bacteria, as well as two linear bishydroxamate siderophores, the nocardichelins, which have structural similarities to desferrioxamine B and the mycobactins and features a long carbon chain of varying length.(134-136) The extracellular siderophores of the related bacterium genus *Rhodococcus*, the heterobactins, were found to consist of a cyclic hydroxamate and a catechol donor group, with heterobactin A featuring a possible salicylate binding mode.(154) While the extracellular siderophore acting in *N. brasiliensis* has not yet been identified, the extracellular siderophores of related bacteria, exochelins MN and MS, have been identified. Additionally, the extracellular siderophores of some related actinomycetes, *Actinomadura madurae*, have been characterized and feature similar structures as those observed in the exochelins.(155) Thus, exochelins MN and MS can be viewed as model siderophores to explore the mechanism of iron uptake in *N. brasiliensis* and for comparison of Fe(III)-complex thermodynamics. Here we have characterized the aqueous thermodynamics of an Fe(III)-brasilibactin analog system and propose that the relatively low Fe(III) affinity

and ease of complex reduction are critical to the role of mycobactins in the iron uptake mechanism of mycobactins and related bacteria.

The mycobactin siderophores play a central role in the mycobacteria iron uptake system, where iron is exchanged from exochelins or carboxymycobactins to membrane-bound mycobactins. Here we assume the validity of Bbtan as an analog that accurately mimics the iron(III) sequestration characteristics of brasilibactin A. It is significant that the Fe(III) affinity of brasilibactin A is so much lower than that of the extracellular component of the uptake system (exochelin). The log formation constants of exochelin MN (39.12) and exochelin MS (28.86) are much higher than the value determined here for a brasilibactin A analog and that previously reported for mycobactin S (Table 2). Based on the higher Fe(III) affinity constants and pFe values for the exochelins, the ability of a mycobactin to remove iron from an exochelin would seem problematic. However, there are a number of additional factors that may lead to the exchange of iron from an exochelin to a mycobactin. First, as mentioned in Section 5.1., the iron uptake system of mycobacteria involves the uptake of exochelin and carboxymycobactin complexes, with membrane-bound mycobactin acting as a transient iron storage pool when the internal processing mechanisms are overwhelmed (Fig. 5.19.).(138) At the inner cellular membrane surface bound mycobactin concentrations are high relative to the iron-exochelin (or iron-carboxymycobactin) complex. The resulting thermodynamic

drive (concentration effect) to exchange iron with mycobactin at the cellular membrane is presumably followed by reduction of the ferri-mycobactin complex.

The relatively low thermodynamic stability of the ferri-mycobactin complexes also may be advantageous considering the role of the ferri-mycobactin reduction in iron transport. It has been shown that the strength of binding of iron(III) by a siderophore is inversely related to the redox potential of the ferri-siderophore complex.(1, 34) This relationship between complex iron(III) affinity and complex redox potential is illustrated in a rearranged form of the Nernst equation, Eq. 5.9. where E^0_{complex} represents the standard redox potential of the Fe-Bbtan complex, E_{aq} represents the potential of the aquated iron(III)/iron(II) redox couple (770 mV vs NHE), β^{III} represents the affinity constant of Bbtan for iron(III) and β^{II} represents the affinity constant of Bbtan for iron(II).(1, 156) As iron(III) has a relatively low affinity for brasilibactin A

$$E^0_{\text{complex}} - E_{\text{aq}} = -59.16 \log(\beta^{\text{III}} / \beta^{\text{II}}) \quad (5.9.)$$

(relative to other siderophores, namely the exochelins), this results in a reduction potential for the complex that is higher than other iron-siderophore complexes (-300 mV), increasing the ease of reduction of the iron center. From Eq. 5.9., we can estimate the value of β^{II} as $10^{8.87}$. This drop in iron affinity upon reduction facilitates the dissociation of Fe(II) from brasilibactin and transport into the cell.

In the case of pathogenic mycobacteria that use carboxymycobactins, however, the difference in stability constants between the ferric-siderophore complex of delivering and receiving siderophores is not an issue as the stability of the Fe(III)-mycobactin complex and of the Fe(III)-carboxymycobactin complex should be very similar due to the similarity of the backbone structure. It is also possible that other processes may play a role in the exchange of iron from exochelins to mycobactins, such as ternary complex formation by small molecules (salicylic acid is a small extracellular chelator capable of ternary complex formation that has been identified in many mycobacteria).(138)

The specific proposed role of brasilibactin in the iron uptake mechanism of *Nocardia brasiliensis*, as well as the generally proposed role of mycobactins in the iron uptake mechanism of mycobacteria, is shown in Fig. 5.19. In the model, the extracellular siderophore of the pathogenic bacterium chelates to iron after removing it from the host iron chelating agent. Upon diffusing back to the cell, the extracellular iron chelator may be either transported across the cell membrane surface by its specific receptor protein, or it may exchange iron with membrane-bound mycobactin. The exchange reaction with membrane-bound mycobactin only takes place once the transport receptors are overwhelmed, suggesting that the concentration of iron-loaded siderophore is low at the membrane envelope and the localized mycobactin concentration is high at the membrane surface, driving the thermodynamics of the Fe(III) exchange reaction towards

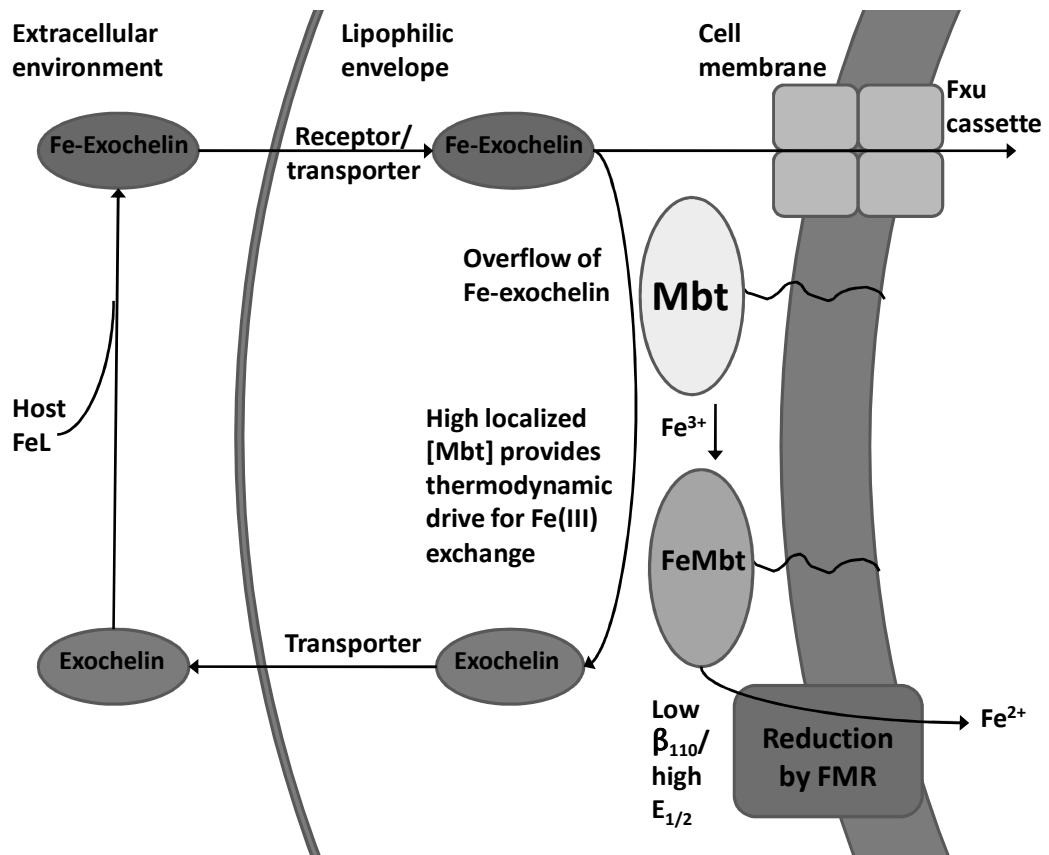


Figure 5.19. Schematic representation of iron acquisition and transport in mycobacteria. Diagram illustrates the effect of high inner cell membrane surface concentration on mycobactin (Mbt) extracting Fe³⁺ from the extracellular Fe-exochelin complex, followed by FMR reduction of Fe-Mbt and passage of Fe²⁺ through the membrane into the cell.

mycobactin. Once iron has been received by the mycobactin, it is held until the complex is reduced by the ferri-mycobactin reductase, FMR. The reduction of the iron-mycobactin complex is facilitated by the relatively high redox potential of the complex as reported here, which is a consequence of low complex stability. Upon reduction, iron(II) is then transported across the membrane envelope through an uncharacterized transport process.

A possible role for the hydrolysis of the mycobactin backbone in natural systems may be speculated upon based on the results discussed above. It is possible that hydrolysis of the mycobactin backbone takes advantage of three phenomena to facilitate the exchange of iron from the mycobactin complex. As mentioned in Chapter 1, a decrease in complex denticity results in an increase of complex redox potential and a decrease in complex stability due to the chelate effect. In addition, complexes featuring lower denticity chelators exhibit higher kinetics of exchange. Hydrolysis of the mycobactin backbone would produce a complex with a bidentate chelator and a tetradentate chelator, which would have a more positive redox potential and lower complex stability than the hexadentate mycobactin complex resulting in easier reduction by ferric mycobactin reductase, as well as an increased thermodynamic drive for iron release. Additionally, the EDTA competition experiments exhibited slow exchange of iron from Bbtan to EDTA, and hydrolysis of the mycobactin backbone could accelerate such exchange reactions to the point where they are viable for biological applications.

5.6. Conclusion

Mycobacteria are a significant health concern throughout the world.

Understanding the role of mycobactins in the iron uptake pathways of mycobacteria is an important aspect of understanding the biological processes that are related to virulence of the bacteria. Bbtan is a synthetic model for a variety of mycobactin and carboxymycobactin molecules, which forms a stable complex with iron ($\log \beta_{110} = 26.96$, $pFe = 22.73$) and exhibits a relatively positive redox potential for the iron-Bbtan complex ($E_{1/2} = -300$ mV vs NHE). These observations are consistent with the proposal of the role of mycobactins as secondary iron chelators which receive iron from exochelins in conditions where the uptake pathways of the exochelins are overloaded. Upon receiving iron from the exochelins, the iron is stored until needed, at which time reductases reduce the iron to the 2+ oxidation state, which facilitates the release and transport of the iron across the cell membrane for use by the bacterium.

6. Characterization of the iron binding ability of the Trojan Horse antimicrobial agent, PF-02538084

6.1. Introduction

One moiety that has been shown to be a potent feature in antimicrobial agents is the β -lactam functional group. There are presently a number of proposed and commercially available antimicrobial agents featuring the β -lactam moiety, including the penicillins, cephalosporins, nocardicin A, aztreonam, and fortam (Fig. 6.1.). β -lactam antibiotics generally act by inhibiting proper formation of the peptidoglycan cell wall of the bacterium, which leads to death.(157) In the case of aztreonam (Fig. 6.1.), the molecule has shown high efficacy against a range of gram-negative bacteria, but it has been found to be ineffective at treating infections of *Pseudomonas* species of bacteria.(158, 159) Infections by *Pseudomonas* species bacteria contribute to a number of diseases in mammals and plants, and are of special concern in immunocompromised patients.(160) Patients who suffer from severe burns or cystic fibrosis are particularly susceptible to diseases caused by *Pseudomonas*, which could result in complications in their treatment and possibly death. Due to the risk associated with *Pseudomonas* infection and the possibility of the development of multi-drug resistant strains of *Pseudomonas*, developing new and effective treatments for *Pseudomonas* infection is highly desirable.

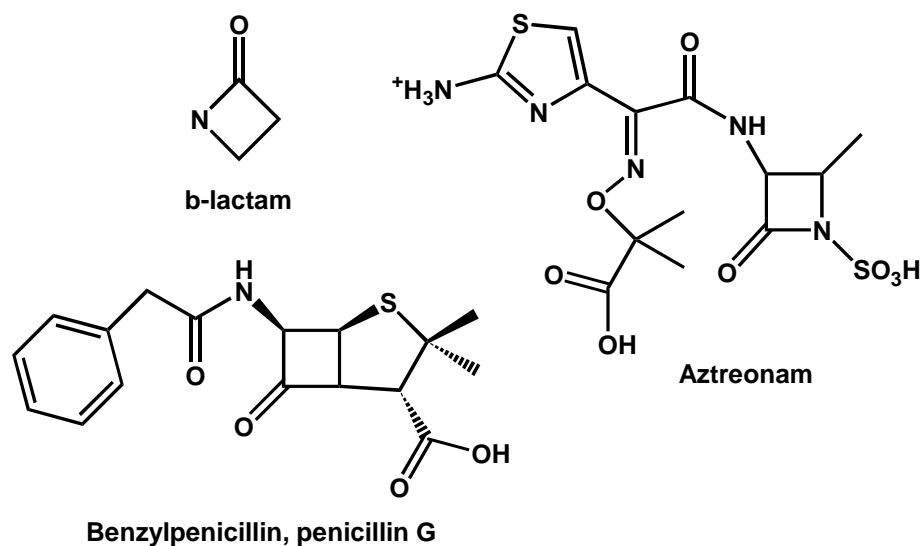


Figure 6.1. Chemical structures of the β -lactam moiety utilized in antimicrobial agents, such as the commercially-available Aztreonam and penicillin G.

One possible solution is the development of a Trojan Horse drug featuring the β -lactam moiety. As mentioned in Chapter 1, in the context of this dissertation, a Trojan Horse drug is a molecule that incorporates two functional segments: an iron binding moiety and an antimicrobial moiety. The Trojan Horse drug bypasses normal defense mechanisms of bacteria by making use of normal iron-uptake pathways of the microbe, transporting the antimicrobial moiety, such as the β -lactam moiety, into the microbe, where it is activated. One such molecule that has been developed and studied is pirazmonam, shown in Fig. 6.2. It features a tail with a β -lactam moiety and high structural similarity to aztreonam attached to a 3-hydroxy-4-pyridinone donor group. PF-02538084 (L^{PF}), also shown in Fig. 6.2., is a β -lactam-based molecule, which could have interesting potential as an antimicrobial agent. Although the mechanism of uptake

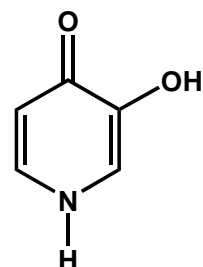
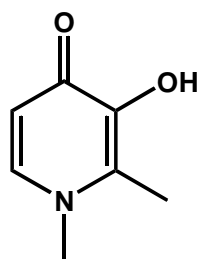
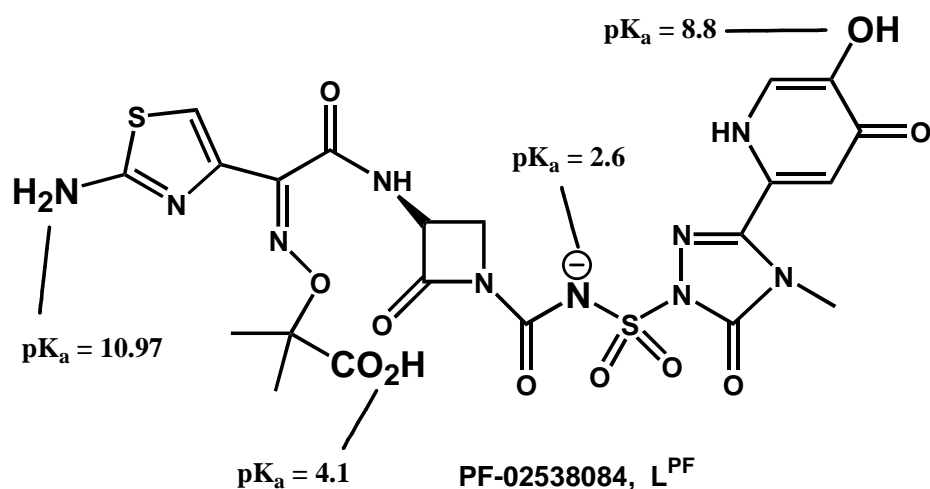
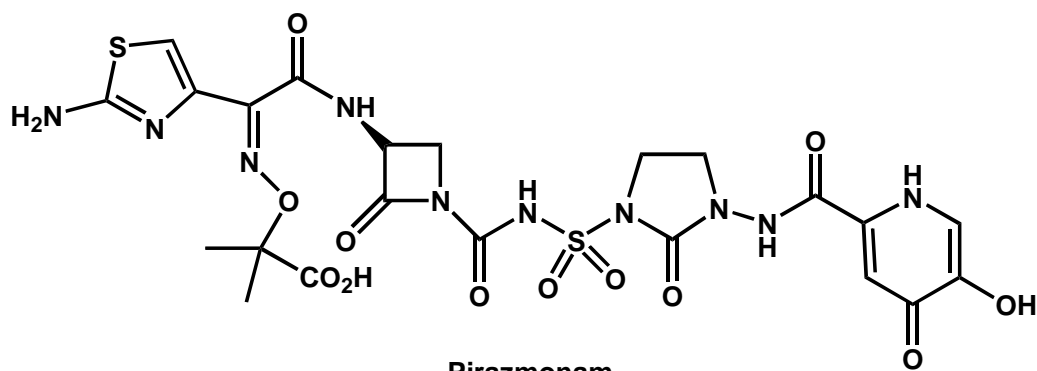


Figure 6.2. Representative structures of β -lactam based Trojan horse antibiotics, Pirazmonam and PF-02538084 (L^{PF}). The ionizable groups of L^{PF} are highlighted in larger text. Also shown are the analogous hydroxypyridinone iron chelators, 1,2-dimethyl-3-hydroxy-4-pyridinone, DMHP, and 3-hydroxy-4-pyridinone, 3,4-HOPO.

of the molecule has not yet been characterized, the molecule has been shown to interact strongly with penicillin-binding protein (PBP 3) of *E. coli* and has strong resistance to inactivation by β -lactamase.(161) In this study, the term L^{PF} is meant to represent the collective protonated forms of PF-02538084, while specific protonated forms of the ligand will be referred to as H_4L^{PF+} , H_3L^{PF} , H_2L^{PF-} , etc. The molecule L^{PF} also contains a 3-hydroxy-4-pyridinone moiety, intended to promote sequestration of iron. Thus, L^{PF} is viewed as a Trojan Horse drug, as it features a common antimicrobial moiety (the β -lactam moiety) attached to a moiety that is selective for binding iron and can facilitate uptake of the entire molecule through normal iron uptake pathways. This provides a method of action in some species of bacteria that have proven resistant to other β -lactam-based antimicrobial agents or in multi-drug resistant bacteria.

One method of assessing the effectiveness of an antimicrobial agent is through its minimum inhibitory concentration (MIC), which is defined as the minimum concentration of the molecule required to prevent visible colonies of bacteria from growing in culture overnight.(162) L^{PF} has been found to have a low MIC in *P. aeruginosa* compared to aztreonam and similar MIC values to aztreonam for other gram negative bacteria. It has also been shown that L^{PF} has much lower affinity for penicillin-binding protein in some species of gram negative bacteria than aztreonam making it a possible candidate for treatment of *Pseudomonas* species infections.(161)

6.2. Statement of chapter objectives

It is the purpose of this study to examine the iron binding capabilities of L^{PF} to determine the mode of binding, complex stoichiometry, and ligand Fe(III) affinity. This has been done through a series of potentiometric and spectrophotometric titrations, as well as electrochemical characterization of the complex over a range of pH. This characterization yields some information on the role of iron binding in the potential effectiveness of L^{PF} as an antimicrobial agent.

If a complexing agent is to be used in biological systems, it is important to ensure that the complex exhibits a reduction potential outside of the range of biological reductants to prevent redox cycling in the patient (see Sec. 1.5.). Due to these factors, it is also desirable to investigate the redox chemistry of iron-siderophore complexes.

6.3. Experimental

6.3.1. Materials

Samples of PF-02538084 (L^{PF}) were obtained from Pfizer, prepared as previously reported and were used as received without further purification (see Appendix D).(163)

ESI mass spectra of the compound exhibited an M^+ peak of 655, suggesting purity and identity of the product. H-NMR spectra also supported high purity of the product (see Appendix D). Solid NaClO_4 (99.99%, Sigma-Aldrich) was obtained for preparation of background electrolyte. Solutions of 0.10 M NaOH and 0.10 M HClO_4 were prepared and standardized to the phenolphthalein endpoint against KHP and standardized NaOH, respectively. Stock solutions of $\text{Fe}(\text{ClO}_4)_3$ in 0.10 M HClO_4 were prepared and standardized by reduction with SnCl_2 and titration with $\text{K}_2\text{Cr}_2\text{O}_7$.(93)

6.3.2. Protonation constant determination

Initial experiments were performed to characterize the protonation constants of L^{PF} , involving potentiometric and spectrophotometric titrations of the molecule. Spectrophotometric titrations were performed on solutions of 30 μM ligand in 0.10 M NaClO_4 background electrolyte. Solution pH was adjusted by titration with 0.10 M NaOH. All pH measurements were made with an Orion 230 A+ pH/ion meter equipped with an Orion Ross pH electrode filled with 3 M NaCl solution. The electrode was calibrated by the "classical method," titration of standardized 0.10 M HClO_4 with standardized 0.10 M NaOH.(95) Calibration data were analyzed using the computer program, GLEE.(96) UV-visible spectra were recorded with the Cary-50 spectrophotometer equipped with an external dip probe (Hellma, USA). Analysis of the measured spectra was performed using the program, HYPERQUAD, using a 4-proton model.(143)

6.3.3. Solution equilibria

Experiments were performed to determine the stoichiometry of the Fe(III)-L^{PF} complex. A titration was performed using a solution with a set ratio of Fe(III) to ligand with a solution of free ligand in a buffered solution at pH 7.0. The initial solution was prepared at a molar ratio of 3 moles ligand to 2 moles Fe(III). The ratio of moles ligand per mole Fe(III) was raised in a series of 2.0 mL aliquots and UV-visible spectra were measured of the complexes over a range of L^{PF}:Fe molar ratios from 1.5 to 6.0.

To characterize the stability constant of the fully coordinated complex, a spectrophotometric titration was performed to monitor the competition reaction between the Fe(III)-L^{PF} complex and EDTA. A solution was prepared at a 5:1 molar ratio of L^{PF}:Fe(III) at a pH of 6.03 in solution buffered with 0.25 M MES, a pH chosen to facilitate the formation of the fully coordinated complex. Additions of 0.10 M EDTA solution in the MES buffered solution over a range of EDTA:Fe(III) ratios from 0:1 to 10:1 were performed and spectra were measured at each EDTA concentration after allowing overnight equilibration. The equilibrium being monitored in this reaction is shown in Eqs. 6.1.-6.2. Spectra measured in the competition reaction with EDTA are



$$K_{\text{obs}} = \frac{[\text{Fe}(\text{EDTA})^-][\text{H}_2\text{L}^{\text{PF}-}]^3}{[\text{Fe}(\text{HL}^{\text{PF}})_3^{3-}][\text{H}_2\text{EDTA}^{2-}][\text{H}^+]} \quad (6.2)$$

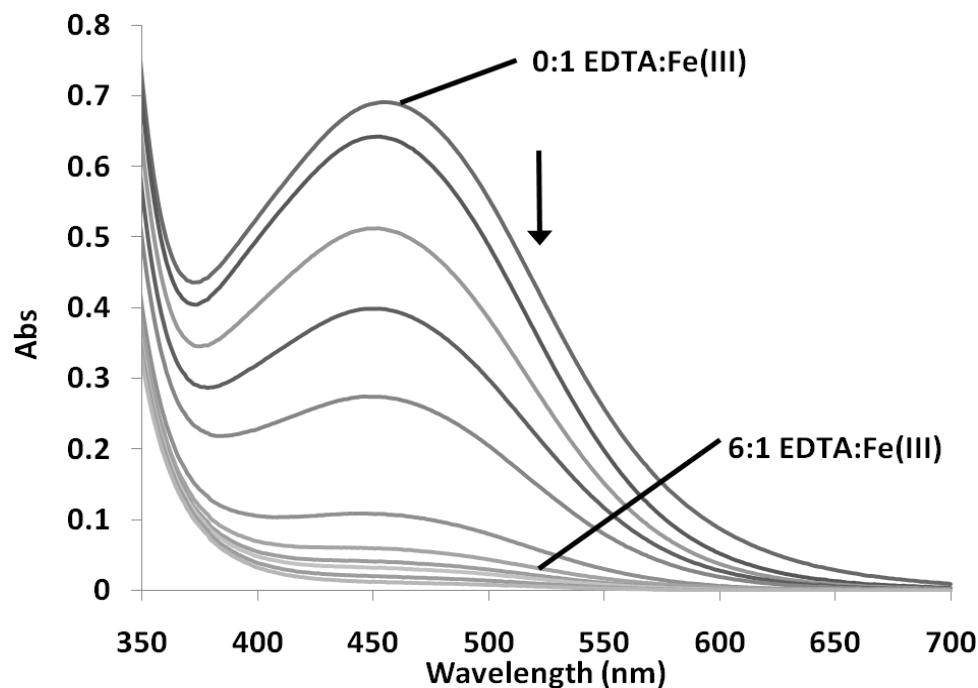


Figure 6.3. UV-Visible spectra obtained from the competition experiment between the $\text{Fe}(\text{HL}^{\text{PF}})_3^{3-}$ complex and EDTA. The concentration ratio of EDTA to iron(III) ranges from 0 equivalents EDTA to 10 equivalents EDTA. Experiment was performed in 0.25 M MES buffer at pH 6.03, $T = 25\text{ }^\circ\text{C}$ and $\mu=0.10\text{ M}$ (NaClO_4).

shown in Fig. 6.3. The equilibrium spectra were analyzed with the program, HYPERQUAD, using a model featuring only one pK_a from L^{PF} corresponding to the hydroxypyridinone group, the determined iron-binding group of the molecule (see below).

pH-dependent spectrophotometric titrations were performed to characterize the binding state of the complex over a range of pH values and to determine the stability constants of those complexes. Three separate sets of titrations were performed, going from low pH to high pH (pH 2 to 11), high to low pH (pH 12 to 2) and low to lower pH (pH 6 to approximately 0.5). In all three titrations, 5:1 molar ratio $L^{PF}:Fe$ solutions were prepared in 0.10 M $NaClO_4$. In the low-to-high pH titration, the solution was titrated with standardized 0.10 M $NaOH$. In the high-to-low pH titration, the solution was titrated with 0.10 M $HClO_4$. In the low-to-lower pH titration, the solution was titrated with 1.0 M $HClO_4$. In the high-to-low titration and the low-to-lower pH titration, 15 minutes equilibration time was given after each addition to ensure complete reaction of the complex. Spectra were analyzed with the program HYPERQUAD to determine the stepwise equilibrium constants for the $Fe-L^{PF}$ complexes.

6.3.4. Electrochemical studies of the $Fe-L^{PF}$ system

Cyclic voltammetric experiments were performed on the $Fe(III)-L^{PF}$ system. A 5:1 $L^{PF}:Fe(III)$ solution was prepared in 0.10 M $NaClO_4$ and the solution was titrated with 0.10 M $NaOH$. Measurements were taken using a BASi Controlled Growth Mercury Electrode set to the static mercury drop electrode mode as the working electrode, a $Ag/AgCl$ in 3.5 M KCl reference electrode and a platinum wire auxiliary electrode. The working electrode potential was controlled by a Princeton Applied Research Model 263

potentiostat, controlled by the PowerSuite computer software. The solution pH was varied using standardized NaOH over the pH range of 1 to 9 and cyclic voltammograms were measured periodically. To investigate the possibility of reduction of the ligand, a cyclic voltammogram was measured for L^{PF} alone in a solution buffered at pH 7.2. All potentials are reported versus NHE by applying a 205 mV correction to the observed values.

6.4. Results and Discussion

6.4.1. Ligand protonation constants

Characteristic spectra obtained from the spectrophotometric titration of L^{PF} are shown in Figure 6.4. Over the pH range of approximately pH 2 to pH 12, there are three separate equilibria observed, as suggested by three distinct isosbestic points observed over the pH ranges of 2.1 to 5.6 (Fig. 6.4.A), 6.9 to 9.2 (Fig. 6.4.B), and above 10 (Fig. 6.4.C). The L^{PF} molecule contains four ionizable groups, shown in Figure 6.2. Protonation constants were determined from three replicate titrations using the program, HYPERQUAD using a 4-proton model, and the resulting pK_a 's are shown in Table 6.1. and Fig. 6.2.

The values measured are consistent with expected ranges of protonation constants of the predicted ionizable groups. The protonation constant, $pK_{a4} = 10.97$,

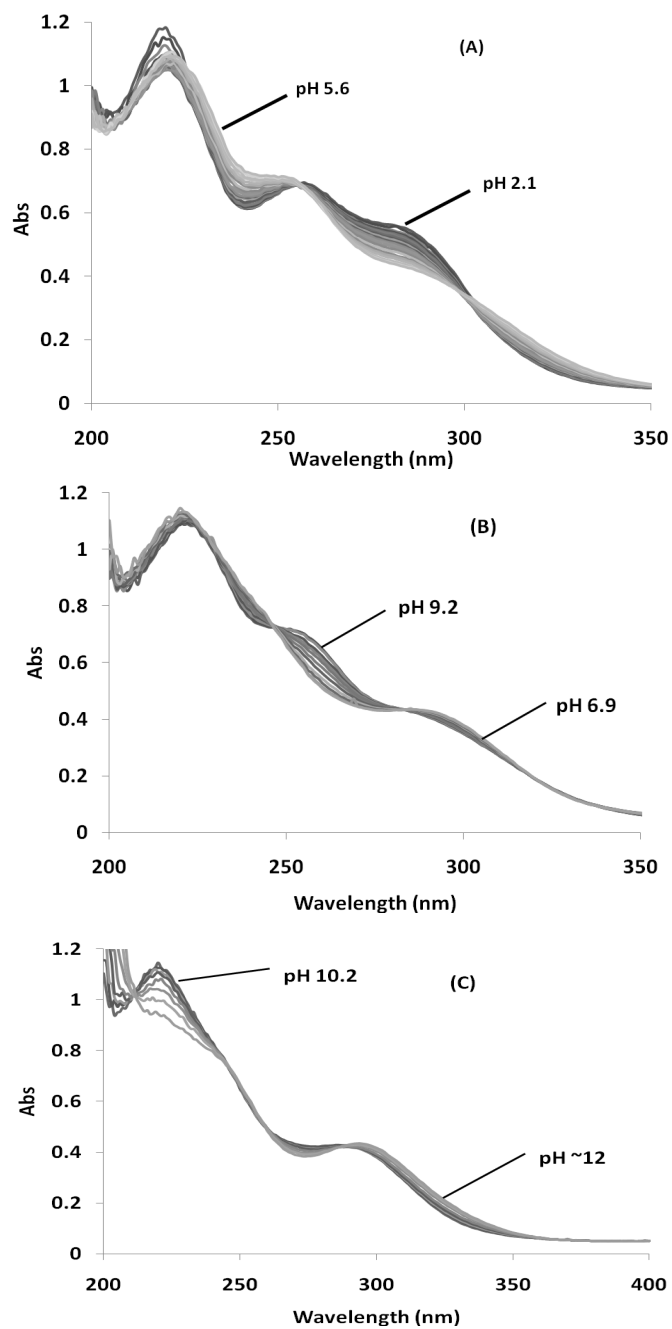


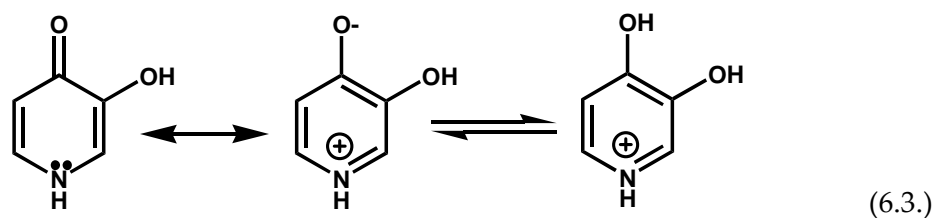
Figure 6.4. Spectra of three separate equilibria observed in the spectrophotometric titration of L^{PF} . $[L^{PF}]_{tot} = 30 \mu\text{M}$, $\mu = 0.10 \text{ M (NaClO}_4\text{)}$, $T = 25 \text{ }^\circ\text{C}$. (A) pH 2.1 to 5.6, (B) pH 6.9 to 9.2, (C) above pH 10.

Table 6.1. Equilibrium constants determined for the proton-dependent and proton-independent reactions of L^{PF} with Fe(III). Numbers shown in parentheses are the standard deviation of the value as determined from the program, HYPERQUAD. All experiments were performed at T = 25 °C and μ = 0.10 M (NaClO₄).

Reaction	K or β	log K
$L^{PF\ 3-} + H^+ \rightleftharpoons HL^{PF\ 2-}$	pK _{a1}	10.97 (0.07)
$HL^{PF\ 2-} + H^+ \rightleftharpoons H_2L^{PF\ -}$	pK _{a2}	8.8 (0.6)
$H_2L^{PF\ -} + H^+ \rightleftharpoons H_3L^{PF}$	pK _{a3}	4.1 (0.2)
$H_3L^{PF} + H^+ \rightleftharpoons H_4L^{PF\ +}$	pK _{a4}	2.6 (0.2)
$Fe(H_2O)_6^{3+} + 3 HL^{PF\ 2-} \rightleftharpoons Fe(HL^{PF})_3^{3-} + 6 H_2O$	β ₁₃₀	31.91 (0.02)
$Fe(H_2O)_6^{3+} + 3 H_2L^{PF\ -} \rightleftharpoons Fe(HL^{PF})_3^{3-} + 3 H^+ + 6 H_2O$	K ₁₃₀	5.5 (0.3)
$Fe(H_2O)_6^{3+} + 2 HL^{PF\ 2-} \rightleftharpoons Fe(HL^{PF})_2(H_2O)_2^{2-} + 4 H_2O$	β ₁₂₀	22.07 (0.09)
$Fe(HL^{PF})_2(H_2O)_2^{2-} + (HL^{PF})^{2-} \rightleftharpoons Fe(HL^{PF})_3^{3-}$	β ₃	9.84 (0.09)
$Fe(HL^{PF})_2(H_2O)_2^{2-} + H_2L^{PF\ -} \rightleftharpoons Fe(HL^{PF})_3^{3-} + H^+$	K ₃	1.0 (0.2)
$Fe(H_2O)_6^{3+} + 2 H_2L^{PF\ -} \rightleftharpoons Fe(HL^{PF})_2(H_2O)_2^{2-} + 2 H^+ + 4 H_2O$	K ₁₂₀	4.5 (0.3)
$Fe(H_2O)_6^{3+} + HL^{PF\ 2-} \rightleftharpoons Fe(HL^{PF})(H_2O)_4^{+} + 2 H_2O$	β ₁₁₀	11.347 (0.005)
$Fe(H_2O)_6^{3+} + H_2L^{PF\ -} \rightleftharpoons Fe(HL^{PF})(H_2O)_4^{+} + H^+ + 2 H_2O$	K ₁₁₀	2.5 (0.2)
$Fe(HL^{PF})(H_2O)_4^{+} + HL^{PF\ 2-} \rightleftharpoons Fe(HL^{PF})_2(H_2O)_2^{2-} + 2 H_2O$	β ₂	10.6 (0.2)
$Fe(HL^{PF})(H_2O)_4^{+} + H_2L^{PF\ -} \rightleftharpoons Fe(HL^{PF})_2(H_2O)_2^{2-} + H^+$	K ₂	1.8 (0.3)
$Fe(HL^{PF})_3^{3-} \rightleftharpoons Fe(HL^{PF})_2(L^{PF})^4 + H^+$	K _{aFe1}	9.0 (0.2) ^a
$Fe(HL^{PF})_2(L^{PF})^4 \rightleftharpoons Fe(HL^{PF})(L^{PF})_2^4 + H^+$	K _{aFe2}	9.9 (0.4) ^a

^a The equilibria shown in these equations represent the sequential loss of two protons from the Fe(HL^{PF})₃³⁻ complex at higher pH

corresponding to tertiary amines ($pK_a \sim 10$), while $pK_{a3} = 8.8$, consistent with the literature protonation constant of hydroxypyridinone moieties ($pK_a = 8-9$). The observed $pK_{s2} = 4.1$, corresponding to the carboxylic acid moiety ($pK_a \sim 4$), and $pK_{a1} = 2.8$, similar to sulfonamide moieties ($pK_a \sim 2.6$).^(130, 164) The spectrophotometric titration demonstrates only three spectral shifts, which would suggest only three ionizable groups. However, the optimal fit of determined protonation constants to experimental data was obtained using a 4-protonation constant model. This suggests either a spectrally silent protonation reaction, or two spectrally similar protonation transitions. The molecule contains other amide protons, which might have lower protonation constants, but these would not be observable at the pH range in which these experiments were performed. Literature reports also suggest that a second protonation constant corresponding to protonation of the neutral hydroxypyridinone donor group would be observable at low pH (Eq. 6.3.), but it is also probable



that electrostatics and electronic structure of the molecule would prevent the observation of such an equilibrium in this system.

Potentiometric titrations were also performed to characterize the protonation constants for L^{PF} (Fig. 6.5). However, when solving for the protonation constants using HYPERQUAD, the fit of the determined protonation constants to the experimental data was less precise than that obtained from the spectrophotometric titration. As spectrophotometric titrations are a more sensitive measurement of the protonation state of the molecule, the values obtained from spectrophotometric titration were taken as the actual deprotonation constants of L^{PF} . A speciation diagram for the protonation of L^{PF} is shown in Fig. 6.6.A.

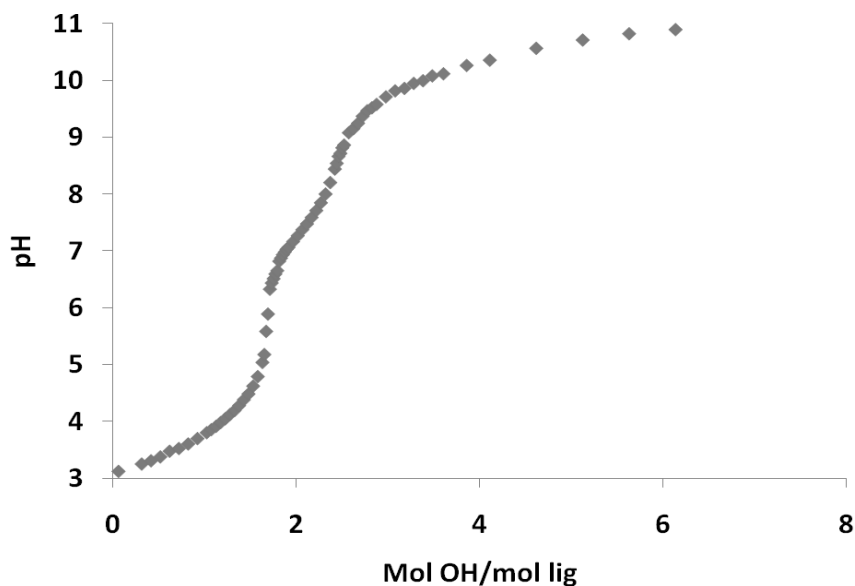


Figure 6.5. Potentiometric titration of L^{PF} , showing the plot of pH versus mol OH/mol ligand. Conditions: $[L^{PF}]_{tot} = 1.0 \text{ mM}$, $\mu = 0.10 \text{ M}$ (NaClO_4), $T = 25 \text{ }^\circ\text{C}$.

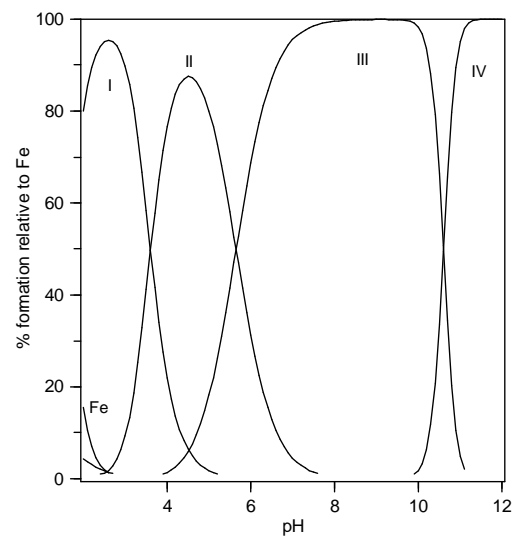
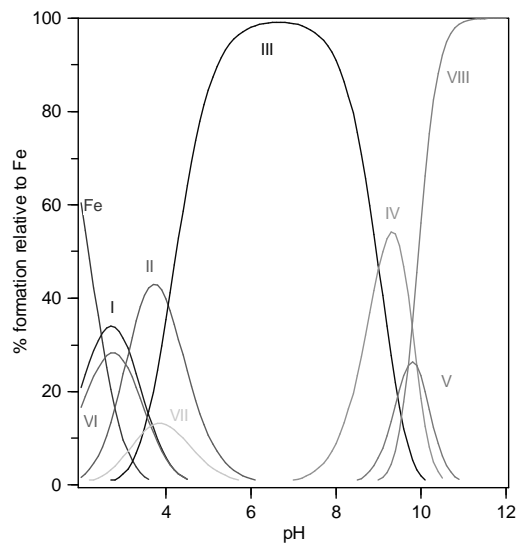
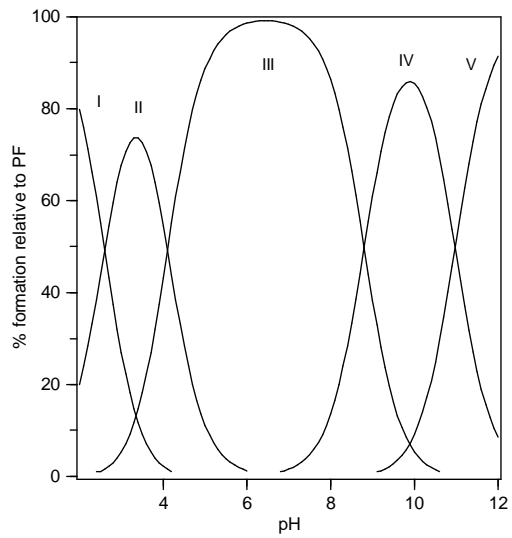


Figure 6.6. Speciation diagram for (A) the free ligand L^{PF} , (B) the Fe(III)- L^{PF} system and (C) the Fe(III)-DMHP system, calculated using the determined and literature equilibrium constants.⁽¹⁶⁵⁾ Graph shows relative amount of total iron in different forms over a range of pH values. In graph (A), $[Fe^{3+}]_{tot} = 0$ M, $[L^{PF}]_{tot} = 10^{-5}$ M, $T = 25$ °C and $\mu = 0.10$ (NaClO₄). In graphs (B) and (C), $[Fe^{3+}]_{tot} = 10^{-6}$ M, $[L]_{tot} = 10^{-5}$ M, $T = 25$ °C and $\mu = 0.10$ (NaClO₄). Key: (A) I = H_4L^{PF+} , II = H_3L^{PF} , III = H_2L^{PF-} , IV = HL^{PF2-} , and V = L^{PF3-} . (B) I = $Fe(HL^{PF})(H_2O)_4^+$, II = $Fe(HL^{PF})_2(H_2O)_2^+$, III = $Fe(HL^{PF})_3^+$, VI = $Fe(HL^{PF})_2(L^{PF})_4^-$, and V = $Fe(HL^{PF})(L^{PF})_2^{5-}$. VI-VIII represent hydrolyzed forms of free metal ion, $Fe(OH)^{2+}$, $Fe(OH)_2^+$, and $Fe(OH)_4^-$, respectively. (C) I = $Fe(DMHP)(H_2O)_4^{2+}$, II = $Fe(DMHP)_2(H_2O)_2^+$, III = $Fe(DMHP)_3$, and IV = $Fe(OH)_4^-$. In both (B) and (C), Fe represents free aqueous iron(III).

6.4.2. Iron complex equilibria: complex structure

Based on titrations designed to determine the stoichiometry of the complex described below, it will be demonstrated that one mole of iron(III) will bind to 3 moles of L^{PF} , forming an FeL_3 complex at physiological pH. Further, it will be shown that comparisons of the spectrophotometric handles of the complex over a range of solution pH values to literature studies of 3-hydroxy-4-pyridinone complexes showed that L^{PF} binds to iron(III) exclusively via the 3-hydroxy-4-pyridinone moiety.

It was observed that in the preparation of these solutions, at low molar ratios, such as 1:1, iron(III) would precipitate out of solution in the form of a brown precipitate, presumably iron hydroxide, in the pH range of approximately 2-3, followed by a slow dissolution at higher pH values (dissolution time varying from 5 minutes to 2 hours dependent on the concentration of the ligand and the solution pH). A minimum molar ratio of 3 L^{PF}:2 Fe would prevent precipitation of iron(III), and an increase in the L^{PF}:Fe ratio resulted in increased complex formation through 4:1 L^{PF}:Fe ratio (Fig. 6.7.). The

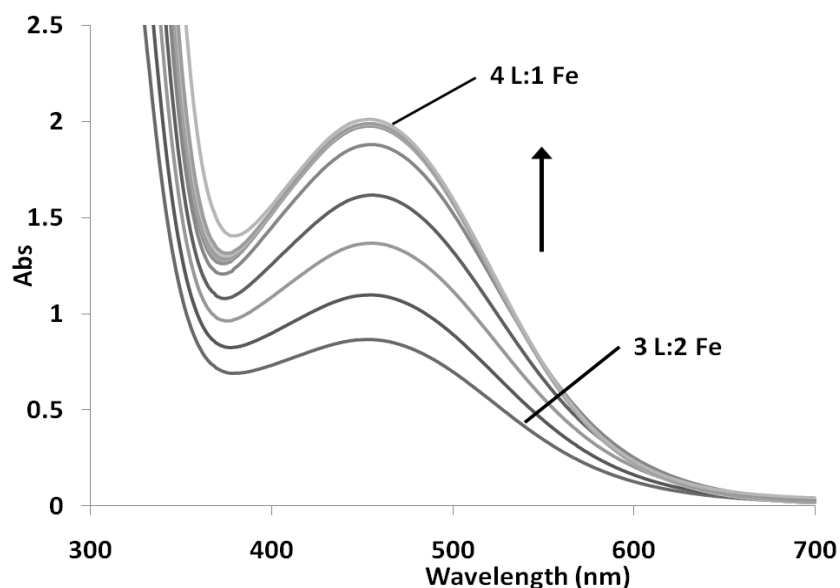


Figure 6.7. Spectrophotometric titration of the Fe(III)-L^{PF} system over a range of L^{PF}:Fe ratios from 3:2 to 4:1. Absorbances are corrected for dilution. Conditions: [Fe³⁺]_{tot} = 3.0 × 10⁻⁴ M, pH = 7.01 (0.25 M MES buffer), μ = 0.10 M (NaClO₄), T = 25 °C. Arrow indicates the change in spectral intensity as the L^{PF}:Fe ratio increased. Solutions were stored out of the light until measurement to prevent complex degradation.

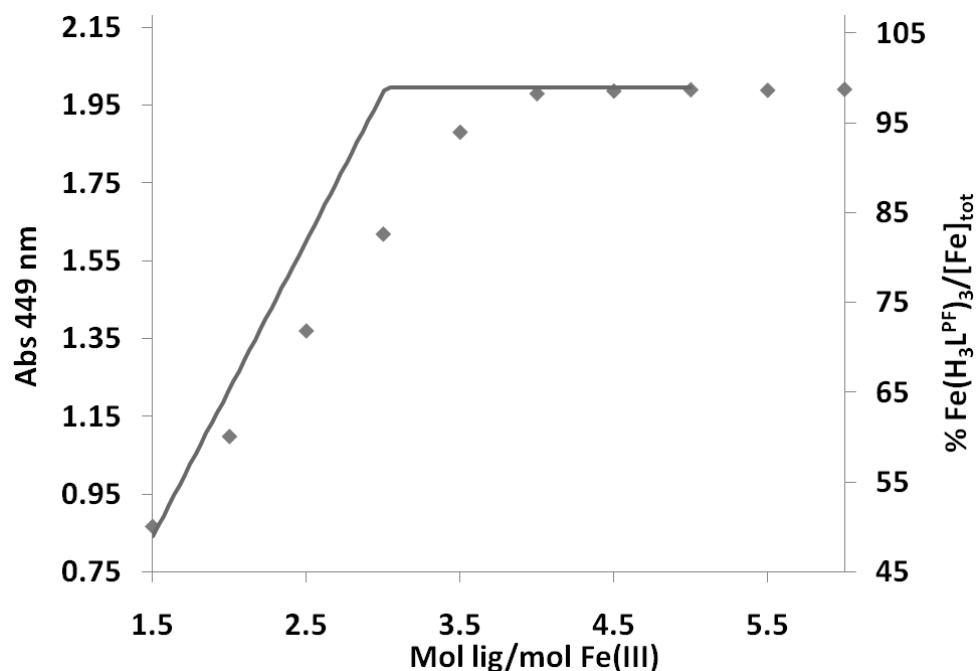


Figure 6.8. Diamonds/left y-axis represents a plot of absorbance at 449 nm for a series of spectra measured over a range of ratios of ligand to metal for the Fe-L^{PF} system.

The line/right y-axis represents a theoretical fit of percent iron bound in the Fe(HL^{PF})₃³⁻ complex as a function of moles ligand:moles Fe(III). The theoretical fit was calculated from the speciation simulation of the Fe-L^{PF} system using the determined complex formation constants and the protonation constant of the hydroxypyridinone donor group as described in the text. Spectra were measured in a 0.10 M NaClO₄ solution buffered at pH 7.01 with 0.25 M MES, T = 25 °C. Solutions were stored out of the light until measurement to prevent complex degradation.

graph of the absorbance measured at the λ_{\max} , 449 nm from this experiment, adjusted for dilution, plotted as a function of the number of moles of ligand per mole Fe(III) is shown in Figure 6.8. The observed maximum absorbance at a 4:1 L^{PF} :Fe ratio suggests that the equilibrium occurring in solution at the experimental conditions involved the formation of the FeL_3 complex. The spectra measured during the titration were also used to calculate the λ_{\max} and molar absorptivity of the FeL_3 complex (Table 6.2.).

The spectra measured from pH-dependent spectrophotometric titrations of the system are shown in Figs. 6.9.-6.11., where clean isosbestic points indicated conversion between two complexes. In the low-to-high pH titration (Figure 6.10.), one spectral shift was observed over the pH range of 2.3 to 5.5, with an initial λ_{\max} of 483 nm and a final λ_{\max} of 452 nm. A second equilibrium was observed over the range of pH 6.1 to pH 7.9, with a final λ_{\max} of 458 nm. The final shift was observed from pH 8.2 to pH 10.6, with a

Table 6.2. Observed wavelengths of maximum absorbance for the iron(III)- L^{PF} complex system and molar absorptivities of the complexes, calculated by the program HYPERQUAD. Literature values for the FeL through FeL_3 complexes of the iron(III)-DMHP system are shown for comparison. L represents the respective hydroxypyridinone-donor chelators, L^{PF} or DMHP.

Complex	λ_{\max} (nm) L = L^{PF}	ϵ ($M^{-1} cm^{-1}$) L = L^{PF}	$\lambda_{\max, lit}$ (nm) ^a L = DMHP
ML	543	2660	538
ML ₂	499	4480	488
ML ₃	451	7160	446
ML ₃ H-	458	5895	
ML ₃ H ₂ -	472	6950	

^aLiterature values are taken from Ref (165).

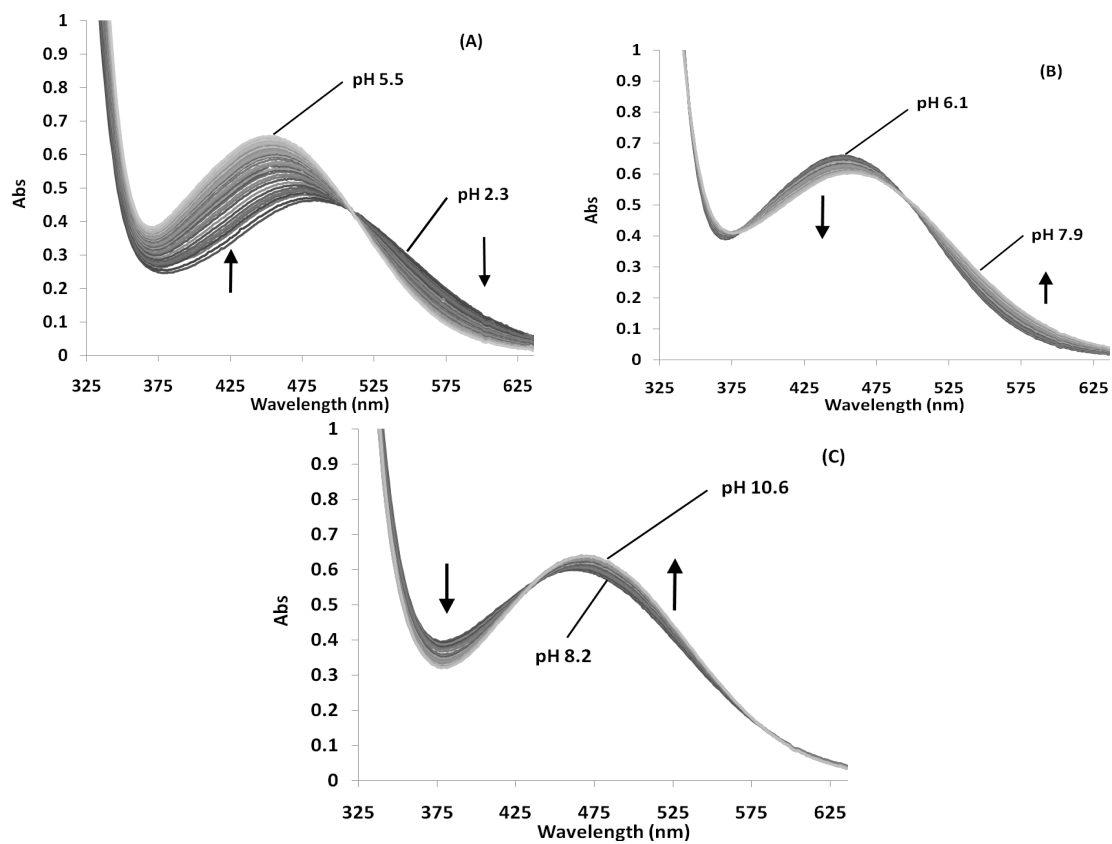


Figure 6.9. Spectrophotometric titration of the 5:1 $L^{PF}:Fe$ system as a function of pH from pH 2.3 to 10.6. (A) Spectra measured over the pH range of 2.3 to 5.5. (B) Spectra measured over the pH range of 6.1 to 7.9. (C) Spectra measured over the pH range of 8.2 to 10.6. Conditions: $[Fe^{3+}]_{tot} = 1.05 \times 10^{-4} M$, $[L^{PF}]_{tot} = 5.26 \times 10^{-4} M$, $T = 25 \text{ }^\circ C$, $\mu = 0.10$ ($NaClO_4$). Arrows indicate the direction of spectral shifts with changes in pH.

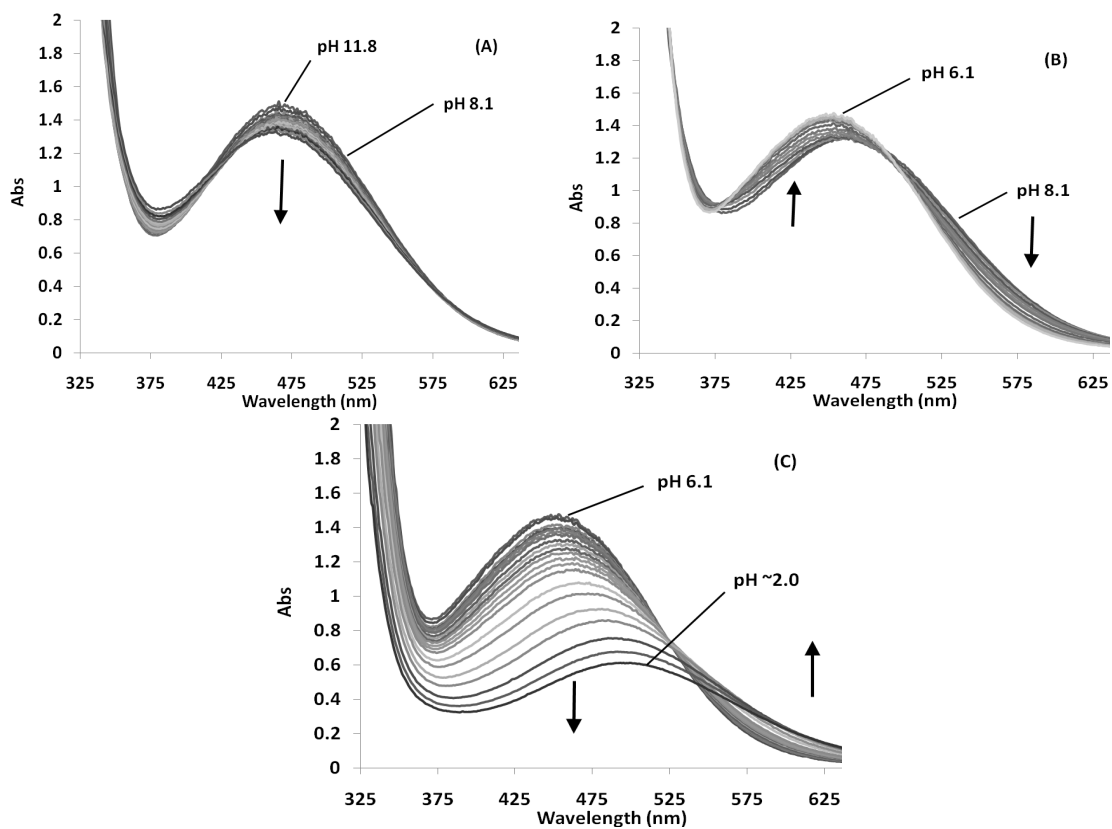


Figure 6.10. Spectrophotometric titration of the 5:1 L^{PF} :Fe system as a function of pH over the pH range of 11.8 to ~2.0. (A) Spectra measured over the pH range of 11.8 to 8.1. (B) Spectra measured over the pH range of 8.1 to 6.1. (C) Spectra measured over the pH range of 6.1 to ~2.0. Conditions: $[Fe^{3+}]_{tot} = 2.9 \times 10^{-4} M$, $[L^{PF}]_{tot} = 1.5 \times 10^{-3}$, $\mu = 0.10 M$ ($NaClO_4$), $T = 25 \text{ }^\circ C$. Arrows indicate the direction of spectral shifts with decreasing pH.

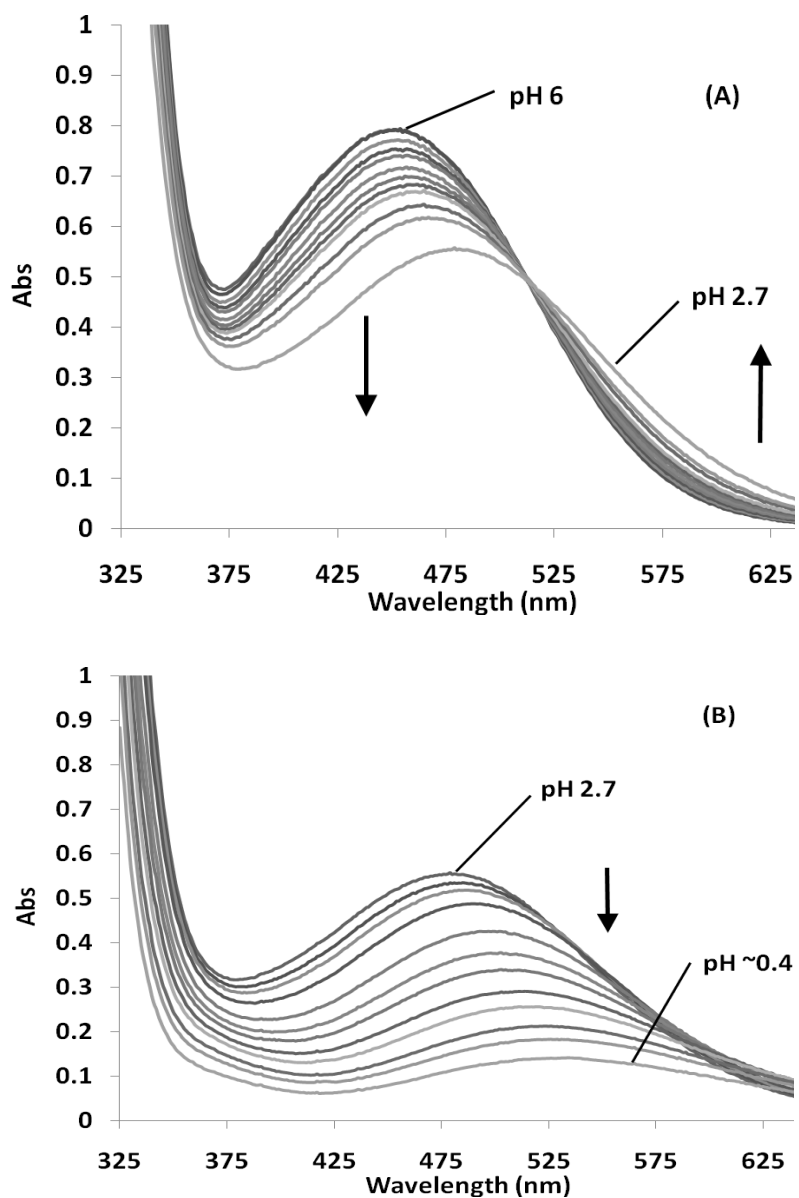


Figure 6.11. Spectrophotometric titration of the 5:1 L^{PF}:Fe system as a function of pH from pH 6.3 to ~0.4. (A) Spectra measured over the pH range of 6 to 2.7. (B) Spectra measured over the pH range of 2.7 to ~0.4. Conditions: [Fe³⁺]_{tot} = 1.19 × 10⁻⁴ M, [L^{PF}]_{tot} = 6.7 × 10⁻⁴ M, T = 25 °C, μ = 0.10 (NaClO₄). Arrows indicate the direction of spectral shifts with decreasing pH.

final λ_{\max} of 472 nm. The spectrophotometric titration of the Fe(III)-L^{PF} system going from pH 11.8 to 2.0 is shown in Fig. 6.9., where the spectral shifts exhibited were very similar to those observed from increasing the solution pH over the same range (Fig. 6.10.). A second low-pH spectrophotometric titration from pH 6 to ~0.4 (Fig. 6.11.) exhibited a second spectral transition below pH 2.7 (Fig. 6.11.B), where the λ_{\max} increased from 481nm and the spectral intensity decreased, partly due to dilution from increasing volumes required to change the pH. The shifts in spectral handles over a range of solution pH values can be used to characterize the species present in solution, as well as the L^{PF} complex equilibria (shown in Table 6.1.), as will be discussed later.

The composition of the species observed in these equilibria were determined by comparison with the observed λ_{\max} values of 3-hydroxy-4-pyridinone complexes from a previous study (Table 6.2.).⁽¹³⁰⁾ The λ_{\max} values observed in the spectrophotometric titrations correspond closely to those observed in previous experiments for complexes of 3-hydroxy-4-pyridinone ligands with Fe(III), suggesting that the binding mode of the ligand to iron(III) is exclusively through the 3-hydroxy-4- pyridinone donor group (Fig. 6.12.). The observed λ_{\max} of the solution around pH 2.5 and 6.1 correspond closely to the literature values for 3-hydroxy-4-pyridinone ligands, suggesting binding of L^{PF} with Fe(III) through the hydroxypyridinone moiety, with additional loss of protons from the complex above pH 6.1 at remote sites on the ligands.

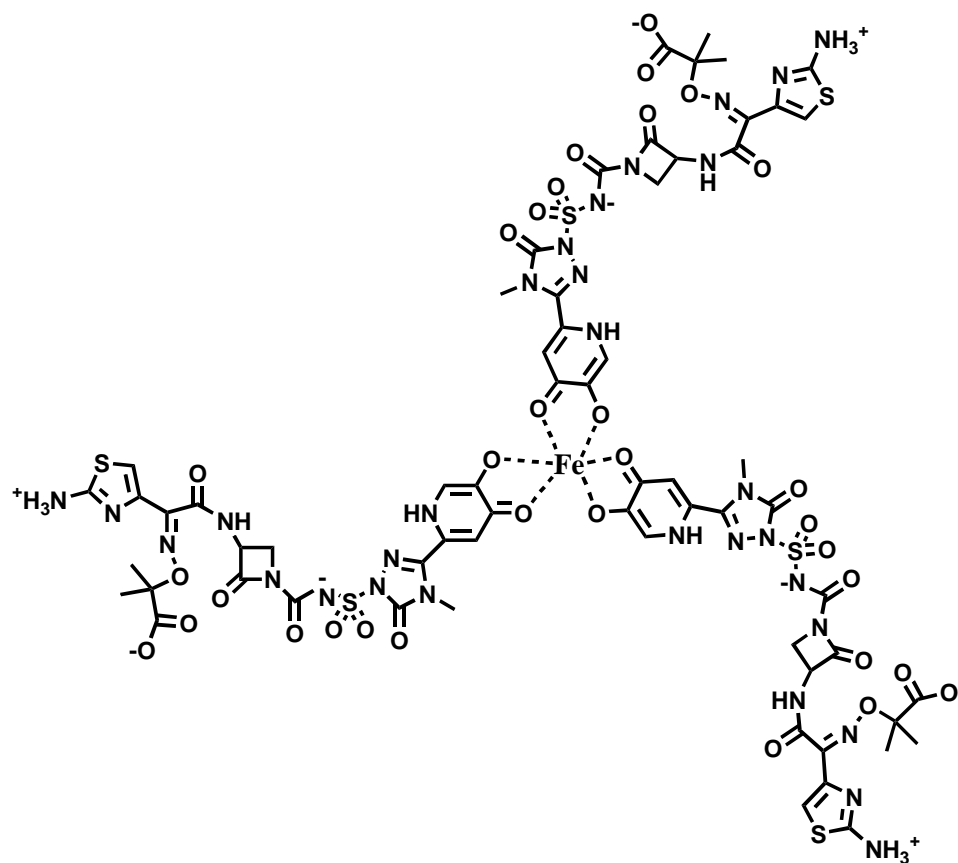


Figure 6.12. Proposed structure of the 3:1 $L^{PF}:Fe$ complex at physiological pH,



Additional evidence for the structure comes from HPLC/ESI-MS/MS experiments performed on the Fe(III)-L^{PF} system (performed by John O'Connell, et al, see Appendix C for more details). ESI mass spectra were measured of the ligand alone in positive ion mode by extracted ion chromatography, which exhibited a peak at a *m/z* ratio of 655, corresponding to the molecular weight of L^{PF}. Addition of iron to the solution resulted in observation of a peak at a *m/z* ratio of 673 units, which can be assigned to the Fe(HL^{PF})₃³⁺ complex. Additionally, collision induced dissociation spectra were measured for both the L^{PF} and the Fe(HL^{PF})₃³⁺ complex, and both exhibited fragmentation patterns consistent with the structure of L^{PF} (see Appendix C for more details).

6.4.3. Iron complex equilibria: determination of stepwise formation constants

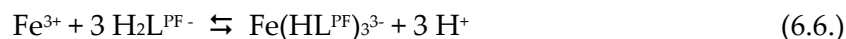
It is difficult to directly determine the equilibrium constant of the complex formation reaction between iron(III) and hydroxypyridinone chelators. The strength of binding is so high that the ligand reacts stoichiometrically, preventing accurate determination by direct titration. Therefore, a spectrophotometric competition titration with EDTA was performed to indirectly determine the complex stability constant of the Fe(III)-L^{PF} system (see Section 6.2.3.). While the stoichiometry of the fully formed Fe(III)-L^{PF} complex was determined to be 3:1 L^{PF}:Fe³⁺ (see previous section), the ligand-to-metal molar ratio of 3:1 is insufficient to provide full formation of the Fe(HL^{PF})₃³⁻ complex (see Fig. 6.8.). The EDTA competition experiment was designed at a 5:1 molar ratio of L^{PF}:Fe,

which gives complete formation of the $\text{Fe}(\text{HL}^{\text{PF}})_3^{3-}$ complex. In computing the equilibrium constants of the $\text{Fe}(\text{III})\text{-L}^{\text{PF}}$ system, it is only necessary to use the protonation constant assigned to the hydroxypyridinone O-H proton, as this group is the only group involved in the binding interaction with iron(III) as deduced from the structure of the molecule, the stoichiometry of the complex at circumneutral pH and the spectral observations of the previous section. Any further deprotonation reaction will affect the electrostatics of the interaction of the molecule with Fe^{3+} , but should not directly factor into the binding equilibria. The equilibrium constant for the formation of the $\text{Fe}(\text{HL}^{\text{PF}})_3^{3-}$ complex is shown below and in Table 6.1. The value obtained from the competition titration is the proton independent stability constant, $\log \beta_{130}$ (Eq. 6.4.-6.5.).



$$\beta_{130} = \frac{[\text{Fe}(\text{HL}^{\text{PF}})_3]}{[\text{Fe}^{3+}][\text{HL}^{\text{PF}}]^3} \quad (6.5.)$$

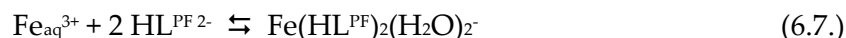
However, in solution, protons will be present to compete with iron for binding to the hydroxypyridinone moiety (Eq. 6.6.). This results in the necessity to determine the



proton-dependent stability constants, which can be done by using the protonation constant of the hydroxypyridinone moiety of the molecule. The pH-dependent and independent equilibria and determined stability constants for all reactions of the iron(III)-L^{PF} system are shown in Table 6.1.

The value determined for the log β_{130} of the complex (log $\beta_{130} = 31.91$) is lower than that of unsubstituted 3,4-HOPO (log $\beta_{130} = 34.91$) or of 1,2-dimethyl-3-hydroxy-4-pyridinone (log $\beta_{130} = 35.88$).^(165, 166) This is likely due to steric effects and decreased electron donating ability of the molecule due to the extensive conjugated electron system. A simulation of the percent iron found in the Fe(HL^{PF})₃³⁻ complex at conditions mimicking those of the complex ratio titration and using the determined log β_{130} is shown in Fig. 6.8., demonstrating good agreement between the experimental data and the theoretical calculations using our model featuring 3:1 L^{PF}:Fe³⁺ complex formation.

The low-to-high pH titrations of the Fe(HL^{PF})₃³⁻ complex (Fig. 6.10.) were used to determine the stability constant of the Fe(HL^{PF})₂²⁻ complex corresponding to Eq. 6.7., as well as the stability constant of the Fe(HL^{PF})₃³⁻ complex, Eq. 6.8., giving the proton independent overall equilibrium constant.



The high-to-low pH titration (Fig. 6.9.) displayed similar λ_{\max} values as those observed in the low-to-high pH titration (Fig. 6.10.), suggesting that the same equilibria are active during the course of the experiment. The equilibrium constants involving the $\text{Fe}(\text{HL}^{\text{PF}})^+$ complex were determined using spectra obtained from the spectrophotometric titration below pH 2.5. The spectra obtained from the spectrophotometric titration below pH 2.5. Therefore the values may be less accurate than the other determinations due to the high dilution factor.

There were two separate spectral transitions observed, one from the pH range of 6.3 to 2.7, corresponding to the transition from the $\text{Fe}(\text{HL}^{\text{PF}})_3^{3-}$ complex to the $\text{Fe}(\text{HL}^{\text{PF}})_2(\text{H}_2\text{O})_2^-$ complex (Fig. 6.11.A). Below pH 2.7, a second spectral transition was observed (Fig. 6.11.B), where the spectral λ_{\max} increased and the spectral intensity decreased, partly due to dilution from increasing volumes required to change the pH. The spectra obtained were used with the program HYPERQUAD to determine the equilibrium constants for the lower order complexes observed, namely the $\text{Fe}(\text{HL}^{\text{PF}})^+$ complex. This titration was then used to determine the stability constants of the FeL complex, however this value may be less accurate than the other determinations due to the high dilution factor present in the low pH titration.

The determined equilibrium constants and protonation constants were used to calculate the pFe value as a function of pH, shown in Fig. 6.13., and to calculate speciation models over a range of biologically relevant pH values (Fig. 6.6.). The calculated pFe value for the standard conditions at pH 7.4 is 18.2, relatively low for an iron chelator, and a plot of pFe values over a range of pH values is shown in Figure 6.13. The determined pFe value is somewhat lower than that of 3,4-HOPO, the bidentate

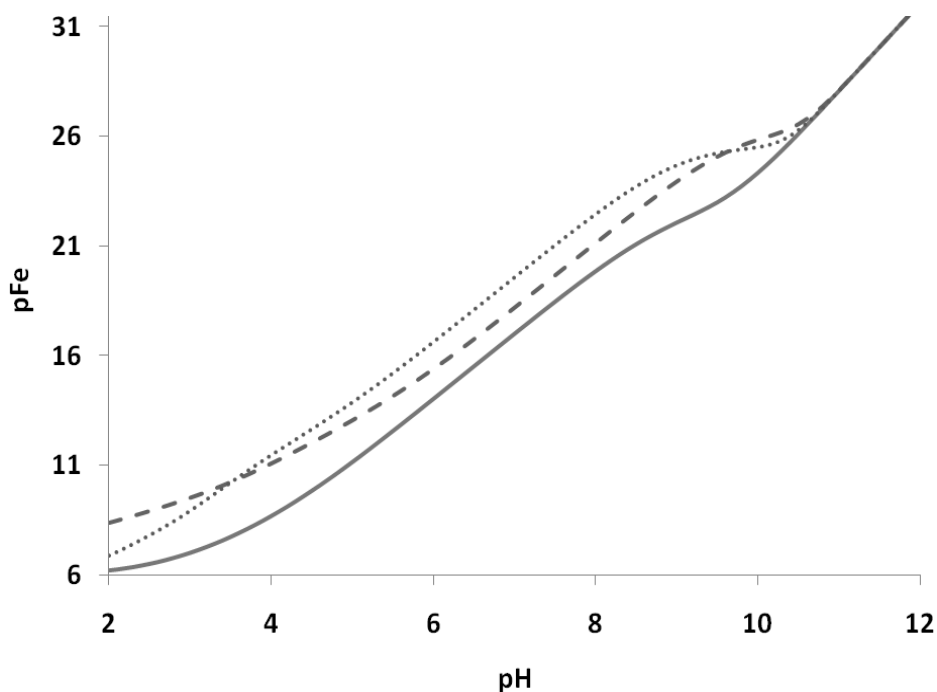


Figure 6.13. Plot of pFe values over a range of pH values for the Fe(III)-L^{PF} system (solid line), the Fe(III)-3,4-HOPO system (dotted line) and the Fe(III)-DMHP system (dashed line). For both graphs, $[\text{Fe}^{3+}]_{\text{tot}} = 10^{-6} \text{ M}$, $[\text{L}]_{\text{tot}} = 10^{-5} \text{ M}$, and all constants used in the analysis were measured at 25 °C and $\mu = 0.10 \text{ (NaClO}_4\text{)}$.

analog of L^{PF} ($pFe = 20.72$), as well as that of 1,2-dimethyl-3-hydroxy-4-pyridinone (DMHP; $pFe = 19.4$). This is illustrated in Fig. 6.13. The differences in pFe values are due in part to the lower $\log \beta_{130}$ of the L^{PF} complex compared to 3,4-HOPO and DMHP. These differences likely arise from steric factors due to the bulkier backbone of L^{PF} , as well as differences in ligand acidity and the electronic structure of the backbone.

A speciation diagram for the $Fe-L^{PF}$ system was generated using the determined stability constants (Table 6.1.) over a range of pH values to show the form of the complex at a variety of conditions (Figure 6.6.B). The speciation diagram of the $Fe-L^{PF}$ system is somewhat simplified from the actual speciation of the complex in solution. Below pH 5, the protonation constants of the carboxylate and sulfonamide group begin to factor into speciation of the ligand. As these groups are not involved in iron(III) complex formation, it is likely that the protonation constants of the groups will be minimally affected by the formation of the $Fe(HL^{PF})_x$ complexes. This suggests that at low pH values, the speciation of the $Fe(HL^{PF})_x$ complex will involve the additional protonation of the carboxylate and sulfonamide moieties. The protonation states of those remote sites will change the overall charge of the complex, which is in turn related to the bioavailability of the complex. Because of the deprotonation of the remote sites on the molecules, the overall charge of the complex at most biologically relevant conditions, pH 5-8, is 3-. The structure of the complex is illustrated in Figure 6.12.

The complex is seen to be relatively weak binding compared to other iron chelators, as at lower pH values, the ligand is not able to effectively compete with hydrolysis of the metal ion. However, between pH 6 and pH 8.5, the concentration of unbound iron is relatively low (Fig. 6.6.B.), indicating high stability of the complex around physiological pH. The speciation diagram of the Fe(III)-DMHP system is also shown for comparison (Fig. 6.6.C.). As suggested by the differences in stability constants, chelation by DMHP is more stable than that of L^{PF} , resulting in the absence of hydrolyzed forms of the metal ion from the speciation diagram at low pH values. This observation is consistent with the formation of iron(III) hydroxide precipitate at lower pH values in the L^{PF} system. However, comparison of the two speciation diagrams (Fig. 6.6.B. and 6.6.C.) shows that around physiological pH values, a higher percentage of iron is found as the FeL_3 complex in the presence of L^{PF} than in the presence of DMHP. This suggests that while the chelation of Fe(III) by L^{PF} is not stronger than DMHP (lower pFe values, Fig. 6.13.), L^{PF} is more likely to form the fully chelated complex than DMHP at circumneutral pH.

6.4.4. Electrochemical characterization

The voltammograms measured for the Fe(III)- L^{PF} system can be classified by three separate pH ranges: pH ~1 to 2.5, pH 2.5 to pH 4, and above pH 4. Representative voltammograms are shown in Figure 6.14. Below pH 2.5 (Fig. 6.14.A.), there were two observable irreversible reductions at ~ -500 mV vs NHE and a pH-dependent

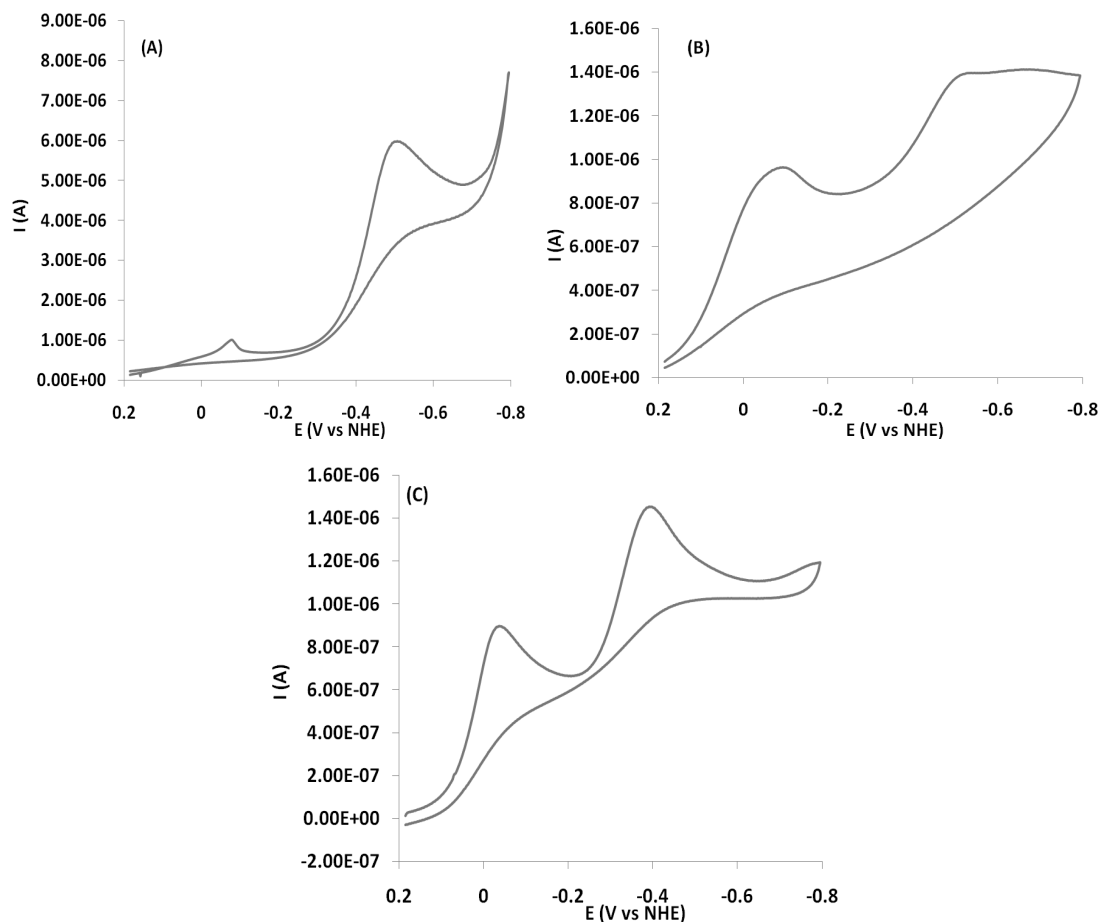


Figure 6.14. Cyclic voltammetric titration of a 1:5 M:L molar ratio solution of the Fe(III)-L^{PF} system. Representative voltammograms are shown for the three pH ranges observed during the titration. (A) – pH 1.4, $E_{red1} = -70$ mV vs NHE, $E_{red2} = -500$ mV vs NHE, (B) – pH 3.8, $E_{red1} = -84$ mV vs NHE, $E_{red2} = -506$ mV vs NHE, (C) – pH 7.4, $E_{red1} = -30$ mV vs NHE, $E_{red2} = -385$ mV vs NHE. Conditions: $[Fe^{3+}]_{tot} = 1$ mM, $[L^{PF}]_{tot} = 5$ mM, $T = 25$ °C, $\mu = 0.20$ (NaClO₄), reference electrode: Ag/AgCl, 3.5 M KCl, auxiliary electrode: Platinum wire, working electrode: hanging drop mercury electrode, scan rate: 20 mV/sec.

irreversible reduction over the range of 0 to -200 mV vs NHE. From pH 2.5 to pH 4 (Fig. 6.14.B.), the more negative reduction signal shifted further to more negative potentials and decreased in intensity until it was replaced with a reduction peak current at -300 mV vs NHE. The more positive reduction peak current decreased in intensity until it was replaced with a reduction at -30 mV vs NHE. Above pH 4 (Fig. 6.14.C.), there were two irreversible reductions observed, one pH-independent reduction peak current at -30 mV vs NHE and a second pH-dependent reduction peak over the potential range of -300 mV to -415 mV vs NHE. At physiological pH, there are two irreversible reductions observed, at -30 mV vs NHE and at -385 mV vs NHE.

The representative voltammograms in Figure 6.14. show good agreement with the speciation diagram shown in Figure 6.6.B., as below pH 4, the predominant species is the $\text{Fe}(\text{HL}^{\text{PF}})_2(\text{H}_2\text{O})_2^-$ complex, with a large fraction of the iron found as $\text{Fe}(\text{H}_2\text{O})_6^{3+}$ or $\text{Fe}(\text{OH})_x$. Meanwhile, above pH 4, the $\text{Fe}(\text{HL}^{\text{PF}})_3^{3-}$ complex is predominant, and is stable until about pH 9.

The cyclic voltammogram measured for L^{PF} in the absence of iron(III) is shown in Figure 6.15. A single irreversible reduction is observed at -50 mV vs NHE, consistent with the observed higher (less negative) peak currents measured for the iron complex. This reduction can be assigned to the β -lactam moiety. There have been studies performed on the electrochemical reduction of a variety of β -lactam-based antibiotics,

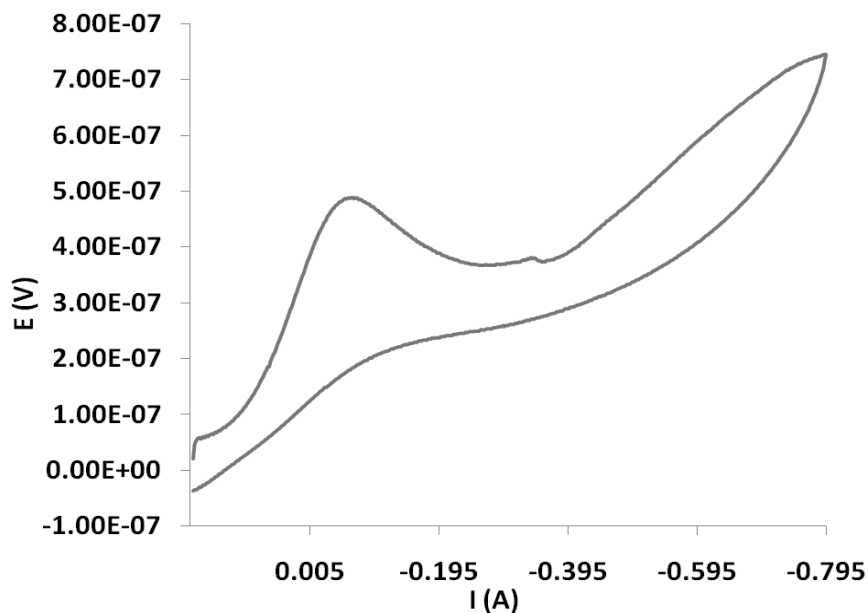


Figure 6.15. Cyclic voltammogram of a 2.5×10^{-3} M solution of L^{PF} in the absence of Fe(III) in 0.50 M KCl/0.50 M MOPS at pH 7.2. T = 25 °C, reference electrode: Ag/AgCl, 3.5 M KCl, auxiliary electrode: Platinum wire, working electrode: hanging drop Hg electrode, scan rate: 20 mV/sec.

including the structurally similar aztreonam, which shows an irreversible reduction occurring at a more negative potential around physiological pH ($E_{1/2} < -0.26$ V vs NHE) that was proposed to correspond to the 2-proton reduction of the ketone moiety of the β -lactam group to a cyclobutanol moiety.⁽¹⁶⁷⁾ It is possible that the differing side chains connected to the β -lactam shift the reduction potential from those seen in the literature studies of similar structures.

A voltammogram featuring two irreversible reductions is unexpected for an iron(III) complex, as the commonly attainable oxidation states for iron in nature are +3 and +2. Using the DMHP ligand as a L^{PF} binding site analog, cyclic voltammograms were obtained for Fe(III) in the presence of excess DMHP. A representative cyclic voltammogram for Fe(III) in the presence of 5-fold excess DMHP is shown in Fig. 6.16. This shows a single reversible reduction with $E_{1/2}$ at -486 mV vs. NHE at physiological pH (Fig. 6.16.). This is consistent with assigning the more negative peak in the Fe(III)- L^{PF} system to a Fe(III)/Fe(II) centered irreversible reduction. Presumably the irreversible

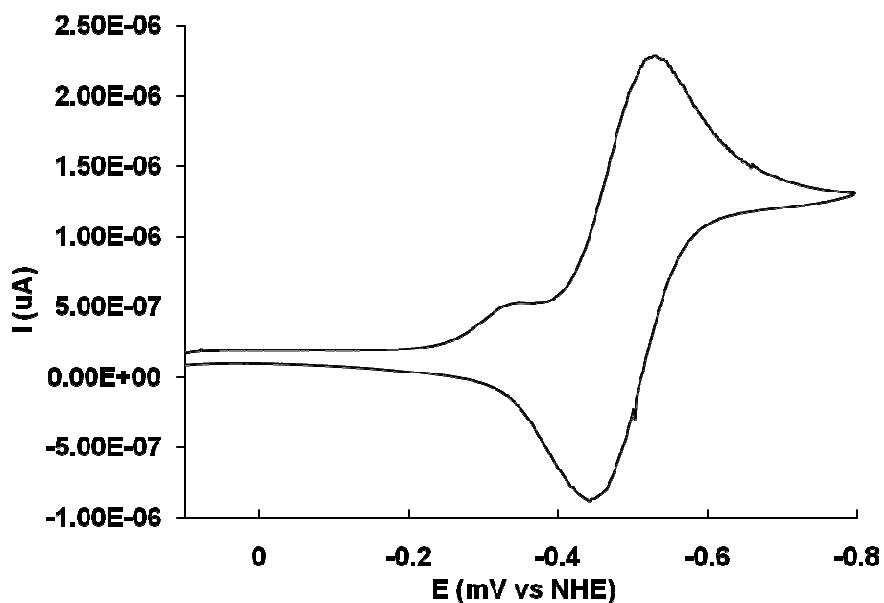
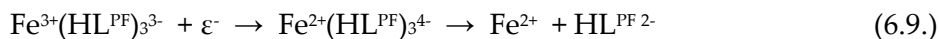


Figure 6.16. Cyclic voltammogram of a 5:1 L:M solution of Fe(III) and DMHP in 0.10 M NaNO_3 /0.20 M MOPS at pH 7.2. $[\text{Fe}^{3+}]_{\text{tot}} = 1.5 \times 10^{-3}$ M, $[\text{DMHP}]_{\text{tot}} = 7.6 \times 10^{-3}$ M, $T = 25$ °C, reference electrode: Ag/AgCl, 3.5 M KCl, auxiliary electrode: Platinum wire, working electrode: hanging drop mercury electrode, scan rate: 20 mV/sec.

character comes from dissociation of Fe²⁺ from the Fe-L^{PF} complex upon reduction. This is illustrated below for Fe(HL^{PF})₃³⁻ (Eq. 6.9).



This Fe(III)/Fe(II) centered reduction occurs at a more positive potential than other siderophore and siderophore mimic systems, and is more positive than other iron-bidentate hydroxypyridinone complexes. This more positive reduction potential for L^{PF} (E_{red} = -385 mV vs NHE for Fe(HL^{PF})₃³⁻; E_{1/2} = -486 mV vs NHE for Fe(DMHP)₃) is possibly due to the presence of the extended conjugated electron system of the backbone of L^{PF}.

6.5. Conclusions

The chelator L^{PF} has been shown to be a relatively strong chelator of iron(III) at physiological pH (see complex formation constants in Table 6.1.), although the strength of binding is less than analog chelators. The binding occurs exclusively through the 3-hydroxy-4-pyridinone donor group and allows the formation of a 3:1 L^{PF}:Fe³⁺ complex with log β₁₃₀ = 31.91. The complex exhibits two irreversible reductions, one corresponding to bound iron(III) and another corresponding to L^{PF} itself. The weak binding of L^{PF} compared to natural iron chelators makes it unclear whether iron chelation is able to compete with natural molecules for binding iron(III), but the effectiveness of the molecule as an antimicrobial agent makes it a possible route for

additional drug development. The demonstrated ability of L^{PF} to bind iron stably and its observed low MIC values suggest that it acts as an effective Trojan Horse drug and can serve as a model in the future development of Trojan Horse antimicrobial agents.

7. Computational comparison of strain energies in synthetic saccharide-backbone siderophore mimics

7.1 Introduction

As discussed previously (see Section 1.7.1.), patients suffering from iron overload are often treated by chelation therapy, which acts to remove non-transferrin bound iron and to remove excess transferrin-bound iron from the body of the patient. Most chelation treatments currently in use or under investigation use synthetic siderophore mimics to chelate and remove iron from the patient due to low bioavailability of the iron-chelator complex. The design of these agents is important as it related to strength of binding and bioavailability of the chelating agent, which is in turn related to the clinical efficacy of the agent. Many natural siderophores exhibit low solubility in aqueous systems that makes them more likely to be taken into a mammalian subject but also more likely to be removed during first pass metabolism. This can result in a short serum half-life, which increases the amount of the siderophore that must be used in the treatment. This increases the cost, length of time, discomfort to the patient, and frequency with which treatments must be administered to the patient, adversely effecting patient compliance rates.

One way of increasing the solubility of siderophore mimics is by functionalizing them or by using synthetic analogues of the siderophore(168, 169). These analogues can

be designed to have similar binding ability as the natural siderophores for which they are models, as well as having increased solubility. One method of increasing the solubility of synthetic siderophore analogues is by using a saccharide-based backbone. The saccharide backbone improves solubility through increasing hydrogen bond donor and acceptor sites located around the central ring system and acts as a reasonable model for natural exocyclic siderophores, such as enterobactin. The nature of the donor groups can then be varied to mimic a wide variety of siderophores. One example of this was the study of the binding of an exocyclic tris-catecholate synthetic siderophore based around a saccharide backbone with Fe(III), which was found to bind strongly to Fe(III) and acts as a structural model for enterobactin.(170) Some synthetic analogs of ferrichrome have been synthesized that feature central ring systems with low hydrophilicity as potential therapeutic iron chelation agents.(171)

Previous work performed in our group determined the stability of binding of two hydroxamate-donor group saccharide-backbone siderophores, $H_3L_R^{234}$ and $H_3L_N^{236}$ (Figure 7.1.) with Fe(III).(172) In these exocyclic hydroxamate siderophore mimics, there are a number of constitutional isomers which can exhibit variable binding stability. One source of isomerism in hydroxamic acid chelators is the donor group, which can exhibit either normal ($R_1\text{-NOH-CO-R}_2$) or retro-hydroxamate ($R_1\text{-CO-NOH-R}_2$) structure. In the nomenclature of the structures studied here (Fig. 7.1.), the subscript N corresponds to normal hydroxamate type donor groups, while subscript R represents

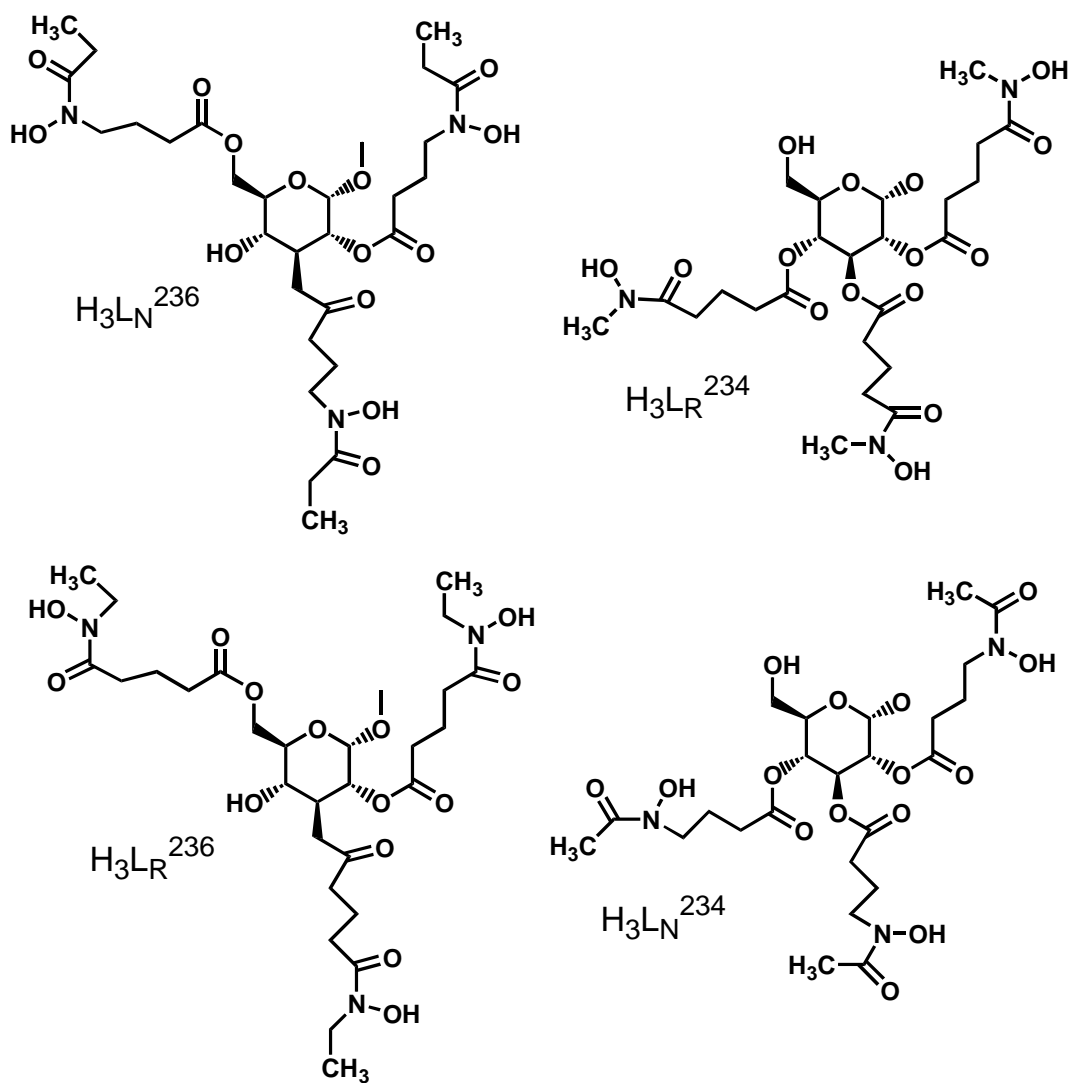


Figure 7.1. Chemical structures of the exocyclic siderophore mimics studied here by computational simulations.

retrohydroxamate type donor groups. Exocyclic siderophore mimics may also exhibit isomerism due to the placement of the donor group arms around the central ring. In the ligands studied here, the superscript numbers represent the carbons of the saccharide rings where the arms are attached. A slight difference in stability was observed for the two siderophores ($\log \beta_{110, H3LR234} = 31.86$, $\log \beta_{110, H3LN236} = 31.17$) which had very similar structures, differing only in the location of one binding arm and the use of hydroxamate or retrohydroxamate donor groups. (172, 173)

7.2. Statement of chapter objectives

In this study, we will investigate the effects of ligand architecture on the stability of binding of the exocyclic siderophore mimics, $H_3L_N^{234}$, $H_3L_R^{234}$, $H_3L_N^{236}$, and $H_3L_N^{236}$, with iron(III). Comparisons will be made between the systems based on molecular mechanics computational simulations of the strain energy of complex formation of the iron(III)-siderophore complexes. The comparisons will make it possible to discern the architectural factors that give rise to complex stability by comparing the strain energy of complex formation of normal and retrohydroxamate donor groups, as well as arm placement on the central ring of H_3L^{234} and of H_3L^{236} . Computation of the strain energy of complex formation of siderophore mimics upon removing one arm will be used to predict the mechanism of proton-driven complex dissociation. Finally, the calculated strain energies will be used to predict relative complex stability of the iron(III)-exocyclic hydroxamate donor group siderophore mimics.

7.3. Experimental

All strain energy calculations were performed using Spartan '02 by Wavefunction, Inc. (174) Calculations were performed for the iron(III) complexes of $H_3L_N^{236}$, $H_3L_R^{236}$, $H_3L_N^{234}$, and $H_3L_R^{234}$ whose structures are shown in Figure 7.1. In order to check the validity of our approach, similar calculations were also performed for the iron(III) complexes of desferrioxamine B, desferrioxamine D, and desferrioxamine E, for which crystal structures are available. (175-177)

The complex structural simulation was performed as follows. A model was made of the iron(III) complex using the basic building tools of the Spartan program. The Fe-O bond lengths and O-Fe-O bite angles of the complex were then constrained to lengths corresponding to the average bond lengths of similar iron(III)-hydroxamate complexes taken from a series of crystal structures found in the Cambridge Crystallographic Structural Database and a previous publication. (168, 175, 178) The iron complex structures were then optimized by semi-empirical calculations under the PM3 basis set with a neutral charge and a spin multiplicity of 6. Upon optimization, the iron was removed from the complex structure and a single-point molecular mechanics measurement was taken under the MM+ force field to determine the strain energy of the entire molecule without the iron atom (shown in Table 1 in the column marked "Total Strain Energy"). The complex structure was then re-optimized by re-inserting the iron

and removing the constraints on the O-Fe bond lengths and the O-Fe-O bond angles. This second optimization was performed by molecular mechanics calculations under the MM+ force field. The iron was removed again and another single point reading was taken under the MM+ force field to give the strain energy of the molecular structure optimized without the primary coordination sphere constraints (shown in Table 7.1. in the column labeled “Unstrained Energy”). Both strain energies determined in the

Table 7.1. Strain energy calculations for iron(III) complexes of desferrioxamine B, desferrioxamine D, desferrioxamine E, H₃LN²³⁶, H₃LR²³⁴, H₃LR²³⁶, and H₃LN²³⁴

Complex	Total strain Energy ^a (kcal/mol)	Unstrained Energy ^b (kcal/mol)	Strain Energy of complexation ^c (kcal/mol)
FeLN ²³⁶	682	439	242
FeLR ²³⁴	660	458	202
FeLR ²³⁶	696	470	226
FeLN ²³⁴	704	448	256
Ferrioxamine B	486	205	281
	600 ^d	315 ^d	285 ^d
Ferrioxamine D	572	295	277
	602 ^d	318 ^d	284 ^d
Ferrioxamine E	498	285	213

^a Calculated by semi-empirical calculations at PM3 level of theory with primary coordination sphere constraints

^b Calculated by molecular mechanics calculations at MM+ level of theory with no primary coordination sphere constraints

^c Column 2 minus column 3

^d Calculations performed without pendant tail

absence of iron are shown in Table 7.1. The difference between the strain energy from the PM3 optimization (Table 7.1., column 2) and the strain energy from the MM+ calculation (Table 7.1., column 3) was taken as the strain energy brought about by complexation with iron(III) (Table 7.1., column 4). These results were qualitatively validated by applying the same method to ferrioxamine B, D and E (Fig. 7.2.), where crystal structures and stability constants are known. (175-177)

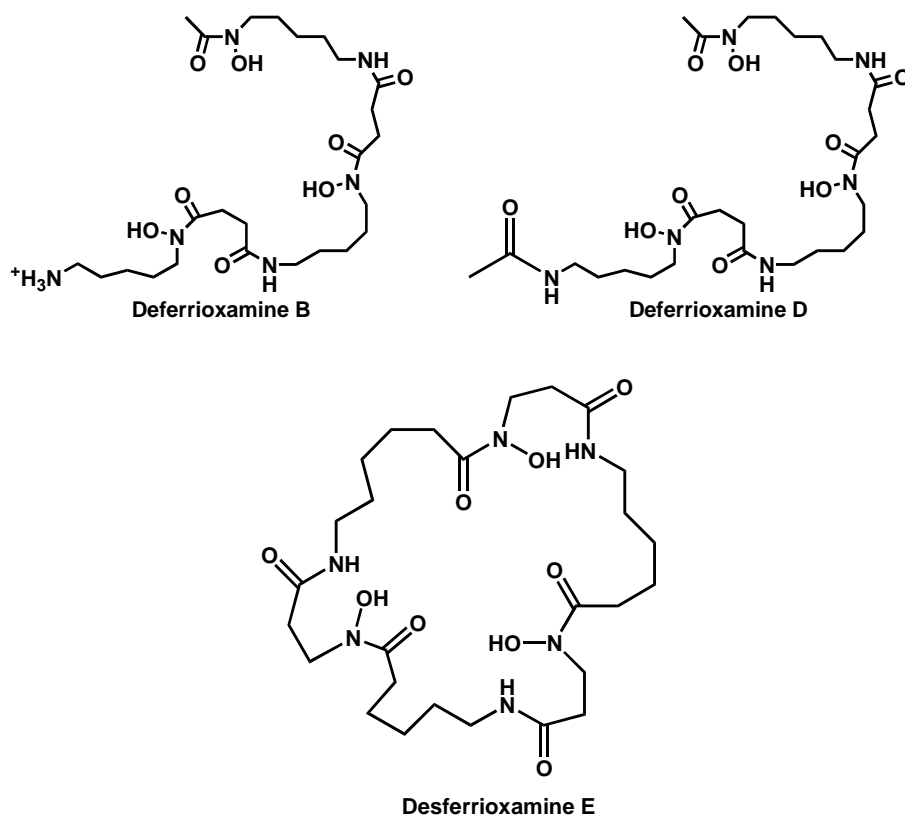


Figure 7.2. Chemical structures of three ferrioxamines, B, D, and E. The strain energy of complex formation of these ligands was calculated to verify the method for use on the tris-hydroxamate siderophore mimics.

7.4. Results

For the ferrioxamines B ($\log \beta_{110} = 30.6$) and D ($\log \beta_{110} = 31.40$), two calculations each were performed, one with the pendant tail and a second with the pendant tail removed. In the calculations performed with the pendant tail included in the structures, ferrioxamine B yielded slightly higher strain energy of complex formation than ferrioxamine D (Table 7.1.). However, ferrioxamine B and D gave effectively the same strain energies without consideration of the pendant tail. Ferrioxamine E showed lower strain energy of complexation than both ferrioxamines B and D, consistent with the higher iron binding constant for desferrioxamine E ($\log \beta_{110} = 32.21$).^(20, 179) This demonstrates that the strain energies of complex formation may be correlated to relative stabilities of iron(III)-siderophore complexes, a technique which we will apply to the exocyclic hydroxamate siderophore mimics, $H_3L_N^{234}$, $H_3L_R^{234}$, $H_3L_N^{236}$, and $H_3L_R^{236}$.

Results of calculations for the saccharide hydroxamic acid ligands shown in Table 7.1. were performed assuming a facial coordination geometry (Fig. 7.3.), consistent with reported crystal structures for tris-hydroxamic acid complexes (15 of 18 reported unique iron-hydroxamate donor molecule structures exhibited facial geometry, while one was a mer/fac mixture, Table 7.2.).⁽¹⁶⁸⁾ The Fe-O-C bond angles from calculated structures are shown in Table 7.3. for comparison to those reported in the literature and shown in Table 7.2. Strain calculations were also performed to compare facial and meridional geometrical isomers (Fig. 7.3., Table 7.4.), with FeL_N^{234} and FeL_N^{236} showing

Table 7.2. Average Fe-O-C bond angles of hydroxamate iron(III) complex crystal structures in the Cambridge Data Base.(178)

Compound	Architecture	normal/retro	mer/fac	Fe-O-C bond angle	Crystallographic database deposition number
6-L-alanine-ferrirubin	Exocyclic	normal	fac	113.27	BOPMUO01
Tris-[3-(N-acetyl-N-hydroxyl)glycyl-amino)propyl]ammonium	Tripodal	normal	fac	113.78	BUHQQU
N-(4-cyanophenyl)-acetohydroxamate	Monohydroxamate	n/a	fac	113.37	BURDIB
Neurosporin	Endocyclic	n/a	fac	112.50	CETWIH
Isotriornicin	Linear	n/a	mer	113.98	COFDIK10
Ferrioxamine D	Linear	n/a	fac	113.06	DUPJON
Ferricrocin	Exocyclic	normal	fac	112.03	FERCRN10
Ferrichrome A	Exocyclic	normal	fac	113.46	FERMAH10
Ferrioxamine E	Endocyclic	normal	fac	112.34	FEROXE10
N, N', N''-triacetylfusarinine	Endocyclic	n/a	fac	114.17	FTAFUS10
Ferrirhodin	Exocyclic	normal	fac	113.36	JEPHAX
Tris(2-(((N-acetyl-N-oxy)glycylamino)ethyl)amine	Tripodal	normal	fac	111.97	OCELOX
Ferrioxamine B	Linear	n/a	Fac	112.94	OFUYET
Retro-ferrioxamine E	Endocyclic	retro	fac	113.22	SIPMEJ
Acetohydroxamic acid	Monohydroxamate	n/a	mer/fac ¹	111.59	SUXREI
Alcaligin	Endocyclic, bishydroxamate	n/a	mer ²	113.72	TEQKUV

¹The structure recorded is a 50:50 mixture of the mer and fac isomers.

²This structure corresponds to the M₂L₃ Fe⁺³-alcaligin complex

Table 7.3. Fe-O-C bond angles for calculated structures of iron-tris-hydroxamate complexes.

Hydroxamate containing arm(s) dissociated	Fe ³⁺ (L _N ²³⁶)	Fe ³⁺ (L _R ²³⁴)	Fe ³⁺ (L _R ²³⁶)	Fe ³⁺ (L _N ²³⁴)
2-arm	110.8	102.7	104.5	115.0
3-arm	107.3	107.4	108.8	106.6
4-arm	n/a	115.6	n/a	109.9
6-arm	115.1	n/a	106.7	n/a
Average	111.07	108.6	106.7	110.5

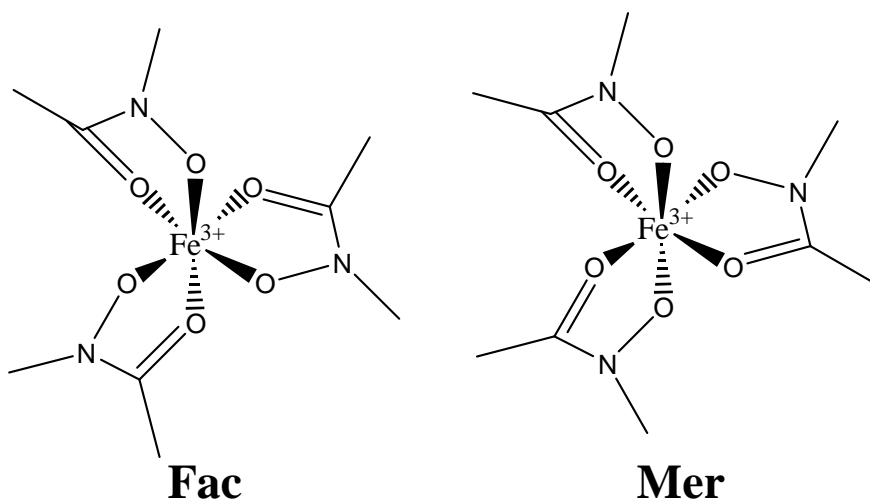


Figure 7.3. General structures of the mer- and fac- isomers of a series of tris-hydroxamic acid synthetic chelators.

Table 7.4. Strain energies of complexation for *fac* and *mer* isomers of normal and retro hydroxamate saccharide models for ferrichrome.

Complex	Strain E of complexation (kcal/mol)
<i>fac</i> -FeL _N ²³⁶	410
<i>mer</i> -FeL _N ²³⁶	415
<i>fac</i> -FeL _R ²³⁴	384
<i>mer</i> -FeL _R ²³⁴	409

no difference between isomers and FeL_R^{234} and FeL_R^{236} slightly favoring the facial isomer. However, the qualitative conclusions arrived at in this study are not influenced by whether the comparisons are made with the facial or meridional isomers.

In order to predict which pendant arm dissociates with the first protonation of FeL_N^{236} and FeL_R^{234} , strain energy calculations were made with one arm completely removed from the complexes. These results are listed in Table 7.5. Comparisons may be made within a ligand system omitting a single arm, but not between ligands as a different number of atoms are involved in the calculations involving the two ligands.

All of the calculations performed here assume the molecules are in a vacuum where the energy of complexation, energy of ionic interaction and energy of ligand conformation are considered, but where medium effects, solvation effects, entropic considerations, and other real solution contributions are ignored. Consequently, the results of these calculations are only considered qualitatively in order to compare relative stabilities

Table 7.5. Calculated complexation strain energies for FeL_N^{236} and FeL_R^{234} after removal of a single hydroxamate moiety and pendant arm.

Hydroxamate containing 2, 3, 4 or 6-arm dissociated	FeL_N^{236}	FeL_R^{234}
2-arm	71	79
3-arm	210	95
4-arm	N/A	71
6-arm	168	N/A

between ligands. It is also likely that solvent effects and other entropic effects will be the same between the isomers studied here.

7.5. Discussion

The effectiveness of iron chelators is indirectly linked to the architecture of the molecule. As donor groups move farther away from their ideal conformation to facilitate the formation of iron complexes due to changes in ligand architecture, there is a strain energy value inherent upon shifting the donor groups away from that conformation. With increased strain energy of complexation comes a lower strength of chelation of iron(III) by the chelators (in many cases, although there are generally more factors involved). In the case of exocyclic siderophores, the placement of the arms around the central ring affects the ease of presentation of donor groups to iron for coordination. Additionally, the identity of the hydroxamate donor group as either hydroxamate or retrohydroxamate will affect the O-Fe-O bite angle upon coordination of iron by the hydroxamate. The change in conformation of the arm with the change of terminal hydroxamate group from normal to retro- (or vice-versa) to facilitate the formation of this bite angle can result in increased strain energy and a corresponding decrease in thermodynamic stability constant.

The calculations of the ferrioxamine complexes to validate the computational technique shows that the strain energy of coordination of iron(III) is very similar for the desferrioxamines B and D, both with and without the pendant tail of the ligand. The calculations performed with the tails represents the entire molecule, and while the inner coordination sphere will remain unchanged between the two systems, there is a small contribution to the strain energy of complexation due to hydrogen bonding interactions between the terminal group of the pendant tail and a peptide N-H from the backbone of the siderophore. The interaction in the case of desferrioxamine D is slightly more stabilizing than in desferrioxamine B, as induction of electron density from the nitrogen by the amide O in the tail of desferrioxamine D allows a more stable hydrogen bond to form than with the pendant amine tail of desferrioxamine B. The removal of the pendant tail leaves only the inner coordination sphere, which is the same between the two systems, resulting in identical strain energies of complexations. Both of these strain energies of complexation, however, are much higher than that of the macrocyclic desferrioxamine E, likely due to preorganization afforded by its macrocyclic structure. Additionally, the strain energy values calculated are consistent with the observation that the ferric complex of desferrioxamine D ($\log \beta_{110} = 31.40$) is slightly more stable than that of desferrioxamine B ($\log \beta_{110} = 30.6$), while desferrioxamine E forms a much more stable complex than either B or D ($\log \beta_{110} = 32.21$).

Comparison between the ferric complexes of the two ligands $H_3L_R^{234}$ and $H_3L_N^{236}$ showed a lower strain energy of complex formation for $H_3L_R^{234}$ (Table 7.1.), consistent with the comparison of $\log \beta_{110}$ for the two systems (for $H_3L_R^{234}$, $\log \beta_{110} = 31.86$; for $H_3L_N^{236}$, $\log \beta_{110} = 31.14$).^(172, 173) Calculations were performed to determine the strain energy of complex formation of the two remaining isomers, $H_3L_R^{236}$ and $H_3L_N^{234}$, to allow comparison of the structural factors between all four constitutional isomers that would contribute to increased complex stability in exocyclic siderophore structures.

7.5.1. Ligand design related to complex strain

Calculations were performed to determine the strain energy of complexation of the analogs L_N^{234} and L_N^{236} as well as L_R^{236} and L_R^{234} . While the stability constants of all of these siderophore mimics were not determined, these comparisons can allow some predictions to be made about their relative stability. Comparison of the strain energy between the complexes of L_N^{234} and L_N^{236} showed higher strain energy of complexation for the 234 arm configuration by 14 kcal/mol, while comparison between L_R^{236} and L_R^{234} showed higher strain energy for the 236 arm configuration by 24 kcal/mol (Table 7.1.). This inconsistency between the normal and retrohydroxamate configuration ligands suggests that more factors are at play in the complex formation reaction than just arm placement. It is possible that the hydroxamate configuration donor group favors the 234 arm configuration due to the bite angle between the donor groups and iron.

Similar comparisons can be made between the normal hydroxamate and retrohydroxamate donor group versions of the molecules. Comparison of the strain energy of complexation of L_N^{234} and L_R^{234} shows a lower strain energy for the complex of the retrohydroxamate isomer by 54 kcal/mol (Table 7.1.). The same is the case for comparison of L_N^{236} and L_R^{236} , which favors the retrohydroxamate isomer by 16 kcal/mol. This demonstrates that with the same scaffold structure, the normal hydroxamate architecture is favored over retrohydroxamate in complex formation.

The two comparisons provided here for arm placement and normal/retrohydroxamate suggest that the two structural variations act in opposing directions, with the retrohydroxamate donor groups conferring stability on L_R^{234} and the 236 arm placement acting to stabilize L_N^{236} . However, the destabilization by the 234 arm placement seems less than the stabilization of the retrohydroxamate group, resulting in overall slightly higher stability for the Fe- L_R^{234} complex. Interestingly, it also appears from these calculations that the L_R^{234} isomer forms the complex with the highest stability of the four isomers studied here, although the iron complexes of L_R^{236} and L_N^{234} have yet to be characterized thermodynamically.

One indicator of the strain energy of complexation that focuses on the donor group is a measure of the Fe-O-C bond angle. The carbonyl oxygen is partially hybridized as a part of the hydroxamate donor group, and so features a characteristic

that is partially sp^2 and partially sp^3 in nature. This suggests that the ideal Fe-O-C bond angle should measure somewhere between 120° and 109.5° . A survey of observed literature values of the Fe-O-C bond angles from iron-hydroxamate complexes registered in the Cambridge Crystallographic Structural Database, shown in Table 7.2., finds the angles to be approximately 113° .⁽¹⁷⁸⁾ The computational simulations of the Fe-saccharide backbone siderophore mimics, however, predicts a range of Fe-O-C bond angles from 106° for FeL_R^{236} to 111.1° for FeL_N^{236} . This suggests some distortion from predicted values based on observations in the literature, possibly due to the calculation method used.

7.5.2. Ligand design related to complex stereochemistry

Calculations showed a slight decrease in strain energy of complexation for the *fac*- isomer compared to the *mer*-isomer in FeL_N^{234} and FeL_R^{234} (Fig. 7.3., Table 7.4.). This shows a marked preference for formation of the *fac* isomer in hydroxamate donor group complexes, which is consistent with a survey of crystal structures recorded in the Cambridge Crystallographic database (Table 7.2.).⁽¹⁷⁸⁾ The majority of exocyclic hydroxamate siderophores feature normal hydroxamate donor groups, and almost all of the structures included feature *fac*- geometry. However, the prevalence of normal hydroxamates is likely attributable to the modification of lysine and ornithine residues in the production of siderophores. Also, the observation of a preference for *fac*- geometry may not be attributed to a number of possible architectures so much as it is

due to symmetry in the production of polyhydroxamate siderophores. In tris-hydroxamate siderophores, such as those studied here, it is much more likely that the hydroxamate donors will coordinate in similar modes to produce *fac*- geometry than that they will undergo the conformational changes necessary to form the *mer*-isomer. In this light, it is not surprising that the crystal structure of acetohydroxamic acid would exhibit a 50:50 mix of *mer*- and *fac*-isomer. It is, however, still interesting that N-(4-cyanophenyl)-acetohydroxamate, a monhydroxamate ligand, would exhibit preferential formation of the *fac*-isomer, considering the bulky N-substituent.

7.5.3. Complex protonation scheme

By calculating the strain energy of complex formation of the isomers after removing individual arms from the model, it is possible to gain some insight into the mechanism of sequential dissociation of the hydroxamate donor groups from the iron center. This type of calculation can provide more insight into the mechanism of complex dissociation and the order of donor group dissociation than complex protonation constants determined by spectrophotometric or potentiometric titration, as all donor groups are identical acidic moieties which would produce identical spectral shifts upon dissociation. It was possible to calculate the strain energy of complexation of the iron complexes of L_N^{234} and L_R^{234} upon the dissociation of a donor arm by removing the arms before performing the calculations. This ignores the variability of the structure of the arm that is floating free in solution, which would make determination of the strain

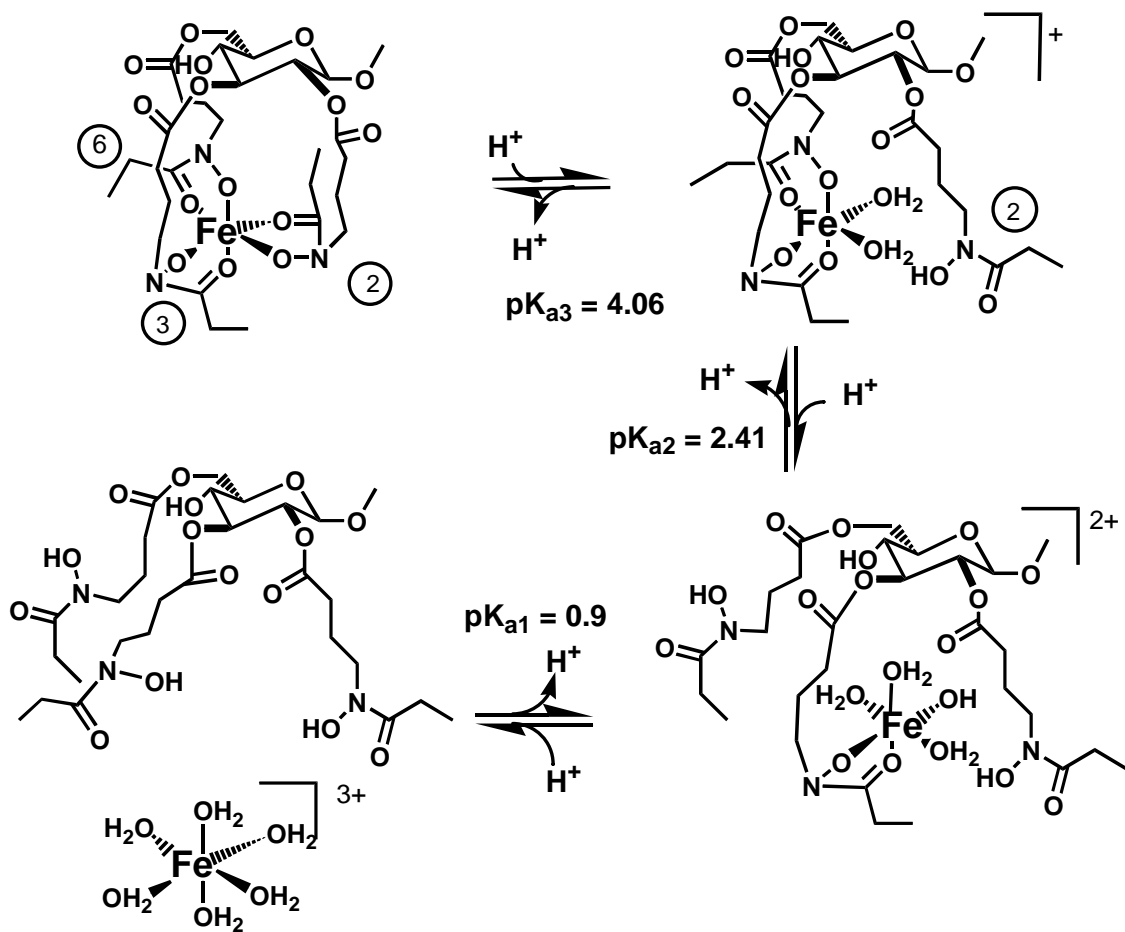
energy of complexation incredibly difficult due to the variability of the conformation of the free arm and the likely existence of localized energy minima. Using this method, the structure with the lowest calculated strain energy of calculation can be seen as predicting which arm will dissociate during the first protonation equilibrium for the iron complex in solution. The strain energies of complexation for the ligands L_N^{234} and L_R^{234} are shown in Table 7.5. These calculations were performed for the first two protonation steps of each ligand, but the results for the second protonation are not shown, as the only remaining strain energy of complexation would correspond to a simple hydroxamate donor, which is invariable with respect to the architecture of the ligand molecule. Also, with respect to the calculations, the remaining structure of the central ring would be allowed to float free in the system, making consistent solution of the energy very difficult for the same reason as the free arms in solution in the singly dissociated structures. From these observations, it is reasonable to propose that either of the remaining arms is equally likely to dissociate during the second protonation reaction.

For the $Fe-L_N^{236}$ complex, the lowest strain energy of complexation was determined for dissociation of the arm attached to the 2-carbon position on the saccharide backbone, suggesting that it is the most likely to dissociate during the first protonation reaction of the complex. This is likely due to its proximity to the 3-carbon arm as well as steric interactions with the substituent of the 1-carbon. For the $Fe-L_R^{234}$,

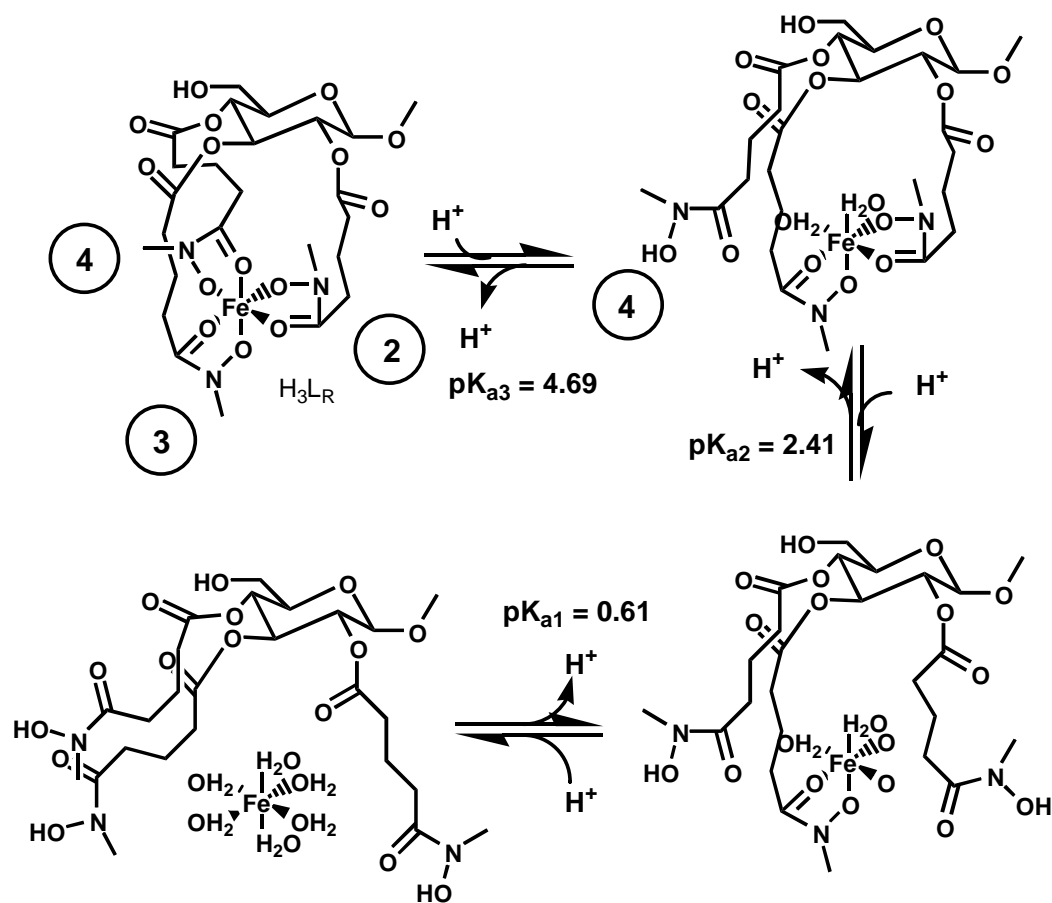
the lowest strain energy of complexation was determined for dissociation of the 4-carbon arm, suggesting that it is most likely to dissociate during the first protonation reaction of the complex. The ease with which any given arm dissociates from iron depends on the steric interactions between all three coordinated arms, as well as how much strain on the entire molecule is relieved by its dissociation. Based on the results of the strain energy calculations, the proposed protonation schemes for L_R^{234} and L_N^{236} are shown in Schemes 7.1. and 7.2.

7.6. Conclusions

The stability of complexation of synthetic iron chelators is one important factor in the development of novel chelation therapy agents. In the case of exocyclic iron chelators, the placement of arms around the central ring system can contribute to changes in complex stability. Computational simulations performed here suggest that in the case of saccharide-based siderophore mimics, the placement of donor group arms around the central ring contributes to complex stability, although the degree to which it contributes can vary based on the identity of the donor groups. Comparison of retrohydroxamate and normal hydroxamate donor groups suggests that the retrohydroxamate configuration provides more stable complexation to iron due to lower strain energy of complexation.



Scheme 7.1. Counter-clockwise from bottom-left to top-left illustrates the step-wise chelation of Fe^{3+} by $\text{H}_3\text{LN}^{236}$ showing equilibrium constants (pK_n) for each step and position of coordinated arms. Clockwise from top-left illustrates proton-driven dissociation of pendant arms starting with the 2-arm.



Scheme 7.2. Counter-clockwise from bottom-left to top-left illustrates the step-wise chelation of Fe³⁺ by H₃L_R²³⁴ showing equilibrium constants (pK_n) for each step and position of coordinated arms. Clockwise from top-left illustrates proton-driven dissociation of pendant arms starting with the 4-arm.

8. Heavy metal toxicity and the protective effects of chelating agents on *Caenorhabditis elegans* growth

8.1. Introduction

A number of transition metal ions are essential to biological processes crucial to maintaining life. A deficiency of the metals will result in the inability of the organism to perform important biological processes ranging from small molecule transport (iron in hemoglobin and copper in hemocyanin) to epigenetic regulation of gene expression (zinc in histone deacetylase).(180) Exposure of organisms to an excess of metals can result in toxicity due to undesirable reactions including oxidative damage to biomolecules, clogging ion channels, and cross-linking DNA. Organisms have developed stress responses to protect the organism from metal toxicity or to remove toxic metals from the system. However, when those stress responses are overwhelmed, the organism will suffer from metal toxicity. For humans, it is important to understand the toxicity of metals due to the prevalence of transition metals in a variety of products and industrial processes.

One potential avenue of treatment of metal ion toxicity is chelation therapy, where chelating agents are administered to the patient, which will bind to the metal, prevent further reactivity, and remove the metal safely from the patient. The effectiveness of chelation therapy can be related to a number of factors involving the

interaction between the target metal and the chelating agent.(181) First, the chelating agent must bind the metal stronger than any competing chelator in the biological system (taking into account physiological concentrations of endogenous chelators). One expression representing strength of chelation is expressed through the pM value. The pM value is a unitless quantity that is analogous to the pFe value discussed in previous chapters, and which can be compared for a number of metal ions. The degree of complex formation is dependent on the concentrations of the metal and chelator present in the system, making the amount of chelating agent administered important to the efficacy of the treatment. One common competing chelating agent in biological systems is citrate, which can bind to metals via a constellation of carboxylate groups. As the competing biological chelators also have complex stability equilibrium constants with the metals, the concentration of the competing chelators is also important. Second, the chelated form of the metal cannot be bioavailable to the organism in order for it to be removed. If the complex is bioavailable to the organism, then the metal will remain in the biological system and can potentially continue to cause damage to the organism over time.

Chelation therapy treatments for some metals are already in clinical use.

Treatment of iron overload in β -thalassemia patients through chelation therapy has been performed using the chelating agent Desferal, or desferrioxamine B, which is a bacterial iron-specific chelator (Fig. 8.1.). More recently, a second chelating agent has been implemented in iron chelation therapy in Europe, Deferriprone (1,2-dimethyl,3-

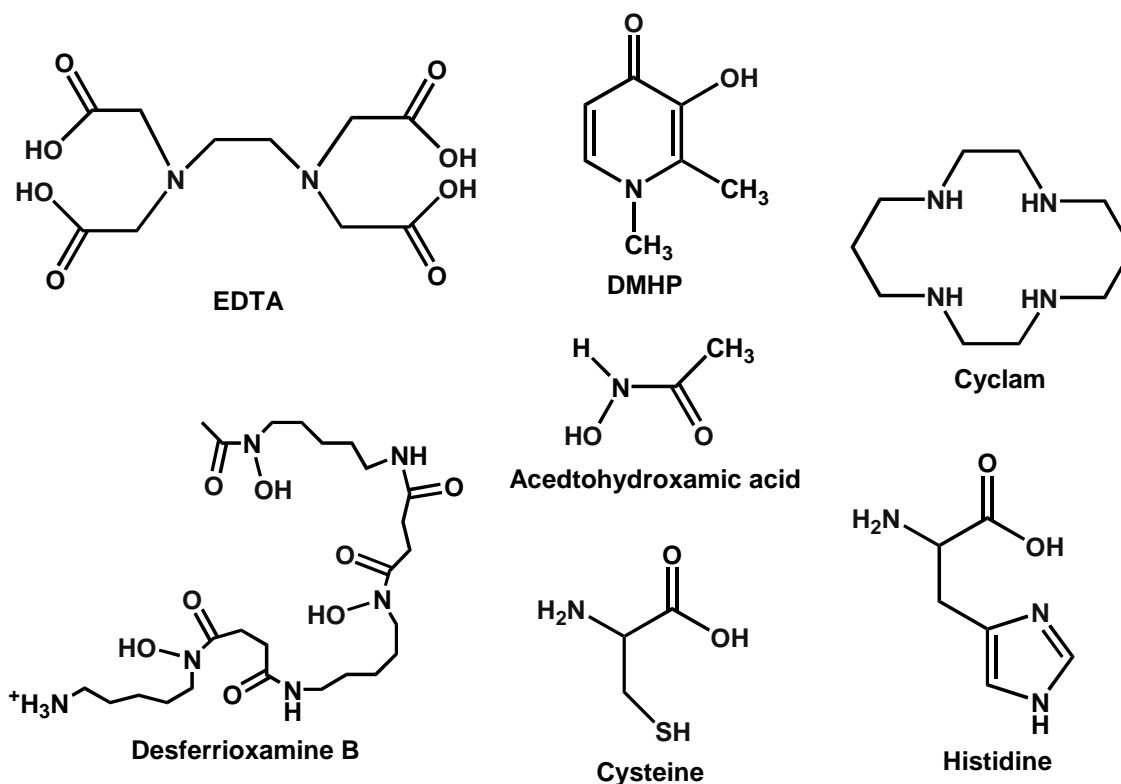


Figure 8.1. Chemical structures of the chelating agents studied here for toxicity and protective effects from metals.

hydroxy,4-pyridinone or DMHP; Fig. 8.1.).(63) Disodium calcium EDTA (Fig. 8.1.) has been used clinically as a treatment for heavy metal toxicity, while there have been reports that disodium EDTA is harmful to patients, resulting in hypocalcemia and sometimes death.(182) The use of chelation therapy has been derided as poor science in some circles due to its misappropriation as a treatment for numerous health problems, such as congenital heart disease and autism. While scientific studies on these uses have shown no medical benefit in cases of congenital heart disease and autism, chelation therapy still remains an effective tool in the treatment of heavy metal toxicity.(183)

Caenorhabditis elegans is a small soil-based nematode whose anatomy and genetics have been studied thoroughly since 1965.(184-186) It is viewed as a model for higher order organisms at the biomolecular level, expressing many similar stress response genes as are observed in vertebrate systems.(187-192) It is also ideal as a model system due to its relatively short life cycle, the thoroughness of understanding of its biology, and the ease of observing the cells in the organism with light microscopy.(193) The organism is approximately 1 mm long, translucent, and is one of two sexes, male and hermaphrodite, which have specialized reproductive systems and structures. They have a fixed number of cells at each stage of development, which is invariable and results in the inability of the organism to replace injured body parts. The larval phase of their life span is divided into four periods, L1-L4, which last a total of approximately 72 hours.(194, 195) The growth phases are punctuated with molts of the cuticle between periods of growth.

C. elegans has been used as a model in studying toxicity of a variety of chemicals due to the expression of stress responses that are similar to those observed in other organisms.(196) A number of criteria can be used to investigate the toxicity of chemicals to *C. elegans*, including organism growth, reproductive rate, feeding, and coordination of movement. Medium- and high-throughput methods for studying as many as 6000 nematodes/minute using the COPAS biosort flow sorting system have been developed, allowing rapid evaluation of a number of potential toxicants over a range of concentrations.(193) The COPAS biosort flow sorting system measures biological

samples based on the criteria of extinction (EXT), or optical density of each individual of the sample population, and time of flight (TOF), or length of each individual of the sample population, are used to determine the rate of growth of the nematode with time. Study of the growth of *C. elegans* has also resulted in the development of a mathematical model for the growth of the nematode over time.(197) This model of the growth of *C. elegans* has previously been used to determine the effect of a number of toxicants on growth of the organism.(198)

8.2. Statement of chapter objectives

The nematode, *C. elegans*, can be used as a model organism to investigate the toxic effects of chemicals on biological organisms, using the COPAS biosort method and the mathematical model of growth. The objective of the study described in this chapter is to use *C. elegans* to investigate the toxic properties of potential chelating agents, as well as to determine the protective effect of the chelating agents from the toxicity of some metal ions. It is important to examine, not only the potential protective effects of the chelators, but also their toxicity, as it is possible that the chelators can have undesirable toxic effects due to chelation of essential metals resulting in a deficiency. By combining the metals and the chelating agents in a single treatment, it will be possible to determine the protective effect of the chelating agents in the presence of toxic concentrations of metals. This study will also provide information about which chelating agent is most appropriate for protecting against toxic exposure to each metal based on a combination

of limited toxicity of the chelating agent and maximized protective effect. The metals to be studied here are cadmium(II), copper(II), iron(III), nickel(II), and zinc(II). The chelating agents of interest are desferrioxamine B and DMHP, two clinically approved iron chelation therapy agents, acetohydroxamic acid (AHA), a specific iron chelator but proposed teratogen, cyclam (Fig. 8.1.), which has been proposed to chelate excess zinc(II) and copper(II) and act as a neuroprotective agent, cysteine and histidine, amino acids which should bind effectively to copper, and Na₂CaEDTA, a stable chelator for a number of heavy metal ions including iron(III) and lead(II).(199)

8.3. Experimental

8.3.1. Nematode culture

The Bristol N2 (wild-type) strain of *C. elegans* was obtained from the *Caenorhabditis* Genetic Center (Minneapolis, MN), and maintained at 20°C on K-agar plates (2% bacto-agar, 0.25% bacto-peptone, 51 mM sodium chloride, 32 mM potassium chloride, 13 µM cholesterol) seeded with *E. coli* OP50.(186, 200) Age-synchronized adult nematodes were prepared as previously described.(201)

8.3.2. Materials

All solutions were prepared in K-medium (51 mM sodium chloride, 32 mM potassium chloride) to maintain osmotic pressure in the nematode culture. Zinc

chloride (97%), FeCl₃ hexahydrate (97%), anhydrous NiCl₂ (98%), anhydrous CdCl₂ (99.99+%), and CuCl₂ dihydrate (99.999+%) were obtained from Sigma-Aldrich and used as received to prepare metal solutions. Iron(III) solutions were prepared in 0.10 M HCl, then added slowly with stirring to potassium citrate (Baker analyzed 100.5%, J.T. Baker) dissolved in K-medium. The pH was adjusted to approximately 6 by slow addition of 0.10 M NaOH solution after iron(III) was added. The solution was allowed to equilibrate in the dark overnight.

Desferrioxamine B mesylate salt (95%), 1,2-dimethyl-3-hydroxy-4-pyridinone (98%), L-histidine (98%), acetohydroxamic acid (98%), 1,4,7,11-tetrazacyclotetradecane (cyclam, 98%), and calcium disodium ethylenediaminetetracetic acid (CaNa₂EDTA) were all obtained from Sigma-Aldrich and used as received to prepare chelator solutions. The pH was adjusted to between 5 and 8 for use in exposure growth assays using 0.10 M NaOH and concentrated HCl (for cyclam solution).

8.3.3. Growth assay

All assays used the COPAS Biosort flow sorting system (Pulak 2006) (Union Biometrica Inc., Somerville, MA, USA).(202) The Biosort was used to dispense samples into 96-well exposure plates containing complete K-medium (Boyd et al. 2009) (51 mM sodium chloride, 32 mM potassium chloride, 3 mM calcium chloride, 3 mM magnesium sulfate, 13 µM cholesterol), varying concentrations of the chelating agents and metals,

and OP50 *E. coli* as a food source for nematodes. Sample pH was maintained in the pH range of 6 to 8 to prevent additional stress to the nematodes. After exposure, the samples were aspirated from exposure plates using the COPAS Biosort ReFlx and all measurements of individual nematodes were recorded by the Biosort.

Growth assays were modified from Boyd et al., 2009.(203) Fifty L1 stage nematodes were dispensed to each exposure well and incubated for 48h at which time untreated nematodes had reached the L4 stage. The Biosort was used to measure two size characteristics of individual nematodes, the length or 'time of flight,' log(TOF) and optical density or 'extinction,' log(EXT). To determine the toxicological effects of the chelators, a range-finding experiment was performed. Nematodes were exposed to concentrations of chelators ranging from 0.42 mM to 42.5 mM with one set of control wells containing no chelator. After exposure, the effects of the chelators were observed visually and the concentration response to the chelator was classified based on movement and relative size and extinction of the nematodes compared to the control well as measured by the COPAS Biosort.

To determine the concentration of metal appropriate for the toxicity protection assays, a similar series of range-finding experiments were performed using only the metals. A series of 12 wells were prepared for each metal containing concentrations ranging from 32 to 600 μM of each metal, Cd^{2+} , Cu^{2+} , Ni^{2+} , and Zn^{2+} and one control well.

In each well, fifty L1 stage nematodes were exposed and after 48 hours, the TOF and EXT for the nematodes were observed, both visually and by measurement with the COPAS biosort.

To determine the protective effects of the chelators, 48-hour growth assays were performed where the nematodes were exposed to both metal and chelator. A single concentration of both metal and chelator were used for exposure studies. For each metal-chelator pair, a speciation plot was produced (see Appendix E) using the literature values of the metal-ligand stability constants to allow determination of the minimum concentration of chelator that would provide chelation of the metal while not producing toxic effects due to the ligand alone.⁽²⁰⁴⁾ The speciation simulations were calculated at a constant pH of 6.5 to give an estimate of complex formation in solution. In the cases where little or no complex formation was predicted to occur, the maximum concentration of chelator that would not produce a toxic effect was used. Each 96-well plate corresponded to a single metal being tested. Each row of wells corresponded to a single chelator that was being tested with a single row treated with no chelator (control and metal-treated worms for comparison). Each row consisted of four replicate wells of chelator only treatment, four replicate wells of metal-chelator combined treatment, and four wells of DI water for use by the COPAS biosorter as wash-wells. For each metal, at least 3 replicate plates were performed. Fifty nematodes were dispensed in each well

containing a treatment and were exposed over 48 hours, followed by visual inspection and measurement by the COPAS biosorter.

8.4. Results

8.4.1. Chelator and metal toxicity assays

Toxic responses based on visual inspection were graded loosely as one of three levels of response: 1) non-toxic for specimens that did not differ significantly in size or level of activity from the control nematodes; 2) slightly toxic for nematodes that exhibited slightly less growth or levels of activity than the controls; and 3) toxic for greatly diminished growth and activity compared to the control nematodes. Treatment of metal-exposed subjects was done using only slightly toxic or non-toxic concentrations of chelators, as will be addressed later.

Acetohydroxamic acid was nontoxic to the nematodes up to a concentration of 1.7 mM, showing no loss of growth or activity levels. Above that, a slightly toxic response was obtained through 11 mM, with some loss of growth and decrease in activity levels of the worms as evaluated by decreased head thrashing or whole body movement in solution. A toxic response was observed, with severe growth loss and death at the highest concentration. Cysteine produced no toxic response through 2.7 mM, above which a precipitate was observed in the wells, accompanied by death of the nematodes. Desferrioxamine B produced no toxic response at all concentrations through

the maximum measured (see Section 8.3.3.). DMHP was nontoxic up to 0.67 mM concentration, slightly toxic through 2.7 mM, and toxic above that. Cyclam was nontoxic through 17 mM and slightly toxic above that. Na₂CaEDTA was slightly toxic through 4.25 mM and toxic at higher concentrations. Histidine was also observed to be nontoxic at all concentrations.

The metals were found to be toxic at much lower concentrations than the chelators. Cadmium produced a toxic response at concentrations as low as 200 μM. Copper produced a toxic response at concentrations as low as 320 μM. Nickel produced a toxic response at 225 μM, and zinc produced a toxic response at 500 μM. Surprisingly, no toxic response was observed in the presence of iron(III) up to a concentration of 10 mM.

8.4.2. Metal chelation protection assays

The results of the visual inspection of the metal-chelator protection assays are shown in Table 8.1. Statistical analysis of the p-values of protection of specimens from metal toxicity by chelator treatments are shown in Table 8.2. In the context of these experiments, p-values are statistical values that represent the probability that a treatment is unrelated to the outcome observed in the subjects (the probability that an outcome arose due to chance instead of due to the treatment). The outcome is a population distribution of log(EXT) values and the treatment is the presence of a

Table 8.1. Results of metal-chelator protection assays. Concentrations of metal are listed at the top of the column, while concentrations of each chelator used is listed in each box. Symbols: 0 – no protection, + - slight protection, ++ - full protection, -- - death of all specimens.

	<i>Cd(II)</i> (350 μ M)	<i>Cu(II)</i> (320 μ M)	<i>Ni(II)</i> (320 μ M)	<i>Zn(II)</i> (600 μ M)
AHA	0 (4.25 mM)	0 (1.1 mM)	0 (1.7 mM)	0 (4.25 mM)
Cyclam	0 (11 mM)	+ (1.7 mM)	++ (0.425 mM)	+ (0.67 mM)
Cysteine	0 (2.7 mM)	+ (1.1 mM)	0 (1.7 mM)	0 (1.7 mM)
DMHP	0 (1.7 mM)	++ (1.7 mM)	0 (1.1 mM)	0 (1.7 mM)
DFB	0 (29.7 mM)	++ (1.7 mM)	0 (27.2 mM)	0 (2.7 mM)
EDTA	++ (0.425 mM)	++ (0.425 mM)	++ (0.425 mM)	++ (0.67 mM)
Histidine	+ (29.7 mM)	++ (2.7 mM)	++ (1.1 mM)	-- (6.7 mM)

chelator. The population distribution of log(EXT) values when treated by the chelator with and without metal are compared to the population distribution of log(EXT) values without chelation treatment in the absence and presence of metal. For these experiments, statistical analysis was performed using a 2-way anova (two independent factors that can be analyzed separately) to allow analysis based on either number of specimens recovered alive or log EXT values measured by the COPAS Biosort. Analysis

Table 8.2. Statistical analysis of the results of metal-chelator protection assays.^a

Concentrations of all chemicals are the same as in Table 8.1.

	Cadmium ^b	Copper ^c	Nickel ^c	Zinc ^c
AHA	0.7513	0.8393 0.1064	0.3750 0.9113	0.7093 0.9435
Cysteine	0.6251	0.5607 0.7665	0.1677 0.7098	0.4477 0.9510
Cyclam	0.9177	0.8141 0.4527	0.0457 0.2231	0.2145 0.4818
DMHP	0.3658	0.9163 0.0929	0.4614 0.8220	0.2763 0.9999
DFB	0.9516	0.2143 0.0516	0.6252 0.4796	0.6267 0.5774
EDTA	0.0005	0.1660 0.0125	0.0019 0.0720	0.0051 0.0037
Histidine	0.0640	0.2550 0.0029	0.0005 0.3116	0.2802 0.1578

^a Values listed in boxes are P-values, or representative of the probability that the observed result of treatment by chelator could have arisen in the *C. elegans* population by chance. I.E. – lower P-values are more suggestive of a protective effect on the specimens due to treatment with chelator.

^b P-values for cadmium assays were calculated using the number of specimens recovered alive, as treatment with the metal resulted in death in the absence of the chelator.

^c P-values for copper, nickel, and zinc were calculated both by comparing the number of specimens recovered alive in the presence and absence of chelator (top value) and by comparing the log EXT values of metal-treated specimens to log EXT values of metal-and-chelator-treated specimens (bottom value).

of log(EXT) values was graciously performed by Marjolein Smith of SRA International, Inc (see Appendix E for more details on statistical analysis). In Tables 8.1. and 8.2., concentrations of metal and chelator used in each assay are listed along with the protective effect of each assay. For this study, a p-value of 0.25 or less is suggestive of a slight protective effect, while a p-value of 0.05 or less is suggestive of a strong protective effect. For each metal, a concentration was used that was above the minimum concentration required to produce a toxic effect to ensure reproducible toxic effects were obtained for the metal treatment. Some chelators required higher concentrations than would just provide full complex formation (>90% of metal chelated in some form), as lower concentrations provided little or no protection.

In the absence of chelators, cadmium exposure resulted in the death of almost all specimens. Additionally, it produced a toxic effect in the presence of all chelators except Na₂CaEDTA (full protection) and histidine (partial protection). This is observed in the p-values of Table 8.2., where Na₂CaEDTA has an extremely low p-value, which is strongly suggestive of protection of the specimens from metal toxicity by the ligand. This is also true for histidine, which exhibits a low P-value (0.064), suggestive of some protective effect by histidine. The toxic effect due to exposure to copper was not observed in the presence of DFB, DMHP, CaEDTA, and histidine based on visual inspection of the specimens. Partial protection was observed in the presence of cysteine and cyclam based on visual inspection of nematode subjects. p-value analysis, however, suggests little effect due to exposure to cysteine (p-value = 0.766) and cyclam (p-value =

0.453). Visual inspection suggested that acetohydroxamic acid provided no protection from copper toxicity, while p-value analysis suggested a slight effect based on log EXT values of recovered specimens (p-value = 0.106). Nickel toxicity was alleviated by treatment of the nematodes with cyclam (p-value = 0.046), CaEDTA (p-value = 0.002), and histidine (p-value = 0.0005). Zinc toxicity was not observed in the presence of cyclam (partial protection from visual inspection, p-value = 0.215) and CaEDTA (p-value = 0.005). While histidine alone did not produce a toxic effect, histidine in the presence of zinc was observed to kill the specimens consistently during the L3 phase.

8.5. Discussion

Development of novel chelation therapy agents is a lengthy process with multiple levels of testing, from the basic science of characterizing complex stability constants and membrane permeability (lipophilicity) to testing in animal models before moving on to human testing. The nematode, *C. elegans*, is an animal model that could provide another route for testing chelation agents before proceeding into tests of higher order organisms. One of the great strengths of *C. elegans* as a test model is how highly conserved their stress responses are at a genetic level compared to higher order organisms.⁽¹⁸⁴⁾ The assay developed here serves as a simple demonstration of the use of *C. elegans* as a model in the study of chelation therapy agents.

8.5.1. Chelator and metal toxicity assays

The response of the organisms to the chelators studied here are of interest in and of themselves, as this is a strong indicator of deleterious effects of the chelating agents. One important requirement for a chelation therapy agent is that the treatment cannot harm the subject on its own, as this brings into question the use of the agent at all. None of the molecules investigated here were highly toxic on their own, and only some were found to exhibit toxic effects in the subjects tested. Acetohydroxamic acid was chosen as a model chelator of hard metal ions, but it was found to be toxic at moderate concentrations (see Sec. 8.4.1). This is not surprising, as Acetohydroxamic acid has been observed to have a toxic effect in humans and is a proposed teratogen. Cysteine was found to be toxic at a moderate concentration (see Sec. 8.4.1), as well as promoting the formation of a precipitate in the wells. One potential source of toxicity of cysteine is oxidation over time in aqueous solution, forming reactive oxygen species that would harm the organism.⁽²⁰⁵⁾ Cyclam is a stable molecule with high hydrophilicity and low bioavailability, which results in low toxicity of the molecule until higher concentrations (see Sec. 8.4.1). Desferrioxamine B has been thoroughly characterized as a chelating agent for iron(III), and it is known to have low bioavailability and low serum half-life. The short residence of the compound in the organism is likely related to the lack of toxicity of the compound (see Sec. 8.4.1). 1,2-dimethyl-3-hydroxy-4-pyridinone has also been characterized as an iron(III) chelator and as stated earlier, there are some concerns about the toxicity of the molecule in the treatment of humans. This concern is reflected by the observed toxicity of the molecule at low concentrations in *C. elegans* (see Sec.

8.4.1). Calcium disodium EDTA was observed to have a slight toxic effect at low concentrations (see Sec. 8.4.1), likely due to the chelation of essential metals by the molecule, as it is a stable chelator for a variety of metals. Histidine exhibited low toxicity, likely because it is mostly unreactive and is an essential amino acid for all organisms.

The metals studied have all been found to have a toxic effect in organisms at relatively low concentrations, resulting in a concern with regards to their toxicity. Cadmium results in a toxic effect due to the inhibition of superoxide dismutase and other protective enzymes.⁽²⁰⁶⁾ Nickel, copper, and zinc, are essential metals in biological systems, but there is a certain level where the concentration of the metal exceeds that required for sustaining life. Copper acts as a catalyst, in addition to its role in small molecule transport in some organisms. However, it can also crosslink DNA strands, resulting in mutations in cells and aggregation of proteins. Additionally, there is the possibility that it can redox cycle in the presence of reactive oxygen species, resulting in the formation of oxygen radicals that can harm organisms. Buildups of the metal in plaques have been associated with Alzheimer's disease. Nickel is required for the production of hormones, but in excess it acts as a carcinogen. Zinc is an essential metal ion for a wide variety of processes including signaling and epigenetic regulation, resulting in its higher tolerance than other metal ions. An excess, however, will result in interference with the metabolism of other metal ions. All three of these would likely be available to the organism through uptake by the divalent metal transporter protein, as

well as possibly specialized uptake systems (Nik uptake cassette).(207, 208) While most of the above effects have been characterized only in human systems, it is very likely that they would remain relevant to the *C. elegans* model, which features numerous highly conserved genes to higher organisms as stated above.

8.5.2. Metal chelation protection assays

The toxicity of metals is related to the bioavailability of the metal, which is in turn related to a number of factors. The bioavailability of any species is influenced by the size, shape, and charge of the species, as these are the characteristics that allow a species to interact with any number of uptake pathways in the biological system.

Complexation of a metal changes all of these factors, as a change in the inner coordination sphere can result in an increase in the effective size of the metal complex compared to the metal ion, as well as the shape. Also, as most of the ligands used here feature ionizable sites, complexation of the metal will result in a more negative charge for the complex compared to the aquated metal ion. For the purposes of this study, chelation does not necessarily have to be complete or in the highest order of complex to be seen as protective from metal toxicity, as partial chelation could still reduce the effective concentration of metal available to the organism due to the changes in shape, size, and charge from even partial chelation.

Table 8.3. pM value of the chelators studied here for the metals used in this study.^a

Metal	Cd(II)	Cu(II)	Ni(II)	Zn(II)
Chelator				
AHA	6.00	7.201	6.029	6.033
Cyclam	11.83	6.409	6.007	6.006
Cysteine	6.028	21.64	13.65	9.055
DMHP	^b	10.38	6.094	6.167
DFB	6.00	11.46	6.381	6.770
EDTA	14.58	15.44	16.68	14.68
Histidine	6.007	9.728	7.626	6.090

^apM values were calculated at the following conditions:

$[M]_{\text{tot}} = 10^{-6} \text{ M}$, $[L]_{\text{tot}} = 10^{-5} \text{ M}$, pH = 7.4, T = 25 °C,

$\mu = 0.10 \text{ M}$.

^bStability constants for the Cd-DMHP system have yet to be characterized.

Table 8.3. provides calculated pM values for the metal-chelator systems studied here. Figures 8.2.-8.5. show histograms that correlate the calculated pM values to observed p-values for treatment by metal-ligand systems. In order to be able to make a statement about the relationship between high pM value and protective ability of the chelator, it would be necessary to observe a pairing of high pM bar ($pM > 10$) with a low p-value calculated from either survival or growth ($\log(\text{EXT})$ values), or conversely a pairing of low pM value and high p-value. Acetohydroxamic acid was found to be ineffective at protecting the organisms from any metal studied here, despite the high order of complex formation in the case of copper, zinc, and nickel. At the concentrations of ligand used in each of those experiments, at least 65% of the metal was chelated by ligand in some form (much greater for copper, see speciation diagrams in Appendix E), suggesting that other mechanisms are at work in this system that would prevent protection by acetohydroxamic acid. In the case of cadmium, no complexation was predicted, suggesting that the low affinity of the metal for AHA was related to the inability of AHA to protect from cadmium toxicity.

Cysteine only provided partial protection from copper toxicity (Fig. 8.3.), despite forming a stable complex with cadmium as well (Fig. 8.2.). Its inability to protect against zinc and nickel toxicity is likely related to its inability to chelate those metals, although there is also the possibility of the catalysis of side reactions due to the presence of metals. Cyclam was predicted to form stable complexes with copper, zinc, and nickel, and it also exhibited some protective effect from all three of those metals, although it

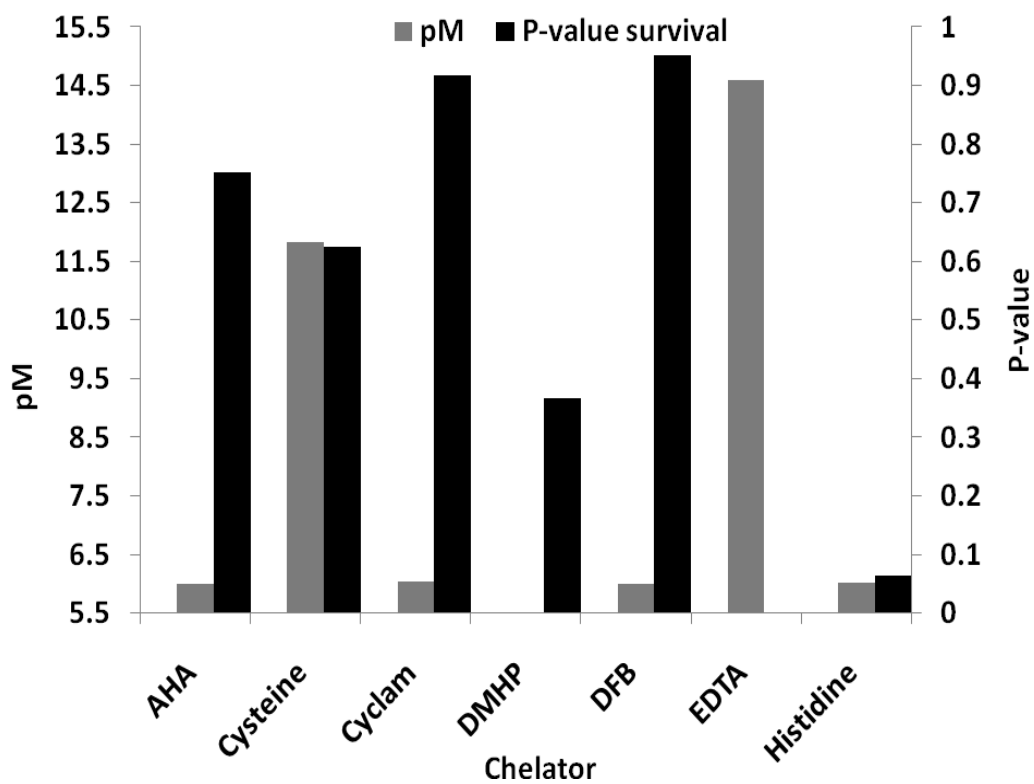


Figure 8.2. Histogram comparing pM value of chelator with cadmium with calculated P-value of treatment of *C. elegans* with metal and chelator. pM values taken from Table 8.3. and P-values taken from Table 8.2.

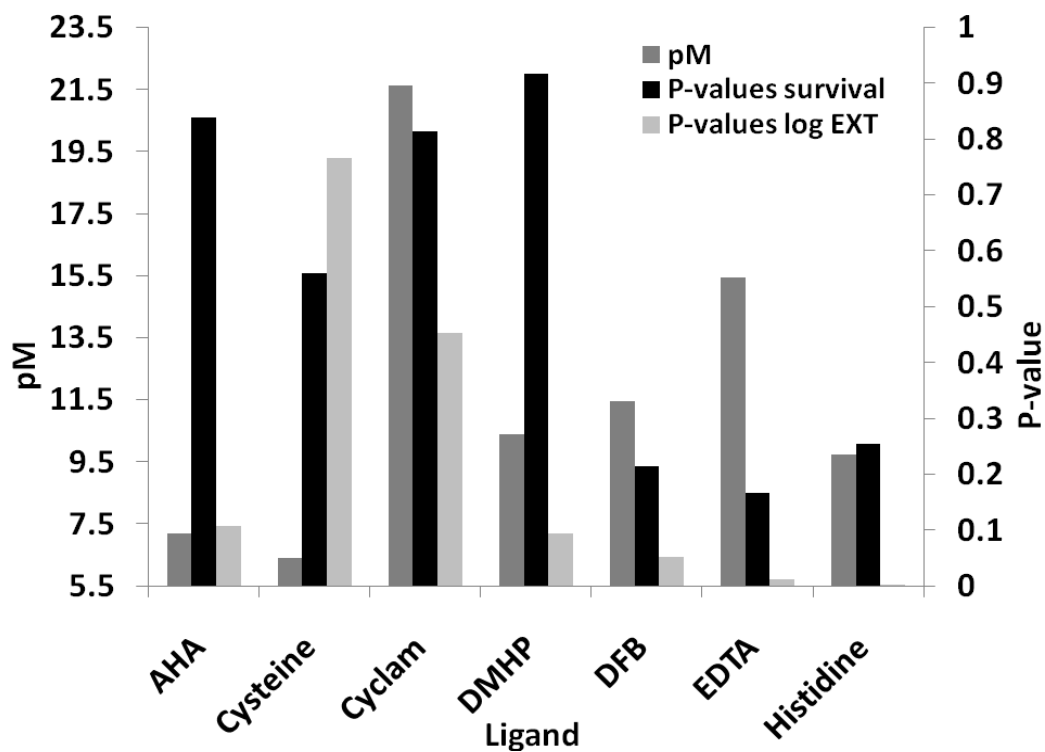


Figure 8.3. Histogram comparing pM value of chelator with copper with calculated P-value of treatment of *C. elegans* with metal and chelator. pM values taken from Table 8.3. and P-values taken from Table 8.2.

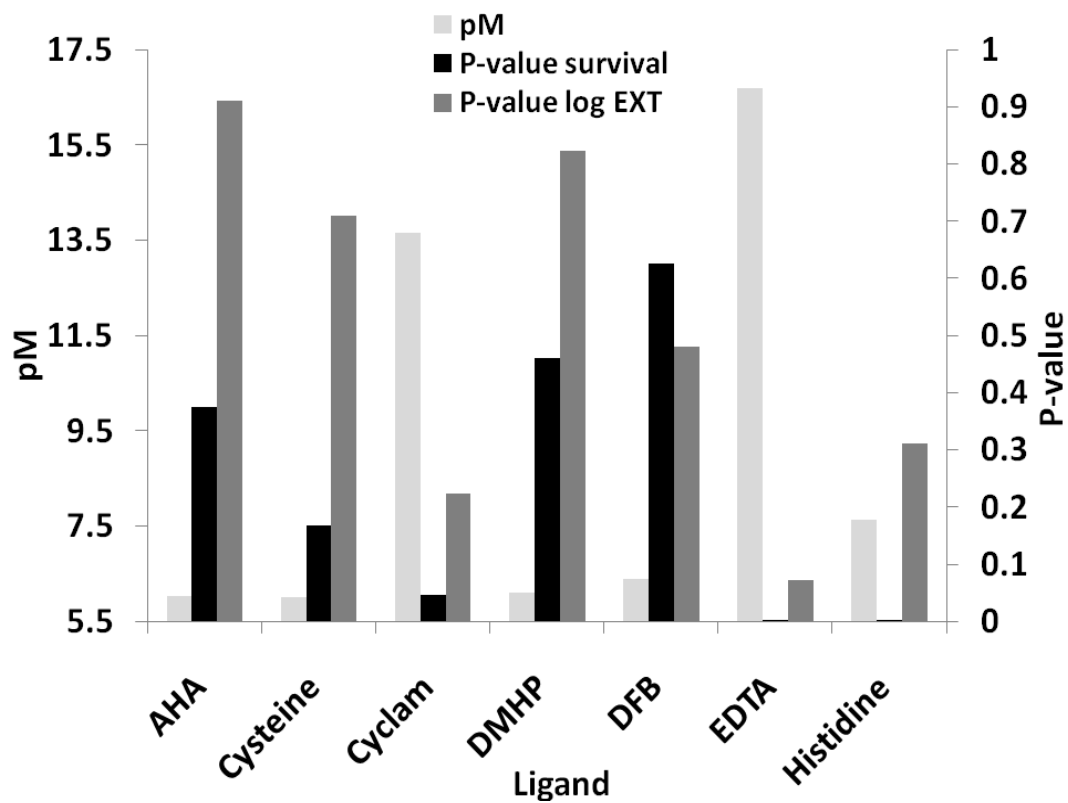


Figure 8.4. Histogram comparing pM value of chelator with nickel with calculated P-value of treatment of *C. elegans* with metal and chelator. pM values taken from Table 8.3. and P-values taken from Table 8.2.

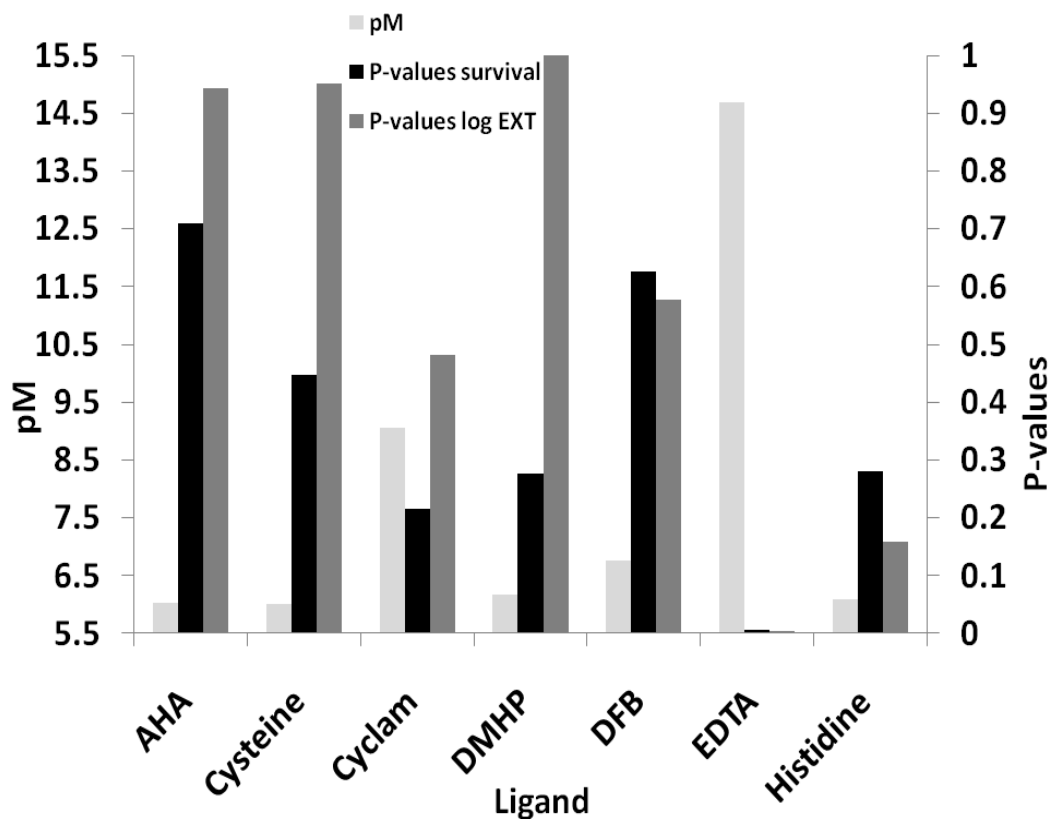


Figure 8.5. Histogram comparing pM value of chelator with zinc with calculated P-value of treatment of *C. elegans* with metal and chelator. pM values taken from Table 8.3. and P-values taken from Table 8.2.

only exhibited full protection against nickel toxicity. Desferrioxamine B chelates copper, nickel, and zinc relatively strongly, but only provided protection against copper toxicity. This is likely due to the relative strength of chelation. The chelated groups are protonated relatively easily in the nickel and zinc complexes, resulting in a low relative stability of the complex as solution pH changes. DMHP chelates copper relatively strongly and provides partial chelation of nickel and zinc based on the simulations performed (see Appendix D). This low degree of complex stability is likely related to the inability to protect from nickel and zinc toxicity. The stability of the cadmium-DMHP complex has yet to be characterized, although it is likely that the complex stability is relatively low, as DMHP features hard donor atoms and cadmium is a moderate Lewis acid.(22)

CaNa₂EDTA was the only chelator that provided protection from all four metals studied here. EDTA is known as a stable chelator of many metals, resulting in its widespread application. As mentioned previously, it is also currently used to treat toxicity of a number of metals. The use of CaNa₂EDTA is favorable over a number of other chelators, including Na₂EDTA, as it is less likely to coordinate and remove essential metal ions. The use of Na₂H₂EDTA has been associated with hypocalcemia in patients and other metal-deficient conditions.(182) By using the calcium coordinated form of the chelator, the removal of calcium from the system is avoided, and by using approximately the same concentration of chelator as metal present in the system prevents a large excess of chelator that would chelate other essential metals.

Interestingly, histidine was found to have a protective effect against most of the metals studied here, despite its relatively low degree of chelation of cadmium and nickel. One study suggested that excess histidine abrogates nickel toxicity through other mechanisms than chelation of the metal, possibly involving the storage of excess histidine in vacuoles in the cell.(209)

The above results demonstrate that while in most cases strong thermodynamics of complex formation (i.e. – high pM value) is necessary for explaining efficacy of chelation therapy, that factor alone is not sufficient for the development of effective chelating agents. One probable reason for this is the variety of environments that the metal complex encounters in the experimental environment. While the complexes may encounter approximately neutral environments in the wells of the 96-well plate, the primary route of entry of the toxicant into the worm is through ingestion. The environment of the gut of the worm is more acidic than the external environment (this has been inferred based on the optimal pH for proteases found in the lumen of *C. elegans*), which suggests that some complexes that were simulated as stable around pH 6.5 may dissociate, making the metal bioavailable again upon ingestion.(210) Also, it is unclear what mechanism results in the bioavailability of the metal in the worm, so while some metals may remain even partially chelated, these complexes may still be bioavailable upon ingestion.

Additional work is required using this model to fully develop the assay into a tool for the investigation of chelation therapy agents. While the metals investigated here all exhibited toxic responses at low concentrations, it is unclear that all known toxic metals would produce a toxic effect. Primary investigations were done with the iron(III) complexes of nitrilotriacetic acid and citric acid to investigate the toxicity of iron(III) in the *C. elegans* system, but no toxic effect was observed through higher concentrations (10 mM) for either complex. Also, additional complexing agents would have to be tested to ensure the reliability of the test in predicting quality of chelating agent. Additionally, the tests performed here did not address the chelator concentration dependence of the toxic response. These experiments would provide information with regards to the minimum concentration of chelator required to protect the subject from the toxic effects of the metal.

While the assay developed here seems to have some strength in the identification of potential chelation therapy agents, the assay is not directly analogous to chelation therapy agents. In chelation therapy, the subject likely will have already been exposed to the metal for some time before the administration of the chelating agent, while the assay developed here exposes the nematodes to metal and chelator at the same time. Thus, it is foreseeable that another assay would be useful involving the testing of the administration of the chelator some time after exposure of the subject to the toxic metal. Also, while the ideal chelation therapy agent will be bioavailable, allowing oral administration, many chelation therapy agents are administered parenterally,

suggesting that exposure of chelate complexes to the acidic environment of the gut skews the results of protection assays due to complex dissociation. Despite the limitations described above, the experiments described here demonstrate the strength of *C. elegans* as a model system for studying the toxicity and protective effects of potential chelation therapy agents.

8.5.3. Alternative applications

While the stated purpose of the assay developed here is to aid in the development of chelation therapy agents, there is an additional application for the assay in the field of soil remediation. The exposure of soil to toxic metals and the bioavailability of the toxic metals is a concern, resulting in the need to remove the toxic metals from the environment. One potential approach to this would be to significantly decrease the bioavailability of the toxic metal in the soil through the application of chelating agents. As the main focus of this treatment would be to decrease the bioavailability of metals, the assay described here would be an invaluable tool in predicting chelators that would remove the toxic effects of the metals in the environment.

8.6. Conclusions

The development of chelation therapy agents can be a lengthy, complicated process involving testing a wide variety of compounds. A method to quickly and

effectively assess the abilities of a particular chelating agent to protect an organism from metal toxicity would be a great benefit to the development of new, more effective chelation therapy agents. The model developed here makes use of the nematode, *C. elegans* to evaluate the protective effect of a wide variety of chelation therapy agents, which can serve as initial testing for effectiveness of a chelator. The results presented above demonstrate that (A) high complex stability (as evidenced by pM values) is necessary, but not sufficient, to provide effective protection of an organism from metal toxicity, and (B) *C. elegans* can serve as an effective model for higher organisms in the testing of chelation therapy agents.

Appendix A: Calculation of pFe values

As discussed in Chapter 1, pFe values are useful in comparison of complex stability between ligand systems where ligand denticity and acidity can vary greatly depending on the type of donor group. The calculation of these values can be a complicated process due to the great number of variables involved in the chemical equilibria, especially in cases where complex formation involves multiple complex stoichiometries depending on the solution conditions. This appendix will discuss the calculation of pFe values from known iron complex formation constants ($\log \beta$ values) and ligand protonation constants. The first example will illustrate the calculations necessary to determine the pFe value of a simple system where a single ligand interacts with iron to form a 1:1 complex, and the subsequent discussion will focus on computational methods of determining pFe in more complex systems.

Calculation of pFe in a 1:1 M:L complex system

The determination of pFe values requires knowledge of equilibrium constants of complex formation, as well as ligand protonation constants. Due to ligand protonation in aqueous solvent systems, competition is observed between protons and the metal for accepting electron density from the ligand donor groups. A value representing the degree of protonation of the free ligand or metal-ligand complex in solution is called the Ringbom Coefficient. The Ringbom coefficient for a particular system is determined from the mass balance equation for that system. An example of this value for the ligand is shown below.

$$L_{tot} = [L] + [LH] + [LH_2] + \dots \quad (\text{A.1.})$$

$$L_{tot} = [L] + K_{a1}[L][H^+] + \beta_{a2}[L][H^+]^2 + \dots \quad (\text{A.2.})$$

$$L_{tot} = [L](1 + K_{a1}[H^+] + \beta_{a2}[H^+]^2 + \dots) \quad (\text{A.3.})$$

$$\alpha_L = 1 + K_{a1}[H^+] + \beta_{a2}[H^+]^2 + \dots \quad (\text{A.4.})$$

$$L_{tot} = [L]\alpha_L \quad (\text{A.5.})$$

A similar value of the Ringbom coefficient exists for the metal-ligand complex, α_{FeL} , but for the sample calculations shown here, the Ringbom Coefficient for the metal is ignored, as it is assumed that the free metal ion present in solution is hydrolyzed to a relatively small extent.

$$\alpha_{FeL} = 1 + K_{a1}[H^+] + \beta_{a2}[H^+]^2 + \dots \quad (\text{A.6.})$$

$$[FeL]_{tot} = [FeL]\alpha_{FeL} \quad (\text{A.7.})$$

While the unconditional complex stability constant, $\log \beta_{110}$ is the equilibrium constant that is most often associated with iron-siderophore complexes, it is possible to define modified form of the complex formation constant, which shall be referred to as β_{110}' .

$$\beta_{110}' = \frac{[FeL]_{tot}}{[Fe]_{tot}[L]_{tot}} \quad (\text{A.8.})$$

By substituting Equations A.5. and A.7. into Equation A.8., one obtains

$$\beta_{110}' = \frac{\alpha_{FeL} [FeL]}{[Fe]_{tot} \alpha_L [L]} \quad (A.9.)$$

Using the assumption that the total uncomplexed metal ion is found in solution as the free aqueous metal, or $[Fe]_{tot} = [Fe]$ and then substituting in the expression for the unconditional complex stability constant, β_{110} , it can be shown that

$$\beta_{110}' = \beta_{110} \frac{\alpha_{FeL}}{\alpha_L} \quad (A.10.)$$

The conditions at which most pFe values are reported in the literature are $[Fe]_{tot} = 1 \times 10^{-6}$ M and $[L]_{tot} = 1 \times 10^{-5}$ M. As such, it is possible to arrange a concentration table as shown below:

Table A.1. Concentration table for the calculation of pFe values from standard conditions.

	$[Fe^{3+}]$	$[L]$	$[FeL]$
Initial Total	1×10^{-6} M	1×10^{-5} M	0
Stoichiometric reaction	0 M	9×10^{-6} M	1×10^{-6} M
Final concentration	x	$9 \times 10^{-6} + x$ M	$1 \times 10^{-6} - x$ M

As the complex formation reactions of iron-siderophore complexes are highly thermodynamically favored, it is generally safe to assume that the concentration of free iron(III) at equilibrium is much smaller than the concentrations of ligand and metal-ligand complex. Using these equilibrium concentration expressions and the previous assumption, it is possible to express the equilibrium constant, β_{110}' as

$$\beta_{110}' = \frac{(1 \times 10^{-6})}{[Fe]_{tot} (9 \times 10^{-6})} \quad (\text{A.11.})$$

By substitution of Equation A.11. into Equation A.10., the expression for determination of the free metal ion at low proton concentrations (moderate to high pH values, usually 4-10) is

$$[Fe]_{aq} = \frac{\alpha_L}{9\alpha_{FeL}\beta_{110}} \quad (\text{A.12.})$$

If it is necessary to determine the pFe value of a complex at low pH values, the degree of protonation of the ligand and the metal-ligand complex becomes significant, and the concentration of free metal ion in solution becomes comparable to the concentration of L and the FeL complex at equilibrium, so the assumptions used to derive Equation A.11. become invalid. At such conditions, it is necessary to solve for the free iron concentration rigorously. In order to solve rigorously for the free metal ion concentration, the expression for β_{110} takes the form of

$$\beta_{110} = \frac{(1 \times 10^{-6} - x)\alpha_L}{x(9 \times 10^{-6} + x)\alpha_{FeL}} \quad (\text{A.13.})$$

By distributing all terms, multiplying both sides by the denominator, and then setting the equation equal to zero, the expression becomes

$$\alpha_{FeL}\beta_{110}x^2 + (9.0 \times 10^{-6}\alpha_{FeL} + \alpha_L)x - 1.0 \times 10^{-6}\alpha_L = 0 \quad (\text{A.14.})$$

From Equation A.14., it is possible to determine the concentration of iron present in solution from the quadratic equation:

$$[Fe^{3+}] = x = \frac{-b \pm \sqrt{b^2 - 4ac}}{2a} \quad (\text{A.15.})$$

Where $a = \alpha_{FeL}\beta_{110}$, $b = 9.0 \times 10^{-6}\alpha_{FeL} + \alpha_L$, and $c = 1.0 \times 10^{-6}\alpha_L$. This calculation provides the concentration of free iron present in solution over a range of pH values, and is approximately the same value as that provided by Equation A.12. at moderate and high pH values.

Calculation of pFe in higher stoichiometry iron-ligand complexes

The calculation of pFe values in systems where more than one complex may be present or where the complex stoichiometry is higher than 1:1 is usually more difficult

due to more complex solution thermodynamics. In such cases, it may be simpler to determine the concentration of free iron present in solution using a computer-based speciation simulation program, such as HySS.(131)

The use of HySS requires knowledge of all of the complex stability constants and ligand protonation constants for the system of interest. Upon starting the program, you will be asked to choose an existing system or to design a new system. For the purposes of this discussion, we will go through the process of designing a new system. Upon choosing the “New Project” option, the box shown in Fig. A.1. will appear.

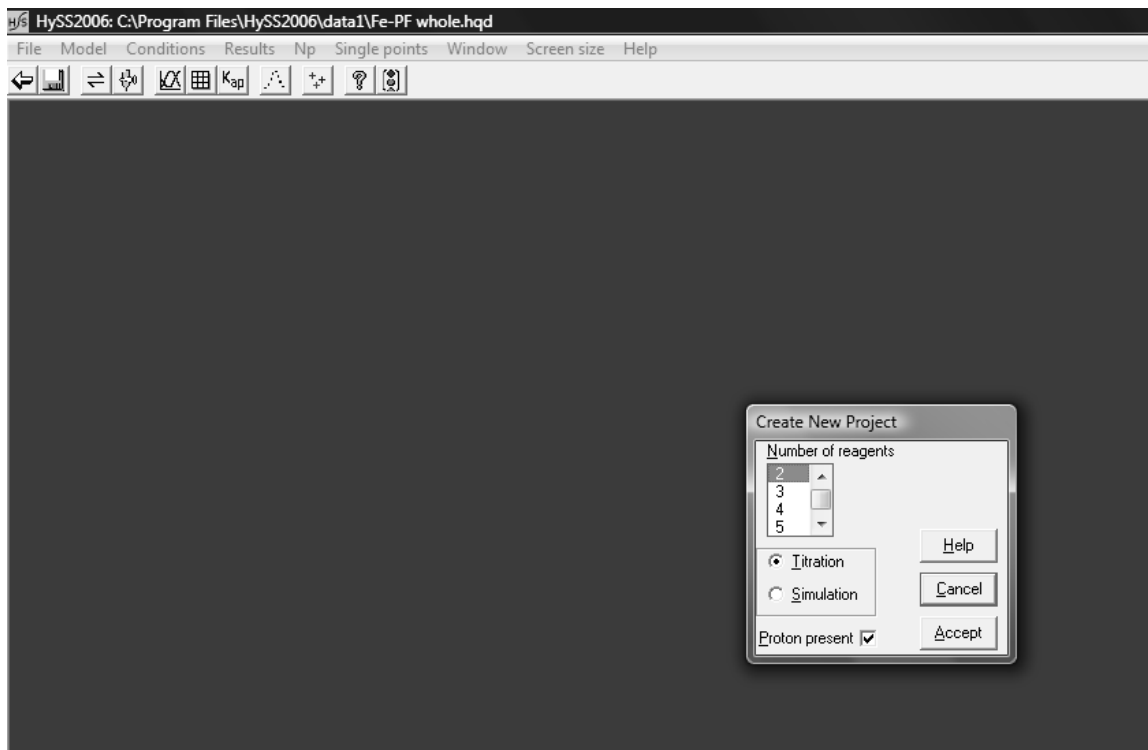


Figure A.1. Upon choosing to create a new project in HySS, a box will appear requesting the number of reagents present in the system, including protons.

The box shown in Fig. A.1. requests the number of reagents present in the system. This feature allows the user to model complex systems where a large number of metals and ligands are present at the same time, but in the context of the discussion here, the user should select 3 reagents, iron, the ligand, and protons, as well as clicking the “Simulation” option, followed by “Accept.” Next, a new box will appear for the user to input the file name and save the file. Upon selection of a file name, a new box will appear where the user can specify all of the known equilibrium constants for the system of interest. The input of HySS involves specifying the stoichiometry of each reagent involved in the equilibrium, as well as the overall equilibrium constant, or the β value of the equilibrium. Fig. A.2. shows the example of the L^{PF} system, discussed in Chapter 6.

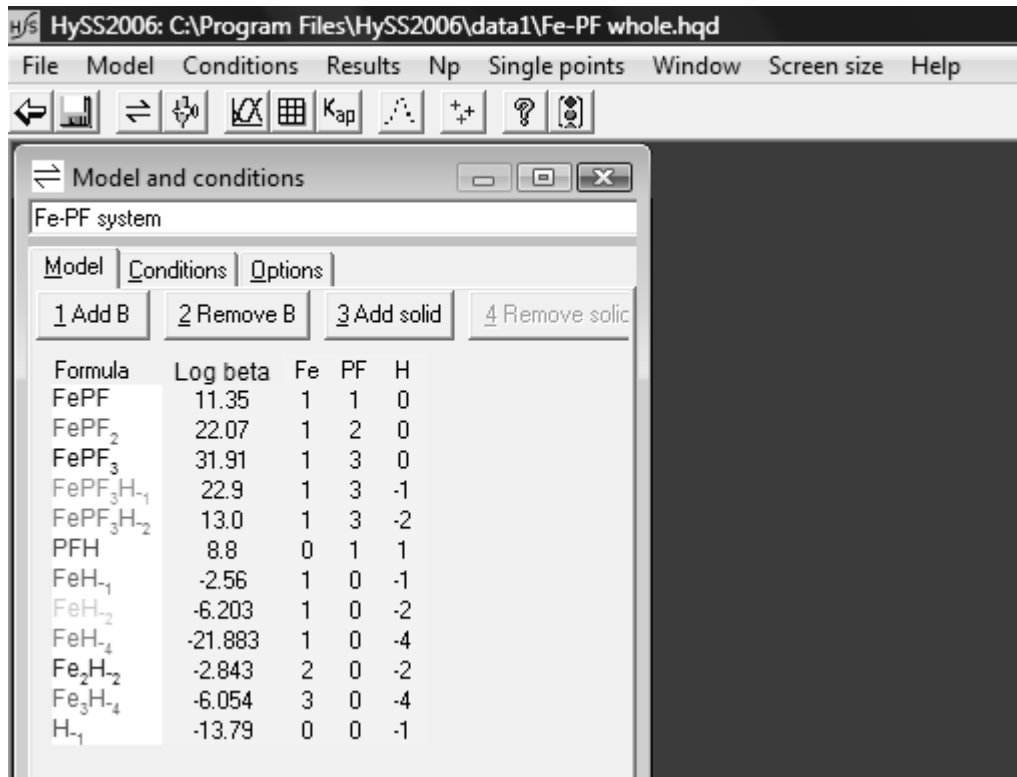


Figure A.2. Sample input screen for the Fe- L^{PF} system from Chapter 6.

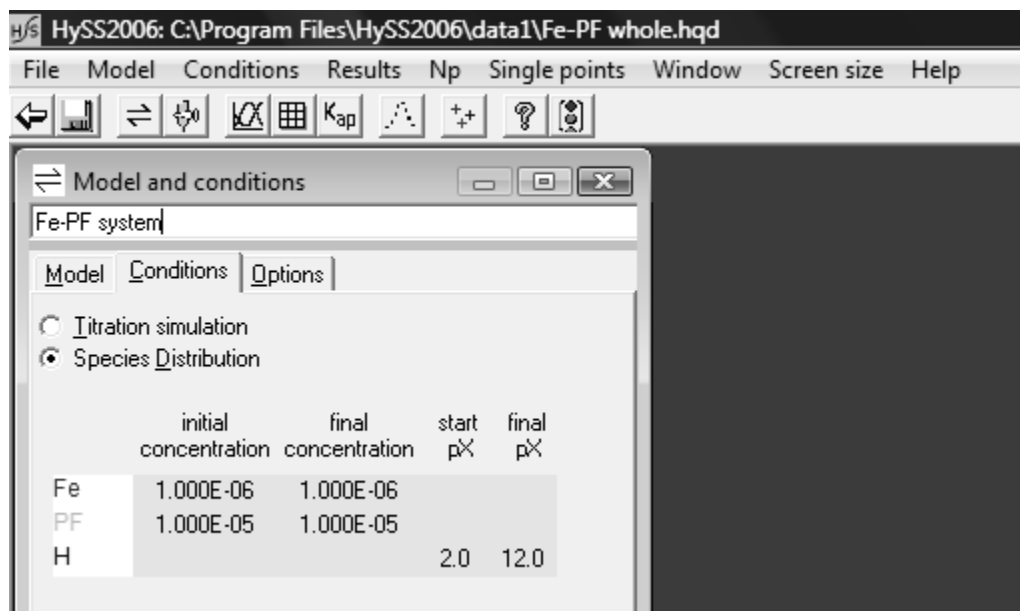


Figure A.3. The conditions tab allows input of the concentrations of each reagent, as well as the range of pH values of interest.

Upon entering the equilibrium constants for the metal-ligand model, it is necessary to specify the concentrations of each reagent in solution by clicking on the “Conditions” tab, shown in Fig. A.3. In the example shown above, the concentrations being used to calculate the speciation model for the system are the standard concentrations of 10^{-6} M metal and 10^{-5} M ligand. The calculation of the speciation model can be performed over a range of pH values, which allows rapid determination of pFe values as a function of pH, which may be of interest due to changing pH values in biological systems.

Once the concentrations of the reagents have been entered, the user can generate a speciation diagram using the specified conditions by pressing the “Draw Graph”

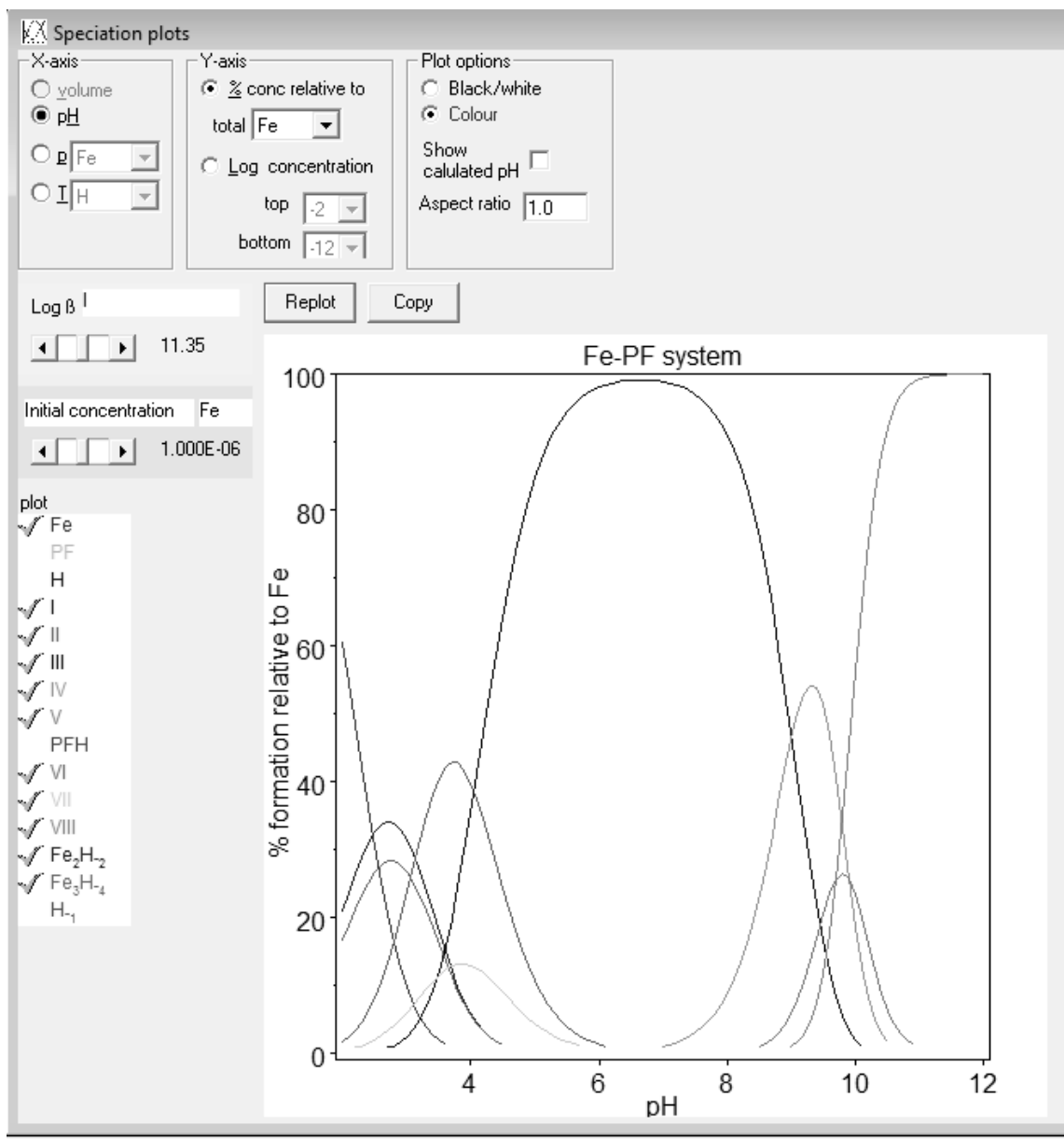


Figure A.4. Speciation diagram produced by HySS using the entered equilibrium constants and reagent concentrations.

button on the tool bar or by selecting "Plot" from the "Results" drop-down menu. One such plot is shown in Fig. A.4. By clicking on the curves contained on the plot, the program will provide a label of the species represented by the curve. In most

siderophore systems, aside from very low pH conditions, the curve representing free iron will be too low to be plotted on the speciation diagram. A more accurate representation of the free iron concentration can be obtained by clicking the “Concentrations’ Table” box in the tool bar or by clicking the “Table” option on the “Results” drop-down menu. By doing so, a table of the concentration of each species present in solution will appear, as shown in Fig. A.5. From this window, it is possible to copy the concentration table by clicking on the “Copy to Clipboard” button, highlighted in red on Fig. A.5. After copying the data to the clipboard, the concentration table can be pasted into a spreadsheet program, such as Excel. From there, it is possible to calculate the pFe value of the system over a range of pH values, as well as speciation plots in Excel. Note that, as discussed in Chapter 1, the pFe value only includes the concentration of non-

HySS - Concentration table. Created at 4/14/2010 4:00:57 PM

Concentrations / mol dm-3: Fe-PF system

	total Fe	total PF	total H	free Fe	free PF	p(H)	FePF	FePF2	FePF3	FePF3H-1	FePF3H-2	PFH	FeH-1	FeH-2
1	1.0000E-06	1.0000E-05	1.0010E-02	6.038e-07	1.546e-12	2.00	2.090e-07	1.696e-08	1.814e-10	1.773e-17	2.232e-25	9.757e-06	1.663e-07	3.76
2	1.0000E-06	1.0000E-05	7.9528E-03	5.449e-07	1.938e-12	2.10	2.364e-07	2.405e-08	3.225e-10	3.968e-17	6.288e-25	9.715e-06	1.889e-07	5.41
3	1.0000E-06	1.0000E-05	6.3190E-03	4.839e-07	2.429e-12	2.20	2.631e-07	3.353e-08	5.634e-10	8.726e-17	1.741e-24	9.668e-06	2.112e-07	7.61
4	1.0000E-06	1.0000E-05	5.0212E-03	4.226e-07	3.041e-12	2.30	2.877e-07	4.592e-08	9.663e-10	1.884e-16	4.733e-24	9.618e-06	2.322e-07	1.05
5	1.0000E-06	1.0000E-05	3.9904E-03	3.625e-07	3.807e-12	2.40	3.090e-07	6.173e-08	1.626e-09	3.991e-16	1.262e-23	9.563e-06	2.508e-07	1.42
6	1.0000E-06	1.0000E-05	3.1715E-03	3.053e-07	4.763e-12	2.50	3.256e-07	8.138e-08	2.682e-09	8.287e-16	3.239e-23	9.504e-06	2.659e-07	1.91
7	1.0000E-06	1.0000E-05	2.5210E-03	2.523e-07	5.956e-12	2.60	3.364e-07	1.052e-07	4.334e-09	1.686e-15	8.450e-23	9.440e-06	2.767e-07	2.50
8	1.0000E-06	1.0000E-05	2.0043E-03	2.045e-07	7.445e-12	2.70	3.409e-07	1.332e-07	6.859e-09	3.360e-15	2.120e-22	9.372e-06	2.823e-07	3.21
9	1.0000E-06	1.0000E-05	1.5938E-03	1.626e-07	9.299e-12	2.80	3.385e-07	1.652e-07	1.063e-08	6.553e-15	5.205e-22	9.299e-06	2.825e-07	4.05
10	1.0000E-06	1.0000E-05	1.2678E-03	1.267e-07	1.161e-11	2.90	3.293e-07	2.006e-07	1.611e-08	1.251e-14	1.251e-21	9.221e-06	2.772e-07	5.00
11	1.0000E-06	1.0000E-05	1.0087E-03	9.676e-08	1.448e-11	3.00	3.137e-07	2.384e-07	2.389e-08	2.335e-14	2.939e-21	9.138e-06	2.665e-07	6.06
12	1.0000E-06	1.0000E-05	8.0298E-04	7.241e-08	1.805e-11	3.10	2.927e-07	2.773e-07	3.464e-08	4.261e-14	6.754e-21	9.049e-06	2.511e-07	7.15
13	1.0000E-06	1.0000E-05	6.3951E-04	5.307e-08	2.249e-11	3.20	2.672e-07	3.154e-07	4.909e-08	7.603e-14	1.517e-20	8.955e-06	2.316e-07	8.35
14	1.0000E-06	1.0000E-05	5.0964E-04	3.808e-08	2.800e-11	3.30	2.388e-07	3.509e-07	6.798e-08	1.325e-13	3.329e-20	8.856e-06	2.093e-07	9.50
15	1.0000E-06	1.0000E-05	4.0646E-04	2.676e-08	3.484e-11	3.40	2.087e-07	3.816e-07	9.199e-08	2.258e-13	7.141e-20	8.752e-06	1.851e-07	1.05
16	1.0000E-06	1.0000E-05	3.2448E-04	1.840e-08	4.333e-11	3.50	1.785e-07	4.059e-07	1.217e-07	3.759e-13	1.497e-19	8.645e-06	1.603e-07	1.15
17	1.0000E-06	1.0000E-05	2.5934E-04	1.239e-08	5.385e-11	3.60	1.494e-07	4.221e-07	1.573e-07	6.118e-13	3.066e-19	8.535e-06	1.358e-07	1.22
18	1.0000E-06	1.0000E-05	2.0758E-04	8.167e-09	6.690e-11	3.70	1.223e-07	4.295e-07	1.988e-07	9.735e-13	6.143e-19	8.422e-06	1.127e-07	1.28
19	1.0000E-06	1.0000E-05	1.6644E-04	5.272e-09	8.309e-11	3.80	9.807e-08	4.277e-07	2.458e-07	1.516e-12	1.204e-18	8.309e-06	9.162e-08	1.31
20	1.0000E-06	1.0000E-05	1.3375E-04	3.335e-09	1.032e-10	3.90	7.703e-08	4.171e-07	2.977e-07	2.311e-12	2.311e-18	8.195e-06	7.296e-08	1.31
21	1.0000E-06	1.0000E-05	1.0777E-04	2.068e-09	1.281e-10	4.00	5.931e-08	3.987e-07	3.534e-07	3.453e-12	4.347e-18	8.083e-06	5.695e-08	1.25
22	1.0000E-06	1.0000E-05	8.7112E-05	1.258e-09	1.591e-10	4.10	4.479e-08	3.739e-07	4.115e-07	5.063e-12	8.024e-18	7.973e-06	4.361e-08	1.24
23	1.0000E-06	1.0000E-05	7.0692E-05	7.508e-10	1.976e-10	4.20	3.321e-08	3.444e-07	4.707e-07	7.290e-12	1.455e-17	7.866e-06	3.278e-08	1.18

Figure A.5. Concentration table generated by HySS, which can be used to calculate pFe, as well as complex speciation plots.

hydrolyzed metal, so the only column that should be used to calculate pFe is the column labeled “Free Fe.”

The Unsuccessful Ligand

In Chapter 1, it was discussed that the pFe value only represents the concentration of completely aquated iron(III), which is not the sole constituent of soluble iron. Of the total soluble iron concentration at any given pH, a significant portion of the total will be partially hydrolyzed iron, such as $\text{Fe}(\text{OH})_2^+$ and $\text{Fe}(\text{OH})_4^-$. Thus, as the pH increases, the pFe value will always increase, due to the conversion of aqueous iron to hydrolyzed forms, and the difference between the pFe and the pFe_{tot} , or the negative logarithm of the total concentration of soluble iron will always increase, as well. This can be demonstrated by comparison of a plot of pFe as a function of pH with a plot of pFe_{tot} as a function of pH, shown in Fig. A.6.

The techniques described in the previous section can also be used in calculating the pFe value of an “unsuccessful ligand,” where the molecule is unable to bind appreciably to iron. In such a case, the use of HySS would provide a pFe value of aqueous iron in the absence of a chelating ligand, essentially the pFe value of water.

Calculation of the concentration of free, fully aqueous iron provides a pFe value of 14.65, suggesting that for chelation to be strong enough to prevent precipitation of iron hydroxides, the pFe value of the ligand must be at least 14.65.

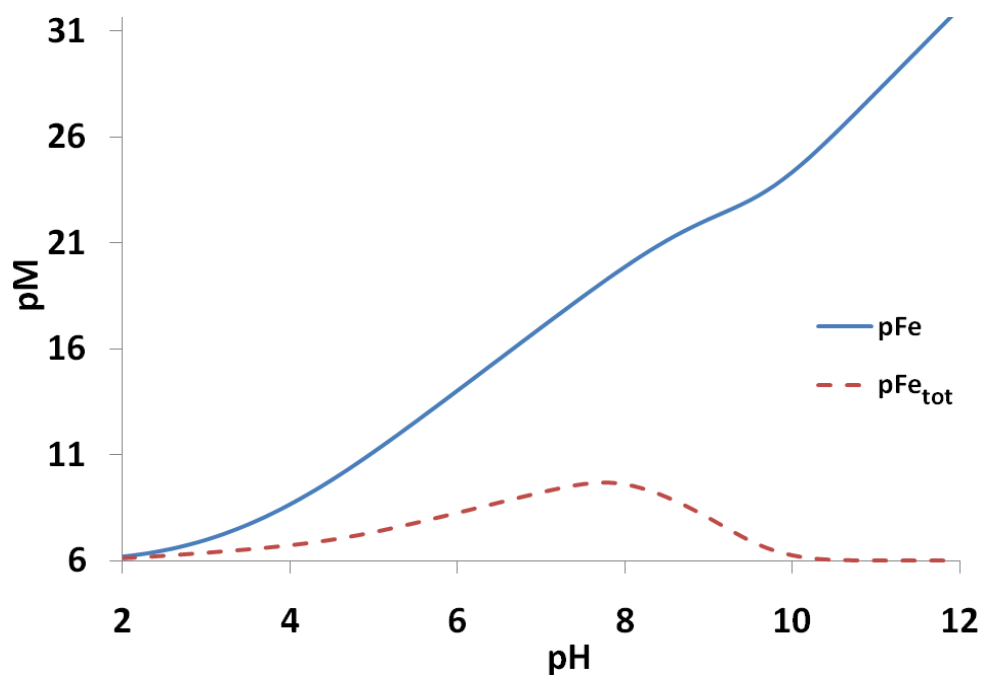


Figure A.6. Plot of pM as a function of pH. Values shown on the plot are pFe (solid line), which represents the concentration of fully aquated iron(III) in solution, and pFe_{tot} (dashed line), which represents the total concentration of soluble, unchelated iron present in solution. The pM values are calculated for the L^{PF} system, described in

Chapter 6. Conditions: [Fe]_{tot} = 10⁻⁶ M, [L^{PF}]_{tot} = 10⁻⁵ M, T = 25 °C, μ = 0.10 M.

Appendix B: Synthesis of 3-hydroxy-2-pyridinone siderophore mimics

Synthesis of the 3-hydroxy-2-pyridinone siderophore mimics was performed by the Gopalan Lab at New Mexico State University under the supervision of Hollie Jacobs and Sumathi Chittamuru

General procedures. Infrared spectra were recorded on a Perkin Elmer FT-IR 1720X spectrometer. ^1H NMR (200 MHz) and ^{13}C NMR (50 MHz) were obtained on a Varian XL 200. Spectra obtained in CDCl_3 were recorded using tetramethylsilane as an internal reference. ^1H NMR spectra recorded in D_2O used the HOD peak as an internal reference (4.72 ppm). 1,4-Dioxane (66.5 ppm) was used as an internal reference for ^{13}C NMR spectra recorded in D_2O . Elemental analyses were performed by Desert Analytics, Tucson, Arizona.

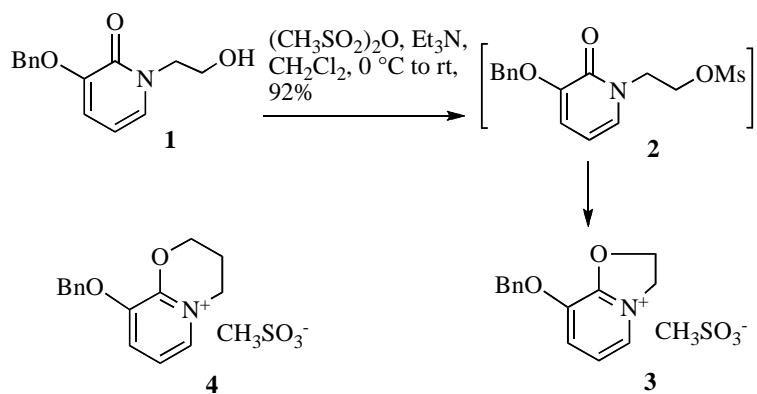
Hydroxypyridinone alcohol **1** and $\text{N}^2(\text{prLH})_2$ were prepared by published procedures.^(94, 211) Reagents were generally obtained from Aldrich Chemical Company and were used without further purification unless otherwise indicated. All solvents were HPLC grade and were obtained from Fisher Scientific or VWR Scientific. Column chromatography was done on silica gel (60-200 mesh).

*N*₂(*prLH*)₂ synthesis. IR (KBr): 3229, 1651, 1600 cm⁻¹; ¹H NMR (200 MHz, D₂O) δ 2.0 (m, 4H), 2.43 (m, 8H), 2.55 (m, 4H), 4.05 (t, *J*=6.9Hz, 4H), 6.14 (t, *J*=7.2 Hz, 2H), 6.79 (dd, *J*=7.4, 1.7 Hz, 2H), 6.82 (dd, *J*=7.0, 1.6 Hz, 2H); ¹³C (50 MHz, D₂O) δ 23.3, 46.6, 48.6, 53.7, 108.9, 118.9, 128.9, 145.4158; Anal. calc'd for C₂₀H₂₈N₄O₄·2HBr: C, 43.65; H, 5.50; N, 10.18. Found: C, 43.45; H, 5.54; N, 9.79.

Iminium salt (3). A solution of methanesulfonic anhydride (2.5g, 14.4 mmol) in anhydrous dichloromethane (5 mL) was added dropwise to a solution of alcohol **1** (2.5g, 9.6 mmol) and triethylamine (1.95g, 19.3 mmol) in anhydrous dichloromethane at 0°C under N₂. The reaction was stirred at 0°C for 1 h and then at rt for 1 h. The dichloromethane was removed under reduced pressure and the residue was stirred in chloroform (50 mL) overnight. The chloroform was removed and the solid was triturated with hot ethyl acetate (4 x 30 mL) to give **3** as a pale white solid (3.0 g, 92%). mp 102-104 °C; IR (KBr): 3436, 1646, 1591 cm⁻¹; ¹H (200 MHz, CDCl₃) δ 2.64 (s, 3H), 5.13-5.46 (m, 6H), 7.27-7.48 (m, 6H), 7.77 (d, *J*=8.6 Hz, 6 H), 8.49 (d, *J*=6.2Hz, 6H); ¹³C (50 MHz, CDCl₃) δ 39.4, 52.1, 72.0, 72.3, 119.7, 127.9, 128.0, 128.8, 129.5, 134.2, 142.8, 153.7; Anal. calc'd for C₁₅H₁₇NO₅S: C, 55.71; H, 5.30; N, 4.33. Found: C, 55.39; H, 5.35; N, 4.45. The synthetic procedure used for this product is shown in Scheme 001.

*Benzyl-protected N*₂(*etLH*)₂ (**5**). A mixture of the iminium salt, **3**, (0.569g, 1.76 mmol), piperazine (0.050g, 0.58 mmol) and triethylamine (0.23g, 2.3 mmol) in dry acetonitrile (5

Scheme B.1. Synthesis of electrophilic HOPO iminium salt, 3.



mL) was stirred under N₂ at rt for 7 h. The reaction mixture was diluted with dichloromethane (60 mL) and washed with sat'd NaHCO₃ (60 mL). The aqueous layer was extracted again with dichloromethane (50 mL) and the combined organic extracts were dried (Na₂SO₄) and the solvent removed in vacuo. The crude product was purified by silica gel chromatography (30% methanol/ethyl acetate) to give **4** (0.311 g, 96.9%) as an off-white solid. mp 150-152°C ;IR (KBr) 2944, 1651, 1603 cm⁻¹; ¹H (200 MHz, CDCl₃) δ 7.43-7.2 (m, 10H), 6.92 (d, *J* = 6.7Hz, 2H), 6.63 (d, *J* = 7.5Hz, 2H), 5.98 (t, *J* = 7.1Hz, 2H), 5.07 (s, 4H), 4.0 (t, *J* = 6.6Hz, 4H), 2.67 (t, *J* = 6.6Hz, 4H), 2.49 (s, 8H); ¹³C (50 MHz, CDCl₃) δ 157.7, 148.3, 136.1, 129.5, 128.1, 127.5, 127.0, 115.6, 103.8, 70.4, 56.0, 52.9, 46.7; Anal. calc'd for C₃₂H₃₆N₄O₄·0.25H₂O: C, 70.52; H, 6.74; N, 10.27. Found: C, 70.46; H, 6.57; N, 10.14.

*N*²(*etLH*)₂ synthesis. A solution of 1:1 concentrated HBr/glacial acetic acid (3 mL) was added to **4** (0.200g, 0.37 mmol) and stirred at rt. After 4 d, the solvents were removed

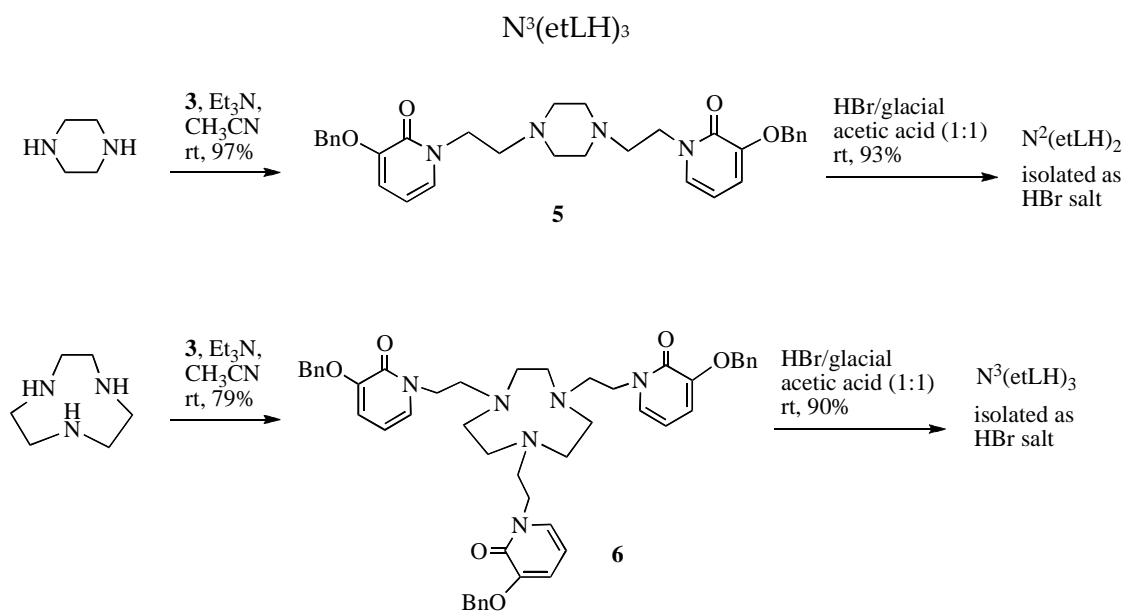
and the residue was washed with methanol. The resulting powder was dried in *vacuo*. The resulting solid was dissolved in water and lyophilized to give $N_2(etLH)_2$ (0.180g, 93%) as the dihydrobromide salt. mp 295-297 °C; IR (KBr) 3400, 1651, 1585 cm^{-1} ; 1H NMR (200 MHz, D_2O) δ 7.14 (d, $J = 6.6$ Hz, 2H), 6.96 (d, $J = 7.3$ Hz, 2H), 6.36 (t, $J = 7$ Hz, 2H), 4.38 (t, 4H), 3.49 (m, 12H); ^{13}C (50 MHz, D_2O) δ 159.4, 145.6, 128.9, 119.2, 109.1, 55.7, 49.6, 45.1; Anal. calc'd for $C_{18}H_{24}N_4O_4 \cdot 2HBr$: C, 41.4; H, 5.07; N, 10.74. Found: C, 41.53; H, 5.07; N, 10.73. The synthetic procedure used to produce this ligand is shown in Scheme 002.

Benzyl protected $N^3(etLH)_3$ (6) synthesis. A mixture of the iminium salt, **3**, (2.1 g, 6.5 mmol), N, N', N''-1,4,7-triazacyclononane (0.185g, 1.44 mmol) and triethylamine (0.876 g, 8.66 mmol) in dry acetonitrile (15 mL) was stirred under N_2 at rt for 16 h. The reaction mixture was diluted with dichloromethane (60 mL) and washed with sat'd $NaHCO_3$ (60 mL). The aqueous layer was extracted again with dichloromethane (50 mL) and the combined organic extracts were dried (Na_2SO_4) and the solvent removed in *vacuo*. The residue was dissolved in minimum methanol and ethyl acetate added to precipitate the product. After refrigerating overnight, the solvent was decanted and the residue dried in *vacuo*. The remaining powder was washed with ethyl acetate to give **5** (0.950, 79%) as an off-white solid. mp 50-52 °C; IR (KBr) 2926, 1652, 1601 cm^{-1} ; 1H (200 MHz, $CDCl_3$) δ 7.44-7.26 (m, 15H), 6.89 (dd, $J = 6.8, 1.5$ Hz, 3H), 6.62 (dd, $J = 7.4, 1.5$ Hz, 3H), 5.96 (t, $J = 7.1$ Hz, 3H), 5.07 (s, 6H), 3.96 (t, $J = 6.2$ Hz, 6H), 2.80 (t, $J = 6.3$ Hz, 6H), 2.66 (s, 12H); ^{13}C (50 MHz, $CDCl_3$), δ 157.9, 148.5, 136.2, 129.5, 128.2, 127.6, 127.1, 115.6, 103.9, 70.5, 56.6, 55.9,

47.8; Anal. calc'd for $C_{48}H_{54}N_6O_6 \cdot 1.5 H_2O$: C, 68.80; H, 6.85; N, 10.03. Found: C, 68.77; H, 6.63; N, 9.72.

$N^3(etLH)_3$ synthesis. A solution of 1:1 concentrated HBr/glacial acetic acid (6 mL) was added to **5** (0.540 g, 0.6 mmol) and stirred at rt. After 5 d, the solvents were removed and the residue was washed with methanol. The resulting powder was dried in *vacuo* and then lyophilized from water to give $N^3(etLH)_3$ (0.421 g, 89.6%) as the trihydrobromide salt. mp 156-158 °C; IR (KBr) 3397, 1645, 1552 cm^{-1} ; 1H NMR (200 MHz, D_2O) δ 7.15 (d, $J=6.6$ Hz, 3H), 6.9 (d, $J=7.4$ Hz, 3H), 6.36 (t, $J=7.1$ Hz, 3H), 4.35 (t, $J=5.1$ Hz, 6H), 3.45 (s, 18 H); ^{13}C (50 MHz, D_2O) δ 158.7, 145.5, 129.1, 119.1, 109.2, 55.4, 49.8, 45.5; Anal. calc'd for $C_{27}H_{36}N_6O_6 \cdot 3HBr$: C, 41.4; H, 5.02; N, 10.73. Found: C, 41.77; H, 5.22; N, 10.85. The synthetic procedure used to produce this ligand is also shown in Scheme 002.

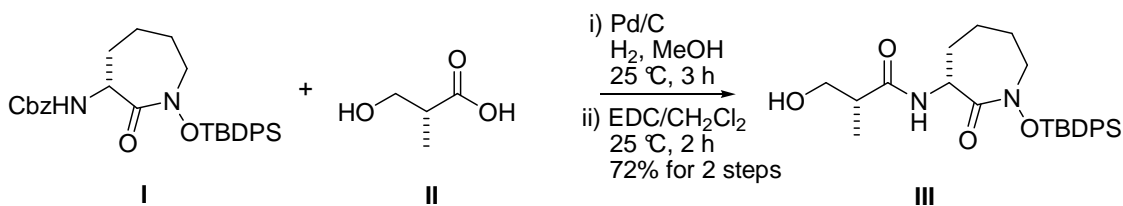
Scheme B.2. Synthesis of 3-hydroxy-2-pyridinone siderophore mimics $N^2(etLH)_2$ and



Appendix C: Synthesis of an analog of the cytotoxic siderophore Brasilibactin A

The brasilibactin A analog, Bbtan was produced by Jiyong Hong, Heekwang Park, and Yongcheng Ying at Duke University.

Preparation of cyclic hydroxamate alcohol (III)

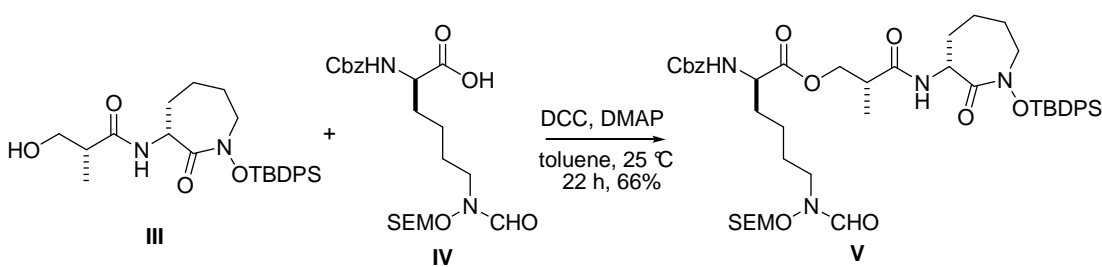


Scheme C.1.

To a solution of Cbz protected hydroxamate **I** (255 mg, 0.49 mmol) in MeOH (3.0 mL) was added Pd/C (10%, 50 mg) at 25 °C. The reaction mixture was flushed with H₂, then stirred under H₂ atmosphere for 3 h. After filtration through celite, the reaction mixture was concentrated under reduced pressure to afford the corresponding free amine. To a solution of free amine in CH₂Cl₂ (20.0 mL) was added β-hydroxy carboxylic acid **II** (79 mg, 0.76 mmol) and EDC·HCl (284 mg, 1.48 mmol) at 25 °C. After being stirred for 2 h at 25 °C, the reaction mixture was concentrated and purified by column chromatography (silica gel, EtOAc/hexanes, 1/2) to afford cyclic hydroxamate alcohol **III** (168 mg, 72% for 2 steps) as a colorless oil. ¹H NMR (400 MHz, CDCl₃) δ 1.08 (d, *J* = 7.2 Hz, 3H), 1.13 (s, 9H), 1.18–1.29 (m, 1H), 1.36–1.46 (m, 1H), 1.52–1.61 (m, 2H), 1.78 (d, *J* = 10.0 Hz, 2H),

2.39–2.47 (m, 1H), 3.30 (br, s, 1H), 3.46–3.47 (m, 2H), 3.54–3.61 (m, 2H), 4.26 (dd, $J = 6.8$, 10.0 Hz, 1H), 6.73 (d, $J = 6.8$ Hz, 1H), 7.34–7.47 (m, 6H), 7.71–7.75 (m, 4H); ^{13}C NMR (100 MHz, CDCl_3) δ 175.15, 170.03, 136.25, 136.15, 132.15, 131.68, 130.37, 130.33, 127.69, 127.63, 65.26, 54.31, 51.71, 42.39, 30.64, 27.40, 26.98, 25.44, 19.66, 13.71.

Preparation of cyclic hydroxamate ester (V)

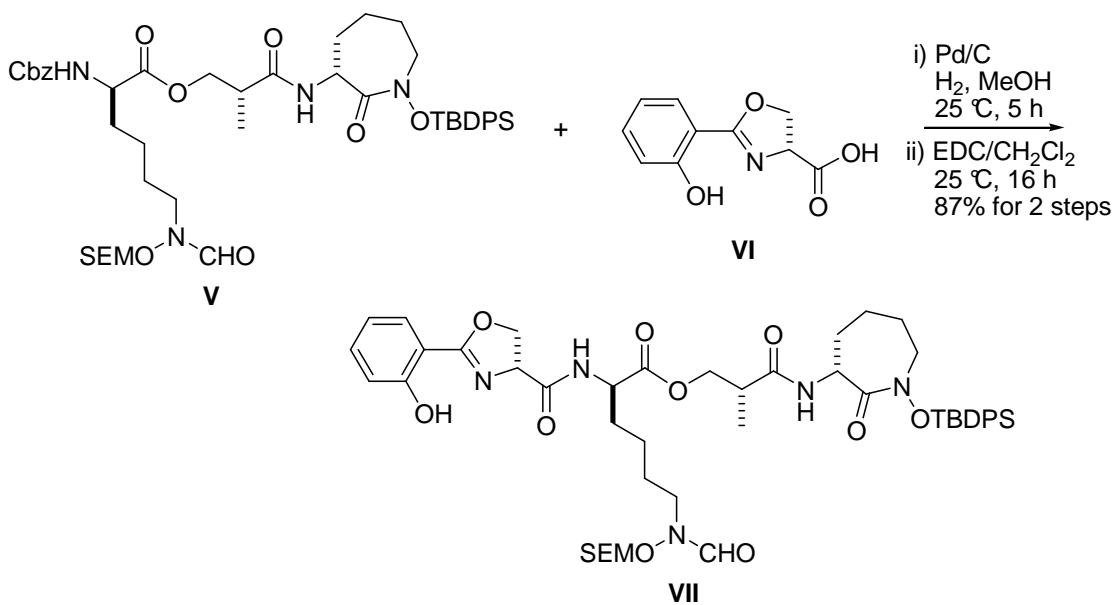


Scheme C.2.

To a solution of **III** (78 mg, 0.17 mmol) in toluene (4.0 mL) was added a solution of **IV** (96 mg, 0.21 mmol) in toluene (4.0 mL) and followed by the addition of DCC (138 mg, 0.69 mmol) and DMAP (82 mg, 0.69 mmol) at 25 °C. After being stirred for 22 h at 25 °C, the reaction mixture was concentrated and purified by column chromatography (silica gel, EtOAc/hexanes, 1/1) to afford cyclic hydroxamate ester **V** (100 mg, 66%) as a colorless oil. ^1H NMR (400 MHz, CDCl_3) δ 0.02 (s, 9H), 0.95 (t, $J = 8.4$ Hz, 3H), 0.97–1.91 (m, 27H), 2.53 (m, 1H), 3.42–3.57 (m, 4H), 3.72 (t, $J = 8.0$ Hz, 2H), 4.09–4.20 (m, 4H), 4.30–4.32 (m, 1H), 4.84 (s, 1H), 5.10 (s, 2H), 5.58 (d, $J = 8.0$ Hz, 1H), 6.93 (d, $J = 4.8$ Hz, 1H), 7.29–7.38 (m, 11H), 7.71–7.73 (m, 4H), 8.30 (s, 0.8H); ^{13}C NMR (100 MHz, CDCl_3) δ 172.31, 172.05, 169.60, 163.71, 156.21, 136.57, 136.33, 136.21, 132.16, 131.73, 130.50, 130.37, 128.66,

128.25, 127.70, 114.21, 98.25, 54.38, 54.03, 51.78, 44.82, 40.21, 39.00, 33.35, 32.08, 31.84,
31.16, 30.44, 31.00, 29.84, 29.50, 27.44, 27.06, 26.88, 26.45, 26.06, 25.43, 22.83, 22.38, 19.73,
18.21, 14.30, -1.31.

Preparation of SEM and TBDPS protected depsipeptide (VII)

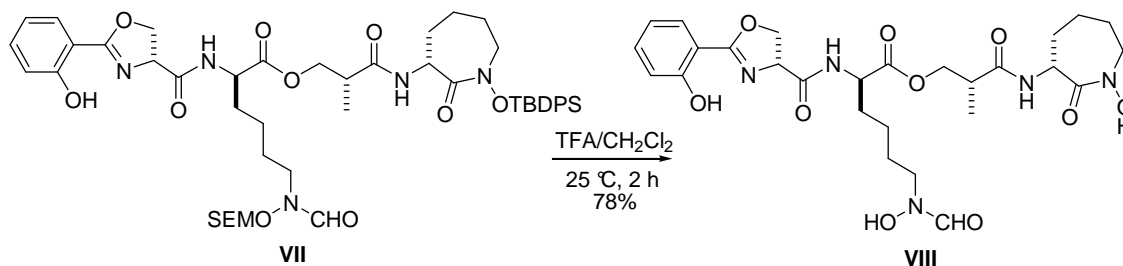


Scheme C.3.

To a solution of Cbz protected hydroxamate ester **V** (101 mg, 0.11 mmol) in MeOH (2.0 mL) was added Pd/C (10%, 15 mg) at 25 °C. The reaction mixture was flushed with H₂, then stirred under H₂ atmosphere for 5 h. After filtration through celite, the reaction mixture was concentrated under reduced pressure to afford the corresponding free amine. To a solution of free amine in CH₂Cl₂ (10.0 mL) was added oxazoline carboxylic acid **VI** (60 mg, 0.20 mmol) and EDC·HCl (65 mg, 0.34 mmol) at 25 °C. After being stirred for 16 h at 25 °C, the reaction mixture was concentrated and purified by column chromatography (silica gel, acetone/hexanes, 2/7) to afford SEM and

TBDPS protected depsipeptide **VII** (94 mg, 87%) as a colorless oil. ^1H NMR (400 MHz, CD_3OD) δ 0.02 (s, 9H), 0.94 (t, $J = 11.2$ Hz, 3H), 1.04 – 1.91 (m, 27H), 2.61 (dd, $J = 11.2, 17.6$ Hz, 1H), 3.49–3.57 (m, 4H), 3.70 (t, $J = 11.2$ Hz, 2H), 4.17–4.26 (m, 2H), 4.47–4.53 (m, 1H), 4.61–4.68 (m, 2H), 4.80 (s, 1H), 4.95 (dd, $J = 10.4, 14.0$ Hz, 1H), 6.91 (t, $J = 7.6$ Hz, 1H), 6.97–7.03 (m, 3H), 7.33–7.46 (m, 7H), 7.68–7.76 (m, 5H), 7.96 (s, 0.2H), 8.22 (s, 0.8H), 11.29 (br, s, 1H); ^{13}C NMR (100 MHz, CDCl_3) δ 171.24, 171.42, 170.48, 169.76, 163.73, 159.95, 136.25, 136.16, 134.27, 132.08, 131.76, 130.37, 128.68, 127.66, 119.11, 117.07, 98.20, 69.56, 68.09, 67.22, 54.39, 52.42, 51.80, 40.11, 31.00, 27.38, 26.99, 26.24, 25.42, 22.30, 19.70, 18.14, 14.41, -1.35.

Preparation of brasilibactin A analogue (Bbtan; **VIII**)



Scheme C.4.

Depsipeptide **VII** (50 mg, 0.052 mmol) in TFA/ CH_2Cl_2 (1.5 mL, 1:4) was stirred under N_2 atmosphere at 25 $^\circ\text{C}$ for 2 h. The reaction mixture was concentrated and washed with Et_2O (1.0 mL \times 3). The crude mixture was then purified by reverse phase semi-HPLC (Luna C18, Phenomenex, 250 mm \times 10 mm \times 5 μm ; eluent, $\text{CH}_3\text{CN}/\text{H}_2\text{O}$, 40:60; flow rate, 3 mL/min; UV detection, 230 nm and 254 nm) to afford iron-free brasilibactin A analogue **VIII** (24 mg, 78%) as a white solid: ^1H NMR (400 MHz, CD_3OD)

δ 1.14 (d, 3H, $J = 7.2$ Hz), 1.29–1.98 (m, 12H), 2.80–2.90 (m, 1H), 3.47 (t, 1H, $J = 6.8$ Hz), 3.54 (t, 1H, $J = 6.8$ Hz), 3.67 (dd, 1H, $J = 4.8, 16.0$ Hz), 3.93 (dd, 1H, $J = 11.2, 16.0$ Hz), 4.14–4.25 (m, 2H), 4.48 (ddd, $J = 5.2, 8.6, 8.6$ Hz 1H), 4.57–4.63 (m, 3H), 5.07 (t, $J = 8.8$ Hz, 1H), 6.90 (t, $J = 7.6$ Hz, 1H), 6.96 (d, $J = 8.0$ Hz, 1H), 7.41 (t, $J = 8.0$ Hz, 1H), 7.68 (dd, $J = 2.0, 8.0$ Hz, 1H), 7.90 (br s, 0.6H), 8.22 (br s, 0.4H); ^{13}C NMR (100 MHz, CD_3OD) δ 175.58, 172.91, 170.83, 168.50, 163.93, 160.94, 159.43, 135.02, 129.48, 120.04, 117.67, 111.51, 70.43, 69.15, 67.75, 54.08, 53.84, 52.69, 51.00, 47.08, 40.91, 31.86, 28.69, 27.49, 26.91, 26.80, 23.64, 23.46, 14.41; LCMS (FAB) m/z calcd for $\text{C}_{27}\text{H}_{37}\text{N}_5\text{O}_{10}$ ($\text{M} + \text{H}$) $^+$ 592.25, found 592.21.

Appendix D: Synthesis and purity analysis of 2-({[(1E)-1-(2-amino-1,3-thiazol-4-yl)-2-{{[(3S)-1-({[4-methyl-3-(5-hydroxy-4-oxo-1,4-dihydropyridin-2-yl)-5-oxo-4,5-dihydro-1H-1,2,4-triazol-1-yl]sulfonyl}carbamoyl)-2-oxoazetidin-3-yl]amino}-2-oxoethylidene]amino}oxy)-2-methylpropanoic acid (PF-02538084).

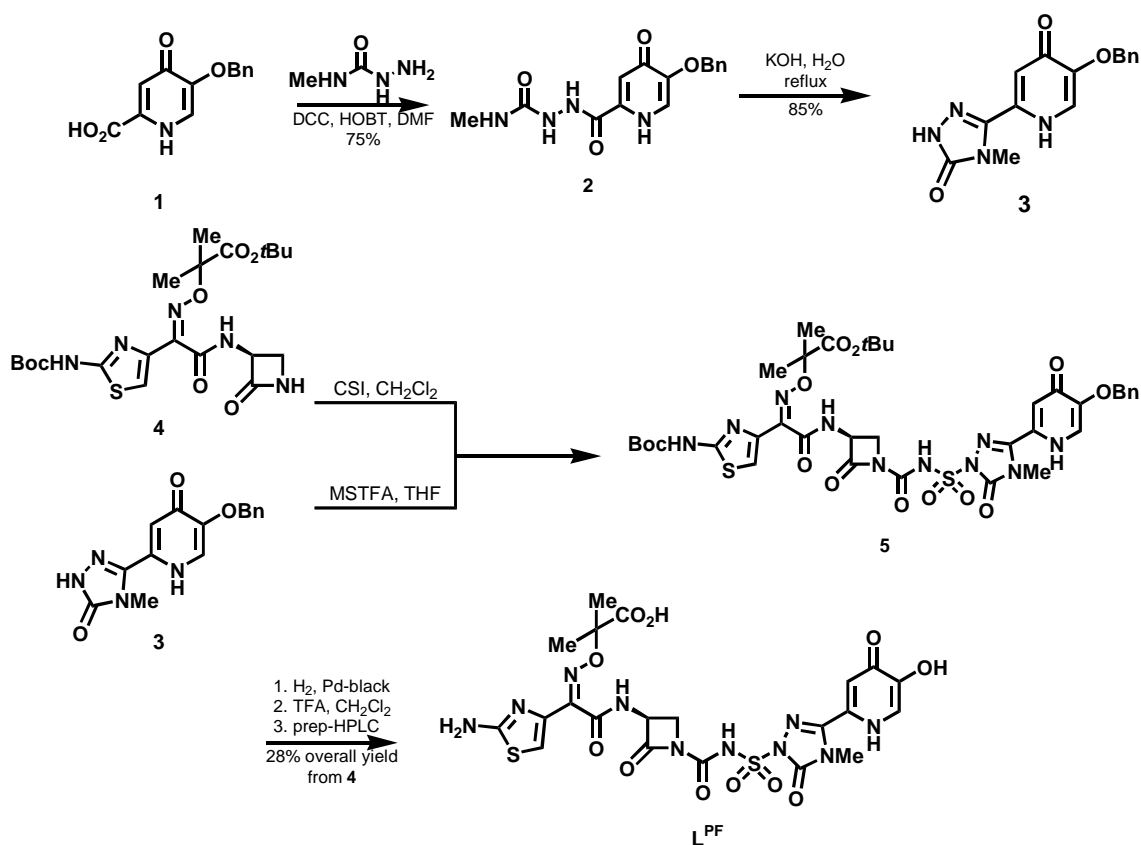
PF-02538084 was prepared as described in the literature (Scheme D.1.). The crude product was dissolved in a minimum amount of DMSO filtered and purified by preparative HPLC (Symmetry C8, 13 to 33 % acetonitrile in water with 0.1 % formic acid modifier). The pooled fractions were concentrated using the rotary evaporator to afford PF-02538084 as a light pink solid. LCMS m/z 652.9 (M-1). ^1H NMR (400 MHz, DMSO- d_6) δ 9.01 (d, $J = 8.2$ Hz, 1H), 8.01 (s, 1H), 7.37 (s, 1H), 6.82 (s, 1H), 4.90 (m, 1H), 3.70 (m, 1H), 3.35 – 3.39 (br s, 4H), 1.42 (s, 6H).

HPLC/ESI/MS/MS Characterization of Fe:L^{PF3} Complex

Experimental

HPLC/ESI-MS/MS experiments were graciously performed by John O'Donnell and Jennifer Winton of Pfizer, Inc.

A 1 mL solution consisting of 50 μM Fe(ClO₄)₃ and 75 μM PF-02538084 was prepared in 25 mM Tris-HCl pH 7.0. The reaction was allowed to proceed for 15 minutes at room temperature prior to transferring 200 μL to an HPLC injection vial. HPLC/ESI/MS/MS



Scheme D.1. Synthetic scheme of the ligand, PF-02538084 or L^{PF} .

analysis was performed using a Shimadzu LC-20AD HPLC in line with a Sciex API-3000 triple quadrupole mass spectrometer operated in the positive ion mode. Post column flow was split such that mobile phase was introduced into the mass spectrometer at a rate of 100 $\mu\text{L}/\text{min}$. The ion spray interface temperature was 300°C and the ion spray voltage was set at 3.5 kV. The orifice voltage was optimized at 40 eV and the sample injection volume was 10 μL . Nitrogen was used as both the nebulizing and collision gas. Total ion (Q1) experiments were performed at a range of 75 to 1000 m/z at unit resolution. A collision energy of 20 eV was used for collision induced dissociation (CID) product ion scan experiments. Separation of the iron-ligand complex and free PF-

02538084 was achieved on a Phenomenex Onyx Monolithic C18 column (3 × 100 mm) utilizing a binary HPLC gradient consisting of 90:10 0.1% formic acid : acetonitrile (mobile phase A) and acetonitrile (mobile phase B). The HPLC gradient schedule consisted of the following:

Time (min)	Flow Rate	A(%)	B(%)
0	850	90	10
6	850	90	10
6.1	850	5	95
11.1	850	5	95
11.2	850	90	10
12.8	850	90	10

The compound L^{PF} alone exhibited a retention time of 1.75 minutes (Fig. D.1.), and the ESI-mass spectrum of this peak exhibited a M+1 peak of 655 m/z units (Fig. D.2.A.). This mass-to-charge ratio can be assigned to the molecular peak of L^{PF} . The collision induced dissociation product ion mass spectrum of the peak at 655 m/z is shown in Fig. D.2.B. The fragmentation pattern exhibited is consistent with that shown in Fig. D.3. The liquid chromatogram of the Fe- L^{PF} solution exhibits a second peak at 0.98 minutes (Fig. D.1.). The ESI-mass spectrum of L^{PF} in the presence of iron (Fig. D.4.A.) exhibits a peak at 673 m/z units, which corresponds to the ML_{3+3} peak of the $Fe(H_3L^{PF})_3^{3+}$ peak, indicative of complex formation in a 3:1 ratio. Additionally, the collision induced dissociation product ion spectrum of the 673 m/z peak exhibits the

same fragmentation as that observed in the CID product ion spectrum of the 655 m/z peak, further suggesting that this peak corresponds to the $\text{Fe}(\text{H}_3\text{L}^{\text{PF}})_{3^{3+}}$ complex.

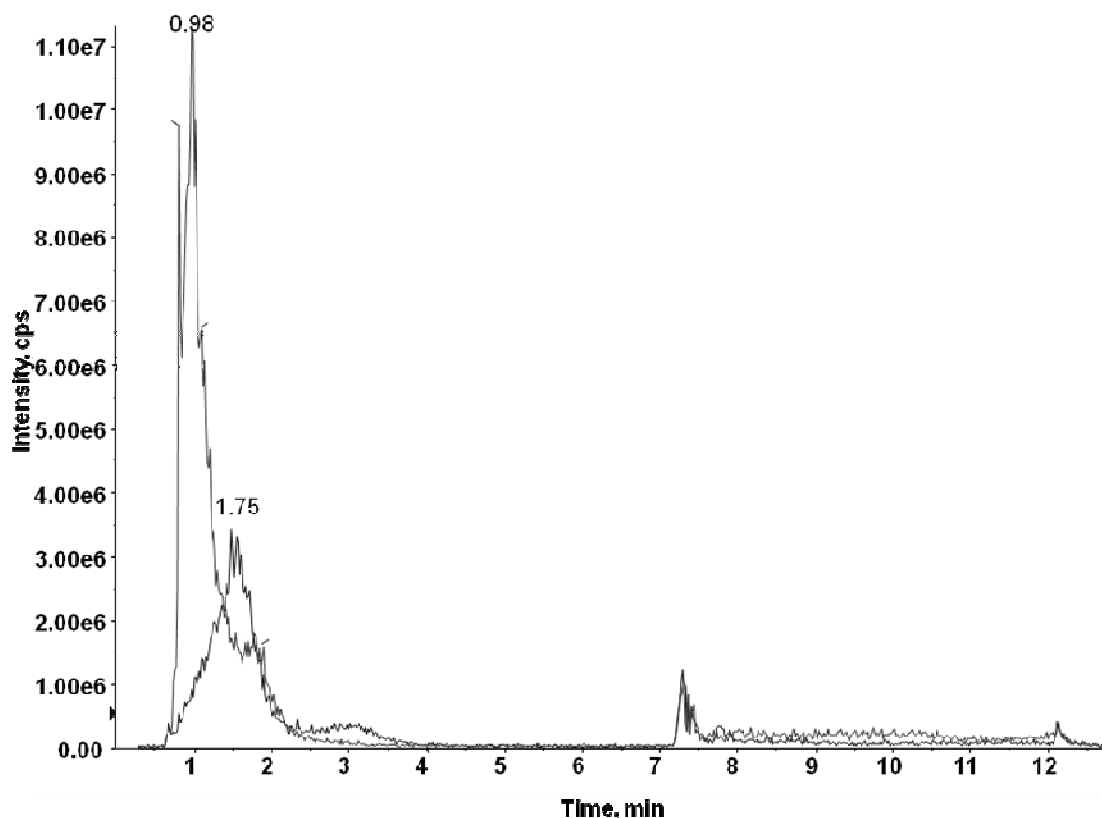


Figure D.1. Extracted ion chromatogram of the Fe-L^{PF} system in solution. The top trace (retention time = 0.98 minutes) corresponds to the chromatogram of the Fe-L^{PF} complex, while the lower trace (retention time = 1.75 minutes) corresponds to the chromatogram of the ligand alone. Conditions: Phenomenex Onyx Monolithic C18 column (3 x 100 mm), mobile phase: 90:10% formic acid:acetonitrile and acetonitrile following the gradient program described in the experimental section.

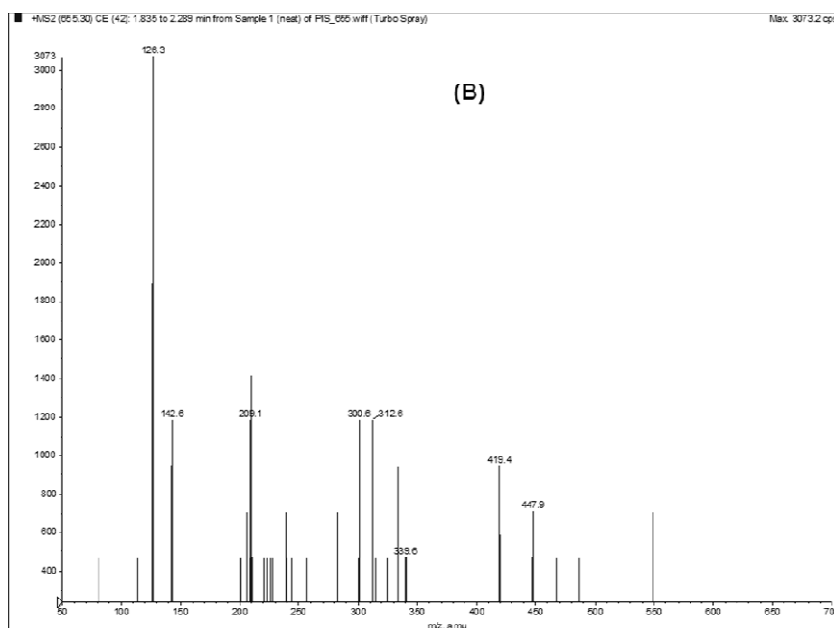
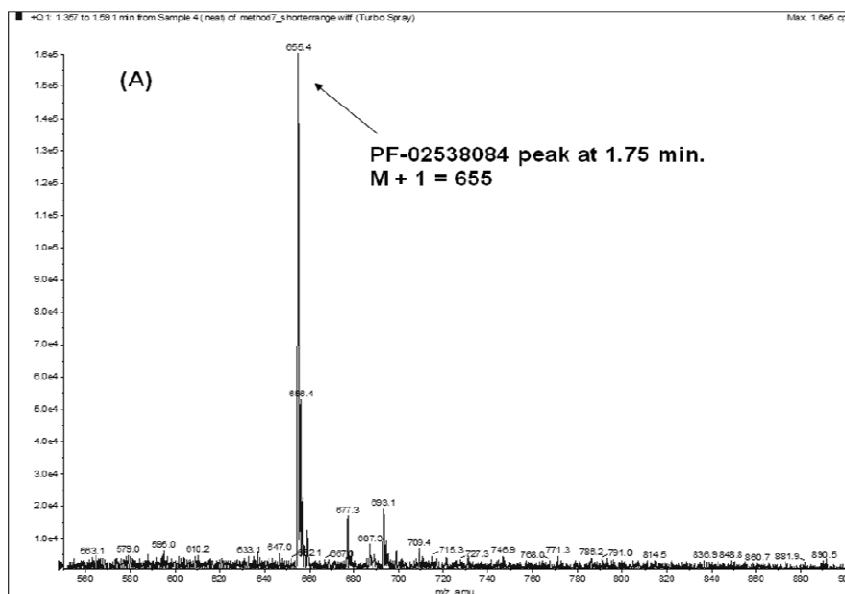


Figure D.2. ESI-mass spectra of the ligand L^{PF} in the absence of iron(III). (A) ESI mass spectrum of the compound. (B) Collision-induced dissociation product ion spectrum of the peak observed at 655 m/z units. Conditions: pH 3.0, $T = 300\text{ }^{\circ}\text{C}$, ion spray voltage = 3.5 kV, orifice voltage = 40 eV, collision energy = 20 eV, collision and nebulizing gas: N_2 .

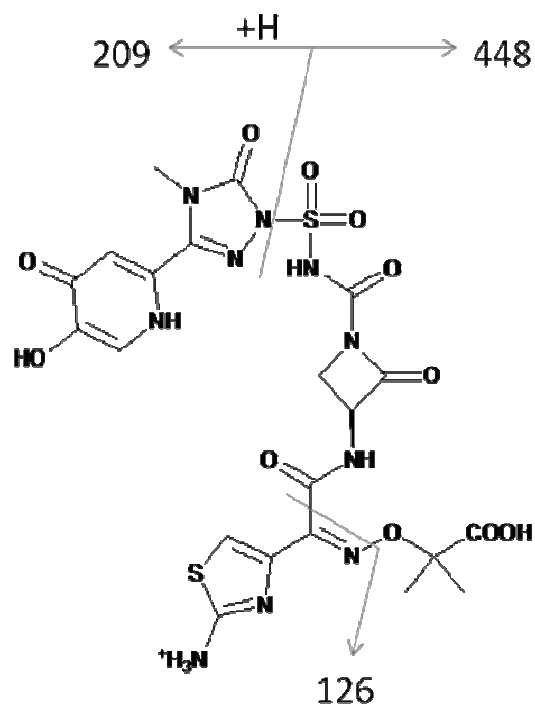


Figure D.3. Structural assignments for fragment ions at 126 m/z units, 209 m/z units, and 448 m/z units observed in CID product ion mass spectra of L^{PF} and the Fe- L^{PF} complex.

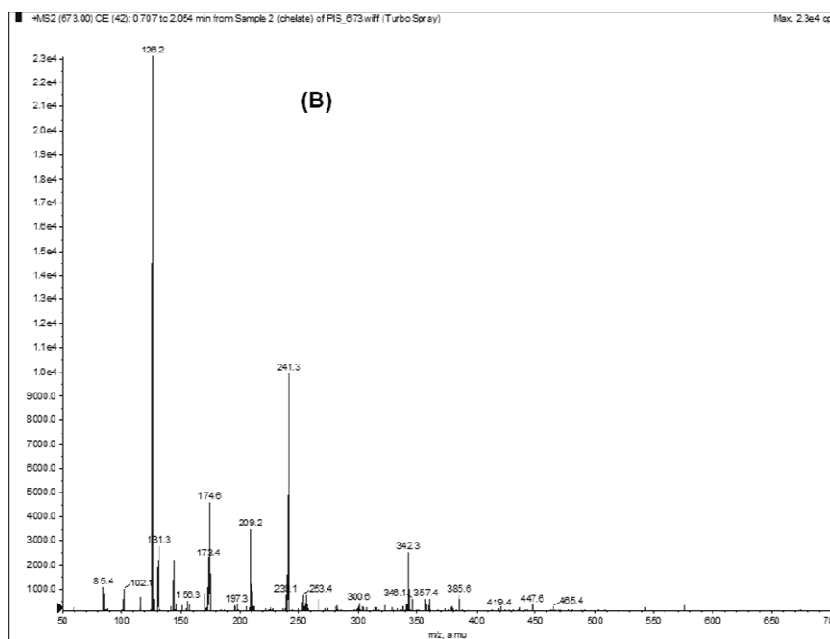
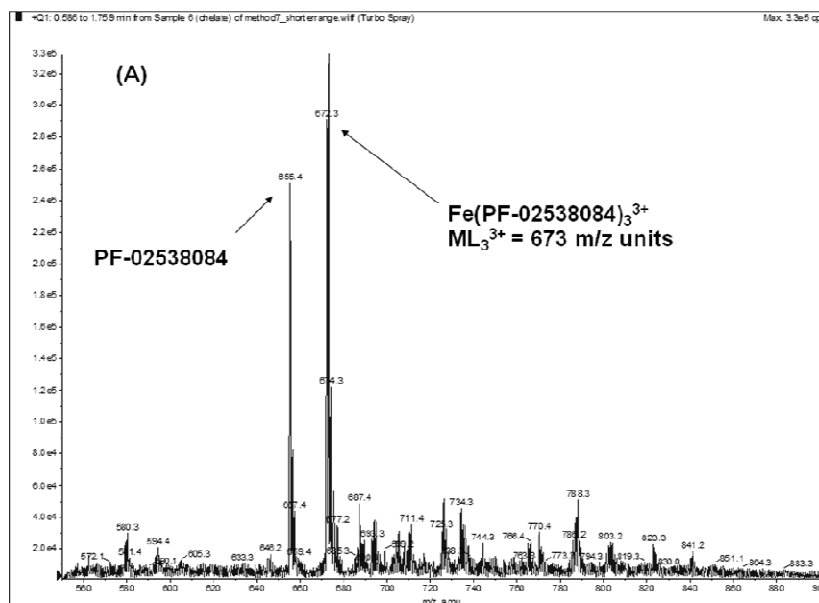


Figure D.4. ESI-mass spectrum of the Fe-L^{PF} system. (A) ESI mass spectrum of the compound at 0.98 minute retention time. Both L+1 and ML₃+3 peaks are observed, suggesting incomplete complex formation. (B) Collision induced dissociation product ion spectrum of the peak observed at 673 m/z units. Conditions: pH 3.0, T = 300 °C, ion spray voltage = 3.5 kV, orifice voltage = 40 eV, collision energy = 20 eV, N₂ gas used as collision and nebulizing gas.

Appendix E: Statistical analysis and speciation diagrams for the metal-ligand systems of toxicity studies with *C. elegans*

Statistical analysis of metal-chelator systems

In metal-chelator treatment assays, 4 populations of *C. elegans* were exposed to no treatment (control population), treatment by chelator only, treatment by metal only, and treatment by metal and chelator at set concentrations. The outcome is a population distribution of $\log(\text{EXT})$ values and the treatment consists of 2 factors: the presence of a metal and the presence of a chelator. The interest is in the interaction between the chelator and the metal. In the plot shown in Fig. E.1., samples with and without metal are plotted, as shown by the horizontal axis. The vertical axis shows $\log(\text{EXT})$ values.

The plot shown in the solid line represents the case where no chelator is present and demonstrates a loss of growth ($\log(\text{EXT})$) in the presence of a toxic metal ion. In the case of the dashed line, the chelator is present and affects the outcome variable ($\log(\text{EXT})$), but does not interact with the metal. I.e, while the presence of the chelator may decrease the growth of the organism on its own (as evidenced by the different y-intercepts of the solid and dashed line), the difference between the sample with metal and the sample without metal is not affected by the presence of the chelator (as evidenced by the same slope for the solid and dashed line).

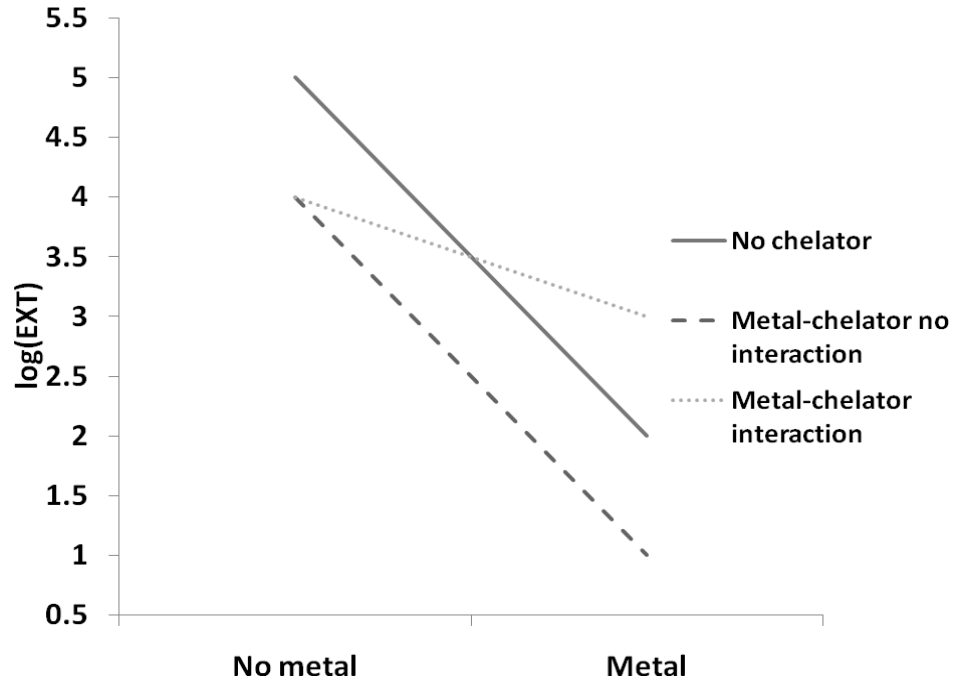


Figure E.1. Plot of response to treatment against two treatments in three cases, where no chelator is present, where a chelator is present and produces no interaction with the metal, and where a chelator is present and exhibits interaction with the metal.

In the case of the dotted line, the chelator is again present, but this time affects the difference between the samples with and without metal. Ie, the difference between the population untreated by metal and treated by metal is smaller with the chelator present. The 2 lines (solid and dotted) exhibiting differing slopes means there is an interaction effect present. This is what we tested for.

Thus, the null hypothesis is that there is no interaction between chelator and metal. This situation is represented by the solid and dashed line. To test such a hypothesis, a 2-way ANOVA analysis is used (or statistical analysis of variables using

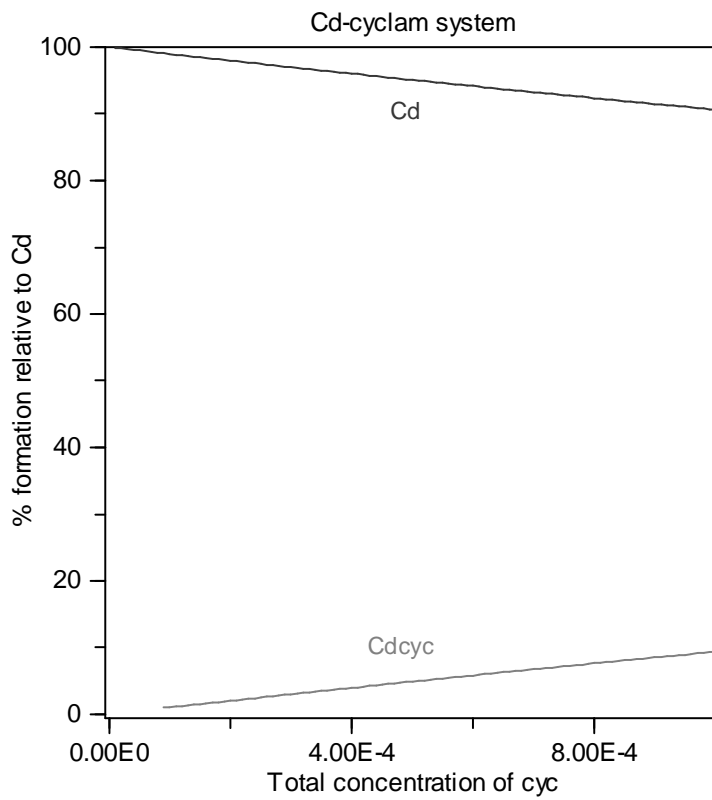
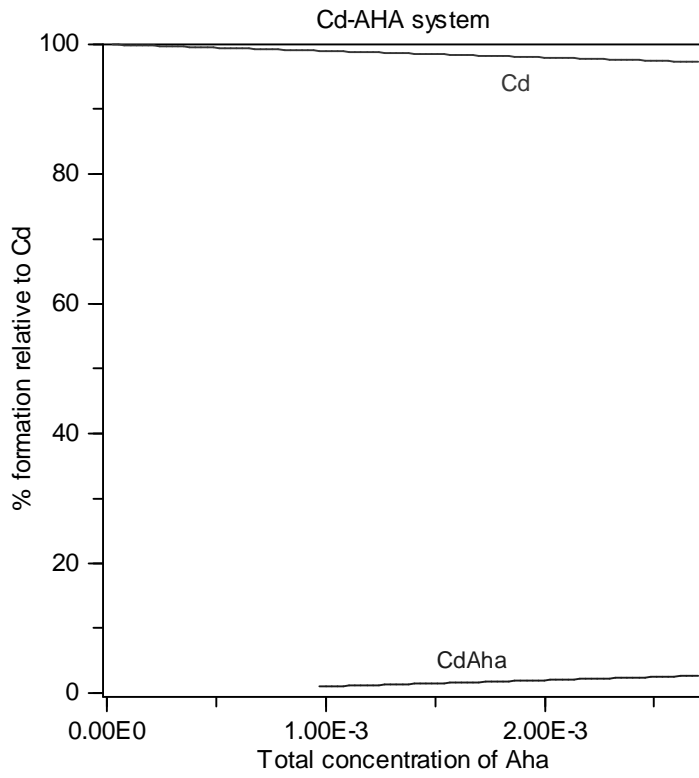
two forces). The result of the ANOVA analysis is the probability (a 'p-value' stands for 'probability value'), that the data is consistent with the null hypothesis of no interaction. A very low probability value indicates that the probability of seeing the data produced without an interaction effect being present is very low – ie significant.

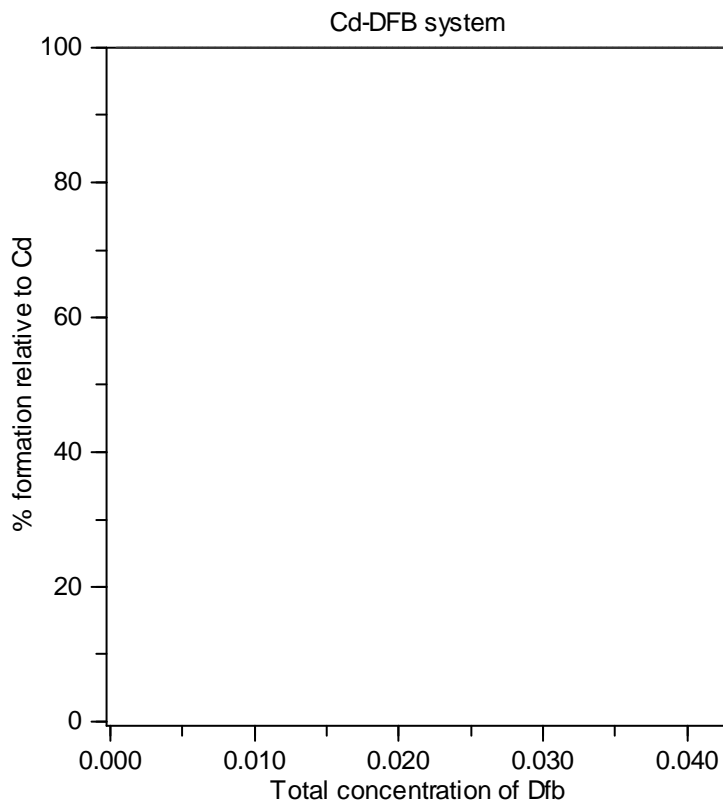
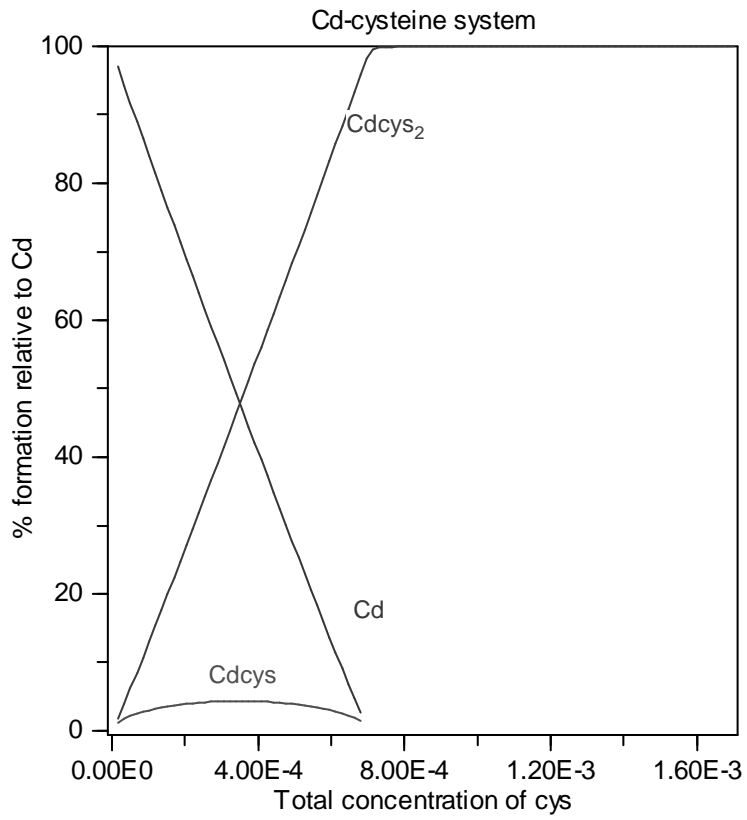
The calculation of the p-values for each data set is beyond the scope of this work, and will not be described at length here.

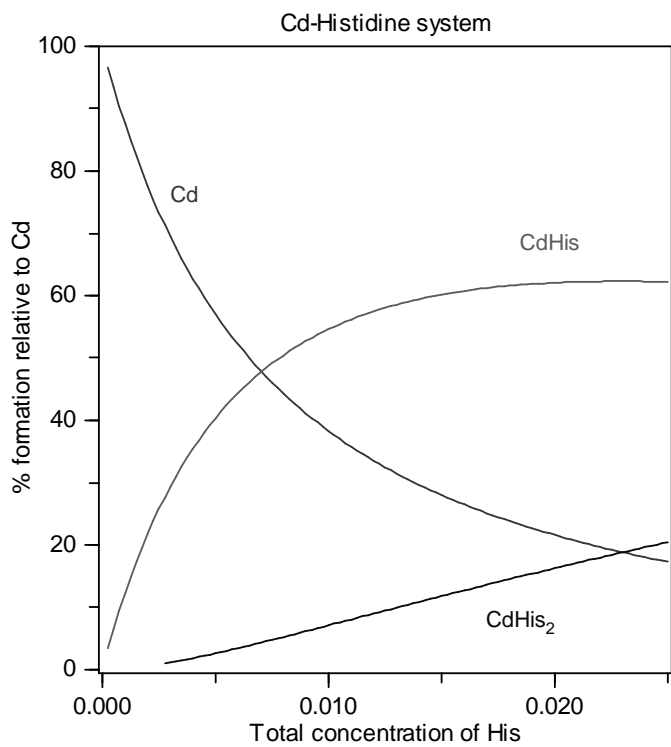
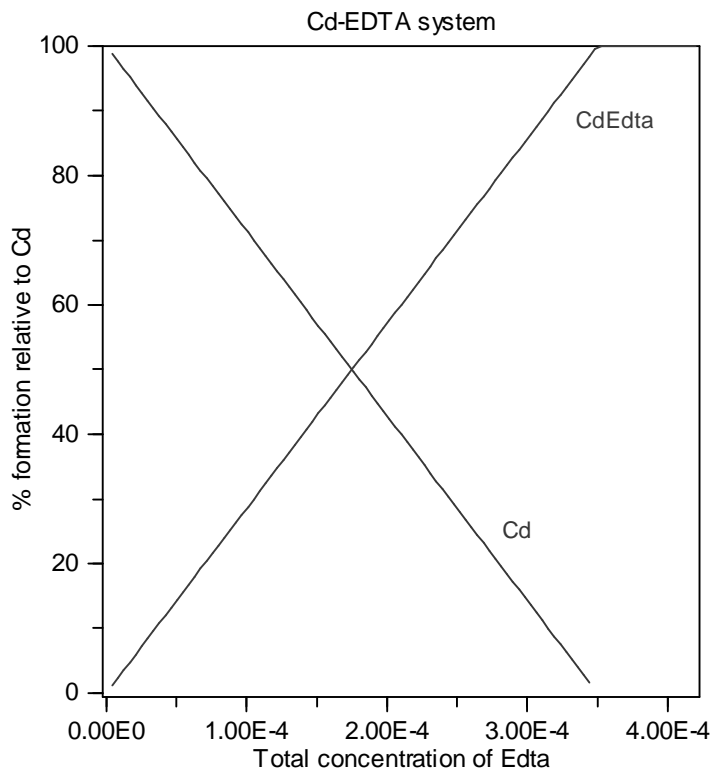
Speciation diagrams for metal-chelator systems

Speciation diagrams were calculated for metal-ligand systems using stability constants obtained from the IUPAC Stability Constant Database using the program, HySS by Protonic Software.(131, 204) Speciation diagrams were calculated at a constant pH and metal ion concentration, which are noted above each section of speciation diagrams, and varying ligand concentration.

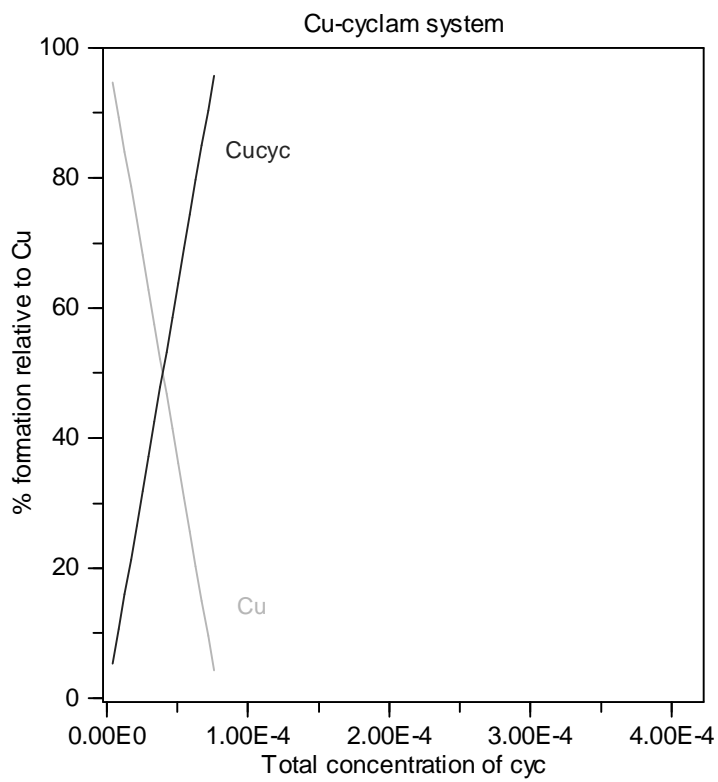
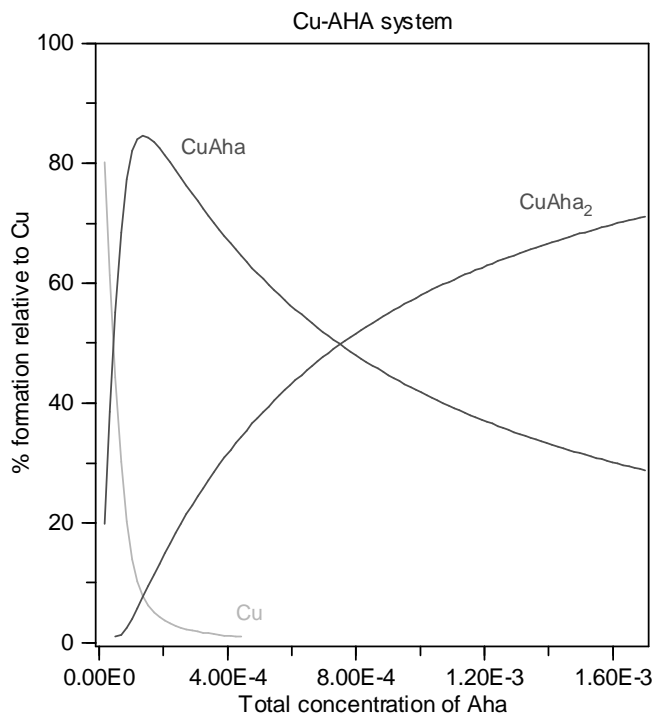
Conditions: pH 6.5, 350 μM Cd

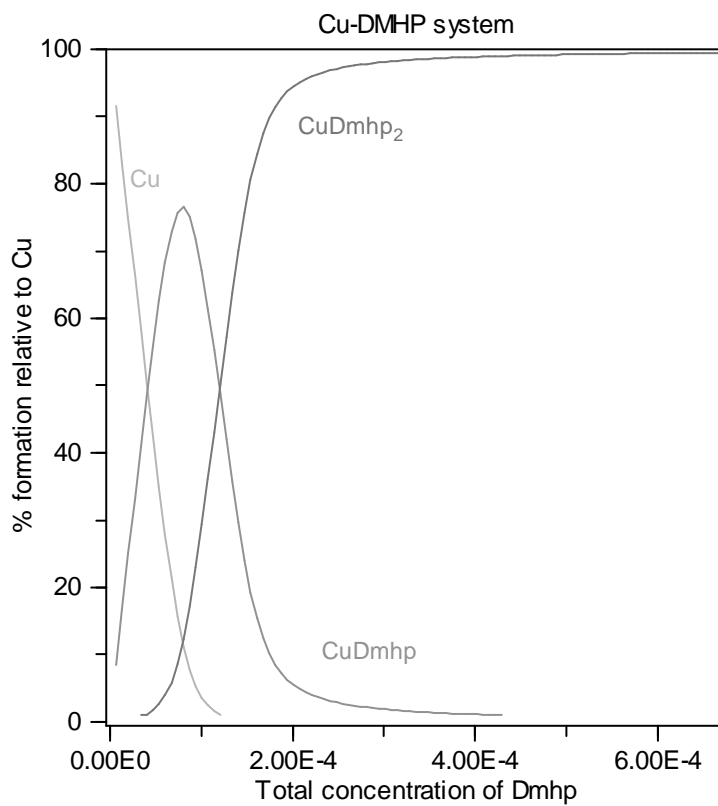
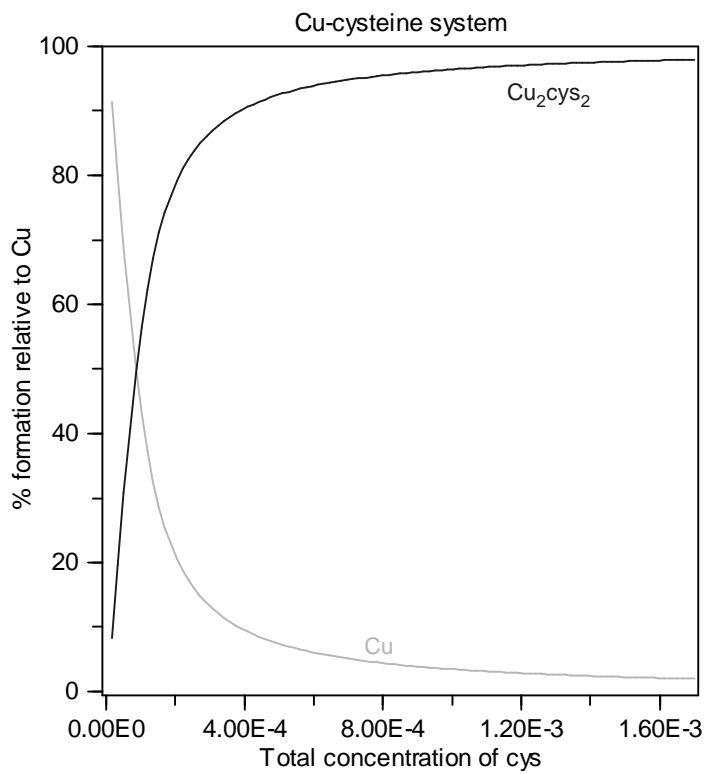


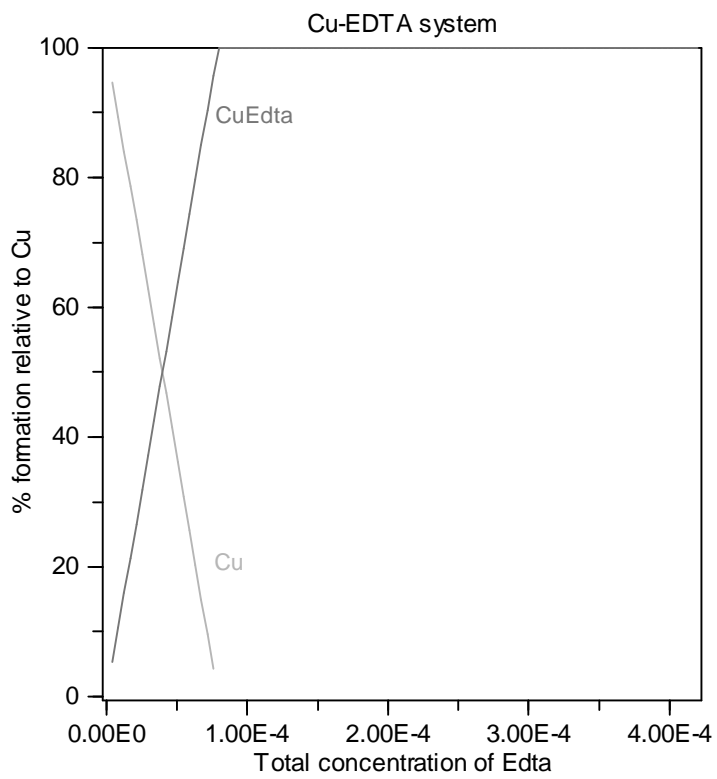
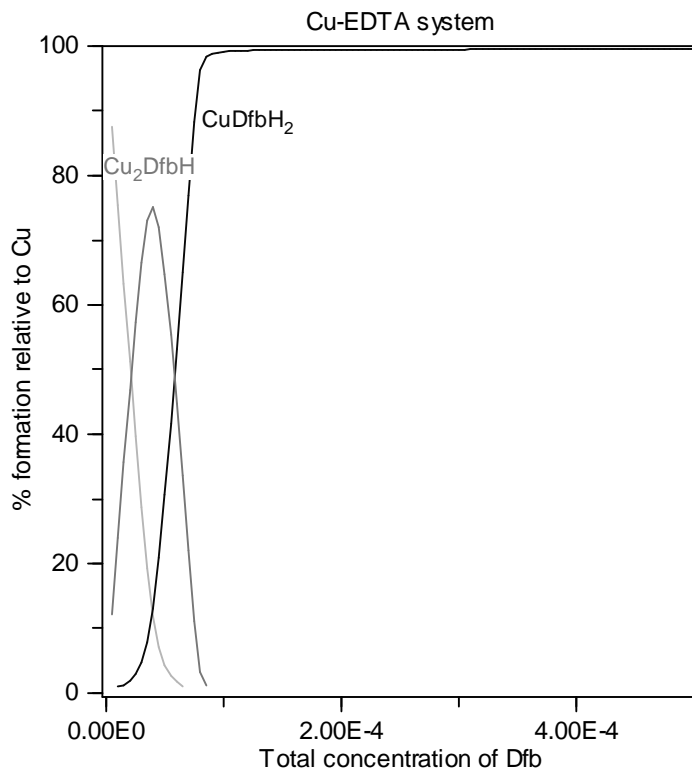


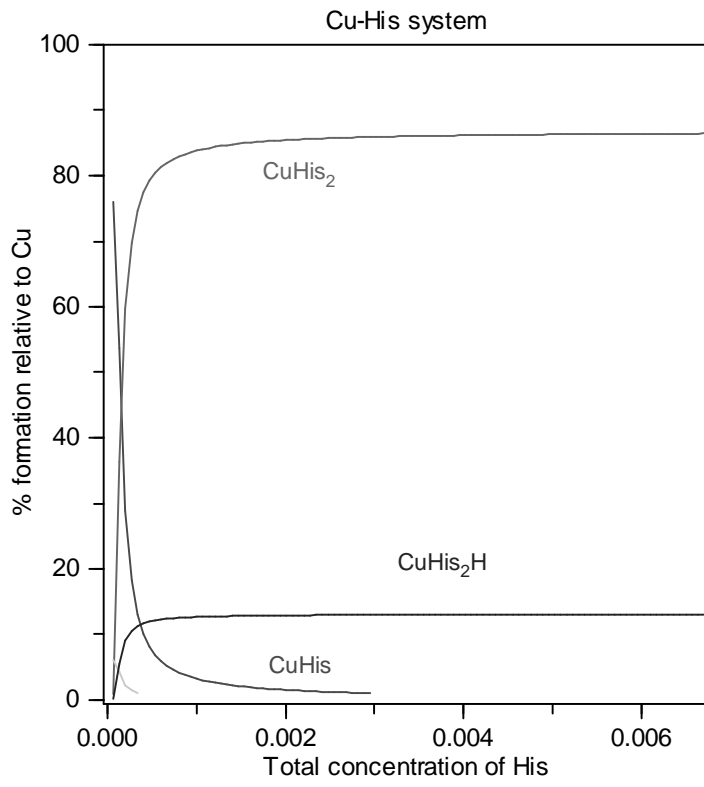


pH 6.5, 79 μM Cu^{2+}

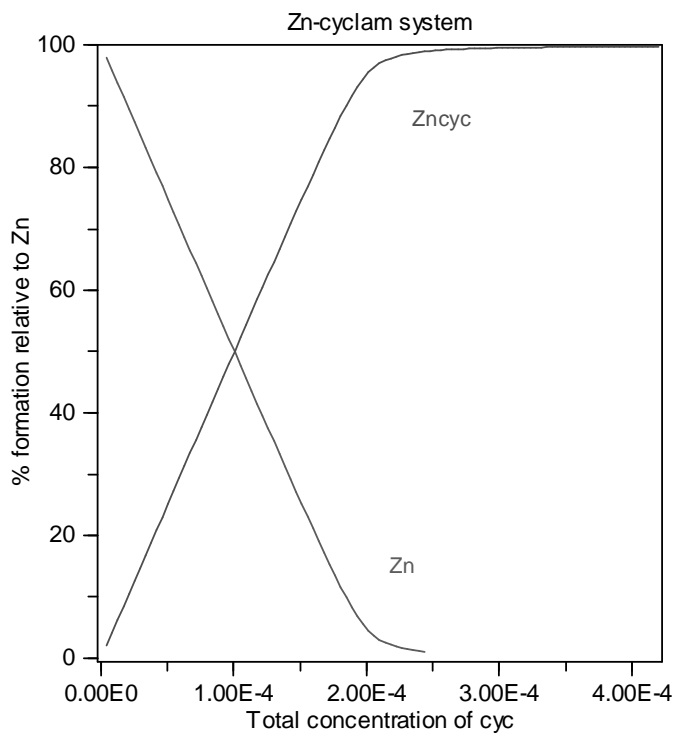
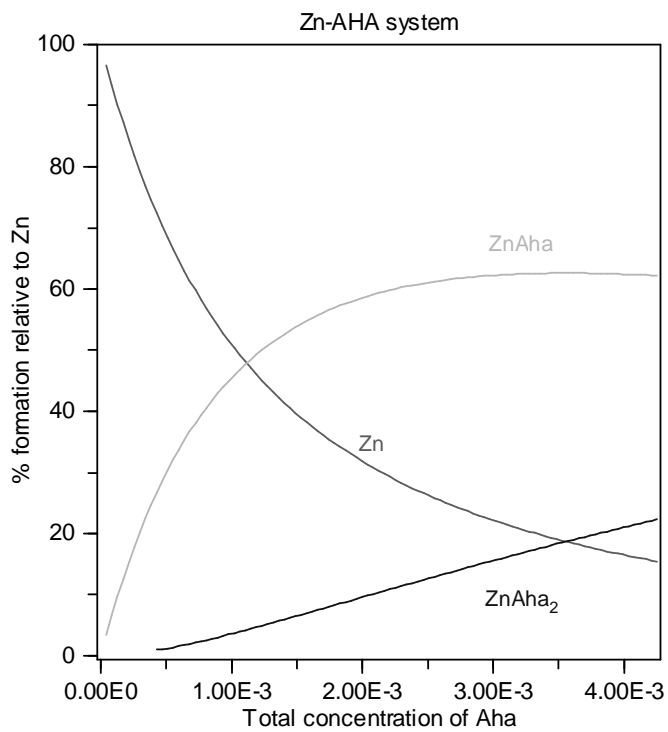


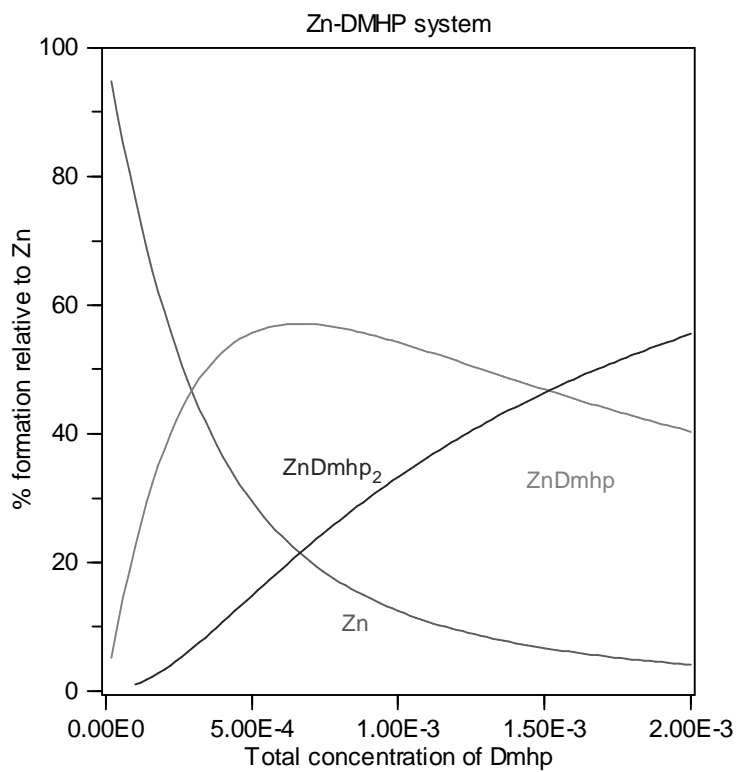
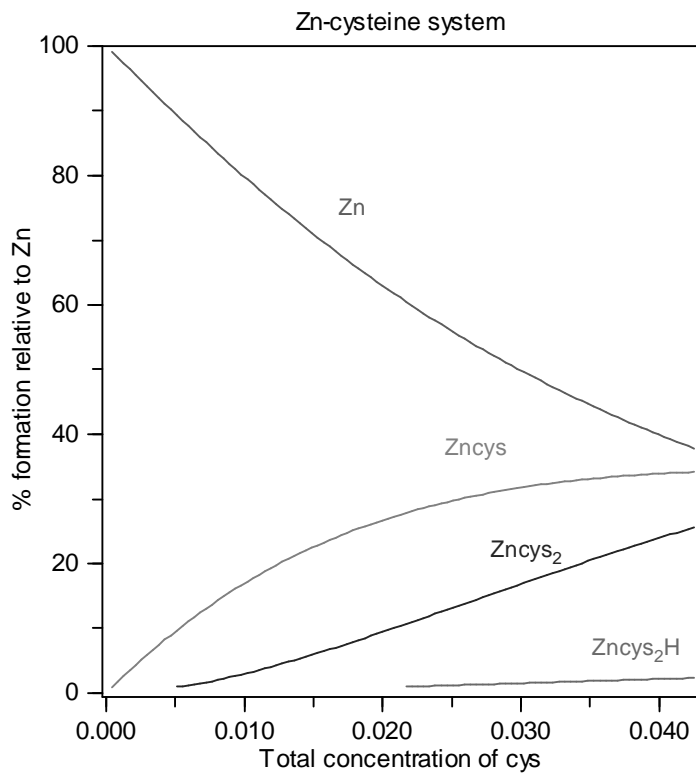


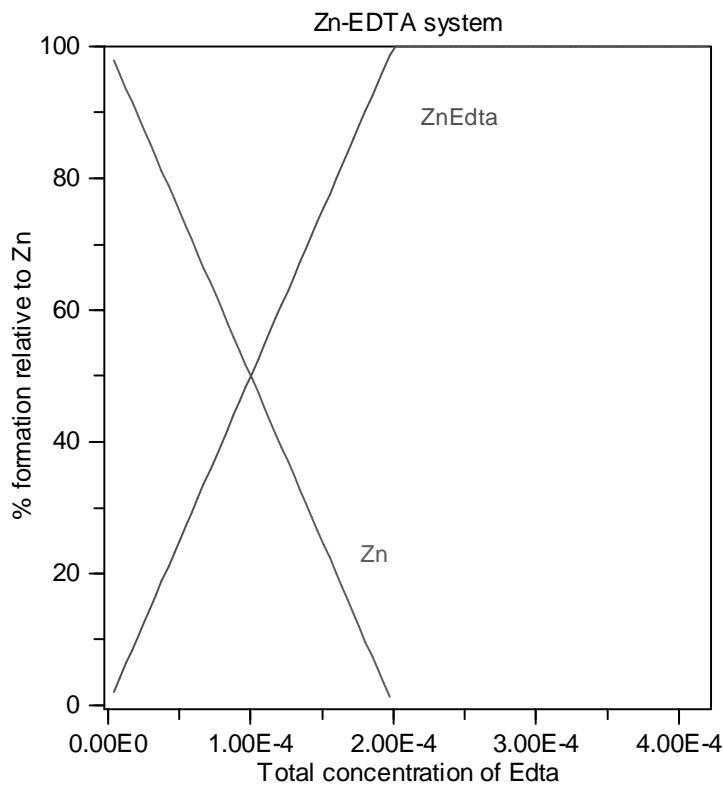
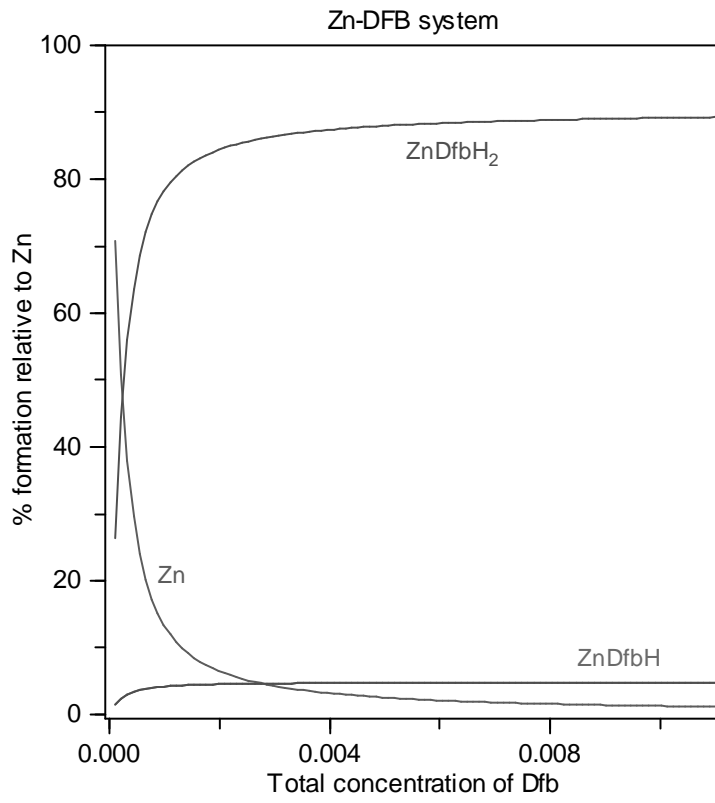


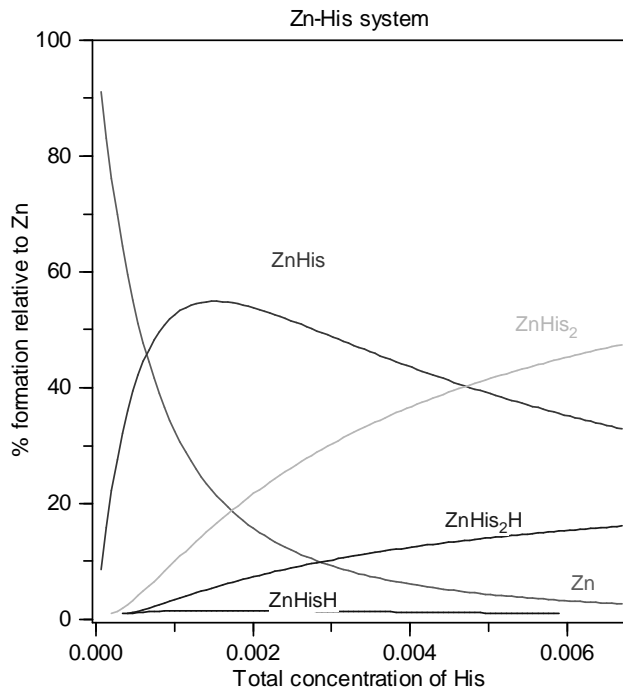


pH 6.5, 200 μM Zn^{2+}

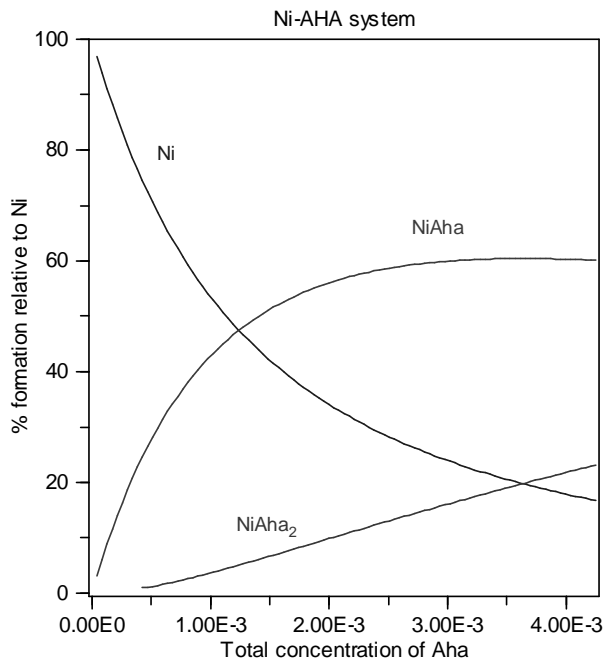


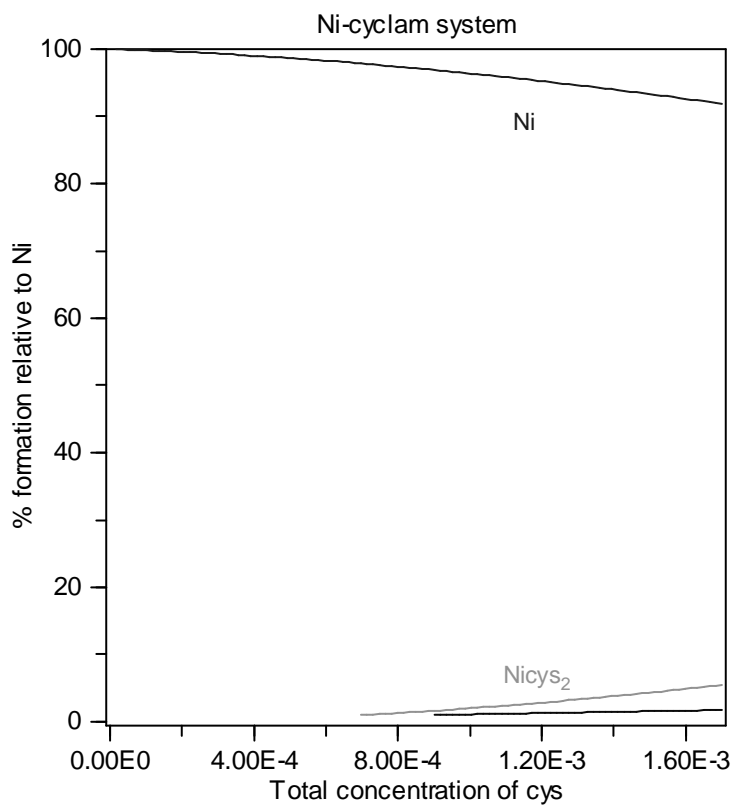
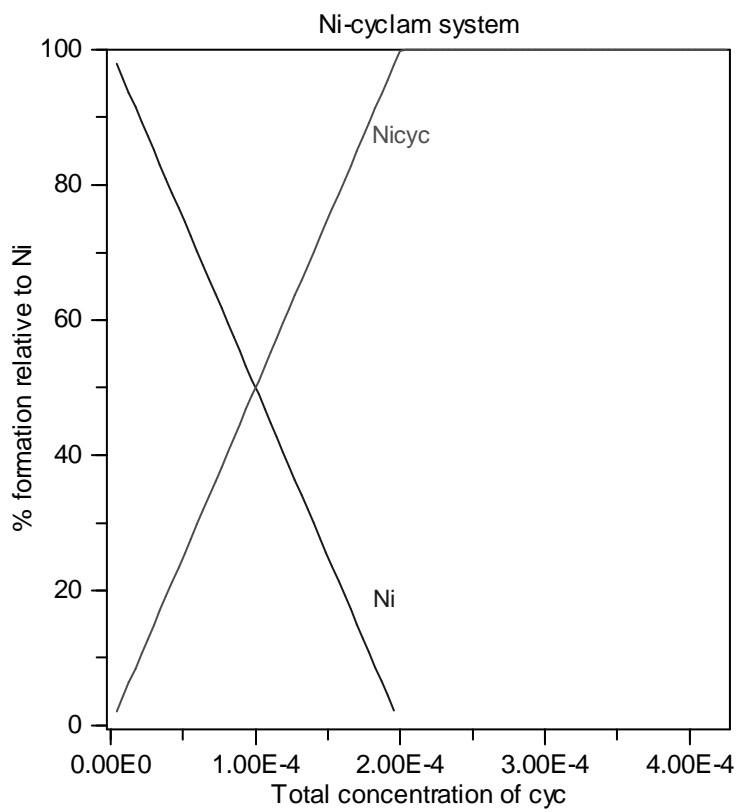


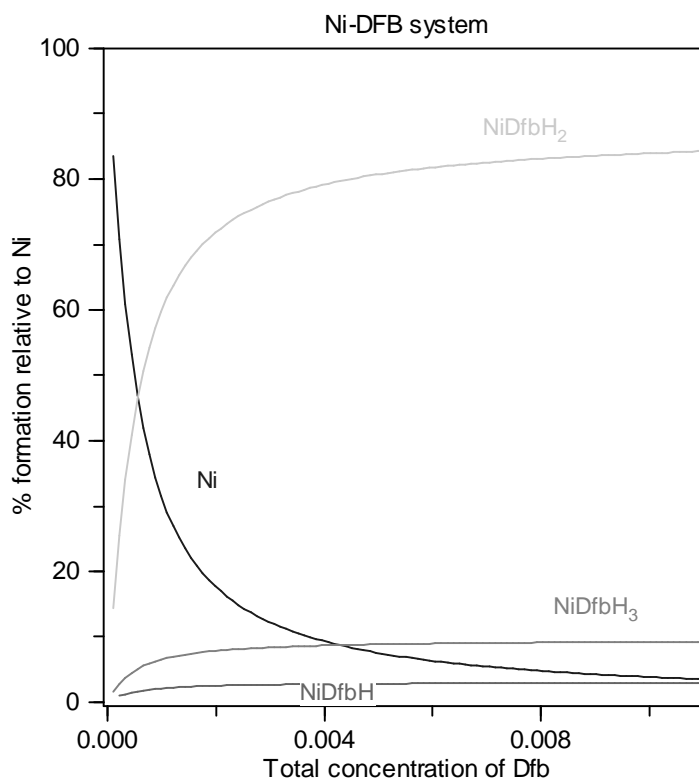
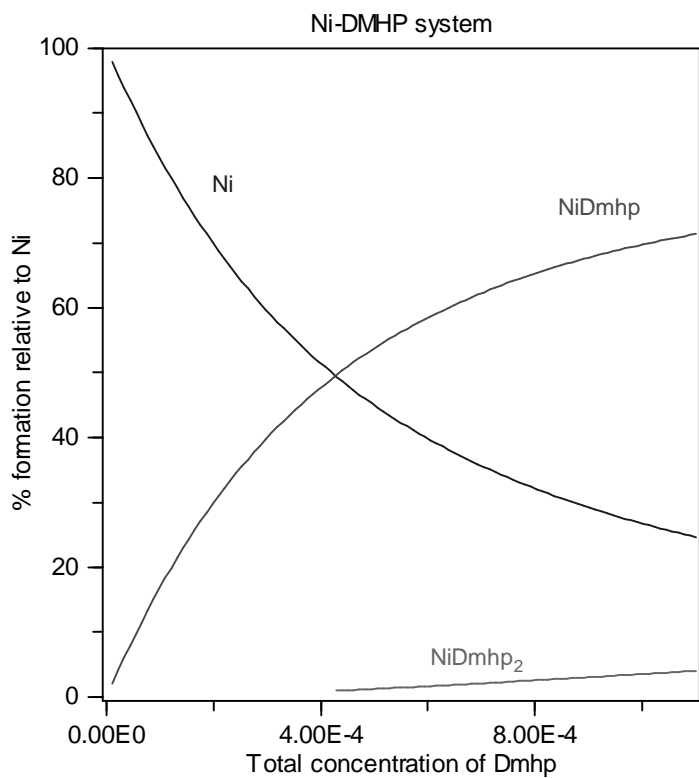


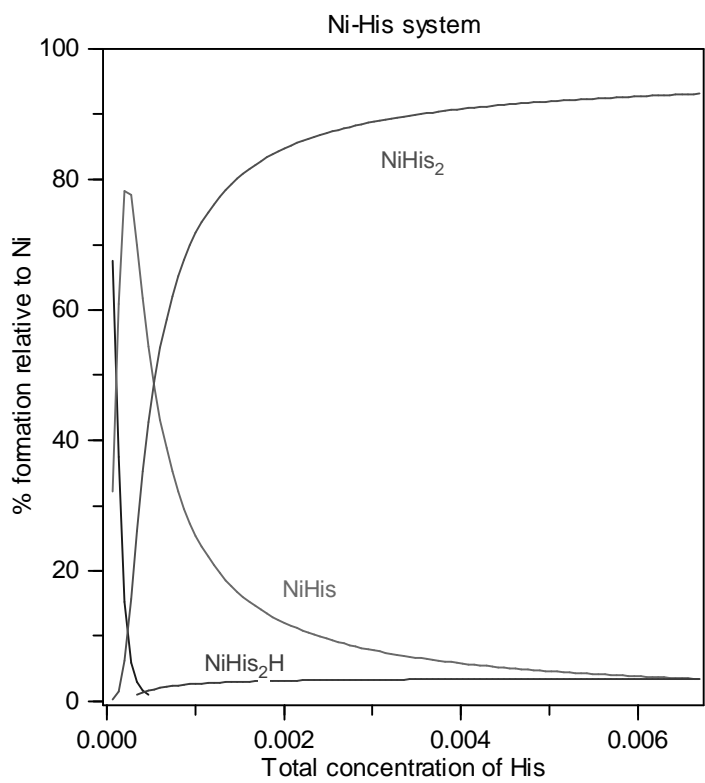
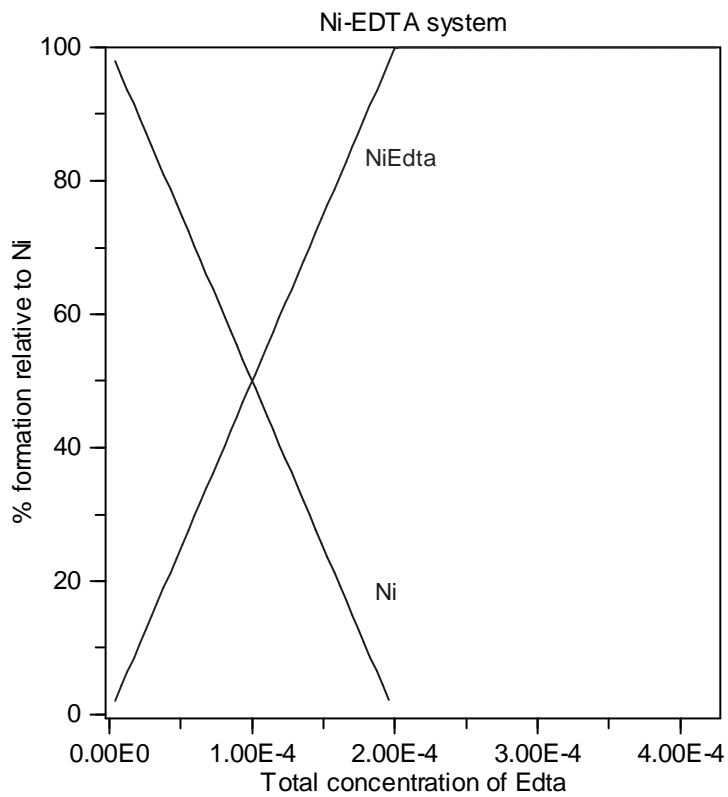


pH 6.5, 200 $\mu\text{M Ni}^{2+}$









References

1. A. L. Crumbliss, J. M. Harrington, in *Adv. Inorg. Chem.* (2009), vol. 64, pp. 179-250.
2. W. F. McDonough, S.-s. Sun, *Chem. Geol.* **120**, 223 (1995).
3. C. J. Baes, R. C. Mesmer, *The Hydrolysis of cations.* (Wiley, New York, 1976).
4. L. E. Hersman, in *Environmental Microbe-Metal Interactions*, D. R. Lovely, Ed. (ASM Press, Washington, D.C., 2000), pp. 145.
5. S. M. Kraemer, *Aquat. Sci.* **66**, 3 (2004).
6. S. Dhungana, C. R. Anthony III, L. E. Hersman, *Appl. Environ. Microbiol.* **73**, 3428 (2007).
7. E. Farkas, E. A. Enyedy, I. Fabian, *Inorg. Chem. Commun.* **6**, 131 (2003).
8. E. Farkas, E. A. Enyedy, L. Zekany, G. Deak, *J. Inorg. Biochem.* **83**, 107 (2001).
9. S. Dhungana, A. L. Crumbliss, *Geomicrobiol. J.* **22**, 87 (2005).
10. S. Dhungana, C. R. Anthony III, L. E. Hersman, *Geochim. Cosmochim. Acta* **71**, 5651 (2007).
11. Z. Hou, K. N. Raymond, B. O'Sullivan, T. W. Esker, T. Nishio, *Inorg. Chem.* **37**, 6630 (1998).
12. I. Spasojević, S. K. Armstrong, T. J. Brickman, A. L. Crumbliss, *Inorg. Chem.* **38**, 449 (1999).
13. R. J. Abergel, J. A. Warner, D. K. Shuh, K. N. Raymond, *J. Am. Chem. Soc.* **128**, 8920 (2006).
14. K. A. Mies, P. Gebhardt, U. Mollmann, A. L. Crumbliss, *J. Inorg. Biochem.* **102**, 850 (2008).
15. M. T. Caudle, R. D. Stevens, A. L. Crumbliss, *Inorg. Chem.* **33**, 6111 (1994).
16. C. J. Carrano, S. R. Cooper, K. N. Raymond, *J. Am. Chem. Soc.* **101**, 599 (1979).
17. Z. Hou, C. J. Sunderland, T. Nishio, K. N. Raymond, *J. Am. Chem. Soc.* **118**, 5148 (1996).
18. A. M. Albrecht-Gary, A. L. Crumbliss, in *Metal Ions in Biological Systems*, A. Sigel, H. Sigel, Eds. (M. Dekker, New York, 1998), pp. 234.
19. A. L. Crumbliss, in *Handbook of Microbial Chelates*, G. Winkelmann, Ed. (CRC Press, Boca Raton, FL, 1991), pp. 177.

20. G. Schwarzenbach, K. Schwarzenbach, *Helv. Chim. Acta.* **46**, 1390 (1963).
21. M. Streator, P. D. Taylor, R. C. Hider, *J. Med. Chem.* **33**, 1749 (1990).
22. R. G. Pearson, *Chemical Hardness*. (Wiley-VCH, Weinheim, Germany, 1997).
23. I. Cukrowski, E. Cukrowska, R. D. Hancock, G. Anderegg, *Anal. Chim. Acta* **312**, 307 (1995).
24. M. Luo, E. A. Fadeev, J. I. Groves, *Nat. Chem. Bio.* **1**, 149 (2005).
25. R. C. Scarrow, D. L. White, K. N. Raymond, *J. Am. Chem. Soc.* **107**, 6540 (1985).
26. J. C. Renshaw *et al.*, *Mycol. Res.* **106**, 1123 (2002).
27. M. T. Caudle, A. L. Crumbliss, *Inorg. Chem.* **33**, 4077 (1994).
28. B. Monzyk, A. L. Crumbliss, *J. Am. Chem. Soc.* **101**, 6203 (1979).
29. S. M. Kraemer, A. Butler, P. Borer, J. Cervini-Silva, *Rev. in Mineralo. Geochem.* **59**, 53 (2005).
30. K. Barbeau, E. L. Rue, K. W. Bruland, A. Butler, *Nature* **413**, 409 (2001).
31. K. Barbeau, E. L. Rue, C. G. Trick, K. W. Bruland, A. Butler, *Limnol. Oceanogr.* **48**, 1069 (2003).
32. W. R. Harris, C. J. Carrano, K. N. Raymond, *J. Am. Chem. Soc.* **101**, 2722 (1979).
33. M. Valdebenito, A. L. Crumbliss, G. Winkelmann, K. Hantke, *Int. J. Med. Microbiol.* **296**, 513 (2006).
34. J. M. Harrington, A. L. Crumbliss, *Biometals* **22**, 679 (2009).
35. H. Boukhalfa, A. L. Crumbliss, *Biometals* **15**, 325 (2002).
36. H. Boukhalfa, A. L. Crumbliss, *Biometals* **15**, 325 (2002).
37. S. Dhungana, S. Heggemann, P. Gebhardt, U. Möllmann, A. L. Crumbliss, *Inorg. Chem.* **42**, 42 (2003).
38. S. Dhungana, M. J. Miller, L. Dong, C. Ratledge, A. L. Crumbliss, *J. Am. Chem. Soc.* **125**, 7654 (2003).
39. S. Dhungana, J. M. Harrington, P. Gebhardt, U. Möllmann, A. L. Crumbliss, *Inorg. Chem.* **46**, 8362 (2007).
40. S. R. Cooper, J. V. McArdle, K. N. Raymond, *Proc. Nat. Acad. Sci. USA* **75**, 3551 (1978).

41. R. Helman, G. D. Lawrence, *Biochem. Bioenerg.* **22**, 187 (1989).
42. A. El-Jammal, D. M. Templeton, *Inorg. Chim. Acta* **245**, 199 (1996).
43. S. Dhungana, M. J. Miller, L. Dong, C. Ratledge, A. L. Crumbliss, *J. Am. Chem. Soc.* **125**, 7654 (2003).
44. K. A. Mies, J. I. Wirgau, A. L. Crumbliss, *Biometals* **19**, 115 (2006).
45. G. Weber, N. von Wiren, H. Hayen, *Biometals* **21**, 503 (2008).
46. C. Klumpp, A. Burger, M. L. Mislin, M. A. Abdallah, *Bioorg. Med. Chem. Lett.* **15**, 1721 (2005).
47. D. Cobessi, H. Celia, F. Pattus, *J. Mol. Biol.* **352**, 893 (2005).
48. E. G. Olmstead, S. W. Harman, P. L. Choo, A. L. Crumbliss, *Inorg. Chem.* **40**, 5420 (2001).
49. H. J. H. Fenton, *J. Chem. Soc., Trans.* **65**, 899 (1894).
50. E. Barchini, R. E. Cowart, *Arch. Microbiol.* **166**, 51 (1996).
51. K. T. Greenwood, R. K. J. Luke, *Biochem. Biophys. Acta* **525**, 209 (1978).
52. J. L. Pierre, M. Fontecave, R. R. Crichton, *Biometals* **15**, 341 (2002).
53. K. N. Raymond, E. A. Dertz, in *Iron Transport in Bacteria*, J. H. Crosa, A. R. Rey, S. M. Payne, Eds. (ASM Press, Washington, D.C., 2004), pp. 3.
54. D. T. Richens, *Chem. Rev.* **105**, 1961 (2005).
55. R. G. Wilkins, *Kinetics and Mechanism of Reactions of Transition Metal Complexes*. (VCH, Weinheim, Germany, ed. 2, 1991).
56. Y. Deugnier, B. Turlin, *World J. Gastroenterol.* **13**, 4755 (2007).
57. J. B. Porter, *Am. J. Haematol.* **82**, 1136 (2007).
58. C. Borgna-Pignatti *et al.*, *Haematologica* **89**, 1187 (2004).
59. P. V. Bernhardt, *Dalton Trans.*, 3214 (2007).
60. G. Faa, G. Crisponi, *Coord. Chem. Rev.* **184**, 291 (1999).
61. A. J. Jacobs, in *Development of Iron Chelators for Clinical Use*, A. E. Martell, W. F. Anderson, D. B. Badman, Eds. (Elsevier, North Holland, 1981), pp. 29.
62. E. Vichinsky, *Am. J. Haematol.* **83**, 398 (2008).

63. R. Galanello, *Ther. Clin. Risk Manag.* **3**, 795 (2007).
64. P. Lee *et al.*, *Drug Met. Disp.* **21**, 640 (1993).
65. G. J. Kontoghiorghes, *Expert Opin Drug Saf* **6**, 235 (2007).
66. N. F. Olivieri *et al.*, *N. Eng. J. Med.* **339**, 417 (1998).
67. S. F. Wu, C. T. Peng, K. H. Wu, C. H. Tsai, *Hemoglobin* **30**, 215 (2006).
68. J. M. Roosenberg II, Y. M. Lin, Y. Lu, M. J. Miller, *Curr. Med. Chem.* **7**, 159 (2000).
69. R. L. Jones, R. W. Gray, *Eur. J. Clin. Microbiol.* **2**, 411 (1983).
70. M. Miethke, M. A. Marahiel, *Microbiol. Mol. Biol. Rev.* **71**, 413 (2007).
71. T. Kline *et al.*, *Bioorg. Med. Chem.* **8**, 73 (2000).
72. J. L. Buss, B. T. Greene, J. Turner, F. M. Torti, S. V. Torti, *Curr. Top. Med. Chem.* **4**, 1623 (2004).
73. A. Gupta, A. L. Crumbliss, *J. Lab. Clin. Med.* **136**, 371 (2000).
74. J. M. Harrington *et al.*, Submitted (2010).
75. R. C. Hider, G. J. Kontoghiorghes, J. Silver. (Brit. UK Pat. Appl., Great Britain, 1984), pp. 17.
76. R. C. Hider, Kontoghiorghes, G.J., Silver, J. and Stockton, M.A. (Brit. UK Pat. Appl., Great Britain, 1984), pp. 19.
77. A. C. Veeck *et al.*, *Solv. Extr. Ion Exch.* **22**, 1037 (2004).
78. G. J. Kontoghiorghes, A. Efstathiou, S. Ioannou-Loucaides, A. Kolnagou, *Hemoglobin* **32**, 217 (2008).
79. Y. Miao *et al.*, *Clin. Cancer Res.* **11**, 5616 (2005).
80. V. C. Pierre, M. Botta, S. Aime, K. N. Raymond, *J. Am. Chem. Soc.* **128**, 5344 (2006).
81. K. N. Raymond, V. C. Pierre, *Bioconjugate Chem.* **16**, 3 (2005).
82. D. E. Reichert, J. S. Lewis, C. J. Anderson, *Coord. Chem. Rev.* **184**, 3 (1999).
83. M. K. Thompson *et al.*, *J. Med. Chem.* **48**, 3874 (2005).
84. E. J. Werner *et al.*, *J. Am. Chem. Soc.* **129**, 1870 (2007).
85. E. J. Werner, A. Datta, C. J. Jocher, K. N. Raymond, *Angew. Chem.* **47**, 8568 (2008).

86. T. N. Lambert, Chittamuru, S., Jacobs, H. K., Gopalan, A. S., *Tetrahedron Letters* **43**, 7379 (2002).
87. B. L. Rai, H. Khodr, R. C. Hider, *Tetrahedron* **55**, 1129 (1999).
88. M. Meyer *et al.*, *J. Am. Chem. Soc.* **119**, 10093 (1997).
89. G. L'Heureux, A. E. Martell, *J. Inorg. Nucl. Chem.* **28**, 481 (1966).
90. A. E. Martell, R. M. Smith, *Critical Stability Constant Database*. (National Institute of Science and Technology (NIST), Gaithersburg, MD, 2003).
91. E. T. Clarke, A. E. Martell, *Inorg. Chim. Acta* **196**, 185 (1992).
92. A. Avdeef, S. R. Sofen, T. L. Bregante, K. N. Raymond, *J. Am. Chem. Soc.* **100**, 5362 (1978).
93. A. I. Vogel, *A Text-Book of Quantitative Inorganic Analysis*. (Longmans, Green, and Co Ltd, London, ed. 3rd, 1961).
94. T. N. Lambert, S. Chittamuru, H. K. Jacobs, A. S. Gopalan, *Tetrahedron Letters* **43**, 7379 (2002).
95. A. E. Martell, R. J. Motekaitis, *Determination and Use of Stability Constants*. (VCH Publishers, New York, ed. 2nd, 1992).
96. P. Gans, B. O'Sullivan, *Talanta* **51**, 33 (2000).
97. E. J. Billo, *EXCEL for Chemists*. (Wiley-VCH, New York, 2001).
98. H. Gampp, M. Maeder, C. J. Meyer, A. D. Zuberbuehler, *Talanta* **32**, 257 (1985).
99. P. Gans, A. Sabatini, A. Vacca, *Talanta* **43**, 1739 (1996).
100. P. Gans, O'Sullivan, B. (VLpH (see: <http://www.hyperquad.co.uk/vlph.htm>), Unpublished).
101. C. Bull, G. J. McClune, J. A. Fee, *J. Am. Chem. Soc.* **105**, 5290 (1983).
102. A. E. Martell, Smith, R.M., *Critical Stability Constant Database*. (National Institute of Science and Technology (NIST), Gaithersburg, MD, 2003).
103. P. T. Kissinger, W. R. Heineman, *Laboratory Techniques in Electroanalytical Chemistry*. A. J. Bard, Ed., (Marcel Dekker, Inc., New York, 1984), pp. 751.
104. F. Khalili, A. Henni, A. L. L. East, *J. Chem. Eng. Data*, doi: 10.1021/je9000005c.
105. R. Luckay, R. D. Hancock, I. Cukrowski, J. H. Reibenspies, *Inorg. Chim. Acta* **246**, 159 (1996).

106. R. C. Scarrow, P. E. Riley, K. Abu-Dari, D. L. White, K. N. Raymond, *Inorg. Chem.* **24**, 954 (1985).
107. G. Ambrosi, Formica, M., Fusi, V., Giorgi, L., Guerri, A, Lucarini, S., Micheloni, M., Paoli, P., Rossi, P, Zappia, G., *Inorg. Chem.* **44**, 3249 (2005).
108. B. Noszal, in *Biocoordination Chemistry: Coordination equilibria in Biologically Active Systems*, K. Burger, Ed. (Ellis Horwood, New York, 1990), pp. 18-55.
109. C. F. G. C. Geraldles, M. C. Alpoim, M. P. M. Marques, A. D. Sherry, M. Singh, *Inorg. Chem.* **24**, 3876 (1985).
110. Y. M. Nesterova, T. N. Polynova, L. I. Martynenko, N. I. Pechurova, *Zhu. Struk. Khim.* **12**, 1110 (1971).
111. Z. D. Liu, R. C. Hider, *Coord. Chem. Rev.* **232**, 151 (2002).
112. Z. D. Liu, H. H. Khodr, L. D.Y., S. L. Lu, R. C. Hider, *J. Med. Chem.* **42**, 4814 (1999).
113. S. Steinhauser *et al.*, *Eur. J. Inorg. Chem.* **2004**, 4177 (2004).
114. R. J. Abergel, K. N. Raymond, *Inorg. Chem.* **45**, 3622 (2006).
115. W. R. Harris, C. J. Carrano, K. N. Raymond, *J. Am. Chem. Soc.* **101**, 2722 (1979).
116. I. De Dominicco, D. M. Ward, J. Kaplan, *Nat. Rev. Mol. Cell Biol.* **9**, 72 (2008).
117. C. M. Craven *et al.*, *Proc. Nat. Acad. Sci. USA* **84**, 3457 (1987).
118. I. Turcot, A. Stintzi, J. Xu, K. N. Raymond, *J. Biol. Inorg. Chem.* **5**, 634 (2000).
119. A. Katoh, H. Kudo, R. Saito, *Heterocycles* **66**, 285 (2006).
120. H. Boukhalfa, A. L. Crumbliss, *Inorg. Chem.* **40**, 4183 (2001).
121. E. M. Tristani, G. R. Dubay, A. L. Crumbliss, *J. Incl. Phenom.* **64**, 57 (2009).
122. G. Serratrice, F. Biaso, J.-L. Pierre, S. Blanc, A.-M. Albrecht-Gary, *Eur. J. Inorg. Chem.* **2007**, 3681 (2007).
123. H. Boukhalfa, A. L. Crumbliss, *Inorg Chem* **39**, 4318 (2000).
124. I. Spasojević, H. Boukhalfa, R. D. Stevens, A. L. Crumbliss, *Inorg. Chem.* **40**, 49 (2001).
125. H. Boukhalfa, T. J. Brickman, S. K. Armstrong, A. L. Crumbliss, *Inorg. Chem.* **39**, 5591 (2000).
126. B. Monzyk, A. L. Crumbliss, *J. Inorg. Biochem.* **19**, 19 (1983).

127. R. J. Motekaitis, A. E. Martell, *Inorg. Chim. Acta* **183**, 71 (1991).
128. T. P. Tufano, K. N. Raymond, *J. Am. Chem. Soc.* **103**, 6617 (1981).
129. L. Helm, A. E. Merbach, *Chem. Rev.* **105**, 1923 (2005).
130. R. C. Scarrow, Riley, P. E., Abu-Dari, K., White, D. L., Raymond, K. N., *Inorg. Chem.* **24**, 954 (1985).
131. L. Alderighi *et al.*, *Coord. Chem. Rev.* **184**, 311 (1999).
132. M. Tsuda *et al.*, *J. Nat. Prod.* **68**, 462 (2005).
133. I. Sliskovic, B. Mutus, *FEBS Lett* **580**, 2233 (2006).
134. Y. Ikeda, H. Nonaka, T. Furumai, H. Onaka, Y. Igarashi, *J. Nat. Prod.* **68**, 1061 (2005).
135. K. Schneider *et al.*, *J. Nat. Prod.* **70**, 932 (2007).
136. K. A. Fennell, U. Mollmann, M. J. Miller, *J. Org. Chem.* **73**, 1018 (2008).
137. J. M. Roosenberg II., Y. M. Lin, Y. Lu, M. J. Miller, *Curr. Med. Chem.* **7**, 159 (2000).
138. C. Ratledge, *Tuberculosis* **84**, 110 (2004).
139. G. A. Snow, *Bacteriol. Rev.* **34**, 99 (1970).
140. H. J. MacCordick, J. J. Schleiffer, G. Duplatre, *Radiochim. Acta* **38**, 43 (1985).
141. Y. Ying, J. Hong, *Tetrahed. Lett.* **48**, 8104 (2007).
142. J. M. Harrington, H. Park, Y. Ying, J. Hong, A. L. Crumbliss, manuscript in preparation (2010).
143. P. Gans, Sabatini, A., and Vacca, A., *Talanta* **43**, 1739 (1996).
144. M. K. Nguyen-van-Duong *et al.*, *Inorg. Chem.* **40**, 5948 (2001).
145. S. Yamamoto, N. Okujo, T. Yoshida, S. Matsuura, S. Shinoda, *J. Biochem.* **115**, 868 (1994).
146. S. Dhungana, M. J. Miller, L. Dong, C. Ratledge, A. L. Crumbliss, *J. Am. Chem. Soc.* **125**, 7654 (2003).
147. R. Kikkeri *et al.*, *Inorg. Chem.* **46**, 2485 (2007).
148. J. J. De Voss, K. Rutter, B. G. Schroeder, C. E. Barry III, *J. Bacteriol.* **181**, 4443 (1999).

149. J. J. De Voss, K. Rutter, B. G. Schroeder, C. E. Barry, *J. Bacteriol.* **181**, 4443 (1999).
150. K. A. Mies, P. Gebhardt, U. Mollmann, A. L. Crumbliss, *J. Inorg. Biochem.* **102**, 850 (2008).
151. F. C. Küpper, C. J. Carrano, J. U. Kuhn, A. Butler, *Inorg. Chem.* **45**, 6028 (2006).
152. S. Dhungana, C. Ratledge, A. L. Crumbliss, *Inorg. Chem.* **43**, 6274 (2004).
153. C. M. Ryan, E. Kariv-Miller, *Tetrahedron* **44**, 6807 (1988).
154. C. J. Carrano, M. Jordan, H. Dreschel, D. G. Schmid, G. Winkelmann, *Biometals* **14**, 119 (2001).
155. K. Harada *et al.*, *J. Antibiot.* **57**, 125 (2004).
156. D. A. Skoog, F. J. Holler, T. A. Nieman, *Principles of Instrumental Analysis*. (Thomson Learning, Toronto, Ontario, ed. 5, 1998), pp. 957.
157. D. J. Tipper, in *B-lactam Antibiotics for Clinical Use*, S. F. Queener, J. A. Webber, S. W. Queener, Eds. (Marcel Dekker, Inc., New York, 1986), pp. 17-48.
158. D. E. Sentochnik, G. M. Eliopoulos, M. J. Ferraro, J. Moellering, R.C., *Antimicrob. Agents Chemother.* **33**, 1232 (1989).
159. J. R. Edwards *et al.*, *Antimicrob. Agents Chemother.* **33**, 215 (1989).
160. K. V. I. Rolston, G. P. Bodey, *Cancer Investigation* **10**, 43 (1992).
161. G. E. Zurenko, S. E. Truesdell, B. H. Yagi, R. J. Mourey, A. L. Laborde, *Antimicrob. Agents Chemother.* **34**, 884 (1990).
162. J. M. Andrews, *J. Antimicrob. Chemother.* **48**, 5 (2001).
163. M. R. Barbachyn, T. C. Tuominen, *J. Antibiot.* **43**, 1199 (1990).
164. D. S. Williamson, D. L. Nagel, R. S. Markin, S. M. Cohen, *Fd Chem. Toxic.* **25**, 211 (1987).
165. R. J. Motekaitis, A. E. Martell, *Inorg. Chim. Acta* **183**, 71 (1991).
166. E. T. Clarke, A. E. Martell, *Inorg. Chim. Acta* **196**, 185 (1992).
167. N. A. El-Maali, *Bioelectrochem. Bioenerg.* **45**, 281 (1998).
168. Z. D. Liu, R. C. Hider, *Coord. Chem. Rev.* **2002**, 151 (2002).
169. D. R. Richardson, *Critical Reviews in Oncology/Hematology* **42**, 267 (2002).
170. S. Dhungana *et al.*, *Inorg Chem* **40**, 7079 (2001).

171. C. Y. Ng, S. J. Rodgers, K. N. Raymond, *Inorg. Chem.* **28**, 2062 (1989).
172. S. Dhungana, Harrington, J.M., Gebhardt, P., Mollmann, U., Crumbliss, A.L., *Inorg Chem* **46**, 8362 (2007).
173. S. Dhungana, Heggemann, S., Gebhardt, P., Mollmann, U., Crumbliss, A.L., *Inorg Chem* **42**, 42 (2003).
174. I. Wavefunction. (18401 Von Karman Ave, Suite 370, Irvine, CA 92612 USA).
175. S. Dhungana, P. S. White, A. L. Crumbliss, *J. Biol. Inorg. Chem* **6**, 810 (2001).
176. M. B. Hossain, M. A. F. Jalal, D. van der Helm, *Acta Crystallogr. Sect. C.* **42**, 1305 (1986).
177. D. van der Helm, M. Poling, *J. Am. Chem. Soc.* **98**, 82 (1976).
178. F. H. Allen, *Acta. Cryst. B* **58**, 380 (2002).
179. S. Konetschny-Rapp, G. Jung, K. N. Raymond, K. N. Miewes, H. Zahner, *J. Am. Chem. Soc.* **114**, 2224 (1992).
180. J. J. R. Frausto da Silva, R. J. P. Williams, *The Biological Chemistry of the Elements.* (Oxford University Press, New York, 2001).
181. R. S. Waters, N. A. Bryden, K. Y. Patterson, C. Veillon, R. A. Anderson, *Biological Trace Element Research* **83**, 207 (2001).
182. M. J. Brown, T. Willis, B. Omalu, R. Leiker, *Pediatrics* **118**, 534 (2006).
183. M. Mitka, *J. Am. Med. Assoc.* **300**, 2236 (2008).
184. T. C. elegans sequencing consortium, *Science* **282**, 2012 (1998).
185. *C elegans II.* D. L. Riddle, T. Blumenthal, B. J. Meyer, J. R. Priess, Eds., (Cold Spring Harbor Laboratory Press, Plainview, N.Y., 1997).
186. S. Brenner, *Genetics* **77**, 71 (1974).
187. J. H. Freedman, L. W. Slice, D. Dixon, A. Fire, C. S. Rubin, *J. Biol. Chem.* **268**, 2554 (1993).
188. A. M. Giglio, T. Hunter, J. V. Bannister, W. H. Bannister, G. Hunter, *Biochem. Mol. Biol. Int.* **33**, 41 (1994).
189. M. F. Heschl, D. L. Baillie, *Comp. Biochem. Physiol. B* **96**, 633 (1990).
190. E. G. Stringham, D. Jones, E. P. Candido, *Gene* **113**, 165 (1992).
191. K. Weston, J. Yochem, I. Greenwald, *Nucleic Acids Res.* **17**, 2138 (1989).

192. M. Wolf, F. Nunes, A. Henkel, A. Heinek, R. J. Paul, *J. Cell. Physiol.* **214**, 721 (2008).
193. W. A. Boyd, M. V. Smith, G. E. Kissling, J. H. Freedman, *Neurotox. Teratol.* **32**, 68 (2009).
194. D. H. Hall, Z. F. Altun, *C. elegans Atlas*. (Cold Spring Harbor Laboratory Press, Cold Spring Harbor, N.Y., 2008).
195. W. B. Wood, in *The Nematode Caenorhabditis elegans*, W. B. Wood, Ed. (Cold Spring Harbor Laboratory Press, Cold Spring Harbor, N.Y., 1988), pp. 1-16.
196. W. A. Boyd, M. V. Smith, G. E. Kissling, J. H. Freedman, *Neurotoxicol. Teratol.*, doi: 10.1016/j.ntt.2008.12.004 (2009).
197. M. V. Smith *et al.*, *PLoS ONE* **4**, e7018. doi: 10.1371/journal.pone.0007018 (2009).
198. W. A. Boyd *et al.*, *Plos One* **4**, e7204. doi: 10.1371/journal.pone.0007024 (2009).
199. T. Chen *et al.*, *Inorg. Chem.* **48**, 5801 (2009).
200. P. L. Williams, D. B. Dusenbery, *Toxicol. Ind. Health* **4**, 469 (1988).
201. N. Khanna, C. P. Cressman III, C. P. Tataara, P. L. Williams, *Arch. Environ. Contam. Toxicol.* **32**, 110 (1997).
202. R. Pulak, *Methods Mol. Biol.* **351**, 275 (2006).
203. W. A. Boyd *et al.*, *manuscript in preparation*, (2009).
204. K. J. Powell. (Academic Software, Timble, Otley, Yorks, UK).
205. E. G. Gerwe, *Science* **76**, 100 (1932).
206. T. Hussain, G. S. Shukla, S. V. Chandra, *Pharmacol. Toxicol.* **60**, 355 (1987).
207. H. Fujishiro, T. Sakurai, S. Himeno, *Biomed. Res. Trace Elem.* **17**, 349 (2006).
208. M. V. Cherrier *et al.*, *J. Am. Chem. Soc.* **127**, 10075 (2005).
209. D. A. Pearce, F. Sherman, *J. Bacteriol.* **181**, 4774 (1999).
210. G. J. Sarkis, M. R. Kurpiewski, J. D. Ashcom, L. Jen-Jacobson, L. A. Jacobson, *Arch. Biochem. Biophys.* **261**, 80 (1988).
211. T. N. Lambert, L. Dasaradhi, V. J. Huber, A. S. Gopalan, *J. Org. Chem.* **64**, 6097 (1999).

Biography of the author

James Michael Harrington was born on September 25th, 1982 in Greensboro, North Carolina. He lived his entire life in the same city, graduating from Southeast Guilford High School in 2000. He completed his Bachelor's Degree with Departmental Honors in Chemistry at the University of North Carolina at Wilmington in December 2004 working in the laboratory of Dr. Robert D. Hancock, studying transition metal complexes, specifically cadmium and indium complex stability constants. His undergraduate thesis was titled "The Possible Role of Relativistic Effects in the Formation of Cadmium Complexes with Crown Ethers."

Since then, he has performed research under the guidance of Alvin L. Crumbliss on the topic of siderophore-mediated iron uptake systems in bacteria and fungi. He has given numerous research presentations at academic conferences including the National Meetings of the American Chemical Society in Boston (2007) and Washington (2009) and has currently published 8 peer-reviewed articles including 2 review articles on the topic of siderophore chemistry and the redox chemistry of iron-siderophore complexes. He is currently performing research as a postdoctoral researcher at North Carolina State University under the guidance of Owen Duckworth on the topic of siderophore-mediated geochemical cycling of metals besides iron.